

MONITORING AND MODELING TERRESTRIAL ECOSYSTEMS' RESPONSE TO CLIMATE CHANGE

GUEST EDITORS: DONG JIANG, SHENGLI HUANG, AND DAWEI HAN





Monitoring and Modeling Terrestrial Ecosystems' Response to Climate Change

Advances in Meteorology

Monitoring and Modeling Terrestrial Ecosystems' Response to Climate Change

Guest Editors: Dong Jiang, Shengli Huang, and Dawei Han



Copyright © 2014 Hindawi Publishing Corporation. All rights reserved.

This is a special issue published in “Advances in Meteorology.” All articles are open access articles distributed under the Creative Commons Attribution License, which permits unrestricted use, distribution, and reproduction in any medium, provided the original work is properly cited.

Editorial Board

Paulo Artaxo, Brazil
Guy Brasseur, USA
M. Ćurić, Serbia
Raymond Desjardins, Canada
Klaus Dethloff, Germany
P. S. Devara, India
Julio Diaz, Spain
Shouting Gao, China
Luis Gimeno, Spain

Sven-Erik Gryning, Denmark
Ismail Gultepe, Canada
H. Hashiguchi, Japan
D. Hauglustaine, France
Ivar S A Isaksen, Norway
Yasunobu Iwasaka, Japan
Hann-Ming H. Juang, USA
George Kallos, Greece
Harry D. Kambezidis, Greece

Richard Leitch, Canada
M. Leclerc, USA
Gwo-Fong Lin, Taiwan
Edward Llewellyn, Canada
Kyaw T. Paw, USA
Sara C. Pryor, USA
Eugene Rozanov, Switzerland
Zhihua Zhang, China

Contents

Monitoring and Modeling Terrestrial Ecosystems' Response to Climate Change, Dong Jiang, Shengli Huang, and Dawei Han
Volume 2014, Article ID 429349, 2 pages

An Integrated Model for Simulating Regional Water Resources Based on Total Evapotranspiration Control Approach, Jianhua Wang, Xuefeng Sang, Zhengli Zhai, Yang Liu, and Zuhao Zhou
Volume 2014, Article ID 345671, 10 pages

Spatial and Temporal Characteristics of Meteorological Drought in Shandong Province, China, from 1961 to 2008, Xiaoli Wang, Xiyong Hou, Zhi Li, and Yuandong Wang
Volume 2014, Article ID 873593, 11 pages

The Review of GRACE Data Applications in Terrestrial Hydrology Monitoring, Dong Jiang, Jianhua Wang, Yaohuan Huang, Kang Zhou, Xiangyi Ding, and Jingying Fu
Volume 2014, Article ID 725131, 9 pages

Forest Phenology Dynamics and Its Responses to Meteorological Variations in Northeast China, Xinfang Yu, Qiankun Wang, Huimin Yan, Yong Wang, Kege Wen, Dafang Zhuang, and Qiao Wang
Volume 2014, Article ID 592106, 12 pages

The Impact of Urbanization on the Annual Average Temperature of the Past 60 Years in Beijing, Yong Wang, Wei Ji, Xinfang Yu, Xinliang Xu, Dong Jiang, Zhangang Wang, and Dafang Zhuang
Volume 2014, Article ID 374987, 9 pages

A System Dynamics Approach to Modeling Future Climate Scenarios: Quantifying and Projecting Patterns of Evapotranspiration and Precipitation in the Salton Sea Watershed, Michael E. Kjelland, Todd M. Swannack, and William E. Grant
Volume 2014, Article ID 135012, 15 pages

Improving Carbon Mitigation Potential through Grassland Ecosystem Restoration under Climatic Change in Northeastern Tibetan Plateau, Lin Huang, Xinliang Xu, Quanqin Shao, and Jiyuan Liu
Volume 2014, Article ID 379306, 11 pages

Modeling and Monitoring Terrestrial Primary Production in a Changing Global Environment: Toward a Multiscale Synthesis of Observation and Simulation, Shufen Pan, Hanqin Tian, Shree R. S. Dangal, Zhiyun Ouyang, Bo Tao, Wei Ren, Chaoqun Lu, and Steven Running
Volume 2014, Article ID 965936, 17 pages

Comparison of Satellite and Ground-Based Phenology in China's Temperate Monsoon Area, Huanjiong Wang, Junhu Dai, and Quansheng Ge
Volume 2014, Article ID 474876, 10 pages

Integrated Monitoring and Assessment Framework of Regional Ecosystem under the Global Climate Change Background, Qiao Wang, Peng Hou, Feng Zhang, and Changzuo Wang
Volume 2014, Article ID 896453, 8 pages

Monitoring Grassland Tourist Season of Inner Mongolia, China Using Remote Sensing Data,
Quansheng Ge, Xi Yang, Zhi Qiao, Haolong Liu, and Jun Liu
Volume 2014, Article ID 859765, 5 pages

Characteristics of Spring Phenological Changes in China over the Past 50 Years, Junhu Dai,
Huanjiong Wang, and Quansheng Ge
Volume 2014, Article ID 843568, 8 pages

Influences of Urban Expansion on Urban Heat Island in Beijing during 1989–2010, Zhi Qiao,
Guangjin Tian, Lixiao Zhang, and Xinliang Xu
Volume 2014, Article ID 187169, 11 pages

Trends in Moisture Index, Farmland Area, and Their Combined Effects on Grain Production in Northern China, Qingshui Lu, Zhiqiang Gao, Xinliang Xu, Jicai Ning, and Xiaoli Bi
Volume 2014, Article ID 606787, 9 pages

Evaluating the Marginal Land Resources Suitable for Developing Bioenergy in Asia, Jingying Fu,
Dong Jiang, Yaohuan Huang, Dafang Zhuang, and Wei Ji
Volume 2014, Article ID 238945, 9 pages

Changes in Production Potential in China in Response to Climate Change from 1960 to 2010, Luo Liu,
Xi Chen, Xinliang Xu, Yong Wang, Shuang Li, and Ying Fu
Volume 2014, Article ID 640320, 10 pages

NDVI-Based Vegetation Change in Inner Mongolia from 1982 to 2006 and Its Relationship to Climate at the Biome Scale, Linghui Guo, Shaohong Wu, Dongsheng Zhao, Yunhe Yin, Guoyong Leng, and Qingyu Zhang
Volume 2014, Article ID 692068, 12 pages

Spatially Explicit Assessment of Ecosystem Resilience: An Approach to Adapt to Climate Changes,
Haiming Yan, Jinyan Zhan, Bing Liu, Wei Huang, and Zhihui Li
Volume 2014, Article ID 798428, 9 pages

Editorial

Monitoring and Modeling Terrestrial Ecosystems' Response to Climate Change

Dong Jiang,¹ Shengli Huang,² and Dawei Han³

¹ Key Laboratory of Resources Utilization and Environmental Remediation, Institute of Geographical Sciences and Natural Resources Research, Chinese Academy of Sciences, Beijing 100101, China

² USGS EROS, Sioux Falls, SD 57198, USA

³ Department of Civil Engineering, University of Bristol, Bristol BS81TR, UK

Correspondence should be addressed to Dong Jiang; jiangd@igsnr.ac.cn

Received 21 July 2014; Accepted 21 July 2014; Published 5 August 2014

Copyright © 2014 Dong Jiang et al. This is an open access article distributed under the Creative Commons Attribution License, which permits unrestricted use, distribution, and reproduction in any medium, provided the original work is properly cited.

Global average land and sea surface temperatures have increased since 1850, which is likely due to the observed increase in anthropogenic greenhouse gas concentrations [1] and other possible influences include solar, volcanic, and greenhouse gas factors and natural variability that is internal to the climate system [1, 2]. There is ample evidence of the ecological impacts of recent climate change, from polar terrestrial to tropical marine environments [2]. These observed ecological changes are heavily biased in the directions predicted from global warming and have been linked to local or regional climate change through correlations between climate and biological variation, field and laboratory experiments, and physiological research [3]. Monitoring spatiotemporal dynamics of ecosystems response to climate change have drawn much attention in recent years [4].

This special issue consists of 18 articles and the topics include terrestrial water cycle, ecological changes in the phenology, ecosystem production, and ecosystem health monitoring.

Global change has led to the changes in the terrestrial hydrology. Four papers in this special issue focus on the spatial and temporal changes of the distribution and total amount of water resources. J. Wang et al. developed a water allocation and simulation (WAS) model for simulating the water cycle and output different evapotranspiration (ET) values for natural and artificial water use. The model was applied in Tianjin City of China, and the results demonstrate that ET of irrigation lands is a priority in ET control for water management. M. E. Kjelland et al. developed a Salton Sea Stochastic Simulation Model (S4M) with a higher degree of climate

forecasting resolution. The model could be used to assist planners and residents of the Salton Sea (SS) transboundary watershed (USA and Mexico) in making sound policy decisions regarding complex water-related issues. X. Wang et al. evaluated the spatiotemporal characteristics of meteorological drought in Shandong Province of China from 1961 to 2008 by using the meteorological drought composite index (CI). D. Jiang et al. present a review of recent applications of the Gravity Recovery and Climate Experiment (GRACE) satellite data in terrestrial hydrology monitoring. It was found that GRACE data could be used for improving the monitoring result of the spatial and temporal changes of water cycle at large scale quickly.

Climate change has resulted in a significant effect on vegetation dynamics during the past decades. Lots of existing literatures have investigated seasonal variations in vegetation and their responses to climate changes, with both *in situ* and satellite observations. Q. Ge et al. presented a valid methodology for detecting the grassland tourist season. The beginning, the best, and the end of grassland tourist season of Inner Mongolia could be determined with remote sensing data. X. Yu et al. used time series of Moderate Resolution Imaging Spectroradiometer (MODIS) Enhanced Vegetation Index (EVI) data (2000–2009) to evaluate forest phenology dynamics and its responses to climate changes in the cool-temperate needle leaf forest region. J. Dai et al. provided the characteristics of spring phenological changes in China over the past 50 years based on observation data at 33 sites from the Chinese Phenological Observation Network (CPON). L. Guo et al. analyzed vegetation change of the six major

biomes across Inner Mongolia at the growing season and the monthly timescales and estimated their responses to climate change between 1982 and 2006. H. Wang et al. compared satellite and ground-based phenology in China's temperate monsoon area. Five methods to estimate start of season (SOS) from the Advanced Very High Resolution Radiometer (AVHRR)/normalized difference vegetation index (NDVI) dataset were employed and evaluated. The results show that the variability of SOS time series is significantly different from ground phenology except for HANTS, Polyfit, and Midpoint methods.

Terrestrial net primary production (NPP) is a key component of energy and mass transformation in terrestrial ecosystems and also the key indicator of ecosystem functioning. In this special issue, four articles provided major approaches to monitoring and predicting terrestrial primary production in a changing global environment. S. Pan et al. provided a comprehensive review of three major approaches to monitoring and predicting terrestrial primary production, including ground-based field measurements, satellite-based observations, and process-based ecosystem modeling. The performance of the dynamic land ecosystem model (DLEM) at various scales from site to region to global was presented as case study. J. Fu et al. presented the evaluation of the marginal land resources suitable for developing bioenergy in Asia. A multiple factor analysis method was used to identify marginal land using multiple datasets including remote sensing derived land cover and meteorological data. Productions and biofuel potential were then estimated. Q. Lu et al. analyzed the combined effects of land use and climate change on grain production in northern China during 1988–2008, with the remote sensing derived farmland map, the moisture index (MI) from meteorological data, and unit grain production from statistical yearbooks. L. Liu et al. assessed the changes in production potential in China in response to climate change from 1960 to 2010, with the Global Agro-Ecological Zone (GAEZ) model. It was found that an increase of approximately 1.58 million tons/decade in production potential correlated with climate change.

Routine monitoring of regional ecosystem plays much important role in the research of global change. Q. Wang et al. proposed an integrated framework for monitoring ecosystem at regional scale. H. Yan et al. developed a conceptual model of the ecosystem resilience of forests. The result suggests that there is significant spatial heterogeneity of the ecosystem resilience of forests, indicating that it is feasible to generate large-scale ecosystem resilience maps with this assessment model. L. Huang et al. explored the dynamics of grassland degradation and restoration from 1990 to 2012 in the North-eastern Tibetan Plateau and its relationship with climate mitigation to provide a definite answer as to the forcing and response of grassland degradation and restoration to climate change. Y. Wang et al. presented a study on the impact of urbanization on the annual average temperature of the recent 60 years in Beijing. Meanwhile, Z. Qiao et al. focused on the influences of urban expansion on urban heat island in Beijing during 1989–2010. The results suggested that urban design based on urban form would be effective for regulating the thermal environment.

This special issue aims to summarize the most recent developments and ideas in monitoring and modeling terrestrial ecosystems response to climate change. Contributions presented here will promote the illustration of the relationship between terrestrial ecosystems and global climate change.

Acknowledgments

We would like to thank all the authors and reviewers who contributed to this special issue.

Dong Jiang
Shengli Huang
Dawei Han

References

- [1] IPCC, "Summary for policymakers," in *Climate Change 2013: The Physical Science Basis. Contribution of Working Group I to the Fifth Assessment Report of the Intergovernmental Panel on Climate Change*, T. F. Stocker, D. Qin, G. K. Plattner et al., Eds., pp. 3–29, Cambridge University Press, Cambridge, UK, 2013.
- [2] G. Walther, E. Post, P. Convey et al., "Ecological responses to recent climate change," *Nature*, vol. 416, no. 6879, pp. 389–395, 2002.
- [3] C. Parmesan, "Ecological and evolutionary responses to recent climate change," *Annual Review of Ecology, Evolution, and Systematics*, vol. 37, pp. 637–669, 2006.
- [4] Q. Ge, H. Wang, R. This, and J. Dai, "Phenological response to climate change in China: a meta-analysis," *Global Change Biology*, 2014.

Research Article

An Integrated Model for Simulating Regional Water Resources Based on Total Evapotranspiration Control Approach

Jianhua Wang, Xuefeng Sang, Zhengli Zhai, Yang Liu, and Zuhao Zhou

State Key Laboratory of Simulation and Regulation of Water Cycle in River Basin,
China Institute of Water Resources and Hydropower Research, 100038, China

Correspondence should be addressed to Xuefeng Sang; xuefengsang@gmail.com

Received 29 January 2014; Revised 3 June 2014; Accepted 24 June 2014; Published 14 July 2014

Academic Editor: Dawei Han

Copyright © 2014 Jianhua Wang et al. This is an open access article distributed under the Creative Commons Attribution License, which permits unrestricted use, distribution, and reproduction in any medium, provided the original work is properly cited.

Total evapotranspiration and water consumption (ET) control is considered an efficient method for water management. In this study, we developed a water allocation and simulation (WAS) model, which can simulate the water cycle and output different ET values for natural and artificial water use, such as crop evapotranspiration, grass evapotranspiration, forest evapotranspiration, living water consumption, and industry water consumption. In the calibration and validation periods, a “piece-by-piece” approach was used to evaluate the model from runoff to ET data, including the remote sensing ET data and regional measured ET data, which differ from the data from the traditional hydrology method. We applied the model to Tianjin City, China. The Nash-Sutcliffe efficiency (Ens) of the runoff simulation was 0.82, and its regression coefficient R^2 was 0.92. The Nash-Sutcliffe Efficiency (Ens) of regional total ET simulation was 0.93, and its regression coefficient R^2 was 0.98. These results demonstrate that ET of irrigation lands is the dominant part, which accounts for 53% of the total ET. The latter is also a priority in ET control for water management.

1. Introduction

Water resources are becoming increasingly interconnected with social, economic, environmental, and political issues at national, regional, and even international levels [1]. A hydrological cycle study usually takes into account precipitation, surface runoff, rivers, and groundwater, but it should now also incorporate four components of the human water cycle: uptake of water, transportation of water, use of water, and drainage and regress. Thus, recent hydrological cycles have the characteristics of both a natural process and a human intervention [2].

In general, hydrological models can be classified into lumped models and distributed models, which are also called data-driven models and mechanistic models [3]. Lumped models, such as linear time series models, nonlinear time series analysis [4–6], and regression models [7], can be used for various purposes, such as forecasting and modelling rainfall runoff and estimation of missing hydrological data. In past decades, distributed hydrological models, for example, the SWAT model [8], TOPMODEL [9], MODFLOW [10], FEFLOW [11], MIKE-SHE model [12], SVM model [13],

HSPF model [14], and VIC model [15], have been developed and widely used for water planning and management.

Nonetheless, a pragmatic model should include not only natural factors such as plants, soil, and climate but also water use in society and in the economy [16]. The above-mentioned specialized hydrological models used for water management have limitations in regions affected by human activities. It is known that the remote sensing (RS) technique can objectively quantify different types of evapotranspiration (ET) as a function of time [17]. In this work, we developed the water allocation and simulation (WAS) model to simulate different types of natural ET and various types of artificial water consumption; a “piece-by-piece” approach was utilised to evaluate the model from runoff to ET.

2. The WAS Model

The WAS model can simulate dually natural-artificial water cycles influenced by both nature and humans. It consists of two interoperative computational modules: SWAT and the artificial water optimized allocation module (AWOM), which was developed in this study. In particular, AWOM, which

TABLE 1: Generalized elements of the system of water resources in AWOM.

Elements	Class	The representative system
Points	Supply	Reservoir, diversion works, well project, lakes, and marshes
	Water use	City residents, rural residents, industry, agriculture, urban ecology, lake ecology, and wetland ecology
	Convergence	Catchment zones and outflow, such as an ocean or a lake
	Water control	Key section of a river or channel
Lines	River	Natural rivers
	Channel	Artificial channels

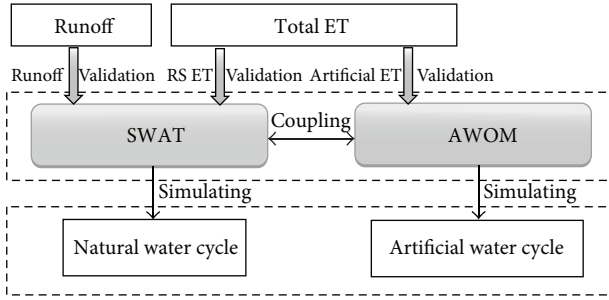


FIGURE 1: The structure of the WAS model (RS ET is ET data retrieval with remote sensing).

can implement optimization of regional water utilization by regional ET control, is the core for regional water resource management. SWAT provides basal data to AWOM. Synchronously, the SWAT and AWOM are the key to ET control of a region because regional ET includes not only natural ET such as ET of soil, grass, crops, and water (which can be obtained from SWAT and verified with data from RS) but also artificial ET-like consumptive use (ET) by residential buildings and by the industry, which can be provided by AWOM. Total regional ET can be verified using the water balance method and simulated using the WAS model, which is shown in Figure 1. Figure 1 shows the general architecture and state information flows of the WAS model, and Figure 2 illustrates the overall cyclic flow of this model.

2.1. Development of the SWAT Model. SWAT was initially developed by the United States Department of Agriculture for comprehensive modelling of the impact of management practices on water yield, sediment yield, and crop growth in large complex watersheds [8]. There are some disadvantages of SWAT. One example is that its artificial water simulation is limited and the scenarios are set passively; therefore, it cannot actively resolve conflicting water allocation options using data from social, economic, environmental, and water resources. In our study, some functions of SWAT were developed to incorporate the impact of human activities as follows. (1) We improved the agriculture module by adding an irrigation function that can locate more water sources for irrigation water within the same time frame. (2) We developed the consumptive water use module, which may be adapted to spatial and temporal variability of water use in different years; these data have been published previously [18].

2.2. Development of AWOM. Allowing for natural and artificial “dualistic” characteristics of a hydrological cycle, AWOM that is based on the ET control theory has been utilised in this work to simulate the artificial water cycle.

2.2.1. Description of the Water System Methodology. A water system methodology for the regional water resources is used here to describe an actual water system in AWOM, which includes five components (Figure 3): (a) multiple water sources, such as surface water, ground water, transfer water, recycled water, and desalination and brackish water; (b) multiple storage facilities, such as reservoirs, diversion works, well projects, lakes, and marshes; (c) multiple transfer systems, such as natural rivers, artificial channels, and the pipe network; (d) multiple users, including city residents, rural residents, industry, agriculture, ecology, and shipping; and (e) multiple drainage systems, including rivers, rainwater channels, and sewage channels.

2.2.2. Generalized Methodology of the Water System. Because of the complexity of the real-world system of water resources, we need to abstract the main characteristics and processes of a real water resource system according to an actual situation in the region. According to the similarity principle, the regional system of water resources is usually generalized as point elements and line elements to describe generalized water resources (Table 1).

2.2.3. The Delineation Method for Subzones. A study area may be divided into water allocation units (WAUs). WAUs are portions of a subbasin that possess unique subwatersheds or attributes of administrative divisions. The delineation process requires a digital map of subwatersheds and a map of administrative divisions in the shape (PolyLine) format. WAUs should be delineated via superimposition of the two above-mentioned maps in ArcGIS software (Figure 4).

2.2.4. The Relationship between Data from AWOM and SWAT. The holistic approach can objectively and clearly demonstrate the amount of allocation and drainage of water and show where it comes from and where it goes. In particular, AWOM is suitable for optimisation of the profit from water resources according to water availability per capita and a higher value of use considering regional ET control, groundwater exploitation control, among other factors that can improve development of water resources and of the regional economy. In fact, some input data for AWOM, such as runoff, groundwater, and

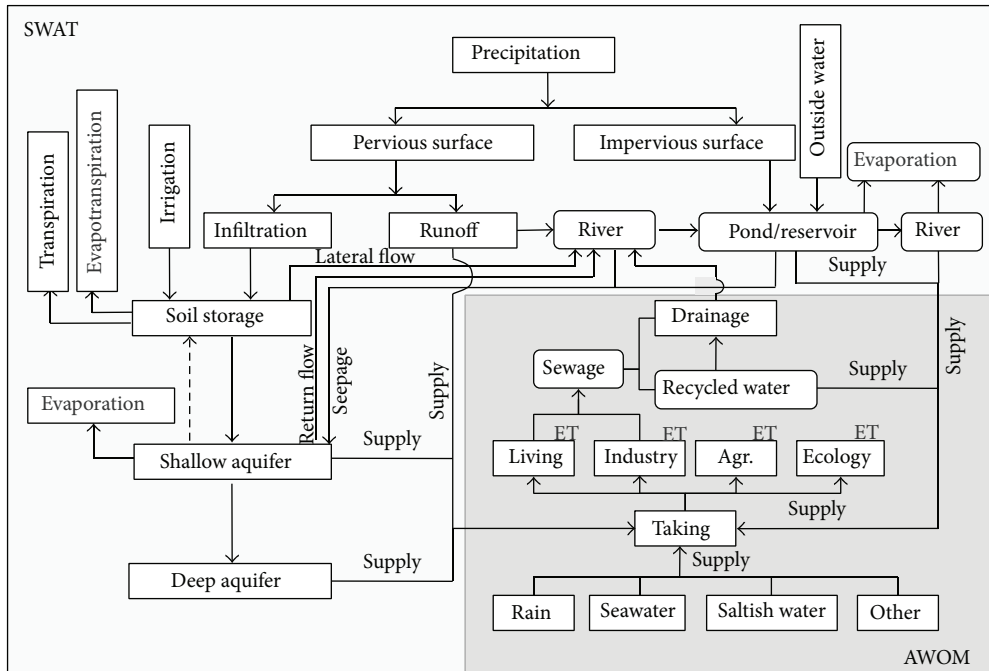


FIGURE 2: The flow chart of the WAS model.

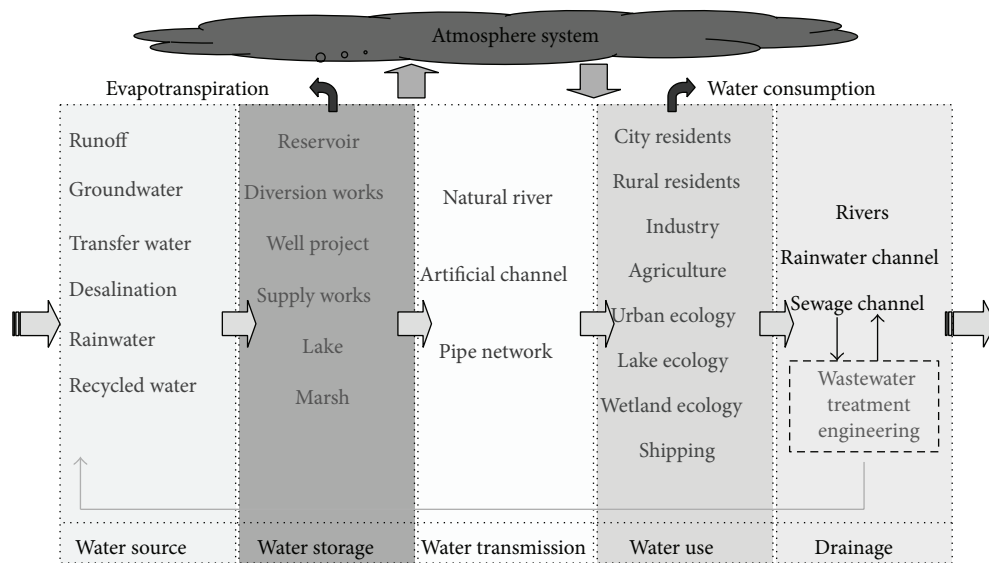


FIGURE 3: Description of the water system in AWOM.

water of sluice facilities, are as important as the output data on water resources demanded by users. In this study, water source data are provided as output of SWAT. Homoplastically, output variables of AWOM for a study region (which reflect the artificial consumptive water process) can be spatially and temporally assimilated into SWAT and used for calculations.

3. Practical Application of the Model

The WAS model described above was applied to Tianjin City, which has an area of 11,920 km² and had a population of 13.6

million in 2011. Tianjin City is located in the northern part of China and is the last city downstream of the Hai River flowing into the Bo Sea.

3.1. Materials

3.1.1. Hydrological Data. The input of the WAS model involves a large amount of data, which include the following: (1) the DEM of Tianjin is SRTM 30 m digital elevation data (downloaded from <http://srtm.csi.cgiar.org/>); (2) data on a regional river system on the scale of 1:250,000, obtained from the Water Resource Department of Tianjin (Figure 5);

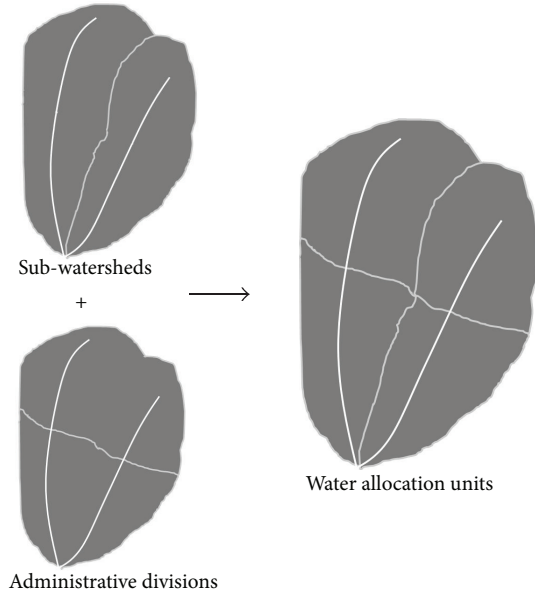


FIGURE 4: Delineation of water allocation units.

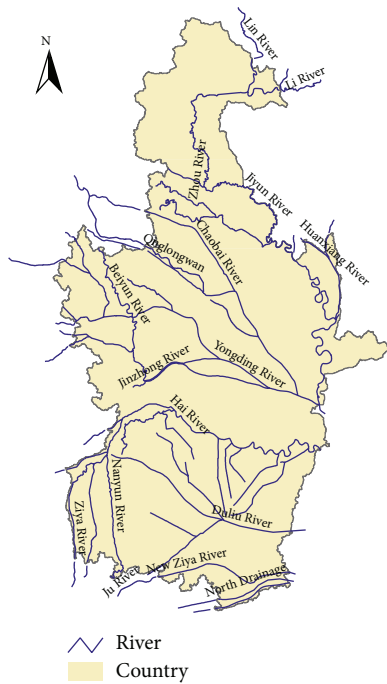


FIGURE 5: Rivers in Tianjin.

(3) daily weather data, including information on precipitation, temperature, wind speed, solar radiation, and relative humidity, supplied by the National Meteorological Site of China; (4) regional river inflow data obtained from the Water Resource Department of Tianjin; (5) soil types and types of land use (Figures 6 and 7) provided by the Water Resource Department of Tianjin; (6) infiltration recharge data from rainfall, rivers, reservoirs, wetlands, and irrigation and data on geological parameters for the groundwater

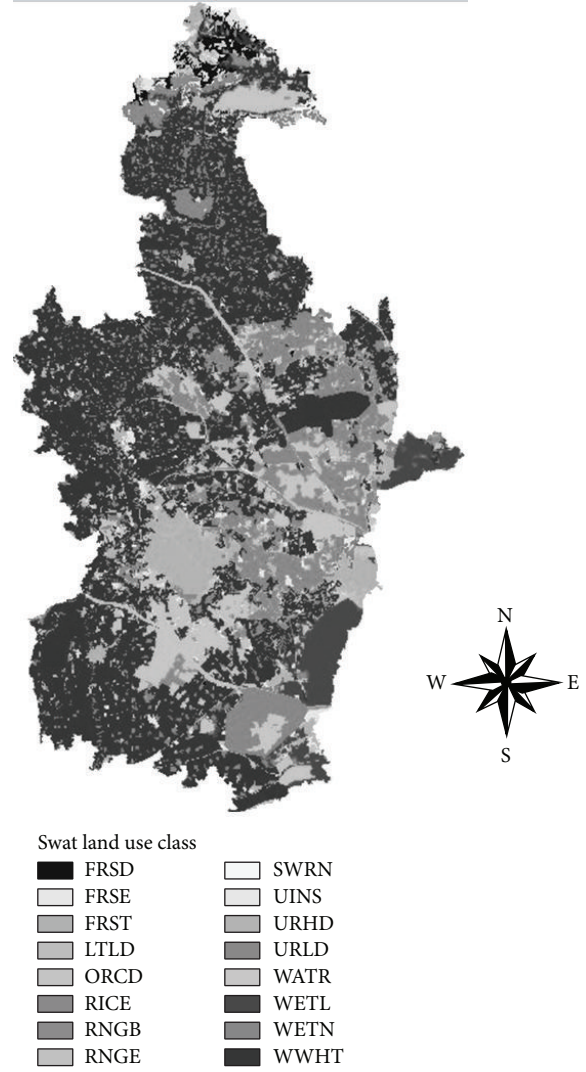


FIGURE 6: Land use in Tianjin.

aquifer, obtained from the Water Resource Department of Tianjin.

3.1.2. Artificial Data. The artificial data comprises five components: (1) the volume of water demanded by a city and industry; (2) the data on the schedule of irrigation, crop planting, fertilization, and other parameters related to farming management; (3) the volume of waste water drained by the city and industry; (4) the water supply source of each zone; and (5) the relationship of supply and drainage among various supply systems and demand zones. All of the above data were obtained from Tianjin water resource departments.

3.2. Development of the Model. The boundaries of the model follow the borders of the Tianjin district and some natural features, such as rivers, creeks, and coastline. As for the land surface, the research area was divided into 325 subbasins and 1,414 hydrologic response units in the SWAT model based on DEM, soil type, and land use of Tianjin (Figure 8). The water resource system of the Tianjin basin was generalized

TABLE 2: The delineated subzones of Tianjin in AWOM.

Unit name	MAJX	PAJX	PABD	PANH	PAHG	PAWQ	PABC	PBBC	PBXQ	PBCQ	PBJN	PBDL	PBTG	PBDG	PBJH
Water resources name	North three mountain areas	North four plain areas					Daqing River plain area								
District name	Jixian	Jixian	Baodi	Ninghe	Hangu	Wuqing	Beichen	Beichen	Xiqing	Central urban	Jinnan	Dongli	Tanggu	Dagang	Jinghai



FIGURE 7: Soils in Tianjin.

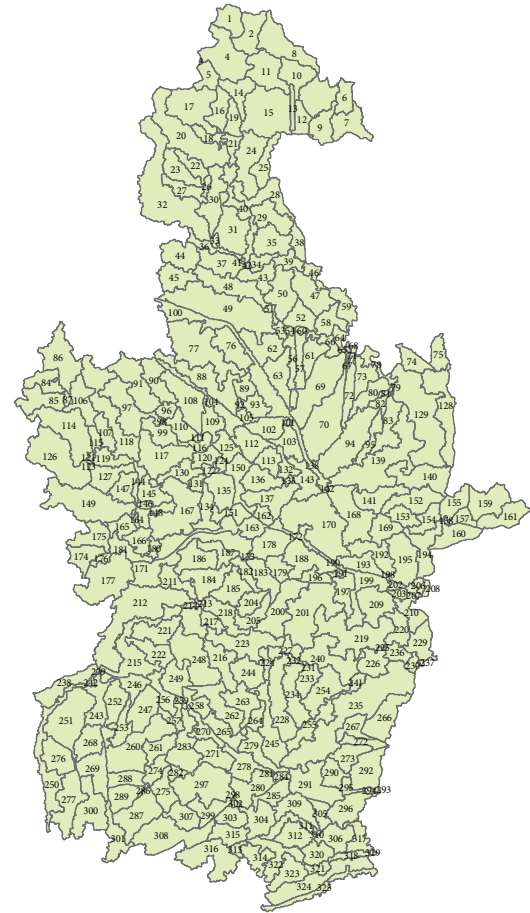


FIGURE 8: Delineation of watersheds in the Tianjin basin.

to describe the four processes of the Tianjin artificial water cycle (Figure 9). The artificial zones were delineated as 15 subzones in AWOM using the method that superimposes the watershed and the district.

The name of a subzone is an abbreviation, composed of four letters; the first two letters represent the regionalisation of water resources and the last two letters represent district regionalization. Table 2 shows descriptions of subzones.

4. Results and Discussion

A “piece-by-piece” approach was used here to evaluate the WAS model from runoff to ET. The idea behind the piece-by-piece approach is to provide the model with rational and available results step by step. The WAS model, like other large models, is subdivided into several pieces and then solved step by step with one piece solved at each step. At each step, the solution of the current partial model begins with a solution found in the previous step, and the solution from the current step is saved for the next step. At the final step, the model contains all pieces and the whole model is then calibrated. Verification of the WAS model is subdivided into

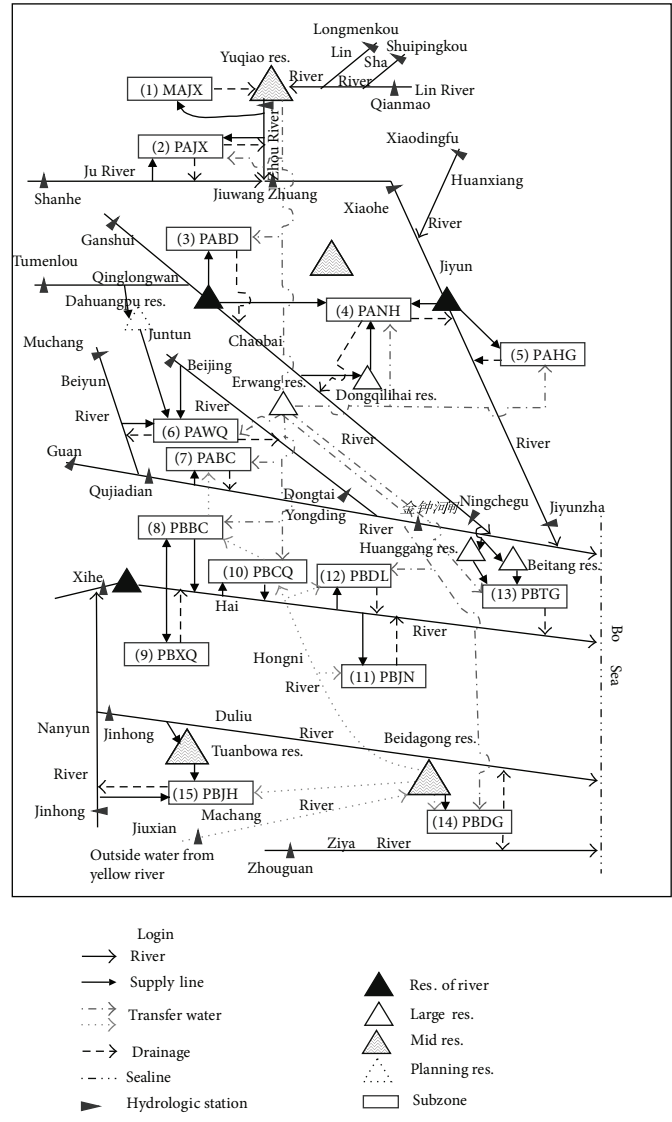


FIGURE 9: Water resource network of Tianjin.

the following three parts: the runoff, the ET measured using water balance analysis, and the ET obtained by means of RS.

4.1. Verification of the Model on Runoff. The surface runoff in the Tianjin basin was calibrated with daily observed streamflow data from 1985 to 1999 from four hydrological stations in Tianjin: on the Jiyun River, on the Chaobai River, on the Hai River, and on the Duliujian River. Comparison of the simulated and observed daily stream flow involved model efficiency (Ens) [19] and a regression coefficient (R^2). Surface runoff was calibrated until average measured and simulated surface runoff had monthly $R^2 > 0.6$ and $Ens > 0.5$. The results of the calibration are shown in Figure 10.

The Nash-Sutcliffe efficiency (Ens) of the model was 0.82 on average, with the maximum 0.89 and minimum 0.78; its regression coefficient R^2 was 0.92 on average, with the maximum 0.94 and minimum 0.91 (Table 3).

Several factors may contribute to the discrepancies between the simulation and the observed data. (1) The

hydrological cycle was strongly affected by human activities, and the spatial-temporal distribution of artificial water use in the model fails to reflect a real situation, although the SWAT module was developed to account for human activities. (2) The schedule of irrigation was also an influential factor because irrigation represented the dominant water use (70% of all off-stream uses), and the irrigation data necessitated consideration of precipitation and soil moisture. Overall, the predictions of runoff are relatively acceptable.

4.2. Verification of the Model on ET Measured Using Water Balance. Regional total ET includes natural ET and artificial ET. The ET measured using water balance is calculated from inflow and rainfall data and outflow data in Tianjin from 1980 to 2004; these measurements were made by Tianjin water resource departments (Figure 11).

In this work, ET of various underlying surface features was simulated and analysed using the distributed hydrology

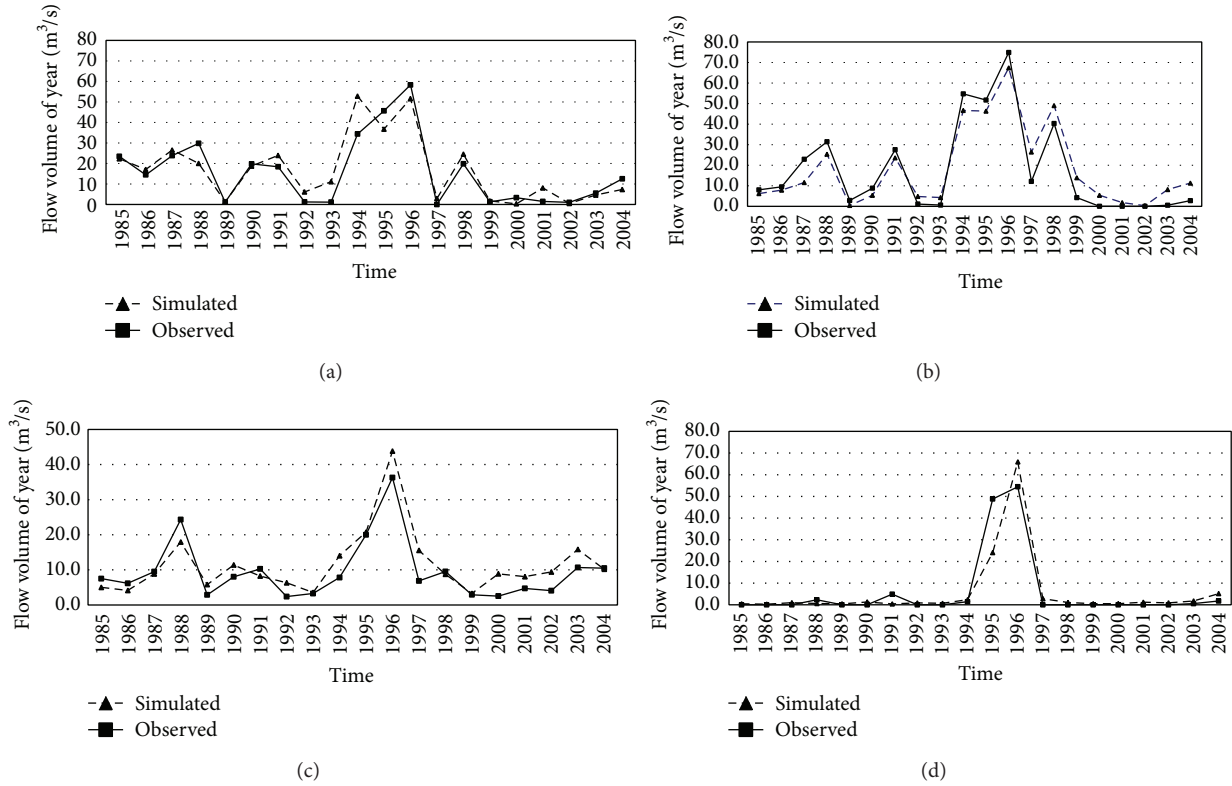


FIGURE 10: Calibration of the model. Comparison between simulated and observed streamflow at the four stations: Jiyun River (a), Chaobai River (b), Hai River (c), and Dulu River (d).

TABLE 3: Correlations at the four observed stations during calibration and validation periods.

ID	Calibration period (1985–1999)					Validation period (2000–2004)				
	a	b	c	d	Average	a	b	c	d	Average
Station	Jinyun	Chaobai	Hai	Dulu		Jinyun	Chaobai	Hai	Dulu	
Nash	0.82	0.89	0.78	0.82	0.82	0.61	0.78	0.65	0.73	0.69
R^2	0.91	0.94	0.92	0.91	0.92	0.67	0.82	0.75	0.78	0.76

Nash: Nash-Sutcliffe efficiency (Ens); R^2 : regression coefficient.

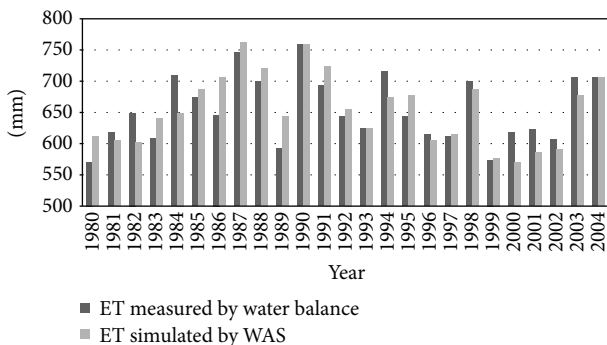


FIGURE 11: Comparison of total ET between simulated and measured data.

model of SWAT, and artificial ET was simulated and calculated in the artificial consumptive water module of AWOM. Figures 5 and 6 show comparisons of integrated regional ET between the simulation and the measured data, which

were obtained in the analysis of water balance in Tianjin. The Nash-Sutcliffe efficiency (Ens) of the model was 0.67, and its regression coefficient R^2 was 0.83. From 1980 to 2004 (Figure 12), 64% of years deviated by less than 5% and 88% of years deviated by less than 8%. The average total ET of 25 years simulated by the WAS model was 654 mm, which equalled the measured ET.

4.3. Verification of the Model on ET Obtained Using RS. Currently, the margin of error of ET obtained using RS can be larger than 15 percentage points, but the relationship of ET with various types of land use is accurate on a spatial scale in the same period. Therefore, we compared the ET results (average value from 2001 to 2004) pertaining to various types of land use between the WAS model and RS in order to validate the results for the model for various types of land use.

We found that the ET simulated by the WAS model was close to the ET data retrieved using the RS technique on different lands, as shown in Figure 13. The Nash-Sutcliffe

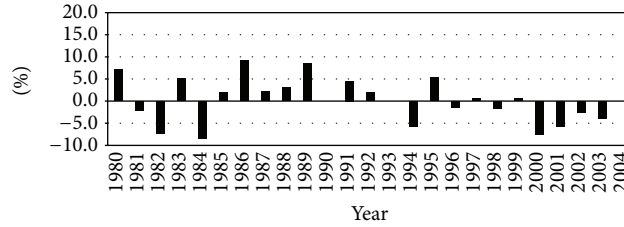


FIGURE 12: The deviation rate of simulated ET compared to measured ET.

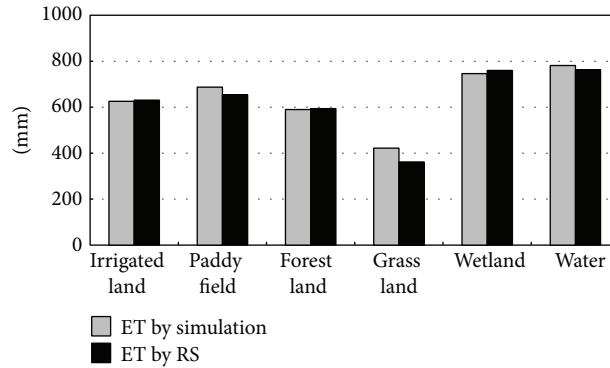


FIGURE 13: Comparison between simulated ET from the model and observed ET from RS in various lands.

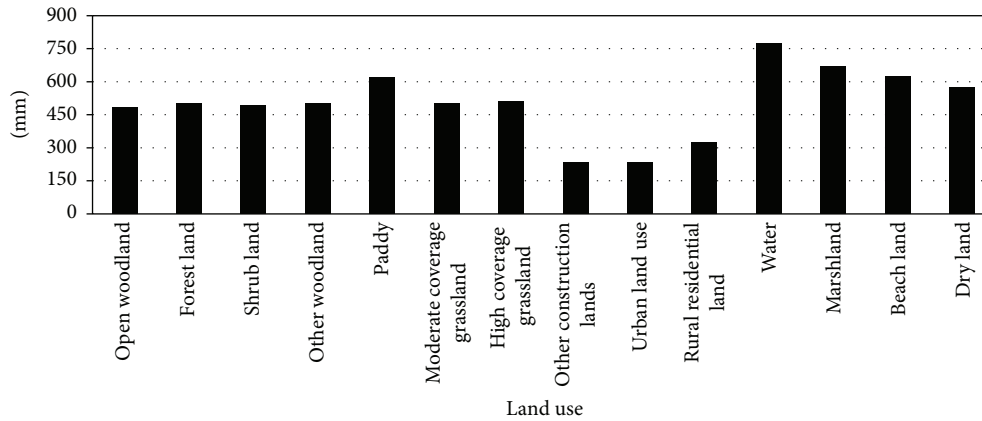


FIGURE 14: Average ET of lands used for various purposes in Tianjin from 1980 to 2004.

efficiency (Ens) of the model was 0.93, and its regression coefficient R^2 was 0.98. The ET from water, wetlands, and paddy lands was higher than that from the irrigated land, forest, and grass land; these results were consistent with the actual context and regional features.

5. Analysis of Regional Total ET

The average ET of various types of land use in Tianjin from 1981 to 2004, calculated by the WAS model, is shown in Figure 14. The water ET is 991 mm on average and was the highest. Marsh land and beach land are the second and the third: 724 mm and 701 mm, respectively. ET of paddy fields and dry lands is also high, 602 mm and 530 mm, respectively. Then follow grassland and forest land, from 482 mm to 501 mm. The rural residential land, urban land, and other

construction lands showed low ET: 326 mm, 236 mm, and 233 mm, respectively.

Figure 15 shows composition and distribution of integrated ET in Tianjin. It demonstrates that ET from irrigation lands is the dominant part that accounts for 53% of the total ET; the second highest ET was from ecology, with 23% from town ecology and 20% from other ecology. Accordingly, the sequence of the feasibility of ET control from easy to difficult is as follows: agriculture, ecology in town, industry, and residential use.

Judging by the results of analysis of ET from various types of land use and industries, the industries showing lower water use efficiency require some improvements. Control of the regional integrated ET can be attained, and regional authorities may finally implement the goals of water use efficiency and reap the resulting benefits.

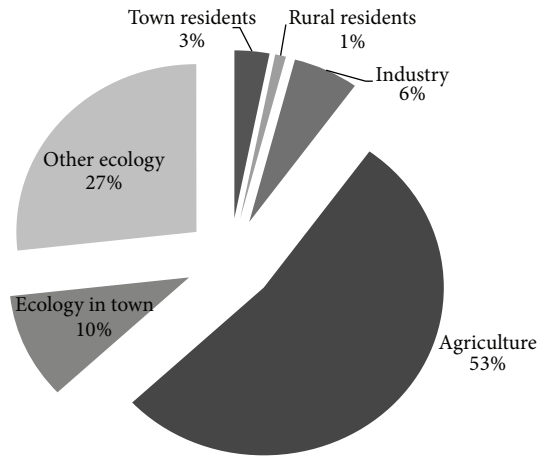


FIGURE 15: Analysis of integrated ET in Tianjin.

6. Conclusions

In this work, a regional WAS model was used to achieve ET control; the model was developed to implement integrated simulation of a natural and artificial water cycle. In the process of calibration and validation, a “piece-by-piece” approach was utilized to solve the model and to obtain rational and effective results from the model step by step. A case study was conducted to explore some of the capabilities of the model in the Tianjin basin.

Among the results of practical application of the model, we can see that the runoff dropped off gradually from 1980 to 2004, and synchronously, the regional total ET changed just like the runoff. This finding demonstrates that the regional total ET strongly correlates with precipitation and the water volume of inflow because the ET mainly comes from various uses of land. Distribution of regional ET also shows that ET of the croplands and other plant lands is higher than that of residential units and industry. The ET from RS estimates the ET of underlying surface features based on the retrieval principle and cannot reflect the regional total ET, such as the ET related to the volume consumed by residential units and industry, but it is used as a tool for evaluating and analyzing the scenario for water resource planning and management. This is because the ET from residential units and industry represents a very small fraction in most regions.

Conflict of Interests

The authors declare that there is no conflict of interests regarding the publication of this paper.

Acknowledgments

This study was funded by the MWR Project “The Theory and Practice of Construction of a Water-Saving Society in China” ([2006]50), a Project of Natural Sciences for Youth Foundation of China (51009149), and IWHR Project (ZJ1224).

References

- [1] A. K. Biswas, “Integrated water resources management: a reassessment,” *Water International*, vol. 29, no. 2, pp. 248–256, 2004.
- [2] J. F. Booker and R. A. Young, “Modeling intrastate and interstate markets for Colorado river water resources,” *Journal of Environmental Economics and Management*, vol. 26, no. 1, pp. 66–87, 1994.
- [3] A. Elshorbagy and L. Ormsbee, “Object-oriented modeling approach to surface water quality management,” *Environmental Modelling and Software*, vol. 21, no. 5, pp. 689–698, 2006.
- [4] A. Porporato and L. Ridolfi, “Nonlinear analysis of river flow time sequences,” *Water Resources Research*, vol. 33, no. 6, pp. 1353–1367, 1997.
- [5] R. S. Govindraj and A. R. Rao, *Artificial Neural Networks in Hydrology*, Kluwer Academic Publishers, Dordrecht, The Netherlands, 2000.
- [6] E. Foufoula-Georgiou and P. K. Kitanidis, “Gradient dynamic programming for stochastic optimal control of multidimensional water resources systems,” *Water Resources Research*, vol. 24, no. 8, pp. 1345–1359, 1988.
- [7] R. M. Hirsch, “A comparison of four streamflow record extension techniques,” *Water Resources Research*, vol. 18, no. 4, pp. 1081–1088, 1982.
- [8] S. L. Neitsch, J. G. Arnold, J. R. Kiniri, and J. R. Williams, *Soil and Water Assessment Tool Theoretical Documentation Version 2000*, Grassland, Soil and Water Research Laboratory and Blackland Research Center, Temple, Tex, USA, 2001.
- [9] M. G. McDonald and A. W. Harbaugh, “A modular three-dimensional finite-difference ground-water flow model,” in *U.S. Geological Survey Techniques of Water-Resources Investigations, Book 6*, chapter A1, pp. 195–286, 1988.
- [10] J. C. Refsgaard and B. Storm, “MIKE SHE,” in *Computer Models in Watershed Hydrology*, V. J. Singh, Ed., pp. 809–846, Water Resource Publications, 1995.
- [11] A. S. Donigan, B. R. Bicknell, and J. C. Imhoff, “Hydrological Simulation Program—Fortran (HSPF),” in *Computer Models of Watershed Hydrology*, V. P. Singh, Ed., pp. 395–442, Water Resources Publications, 1995.
- [12] L. Brown, B. McDonald, J. Tysseling, and C. Dumars, “Water reallocation, market efficiency, and conflicting social values,” in *Water and Agriculture in the Western U.S.: Conservation, Reallocation, and Markets*, G. D. Weatherford, Ed., Westview Press, Boulder, Colo, USA, 1982.
- [13] M. Bray and D. Han, “Identification of support vector machines for runoff modelling,” *Journal of Hydroinformatics*, vol. 6, pp. 265–280, 2004.
- [14] G. Belaine, R. C. Peralta, and T. C. Hughes, “Simulation/optimization modeling for water resources management,” *Journal of Water Resources Planning and Management*, vol. 125, no. 3, pp. 154–161, 1999.
- [15] X. Liang, D. P. Lettenmaier, E. F. Wood, and S. J. Burges, “A simple hydrologically based model of land surface water and energy fluxes for general circulation models,” *Journal of Geophysical Research*, vol. 99, no. 7, pp. 14415–14428, 1994.
- [16] Y. Huang, D. Jiang, D. Zhuang, Y. Zhu, and J. Fu, “An improved approach for modeling spatial distribution of water use profit—a case study in Tuhai Majia Basin, China,” *Ecological Indicators*, vol. 36, pp. 94–99, 2014.
- [17] J. Dong, D. Zhuang, X. Xu, and L. Ying, “Integrated evaluation of urban development suitability based on remote sensing and

- GIS techniques: A case study in Jingjinji area, China,” *Sensors*, vol. 8, no. 9, pp. 5975–5986, 2008.
- [18] X. Sang, Z. Zhou, H. Wang, D. Qin, Z. Zhai, and Q. Chen, “Development of soil and water assessment tool model on human water use and application in the area of high human activities, Tianjin, China,” *Journal of Irrigation and Drainage Engineering*, vol. 136, no. 1, pp. 23–30, 2010.
- [19] J. E. Nash and J. V. Sutcliffe, “River flow forecasting through conceptual models part I—a discussion of principles,” *Journal of Hydrology*, vol. 10, no. 3, pp. 282–290, 1970.

Research Article

Spatial and Temporal Characteristics of Meteorological Drought in Shandong Province, China, from 1961 to 2008

Xiaoli Wang,^{1,2} Xiyong Hou,¹ Zhi Li,³ and Yuandong Wang^{1,2}

¹ Yantai Institute of Coastal Zone Research, Chinese Academy of Sciences, Yantai 264003, China

² University of Chinese Academy of Sciences, Beijing 100049, China

³ College of Natural Resources and Environment, Northwest A&F University, Yangling, Shaanxi 712100, China

Correspondence should be addressed to Xiyong Hou; xyhou@yic.ac.cn

Received 10 February 2014; Revised 20 April 2014; Accepted 5 May 2014; Published 15 June 2014

Academic Editor: Shengli Huang

Copyright © 2014 Xiaoli Wang et al. This is an open access article distributed under the Creative Commons Attribution License, which permits unrestricted use, distribution, and reproduction in any medium, provided the original work is properly cited.

Shandong province is located in the northern part of China and tends to be a drought-prone region. This study is dedicated to making a comprehensive and quantitative analysis of the spatial patterns of drought frequency and its climate trend coefficient, drought grades, and temporal characteristics of drought coverage area, drought duration, and drought intensity from 1961 to 2008 by using the meteorological drought composite index (CI). The results indicated that the occurrence frequency of meteorological drought in Shandong province was generally high and some part of this region such as Jiaodong peninsula had suffered drought pressure with an evident ascending trend. The drought extent and influence were very severe in 1980s and 1990s but very slight in 1964; large-area drought mainly occurred after the 1970s and the yearly and seasonally interdecadal drought duration both showed a fluctuation of 10a periodic cycle approximately. Furthermore, the slight drought mainly appeared in the northwest and southwest while the other grades of drought exhibited much significant spatial and temporal variability. Besides, drought in spring was more serious than that in winter. This study is anticipated to support the mitigation of drought hazards and to improve the management practices of environment system in Shandong province.

1. Introduction

According to the Intergovernmental Panel on Climate Change (IPCC) report [1], the land surface temperatures have risen globally over the past century and a half, which have shown significant regional variations also. And global warming intensifies the global hydrological cycle in terms of the averaged precipitation, evaporation, and runoff; thus it further compounds the drought occurrence around the world [2]. In particular in recent decades, drought occurred frequently, and large-scale intensive drought has been observed in many continents, such as Africa [3, 4], Asia [5, 6], Europe [7, 8], and America [9, 10]. Being located in East Asia, China has been suffering large-scale and long-lasting severe droughts since the early 1950s, which had negative impacts on environment, ecosystem, social-economic development, and people's living conditions [11, 12]. For example, the frequent occurrence of severe droughts in 1997, 1999, and 2002 in

Shandong province, Hebei province, Gansu province, Inner Mongolia Autonomous Region, and so on had caused very serious economic and societal losses [13]. In 1997, the very severe drought in northern China resulted in a period of 226 days with no streamflow in the Yellow River, which is the longest drying-up duration on record [2]. Thus it is of great importance to carry on more thorough drought research at local and regional as well as national scales, especially to those areas with insufficient water resources. However, due to the complexity of drought dynamics and its diverse influencing factors such as temperature, relative humidity, high winds, monsoons, rains, and latitudes, the accurate monitoring and comprehensive evaluating of drought are still a big challenge.

The American Meteorological Society classifies drought into four categories, including meteorological, hydrological, agricultural, and socioeconomic drought [14]. The meteorological drought, which is mainly used for monitoring and assessing the water deficit degree aroused by climate

anomalies in a region within a certain period of time, is the fundamental reason for the occurrence of other droughts. Therefore, it contributes to further researches of other types of drought to explore the meteorological drought's causes and laws and to carry out effective monitoring, early warning, and historical assessment of meteorological drought hazards. As a primary method for assessing the effect of drought, the drought index is a numerical expression of drought parameters, such as intensity, severity, duration, and spatial extent. Many indices have been developed so far to quantify a drought among which some meteorological drought indices have been implemented widely at present, such as the standardized precipitation index (SPI) [15–17], Palmer drought severity index (PDSI) [18, 19], and vegetation condition index (VCI) [20, 21]. Recently, the meteorological drought composite index (CI), which was proposed by China Meteorological Administration, has been used in many regions in China. Compared to meteorological indices previously reported such as SPI and PDSI as well as VCI, CI has the advantage of taking water-heat balance into consideration for drought stress characterization because it combines both precipitation and temperature information; it has the ability to identify the drought onset and termination, severity, and duration as well as drought-hit area; therefore it is suitable for real-time meteorological drought monitoring and assessment of the historical meteorological drought [22]. For instance, Zhao et al. [23] made a prediction of meteorological drought risk with CI in Yunnan province, supporting the quantitative analysis of drought influencing factors such as LUCC in this region. Based on the calculation of CI, Zou et al. [24] studied the drought areas variations for ten major Chinese river basins and China as a whole from 1951 to 2008, revealing the drought areas trends and pointing out the significant drought areas in China. What is more, by employing CI, several other meteorological drought researches had been taken out in eastern [25] and northwest [26] and some other regions in China.

In this study, we made a thorough and quantitative analysis of the spatial-temporal dynamics of the meteorological drought that occurred in Shandong province from 1961 to 2008 by adopting CI which has not been employed in this region. Specifically, we analyzed the spatial patterns of drought frequency and its climate trend coefficient, drought grades, and temporal characteristics of drought coverage area, drought duration, and drought intensity in the expectation of providing reasonable reference and scientific support for alleviating and mitigating the impacts of meteorological drought.

2. Study Area and Data

2.1. Study Area. Shandong province is situated in the downstream area of the Yellow River; it lies between E 114°36'~E 122°43' and N 34°25'~N 38°23', respectively. Being located in the eastern coast area of China, Bohai Sea borders its north and Yellow Sea borders its northeast and southeast (Figure 1). Being affected by the typical warm temperature monsoon climate, Shandong province is characterized by cold and less rain in spring, being hot and rainy in summer, moderate

precipitation and temperature in autumn, and being cold and dry in winter, respectively. The average annual temperature is 11~14°C, increasing from northeast to southwest. The average annual precipitation is generally between 550 and 950 mm, decreasing from southeast to northwest. The seasonal distribution of rainfall is uneven because nearly 60~70% precipitation concentrate in summer, tending to induce or form floods. However, there are so less rainfall in autumn, winter and spring, and the droughts arouses easily in these seasons. Furthermore, with a large population and widespread farmland but limited water resources, Shandong province is facing severe water scarcity due to an increasing demand of water resource by population's livelihood, agriculture, energy, and industry sectors. Therefore, Shandong province becomes a drought-prone region, which threatens regional social-economic development and living standard of local dwellers. However, as for researches that have been reported on drought hazards in Shandong province, it mainly focused on drought causes from the aspect of climatology background in terms of atmospheric circulation and monsoon [27], or drought characters by assessing statistical data such as temperature, precipitation, and disaster losses [28, 29]; there is a shortage of quantitative exploration of meteorological drought from the perspective of spatial-temporal characteristics [30, 31] and different severity levels with a long time series in this region.

2.2. Meteorological Data. The meteorological data records with excellent quality through a strict quality control were selected from the Chinese Terrestrial Climate Information of Daily Datasets. There are 32 representative meteorological stations in these datasets in Shandong province; however, due to the limitation of inconsistency observation records in some stations, we finally choose 18 meteorological stations' daily climate data including measured average temperature and precipitation data from 1961 to 2008. In order to satisfy the requirements of CI calculation, the meteorological records in nearly 50 years were readily preprocessed according to the data processing document.

3. Methodology

3.1. Meteorological Drought Composite Index. In this study, CI was employed to analyze the spatial and temporal characteristics of meteorological drought in Shandong province at time scales of seasonal and interannual. CI is calculated based on standardized precipitation index (SPI) and relative moisture index (MI) as follows [22]:

$$CI = aZ_{30} + bZ_{90} + cM_{30}, \quad (1)$$

where Z_{30} and Z_{90} refer to the SPI of 30 days and 90 days, respectively, M_{30} represents the MI of 30 days, and a , b , and c are coefficients.

SPI was developed for the purpose of defining and assessing drought by McKee et al. [15], and it was computed following Zhang et al. [22] in this paper. MI indicates the

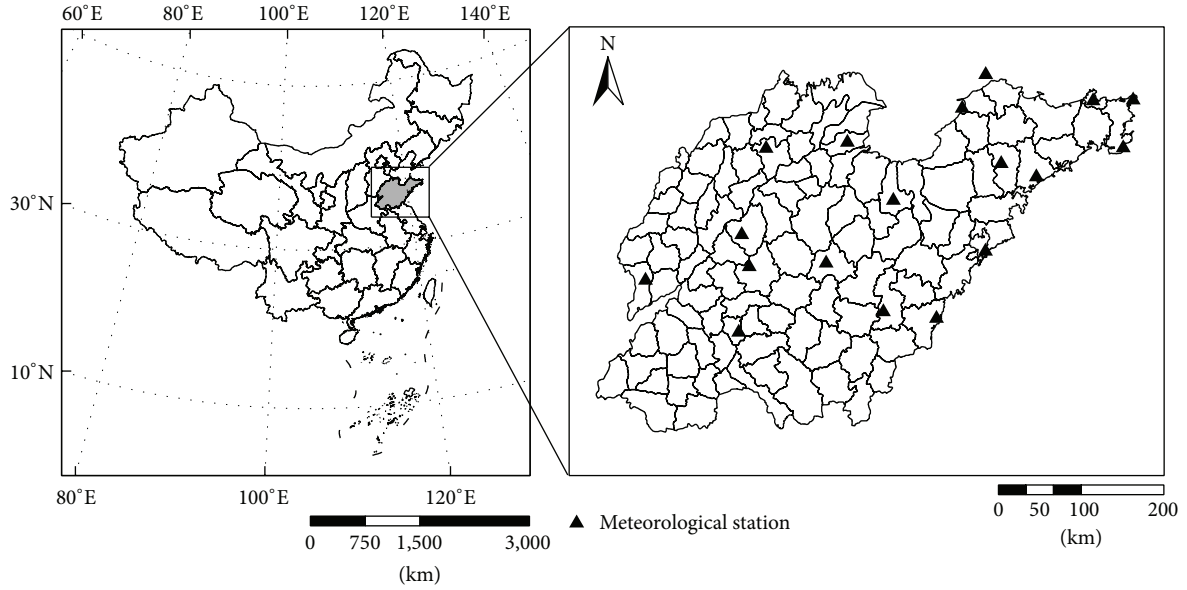


FIGURE 1: Location map of Shandong province and the meteorological stations.

balance between precipitation and evaporation during a period of time, and it was calculated as follows:

$$MI = \frac{P - PE_m}{PE_m}, \quad (2)$$

where P refers to the total amount of precipitation in the recent 30 days (unit: mm) and PE_m is the potential evapotranspiration in the recent 30 days (unit: mm). The potential evapotranspiration was calculated based on the Thornthwaite function according to Zhang et al. [22].

The meteorological data including the daily average temperature and daily precipitation were employed to calculate the CI according to formula (1), and the CI was classified based on Table 1 [23].

3.2. Determination of the Meteorological Drought Process. We adopted CI to determine the meteorological drought process. A meteorological drought process is initiated when CI in 10 consecutive days is above slight drought level ($CI_{10} \leq -0.6$), and this process is terminated until another 10 consecutive nondrought days appear ($CI_{10} > -0.6$). The drought duration refers to the period between the first date and last date of the whole process. A drought event for a specific time scale (month, season, and year) appears when there is at least one occurrence of a drought process and the length of cumulative drought duration exceeds a quarter of the timescale [22]. In addition, the drought intensity is referred to the sum of all CI values above slight drought level during a drought process in which smaller values indicate stronger drought intensity.

In this paper, the annual and seasonal drought duration in Shandong province were obtained by calculating the arithmetic mean of the total number of days of all drought processes for total meteorological stations within the corresponding periods. And the annual drought intensity was defined as the arithmetic mean of the drought intensity for

TABLE 1: Classification standard of the meteorological drought composite index (CI).

Level	Class	CI
1	No drought	$-0.6 < CI$
2	Slight drought	$-1.2 < CI \leq -0.6$
3	Moderate drought	$-1.8 < CI \leq -1.2$
4	Heavy drought	$-2.4 < CI \leq -1.8$
5	Extreme drought	$CI \leq -2.4$

total meteorological stations for each year. The definition of season is as follows: winter covers January, February, and December of last year, spring is from March to May, summer is from June to August, and autumn covers from September to November.

3.3. Drought Frequency and Its Climate Trend Coefficient. The drought frequency is calculated as follows:

$$F = \frac{n}{N} \times 100\%, \quad (3)$$

where F is the drought frequency, n refers to the number of drought years, and N represents the total number of years. In this paper, there were 48 years from 1961 to 2008; thus N took the value of 47 because CI was calculated by rolling back.

The climate trend coefficient is used to describe the temporal characteristics of climate trend change intensity quantitatively [32]; it is calculated as follows:

$$r_{xt} = \frac{\sum_{i=1}^n (x_i - \bar{x})(i - \bar{t})}{\sqrt{\sum_{i=1}^n (x_i - \bar{x})^2 \sum_{i=1}^n (i - \bar{t})^2}}, \quad (4)$$

where r_{xt} refers to the correlation coefficient between factor sequence and natural sequence in n years, x_i is the factor value in the i year, \bar{x} represents the sample mean, and $\bar{t} = (n + 1)/2$.

In this study, the climate trend coefficient of drought frequency was calculated based on the occurrence frequency of drought in five decades for each meteorological station at time scales of year and season. The positive and negative values of r_{xt} reflect linear increase and decrease trends of drought frequency in n years, respectively. And the spatial distribution of drought frequency and its climate trend coefficient as well as different drought grades were obtained by employing the inverse distance weighting (IDW) interpolation method in ArcGIS 9.3 platform.

3.4. Drought Coverage Area. The probability of drought coverage area (PDCA) is defined as the area ratio of drought events that occur for a given timescale in the study region and is calculated as follows:

$$S = \frac{m}{M} \times 100\%, \quad (5)$$

where S is the probability of drought coverage area, m is the number of meteorological stations in which drought events that occur for a given timescale, and M refers to the total meteorological stations. The PDCA of more than 90% is defined as the large-area drought in this research [25].

4. Spatial-Temporal Characteristics of Meteorological Drought

4.1. Spatial Patterns of Drought Frequency and Its Climate Trend Coefficient. There are very significant spatial differences of meteorological drought frequency from 1962 to 2008 in Shandong province. It can be seen that the annual drought frequency decreased both from north to south and from west to east (Figure 2(a)). The annual high drought frequency mainly concentrated in the north and southwest Shandong province, with a maximum percentage of more than 80%. In contrast, low frequency centered in the central and southeastern Shandong province as well as the eastern Jiaodong peninsula, with the lowest occurrence in Taishan about 53.9%. Drought frequency at four seasons also showed very distinct spatial differences. In spring it varied from 63.83% to 80.85%, which is the highest among four seasons, and high values mainly located in northwest and southwest (Figure 2(b)). The scopes of drought frequency in summer (Figure 2(c)) and autumn (Figure 2(d)) were 42.55%~72.34% and 51.06%~74.47%, respectively, exhibiting a similar spatial pattern that the minimum frequency occurred in Taishan and southeast areas and the maximum frequency appeared in north and southwest regions. In winter, the drought frequency varied from 36.17% to 74.46%, which was lower than any other seasons, and low value areas spread widely, including almost the entire central area and most parts of northern area (Figure 2(e)). Overall, the southwest and north areas were prone to high drought frequency, but the central and southeast regions were susceptible of relative low drought frequency.

Furthermore, the temporal trend analysis of drought frequency showed that the meteorological drought in Shandong province tended to be aggravating from 1962 to 2008

(Figure 3(a)). The spatial distribution of drought frequency tendency in spring (Figure 3(b)) was similar to that in autumn (Figure 3(d)) and winter (Figure 3(e)), presenting an ascent trend in eastern and northern area of Shandong province, especially in Jiaodong peninsula. In summer, the increasing trend of drought frequency was observed in finite areas, around Weifang city and Jiaodong peninsula mainly (Figure 3(c)). In general, it demonstrates that regions of significant aggravating drought during 1962 to 2008 mainly concentrated in the northern and southern part and Jiaodong peninsula, showing a certain degree of meteorological drought aggravation, and need to be focused on for mitigating the drought stresses in the future.

4.2. Spatial Patterns of Different Drought Grades. The spatial patterns of different drought grades from 1962 to 2008 in Shandong province are shown in Figure 4. In the respect of annual drought, over the past nearly 50 years, the number of slight drought, moderate drought, and severe and extreme drought days that occurred in Shandong province were between 57~81 d (Figure 4(a)), 32~49 d (Figure 4(b)), and 11~23 d (Figure 4(c)), respectively. Spatially, the days of slight drought decreased from west to east, and the days of moderate drought showed a zonal distribution, with south being more than north, which was conversely with the pattern of severe and extreme drought. Overall, the distributions of high-value centers for every drought grade have no common features whereas low-value centers were all in the Taishan area.

In spring, the annual days of slight drought, moderate drought and severe and extreme drought were 16~25 d (Figure 4(d)), 11~16 d (Figure 4(e)), and 4~9 d (Figure 4(f)), respectively. And the high value centers of slight drought were located in the western and northern regions, with drought days exceeding more than 22 d; on the contrary, the Taishan area and Weihai-Shidao in Jiaodong peninsula were not prone to slight drought. The moderate drought was mostly observed in the west to Weifang-Juxian areas. Moreover, the severe and extreme drought was the most severity in four seasons, exhibiting a high-value in the eastern part of Jiaodong peninsula and low-value in the Taishan area.

In summer, the annual days of slight drought, moderate drought, and severe and extreme drought were 10~17 d (Figure 4(g)), 5~11 d (Figure 4(h)), and 3~7 d (Figure 4(i)), respectively. And the high incidence areas for each drought grades mainly located in the north, northwest, southwest, and the Jiaodong peninsula; whereas the low incidence areas were all in and around the Taishan area.

In autumn, the annual days for the three drought grades were 14~22 d (Figure 4(j)), 9~15 d (Figure 4(k)), and 3~6 d (Figure 4(l)), respectively. The slight drought was likely to occur in the northwest, southwest, and the east area of Jiaodong peninsula. And the moderate drought days were 11~13 d in most areas of the province, except the Yellow River delta and Rizhao city (high-value centers of moderate drought) and Taishan area (low-value center of moderate drought). In addition, the northwest and southwest were vulnerable to severe and extreme drought in autumn, with drought days more than 4 d.

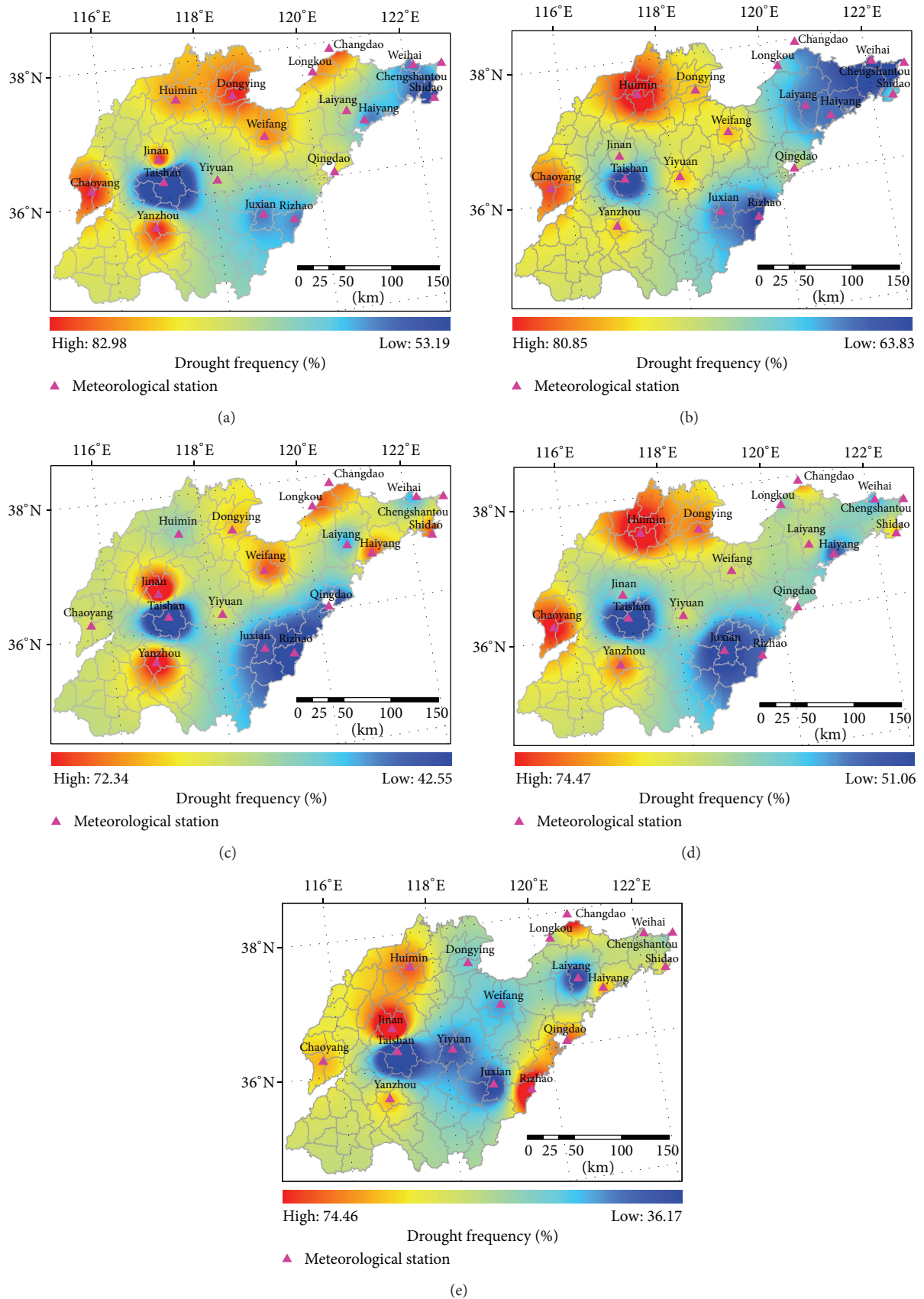


FIGURE 2: Spatial distribution of annual (a), spring (b), summer (c), autumn (d), and winter (e) drought frequency in Shandong province.

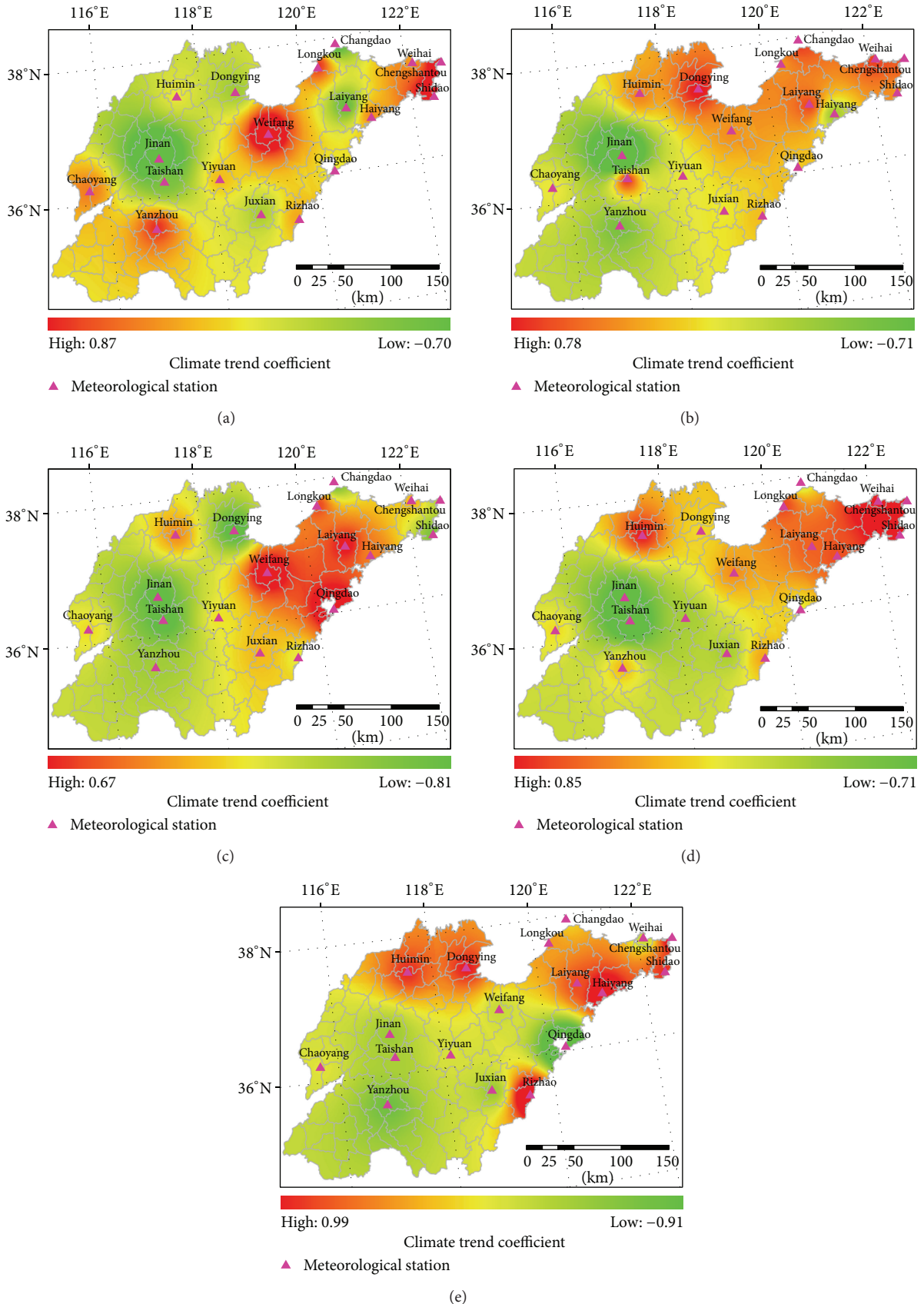


FIGURE 3: Spatial distribution of annual (a), spring (b), summer (c), autumn (d), and winter (e) climate trend coefficient of drought frequency in Shandong province.

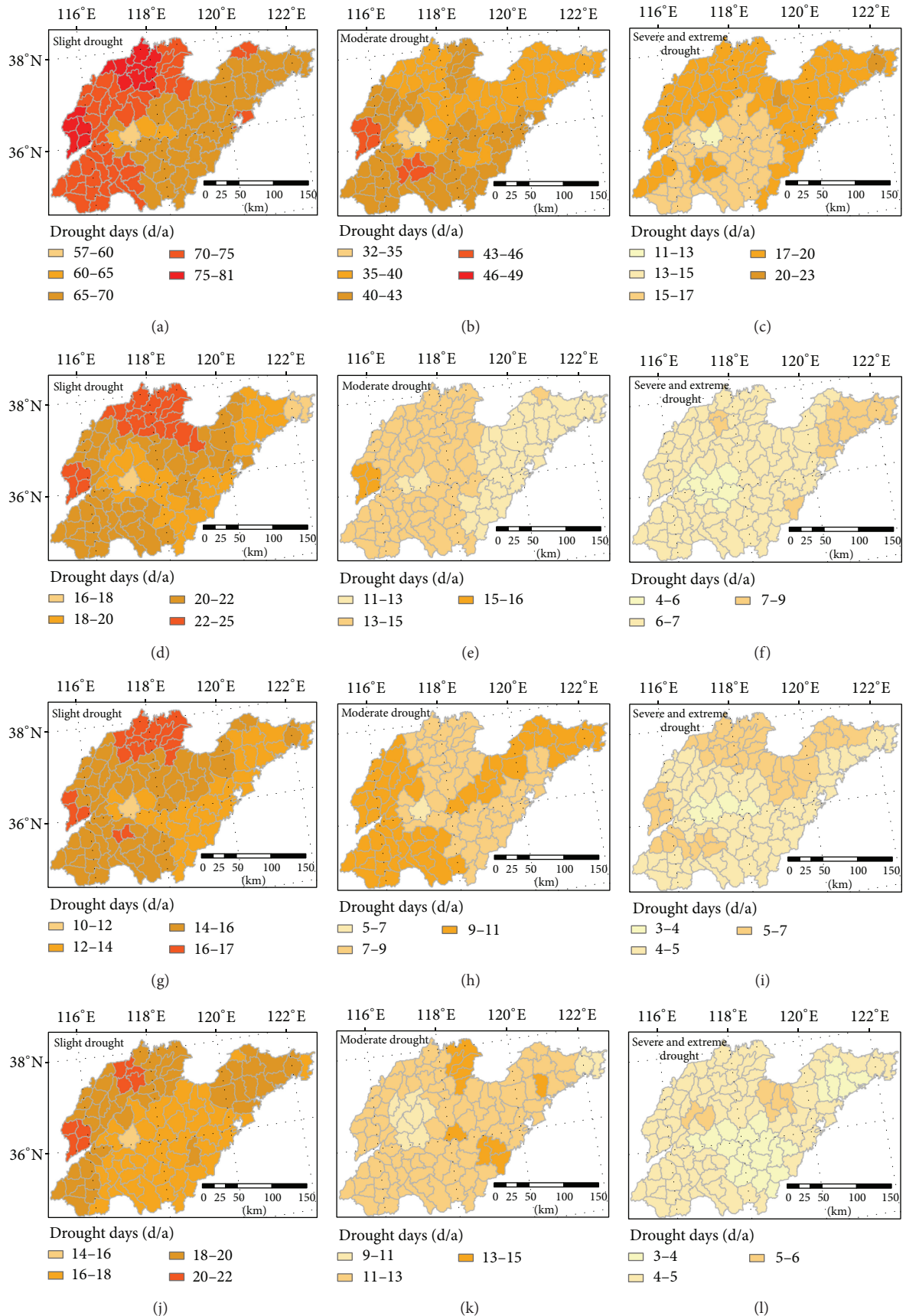


FIGURE 4: Continued.

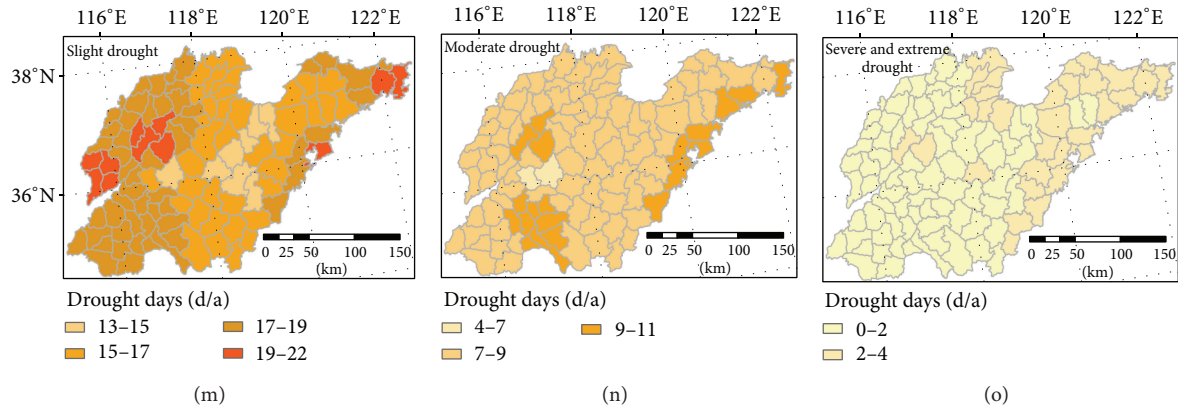


FIGURE 4: Spatial patterns of annual ((a)~(c)), spring ((d)~(f)), summer ((g)~(i)), autumn ((j)~(l)), and winter ((m)~(o)) different drought grades in Shandong province.

In winter, the annual drought days for different grades were 14~22 d (Figure 4(m)), 9~15 d (Figure 4(n)), and 3~6 d (Figure 4(o)), respectively. The northwest, southwest, and eastern coastal areas were prone to slight drought in winter; however, the moderate drought days distributed evenly in the study area, ranging between 7 and 9 d generally. Besides, the severe and extreme drought in winter was the least severity in four seasons, having only 0 to 2 drought days in most parts of the province.

To sum up, each grade of drought that lasts a relatively long time has occurred in Shandong province from 1962 to 2008. And the slight drought was generally observed in the northwest and southwest both for annual and seasonal, but the other grades of drought were observed in different areas for different timescales.

4.3. Temporal Characteristics of Drought Coverage Area. The temporal sequence of PDCA in Shandong province from 1962 to 2008 is shown in Figure 5. The annual average PDCA was 75%, and the annual large-area drought was observed in 14 a which was evenly distributed in the 1980s and 1990s. Relatively, the probabilities of drought extent are zero in 1964 and 2003, revealing that there were no drought events at time scale of year in these two years in Shandong province. For each season, the annual probability of an area affected by a drought in spring, summer, autumn, and winter was 72%, 61%, 65%, and 58%, respectively. There were 21 a of large-area drought which was mainly distributed in the 1980s, 1990s, and early 21 s century in spring, and 9 a, 12 a, and 11 a of large-area drought in summer, autumn, and winter whereas almost all of these years concentrated in the 1980s and 1990s. Meanwhile, the nondrought years for every season were relatively few over the past nearly 50 years, only 4 a in spring, 3 a in summer, and 2 a both in autumn and winter. In summary, the large-area drought at annual and seasonal time scales in Shandong province mostly occurred in the 1980s and 1990s.

Moreover, time-continuous large-area drought events have been observed in a few years in Shandong province; in specific, transseasonal large-area droughts that covers spring, summer, and autumn occurred in 1981, 1988, and 2001, respectively. Autumn-winter continuous large-area droughts

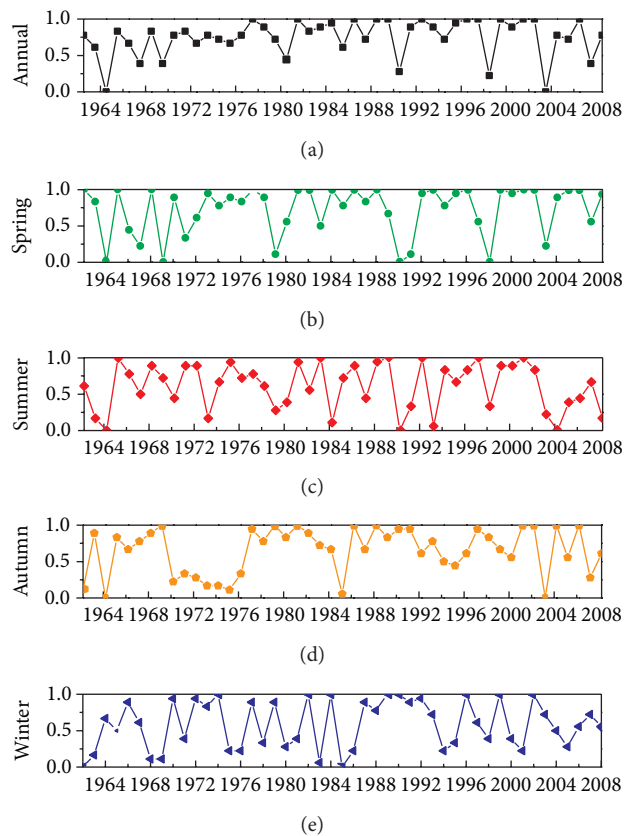


FIGURE 5: Annual, spring, summer, autumn, and winter probability of drought coverage area in Shandong province.

happened in 1990 and 2002, respectively. Serious spring-summer large-area drought occurred in 1992 and summer-autumn large-area drought occurred in 1997, respectively. It can be seen that time-continuous large-area droughts mainly took place after the 1970s in Shandong province, revealing that time-continuous droughts were steadily increasing with time during the study period. However, it is also found that the linear changing tendencies were not obvious in the annual and seasonal PDCA in Shandong province by carrying out

the F significance test with the confidence level of $\alpha = 0.01$ and $\alpha = 0.05$.

4.4. Temporal Characteristics of Drought Duration. As is shown in Figure 6, the annual and seasonal drought durations in Shandong province were both fluctuated significantly from 1962 to 2008. The annual drought duration was 153 d, with the longest drought duration of 291 d in 1999 and the shortest drought duration of 8 d in 1964. There were 15 years that the annual drought duration of which was more than 183 days (half of the total days of a year), and furthermore, these years were mainly in the 1980s and 1990s. On seasonal, the annual drought durations in summer and winter were both 34 d and in spring and autumn were 45 d and 39 d, respectively. Over the past nearly 50 years, there were 24 a, 12 a, 16 a, and 12 a that annual drought duration was more than 46 d (half of the total days of one season) in spring, summer, autumn, and winter, respectively. The longest annual drought duration for spring, summer, autumn, and winter was 84 d in 1988, 76 d in 1992, 78 d in 2002, and 89 d in 1999, respectively; correspondingly, the shortest annual drought duration in spring and summer was 0 d in 1990, while in autumn and winter was 0 d in 1964 and 2003 and 1 d in 1964, respectively.

It reveals that the periodic variation of the annual and seasonal interdecadal drought duration was roughly similar, showing a cycle of 10 a approximately (Table 2). But the linear changing tendencies of drought time duration in Shandong province from 1962 to 2008 were insignificant through executing the F significance test with the confidence level of $\alpha = 0.01$ and $\alpha = 0.05$.

4.5. Temporal Characteristics of Drought Intensity. Over the past nearly 50 years, the annual drought intensity, which is referred to the arithmetic mean of the sum of all the days of CI value that are all above slight drought level for total meteorological stations for each year in Shandong province, showed a fluctuation tendency (Figure 7). The minimum CI value which indicates the strongest drought intensity was -369.93 and appeared in 1988, followed by -333.56 in 1999, and the maximum CI value conversely implying the lightest drought intensity was -15.22 in 1964. There are 19 a that annual drought intensity was above the mean intensity for total years from 1962 to 2008, and those years were mainly in the 1980s, 1990s, and early 21 s century. However, the linear tendency of annual drought intensity has not passed the F significance test with the confidence level of $\alpha = 0.01$ and $\alpha = 0.05$, revealing that the variation tendency of annual drought intensity was much complicated in Shandong province.

The linear tendencies of PDCA and drought duration for annual and seasonal and annual drought intensity were all insignificant; however, it is still obvious that the temporal drought parameters were salient in the 1980s and 1990s than in any other decades, which gives an evidence of the highlighting drought extent and influence in these two decades in Shandong province. In addition, the three temporal drought parameters were all the palest in 1964, demonstrating that the drought was lightest in this year in Shandong province. Moreover, taking into account the annual drought duration and intensity, it is found that the drought duration in 1999

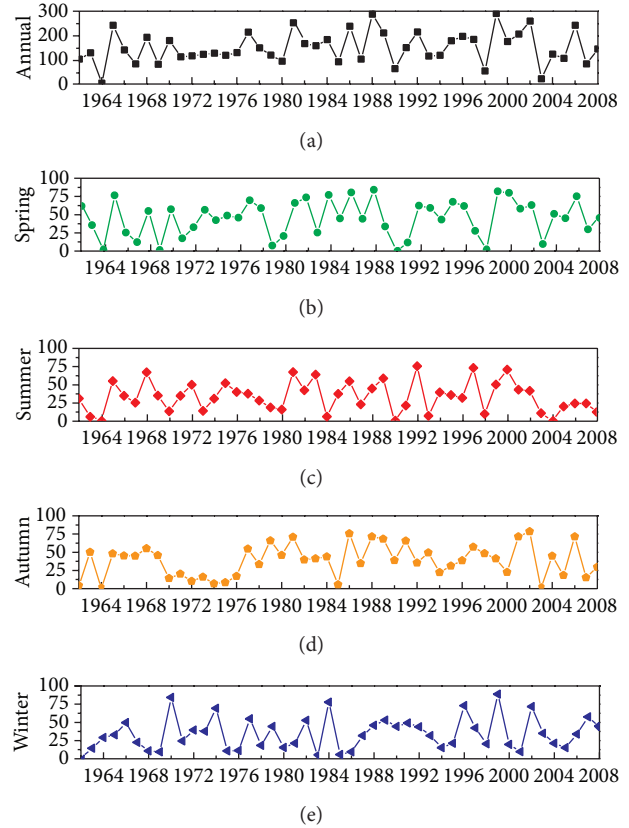


FIGURE 6: Annual, spring, summer, autumn, and winter drought duration in Shandong province.

TABLE 2: Annual and seasonal interdecadal drought duration (d).

Inter-decadal	Timescales				
	Year	Spring	Summer	Autumn	Winter
60 s	124	34	32	37	21
70 s	141	44	32	25	39
80 s	180	55	42	50	32
90 s	159	42	35	43	43
Early 21 s	153	51	32	39	34

was 291 d which was longer than 288 d in 1988, whereas the annual drought intensity was -333.56 in 1999, which was lower than -369.93 in 1988, indicating that the drought cumulative effects in 1988 were more significant than in 1999. In general, the three temporal parameters of drought, namely, PDCA, drought duration, and drought intensity, effectively depict the drought from different aspects and all of them are of great importance to the evaluation of the meteorological drought.

5. Conclusion and Discussion

Owing to various factors such as global warming, abnormality of East Asia monsoon wind, and local precipitation decreasing, the drought hazard in Shandong province is becoming more and more serious. Therefore, on the basis

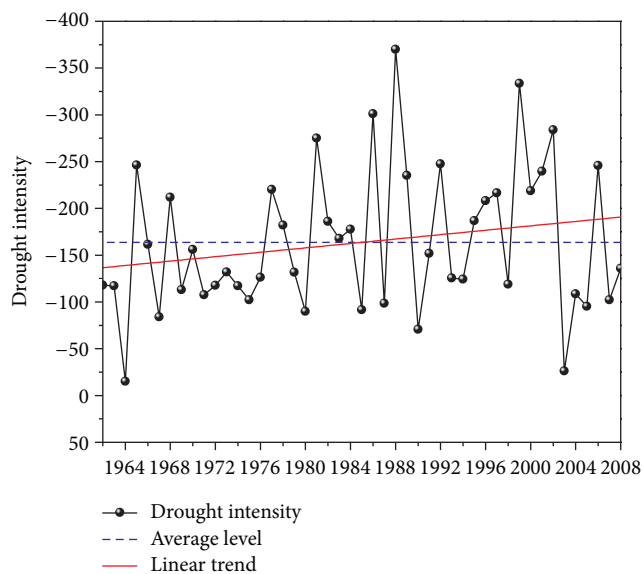


FIGURE 7: The annual drought intensity in Shandong province.

of drought analysis by adopting and calculating the CI for 18 meteorological stations, we comprehensively evaluated the spatial-temporal characteristics of meteorological drought in Shandong province from 1962 to 2008. Main conclusions are as follows.

The frequency of meteorological drought was generally high in Shandong province, and high-frequency regions are mainly concentrated in the southwest and north areas whereas low-frequency regions are generally centered in the central and southeast. The spatial pattern of drought frequency is closely related to the distribution of precipitation which decreases from southeast to northwest and temperature which increases from northeast to southwest.

The seasonal drought frequency followed such an order of spring > autumn > summer > winter. The precipitation is rare in spring but the evaporation is high due to the land surface warming rapidly, which aggravates the spring drought. In contrast, abundant rain falls in summer and low evaporation in winter owing to low temperature result in relatively low drought frequency in these two seasons.

The slight drought, moderate drought, and severe and extreme drought were all observed in Shandong province from 1962 to 2008. And the slight drought generally occurred in the northwest and southwest, but drought of other grades was observed in different areas at different timescales. Additionally, various drought grades were longest in spring but shortest in winter which was consistent with the statistics of the calculated drought parameters and, therefore, further revealed that the spring drought was much more serious than that in the other three seasons.

With respect to the temporal trend of drought frequency, it demonstrated that regions including north, south, and Jiaodong peninsula were all suffering an ascend drought over the past nearly 50 years, but the upward trend in other regions was much evident. Besides, temporal trends of multiple drought parameters including PDCA, drought duration, and drought intensity all indicated that the drought

extent and influence were very severe in the 1980s and 1990s but much mild in 1964; the time-continuous large-area droughts mainly occurred after the 1970s, and the interdecadal drought duration at annual and seasonal scales both showed a fluctuation tendency of 10 a periodic cycle approximately.

In brief, this study proves that Shandong province is a sensitive area to global climate change from the perspective of meteorological drought occurrence. What is more, the much complicated spatial-temporal characteristics of meteorological drought in Shandong province detected by this study do confirm that the regional response to climate change exhibits very significant spatial-temporal differences. The findings summed up above will in turn give us essential knowledge and guidelines on adaptation and mitigation options to address climate change. In specific, in Shandong province, critical works to be carried out are as follows: (1) to conduct more wide and more extensive monitoring and observations in terms of climate change and drought hazards, and to carry out more intensive scientific researches that focus on the dynamics of meteorological drought; (2) to strengthen drought risk management practices in the public sector, especially to choose and enact defense-oriented strategies, and to develop drought emergency plans and measures at the same time; (3) to maintain and make use of the ecosystem functions and services in terms of drought risk defense and water conservation by protecting and restoring ecosystems in ecocritical areas and drought prone areas; (4) to investigate, choose, develop, and promote effective measures of drought defense and prevention among agricultural, industrial, and energy sectors and people's lives, such as dry farming and water-saving agriculture, green-water utilization technologies, industrial water-saving technologies, and domestic water conservation technologies; (5) to promote public education and to motivate public participation with respect to drought defense and prevention, and so on.

Conflict of Interests

The authors declare that there is no conflict of interests regarding the publication of this paper.

Acknowledgments

This research was financially supported by the CAS Strategic Priority Research Program (Grant no. XDA05130703), the Key Research Program of the Chinese Academy of Sciences (Grant no. KZZD-EW-14), and the Research Program of Shandong Association for Science & Technology (Grant no. 20130202). The authors appreciate the reviewers and editors for the positive remarks and insightful comments as well as suggestions.

References

- [1] R. Alley, T. Berntsen, N. L. Bindoff et al., *Climate Change 2007: The Physical Science Basis, Summary for Policy Makers*, Intergovernmental Panel on Climate Change, 2007.

- [2] A. K. Mishra and V. P. Singh, "A review of drought concepts," *Journal of Hydrology*, vol. 391, no. 1-2, pp. 202–216, 2010.
- [3] N. Zeng, "Drought in the Sahel," *Science*, vol. 302, no. 5647, pp. 999–1000, 2003.
- [4] H. Ezzine, A. Bouzuane, and D. Ouazar, "Seasonal comparisons of meteorological and agricultural drought indices in Morocco using open short time-series data," *International Journal of Applied Earth Observation and Geoinformation*, vol. 26, pp. 36–48, 2014.
- [5] S. Agrawala, M. Barlow, H. Cullen, and B. Lyon, *The Drought and Humanitarian Crisis in Central and Southwest Asia: A Climate Perspective*, International Research Institute (IRI) for Climate and Society, 2001.
- [6] X. K. Zou, P. M. Zhai, and Q. Zhang, "Variations in droughts over China: 1951–2003," *Geophysical Research Letters*, vol. 32, no. 4, Article ID L04707, 2005.
- [7] S. Demuth and K. Stahl, *Assessment of the Regional Impact of Droughts in Europe. Final Report to the European Union*, Institute of Hydrology, University of Freiburg, Freiburg, Germany, 2001.
- [8] B. Lehner, P. Döll, J. Alcamo, T. Henrichs, and F. Kaspar, "Estimating the impact of global change on flood and drought risks in Europe: a continental, integrated analysis," *Climatic Change*, vol. 75, no. 3, pp. 273–299, 2006.
- [9] E. R. Cook, R. Seager, M. A. Cane, and D. W. Stahle, "North American drought: reconstructions, causes, and consequences," *Earth-Science Reviews*, vol. 81, no. 1-2, pp. 93–134, 2007.
- [10] K. E. Logan, N. A. Brunsell, A. R. Jones, and J. J. Feddema, "Assessing spatiotemporal variability of drought in the U.S. central plains," *Journal of Arid Environments*, vol. 74, no. 2, pp. 247–255, 2010.
- [11] A. Wang, D. P. Lettenmaier, and J. Sheffield, "Soil moisture drought in China, 1950–2006," *Journal of Climate*, vol. 24, no. 13, pp. 3257–3271, 2011.
- [12] E. Lu, Y. Luo, R. Zhang, Q. Wu, and L. Liu, "Regional atmospheric anomalies responsible for the 2009–2010 severe drought in China," *Journal of Geophysical Research D: Atmospheres*, vol. 116, no. 21, Article ID D21114, 2011.
- [13] Q. Zhang, *Drought and Its Impacts*, China Climate Impact Assessment, China Meteorol Press, Beijing, China, 2003.
- [14] D. Mihajlović, "Monitoring the 2003–2004 meteorological drought over Pannonian part of Croatia," *International Journal of Climatology*, vol. 26, no. 15, pp. 2213–2225, 2006.
- [15] T. B. McKee, N. J. Doesken, and J. Kleist, "The relationship of drought frequency and duration to time scales," in *Proceedings of the 8th Conference on Applied Climatology*, American Meteorological Society, Anaheim, Calif, USA, January 1993.
- [16] T. B. McKee, N. J. Doesken, and J. Kleist, "Drought monitoring with multiple time scales," in *Proceedings of the 9th Conference on Applied Climatology*, pp. 233–236, American Meteorological Society, Dallas, Tex, USA, January 1995.
- [17] C. S. Rim, "The implications of geography and climate on drought trend," *International Journal of Climatology*, vol. 33, no. 13, pp. 2799–2815, 2013.
- [18] W. C. Palmer, "Meteorological drought," Research Paper 45, US Department of Commerce, Weather Bureau, 1965.
- [19] A. Dai, K. E. Trenberth, and T. Qian, "A global dataset of Palmer Drought Severity Index for 1870–2002: relationship with soil moisture and effects of surface warming," *Journal of Hydrometeorology*, vol. 5, no. 6, pp. 1117–1130, 2004.
- [20] F. N. Kogan, "Global Drought Watch from Space," *Bulletin of the American Meteorological Society*, vol. 78, no. 4, pp. 621–636, 1997.
- [21] S. M. Quiring and S. Ganesh, "Evaluating the utility of the Vegetation Condition Index (VCI) for monitoring meteorological drought in Texas," *Agricultural and Forest Meteorology*, vol. 150, no. 3, pp. 330–339, 2010.
- [22] Q. Zhang, X. K. Zou, and F. J. Xiao, *Meteorological Drought Level GB/T20481-2006*, Standards Press, Beijing, China, 2006.
- [23] C. H. Zhao, X. Z. Deng, Y. W. Yuan, H. Yan, and H. Liang, "Prediction of drought risk based on the WRF model in Yuannan province of China," *Advances in Meteorology*, vol. 2013, Article ID 295856, 9 pages, 2013.
- [24] X. K. Zou, G. Y. Ren, and Q. Zhang, "Droughts variations in China based on a compound index of meteorological drought," *Climatic and Environmental Research*, vol. 15, no. 4, pp. 371–378, 2010 (Chinese).
- [25] T. Zhang, B. Zhang, Y. Wang, X. Liu, M. An, and J. Zhang, "Drought characteristics in the Shiyang River Basin during the recent 50 years based on a composite index," *Acta Ecologica Sinica*, vol. 33, no. 3, pp. 975–984, 2013 (Chinese).
- [26] Y. Bao, C. Meng, S. Shen, X. Qiu, P. Gao, and C. Liu, "Temporal and spatial patterns of droughts for recent 50 years in Jiangsu based on meteorological drought composite index," *Acta Geographica Sinica*, vol. 66, no. 5, pp. 599–608, 2011 (Chinese).
- [27] D. Q. Xue, J. G. Wang, X. T. Wang, and D. L. Gong, "Characteristic analysis of change into drought in Shandong Province," *Journal of Natural Disasters*, vol. 16, no. 3, pp. 60–65, 2007 (Chinese).
- [28] Z. Gao, W. Gao, and N. B. Chang, "Integrating temperature vegetation dryness index (TVDI) and regional water stress index (RWSI) for drought assessment with the aid of LANDSAT TM/ETM+images," *International Journal of Applied Earth Observation and Geoinformation*, vol. 13, no. 3, pp. 495–503, 2011.
- [29] H. H. Jiang, "Variance features and correlativity analysis of drought disasters in Shandong Province," *Journal of Catastrophology*, vol. 15, no. 3, pp. 51–55, 2000 (Chinese).
- [30] L. Du, Q. Tian, Y. Huang, and J. Liu, "Drought monitoring based on TRMM data and its reliability validation in Shandong province," *Transactions of the Chinese Society of Agricultural Engineering*, vol. 28, no. 2, pp. 121–126, 2012 (Chinese).
- [31] L. Du, Q. Tian, T. Yu et al., "A comprehensive drought monitoring method integrating MODIS and TRMM data," *International Journal of Applied Earth Observation and Geoinformation*, vol. 23, no. 1, pp. 245–253, 2013.
- [32] B. Gao, J. Z. Fan, Y. G. Jing et al., "Variation characteristics of sunshine hours and its reason analysis over loess plateau of Shaanxi," *Meteorological and Environmental Research*, vol. 2, no. 10, pp. 44–49, 2011.

Review Article

The Review of GRACE Data Applications in Terrestrial Hydrology Monitoring

**Dong Jiang,¹ Jianhua Wang,² Yaohuan Huang,¹
Kang Zhou,³ Xiangyi Ding,² and Jingying Fu¹**

¹ Institute of Geographical Sciences and Natural Resources Research, Chinese Academy of Sciences, Beijing 100101, China

² State Key Laboratory of Simulation and Regulation of Water Cycle in River Basin, Department of Water Resources, China Institute of Hydropower & Water Resources Research, Beijing 100038, China

³ Computer Network Information Center, Chinese Academy of Sciences, Beijing 100190, China

Correspondence should be addressed to Jianhua Wang; wjh@iwhr.com and Yaohuan Huang; huangyh@reis.ac.cn

Received 14 February 2014; Revised 13 May 2014; Accepted 20 May 2014; Published 5 June 2014

Academic Editor: Dawei Han

Copyright © 2014 Dong Jiang et al. This is an open access article distributed under the Creative Commons Attribution License, which permits unrestricted use, distribution, and reproduction in any medium, provided the original work is properly cited.

The Gravity Recovery and Climate Experiment (GRACE) satellite provides a new method for terrestrial hydrology research, which can be used for improving the monitoring result of the spatial and temporal changes of water cycle at large scale quickly. The paper presents a review of recent applications of GRACE data in terrestrial hydrology monitoring. Firstly, the scientific GRACE dataset is briefly introduced. Recently main applications of GRACE data in terrestrial hydrological monitoring at large scale, including terrestrial water storage change evaluation, hydrological components of groundwater and evapotranspiration (ET) retrieving, droughts analysis, and glacier response of global change, are described. Both advantages and limitations of GRACE data applications are then discussed. Recommendations for further research of the terrestrial water monitoring based on GRACE data are also proposed.

1. Introduction

Intensified impact of human activities and global change inevitably lead to the changes in the water cycle, including the spatial and temporal distribution and the total amount of water resources [1, 2]. Terrestrial hydrology, which is an important indicator in global change, affects the global climate system in energy, water, and biogeochemical [3]. Traditional monitoring of terrestrial hydrology mainly depends on site measurements or model simulations, which is costly and time-consuming. Furthermore, for the scale effects of the conversion from observation points to large region, additional error will be brought into spatially continuous data obtained by statistical interpolation methods. The accuracy of interpolation results may significantly decrease in areas far away from observation sites. Hydrological models and land surface models solve the problem of simulation of terrestrial hydrology on the plane scale to some degree. However, the lack of systematic global fine-scale hydrological data

increases the model uncertainty and lowers the simulation accuracy. This restricts the practical application of hydrological models and land surface models in the monitoring of terrestrial hydrology. With the rapid development of remote sensing technology, remote sensing holds significant potential to the regional hydrological researches. By offering a useful and cost-effective approach to rapidly monitor terrestrial hydrological parameters, remote sensing technology has been widely used in hydrology. Recently, combination models of remote sensing technology, observation network, and hydrological models have been common in terrestrial hydrology studies. However, imaging satellite techniques and satellite altimetry can only be used in the monitoring of surface water that represents just one component of total water storage. They can be hardly applied in the monitoring of other components of terrestrial water such as soil water and groundwater, which impeded further applications of these technologies in terrestrial hydrology.

Launched in March 2002, the Gravity Recovery and Climate Experiment (GRACE) can provide an operational product in the form of global gravity fields every ~ 30 days [4]. After several gravity effects have been released (e.g., atmospheric mass variations and ocean tides), precise observations of the time-series global gravity field changes make the spatial monitoring of water storage changes at large scale such as basins possible. Through 10 years of development, GRACE satellite data processing and corresponding TWS retrieval algorithms are improved continuously. They are able to detect the changes of TWS within the accuracy of 1.5 cm on a wide range of spatial scales and seasonal time scales [5]. Compared to imagery remote sensing methods, they provide alternative technical methods for the estimation of glaciers, surface snow, soil water, surface water, groundwater, evaporation, and other components in the terrestrial hydrological system. It provides a new technique for the large-scale monitoring of terrestrial water cycle. The objective of this paper is to present an overview of GRACE data applications in terrestrial hydrology monitoring, including GRACE data processing methods and TWS change retrieval and their application in terrestrial hydrology and related fields.

2. GRACE Data

GRACE gravity satellite program was jointly developed by the National Aeronautics and Space Administration (NASA) of the United States and the German Aerospace Center (DLR) with the objective of providing spatiotemporal variations of the Earth's gravity field. The GRACE satellite program can be also used to detect the atmosphere and ionosphere environment. The US Jet Propulsion Laboratory (JPL) is responsible for the project management of the GRACE gravity satellite program. Monthly gravity field solutions are computed at the University of Texas at Austin Center for Space Research (CSR), the German Research Centre for Geosciences Potsdam (GFZ), JPL, Groupe de Recherche de Geodesie Spatiale (GRGS), and the Delft Institute of Earth Observation and Space Systems (DEOS) as well as Delft University of Technology, among others [4, 6–8]. GRACE utilizes a state-of-the-art technique to trace the spatiotemporal gravity field with an increased sensitivity by tracking the micrometer-precise intersatellite range and range-rate observations between two coplanar, low altitude (300 km \sim 500 km) satellites and the distance between which is about 220 km. To precisely measure the distance changes between two satellites at micron meter level accuracy, a K-band ranging (KBR) system based on carrier phase measurements in the K (26 GHz) and Ka (32 GHz) frequencies is provided. Besides, four key instrumentations of a GPS receiver (space-proofed multichannel, two-frequency), capacitive accelerometer, laser retroreflector (LRR), and star camera are equipped on board of each GRACE satellite [4, 7].

By analyzing the relationship between orbits and forces of GRACE satellites, the Earth's gravity field variety is estimated based on the dynamic equations of satellites motion. It monitors the time-varying characteristics of long-wavelength gravity field on a 15 \sim 30-day or longer time scale. Large-scale

mass redistribution (mass distribution changes over time) in the Earth system reflects the interaction between substances of various forms in the Earth's internal system (atmosphere, oceans and solid crust, viscous mantle, liquid outer core, and solid inner core), which are the important subjects of Earth sciences. Compared to the average Earth's gravity field, the time-varying quantity of the gravity field is very small, but it contains important geophysical information. It reveals the movement, distribution, and changes of all substances in the Earth system and reflects the interaction between the atmosphere, terrestrial water, oceans, and the solid Earth [6].

The time variation of global gravity field caused by the influence of solid Earth (including the inner core and the outer core) is mainly manifested on a 10-year or a longer time scale. However, temporal variation of gravity is mainly caused by the redistribution influence of atmosphere, oceans, and water storages in the surface fluid envelopes of the earth on a seasonal or interannual time scale [9, 10]. The gravity effects of tides (solid Earth, oceans, and atmosphere) and nontidal (atmosphere and oceans) are reduced in the data processing of GRACE gravity field model. Therefore, by excluding the errors in gravity field model and the atmosphere and oceans models, GRACE time-varying gravity field reflects the nonatmospheric and nonocean mass variations due to water mass variations on the continental area. On a seasonal or shorter time scale, it provides information on changes in terrestrial water storage in large river basin [11].

3. Hydrological Applications

3.1. TWS Changes Monitoring. The TWS is the most direct hydrological parameter obtained by GRACE monitoring. For the main goal of GRACE satellite is to monitor the Earth's gravity field variations, early researches are focused on the feasibility and accuracy of TWS retrieval from GRACE data. Wahr et al. [11] pointed out that the GRACE-based TWS retrieval required the consideration of the impacts from short-wave noises and leakage errors, and the TWS retrieval result is valid for large-scale river basins. Further research of Rodell and Famiglietti showed that TWS accuracy could be improved by increasing the monitoring temporal interval and spatial resolution of the monitored area [12, 13]. For regions larger than 200000 km², the TWS changes with intervals on month and longer time scale can be monitored, and the accuracy can reach 1.5 cm and above.

The application of GRACE-based TWS changes data is mainly based on the combination of hydrological models and land surface models. GRACE-based TWS retrieval results offer spatial and temporal distribution of vertically integrated water storage (surface water, soil, groundwater, and snowpack) in large river basins. So the errors due to the use of indirect indicators such as the flow rate and precipitation in some hydrological models can be reduced. In initial researches, the GRACE-based TWS is only considered as a reference to the simulation results from hydrological models (such as GDLAS and CPC), which does not involve the uncertainty of hydrological models in the simulation process. Hu et al. [10] proposed that water storage changes in

Yangtze River could reach a magnitude of 3.4 cm equivalent water height, with the maximum occurring in the spring and early autumn. Using 5-year GRACE-based TWS change data in China, Zhong et al. [14] pointed out that the water storage in the north-central region of China diminished at an annual rate of 2.4 cm water equivalent height. By combining GRACE and GPS network observation data, Wang et al. [15] achieved precise retrieval of TWS change in Nordic region and North America. Their studies showed that, over the past decade, a sharp increase appeared in the water storage in North America and Scandinavia and a water recovery process is underway.

With further study, GRACE data is now considered as an important parameter to assess and improve hydrological model simulation. Swenson and Milly [16] and Syed et al. [17] used GRACE data to verify and improve TWS simulation of five climate models and the Global Land Data Assimilation System (GLDAS), respectively. Niu and Yang [18] and Ngo-Duc et al. [19] used GRACE data for the result verification of common land surface model (CLM) of NCAR and ORCHIDEE and corrected the CLM by applying GRACE-based TWS changes data.

Various quantitative analyses between hydrological models and GRACE-based TWS showed that the two simulation results of large areas are in good consistency on a seasonal or longer time scale [16, 20, 21]. Time-series analyses of South and North America, Southeast Asia, the Ganges River Basin, Africa, Eurasia, and other large-scale regions all showed that GRACE-based TWS reflected a significant seasonal variation. However, given the limitations in the spatial resolution of GRACE data, the consistency of hydrological models and GRACE data in smaller areas is not satisfactory [22]. Excluding the errors of GRACE-based TWS change retrieval, the inconsistency is mainly due to the simulation errors of various TWS components from hydrological models. For example, the generalized deviation in estimating the important elements such as groundwater, surface water, and soil water storage by using hydrological models resulted in smaller magnitudes in TWS changes. The errors in the simulation of rainfall, convergence, and other hydrological processes generated phase deviation in TWS changes time series [17, 23, 24]. In addition, by combination of the measured data of rainfall, recharge, soil water, and groundwater, GRACE-based TWS was used for water storage variation of basin on interannual, annual, seasonal, and monthly time scales [25, 26].

3.2. Hydrological Components Evaluation. With the improvement of GRACE-based TWS change accuracy, the GRACE data is further used in hydrology and water resources research. For specific areas, TWS changes can be expressed as [10]

$$\frac{dW}{dt} = P - E - R, \quad (1)$$

where dW/dt represents TWS changes, and the corresponding equivalent water height can be obtained from GRACE. P represents precipitation, E represents evapotranspiration,

and R represents surface runoff. By combining GRACE-based TWS changes, hydrological models, and the measured data, the water storage components including groundwater, soil water, ET, and $P - E$ can be estimated, respectively.

Groundwater estimation is difficult in remote sensing applications in hydrology. Optical remote sensing methods can only combine measured data with spectral data to construct an empirical model for the estimation of groundwater changes, whose groundwater retrieval accuracy is poor. Considering the contribution of groundwater changes to TWS variation, groundwater remote sensing using GRACE was feasible by combination with ancillary measurements of surface waters and soil moisture. Rodell and Famiglietti [27] firstly used GRACE-based TWS change data, soil water, and other auxiliary data to analyze the possibility of monitoring groundwater changes. Swenson et al. [25] studied the relation between measured value of groundwater plus soil water and GRACE-based TWS changes and presented the possibility and sources of error in groundwater estimation based on GRACE data on multiple time scales. Strassberg et al. [28] compared the spatiotemporal correlation between GRACE-based TWS changes and hydrological model simulations and field monitoring data and proposed the uncertainty of GRACE-based groundwater retrieval. The above studies suggest that, for aquifers larger than 450000 km², the accuracy of GRACE-based groundwater can reach 8.7 mm. Rodell et al. applied GRACE data to the groundwater subsidence monitoring in India and found that excessive irrigation and human activities caused the groundwater in the northwest provinces of India to decline at an annual rate of 3.0 cm~4.0 cm [29].

Evapotranspiration (ET) is an important process parameter to studies of hydrology, which is difficult to measure at a regional or continental scale. Although ET can be indirectly estimated using remote sensing data based on empirical models, energy balance models, or physical models (e.g., Penman-Monteith equation), recent remote-sensed ET estimation is far from satisfactory [30]. For ET is a complex process that related to many variables, its estimation uncertainty based on remote sensing data brings errors to ET retrieval results. Based on terrestrial water balance at scale of river basin, changes of regional ET can be estimated by combining TWS change from GRACE with observed precipitation (P) and runoff data (R). Rodell et al. [31] first used the measured precipitation and runoff data to verify the feasibility of GRACE-based ET retrieval. However, the overdependence on measured data restricts the applicability of this method. Therefore, Ramillien et al. [32] improved this algorithm by using the simulated runoff data from hydrological model. The time-series analysis showed that the ET estimation and WGHM simulation were in good consistency. However, uncertainty of GRACE-based ET estimation increases for its overdependence on accuracy of hydrological model simulated variables such as runoff. In addition, Swenson and Wahr [33] combined GRACE-based TWS changes together with the measured runoff data to estimate the difference between precipitation and evapotranspiration ($P - E$). By comparing with $P - E$ results of a land surface model (GLDAS-Noah),

they found that the errors of GLDAS-Noah estimation are mainly due to model force parameter of precipitation.

3.3. Drought Analysis. Based on time-series analysis of GRACE-based TWS change with high temporal resolution, extreme hydrological disasters can be monitored and alarmed. Droughts for regional and time-series water storage deficit are the most serious natural hazards that can lead to crop losses and economic havoc in many areas. For droughts can be regarded as terrestrial water storage (TWS) changes that are related to integrated bulk variables, analysis relying upon subcomponents (e.g., precipitation) or proxies (e.g., NDVI and CWSI) of TWS is insufficient. Herewith, another hydrological application of GRACE is severe droughts analysis. Combined with the measurements and hydrological model simulations, Leblanc et al. [34] used GRACE data to detect droughts in Southeastern Australia between 2001 and 2008. Based on time-series analysis of TWS changes in summers from 2002 to 2007, 2005 extreme drought event in the Amazon river basin was detected [35], which was regarded as the worst in over a century. GRACE data is more sensitive to droughts than data-assimilating climate and land surface models such as NECEP and GLDAS, which demonstrated the unique potential of GRACE in monitoring large-scale severe drought events. Validated by two independent hydrological estimates of GLDAS and ECMWF and direct gravity observations from superconducting gravimeters, the 2003 excess terrestrial water storage depletion was observed from GRACE, which can be related to the record-breaking heat wave that occurred in central Europe in 2003 [36]. It indicated that GRACE data can be used in heat wave disaster monitoring and evaluation, whose essence is heat wave caused droughts analysis. Combining with imagery remote sensing methods, Frappart and Wilson et al. applied GRACE data to flood monitoring in several flood zones such as the Mekong River Basin and the Amazon River Basin [37, 38]. However, compared to droughts, the water storage changes based on GRACE data of extreme floods are less responsive, which will bring more uncertainty in GRACE-based floods analysis [39].

3.4. Glacier Mass Balance Detection. Driven by global change and population pressure, accelerating of glaciers melting and sea level rise has been a serious global ecological problem. GRACE time-variable gravity field enabled direct measurement of mass loss rates of both mountain glacier and polar glacier systems. As noted by Wouters et al. the GRACE solutions can be used to allow regional estimation of trends, though assessing the mass loss to be dominated by summer events rather than by a linear trend [40]. GRACE-based glacier mass melting volume and rate estimation of Antarctic and Greenland indicate that accelerating polar glacier melting contributes greatly to the current eustatic sea level rise [41–43]. Gardner et al. have also found a rapidly increasing mass loss in the Canadian Arctic Archipelago (CAA) for the period 2004–2009 [44]. Ice loss rate estimation on glaciers of Asia, Alaska, and other global mountains based on GRACE data also agrees with the global tendency of

accelerating glacial loss. Accelerated melting of mountain glaciers worldwide might be contributing to the global sea level rise by 0.73 ± 0.10 mm/yr [45, 46]. Moreover, GRACE-based TWS change can be used for researches of different climate variability impact [47, 48] whereas, for the postglacial rebound effects and unique set of gravity data GRACE mission provided, ice sheet mass change estimation includes large uncertainties [49]. Mass change rates estimated by different GRACE solutions may vary by a factor of two or more. So the glacier mass balance detection needs considerable processing to yield usable mass change data [49].

4. Discussion and Conclusions

Through ten years of development, GRACE data has been widely applied in terrestrial hydrology monitoring. Gravity satellite provides new data sets for hydrology researches based on remote sensing technology. Compared with other kinds of hydrological schemes, GRACE can provide realistic spatiotemporal variations of vertically integrated measurement of water storage (groundwater, soil moisture, surface water, snow water, vegetation water, etc.) at the precision of tens of mm of equivalent water height at large scale. However, the hydrological monitoring based on GRACE data needs further research, for example, retrieval accuracy improvement, more quantitative analyses rather than qualitative analyses, and so forth. The focus of future development includes the following aspects.

(1) *Improving the Accuracy of Gravity Satellite Measurements.* Because of the limitations of GRACE satellite sensors in orbital altitude, vertical gravity gradient measurements, high frequency signal aliasing, and accurate measurement of time-varying gravity signals, the accuracy and spatial resolution of time-varying Earth gravity field signals at medium and long wavelength of GRACE is low, which reduced the TWS change retrieval accuracy. Therefore, the development of key technology in gravity satellite sensors to improve accuracy and spatial resolution of satellite monitored gravity field is the basis for a wider application in terrestrial hydrology monitoring.

(2) *Water Storage Retrieval Models Research.* Recently, the appropriate spatial resolution for GRACE-based TWS change is 400 km, and the data accuracy is generally 1.5 cm. Limited by recent constraints of GRACE satellite, improvement of retrieval models is the only method for spatial resolution and accuracy retrieval of TWS increases. For example, it is feasible to improve TWS accuracy by the atmosphere and ocean models improvement in data preprocessing, reducing the gravity field changes noises caused by factors unrelated to terrestrial water such as tides and circulation of atmosphere and ocean. In addition, by applying different filtering methods such as anisotropic Gaussian filtering and spherical radial basis function filtering, wavelet analysis in different research areas can also improve the spatial resolution and accuracy of TWS retrieval. Water storage retrieval techniques involve various aspects (e.g., GRACE data preprocessing, gravity field retrieval, and TWS changes estimation) of the conversion

of GRACE gravity field data to TWS changes, which are all important in TWS retrieval improvement.

(3) *Further Combination of GRACE Data with Associated Hydrological Models.* For GRACE-based TWS changes retrieval does not involve the hydrological mechanisms, it is necessary to complement GRACE-based TWS by hydrological models for furthering its application in terrestrial hydrology monitoring. Further combination of GRACE and hydrological models needs resolving their consistencies of space, time, and component. Spatial consistency can be solved by adjusting the calculation unit of hydrological models to reflect the spatial variability (such as distributed hydrological models). Temporal consistency requires analysis of upscaling GRACE data and downscaling hydrological models simulation. Component consistency can be achieved by GRACE-based TWS signals subdivision or revising parameters of hydrological models to TWS. Through space, time, and component consistency improvement, the gravity field data and measured data together can become basic dataset to force hydrological models in the future.

Appendices

A. Water Storage Change Retrieval

The changes in terrestrial water storage result in mass redistribution in the Earth's system, thereby causing changes in the gravity field. For a fixed continental region, the changes in water storage (including soil water and surface snow) come from rainfall, evapotranspiration, river transportation, and deep underground infiltration. Except the rainfall which can cause increased water storage, the remaining three processes all reduce it [10]. Using the FG5 absolute gravimeter, Zhang et al. [50] measured the gravity change of nearly $10^{-7} \text{ m}\cdot\text{s}^{-2}$ at the Wuhan University site before and after a rainstorm, which clearly shows the influence of terrestrial water variation on gravity. The Earth's gravity field can be expressed as geoid:

$$N(\theta, \lambda) = a \sum_{n=0}^{\infty} \sum_{m=0}^n [\bar{C}_{nm} \cos(m\lambda) + \bar{S}_{nm} \sin(m\lambda)] \bar{P}_{nm}(\cos\theta), \quad (\text{A.1})$$

where n and m are harmonic degree and order of the gravity field, respectively; a is the Earth's equatorial radius (about 6,371 km); θ and λ are colatitudes (the difference between 90° and latitude) and longitude; \bar{C}_{nm} and \bar{S}_{nm} are spherical harmonic coefficients (dimensionless); \bar{P}_{nm} is the normalized associated Legendre functions. The maximum value N of the order n of ideal gravity field should be infinite ($N \sim \infty$), while the actual order of spherical harmonic coefficients obtained by the gravity satellite has a finite value ($N < \infty$) and the spatial resolution of gravity field data is estimated approximately to be $\pi a/N$ [51]. Geoid height changes ΔN

caused by the movement of substances on the Earth's surface can be expressed as

$$\Delta N(\theta, \lambda) = a \sum_{n=0}^{\infty} \sum_{m=0}^n [\Delta \bar{C}_{nm} \cos(m\lambda) + \Delta \bar{S}_{nm} \sin(m\lambda)] \bar{P}_{nm}(\cos\theta), \quad (\text{A.2})$$

where $\Delta \bar{C}_{nm}$ and $\Delta \bar{S}_{nm}$ are the changes of n -degree m -order spherical harmonic coefficients of geoid and can be expressed as [5, 52]

$$\begin{aligned} & \begin{Bmatrix} \Delta \bar{C}_{nm} \\ \Delta \bar{S}_{nm} \end{Bmatrix} \\ &= \frac{3}{4\pi a \rho_a (2n+1)} \\ & \times \int \Delta \rho(r, \theta, \lambda) \bar{P}_{nm}(\cos\theta) \left(\frac{r}{a}\right)^{n+2} \begin{Bmatrix} \cos(m\lambda) \\ \sin(m\lambda) \end{Bmatrix} \sin\theta d\theta d\lambda dr, \end{aligned} \quad (\text{A.3})$$

where ρ_a is the average density of the Earth (5517 kg/m^3) and $\Delta \rho(r, \theta, \lambda)$ is the change of bulk density at a particular location. In gravity field inversion, because the height change of substances on the Earth's surface H is relatively small compared to the Earth's average radius a in gravity field retrieval ($(r/a) \approx 1$), the changes of the gravity field directly caused by the surface mass can be expressed as

$$\begin{aligned} & \begin{Bmatrix} \Delta \bar{C}_{nm} \\ \Delta \bar{S}_{nm} \end{Bmatrix}_{\text{surf}} \\ &= \frac{3}{4\pi a \rho_a (2n+1)} \\ & \times \int \Delta \sigma(\theta, \lambda) \bar{P}_{nm}(\cos\theta) \begin{Bmatrix} \cos(m\lambda) \\ \sin(m\lambda) \end{Bmatrix} \sin\theta d\theta d\lambda, \end{aligned} \quad (\text{A.4})$$

where $\Delta \sigma$ is surface density change $\Delta \sigma = \int \Delta \rho(r, \theta, \lambda) dr$. Furthermore, the surface mass variation in loads will cause deformation to the solid Earth, which in turn can indirectly cause variations to the gravity field. This can be expressed as [5, 52]

$$\begin{aligned} & \begin{Bmatrix} \Delta \bar{C}_{nm} \\ \Delta \bar{S}_{nm} \end{Bmatrix}_{\text{soild}} \\ &= \frac{3k'_n}{4\pi a \rho_a (2n+1)} \\ & \times \int \Delta \sigma(\theta, \lambda) \bar{P}_{nm}(\cos\theta) \begin{Bmatrix} \cos(m\lambda) \\ \sin(m\lambda) \end{Bmatrix} \sin\theta d\theta d\lambda, \end{aligned} \quad (\text{A.5})$$

where k'_n is load LOVE number of coefficients, and the specific value of k'_n can be found in relevant literature [11].

Thus, the change of the Earth's gravity field caused by mass variations on the Earth's surface is given by

$$\begin{aligned} \begin{Bmatrix} \Delta \bar{C}_{nm} \\ \Delta \bar{S}_{nm} \end{Bmatrix} &= \begin{Bmatrix} \Delta \bar{C}_{nm} \\ \Delta \bar{S}_{nm} \end{Bmatrix}_{\text{surf}} + \begin{Bmatrix} \Delta \bar{C}_{nm} \\ \Delta \bar{S}_{nm} \end{Bmatrix}_{\text{soild}} \\ &= (1 + k'_n) \begin{Bmatrix} \Delta \bar{C}_{nm} \\ \Delta \bar{S}_{nm} \end{Bmatrix}_{\text{surf}}. \end{aligned} \quad (\text{A.6})$$

If the spherical harmonic expansion is performed on the surface density change $\Delta\sigma$, then

$$\begin{aligned} \Delta\sigma(\theta, \lambda) &= a\rho_w \sum_{n=0}^{\infty} \sum_{m=0}^n [\widehat{C}_{nm} \cos(m\lambda) + \widehat{S}_{nm} \sin(m\lambda)] \bar{P}_{nm}(\cos\theta), \end{aligned} \quad (\text{A.7})$$

where ρ_w is the density of water and $\Delta\sigma/\rho_w$ can be considered as mass variation on the Earth's surface expressed in water equivalent height. Wahr et al. [5] proposed that

$$\begin{Bmatrix} \Delta \widehat{C}_{nm} \\ \Delta \widehat{S}_{nm} \end{Bmatrix} = \frac{\rho_a}{3\rho_w} \frac{2n+1}{1+k'_n} \begin{Bmatrix} \Delta \bar{C}_{nm} \\ \Delta \bar{S}_{nm} \end{Bmatrix}. \quad (\text{A.8})$$

The surface density change $\Delta\sigma$ can be calculated using the following equation:

$$\begin{aligned} \Delta\sigma(\theta, \lambda) &= \frac{a\rho_a}{3} \sum_{n=0}^{\infty} \sum_{m=0}^n \frac{2n+1}{1+k'_n} [\bar{C}_{nm} \cos(m\lambda) + \bar{S}_{nm} \sin(m\lambda)] \\ &\quad \times \bar{P}_{nm}(\cos\theta). \end{aligned} \quad (\text{A.9})$$

For ocean and atmosphere mass variations are removed based on Parallel Ocean Program (POP) model, the above equation is the basic equation for the retrieval of surface mass variations based on spatiotemporal changes gravity field. The Earth's surface density changes can be derived from the changes of gravity field coefficients obtained from GRACE satellites.

B. Evaluation Errors

Currently, the latest available GRACE dataset product is the RL05. The accuracy of data provided by CSR and GFZ is better than that provided by JPL. The evaluation errors of GRACE are brought from satellite instruments measurement, retrieval models, and other factors as follows.

- (1) Gravity field data measured by GRACE satellite may be contaminated by satellite measurement errors for the influence of satellite orbit, satellite K-band ranging, and accelerometer measurement [20]. The satellite measurement errors also include poor accuracy of C20 due to the insensitivity of track geometry to

the gravity field's low degree gravitational variations [5, 20]. It is generally released with removing variation of C20 [10] or replacing it by satellite laser ranging (SLR) substitution [20]. In addition, the missing of first-degree spherical harmonic coefficients will also bring error to GRACE. It can commonly be resolved by substituting value calculated from the term of the seasonal changes of the Earth's mass center [53, 54] or ignoring its impact [55].

- (2) In theory, the retrieval of gravity field variation needs to use spherical harmonic coefficients of all degrees from 0 to infinity. However, gravity satellites can only provide definite order data. So the surface density change $\Delta\sigma$ in retrieval models is treated by spherical harmonic expansion to definite orders. For the impact of high-order terms on the Earth's surface density change $\Delta\sigma$ cannot be ignored, it results in truncation errors in gravity field retrieval. RL05 water storage data is estimated by CSR using a retrieval model truncated to degree 60 [8]. Zhu et al. (2008) compared the global water storage retrieval results using models truncated to 15 degrees, 20 degrees, 35 degrees, and 60 degrees [56]. They found that although some information of TWS change may be missing the retrieval result of TWS change became more marked with lower truncation degree. Generally, the water storage retrieval truncated to order 60 is widely adopted [17].
- (3) For terrestrial water monitoring focusing on the mass changes of a particular area (e.g., river basin), it requires the integral process on density change $\Delta\bar{\sigma} = ((\int \Delta\sigma(\theta, \lambda)u(\theta, \lambda)d\Omega)/\Omega)$. The function of regional characteristics $u(\theta, \lambda)$ is equal to 1 inside the particular area and to zero outside. The error will be brought for the discontinuity of $u(\theta, \lambda)$ in the domain of integration. In addition, for the influence of rapid increase of the errors of GRACE gravity field model coefficients with increase of spherical harmonic coefficients degree, signal leakage errors, and the striping pollution [23], filtering methods are proposed to smooth GRACE data for noise reducing, which will result in filtering errors of retrieval results. Proposed filtering methods include spatial averaging, symmetric Gaussian filtering, optimized decorrelation filtering, time-series method, global hydrological model correction method, kernel-independent component analysis, and optimal smoothing kernel method [53, 57–62]. Using filtering for the integral treatment of surface density changes can effectively remove the striping to a certain extent. However, the obtained average surface density is critical for it reduces the useful energy of geophysical signals and results in filtering errors. In addition, the existing filtering methods require the support of a priori knowledge (such as filtering radius and truncation degree). Therefore, in the actual retrieval process, the filter selection and parameter calibration require an understanding of the specific regional characteristics [60, 63].

- (4) TWS changes retrieval based on spatiotemporal variations of gravity field remains considerable uncertainty, which includes errors produced in the removal of tidal movement and the mass migration because of the atmosphere and ocean circulation [11], as well as the errors in hydrological models used for the estimation of other terrestrial water parameters [6].

Conflict of Interests

The authors declare that there is no conflict of interests regarding the publication of this paper.

Acknowledgments

This project was supported by National Natural Science Foundation of China (Grant no. 51309210) and the Chinese Academy of Sciences (Grant no. KZZD-EW-08).

References

- [1] Y. Huang, D. Jiang, D. Zhuang, Y. Zhu, and J. Fu, "An improved approach for modeling spatial distribution of water use profit—a case study in Tuhai Majia Basin, China," *Ecological Indicators*, vol. 36, pp. 94–99, 2014.
- [2] Y.-H. Huang, D. Jiang, D.-F. Zhuang, J.-H. Wang, H.-J. Yang, and H.-Y. Ren, "Evaluation of relative water use efficiency (RWUE) at a regional scale: a case study of Tuhai-Majia Basin, China," *Water Science and Technology*, vol. 66, no. 5, pp. 927–933, 2012.
- [3] J. S. Famiglietti, "Remote sensing of terrestrial water storage, soil moisture and surface waters," in *The State of the Planet: Frontiers and Challenges in Geophysics*, R. S. J. Sparks and C. J. Hawkesworth, Eds., pp. 197–207, 2004.
- [4] B. D. Tapley, S. Bettadpur, M. Watkins, and C. Reigber, "The gravity recovery and climate experiment: mission overview and early results," *Geophysical Research Letters*, vol. 31, no. 9, Article ID L09607, 2004.
- [5] J. Wahr, S. Swenson, V. Zlotnicki, and I. Velicogna, "Time-variable gravity from GRACE: first results," *Geophysical Research Letters*, vol. 31, no. 11, Article ID L11501, 2004.
- [6] A. Güntner, "Improvement of global hydrological models using GRACE data," *Surveys in Geophysics*, vol. 29, no. 4-5, pp. 375–397, 2008.
- [7] G. Ramillien, J. S. Famiglietti, and J. Wahr, "Detection of continental hydrology and glaciology Signals from GRACE: a review," *Surveys in Geophysics*, vol. 29, no. 4-5, pp. 361–374, 2008.
- [8] D. P. Chambers, "Converting 11 Release-04 Gravity Coefficients into Maps of Equivalent Water Thickness," 2007, http://grace-tellus.jpl.nasa.gov/files/GRACE-dpc200711_RL04.pdf.
- [9] M. Becker, W. Llovel, A. Cazenave, A. Güntner, and J.-F. Crétaux, "Recent hydrological behavior of the East African great lakes region inferred from GRACE, satellite altimetry and rainfall observations," *Comptes Rendus Geoscience*, vol. 342, no. 3, pp. 223–233, 2010.
- [10] X. Hu, J. Chen, Y. Zhou, C. Huang, and X. Liao, "Seasonal water storage change of the Yangtze River basin detected by Grace," *Science in China D*, vol. 49, no. 5, pp. 483–491, 2006.
- [11] J. Wahr, M. Molenaar, and F. Bryan, "Time variability of the Earth's gravity field: hydrological and oceanic effects and their possible detection using GRACE," *Journal of Geophysical Research B*, vol. 103, no. 12, pp. 30205–30229, 1998.
- [12] M. Rodell and J. S. Famiglietti, "Detectability of variations in continental water storage from satellite observations of the time dependent gravity field," *Water Resources Research*, vol. 35, no. 9, pp. 2705–2723, 1999.
- [13] M. Rodell and J. S. Famiglietti, "An analysis of terrestrial water storage variations in Illinois with implications for the Gravity Recovery and Climate Experiment (GRACE)," *Water Resources Research*, vol. 37, no. 5, pp. 1327–1339, 2001.
- [14] M. Zhong, J. Duan, H. Xu, P. Peng, H. Yan, and Y. Zhu, "Trend of China land water storage redistribution at medium and large-spatial scales in recent five years by satellite gravity observations," *Chinese Science Bulletin*, vol. 54, no. 5, pp. 816–821, 2009.
- [15] H. Wang, L. Jia, H. Steffen et al., "Increased water storage in North America and Scandinavia from GRACE gravity data," *Nature Geoscience*, vol. 6, no. 1, pp. 38–42, 2013.
- [16] S. C. Swenson and P. C. D. Milly, "Climate model biases in seasonally of continental water storage revealed by satellite gravimetry," *Water Resources Research*, vol. 42, no. 3, Article ID W03201, 2006.
- [17] T. H. Syed, J. S. Famiglietti, M. Rodell, J. Chen, and C. R. Wilson, "Analysis of terrestrial water storage changes from GRACE and GLDAS," *Water Resources Research*, vol. 44, no. 2, Article ID W02433, 2008.
- [18] G.-Y. Niu and Z.-L. Yang, "Assessing a land surface model's improvements with GRACE estimates," *Geophysical Research Letters*, vol. 33, no. 7, Article ID L07401, 2006.
- [19] T. Ngo-Duc, K. Laval, G. Ramillien, J. Polcher, and A. Cazenave, "Validation of the land water storage simulated by Organising Carbon and Hydrology in Dynamic Ecosystems (ORCHIDEE) with Gravity Recovery and Climate Experiment (GRACE) data," *Water Resources Research*, vol. 43, no. 4, Article ID W04427, 2007.
- [20] J. L. Chen, C. R. Wilson, B. D. Tapley, and J. C. Ries, "Low degree gravitational changes from GRACE: validation and interpretation," *Geophysical Research Letters*, vol. 31, no. 22, Article ID L22607, pp. 1–5, 2004.
- [21] R. Klees, E. A. Revtova, B. C. Gunter et al., "The design of an optimal filter for monthly GRACE gravity models," *Geophysical Journal International*, vol. 175, no. 2, pp. 417–432, 2008.
- [22] K.-W. Seo, C. R. Wilson, J. S. Famiglietti, J. L. Chen, and M. Rodell, "Terrestrial water mass load changes from Gravity Recovery and Climate Experiment (GRACE)," *Water Resources Research*, vol. 42, no. 5, Article ID W05417, 2006.
- [23] B. D. Tapley, S. Bettadpur, J. C. Ries, P. F. Thompson, and M. M. Watkins, "GRACE measurements of mass variability in the Earth system," *Science*, vol. 305, no. 5683, pp. 503–505, 2004.
- [24] D. P. Lettenmaier and J. S. Famiglietti, "Hydrology: water from on high," *Nature*, vol. 444, no. 7119, pp. 562–563, 2006.
- [25] S. Swenson, P. J.-F. Yeh, J. Wahr, and J. Famiglietti, "A comparison of terrestrial water storage variations from GRACE with in situ measurements from Illinois," *Geophysical Research Letters*, vol. 33, no. 16, Article ID L16401, 2006.
- [26] L. Xavier, M. Becker, A. Cazenave, L. Longuevergne, W. Llovel, and O. C. R. Filho, "Interannual variability in water storage over 2003–2008 in the Amazon Basin from GRACE space gravimetry, in situ river level and precipitation data," *Remote Sensing of Environment*, vol. 114, no. 8, pp. 1629–1637, 2010.

- [27] M. Rodell and J. S. Famiglietti, "The potential for satellite-based monitoring of groundwater storage changes using GRACE: the High Plains aquifer, Central US," *Journal of Hydrology*, vol. 263, no. 1–4, pp. 245–256, 2002.
- [28] G. Strassberg, B. R. Scanlon, and M. Rodell, "Comparison of seasonal terrestrial water storage variations from GRACE with groundwater-level measurements from the High Plains Aquifer (USA)," *Geophysical Research Letters*, vol. 34, no. 14, Article ID L14402, 2007.
- [29] M. Rodell, I. Velicogna, and J. S. Famiglietti, "Satellite-based estimates of groundwater depletion in India," *Nature*, vol. 460, no. 7258, pp. 999–1002, 2009.
- [30] X. Lu and Q. Zhuang, "Evaluating evapotranspiration and water-use efficiency of terrestrial ecosystems in the conterminous United States using MODIS and AmeriFlux data," *Remote Sensing of Environment*, vol. 114, no. 9, pp. 1924–1939, 2010.
- [31] M. Rodell, J. S. Famiglietti, J. Chen et al., "Basin scale estimates of evapotranspiration using GRACE and other observations," *Geophysical Research Letters*, vol. 31, no. 20, Article ID L20504, 2004.
- [32] G. Ramillien, F. Frappart, A. Güntner, T. Ngo-Duc, A. Cazenave, and K. Laval, "Time variations of the regional evapotranspiration rate from Gravity Recovery and Climate Experiment (GRACE) satellite gravimetry," *Water Resources Research*, vol. 42, no. 10, Article ID W10403, 2006.
- [33] S. Swenson and J. Wahr, "Estimating large-scale precipitation minus evapotranspiration from GRACE satellite gravity measurements," *Journal of Hydrometeorology*, vol. 7, no. 2, pp. 252–270, 2006.
- [34] M. Leblanc, P. Tregoning, G. Ramillien, S. O. Tweed, and A. Fakes, "Basin-scale, integrated observations of the early 21st century multiyear drought in southeast Australia," *Water Resources Research*, vol. 45, no. 4, Article ID W04408, 2009.
- [35] J. L. Chen, C. R. Wilson, B. D. Tapley, Z. L. Yang, and G. Y. Niu, "2005 drought event in the Amazon River basin as measured by GRACE and estimated by climate models," *Journal of Geophysical Research B*, vol. 114, no. 5, Article ID B05404, 2009.
- [36] O. B. Andersen, S. I. Seneviratne, J. Hinderer, and P. Viterbo, "GRACE-derived terrestrial water storage depletion associated with the 2003 European heat wave," *Geophysical Research Letters*, vol. 32, no. 18, Article ID L18405, pp. 1–4, 2005.
- [37] F. Frappart, K. Do Minh, J. L'Hermitte et al., "Water volume change in the lower Mekong from satellite altimetry and imagery data," *Geophysical Journal International*, vol. 167, no. 2, pp. 570–584, 2006.
- [38] M. D. Wilson, P. Bates, D. Alsdorf et al., "Modeling large-scale inundation of Amazonian seasonally flooded wetlands," *Geophysical Research Letters*, vol. 34, no. 15, Article ID L15404, 2007.
- [39] S.-C. Han, C. K. Shum, C. Jekeli, and D. Alsdorf, "Improved estimation of terrestrial water storage changes from GRACE," *Geophysical Research Letters*, vol. 32, no. 7, Article ID L07302, pp. 1–5, 2005.
- [40] B. Wouters, D. Chambers, and E. J. O. Schrama, "GRACE observes small-scale mass loss in Greenland," *Geophysical Research Letters*, vol. 35, no. 20, Article ID L20501, 2008.
- [41] I. Velicogna and J. Wahr, "Measurements of time-variable gravity show mass loss in Antarctica," *Science*, vol. 311, no. 5768, pp. 1754–1756, 2006.
- [42] D. C. Slobbe, P. Ditmar, and R. C. Lindenbergh, "Estimating the rates of mass change, ice volume change and snow volume change in Greenland from ICESat and GRACE data," *Geophysical Journal International*, vol. 176, no. 1, pp. 95–106, 2009.
- [43] P. L. Svendsen, O. B. Andersen, and A. A. Nielsen, "Acceleration of the Greenland ice sheet mass loss as observed by GRACE: confidence and sensitivity," *Earth and Planetary Science Letters*, vol. 364, pp. 24–29, 2013.
- [44] A. S. Gardner, G. Moholdt, B. Wouters et al., "Sharply increased mass loss from glaciers and ice caps in the Canadian Arctic Archipelago," *Nature*, vol. 473, no. 7347, pp. 357–360, 2011.
- [45] J. L. Chen, B. D. Tapley, and C. R. Wilson, "Alaskan mountain glacial melting observed by satellite gravimetry," *Earth and Planetary Science Letters*, vol. 248, no. 1–2, pp. 353–363, 2006.
- [46] K. Matsuo and K. Heki, "Time-variable ice loss in Asian high mountains from satellite gravimetry," *Earth and Planetary Science Letters*, vol. 290, no. 1–2, pp. 30–36, 2010.
- [47] D. García-García, C. C. Ummenhofer, and V. Zlotnicki, "Australian water mass variations from GRACE data linked to Indo-Pacific climate variability," *Remote Sensing of Environment*, vol. 115, no. 9, pp. 2175–2183, 2011.
- [48] W. W. Immerzeel, L. P. H. van Beek, and M. F. P. Bierkens, "Climate change will affect the asian water towers," *Science*, vol. 328, no. 5984, pp. 1382–1385, 2010.
- [49] L. S. Sørensen, S. B. Simonsen, K. Nielsen et al., "Mass balance of the Greenland ice sheet (2003–2008) from ICESat data—the impact of interpolation, sampling and firn density," *Cryosphere*, vol. 5, no. 1, pp. 173–186, 2011.
- [50] W. Zhang, Y. Wang, and C. Zhang, "The preliminary analysis of effects of the soil moisture on gravity observations," *Cartographica Sinica*, vol. 30, no. 2, pp. 108–111, 2001.
- [51] G. Ramillien, J. S. Famiglietti, and J. Wahr, "Detection of continental hydrology and glaciology signals from GRACE: a review," *Surveys in Geophysics*, vol. 29, no. 4–5, pp. 361–374, 2008.
- [52] J. L. Chen, C. R. Wilson, R. J. Eanes, and B. D. Tapley, "Geophysical contributions to satellite nodal residual variation," *Journal of Geophysical Research B*, vol. 104, no. 10, pp. 23237–23244, 1999.
- [53] J. K. Willis, D. P. Chambers, and R. S. Nerem, "Assessing the globally averaged sea level budget on seasonal to interannual timescales," *Journal of Geophysical Research C*, vol. 113, no. 6, Article ID C06015, 2008.
- [54] E. W. Leuliette and L. Miller, "Closing the sea level rise budget with altimetry, Argo, and Grace," *Geophysical Research Letters*, vol. 36, no. 4, Article ID L04608, 2009.
- [55] J. L. Chen, C. R. Wilson, J. S. Famiglietti, and M. Rodell, "Attenuation effect on seasonal basin-scale water storage changes from GRACE time-variable gravity," *Journal of Geodesy*, vol. 81, no. 4, pp. 237–245, 2007.
- [56] G. Zhu, J. Li, H. Wen, and J. Wang, "Study on variations of global continental water storage with GRACE gravity field models," *Journal of Geodesy and Geodynamics*, vol. 28, no. 5, pp. 39–44, 2008.
- [57] S. Swenson and J. Wahr, "Methods for inferring regional surface-mass anomalies from Gravity Recovery and Climate Experiment (GRACE) measurements of time-variable gravity," *Journal of Geophysical Research B*, vol. 107, no. 9, pp. 3–1–3–13, 2002.
- [58] S. Swenson and J. Wahr, "Monitoring changes in continental water storage with grace," *Space Science Reviews*, vol. 108, no. 1–2, pp. 345–354, 2003.
- [59] K.-W. Seo and C. R. Wilson, "Simulated estimation of hydrological loads from GRACE," *Journal of Geodesy*, vol. 78, no. 7–8, pp. 442–456, 2005.

- [60] S. Swenson and J. Wahr, "Post-processing removal of correlated errors in GRACE data," *Geophysical Research Letters*, vol. 33, no. 8, Article ID L08402, 2006.
- [61] G. Ramillien, F. Frappart, A. Cazenave, and A. Güntner, "Time variations of land water storage from an inversion of 2 years of GRACE geoids," *Earth and Planetary Science Letters*, vol. 235, no. 1-2, pp. 283–301, 2005.
- [62] F. Frédéric, G. Ramillien, M. Leblanc et al., "An independent component analysis filtering approach for estimating continental hydrology in the GRACE gravity data," *Remote Sensing of Environment*, vol. 115, no. 1, pp. 187–204, 2011.
- [63] S. Werth, A. Güntner, R. Schmidt, and J. Kusche, "Evaluation of GRACE filter tools from a hydrological perspective," *Geophysical Journal International*, vol. 179, no. 3, pp. 1499–1515, 2009.

Research Article

Forest Phenology Dynamics and Its Responses to Meteorological Variations in Northeast China

Xinfang Yu,¹ Qiankun Wang,^{1,2} Huimin Yan,¹ Yong Wang,¹ Kege Wen,¹
Dafang Zhuang,¹ and Qiao Wang³

¹ State Key Lab of Resources and Environmental Information System, Institute of Geographic Science and Natural Resources Research, Chinese Academy of Sciences, Beijing 100101, China

² Southwest Forestry University, Kunming 650000, China

³ State Environmental Protection Key Laboratory of Satellite Remote Sensing, Satellite Environment Center, Ministry of Environmental Protection of People's Republic of China, Beijing 100094, China

Correspondence should be addressed to Xinfang Yu; yuxf@igsrr.ac.cn

Received 14 February 2014; Revised 30 April 2014; Accepted 15 May 2014; Published 4 June 2014

Academic Editor: Shengli Huang

Copyright © 2014 Xinfang Yu et al. This is an open access article distributed under the Creative Commons Attribution License, which permits unrestricted use, distribution, and reproduction in any medium, provided the original work is properly cited.

Based on time series of Moderate Resolution Imaging Spectroradiometer (MODIS) Enhanced Vegetation Index (EVI) data (2000–2009), we extracted forest phenological variables in Northeast China using a threshold-based method, which included the start of the growing season (SOS), end of the growing season (EOS), and length of the growing season (LOS). The spatial variation of phenological trends was analyzed using the linear regression method. In Northeast China, SOS was delayed at the rate of <1.5 days per year. The delay trend of EOS was well distributed in the entire region with almost the same rates. LOS increased slightly. The analysis of the relationship between forest phenology and meteorological variations shows that SOS was mainly affected by spring temperature, whereas SOS had a negative relationship with precipitation in the warm-temperate deciduous broadleaf forest region. The EOS in temperate steppe region was affected by temperature and precipitation in August, whereas the others were significantly affected by temperature. Because of the increased temperature in spring, the LOS of the temperate steppe region and temperate mixed forest region increased, and the LOS was positively correlated with the mean temperature of summer in the cool-temperate needleleaf forest region.

1. Introduction

Phenology has proven to be a sensitive and integrative indicator of climate variability and vegetation growth responses to climate change [1, 2]. The understanding of phenology brings significant insight into both climate and vegetation interactions and their impacts on different spatial and temporal scales [3]. There is growing evidence that the ecological equilibrium has been altered due to global climate change, resulting in changes in vegetation cover over time and in space. Phenology monitoring can serve as an efficient way to understand the interactions between vegetation and climate, and repeated observations from satellite sensors provide the mechanism to move from plant-specific to regional scale studies of phenology. Satellite-derived vegetation indices are commonly used as indicators of vegetation phenology [4–10]. Justice et al. [4] used Normalized Difference Vegetation

Index (NDVI) to qualitatively assess the global phenology of numerous land cover types. Satellites were later used to interpret phenology as an indicator of land cover changes in South America [5] and to detect phenological dynamics in shrublands [6]. White et al. [7] integrated the basic concepts of traditional meteorologically based phenology modeling with intensive satellite phenology observations and produced biome-specific ecosystem phenology models. Duchemin et al. [8] developed a method that consists of a fit of NDVI predicted by line segment to advanced very high resolution radiometer (AVHRR) NDVI time series to monitor two key stages, budburst and senescence, in the phenological cycle of deciduous forests. Zhang et al. [9, 10] used a series of piecewise logistic functions fit to MODIS Vegetation Index (VI) data to monitor four key transition phases of vegetation dynamics at annual temporal scales. Much related research has demonstrated that environmental drivers such as climate,

topography, and soil properties affect vegetation dynamics at different spatial and temporal scales, ranging from instant to long-term and from local to regional scales [11–18].

Some literatures have described Chinese vegetation phenology research using remotely sensed data. Chen et al. studied the relationship between plant phenology and satellite sensor derived measures of greenness in Eastern China based on field phenological data and NOAA AVHRR data [19–23]. Zhang et al. found that green-up dates in the Tibetan Plateau have continuously advanced from 1982 to 2011 [24]. Guo et al. analyzed Global Inventory Modeling and Mapping Studies (GIMMS) NDVI time series between 1982 and 2003 and found that the start of the growing season of vegetation in Northeast China was significantly influenced by spring temperature [25]. Mao et al. demonstrated that precipitation was a major factor in determining the characteristics of phenology in permafrost regions [26]. Most of these previous studies were limited by spatial resolution (from 1 km to 8 km) and temporal resolution. Since the launch of Terra satellite in late 1999, its MODIS sensor on board provided daily coverage with 250 m spatial resolution.

The objective of this study is to analyze the spatial pattern of key forest phenological variables and to explore the relationship between phenology and meteorological variables in Northeast China. In this study, the 500 m, 8-day composite product from the Terra satellite of Earth Observing System was used to calculate Enhanced Vegetation Index (EVI) for 2000–2009. Spatial distribution maps of vegetation phenological variables were established based on 10-year EVI data, and phenological variables were then analyzed at the regional scale. The relationships between phenology and meteorological variables were analyzed after coupling with meteorological data.

2. Data and Methodology

2.1. Study Area. The study area is in Northeast China ($115^{\circ}09' - 135^{\circ}52'E$ and $38^{\circ}72' - 53^{\circ}55'N$), including Jilin, Heilongjiang, and Liaoning Provinces and eastern Inner Mongolia (Figure 1). The climates in Northeast China are warm-temperate, temperate, and cool-temperate. According to the vegetation regionalization map of 2001, Northeast China is categorized into four vegetation zones, that is, a cool-temperate needleleaf forest region, temperate needleleaf and broadleaf mixed-forest region, warm-temperate deciduous broadleaf forest region, and temperate steppe region (Figure 2) (Editorial Board of Vegetation Map of China, 2001). Northeast China has abundant tree species and a variety of forest types [27]. The forests are widely distributed over mountainous terrain (e.g., Daxinganling and Xiaoxinganling Ranges) and show large variation in species composition across latitudinal domains, elevation gradients, and moisture gradients. At low elevations, the dominant tree species include Korean pine (*Pinus koraiensis*), basswood (*Tilia amurensis*), oak (*Quercus mongolica*), painted maple (*Acer mono*), and ash (*Fraxinus mandshurica*). At high elevations, the major tree species include spruce (*Picea jezoensis* var. *microsperma*), fir (*Abies nephrolepis*), Mongolia pine (*Pinus*

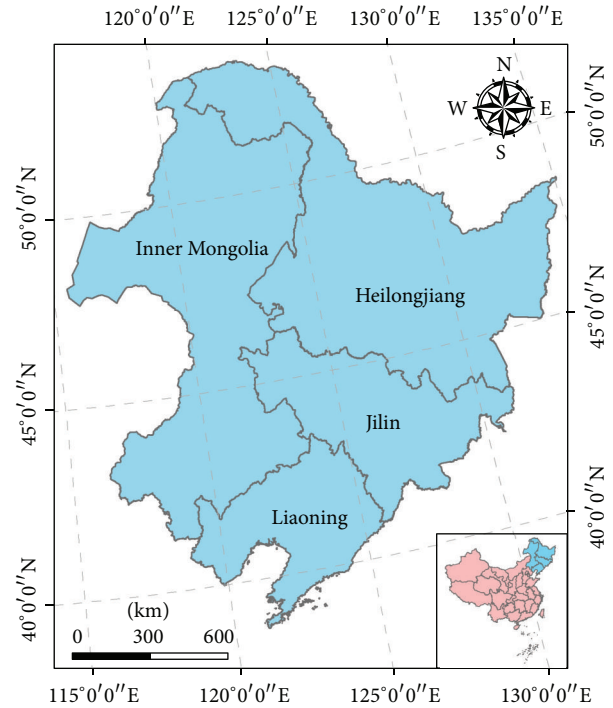


FIGURE 1: Province boundaries in Northeast China.

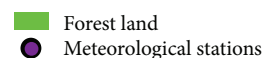
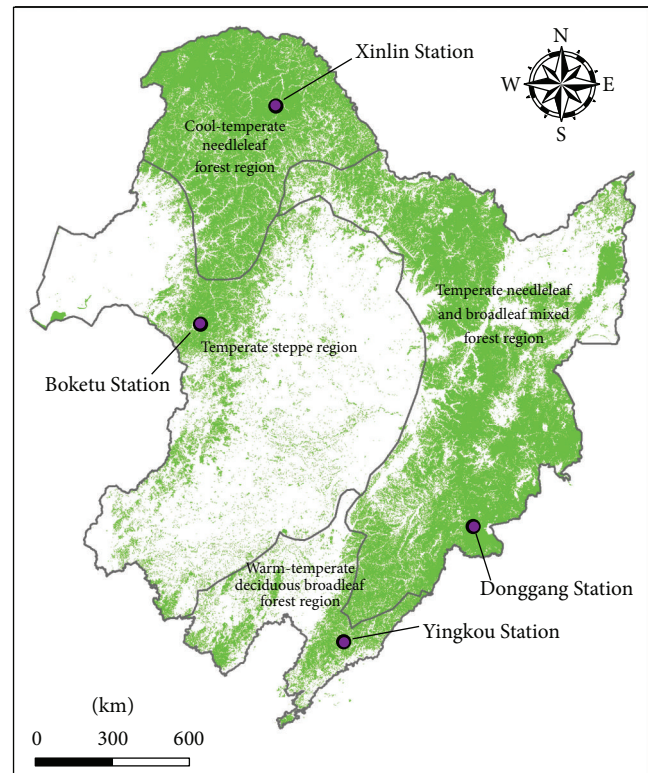


FIGURE 2: Vegetation zones in Northeast China.

sylvestris var. *mongolica*), aspen (*Populus davidiana*), and birch (*Betula platyphylla*). Deciduous coniferous larch (*Larix gmelinii*) forests are widely distributed in the most northern part of Northeast China.

2.2. Materials

2.2.1. MODIS EVI Data. The MODIS Land Science Team provides 8-day composite products for users. The 8-day Land Surface Reflectance product (MOD09A1) from 2000 to 2009 was used in this study. The data were downloaded from the EROS Data Center, US Geological Survey (https://lpdaac.usgs.gov/products/modis_products_table/mod09a1). The MOD09A1 product contains seven spectral bands with a spatial resolution of 500 m. The Enhanced Vegetation Index (EVI) was calculated using three-band reflectance data.

EVI directly adjusts the reflectance in the red band as a function of the reflectance in the blue band, accounting for residual atmospheric contamination (e.g., aerosols), variable soil, and canopy background reflectance [28]. EVI is linearly correlated with the leaf area index and has a higher sensitivity than that of NDVI in areas of high biomass [29]. The equation for EVI is as follows:

$$EVI = 2.5 \times \left(\frac{p_{nir} - p_{red}}{L + p_{nir} + C_1 p_{red} - C_2 p_{blue}} \right), \quad (1)$$

where $C_1 = 6$, $C_2 = 7.5$, and $L = 1$; p_{nir} , p_{red} , and p_{blue} are the reflectance of the blue, red, and near infrared bands, respectively.

2.2.2. Land Use Data. To study forest phenology individually, the forest zones of Northeast China were extracted from the entire region based on the 1:100,000 Land Use Map of China of 2000 from the Data Center for Resources and Environment Sciences, Chinese Academy of Sciences [30].

2.2.3. Climate Data. Air temperature data and rainfall data were acquired from the Chinese Meteorological Data Sharing Service System (<http://cdc.cma.gov.cn/>), including daily average air temperature and precipitation at 343 meteorological stations within the study area from 2000 to 2009. In this study, four representative stations located in Northeast China were used: Xinlin Station (N51.7°, E124.33°) in the cool-temperate needleleaf forest region, Boketu Station (N48.77°, E121.93°) in the temperate steppe region, Donggang Station (N42.1°, E127.57°) in the Temperate needleleaf and broadleaf mixed-forest region, and Yingkou Station (N40.65°, E122.17°) in the warm-temperate deciduous broadleaf forest region.

2.3. Methods. As shown in Figure 3, the double logistic fitting method was used to reduce noise in the time series MODIS EVI data. The threshold-based method was then used to extract forest phenological variables. The least square method was used to analyze the trend of 10 years of phenological variables. Lastly, the change trend was linked to the meteorological variables.

2.3.1. Double Logistic Fitting Method. The double logistic (D.L) function [31, 32] can be used as a basis function as follows:

$$g(t; a_1, \dots, a_4) = \frac{1}{1 + \exp((a_1 - t)/a_2)} - \frac{1}{1 + \exp((a_3 - t)/a_4)}, \quad (2)$$

where a_1 and a_2 determine the position of the left and right inflection points of the curve, respectively, and a_3 and a_4 determine the rate of change at the left and right inflection points, respectively. The TIMESAT software [33] was used to fit the asymmetric Gaussians (AG), D.L, and Savitzky-Golay (SG) models. The AG and D.L functions are superior to the SG with regard to noise reduction [34]. The D.L model was used to fit the time series data in this study. After the data preprocessing of the Double Logistic fitting, the output data had litter noise, and the coefficients of fitted logistic functions were saved for each pixel.

2.3.2. Forest Phenological Variables. Considering the regional characteristics of the forests in Northeast China and the basic rationale of the above methods, the threshold-based method was used to identify forest phenology.

EVI percentage thresholds of 0.2 and 0.27 were used to justify the start of the growing season (SOS) and the end of the growing season (EOS), respectively, according to previous studies [35–37]. For a series of EVI in a given year, we detected EVI_{max} as the maximum EVI and EVI_{min} as the minimum EVI in the first half of the year. The SOS EVI value for a given pixel was calculated using the formula

$$EVI_{start} = EVI_{min} + (EVI_{max} - EVI_{min}) \times 0.2. \quad (3)$$

Then, the day of EVI_{start} was determined as the SOS. The EOS was defined using the same method as follows:

$$EVI_{end} = EVI_{min} + (EVI_{max} - EVI_{min}) \times 0.27, \quad (4)$$

where EVI_{min} is the minimum EVI in the last half of the year.

The processing was performed pixel by pixel to determine EVI_{start} and EVI_{end} . SOS and EOS were then determined using the double logistic fitting results, which can be determined for a specific day with the above EVI thresholds. By using the percentage thresholds, the absolute EVI value could be adapted to each pixel, which makes the phenology more reasonable.

2.3.3. Trend Analysis and Its Linkage to Meteorological Variations. The linear regression method was used to analyze the trends of phenological variables. The least square method is a commonly used method in the analysis of vegetation growth [38] as follows:

$$L = \frac{n \times \sum_{j=1}^n j \times T_j - \sum_{j=1}^n j \sum_{j=1}^n T_j}{n \times \sum_{j=1}^n j^2 - \left(\sum_{j=1}^n j \right)^2}, \quad (5)$$

where n is the number of the years, T_j is the SOS of the j -year, and L is the slope of the trend line. If $L > 0$, the SOS

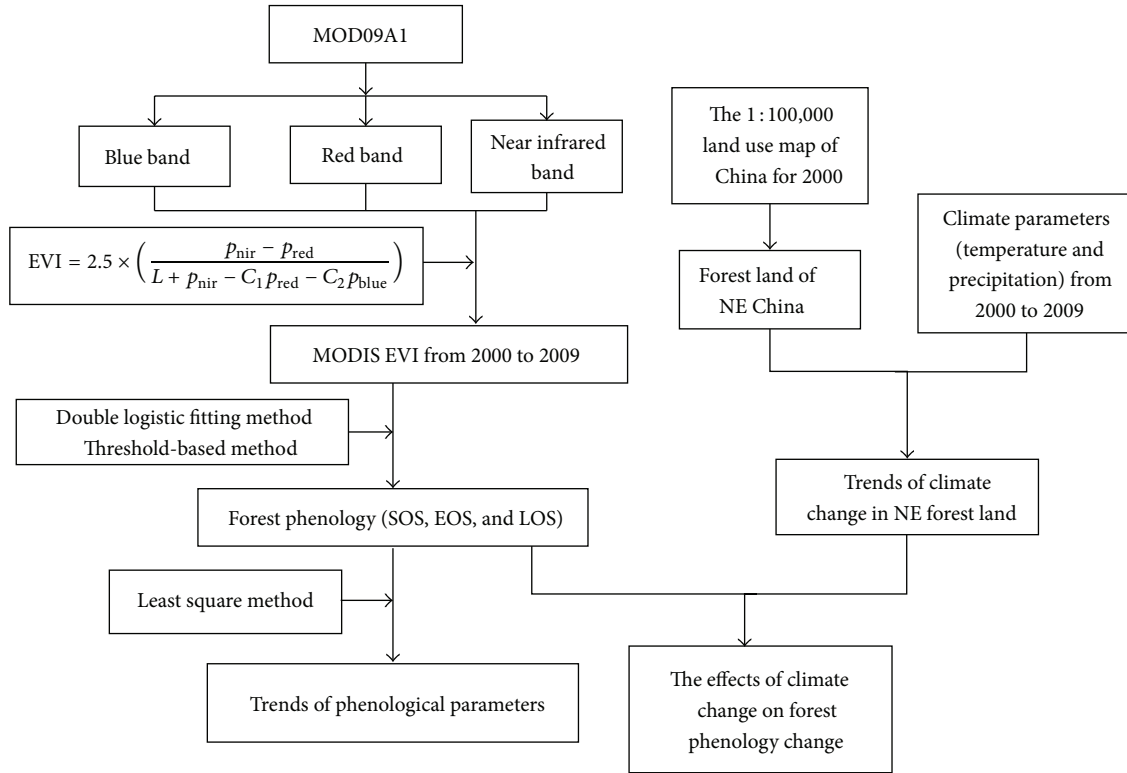


FIGURE 3: Flowchart and schematic of the study analysis.

had a delaying trend during 2000–2009; otherwise, the SOS had an advancing trend. SPSS 16.0 was used for the regression analysis for each pixel.

The interannual variations of phenology variables might be associated with the interannual variations of meteorological variables at regional scales. The connection between the changes in forest phenology (SOS, EOS, and LOS) and meteorological variations was analyzed. The effects of climate change on forest phenology trends were analyzed based on the phenological changes in the four major forest regions.

3. Results

3.1. Spatial Pattern of Forest Phenology. The 10-year annual EVI was calculated for each pixel, and the spatial pattern of forest phenology was generated based on the above-defined thresholds. The spatial distribution of the 10-year average phenological variables (SOS, EOS, and LOS) for Northeast China from 2000 to 2009 is shown in Figure 4. Table 1 shows the maximum, minimum, and average values of the phenological variables in the study area.

Figure 4(a) shows the SOS in Northeast China during DOY (day of the year) 100–140. SOS began earlier in the south, and greening occurred gradually toward the north. This is consistent with the period of tree leaf unfolding in spring. Figure 4(b) shows that the EOS ranges from the DOY 265 to 300, with the end of growth arriving later in lower latitudes, which corresponds to the period of defoliation in autumn. In the cool-temperate needleleaf forest region, there were some patches with an earlier SOS and later EOS, which

TABLE 1: Range of phenological variables in SOE, EOS, and LOS in Northeast China.

Phenology	Maximum	Minimum	Mean
SOS	155	81	114
EOS	343	246	278
LOS	312	108	164

were related to the evergreen needleleaf species of Mongolian pine. In general, the LOS mainly ranged from DOY 130 to 200 along latitudes from north to south in Northeast China, as shown in Figure 4(c).

The spatial patterns of forest phenology in this study are consistent with previous research results [35, 39] and published field-observed phenological data [19–21]. Yu et al. used the threshold-based method to determine the SOS and EOS of Northeast China and found the SOS from DOY 100 to 150, the EOS from DOY 260 to 290, and the LOS mainly from 140–180 DOY [35]. Guo et al. found a DOY of 118–135 for SOS and 252–263 for EOS in Northeast China [39]. Comparison between these results showed that the results derived from the three phenological variables are reasonable in the present study.

3.2. Spatial Change of Phenology Trends. The spatial distribution of trends in the variables SOS and EOS for Northeast China over 10 years from 2000 to 2009 is provided in Figure 5. To evaluate annual trends in the phenological variables, these variables were analyzed at the vegetation zone scale.

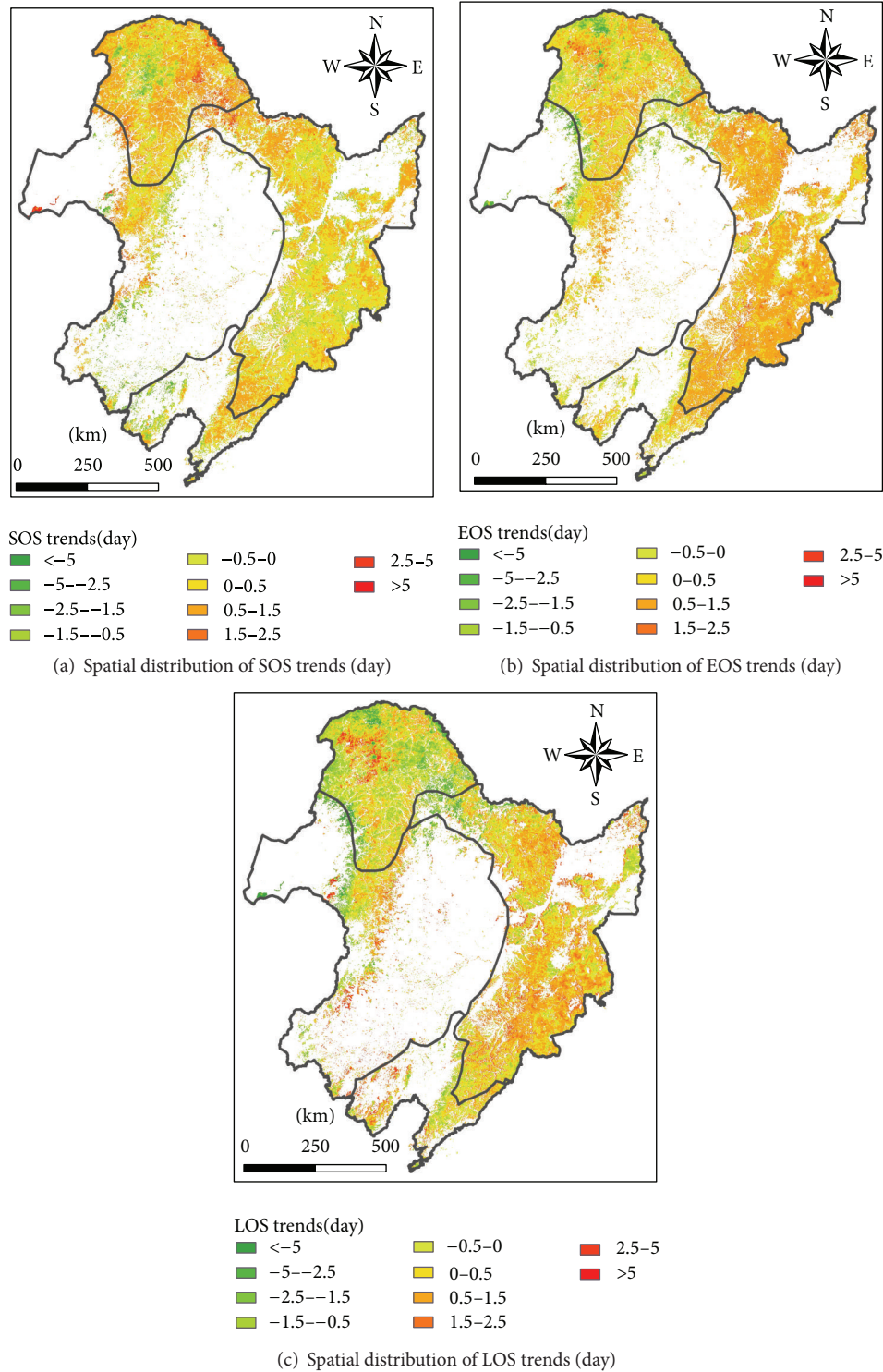


FIGURE 5: Spatial pattern of 10-year forest phenology change trends in Northeast China using MODIS EVI data of 2000~2009.

delayed in all of the vegetation zones. The increased delay in SOS in the cool-temperate needleleaf forest zone caused a decreased LOS (Table 2). The average LOS of the other vegetation zones was increased, and the most positive trend was approximately 0.58 days per year in the warm-temperate deciduous broadleaf forest zone.

3.3. Effects of Climate Change on Forest Phenology Trends

3.3.1. Climate Change. According to the meteorological data, we built the significant trends in meteorological parameters (mean temperature and mean precipitation) for Northeast China over 10 years from 2000 to 2009 (Table 3).

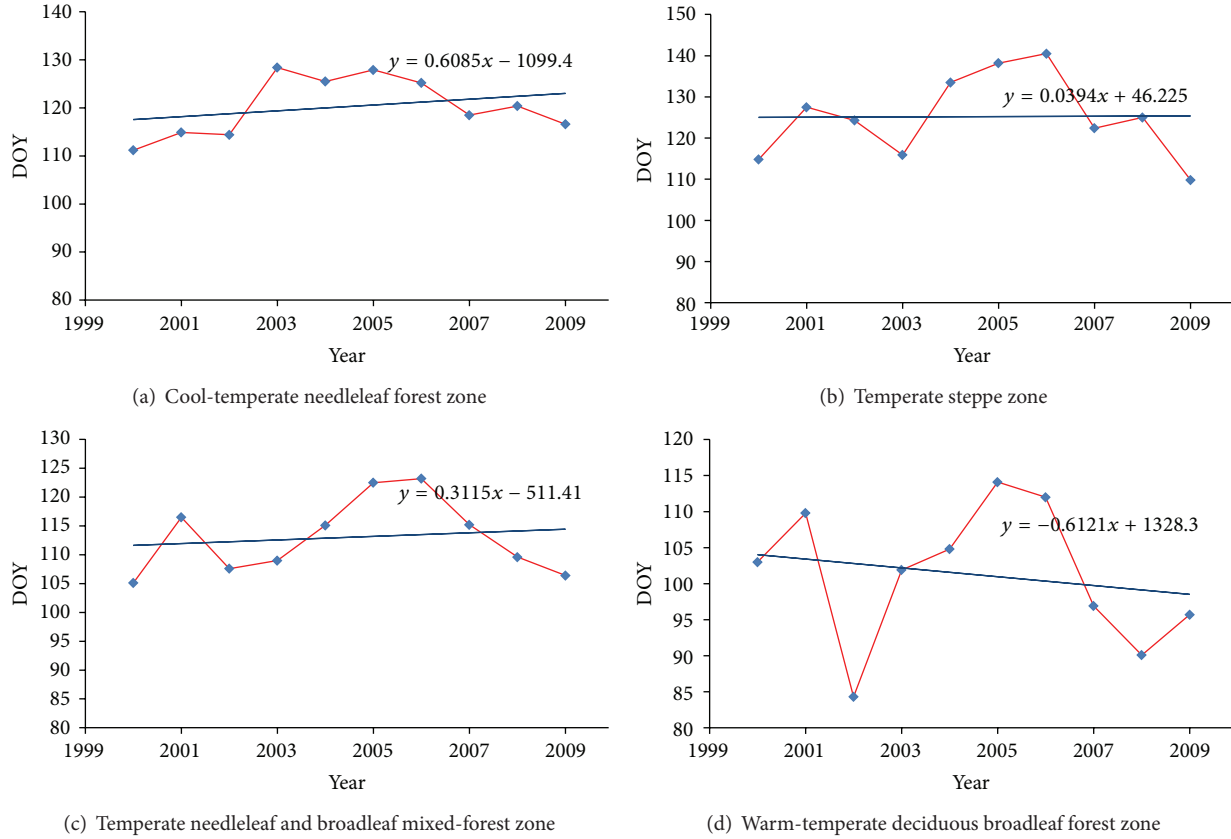


FIGURE 6: The average SOS trends in four forest zones.

TABLE 2: Linear trends of area-averaged phenological variables (SOS, EOS, and LOS) in different vegetation zones of Northeast China.

Regions	SOS trends		EOS trends		LOS trends	
	Slope (d·a ⁻¹)	Variance	Slope (d·a ⁻¹)	Variance	Slope (d·a ⁻¹)	Variance
I	0.50	1.27	0.27	1.54	-0.08	3.08
II	0.24	3.54	0.35	2.47	0.57	5.87
III	0.27	1.17	0.75	0.8	0.58	2.17
IV	-0.06	1.86	0.266	0.66	0.39	2.83

Note. I: cool-temperate needleleaf forest region; II: temperate steppe region; III: temperate needleleaf and broadleaf mixed forest region; IV: warm-temperate deciduous broadleaf forest region.

TABLE 3: Meteorological parameters (temperature and precipitation) in different vegetation zones of Northeast China.

Regions	Temperature (°C)		Precipitation (mm)	
	Mean (°C)	Slope (°C·a ⁻¹)	Mean (mm)	Slope (mm·a ⁻¹)
I	-2.05	0.04	1.42	0.03
II	0.22	0.07	1.11	0.04
III	4.19	0.05	2.18	0.02
IV	10.14	0.05	1.55	-0.03

Note. I: cool-temperate needleleaf forest region; II: temperate steppe region; III: temperate needleleaf and broadleaf mixed forest region; IV: warm-temperate deciduous broadleaf forest region.

The positive linear trend of temperature in the entire study area showed increasing temperature. The largest increase in temperature was observed in the temperate steppe

region, at 0.07°C per year. The precipitation in the warm-temperate deciduous broadleaf forest region decreased at the rate of 0.03 mm per year. The average precipitation in the other three vegetation zones increased by the average rate of 0.03 mm per year.

3.3.2. *Phenology Trends near Meteorological Stations.* Using a window of 20 × 20 pixels centered at the selected meteorological stations, we calculated the average phenology metrics for each area. Figures 6, 7, and 8 show the trends of the average forest phenology for each meteorological station. These trends near the meteorological stations were consistent with each vegetation region.

3.3.3. *Correlation Analysis between Phenology and Meteorological Variations.* To analyze the effects of climate change

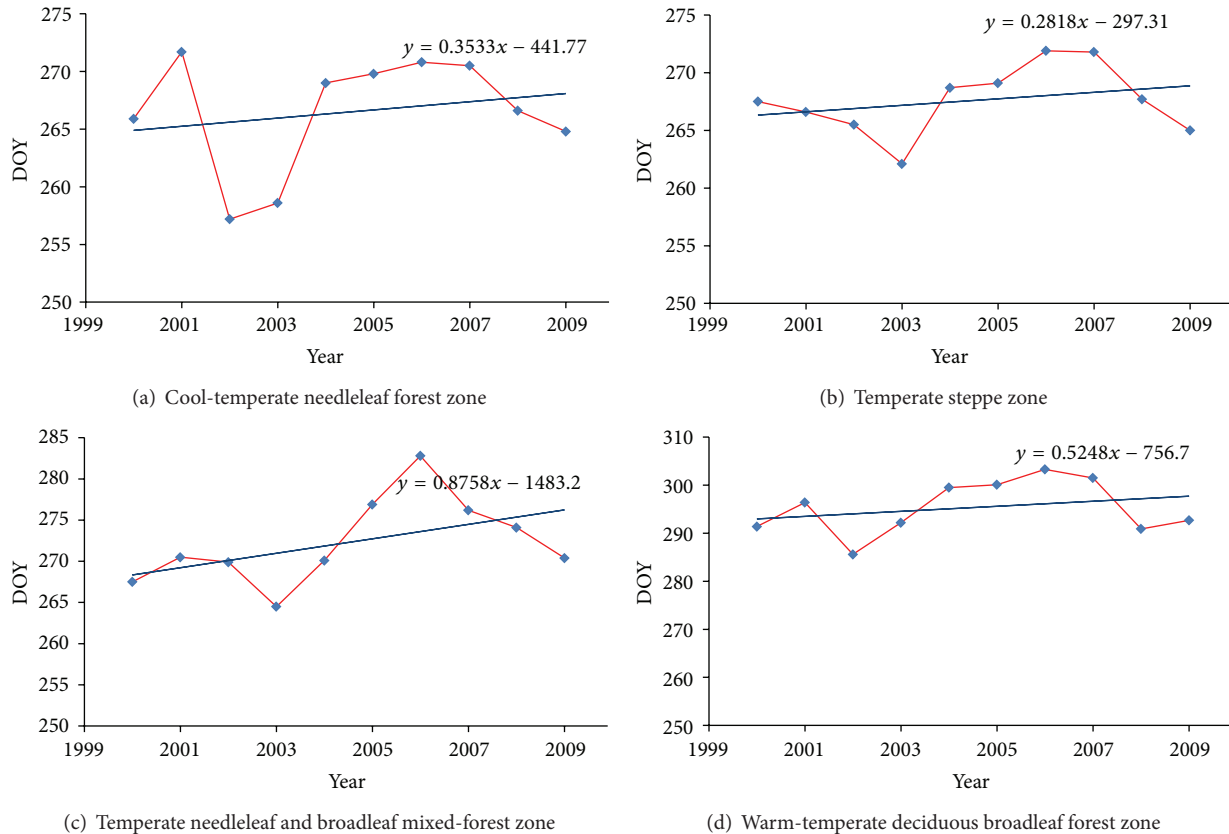


FIGURE 7: The average EOS trends in four vegetation zones.

on forest phenology trends, a correlation analysis between meteorological variations and phenology was used.

During 2000–2009, a series of temporal windows of February, March, April, May, spring (from March to May), the winter of the previous year (from December to the next February), and the entire previous year were used to calculate the mean meteorological variables (temperature and precipitation). These meteorological statistics were used as independent variables because they can represent the regional climate environment when SOS occurred in the study area.

Table 4 shows the correlation between meteorological variations and SOS (Table 4). The SOS of the cool-temperate needleleaf forest region had a relatively high negative relationship with the mean temperature of May ($R = -0.72$, $P < 0.01$). In the temperate steppe region, SOS had a negative relationship with the mean spring temperature ($R = -0.7$, $P < 0.05$), especially with the mean temperature of April ($R = -0.73$, $P < 0.01$). For the total needleleaf forest and temperate steppe region, no significant correlation was found between SOS and mean precipitation in all seasons. Thus, the SOS of the cool-temperate needleleaf forest and temperate steppe region was strongly affected by temperature. The SOS of the temperate needleleaf and broadleaf mixed-forest region showed a negative relationship correlation with the mean temperature of spring ($R = -0.69$, $P < 0.05$) and March ($R = -0.58$, $P < 0.05$), whereas it was positively correlated with the

mean precipitation of the previous year ($R = 0.66$, $P < 0.05$). In addition, in the warm-temperate deciduous broadleaf forest region, SOS had a strongly negative relationship with the mean temperature of March ($R = -0.8$, $P < 0.01$), and the mean precipitation of March had a negative relationship with the SOS ($R = -0.55$, $P < 0.05$). The SOS of the cool-temperate needleleaf forest and temperate steppe region was separately affected by the mean temperature of May and April.

Similar to the SOS correlation analysis, a series of temporal windows of July–November, summer (from June to August), and autumn (from September to November) were used to calculate the mean meteorological variables (temperature and precipitation) for the EOS correlation analysis. Table 5 shows that the EOS of the cool-temperate needleleaf forest region was significantly positively correlated with the mean temperature of autumn ($R = 0.71$, $P < 0.01$) and the mean temperature of November ($R = 0.68$, $P < 0.05$). In the temperate needleleaf and broadleaf mixed-forest region, the EOS was positively correlated with the mean temperature of October ($R = 0.54$, $P < 0.05$), and the EOS of the deciduous broadleaf forest region had a strongly positive correlation with the mean temperature of autumn ($R = 0.79$, $P < 0.01$). For the above-mentioned three regions, EOS was weakly correlated with the mean precipitation in all seasons. Table 5 shows that EOS was affected by temperature more strongly than precipitation. The temperature and precipitation of August both affected the EOS in the temperate steppe region.

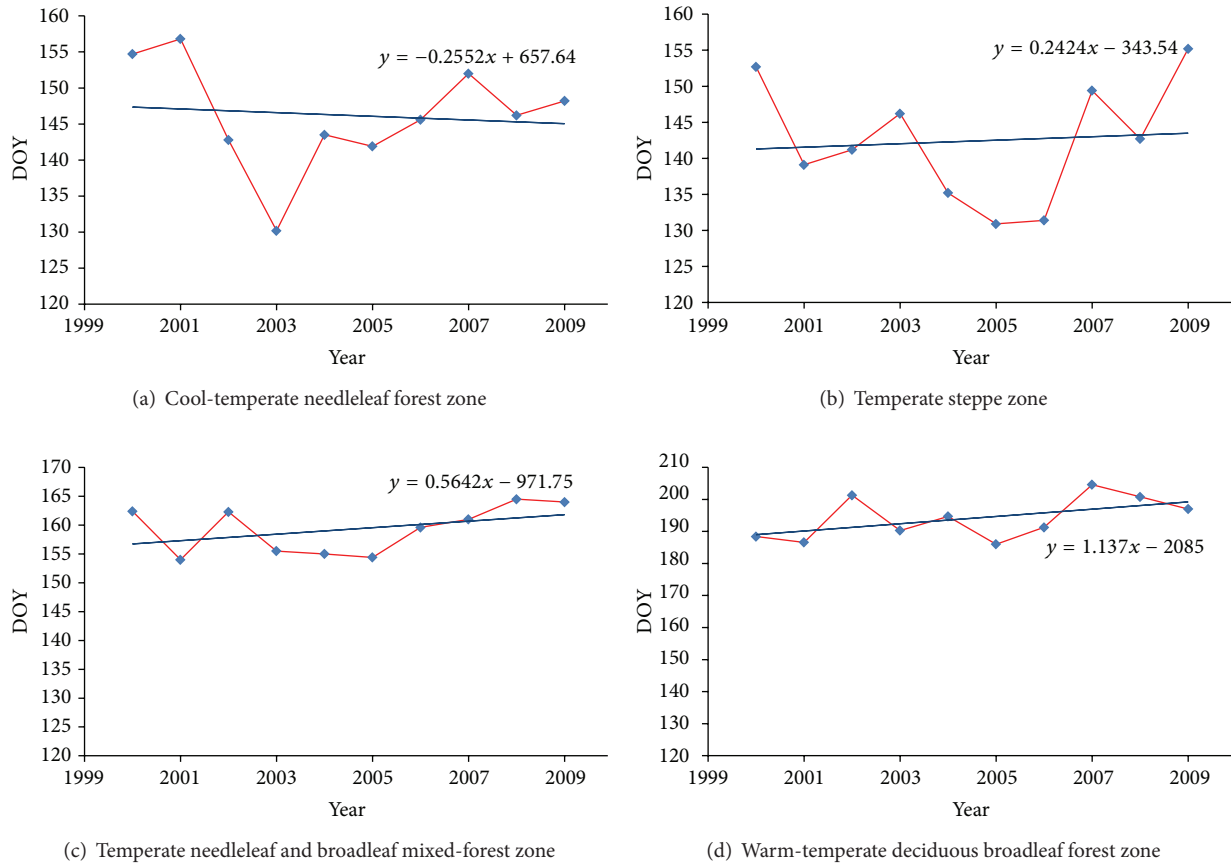


FIGURE 8: The average LOS trends in four vegetation zones.

TABLE 4: The correlation coefficients between climate and forest phenology (SOS) (2000–2009).

	SOS and temperature				SOS and precipitation			
	I	II	III	IV	I	II	III	IV
Annual average	0.44	-0.09	-0.29	0.00	-0.23	-0.33	0.66	-0.03
Spring	-0.30	-0.70*	-0.69*	-0.70*	0.00	0.37	0.43	-0.24
Winter	-0.03	-0.24	-0.35	-0.66	-0.11	0.37	0.00	0.30
February	0.00	-0.35	-0.28	-0.64	0.43	0.25	0.08	0.00
March	0.20	-0.22	-0.58*	-0.80**	0.13	-0.15	0.00	-0.55*
April	-0.45	-0.73**	-0.35	-0.27	0.09	0.27	-0.16	0.03
May	-0.72**	-0.55	-0.45	-0.33	0.37	0.34	0.44	0.45

Note. Trends are significant with ** $P < 0.01$, * $P < 0.05$.

I: cool-temperate needleleaf forest region; II: temperate steppe region; III: temperate needleleaf and broadleaf mixed forest region; IV: warm-temperate deciduous broadleaf forest region.

To carry out the LOS correlation analysis, the mean meteorological variables (temperature and precipitation) of spring (from March to May), summer (from June to August), autumn (from September to November), and the entire year were used as the independent variables to calculate the correlation between climate and phenology (Table 6). The results showed that the LOS of the cool-temperate needleleaf forest region was positively correlated with the temperature of

summer ($R = 0.50, P < 0.05$). In the temperate steppe region and temperate mixed-forest region, the LOS was positively correlated with the temperature of spring ($R = 0.58, P < 0.05$ and $R = 0.64, P < 0.05$, resp.). For these three regions, LOS was weakly correlated with the mean precipitation in all seasons. In the deciduous broadleaf forest region, the LOS had a positive correlation with the mean temperature of the year ($R = 0.74, P < 0.05$), yet it had a negative correlation

TABLE 5: The correlation coefficients between climate and forest phenology (EOS), 2000–2009.

	EOS and temperature				EOS and precipitation			
	I	II	III	IV	I	II	III	IV
Summer	0.38	0.47	0.18	0.09	0.00	-0.57	0.30	0.09
Autumn	0.71**	0.49	0.35	0.79**	-0.24	-0.56	-0.22	-0.45
July	0.14	0.32	0.00	-0.28	-0.08	-0.08	-0.32	0.28
August	0.58	0.73*	0.53	0.09	-0.08	-0.66*	0.36	-0.33
September	0.09	0.64*	0.00	0.29	-0.27	-0.53	-0.05	0.06
October	0.34	0.14	0.54*	0.70*	-0.14	0.00	-0.05	-0.48
November	0.68*	0.40	0.22	0.72*	-0.04	-0.57	-0.47	0.23

Note. Trends are significant with ** $P < 0.01$, * $P < 0.05$.

I: cool-temperate needleleaf forest region; II: temperate steppe region; III: temperate needleleaf and broadleaf mixed forest region; IV: warm-temperate deciduous broadleaf forest region.

TABLE 6: The correlation coefficients between climate and forest phenology (LOS), 2000–2009.

	LOS and temperature				LOS and precipitation			
	I	II	III	IV	I	II	III	IV
Spring	-0.26	0.58*	0.64*	0.31	0.09	-0.34	0.00	0.35
Summer	0.50*	0.05	-0.16	-0.49	-0.24	0.11	-0.49	-0.16
Autumn	0.17	-0.46	-0.56	-0.22	-0.38	0.04	0.23	-0.40
Annual average	0.10	0.21	0.03	0.74*	-0.29	0.00	-0.19	-0.47*

Note. Trends are significant with * $P < 0.05$.

I: cool-temperate needleleaf forest region; II: temperate steppe region; III: temperate needleleaf and broadleaf mixed forest region; IV: warm-temperate deciduous broadleaf forest region.

with the precipitation ($R = -0.47$, $P < 0.05$). Table 6 shows that LOS was positively correlated with temperature throughout the study area.

4. Conclusion and Discussion

In this study, we derived forest phenological variables (start of the growing season, end of the growing season, and length of the growing season) from the MODIS EVI time series data by the threshold-based method. In Northeast China, the average of SOS and EOS are 114 DOY and 278 DOY, respectively. Moreover, the forest phenological variables were found to be related to the distribution of forest types.

Based on the phenological variables extracted from EVI, we built spatial patterns of three forest phenological variables and the linear trends using the linear regression method. In Northeast China, the SOS was delayed, with the rates of 0~1.5 days per year. Although both advanced and delayed EOS were observed, the delay trend was more pervasive, with almost the same rates. As a result, the LOS increased slightly.

The analysis of the relationship between phenology and climate showed that the SOS (start of season) of each region was mainly affected by the spring temperature. Guo et al. came out with the same result using GIMMS NDVI time series between 1982 and 2003, which found that SOS of vegetation in Northeast China was significantly influenced by spring temperature [25]. Only the mean precipitation of March in the warm-temperate deciduous broadleaf forest region had a negative relationship with SOS ($R = -0.55$, $P < 0.05$). Except for the EOS (end of the growing season)

of the temperate steppe region, which was affected by the temperature and precipitation of August, the EOS was significantly affected by temperature in the other study areas. The climate of different seasons had different influences in each area. Because of the increased temperature in spring, the LOS of the temperate steppe region and temperate mixed-forest region increased. The LOS of the cool-temperate needleleaf forest region was positively correlated with the temperature of summer ($R = 0.50$, $P < 0.05$), and the LOS of the deciduous broadleaf forest region was affected by both temperature and precipitation. Furthermore, the LOS was positively correlated with the mean temperature of the year ($R = 0.74$, $P < 0.05$) and negatively correlated with precipitation ($R = -0.47$, $P < 0.05$).

The average start of the growing season in the deciduous broadleaf forest region was advanced, but delayed in the needleleaf forest region, temperate steppe region, and temperate needleleaf and broadleaf mixed forest region. Due to the stronger delay in SOS compared to EOS, the LOS was decreased in the needleleaf forest region, a result that is not consistent with the result derived from the NDVI that needleleaf forest has advanced by rate of 2.5 days per year [39]. The discrepancy is most likely due to the different data and derivation method. The availability of methods and data specially developed for extracting phenological characteristics from remotely sensed data has simplified the data processing and made it more efficient. Vegetation phenology dynamics and its responses to meteorological variations can be described with such research. This study is helpful for phenology-linked climate change research and for

implementing climate-informed monitoring in the context of adaptive management [40].

Conflict of Interests

The authors declare that there is no conflict of interests regarding the publication of this paper.

Acknowledgments

This study was funded by the National Science Foundation of China (no. 41001279), Youth Science Funds of LREIS, CAS and Strategic Priority Research Program—Climate Change: Carbon Budget and Related Issues of the Chinese Academy of Sciences (nos. XDA05050102 and XDA05050602).

References

- [1] A. D. Richardson, T. F. Keenan, M. Migliavacca, Y. Ryu, O. Sonnentag, and M. Toomey, “Climate change, phenology, and phenological control of vegetation feedbacks to the climate system,” *Agricultural and Forest Meteorology*, vol. 169, pp. 156–173, 2013.
- [2] X. Zhao, K. Tan, S. Zhao, and J. Fang, “Changing climate affects vegetation growth in the arid region of the northwestern China,” *Journal of Arid Environments*, vol. 75, no. 10, pp. 946–952, 2011.
- [3] Y. He, K. Lin, and X. Chen, “Effect of land use and climate change on runoff in the Dongjiang basin of south China,” *Mathematical Problems in Engineering*, vol. 2013, Article ID 471429, 14 pages, 2013.
- [4] C. O. Justice, J. R. G. Townshend, B. N. Holben, and C. J. Tucker, “Analysis of the phenology of global vegetation using meteorological satellite data,” *International Journal of Remote Sensing*, vol. 6, no. 8, pp. 1271–1318, 1985.
- [5] T. A. Stone, P. Schlesinger, R. A. Houghton, and G. M. Woodwell, “A map of the vegetation of South America based on satellite imagery,” *Photogrammetric Engineering and Remote Sensing*, vol. 60, no. 5, pp. 541–551, 1994.
- [6] J. Duncan, D. Stow, J. Franklin, and A. Hope, “Assessing the relationship between spectral vegetation indices and shrub cover in the Jornada Basin, New Mexico,” *International Journal of Remote Sensing*, vol. 14, no. 18, pp. 3395–3416, 1993.
- [7] M. A. White, P. E. Thornton, and S. W. Running, “A continental phenology model for monitoring vegetation responses to inter-annual climatic variability,” *Global Biogeochemical Cycles*, vol. 11, no. 2, pp. 217–234, 1997.
- [8] B. Duchemin, J. Goubier, and G. Courrier, “Monitoring phenological key stages and cycle duration of temperate deciduous forest ecosystems with NOAA/AVHRR data,” *Remote Sensing of Environment*, vol. 67, no. 1, pp. 68–82, 1999.
- [9] X. Zhang, M. A. Friedl, C. B. Schaaf et al., “Monitoring vegetation phenology using MODIS,” *Remote Sensing of Environment*, vol. 84, no. 3, pp. 471–475, 2003.
- [10] X. Zhang and M. D. Goldberg, “Monitoring fall foliage coloration dynamics using time-series satellite data,” *Remote Sensing of Environment*, vol. 115, no. 2, pp. 382–391, 2011.
- [11] K. Soudani, G. le Maire, E. Dufrêne et al., “Evaluation of the onset of green-up in temperate deciduous broadleaf forests derived from Moderate Resolution Imaging Spectroradiometer (MODIS) data,” *Remote Sensing of Environment*, vol. 112, no. 5, pp. 2643–2655, 2008.
- [12] P. Lesica and P. M. Kittelson, “Precipitation and temperature are associated with advanced flowering phenology in a semi-arid grassland,” *Journal of Arid Environments*, vol. 74, no. 9, pp. 1013–1017, 2010.
- [13] R. Herdianto, K. Paik, N. A. Coles, and K. Smettem, “Transitional responses of vegetation activities to temperature variations: insights obtained from a forested catchment in Korea,” *Journal of Hydrology*, vol. 484, pp. 86–95, 2013.
- [14] J. Kariyeva and W. J. D. van Leeuwen, “Environmental drivers of NDVI-based vegetation phenology in Central Asia,” *Remote Sensing*, vol. 3, no. 2, pp. 203–246, 2011.
- [15] D. Pouliot, R. Latifovic, R. Fernandes, and I. Olthof, “Evaluation of compositing period and AVHRR and MERIS combination for improvement of spring phenology detection in deciduous forests,” *Remote Sensing of Environment*, vol. 115, no. 1, pp. 158–166, 2011.
- [16] E. G. Beaubien and H. J. Freeland, “Spring phenology trends in Alberta, Canada: links to ocean temperature,” *International Journal of Biometeorology*, vol. 44, no. 2, pp. 53–59, 2000.
- [17] R. de Jong, S. de Bruin, A. de Wit, M. E. Schaepman, and D. L. Dent, “Analysis of monotonic greening and browning trends from global NDVI time-series,” *Remote Sensing of Environment*, vol. 115, no. 2, pp. 692–702, 2011.
- [18] S. Potitthep, S. Nagai, K. N. Nasahara, H. Muraoka, and R. Suzuki, “Two separate periods of the LAI-VIs relationships using in situ measurements in a deciduous broadleaf forest,” *Agricultural and Forest Meteorology*, vol. 169, pp. 148–155, 2013.
- [19] X. Q. Chen, Z. J. Tan, M. D. Schwartz, and C. Xu, “Determining the growing season of land vegetation on the basis of plant phenology and satellite data in Northern China,” *International Journal of Biometeorology*, vol. 44, no. 2, pp. 97–101, 2000.
- [20] X. Q. Chen, C. X. Xu, and Z. J. Tan, “An analysis of relationships among plant community phenology and seasonal metrics of normalized difference vegetation index in the northern part of the monsoon region of China,” *International Journal of Biometeorology*, vol. 45, no. 4, pp. 170–177, 2001.
- [21] X. Q. Chen and W. F. Pan, “Relationships among phenological growing season, time-integrated normalized difference vegetation index and climate forcing in the temperature region of Eastern China,” *International Journal of Climatology*, vol. 22, no. 14, pp. 1781–1792, 2002.
- [22] X. Chen, L. Vierling, D. Deering, and A. Conley, “Monitoring boreal forest leaf area index across a Siberian burn chronosequence: a MODIS validation study,” *International Journal of Remote Sensing*, vol. 26, no. 24, pp. 5433–5451, 2005.
- [23] X. Chen and L. Xu, “Temperature controls on the spatial pattern of tree phenology in China’s temperate zone,” *Agricultural and Forest Meteorology*, vol. 154–155, pp. 195–202, 2012.
- [24] G. Zhang, Y. Zhang, J. Dong, and X. Xiao, “Green-up dates in the Tibetan Plateau have continuously advanced from 1982 to 2011,” *Proceedings of the National Academy of Sciences of the United States of America*, vol. 110, no. 11, pp. 4309–4314, 2013.
- [25] Z. Guo, X. Zhang, Z. Wang, and W. Fang, “Responses of vegetation phenology in Northeast China to climate change,” *Chinese Journal of Ecology*, vol. 29, no. 3, pp. 578–585, 2010 (Chinese).
- [26] D. Mao, Z. Wang, L. Luo, and C. Ren, “Integrating AVHRR and MODIS data to monitor NDVI changes and their: relationships with climatic parameters in Northeast China,” *International Journal of Applied Earth Observation and Geoinformation*, vol. 18, no. 1, pp. 528–536, 2012.

- [27] Y. Ye and X. Fang, "Land use change in Northeast China in the twentieth century: a note on sources, methods and patterns," *Journal of Historical Geography*, vol. 35, no. 2, pp. 311–329, 2009.
- [28] A. R. Huete, H. Q. Liu, K. Batchily, and W. van Leeuwen, "A comparison of vegetation indices over a global set of TM images for EOS-MODIS," *Remote Sensing of Environment*, vol. 59, no. 3, pp. 440–451, 1997.
- [29] A. Huete, K. Didan, T. Miura, E. P. Rodriguez, X. Gao, and L. G. Ferreira, "Overview of the radiometric and biophysical performance of the MODIS vegetation indices," *Remote Sensing of Environment*, vol. 83, no. 1-2, pp. 195–213, 2002.
- [30] J. Liu, W. Kuang, Z. Zhang et al., "Spatiotemporal characteristics, patterns, and causes of land-use changes in China since the late 1980s," *Journal of Geographical Sciences*, vol. 24, no. 2, pp. 195–210, 2014.
- [31] P. S. A. Beck, C. Atzberger, K. A. Høgda, B. Johansen, and A. K. Skidmore, "Improved monitoring of vegetation dynamics at very high latitudes: a new method using MODIS NDVI," *Remote Sensing of Environment*, vol. 100, no. 3, pp. 321–334, 2006.
- [32] P. M. Atkinson, C. Jeganathan, J. Dash, and C. Atzberger, "Inter-comparison of four models for smoothing satellite sensor time-series data to estimate vegetation phenology," *Remote Sensing of Environment*, vol. 123, pp. 400–417, 2012.
- [33] P. Jönsson and L. Eklundh, "TIMESAT—a program for analyzing time-series of satellite sensor data," *Computers and Geosciences*, vol. 30, no. 8, pp. 833–845, 2004.
- [34] J. N. Hird and G. J. McDermid, "Noise reduction of NDVI time series: an empirical comparison of selected techniques," *Remote Sensing of Environment*, vol. 113, no. 1, pp. 248–258, 2009.
- [35] X. Yu, D. Zhuang, X. Hou, and H. Chen, "Forest phenological patterns of Northeast China inferred from MODIS data," *Journal of Geographical Sciences*, vol. 15, no. 2, pp. 239–246, 2005.
- [36] X. Yu, D. Zhuang, H. Chen, and X. Hou, "Forest classification based on MODIS time series and vegetation phenology," in *Proceedings of the IEEE International on Geoscience and Remote Sensing Symposium (IGARSS '04)*, vol. 4, pp. 2369–2372, September 2004.
- [37] U. B. Shrestha, S. Gautam, and K. S. Bawa, "Widespread climate change in the Himalayas and associated changes in local ecosystems," *PLoS ONE*, vol. 7, no. 5, Article ID e36741, 2012.
- [38] G. Ma, L. Dong, and X. Wang, "Study on the dynamically monitoring and simulating the vegetation cover in Northwest China in the past 21 years," *Journal of Glaciology and Geocryology*, vol. 25, no. 2, pp. 1000–0240, 2003 (Chinese).
- [39] Z. Guo, X. Zhang, Z. Wang, and W. Fang, "Simulation and variation pattern of vegetation phenology in Northeast China based on remote sensing," *Chinese Journal of Ecology*, vol. 29, no. 1, pp. 165–172, 2010 (Chinese).
- [40] C. A. F. Enquist, J. L. Kellermann, K. L. Gerst, and A. J. Miller-Rushing, "Phenology research for natural resource management in the United States," *International Journal of Biometeorology*, vol. 58, no. 4, pp. 579–589, 2014.

Research Article

The Impact of Urbanization on the Annual Average Temperature of the Past 60 Years in Beijing

Yong Wang,¹ Wei Ji,^{1,2} Xinfang Yu,¹ Xinliang Xu,¹ Dong Jiang,¹
Zhangang Wang,¹ and Dafang Zhuang¹

¹ State Key Laboratory of Resources and Environmental Information System, Institute of Geographic Sciences and Natural Resources Research, Chinese Academy of Sciences, Beijing 100101, China

² University of Chinese Academy of Sciences, Beijing 100049, China

Correspondence should be addressed to Wei Ji; jiw@reis.ac.cn

Received 14 February 2014; Accepted 4 April 2014; Published 21 May 2014

Academic Editor: Dawei Han

Copyright © 2014 Yong Wang et al. This is an open access article distributed under the Creative Commons Attribution License, which permits unrestricted use, distribution, and reproduction in any medium, provided the original work is properly cited.

Global warming, which is representatively caused by CO₂-based greenhouse gases, has caused widespread concern in the global scientific community and gets the high attention of each government in the world. Human activities impact climate change through greenhouse gas emissions and land use changes. The current study on the impact of urbanization on the annual average temperature of the recent 60 years in Beijing was conducted using 1951–2012 temperature data. Anomaly analysis, quadratic polynomial trend method, and moving average method were employed to indicate the temporal variation of temperature. The results showed that average temperature increased both in urban and rural areas. The temperature of urban Beijing increased during the period from 1951 to 2012, especially from 1971 to 1994. The temperature of rural Beijing showed a faster increase than that of the urban area from 1989 to 1998. However, the rate of temperature increase slowed down in recent years. This type of change was temporally consistent with the process of land use change and urbanization in Beijing. Economic restructuring and improvement of urban planning may have been one of the reasons that the regional warming has been slowed down in the rural area.

1. Introduction

Global warming, which is representatively caused by CO₂-based greenhouse gases, has caused widespread concern in the global scientific community and gets high attention of each government in the world [1, 2]. IPCC (Intergovernmental Panel on Climate Change) (2013) [2] reported that the increase of carbon dioxide and other greenhouse gases is the major part of the human contribution to global warming. Compared with the fourth assessment report, IPCC's fifth assessment report noted that climate change is more serious than previously thought, and is very likely caused by human behavior. According to the 2013 IPCC report [2], climate change is a definite trend and had not been predicted prior to the 1950s. Since the earliest detailed weather records in the 1850s, each of the past three decades has broken the high temperature record. The most recent 30 years may be the hottest 30 years since 1400 in the northern hemisphere. From 1880 to 2012, the average land-ocean surface temperature

trended linearly upward, increasing by 0.85°C. The average temperature from 2003 to 2012 is 0.78°C higher than that of 1850 to 1900 (IPCC, 2013). If surface temperatures continue to rise at the present rate, projections for 2050 indicate that the global temperature will rise 2 to 4°C north and south polar ice will melt significantly, causing the sea level to rise, and some island nations and coastal cities will be submerged, including the famous international cities of New York, Shanghai, Tokyo, and Sydney.

In recent years, many scholars have studied the influence of human activities (such as urbanization) on climate [3–9]. By comparing observational data from cities and surrounding rural areas, analysis showed that urbanization had a significant impact on the temperature. After analyzing the American Historical Climate Network data (1219 Station), Karl et al. [10] noted that the urbanization influence on temperature is approximately 0.06°C (1901–1984) and Kukla et al. [11] noted that in North America the urbanization influence is approximately 0.12°C/10a. Meanwhile, many domestic scholars were

studying the effect of Beijing's urbanization on temperature. Xu [12] noted that the temperature difference between the city and suburb tended to increase. After researching Beijing and surrounding cities' heat island features, Zhang et al. [13] noted that Beijing's urban and suburban temperature changes were in phase, with temperature in suburb always lower than temperature in the city. Beijing city and the suburbs' heat island effect had a noticeable rising trend, comparing the 1990s with the 1980s. Upon comparing the urban and suburban climates of Beijing, Song et al. [14] found that the average rate of temperature increase in urban area is $0.43^{\circ}\text{C}/10\text{a}$ and in suburban is $0.21^{\circ}\text{C}/10\text{a}$. Lin and Yu [15] studied the significant temperature changes in Beijing and noted that its annual variation had large-scale characteristics; there was a change breakpoint in 1981 and the warming rate of the past decade was $0.125^{\circ}\text{C}/10\text{a}$. Zhang et al. [16] analyzed 44 years (1961–2004) of average temperature data from 20 weather stations, and their results showed that Beijing's temperature rose over the 44 years, with a transition in the 1980s after which the warming trend was more significant. Additionally, the warming trend in urban areas was significantly higher than that in the suburbs. Spatially, there was an obvious warming center in urban areas, with warming in January, April, July, and October. The warming trend in urban areas was higher than in the suburbs. Moreover, Yan et al. [17], Zhang et al. [18], and Wang et al. [19] completed in-depth research on the average temperature in Beijing.

In addition to greenhouse gas emissions [20], land use change also has important impact on climate. With the use of numerical simulations and numerical experiments for long term temperature data, many researchers believe that large-scale land use or cover change will affect regional and even global climate [21–30].

Through statistical and modeling analysis of the temperature data, summary of the influence of urbanization on climate change, and research on greenhouse gas emissions, land use change, and other human impacts on temperature, previous studies have obtained many different results, but there are still two shortcomings: (1) regarding average temperature trends, all the results showed that since the 1850s, when the observational data began, the general trend is consistent with the global warming trend, and the warming trend has accelerated over the last 50 years [12, 13, 15, 17–19, 25, 30]. However, was the average temperature trend in Beijing area really consistent over the past 60 years? Are there different trends in different stages? So far, there is no clear research result. (2) Related studies have not revealed the impact of human activities (such as the change of land use types caused by urban expansion activities, industrial plant construction, and new road construction) on climate change and their interactions in the process of urbanization.

Using 1951–2012 Beijing temperature data, anomaly analysis, quadratic polynomial trend method, and moving average method, we analyzed the temperatures in Beijing on different temporal scales, explored the temperature trends, determined whether there was temporal consistency between land use change and urbanization, developed an important scientific reference for predicting future Chinese regional temperature variations, and provided a new observational

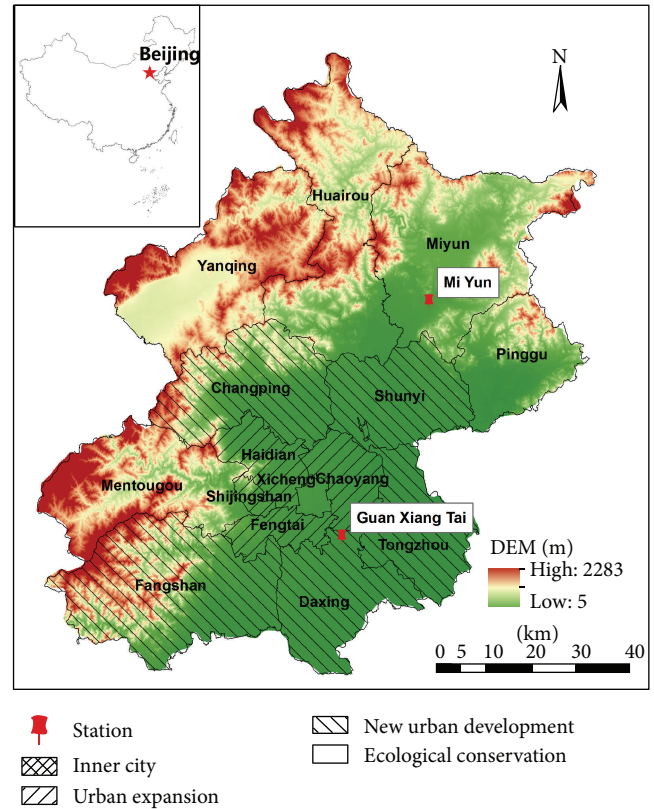


FIGURE 1: The districts, counties, and meteorological stations of Beijing.

basis for studying whether the urban heat island effect and land use status have a significant impact on regional climate change trends.

2. Data and Material

2.1. Study Area. Beijing is situated on the northeast edge of the North China Plain, with its city center located at $39^{\circ}54'20''\text{N}$ and $116^{\circ}25'29''\text{E}$. The city covers a land area of 16,411 square kilometers, including 14 districts and 2 counties (Figure 1). The western, northern, and northeastern parts of the area, accounting for approximately 61.4% of the city, are mountainous and hilly; the remainder is a plain. The city has a typical monsoon-influenced climate, characterized by hot, humid summers due to the East Asian monsoon, and generally cold, windy, dry winters in relation to the vast Siberian anticyclone. Beijing is one place that has experienced high-intensity human activity over the past one hundred years.

According to the urban planning of Beijing, both Dongcheng and Xicheng are traditional core function areas. Chaoyang, Haidian, Fengtai, and Shijingshan are urban expansion districts. Tongzhou, Shunyi, Fangshan, Daxing, and Changping are new urban development districts. Huairou, Pinggu, Mentougou, Miyun, and Yanqing are districts dedicated to ecological conservation.

2.2. Meteorological Data. Meteorological data came from the China Meteorological Data Sharing Service System (<http://cdc.cma.gov.cn/home.do>). In this system, there are two meteorological stations in Beijing—Guan Xiang Tai (GXT) and Mi Yun (MY) (Figure 1). GXT, with an altitude of 31.3 meters, is located in southwestern Beijing. It is the only station that participated in the global meteorological data exchange in Beijing. The observational data from GXT were used to represent the climate conditions of the urban and plain areas of Beijing. MY, with an altitude of 71.8 meters, is located in the northern area of the city. It was named for national reference meteorological stations since 1989 and is intended to represent the weather conditions of the rural area. In this study, the monthly mean temperature data from GTX for the period 1951–2012 and from MY for the period 1989–2010 were collected and used to calculate the annual mean and seasonal mean temperatures. According to meteorological convention in Northern China, spring is from March to May, summer is from June to August, autumn is from September to November, and winter is from December to February of the following year. In addition, Mean Temperature Anomaly (MTA), Quadratic Polynomial Fitting (QPF), and a 3-year moving average were also applied to analyze the temporal variation of the mean temperature. The difference between the mean temperatures at GXT and MY was also calculated to analyze the difference between the urban and rural areas from 1989 to 2010.

2.3. Land Use and Land Cover Data. Land use data for Beijing from 1990, 1995, 2000, 2005, and 2010 were provided by the Data Center for Resources and Environmental Sciences (RESDC) of the Chinese Academy of Sciences and were interpreted from Landsat/TM images. Land use was classified into 6 types (cropland, woodland, grassland, water body, built-up land, and unused land) and 25 subtypes. This dataset has been widely applied in studies of land use, with an overall accuracy of 95% for land use types and 85% for subtypes and a Kappa coefficient above 0.81 validated by intensive field surveys [31–33].

In addition, a land use change detection matrix and dynamic index were introduced to indicate variations in land use in the city [34]. The land use change detection matrix could intelligibly demonstrate the mutual transformation among the various types of land use. The Land Use Dynamic Index (LUDI) and Bilateral Land Use Dynamic Index (BLUDI) are good indicators of the intensity of land use change as follows:

$$\begin{aligned} \text{LUDI}_i &= \frac{(U_{ia} - U_{ib})}{U_{ia}} * \frac{1}{T} * 100\%, \\ \text{BLUDI}_i &= \frac{(\sum U_{ij} + \sum U_{ji})}{U_i} * \frac{1}{T} * 100\%, \end{aligned} \quad (1)$$

where U_{ia} is the area of land use of type i at the beginning of the study period, U_{ib} is the area of type i at the end of the period, $\sum U_{ij}$ is the total area of type i converted into other types, $\sum U_{ji}$ is the total area of type i converted from other

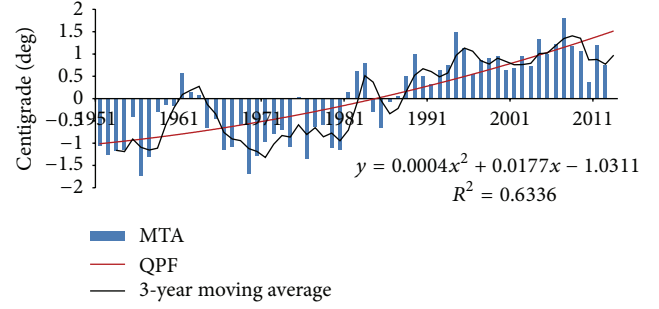


FIGURE 2: The Mean Temperature Anomaly (MTA), Quadratic Polynomial Fitting (QPF), and a 3-year moving average of the annual mean temperature of Guan Xiang Tai (GXT) in the period of 1951–2012.

types, T is the study period, and LUDI_i and BLUDI_i are the dynamic index and bilateral dynamic index of land use type i , respectively [32, 35, 36].

2.4. Socioeconomic Data. The socioeconomic data for this study, including population, building area, length of highway and urban road, and total energy consumption, mainly came from the Beijing Statistical Yearbooks (1978–2012). Data from the fifth and sixth population censuses were also employed in this paper to calculate the Population Growth Rate (PGR) in each town from 2000 to 2010 as follows:

$$\text{PGR} = \frac{(P_{2010} - P_{2000})}{P_{2000}} * 100\%, \quad (2)$$

where P_{2000} and P_{2010} represent the population in 2000 and 2010, respectively.

3. Results and Discussion

3.1. The Temporal Variation of Temperature

3.1.1. Temperature of the Urban Area. Figure 2 shows the temporal variation of the annual Mean Temperature Anomaly (MTA) of GXT from 1951 to 2012. During this period, the average temperature was 12.2°C and an increasing temperature trend was apparent according to the Quadratic Polynomial Tendency (QPF) and a 3-year moving average. The MTA was mainly negative before 1980 but became positive after that year. The annual mean temperature increased dramatically from 1971 to 1994, with the MTA changing from -1.5°C to 1°C . However, the rate of the MTA increase slowed from 1994 to 2007 and even decreased after 2007 according to the 3-year moving average.

The seasonal mean temperatures of GXT from 1951 to 2012 were 13.3°C , 25.2°C , 12.5°C , and -2.3°C for spring, summer, autumn, and winter, respectively. Increasing trends of the mean temperature occurred in all seasons, with the largest variation of the MTA in winter, then spring and autumn, and the smallest variation of the MTA in summer (Figure 3). The transition point of the MTA of the seasonal mean temperature was also 1980, similar to the MTA of the

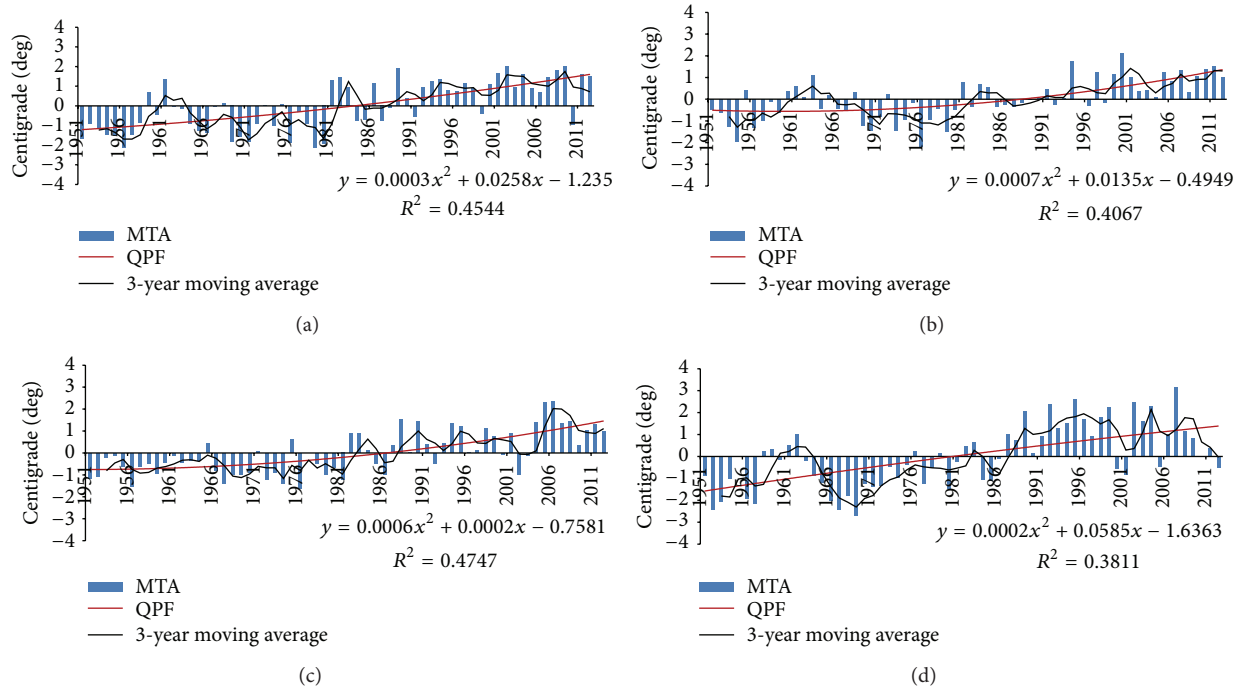


FIGURE 3: The Mean Temperature Anomaly (MTA), Quadratic Polynomial Fitting (QPF), and a 3-year moving average of the mean temperature of spring (a), summer (b), autumn (c), and winter (d) of Guan Xiang Tai (GXT) in the period of 1951–2012.

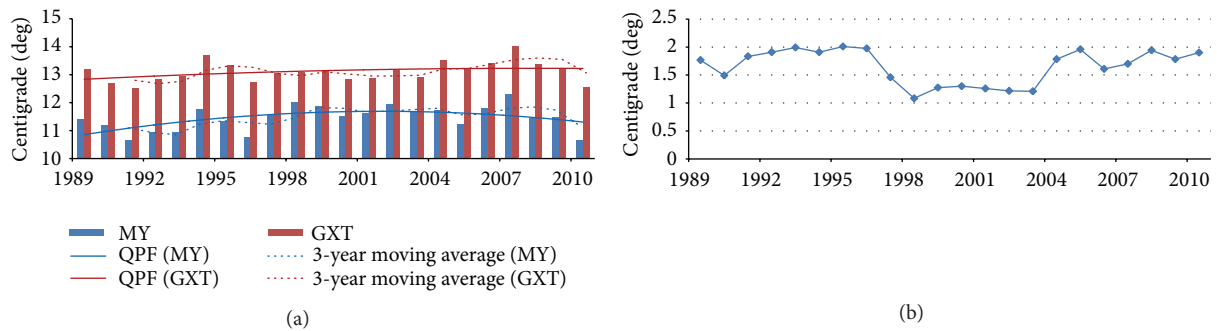


FIGURE 4: The annual mean temperature, Quadratic Polynomial Fitting (QPF), and a 3-year moving average of Guan Xiang Tai (GXT) and Mi Yun (MY) (a) and temperature differences (b) between the two stations in the period of 1989–2010.

annual mean temperature. It is worth noting that while the MTA of the mean spring, autumn, and winter temperatures showed a decrease after 2007, the MTA of the mean summer temperature still increased slowly.

3.1.2. Temperature of the Urban and Rural Areas. Between 1989 and 2010, the average temperatures of GXT and MY were 13.1°C and 11.5°C, respectively, with a mean temperature difference of 1.6°C between the two stations. The annual mean temperature of each station increased slightly from 1989 to 2007 and then decreased slightly (Figure 4). The temporal trends related to the temperature difference between GXT and MY can be divided into three periods: (1) 1989–1996, when the temperature difference was approximately 2°C; (2) 1997–2003, when the temperature difference decreased to

approximately 1.2°C; and (3) 2004–2010, when the temperature difference increased by approximately 0.6°C. Between 1989 and 1998, the annual mean temperature of MY increased faster than that of GXT, causing the decrease of the temperature difference.

The temporal variations of urban-rural differences of the mean temperature in autumn and winter fluctuated during the period from 1989 to 2010, especially after 2000, while those in spring and summer were much more stable and showed slight increases. The QPF of winter decreased slightly for both GXT and MY (Figure 5).

Winter and summer had the largest and smallest temperature differences, respectively, which is mainly due to the coal burning for central heating from November to March in Beijing [1]. The temporal variations of the seasonal temperature differences showed a consistent trend across the annual

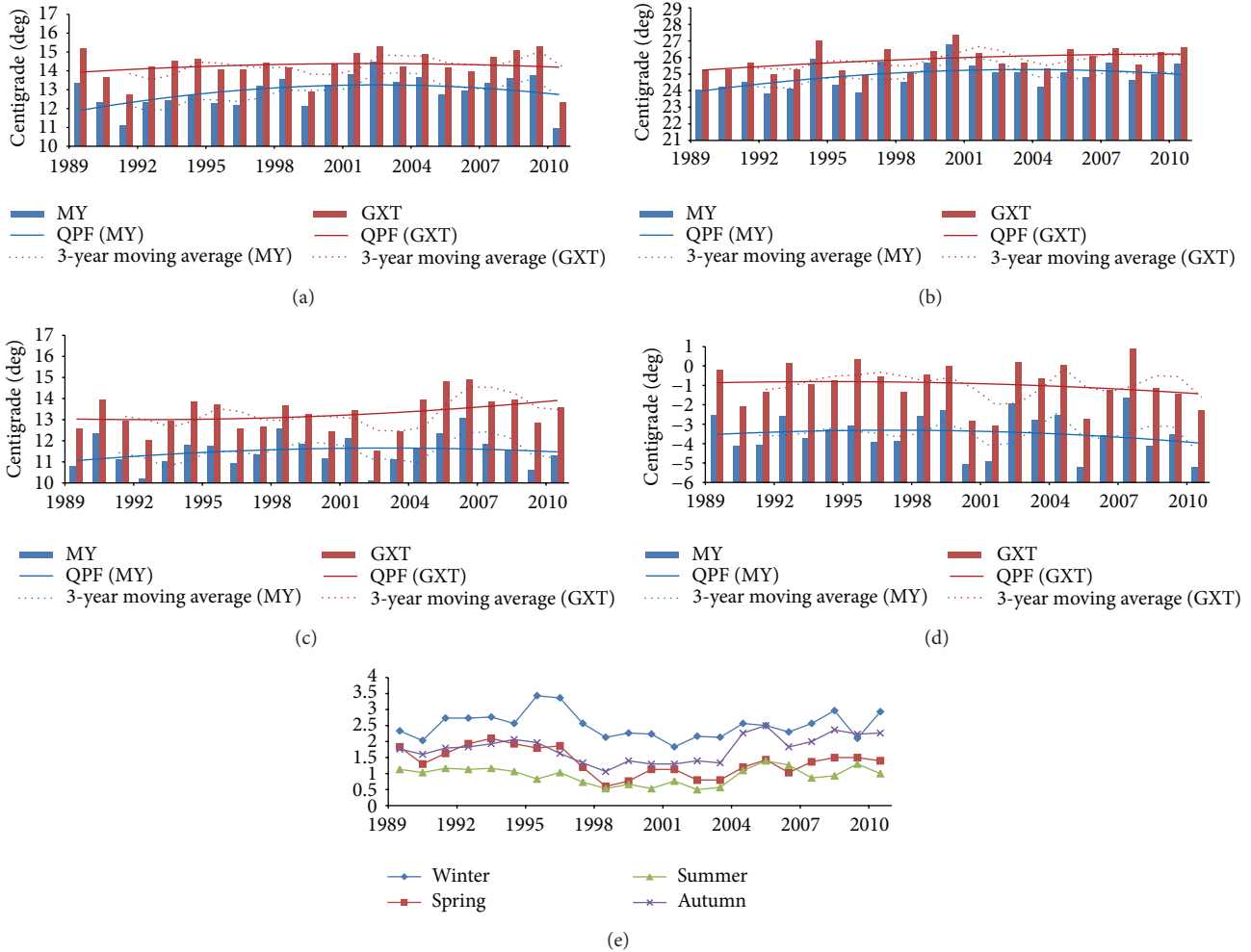


FIGURE 5: The mean temperature and Quadratic Polynomial Fitting (QPF) of Guan Xiang Tai (GXT) and Mi Yun (MY) of spring (a), summer (b), autumn (c), and winter (d), and temperature differences (e) between the two stations in the period of 1989–2010.

temperature differences. Notably, the temperature difference during spring and autumn was similar before 1997. After 1997, the temperature difference of spring decreased more than that of autumn, and after 2004, the temperature difference of spring increased less than that of autumn. Consequently, the temperature difference of spring approached to that of summer, while the temperature difference of autumn tended towards that of winter.

3.2. Urban Development and Temperature Change. As the political, cultural, and educational center of China, Beijing, has attracted a large influx of population. By 2012, Beijing’s resident population reached 20.693 million, which was 2.4 times greater than in 1978, with the population growth rate continuing to accelerate. The urban area of Beijing has grown to 1261 km² in 2012, from 60 km² in 1949, 326 km² in 1978, and 834 km² in 2004. The urban area expanded nearly 17 times. The area under construction increased from 9 million km² in 1978 to 200 million km² in 2012, and the length of highway also increased from 6,562 km to 21,500 km. Industrial development and population growth caused burgeoning energy

consumption, increasing from 19 million tons of standard coal in 1978 to 72 million tons of standard coal in 2012 (Figure 6).

Urbanization has caused an increase of impervious surfaces, industrial energy consumption, domestic heating, and automobile exhaust emissions as well as a decrease of green land and water surface, and it has been shown that city development is changing the thermal conditions of the city in a variety of ways, thus affecting the local temperature [37]. Most studies have shown that Beijing’s temperature increased significantly in the past half century. This study also showed an increasing trend in the annual mean temperature as well as the seasonal mean temperature, especially from 1971 to 1994, mostly due to the large temperature rise in winter and spring.

The urbanization of suburban and rural areas not only promoted the transfer of a large number of high-tech industries from the city to the suburbs and satellite towns, but also attracted a large number of people to these areas. According to the fifth and sixth censuses, the population of Beijing is mostly concentrated in the suburbs and surrounding districts, especially the urban expansion districts of Haidian,

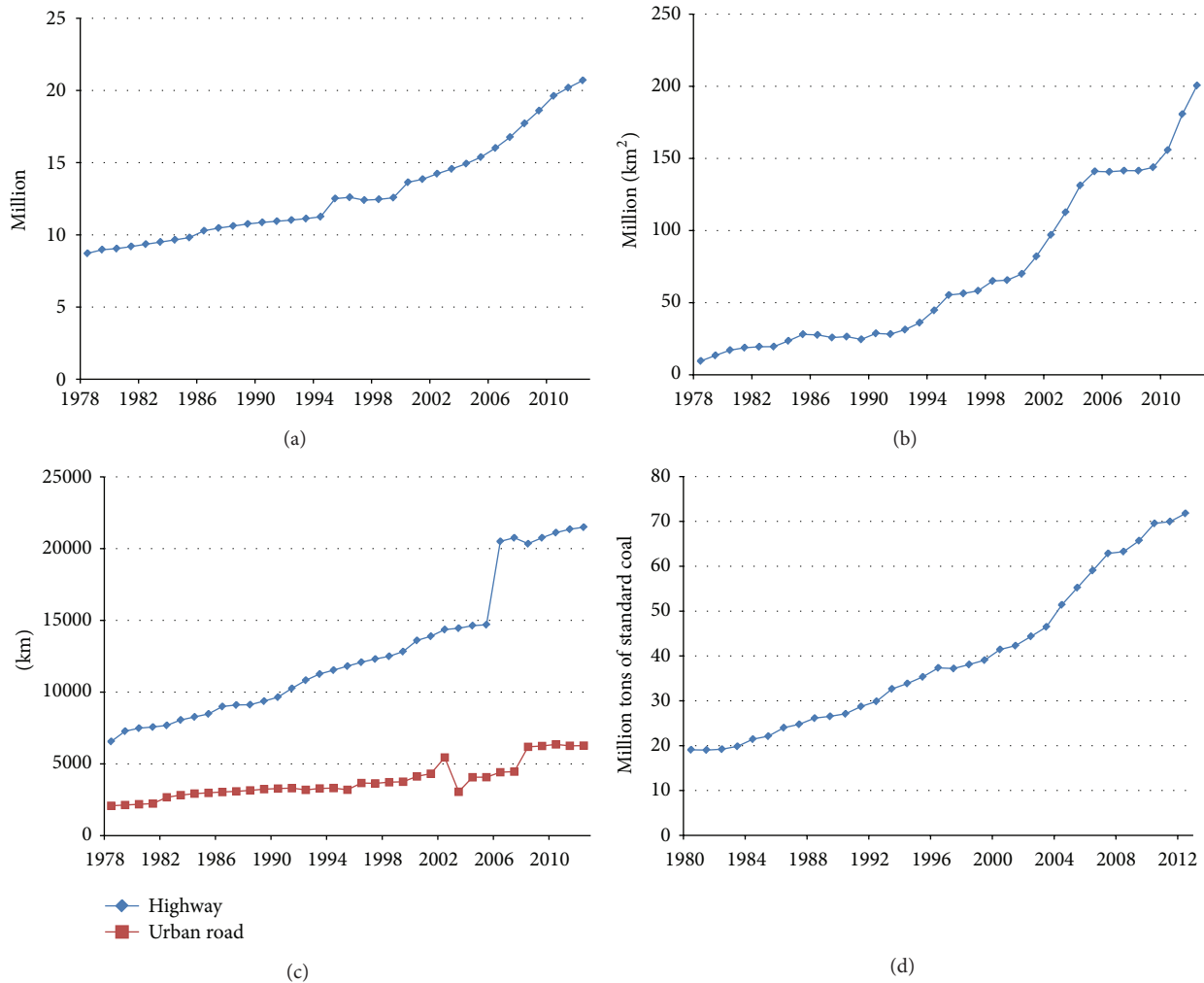


FIGURE 6: Resident population (a), construction area (b), length of highway and urban road (c), and total energy consumption (d) of Beijing in the period of 1978–2012.

Chaoyang, Fengtai, and Shijingshan, which have become the most densely populated areas of the city (Figure 7). The temperature of rural Beijing, represented by the observations at MY, showed a faster increase than the temperature of the urban area during 1989–1998. This change was related to the rapid urbanization and the substantial population increase of the northern suburbs.

3.3. Land Use and Temperature Change. The relationship between temperature and land use change has received considerable research attention, including research on the impact of large-scale land use change on the global climate [38, 39] and the influence of local land use change on regional temperature [30, 40, 41].

From the land use change detection matrix for Beijing in the period of 1990–2010, it can be observed that land use change was more intensive before 2000, when there were many transfers between different land use types, especially an increase of built-up land (Tables 1 and 2). After 2000, transfers from cropland to built-up land continued, but the transfers

between other land use types showed a substantial reduction (Table 3). After 2005, all types of transfers decreased (Table 4).

From 1951 to 2012, the annual mean temperature of GXT showed an overall upward trend, but the rate of the increase slowed after 1994 and there has even been a decrease since 2007. Between 1989 and 2010, the annual mean temperatures of GXT and MY only showed slight increases, and the winter temperatures decreased slightly. The temperature difference between the two stations increased after 2004. From the perspective of land use change, the large increase of built-up land and decrease of green land (cropland, woodland, and grassland) before 2000 have intensified the urban heat island effect and made a positive contribution to the regional warming. However, this part of the contribution was reduced when land use change decreased after 2000.

Since the reform and opening-up of China after 1978, the urbanization of Beijing can be divided into three stages: (1) 1978–1990, a stage of rapid development of urbanization, with an urbanization rate increase from 55% to 73.5% but with

TABLE 1: Land use change detection matrix in the period of 1990–1995 (km²).

1990	1995					
	Cropland	Woodland	Grassland	Water body	Built-up land	Unused land
Cropland	—	610.03	220.14	169.18	845.80	4.70
Woodland	226.02	—	675.49	26.25	57.72	3.55
Grassland	116.90	806.51	—	57.90	16.77	9.48
Water body	28.95	22.05	10.08	—	12.93	0.03
Built-up land	134.81	38.50	15.43	11.57	—	0.60
Unused land	0.06	0.49	0.27	—	—	—
LUDI (%)	-4.58	1.34	-1.26	9.54	9.95	303.64
BLUDI (%)	8.04	6.77	28.29	16.94	15.41	332.18

TABLE 2: Land use change detection matrix in the period of 1995–2000 (km²).

1995	2000					
	Cropland	Woodland	Grassland	Water body	Built-up land	Unused land
Cropland	—	264.82	108.22	36.29	304.86	0.06
Woodland	568.88	—	644.60	163.83	58.78	0.49
Grassland	178.32	710.32	—	10.52	26.79	0.27
Water body	76.45	29.09	28.03	—	27.06	—
Built-up land	288.77	58.34	9.73	16.57	—	—
Unused land	4.47	3.51	9.44	0.03	0.91	—
LUDI (%)	1.78	-0.95	-1.98	2.25	0.41	-18.76
BLUDI (%)	8.11	6.44	27.03	13.12	7.18	20.53

TABLE 3: Land use change detection matrix in the period of 2000–2005 (km²).

2000	2005					
	Cropland	Woodland	Grassland	Water body	Built-up land	Unused land
Cropland	—	11.37	2.07	3.10	375.72	—
Woodland	—	—	0.25	1.21	23.41	—
Grassland	—	2.27	—	0.89	3.58	—
Water body	10.73	0.16	5.86	—	12.76	—
Built-up land	0.67	0.30	—	0.51	—	—
Unused land	—	—	—	—	—	—
LUDI (%)	-1.55	-0.03	0.02	-0.93	3.68	0.00
BLUDI (%)	1.64	0.11	0.23	1.37	3.71	0.00

TABLE 4: Land use change detection matrix in the period of 2005–2010 (km²).

2005	2010					
	Cropland	Woodland	Grassland	Water body	Built-up land	Unused land
Cropland	—	0.07	—	0.85	3.17	—
Woodland	0.05	—	0.03	0.01	1.08	—
Grassland	—	0.02	—	0.01	0.02	—
Water body	11.13	3.50	0.01	—	2.15	—
Built-up land	7.07	1.15	0.02	2.23	—	—
Unused land	—	—	—	—	—	—
LUDI (%)	0.06	0.01	0.00	-0.56	-0.03	0.00
BLUDI (%)	0.10	0.02	0.00	0.81	0.13	0.00

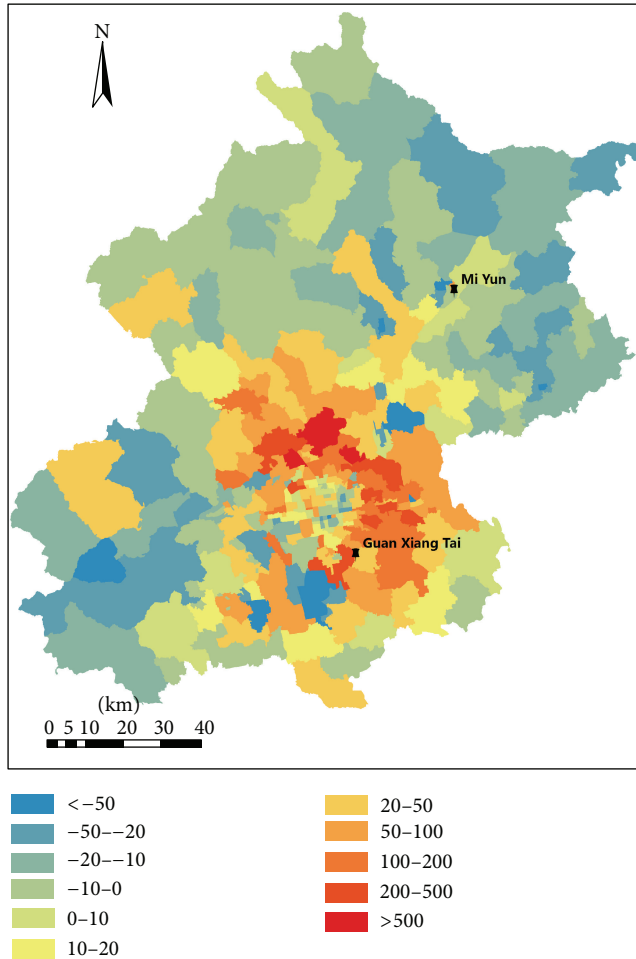


FIGURE 7: Population Growth Rate (PGR) of towns of Beijing in the period of 2000–2010.

a low level of urban infrastructure, without obvious urban sprawl; (2) 1990–2005, a stage of improvement of urbanization, with an urbanization rate increase from 73.5% to 83.6%, and the city underwent intensive expansion; and (3) 2005–2012, a stage of new urbanization, with an urbanization rate increase from 83.6% to 86.2% and urban-rural integration. The process of urbanization showed a temporal consistency with decreased land use change and increased temperatures.

The district of Mi Yun, in which the station MY is located, has been regarded as a district dedicated to ecological conservation. Ecological protection, water conservation, tourism, and ecological agriculture became the main directions of development for this district. Consequently, economic restructuring and improvement of urban planning may have been one of the reasons that the regional warming has been ameliorated.

4. Conclusion

Affected by city development and global warming, the temperature of urban Beijing, represented by the observations at GXT, increased apparently during the period from 1951

to 2012, especially from 1971 to 1994. The temperature of rural Beijing, represented by the observations at MY, showed a faster increase than that of the urban area from 1989 to 1998. However, the rate temperature increase slowed down in recent years, and the winter temperature even decreased slightly between 1989 and 2010. These changes showed temporal consistency with the processes of land use change and urbanization in Beijing. Therefore, economic restructuring and improvement of urban planning may have been one of the reasons that the regional warming has been slowed down in the rural area. Nevertheless, the urban heat island effect in Beijing still needs further research attention, considering the city's large population growth and energy consumption.

Conflict of Interests

The authors declare that there is no conflict of interests regarding the publication of this paper.

Acknowledgments

This study was partially supported and funded by the General Program of Science and Technology Development Project of Beijing Municipal Education Commission (KM201310011010), the China Postdoctoral Science Foundation (20060400496), the Chinese Academy of Sciences (XDA05050102), and the National Scientific and Technological Support Projects of China (2011BAJ07B01-2). The authors are grateful to Professor Shenbin Chen of IGSNRR, CAS for his suggestions on the paper. In addition, the authors thank Ms. Sibou Hou of IGSNRR, CAS for her help in revising the paper.

References

- [1] S. B. Chen and L. Q. Pan, "Effects of urbanization on the annual mean temperature of Beijing," *Acta Geographica Sinica*, vol. 52, no. 1, pp. 27–36, 1997.
- [2] IPCC, "Climate Change," 2013, <http://www.ipcc.ch/report/ar5/wg1/#.UIDShLKBSY8>, <http://www.climatechange2013.org/images/uploads/WGI-AR5.SPMPressRelease.pdf>.
- [3] H. E. Landsberg, *The Urban Climate*, Academic Press, 1981.
- [4] K. P. Gallo, D. R. Easterling, and T. C. Peterson, "The influence of land use/land cover on climatological values of the diurnal temperature range," *Journal of Climate*, vol. 9, no. 11, pp. 2941–2944, 1996.
- [5] K. P. Gallo, T. W. Owen, D. R. Easterling, and P. F. Jamason, "Temperature trends of the U.S. historical climatology network based on satellite-designated land use/land cover," *Journal of Climate*, vol. 12, no. 5, pp. 1344–1348, 1999.
- [6] D. R. Easterling, B. Horton, P. D. Jones et al., "Maximum and minimum temperature trends for the globe," *Science*, vol. 277, no. 5324, pp. 364–367, 1997.
- [7] J. E. Hansen, W. Lawrence, D. Easterling et al., "A closer look at United States and global surface temperature change," *Journal of Geophysical Research: Atmospheres*, vol. 106, no. D20, pp. 23947–23963, 2001.
- [8] T. B. Zhao and C. B. Fu, "Applicability evaluation of surface air temperature from several reanalysis datasets in China," *Plateau Meteorology*, vol. 28, no. 3, pp. 594–606, 2009 (Chinese).

- [9] M. K. Kim and S. Kim, "Quantitative estimates of warming by urbanization in South Korea over the past 55 years (1954–2008)," *Atmospheric Environment*, vol. 45, no. 32, pp. 5778–5783, 2011.
- [10] T. R. Karl, H. F. Diaz, and A. G. Kukl, "Urbanization: its detection and effect in the United States climate record," *Journal of Climate*, vol. 1, no. 11, pp. 1099–1123, 1988.
- [11] G. Kukla, J. Gavin, and T. R. Karl, "Urban warming," *Journal of Climate and Applied Meteorology*, vol. 25, no. 9, pp. 1265–1270, 1986.
- [12] Z. S. Xu, "Discussion on the status of city heat island and its causation in Beijing," *Geographical Research*, vol. 6, no. 3, pp. 159–168, 1987.
- [13] G. Z. I. Zhang, X. D. Xu, J. Z. Wang et al., "A study on the characteristics and evolution of urban heat island over Beijing and its surrounding area," *Journal of Applied Meteorological Science*, vol. 13, pp. 43–50, 2002.
- [14] Y. L. Song, W. J. Dong, S. Y. Zhang et al., "Study on characteristics of climate element in Beijing," *Arid Meteorology*, vol. 21, no. 3, pp. 63–68, 2003.
- [15] X. C. Lin and S. Q. Yu, "Interdecadal changes of temperature in the Beijing region and its heat island effect," *Chinese Journal of Geophysics*, vol. 48, no. 1, pp. 39–45, 2005.
- [16] L. Zhang, Z. X. Xu, and B. Q. Ruan, "Effect of urban heat island on the air temperature and precipitation in Beijing region," *Journal of Natural Resources*, vol. 21, no. 5, pp. 746–755, 2006.
- [17] Z. W. Yan, Z. Li, Q. X. Li, and P. Jones, "Effects of site change and urbanisation in the Beijing temperature series 1977–2006," *International Journal of Climatology*, vol. 30, no. 8, pp. 1226–1234, 2010.
- [18] L. Zhang, G. Y. Ren, J. Liu et al., "Urban effect on trends of extreme temperature indices at Beijing Meteorological Station," *Chinese Journal of Geophysics*, vol. 54, no. 5, pp. 1150–1159, 2011.
- [19] J. Wang, Z. W. Yan, Z. Li, W. D. Liu, and Y. C. Wang, "Impact of urbanization on changes in temperature extremes in Beijing during 1978–2008," *Chinese Science Bulletin*, vol. 58, no. 36, pp. 4679–4686, 2013.
- [20] Intergovernmental Panel on Climate Change, *Climate Change 2007: The Physical Science Basis. Summary for Policymakers*, Cambridge University Press, Cambridge, UK, 2007.
- [21] J. Lean and D. A. Warrilow, "Simulation of the regional climatic impact of Amazon deforestation," *Nature*, vol. 342, no. 6248, pp. 411–413, 1989.
- [22] A. Henderson-Sellers, R. E. Dickinson, T. B. Durbidge, P. J. Kennedy, K. McGuffie, and A. J. Pitman, "Tropical deforestation: modeling local-to regional-scale climate change," *Journal of Geophysical Research*, vol. 98, no. D4, pp. 7289–7315, 1993.
- [23] Y. Xue, "The impact of desertification in the Mongolian and the Inner Mongolian grassland on the regional climate," *Journal of Climate*, vol. 9, no. 9, pp. 2173–2189, 1996.
- [24] R. A. Pielke Sr., G. Marland, R. A. Betts et al., "The influence of land-use change and landscape dynamics on the climate system: relevance to climate-change policy beyond the radiative effect of greenhouse gases," *Philosophical Transactions of the Royal Society A: Mathematical, Physical and Engineering Sciences*, vol. 360, no. 1797, pp. 1705–1719, 2002.
- [25] X. C. Yang, Y. L. Zhang, L. S. Liu, W. Zhang, M. J. Ding, and Z. F. Wang, "Sensitivity of surface air temperature change to land use/cover types in China," *Science in China D: Earth Sciences*, vol. 52, no. 8, pp. 1207–1215, 2009.
- [26] Z. F. Zheng, Y. Zheng, and Q. C. Li, "Effect of urbanization on the temperature of Beijing metropolis in recent 30 years," *Chinese Journal of Eco-Agriculture*, vol. 15, no. 4, pp. 26–29, 2007 (Chinese).
- [27] W. Z. Su, C. L. Gu, and G. S. Yang, "Assessing the impact of land use/land cover on urban heat island pattern in Nanjing City, China," *Journal of Urban Planning and Development*, vol. 136, no. 4, pp. 365–372, 2010.
- [28] W. T. L. Chow and B. M. Svoma, "Analyses of nocturnal temperature cooling-rate response to historical local-scale urban land-use/land cover change," *Journal of Applied Meteorology and Climatology*, vol. 50, no. 9, pp. 1872–1883, 2011.
- [29] M. Wang, X. Yan, X. Liu, and X. Zhang, "The contribution of urbanization to recent extreme heat events and a potential mitigation strategy in the Beijing-Tianjin-Hebei metropolitan area," *Theoretical and Applied Climatology*, vol. 114, no. 3–4, pp. 407–416, 2013.
- [30] W. Cao, Q. Q. Shao, J. Y. Liu et al., "Impact of land use/land cover and its change on climate warming in Beijing area," *Climatic and Environmental Research*, vol. 18, no. 4, pp. 451–460, 2013.
- [31] J. Liu, M. Liu, H. Tian et al., "Spatial and temporal patterns of China's cropland during 1990–2000: an analysis based on Landsat TM data," *Remote Sensing of Environment*, vol. 98, no. 4, pp. 442–456, 2005.
- [32] J. Liu, Z. Zhang, X. Xu et al., "Spatial patterns and driving forces of land use change in China during the early 21st century," *Journal of Geographical Sciences*, vol. 20, no. 4, pp. 483–494, 2010.
- [33] Y. Wang, D. Jiang, D. Zhuang, Y. Huang, W. Wang, and X. Yu, "Effective key parameter determination for an automatic approach to land cover classification based on multispectral remote sensing imagery," *PloS ONE*, vol. 8, no. 10, Article ID e75852, 2013.
- [34] C. A. Berlanga-Robles and A. Ruiz-Luna, "Land use mapping and change detection in the coastal zone of northwest Mexico using remote sensing techniques," *Journal of Coastal Research*, vol. 18, no. 3, pp. 514–522, 2002.
- [35] X. Wang and Y. Bao, "Study on the methods of land use dynamic change research," *Progress in Geography*, vol. 18, no. 1, pp. 81–87, 1999.
- [36] H.-Z. Wang, R.-D. Li, and H.-H. Wu, "Bilateral change dynamic degree model for land use and its application to the land use study of suburban areas of Wuhan," *Remote Sensing for Land & Resources*, vol. 14, no. 2, pp. 20–33, 2002.
- [37] P. Shao and X. Zeng, "Progress in the study of the effects of land use and land cover change on the climate system," *Climate and Environmental Research*, vol. 1, pp. 103–111, 2012.
- [38] T. N. Chase, R. A. Pielke Sr., T. G. F. Kittel, R. R. Nemani, and S. W. Running, "Simulated impacts of historical land cover changes on global climate in northern winter," *Climate Dynamics*, vol. 16, no. 2–3, pp. 93–105, 2000.
- [39] D. Werth and R. Avissar, "The local and global effects of Amazon deforestation," *Journal of Geophysical Research: Atmospheres*, vol. 107, no. D20, pp. LBA 55-1–LBA 55-8, 2005.
- [40] B. Stone Jr., "Land use as climate change mitigation," *Environmental Science & Technology*, vol. 43, no. 24, pp. 9052–9056, 2009.
- [41] W. Wang, W. Shen, X. Liu et al., "Research on the relation of the urbanization and urban heat island effect changes in Beijing based on remote sensing," *Research of Environmental Sciences*, vol. 19, no. 2, pp. 44–48, 2006.

Research Article

A System Dynamics Approach to Modeling Future Climate Scenarios: Quantifying and Projecting Patterns of Evapotranspiration and Precipitation in the Salton Sea Watershed

Michael E. Kjelland,^{1,2} Todd M. Swannack,¹ and William E. Grant²

¹ U.S. Army Engineer Research and Development Center, Environmental Laboratory, Vicksburg, MS 39180-6199, USA

² Department of Wildlife & Fisheries Sciences, Texas A&M University, College Station, TX 77843, USA

Correspondence should be addressed to Michael E. Kjelland; michael.e.kjelland@usace.army.mil

Received 14 February 2014; Revised 17 April 2014; Accepted 18 April 2014; Published 19 May 2014

Academic Editor: Dong Jiang

Copyright © 2014 Michael E. Kjelland et al. This is an open access article distributed under the Creative Commons Attribution License, which permits unrestricted use, distribution, and reproduction in any medium, provided the original work is properly cited.

The need for improved quantitative precipitation forecasts and realistic assessments of the regional impacts of natural climate variability and climate change has generated increased interest in regional (i.e., systems-scale) climate simulation. The Salton Sea Stochastic Simulation Model (S⁴M) was developed to assist planners and residents of the Salton Sea (SS) transboundary watershed (USA and Mexico) in making sound policy decisions regarding complex water-related issues. In order to develop the S⁴M with a higher degree of climate forecasting resolution, an in-depth analysis was conducted regarding precipitation and evapotranspiration for the semiarid region of the watershed. Weather station data were compiled for both precipitation and evapotranspiration from 1980 to 2004. Several logistic regression models were developed for determining the relationships among precipitation events, that is, duration and volume, and evapotranspiration levels. These data were then used to develop a stochastic weather generator for S⁴M. Analyses revealed that the cumulative effects and changes of ± 10 percent in SS inflows can have significant effects on sea elevation and salinity. The aforementioned technique maintains the relationships between the historic frequency distributions of both precipitation and evapotranspiration, and not as separate unconnected and constrained variables.

1. Introduction

The need for improved quantitative precipitation forecasts and realistic assessments of the regional impacts of natural climate variability and climate change has generated increased interest in regional (i.e., systems scale) climate simulation. Because climate warming associated with climate change will exacerbate water sustainability problems, heavily-populated, arid regions such as the Southwest USA are likely to experience some of the highest economic expenses and environmental losses [1]. For example, flows in the Colorado River have been projected to reduce from 10% to 50% by midcentury [2]. Other projections indicated that there would be more frequent and longer lasting droughts particularly in the Colorado River Basin in the latter half of the 21st century, suggesting future

challenges regarding water supplies throughout southwest [3].

Weather generators can be used to produce synthetic weather sequences (which are time series of random numbers that resemble statistically the observations recorded in nature) and are useful for projecting climate into the future [4]. Most weather generators emphasize precipitation (Prpc) as a primary driving variable of interest and other hydroclimatic variables are either directly or indirectly affected by it [5]; for examples, see weather generator (WGEN) by Richardson and Wright [6], a geospatial-temporal (GiST) weather generator by Baigorria and Jones [7], and/or a two-stage resampling algorithm by Leander and Buishand [8]. Weather generators for simulating hourly Prpc and temperature can also be found, for example, downscaling-disaggregation weather GENERator (DD-WGEN) by Mezghani

and Hingray [9] and advanced weather GENERator model (AWE-GEN) by Fatichi et al. [5]. Further, Rajagopalan et al. [10] generated Prcp independently with other climate variables, (e.g., solar radiation, temperature) conditioned on the status of Prcp (i.e., rain or no rain on a given day) using a multivariate nonparametric resampling scheme. The other climate variables can then be generated from either independent statistical distributions fitted separately to each of the variables for each of the two Prcp states (i.e., rain or no rain days) [10].

Stochastic weather models are commonly used because they are easy to calibrate, can be implemented quickly, often pertain to daily time scale [11], and can incorporate data from weather generators easily. Wilks [4] used a first-order, two-state Markov process to simulate daily Prcp, basically based on a conditional probability of a wet day following a dry day and a conditional probability of a wet day following a wet day. An assumption of this type of Markov chain model is that the probability of rainfall on any day depends only on whether it rained on the preceding day; however, the proper Markov order to represent the daily Prcp occurrence process cannot be assumed a priori but can only be determined through observational data analysis or via available results of investigation [12].

Most stochastic models of daily rainfall consist of two parts: a model for the occurrence of dry and wet days and a model for the generation of rainfall volume on wet days [13, 14]. Markov chain models specify each day in a time series as “wet” or “dry,” and develop a relationship between the state of the system at time t (e.g., the current day) current day and the states of the preceding days (time $t - 1, t - 2, \dots, t - n$), where the number of preceding days determines the order of the Markov chain, for example, first order or higher orders [13]. Harrold et al. [15] used four different classes of rainfall amount, categorized according to the number of adjacent wet days whereby the model was conditioned on the rainfall amount of the previous day; this approach accommodates contiguous series of rainfall days (i.e., within-series correlations of rainfall amounts) by using the volume on the previous day as a conditioning variable. Many existing rainfall amount models ignore this correlation structure and assume that the volumes of Prcp at time t are independent of future volumes (i.e., the volume of Prcp at time $t + 1$ is independent of the volume occurring at time t) [15, 16]. However, Buishand [17] and Chapman [13] demonstrated that the distribution of rainfall volumes is different during solitary wet days compared to Prcp occurring over multiple, contiguous days [15]. Srikanthan and Pegram [18] describe a nested multisite daily rainfall stochastic generation model that preserved rainfall characteristics at the daily, monthly, and annual time scales. Srikanthan and Pegram [18] determined that the rainfall volumes on isolated wet days and sequences of wet days did not depend on the duration of the Prcp event as well as they should have.

Evapotranspiration (ETo) changes induced by changing climate conditions are not trivial in hydrologic modeling efforts or water resource management studies [19]. ETo demand is a sensitive parameter that needs to be accounted for; however, often due to limited observational data, it is

often implicitly calculated through calibration efforts or mass balance formulation [19].

Although ETo models and procedures for determining ETo exist (e.g., McMahon et al. [20]), ETo is most often calculated based on the results of Prcp and temperature, for example, Beersma and Buishand [21], or in combination with other weather generated variables (e.g., Snyder et al. [22], Wilks [11]). Miller et al. [19] incorporated changing ETo demands with changing temperatures using the variable infiltration and capacity (VIC) model [23] for streamflow projections over the Colorado River headwater basins. More recently, Baigorria [24] simulated daily minimum and maximum temperatures with regard to covariance with rainfall occurrence, that is, max temperatures on rainy days versus nonrainy days. Snyder et al. [22] describe the development of “Simulation of Evapotranspiration of Applied Water” (SIMETAW) application program for helping California plan future water demand for agricultural purposes. SIMETAW uses only monthly averages of total rainfall volume and the number of rain days for simulating daily weather data and requires information for variables associated with a modified version of the Penman-Monteith equation [25].

There is a need to develop more precise methods for simulating Prcp and ETo that account for the natural interdependency of these two processes. This study utilized nonparametric models to determine the statistical relationships between ETo and Prcp, for incorporation of these relationships into hierarchical nested Markov chain models to preserve the interdependent nature of ETo and Prcp fluctuations. We used the Salton Sea (SS) watershed as a case study for our approach for modeling climate futures.

1.1. Study System. The Salton Sea (SS) watershed spans some 8,360 square miles (21,700 km²) in southeastern California and extends from San Bernardino County through Riverside and Imperial counties and into the Mexicali Valley, in Baja California, Mexico [26]. The terminal lake ecosystem of the SS is located in the Colorado Desert (33° 15' N, 116° W) approximately 35 miles (56 km) north of the US-Mexico border (Figure 1) [27]. The SS is a major hydrologic element of the Lower Colorado River Basin (LCRB) and is considered important to the economic, social, and biological values of the region. However, it is suffering marked degradation as a consequence of human activity and although efforts to rehabilitate the SS ecosystem have been underway for more than a decade, they have had little success.

The present study addresses the need for an integrated systems simulation modeling approach for use in simulating complex water quality and water quantity management policies on both watershed and localized scales. The Salton Sea Stochastic Simulation Model (S⁴M) [28] is a spatially explicit, stochastic, simulation model, formulated as a difference-equation compartment model with a daily time step using STELLA v. 8.0. software [29] representing water flow (i.e., water volume) and quantity of total dissolved salts (TDS) and phosphorus (P) in the LCRB and SS watershed. Unlike previous models constructed for the SS that relied on datasets consisting mainly of monthly or annual averages, the S⁴M

incorporated a high degree of seasonality and climate forecasting resolution. However, the S⁴M initially employed a common technique in modeling the uncertainty in future climate patterns by simply projecting a historic climate data sequence into the future (i.e., deterministic versions of the climate driving variables).

In order to further develop the S⁴M with a higher degree of seasonality and climate forecasting resolution, an in-depth analysis was conducted regarding Prcp and ETo for the semiarid region. ETo is one of the less understood components of the hydrologic cycle [30] but is a major component in terrestrial water balance models [31]. Basically, ETo is the sum of the volume of water used by vegetation (transpired), evaporated from the soil and the intercepted Prcp on vegetation [30, 32]. The difference between evaporation and transpiration is that the latter consists of the vaporization of liquid water contained in plant tissues and the vapor removal to the atmosphere while evaporation occurs at the topsoil if the water is available [30, 33].

Located in one of the most arid regions of North America, maximum temperatures around the Salton Sea may exceed 100°F (38°C) more than 110 days each year, while temperatures seldom drop below freezing. Annual Prcp in the region averages less than 3 inches (7.6 cm), while net evaporation rates from the sea's surface and ETo exceed 66 inches (175 cm) annually [27, 34]. For comparison, the Sahara Desert, much like the Colorado Desert surrounding the SS, is characterized by bare soils and large amounts of available energy allowing for any rainfall to quickly return to the atmosphere [35]. Scott et al. [35] observed that the effect of a Prcp event in the Sahara desert environment had a negative effect on evaporation, but the effect rapidly decreased within the first day. Notably, the timescale of soil moisture storage determines the timescale of the ETo persistence and thus the timescale of humidity persistence in the near-surface atmosphere.

Several other models were developed to address site-specific alternatives for maintaining the Salton Sea. Two hydrodynamic models, RMA-2 and RMA-10, both formulated for the finite element solution method, were applied to simulate the circulation in the sea. This was done to quantify the effects that diked impoundments would have on the sea's circulation and to better understand the sea's circulation via a field monitoring program [36]. Another study conducted a couple of water quality simulations for the -240' and -245' southern impoundments with the BATHTUB model [37, 38]. The BATHTUB model uses a series of empirical submodels to predict the annual nutrient budgets and productivity levels in the water body that predicted mean annual water quality in two proposed impoundment configurations [38]. A UC Davis hydrodynamic model of the Salton Sea was used to estimate the effects of changes in sea elevation [39], while Chung et al. [40] developed a linked hydrodynamic and water quality model.

The primary objective of this study was to develop a more precise methodology for generating ETo and Prcp as interdependent stochastic driving variables that can be used in large-scale systems models. A second objective was to implement the stochastic ETo and Prcp driving variables in

the S⁴M and determine the effects, if any, of a ± 10 percent change of inflow volumes to the SS, thereby addressing future climate change uncertainty of this critically important watershed.

2. Methods

2.1. Determining Statistical Distributions of Historic Data. Following the method of Naoum and Tsanis [30], daily estimates, from 1980 through 2004, of ETo and Prcp were obtained from two meteorological stations [41, 42] in the Salton Sea watershed (Figure 1). Specifically, weather stations in near proximity to the North end and South end of the SS were used, that is, station IDs: Thermal and Indio (TI) and Brawley and Calipatria (BC), respectively. Data points were averaged to get estimates of central tendencies in ETo and Prcp for the SS following methods established in Voinov et al. [43], Bhuyan et al. [44], and Salton Sea Ecosystem Restoration Program [45]. The compiled, averaged 25-year dataset will be henceforth referred to as the averaged dataset.

Daily values of Prcp and ETo data from the averaged weather station data were grouped by month; then each month was tested against thirty-four probability distributions (Table 1) in order to determine the best statistical fit for each month. Monthly distributions were used to preserve seasonality when modeling future climate scenarios, while not solely restricting future climate scenarios to historical values. EasyFit Version 1.3, from MathWave Technologies [46], was used for curve-fitting analyses. The theoretical distribution that provided the "best" fit for each month was determined based on the Kolmogorov-Smirnov (K-S) and Anderson-Darling (A-D) tests of statistical significance, as well as a visual comparison of the fitted curves to the historic frequency distribution.

2.2. Statistical Models Used to Determine Relationship between ETo and Prcp. We hypothesized that different durations of Prcp events would have different effects on ETo, and that the ETo volume of a Prcp event at time $t + 1$ would depend on the volume (or absence thereof) of Prcp at time t . Therefore, individual categories representing single versus multiple Prcp events and corresponding volumes were sorted into subset datasets, along with their respective ETo volumes. In order to thoroughly test these hypotheses, 17 different variables (3 continuous, 14 discrete/categorical) were created from the averaged dataset (Table 2). Because the SS is located in an arid region, many of the daily Prcp values are zeros, 90 percent, or more in many cases. As a result of many days without Prcp, the Prcp data exhibited a mixed distribution with a high number of observations having a value of zero and a continuous distribution when there actually were Prcp events. Traditional time series analysis to account for autocorrelation between observations does not handle datasets with such high zero counts, such as those for ETo and Prcp. Therefore, to determine the relationships among Prcp events and between Prcp events and ETo levels, binomial and multinomial logistic regression models were used [47]. Preliminary analyses indicated that the data were

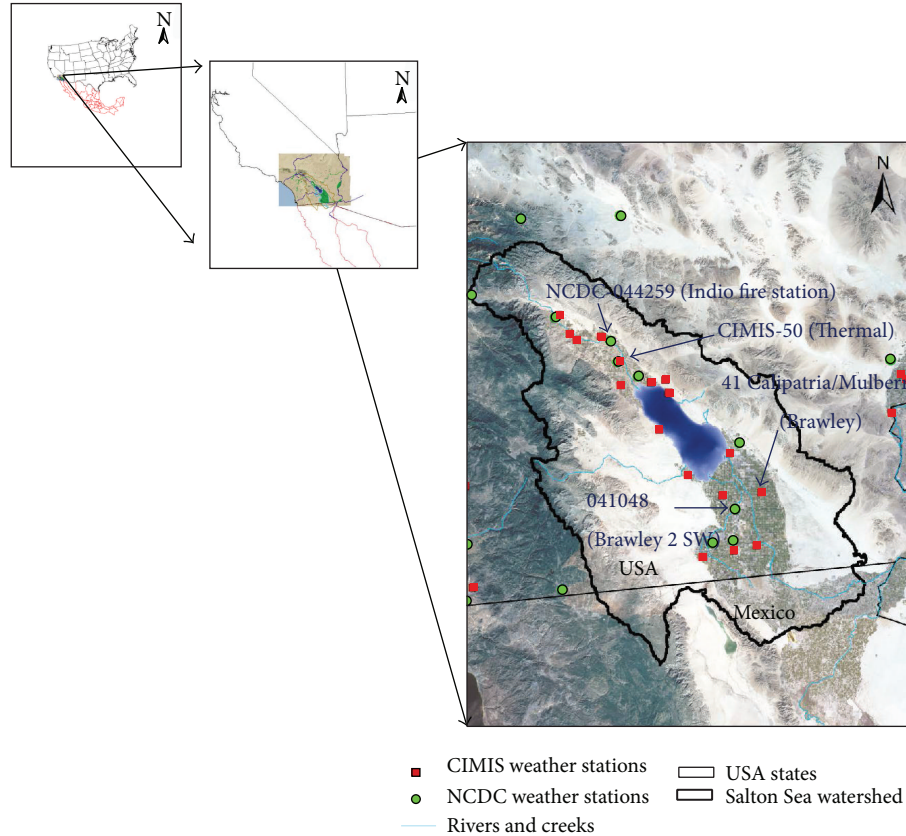


FIGURE 1: Geographic location of the Salton Sea and weather stations within the Salton Sea watershed. Shapefiles were obtained from Redlands Institute, University of Redlands [51].

not overdispersed. From the 17 variables, we developed 16 different statistical models to test the relationship between ETo and Prcp (Table 3). The dependent variables in the logistic regression models were coded as described in Table 2 and tested with binomial or multinomial logistic regression depending on the number of levels [48]. The normality of the standardized residuals, the assumption of linearity in the logit, and a Hosmer-Lemeshow test [48] were used to determine if a model fits the data. A classification table was created using 0.5 as a cut-off point to determine the predictive power of the model, and likelihood ratio tests were used (at $\alpha = 0.05$) to determine model significance [47, 48]. Results from the model selection procedure were used as the new, stochastic climate module for the S^4M . Stata Statistical Software v. 9.0. [49] was used for the binomial and multinomial logistic regression statistical analyses.

2.3. Salton Sea Simulation. The S^4M was constructed to represent water flow in the LCRB as it enters the SS and Colorado River Delta, where it subsequently flows, albeit intermittently, to the Gulf of California. The S^4M specifically accounts for the water volume and water quality in the SS and is formulated as a compartment model based on difference equations with a daily time step using STELLA 8.0 software [29]. ArcGIS v. 9.0. software [50] was utilized for

map making, with SS shapefiles obtained from the University of the Redlands Institute [51].

Previously, the strategy used in modeling the uncertainty in future climate patterns in the S^4M consisted of using a deterministic version of the driving variables in which the historic pattern and number of weather events were preserved, that is, the past and present as the future. Using the methodology described above, a stochastic version of the driving variables was implemented and evaluated. This new module was evaluated by comparing observed and simulated data as a means to assess the performance of the simulation model similar to Tong and Chen [52].

In addition, a climate sensitivity analysis was conducted to observe the cumulative effects of ± 10 percent change of inflow volumes to the SS, if any, on sea elevation and salinity, thereby addressing another aspect of future climate uncertainty. ANOVA and Bonferroni multiple comparisons post hoc tests were performed for SS salinity and elevation variables under both deterministic and stochastic versions of the model using the statistical software SPSS v. 12.0.1. [53].

3. Results and Discussion

A comparison of the averaged weather station historic datasets, that is, TIBC datasets, versus the individual weather

TABLE 1: Probability distributions fit to the historical climate datasets.

(1) Beta
(2) Erlang
(3) Erlang (2P)
(4) Error Function
(5) Exponential
(6) Exponential (2P)
(7) Gamma
(8) Gamma (2P)
(9) Gen. Extreme Value
(10) Gen. Logistic
(11) Gen. Pareto
(12) Gumbel Max
(13) Gumbel Min
(14) Inv. Gaussian
(15) Inv. Gaussian (2P)
(16) Laplace
(17) Logistic
(18) Lognormal
(19) Lognormal (2P)
(20) Normal
(21) Pert
(22) Phased Bi-Exponential
(23) Phased Bi-Weibull
(24) Rayleigh
(25) Rayleigh (2P)
(26) Triangular
(27) Uniform
(28) Wakeby
(29) Weibull
(30) Weibull (2P)
(31) Chi-Squared
(32) Chi-Squared (2P)
(33) Pareto
(34) Student's t

station historic datasets was made for both Prcp and ETo. The TIBC monthly datasets preserved seasonality for both Prcp and ETo as illustrated in the figures (Figures 2–4).

Notably, for the months of February, March, and April the average monthly Prcp volume was lower than the actual weather station historic data. This occurred for two reasons: (1) the disparity in the number of observations between the two weather station datasets and the average resulting in the largest number of observations between the two, and (2) the concomitant decrease in values due to averaging, for example, one weather station having a higher Prcp volume on a given day and the other having a much lower value for the respective day. Instances of missing data in the BC dataset required the replacement of the missing data with TI weather station values, and in such cases, often with a volume of 0 due to the high frequency of days without Prcp events.

The averaging of the weather station data for both Prcp and ETo provided a complete dataset for a 25-year period (1980–2004) for the SS area. Although the pattern of monthly Prcp volumes was preserved when the two separate weather station datasets were averaged, the frequency of Prcp events of a given duration was somewhat inflated. More specifically, the averaging increased the number of consecutive Prcp events when comparing the BC dataset, having a maximum of 7 consecutive events and the TI dataset having a maximum of 9 consecutive events with the TIBC averaged dataset having a maximum of 10 consecutive events. The frequency of smaller events was inflated as well. For example, Prcp events of five or more days in duration were as follows: BC with 7 instances, TI with 13 instances, and the TIBC averaged dataset with 36 instances. Similarly, events of 8 days in duration or more were as follows: BC with 0 instances, TI with 3 instances, and the TIBC averaged dataset with 8 instances. As a result, some months in the TIBC averaged dataset experienced inflated Prcp event durations more than others, for example, January, September, and December. Therefore, the BC weather station dataset statistical relationships, concerning subsequent Prcp events, were implemented and not those based on the averaged dataset. The aforementioned strategy was undertaken as a means to avoid the inflated frequencies of multiple Prcp events being incorporated into the simulation model. The inflated values demonstrate the potential for introduced error in modeling when using averaged data.

3.1. Determining Statistical Distributions of Historic Data. Graphs of the curve fitting results based on the historic frequency distributions for both Prcp and ETo provided a visual aid for determining which theoretic probability distribution gave the “best” fit. The curve providing the “best” fit and associated levels of significance (P -value) for the Kolmogorov-Smirnov (K-S) and Anderson-Darling (A-D) test statistics were recorded for each weather station dataset as well as the TIBC averaged dataset. The results of the two test statistics differed at times, that is, listing two different curves as providing the “best” fit. In the aforementioned situation, a final decision pertaining to the “best” fit was made based on a visual assessment of the figures. A summary of the overall curve fitting results can be found in Kjelland [28].

The curve-fitting exercise resulted in similar distributions providing the “best” fit to the data; however, the distribution for the TIBC averaged dataset for days of individual months often varied, more so in the case of ETo than for Prcp. For example, the most common distribution type providing the “best” fit for both the BC and TI ETo datasets was a Wakeby distribution, but the TIBC averaged dataset (average of the two) more closely resembled Wakeby, General Logistic, and General Extreme Value distributions, depending upon the month in question. The most common distribution types providing the “best” fit for both BC and TI Prcp monthly datasets were Gamma and Exponential distributions, but the TIBC averaged dataset more often resembled Gamma and Rayleigh distributions. The aforementioned differences demonstrate some of the compromises as a result of averaging the datasets.

TABLE 2: Description of variables used for the statistical analyses. Note that event refers to days in which precipitation occurred, either as a one day occurrence or as multiple contiguous days.

Name	Description	Type of variable	Description of levels
Prcp	Daily historic precipitation	Continuous	Daily values from 1982 to 2004
ETo	Daily historic evapotranspiration	Continuous	Daily values from 1982 to 2004
Month	Month of year	Discrete (12 levels)	1 = January, 2 = Feb., . . . , 12 = Dec.
RainEvent	Presence or absence of Prcp event	Discrete (binary)	0 = absent, 1 = present
ETo $\leq 0.21''$	Did ETo exceed $0.21''$?	Discrete (binary)	0 = true, 1 = false
CatEvent	Number of consecutive days of precipitation	Discrete (7 levels)	0 = no prcp, 1 = one day of prcp, . . . , 7 = seven consecutive days of prcp
CatVol	Comparison between volumes (ν) of precipitation between subsequent time steps (i.e., comparing events at time t to events at time $t + 1$)	Discrete (5 levels)	0 = no prcp 1 = single event (a prcp event not followed by another) 2 = $E_{\nu,t} < E_{\nu,t+1}$ 3 = $E_{\nu,t} = E_{\nu,t+1}$ 4 = $E_{\nu,t} > E_{\nu,t+1}$
PrcpAmt	Amount of precipitation per event	Discrete (5 levels)	0 = no Prcp 1 = $\text{Prcp} \leq 0.1''$ 2 = $0.1'' < \text{Prcp} \leq 0.2''$ 3 = $0.2'' < \text{Prcp} \leq 0.5''$ 4 = $0.5'' < \text{Prcp}$
Prcponafter	Denotes first day of event or day after event	Discrete (3 levels)	1 = for first day of prcp event, 2 = day after event, 0 = all other days
Prcpbefafter	Denotes day before event or day after event	Discrete (3 levels)	1 = for day preceding prcp event, 2 = day immediately after event, 0 = all other days
PrcpOn	Denotes first day of event	Discrete (binary)	1 = first day in series of prcp event, 0 = all other days
EToAmt	Amount of ETo per event	Discrete (6 levels)	0 = $\text{ETo} \leq 0.11$ 1 = $0.11 < \text{ETo} \leq 0.21$ 2 = $0.21 < \text{ETo} \leq 0.32$ 3 = $0.32 < \text{ETo} \leq 0.41$ 4 = $0.41 < \text{ETo} \leq 0.5$ 5 = $0.5 < \text{ETo}$
EToPerCh	Percent change in ETo from one time step to next	Continuous	
EToFirst	Compares ETo on day before event to ETo on day of event	Discrete (4 levels)	0 = no prcp or a consecutive day 1 = ETo before prcp event < ETo on day of event 2 = ETo before prcp event = ETo on day of event 3 = ETo before prcp event > ETo on day of event
ETolev2	Compares ETo on day of event to ETo on day after event	Discrete (4 levels)	0 = no prcp 1 = ETo after prcp event < ETo on day of event 2 = ETo after prcp event = ETo on day of event 3 = ETo after prcp event > ETo on day of event
EToOne	Compares ETo on day before an event to ETo on day after event	Discrete (4 levels)	0 = no prcp or a consecutive day 1 = ETo on day after event < ETo day before event 2 = ETo on day after event = ETo day before event 3 = ETo on day after event > ETo day before event

TABLE 2: Continued.

Name	Description	Type of variable	Description of levels
EToTwo	Compares ETo of first day of an event to ETo on day after event	Discrete (4 levels)	0 = no prcp or a consecutive day 1 = ETo on day after event < ETo on first day of event 2 = ETo on day after event = ETo on first day of event 3 = ETo on day after event > ETo on first day of event

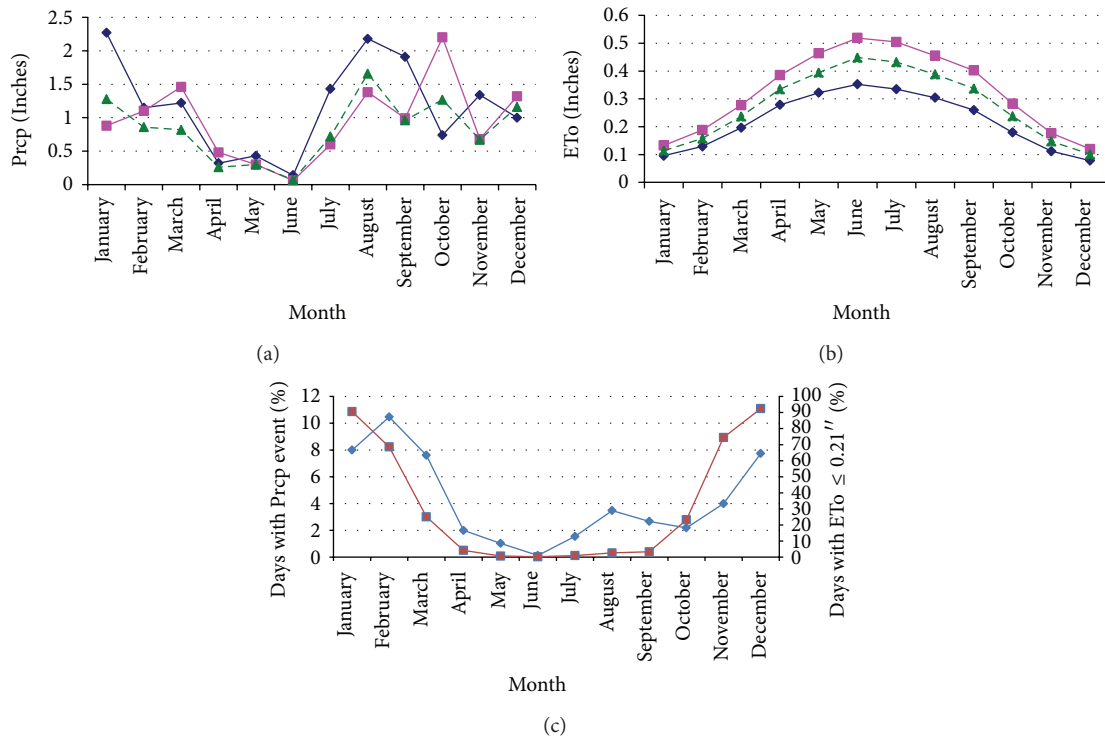


FIGURE 2: (a) Maximum precipitation (Prpc) volumes by month for each weather station (diamond markers = Thermal-Indio (TI), square markers = Brawley-Calipatria (BC)) and their combined average (dashed line). (b) Comparison of mean evapotranspiration (ETo) by month for each weather station (diamond markers = TI, square markers = BC) and their combined average (dashed line). (c) Monthly comparison of precipitation (Prpc) event days and days having evapotranspiration (ETo) ≤ 0.21 inches based on the BC weather station dataset (1982–2004). RainEvent (Prpc event) = percent of observations having some amount of Prcp, that is, a Prcp event, ETo ≤ 0.21 = percent of observations having ETo ≤ 0.21 inches.

3.2. Statistical Models Used to Determine Relationship between ETo and Prcp. It was hypothesized that Prcp and ETo would generally exhibit a negative relationship in the area surrounding the SS, that is, ETo volumes decreasing with Prcp events. Also, the volume and duration of Prcp events would be important factors to consider when exploring any relationship between Prcp and ETo. The two logistic regression models (Equations (1) and (2)) in Table 3 established that some months were significantly different than others concerning the amounts of Prcp and ETo.

The negative relationship between Prcp and ETo was tested statistically using two multinomial logistic regression models and one binomial logistic (logit) regression model (Equations (3), (4) and (5)), respectively (Table 3). The logit model (Equation (3)) resulted in negative coefficients ($P <$

0.05) for all four categories of “PrcpAmt” and had a Prob $> \chi^2$ of < 0.0001 and Pseudo R^2 of 0.105. A likelihood-ratio test for independent variables resulted in a χ^2 of 382.6 and Prob $> \chi^2$ of < 0.0001 . Similarly, the logit model (Equation (4)) resulted in negative coefficients ($P < 0.05$), with an increasing trend, for all five categories of “CatEvent” and had a Prob $> \chi^2$ of < 0.0001 and Pseudo R^2 of 0.124. Also, a likelihood-ratio test for independent variables resulted in a χ^2 of 439.9 and Prob $> \chi^2$ of < 0.0001 . The logit model (Equation (5)) resulted in a statistically significant ($P < 0.05$) and negative coefficient for the variable ETo and an overall Pseudo R^2 of 0.131.

The relationship between the volume of a single Prcp event and subsequent Prcp event volumes and associated changes in ETo was tested statistically using the logit model

TABLE 3: Equations used to test the relationship among seasonality, precipitation, and evapotranspiration. All equations were modeled using the logit link (i.e., logistic equations, Agresti, 1996 [47]).

Equation #	Equation
(1)	Month = $\alpha + \beta * \text{Prcp}$
(2)	Month = $\alpha + \beta * \text{ETo}$
(3)	PrcpAmt = $\alpha + \beta * \text{ETo}$
(4)	CatEvent = $\alpha + \beta * \text{ETo}$
(5)	RainEvent = $\alpha + \beta * \text{ETo}$
(6)	CatVol = $\alpha + \beta * \text{ETo}$
(7)	EToFirst = $\alpha + \beta * \text{PrcpAmt}$
(8)	EToFirst = $\alpha + \beta * \text{ETo}$
(9)	ETolev2 = $\alpha + \beta_1 * \text{PrcpAmt} + \beta_2 * \text{CatEvent}$
(10)	ETolev2 = $\alpha + \beta * \text{ETo}$
(11)	ETolev2 = $\alpha + \beta_1 * \text{PrcpAmt} + \beta_2 * \text{CatVol} + \beta_3 * \text{CatEvent} + \beta_4 * \text{Month}$
(12)	Prcpnafter = $\alpha + \beta * \text{ETo}$
(13)	Prcpnafter = $\alpha + \beta * \text{EToPerCh}$
(14)	Prcpbefafter = $\alpha + \beta * \text{ETo}$
(15)	Prcpbefafter = $\alpha + \beta * \text{EToPerCh}$
(16)	PrcpOn = $\alpha + \beta * \text{EToPerCh}$

(Equation (6)) in Table 3. The model resulted in negative coefficients for all four categories of “CatVol” and had a $\text{Prob} > \chi^2$ of < 0.0001 and Pseudo R^2 of 0.123. The categories 1, 2, and 4 of the nominal categorical variable “CatVol” were significant ($P < 0.05$). Also, a likelihood-ratio test for independent variables resulted in a χ^2 of 433.236 and $\text{Prob} > \chi^2$ of < 0.0001 .

The relationship between different Prcp volumes and associated changes in ETo before a Prcp event and the day of a Prcp event was tested statistically using the logit model (Equation (7)) in Table 3. The model resulted in statistically significant ($P < 0.05$) positive coefficients for categories 1, 2, and 3 of “EToFirst” (using category 0 as the base outcome) and had a $\text{Prob} > \chi^2$ of < 0.0001 and Pseudo R^2 of 0.423. Also, a likelihood-ratio test for independent variables resulted in a χ^2 of 1026.596 and $P > \chi^2$ of < 0.0001 . Another logit model, (Equation (8)) in Table 3, showed that the categories of 1, 2, and 3 of the dependent nominal categorical variable “EToFirst” were less than the base outcome, as all had negative and significant ($P < 0.05$) coefficients.

The relationship between ETo the day of a Prcp event (or the first day in a series of events) and the day after the event (or series of events) was tested statistically using the logit models (Equations (9)–(13)) in Table 3. The logit model (Equation (9)) resulted in positive coefficients ($P < 0.05$) for categories 1, 2, and 3 of “ETolev2,” for both independent variables and had a $\text{Prob} > \chi^2$ of < 0.0001 and Pseudo R^2 of 0.494. Also, a likelihood-ratio test for independent variables resulted in a χ^2 of 82.876 for “PrcpAmt” and 317.128 for “CatEvent” and both had a $P > \chi^2$ of < 0.0001 . Another logit model, (Equation (10)) in Table 3, showed that “ETolev2” categories 1, 2, and 3 all had negative coefficients, although category 1 was not significant, $P > 0.05$. Two additional variables to measure the effect of month (“Month”) and the respective comparisons of Prcp volumes (“CatVol”) associated with single versus subsequent Prcp events were

included in another logit model (Equation (11)) in Table 3. The aforementioned model resulted in some negative coefficients for the independent variables of “CatVol” and “Month” but not “PrcpAmt” and “CatEvent” and had a $\text{Prob} > \chi^2$ of < 0.0001 and Pseudo R^2 of 0.495. The independent variables “CatVol” and “Month” were not significant ($P > 0.05$) for any of the three categories of the dependent nominal categorical variable “ETolev2.” A likelihood-ratio test for independent variables resulted in a χ^2 of 1.541 for “CatVol” and 0.906 for “Month” and $\text{Prob} > \chi^2$ of 0.673 and 0.824, respectively. Models (Equations (12) and (13)) in Table 3, measuring the relationship between Prcp and ETo and the percent change in ETo the day of the event, as compared to after the event, both had statistically significant ($P < 0.05$) and negative coefficients and a Pseudo R^2 of 0.061 and 0.024, respectively.

The relationship between ETo the day before a Prcp event (or sequence of Prcp events) was tested statistically using the logit model (Equation (14)) in Table 3. The logit model (Equation (14)) measuring the relationship between Prcp and ETo before the day of the event had statistically significant ($P < 0.05$) and negative coefficients and a Pseudo R^2 of 0.038.

The relationship between ETo the day after a Prcp event (or after the last Prcp event in the sequence) was tested statistically using the logit model (Equation (15)) in Table 3. The logit model (Equation (15)) measuring the percent change in ETo after the Prcp event had a Pseudo R^2 of 0.016 with positive coefficients for the independent variables. Category 2 of the dependent nominal categorical variable “Prcpbefafter” was statistically significant ($P < 0.05$) whereas category 1 was not ($P = 0.802$).

The general relationship between ETo the day of the first Prcp event (or the first day in a series of events) compared to days without Prcp (or days having Prcp events that are not the first day in the series of events) was tested statistically using the logit model (Equation (16)) in Table 3. The model resulted

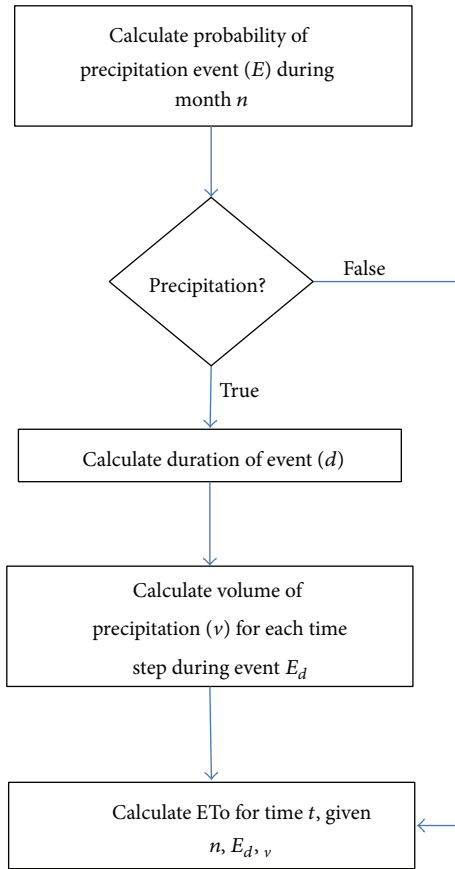


FIGURE 3: Simulation model sampling method for evapotranspiration and precipitation.

in a statistically significant ($P < 0.05$) negative coefficient and had a $\text{Prob} > \chi^2$ of < 0.0001 and Pseudo R^2 of 0.015.

The Prcp data in this study demonstrated that the majority of the rainfall occurred during the winter months. Also, months with a higher percentage of Prcp events had a larger percentage of days with low (0.21 inches or less) ETo (Figure 2(c)). And like the study by Scott et al. [35], where the effect of a Prcp event in the Sahara desert environment had a negative effect on evaporation, the results herein indicated that the same was true for ETo in the semiarid environment around the SS. However, unlike the results of Scott et al. [35] that showed the effect of a Prcp event on evaporation rapidly decreasing within the first day, the results of the present study elucidate a more complex relationship.

There are two important variables that play a role in the relationship between Prcp and ETo amounts, namely, duration (“CatEvent”) and volume (“PrcpAmt”). The results demonstrate that a longer Prcp event is more likely to suppress ETo volumes and for a longer time period. Likewise, larger Prcp volumes suppress ETo volumes more so than the small Prcp volume events; however, larger Prcp volume events also tend to have a higher proportion of the largest ETo volumes compared to small Prcp events. Therefore, the variable “CatEvent” would seem to be a better predictor of

ETo volumes, and the multinomial logistic regression models support this.

The chances of a decrease in ETo the day of a Prcp event compared to the day before the Prcp event were twice as likely (62 percent) than ETo increasing the day of the Prcp event (31 percent). Further, lower Prcp amounts had a slightly higher probability (42 and 43 percent, resp.) for categories 1 and 2 of the ordinal categorical variable “PrcpAmt” versus (35 and 29 percent, resp.) for categories 3 and 4. The probability of ETo more than the day before the Prcp event increased for category 4 of “PrcpAmt” (32 percent) versus (29 percent) for categories 3 and 1, respectively, of the variable “EToFirst.” The overall negative effect of Prcp on ETo levels was supported by Equations (3)–(5) respectively, showing statistically significant ($P < 0.05$) and negative coefficients for all categories of “PrcpAmt,” “CatEvent,” and “RainEvent.” Compared to days without Prcp events, days with Prcp events had significantly lower ETo volumes. Similarly, all categories of the ordinal categorical variable “CatEvent” measuring duration of Prcp events had statistically significant ($P < 0.05$) negative coefficients and showed that the longer the duration of the Prcp event, the larger the decrease in ETo levels, in general. Also, the Pseudo R^2 was somewhat larger for the variable “CatEvent” versus “PrcpAmt” (0.124 versus 0.105, resp.) meaning that the duration of the Prcp event was a slightly better predictor of the decrease in ETo volumes. The nominal categorical variable “CatVol” distinguished between a single or subsequent Prcp event taking into account volume and supported these conclusions based on the logit model (Equation (6)).

The logit model (Equation (8)) with the dependent nominal categorical variable “EToFirst” measured whether ETo the day of a Prcp event was less than, equal to, or greater than before the Prcp event. The logit model (Equation (8)) demonstrated that ETo volumes the day of a Prcp event were significantly less than ETo volumes on days without Prcp. Further, the plot of the Prcp and ETo observations by month (Figure 2) revealed that months with a higher percentage of rain days also had a higher percentage of days with $\text{ETo} \leq 0.21$ inches. ETo and Prcp exhibited a negative relationship overall, as initially hypothesized.

When observing recovery time using the nominal categorical variable “ETolev2” (Equations (9)–(11)) measuring whether ETo is the same after a Prcp event (or the last event in the series of events) as during a Prcp event (or the last day of Prcp in the series of events), there was a greater likelihood of ETo increasing the day after the Prcp event or series of events versus decreasing (38 versus 21 percent, resp.). The greater likelihood of ETo increasing the day after the Prcp event (or series of events), versus decreasing, was also the case for events lasting more than one day, for example, 13 versus 59 percent (resp.) for two-day events. The recovery time or increase in ETo after the Prcp event was more likely with lower Prcp volumes than for higher Prcp volumes, for example, 50 percent for category 1 versus 29 percent for category 4 of the dependent variable “PrcpAmt.” Also, the logit model (Equation (16)) with the dependent nominal categorical variable “PrcpOn” showed a negative change in ETo on the day of a Prcp event, or first day in a series of events

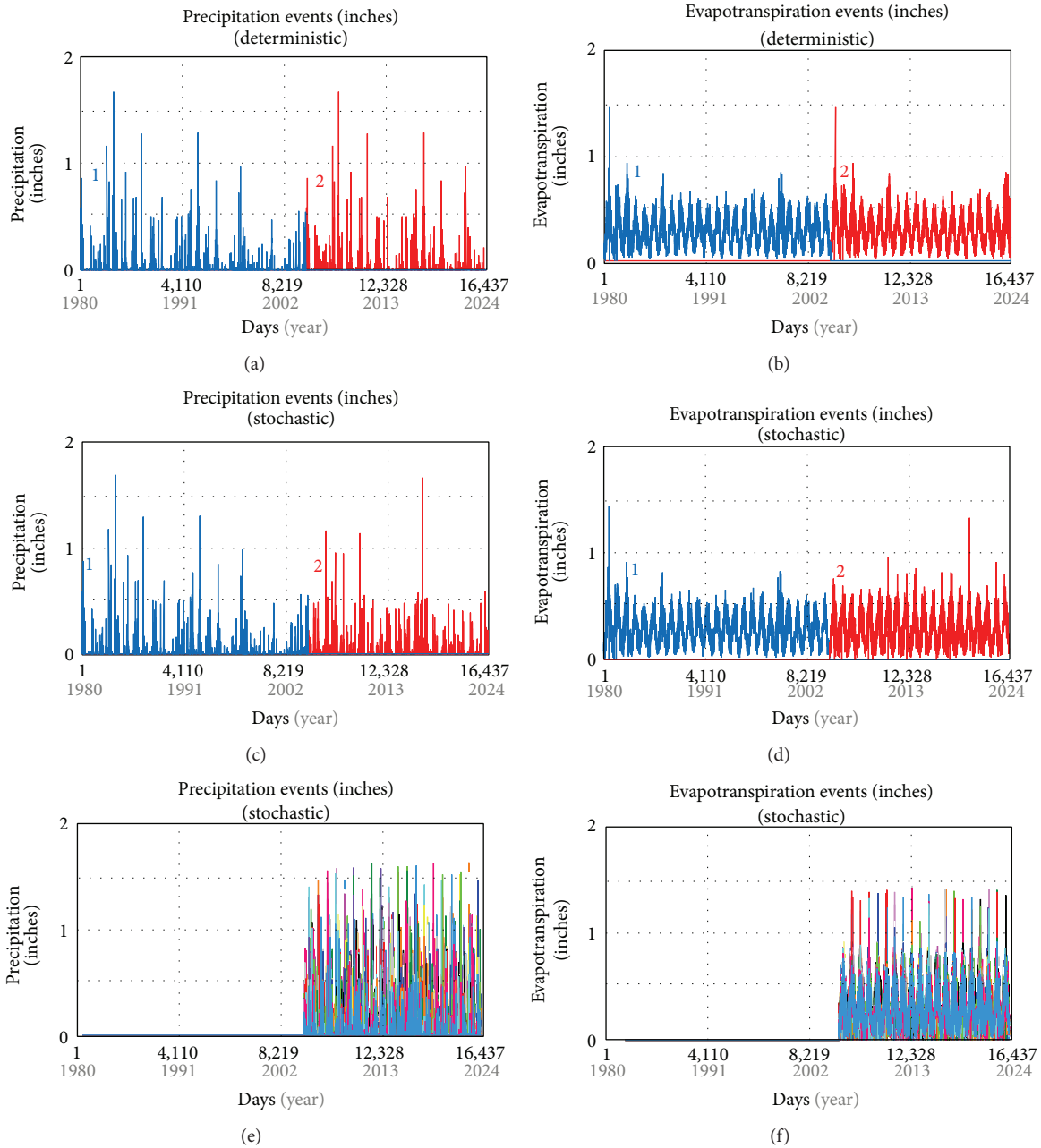


FIGURE 4: Comparison of historic (1) versus simulated (2) and deterministic versus stochastic climates for the S^4M daily time step: (a) precipitation (Prpc) events (inches)—simulated deterministic, (b) evapotranspiration (ETo) events (inches)—simulated deterministic, (c) Prpc events (inches)—simulated stochastic, (d) ETo events (inches)—simulated stochastic, (e) Prpc events (inches)—simulated stochastic (100 repetitions), and (f) ETo events (inches)—simulated stochastic (100 repetitions).

when compared to days without Prpc events. Moreover, the logit model (Equation (12)) with the dependent nominal categorical variable “Prconafter” showed that compared to days without Prpc, the first day of a Prpc event produced a lower ETo volume (coefficient of -5.842) while days after a Prpc event (or the last day in a series of events) also had a lower ETo volume (coefficient of -4.624). Clearly, the first day of the Prpc event had a larger ETo volume than the day after

the Prpc event (or series of events) indicating some recovery from the Prpc event. The recovery time of ETo was tested using another logit model (Equation (13)) using the same dependent variable “Prconafter” but with the independent variable “EToPerCh,” measuring the percent change in ETo from one day to the next. The logit model (Equation (13)) results showed that when compared to days without Prpc, ETo decreased on the first day of a Prpc event. However, a positive

change in ETo the day after the Prcp event (or the last day in a series of events) means ETo increased when compared to days without Prcp events.

An analysis of the frequency of observations for each category of the variable “EToOne” showed that ETo the day after a sequence of Prcp events is generally less than the ETo the day before the sequence of Prcp events. In fact, the ETo volume after the Prcp event is less than the ETo volume the day before the first Prcp events 48 and 50 percent of the time for larger Prcp volume events. Therefore, the frequency that recovery time is within a day of a Prcp event only occurs about 50 percent of the time for larger volume Prcp events.

The logit model (Equation (14)) demonstrated that there is actually less ETo the day before a Prcp event as compared to days without Prcp. Moreover, compared to days without Prcp there is typically less ETo the day after the Prcp event, or last day in a series of events. The other logit model (Equation (15)) reveals a positive increase in ETo before a Prcp event and a positive increase the day after a Prcp event (or series of events) when compared to days without Prcp events. The analysis of single versus subsequent Prcp events result showed the probability of a given Prcp volume for a second consecutive Prcp event based on the Prcp volume of the first Prcp event.

3.3. Salton Sea Stochastic Simulation Model (S^4M). Based on the complex relationships revealed by the logistic regression models, a methodology to generate ETo and Prcp as driving variables in a simulation model other than using the historic data time series (in other words not copying the historic data time series and pasting it to represent the future data time series) was developed for ETo and Prcp data within the SS watershed. However, the technique used in this study maintains the relationships between the historic frequency distributions and interdependency of ETo and Prcp (Figure 2), instead of treating them as separate unconnected variables in the model. Curves for statistical distribution curves were fit to the historical ETo and Prcp data for the occurrence of a precipitation event, the duration of an event, the volume of the event, and the volume of evapotranspiration occurring on that day. The simulation processes the new module following the logic in Figure 3. For any time step for a given month, there are four steps: (1) the probability of a Prcp event occurring is randomly selected from the statistical distribution for that month; (2) if Prcp occurs, then a duration of the event is chosen from the probability distribution of durations for that month (with maximum durations being 7 days); (3) a volume of Prcp is calculated from the probability distributions of volumes for events of that duration for that month; and (4) ETo is generated from the probability distributions associated with Prcp events of that duration for that month (Figure 3). The ability of the S^4M to reasonably simulate the fluctuations in Prcp and ETo volumes, duration of Prcp events, all while preserving the relationships between the patterns between them is evident in Figure 4.

3.4. S^4M Evaluation. The deterministic version of S^4M was evaluated in Kjelland [28]. When the stochastic weather

simulator was added, the model simulated historic sea elevations reasonably well with a difference of only 1 foot at its most disparate point, -228 fasl (simulated) and -229 fasl (historic), and maintained patterns of seasonality. Based on the observed versus simulated sea elevation data, the model has an error rate of less than 1%. These sea elevation results are comparable to IIDWD and CH2MHILL [54], indicating that S^4M has a reasonable ability to simulate the hydrology of the Salton Sea. Figure 4 shows that Prcp and ETo and patterns are similar when comparing the simulated versus historic data, in both magnitude, that is, volumes, and frequency. With regard to TDS, the model validation simulations resulted in the most disparate underestimation of 2,999 mg/L (44,788 mg/L simulated versus 47,787 mg/L observed) compared to the most disparate overestimation of 2,541 mg/L (42,963 mg/L simulated versus 40,422 mg/L observed). Based on the observed versus simulated sea TDS data, the model has an error rate of about 7% at its most disparate points and can be regarded as reasonable given that subsequent years' error rates are much less and the sea's general salinity trend does not change. The model verification results for salinity in a study by IIDWD and CH2MHILL [54] yielded an error rate of approximately 6% at the most disparate point (1980 to 2000), similar to results of the Salton Sea Ecosystem Restoration Program [55].

The S^4M results pertaining to the baseline trends in elevation and salinity projections for the year 2024 are similar to the results from other studies. For example, the *Colorado River Board of California* [56] used sequential cycling of historic conditions as the basis for future inflow conditions and estimated Salton Sea elevations from approximately -231.4 to -233 fasl and a salinity of 67,000 to 79,600 ppm by the year 2020. Cohen and Hyun [27] showed a Salton Sea elevation of -233.6 fasl and a salinity of 60,000 ppm by the year 2018, and an elevation of approximately -245 fasl with salinity between 90,000 and 100,000 ppm by the year 2024. The simulated Salton Sea elevation and salinity results were -234 fasl and 75,000 ppm, respectively, by the year 2030 and assumed reduced future inflow conditions [39]. Moreover, current conditions show that model simulations for salinity are very similar to those of today, about 48,055 ppm (48 g/L) [57] to about 51,000 ppm (approximately 51 g/L) [58].

3.5. Salton Sea Climate Scenarios Using Stochastic Generator.

Three future SS climate scenarios were examined: (1) no change in ETo, Prcp, and river flows (Baseline) versus (2) a scenario of a ten percent increase in Prcp and river flows, and (3) a scenario of a 10 percent decrease in Prcp and river flows (most likely scenario according to Seager et al. [59]). In the climate sensitivity analysis using the historic driving variables ETo, Prcp, and river flows, that is, the past projected into the future version of the model, the elevation of the sea at the end of 2024 was -235.38 fasl with a salinity of 59,292 mg/L under baseline conditions versus -233.38 and -237.09 fasl and salinities of 56,533 and 61,903 mg/L for scenarios 2 and 3, respectively (Figure 5, Table 4). In the stochastic version of the model, the elevation of the sea at the end of 2024 was -235.36 fasl with a salinity of 59,025 mg/L for the baseline

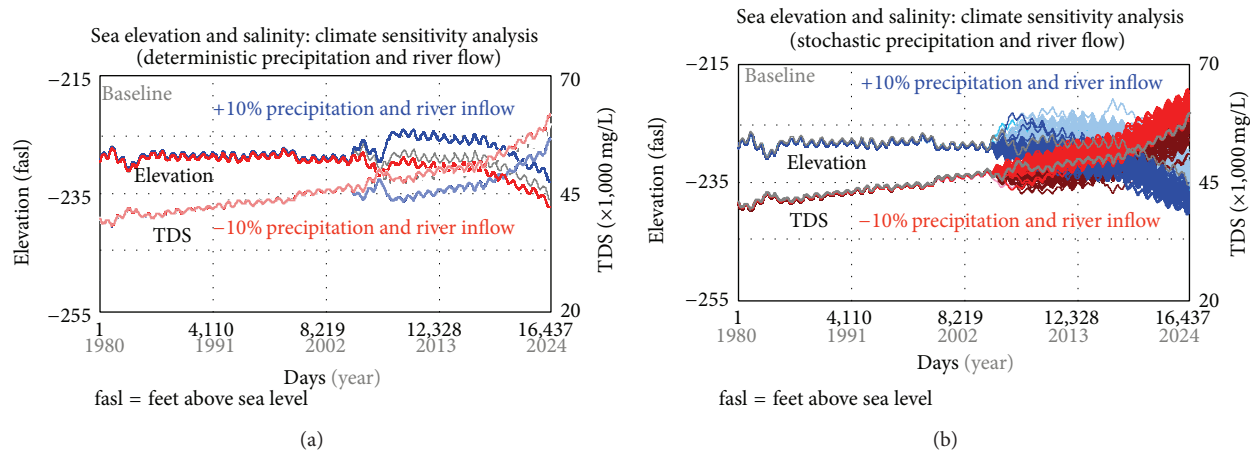


FIGURE 5: Salton Sea Stochastic Simulation Model (S^4M) climate sensitivity analysis: (a) climate sensitivity analysis ($\pm 10\%$ historic) using deterministic driving variables (100 replicates) and (b) climate sensitivity analysis ($\pm 10\%$ historic) using stochastic (100 replicates) driving variables.

version of the model versus -233.4 and -237.06 fasl and salinities of $56,335$ and $61,598$ mg/L for scenarios 2 and 3, respectively (Figure 5, Table 4). For both deterministic and stochastic versions of the model, the ANOVA (Tables 4 and 5) and Bonferroni multiple comparisons post hoc tests results revealed a statistically significant difference ($P < 0.05$) for the sea's elevations and salinities between the baseline climate scenario versus climate scenarios 2 and 3, as well as the elevations and salinities between climate scenarios 2 and 3 themselves.

4. Conclusions

The results of the logistic regression and curve fitting analyses provided valuable insight into the dynamics between single versus multiple Prcp events and the interaction between ETo and Prcp in the SS watershed, both of which are essential to the development of the aforementioned future climate scenario methodology. Results show that months with a larger percentage of Prcp events had a larger percentage of days with low ETo. Similar to the Sahara desert study by Scott et al. [35], the effect of a Prcp event had a negative effect on ETo in the semiarid environment around the SS but elucidated a more complex relationship. The results demonstrate that the longer the duration of the Prcp event, the larger the decrease in ETo volumes, in general, and for a longer period of time. Likewise, larger Prcp volume events suppress ETo volumes more so than smaller Prcp events. Based on the multinomial logistic regression models, the duration of the Prcp event is a slightly better predictor of ETo volumes than the Prcp volume associated with the Prcp event. Overall, ETo and Prcp exhibited a negative relationship.

The present study quantifies the relationships between ETo and Prcp in a semiarid region and provides a technique for maintaining these relationships in research involving stochastic climate simulation modeling. The overall low Pseudo R^2 values of the multinomial regression models

lend support for using this strategy. The curve-fitting results for each monthly dataset resulted in similar distributions providing the "best" fit to the data; however, the distributions for the averaged monthly TIBC dataset often varied, more so for ETo than Prcp. Therefore, if more detailed weather patterns and accuracy in resulting fluctuations are important to the research question being addressed, then individual distributions should be incorporated for respective months when modeling future climate scenarios, such as in the SS watershed.

Concerning climate futures, a comparison can be made between the two strategies that were used in modeling the uncertainty in future climate projections: (1) the deterministic version of the driving variables and (2) the stochastic version of the driving variables. The difference between end simulation baseline mean elevations between the two strategies was less than 3 feet, that is, range of baseline minimum and maximum. The climate sensitivity analyses revealed that the cumulative effects and change of ± 10 percent in SS inflows over the period of analysis can have significant effects ($P < 0.05$) on sea elevation and salinity, thereby demonstrating the importance of including climate uncertainty in the model.

According to climate model projections by Seager et al. [59], the Colorado River headwaters are expected to have an annual stream flow decline of 10 percent and as much as a 20 percent drop in spring runoff in California and Nevada, as warmer temperatures of $1\text{--}2^\circ\text{C}$ also boost evaporation in 2021–2040. Given that the S^4M has been constructed, tested, and validated, one can use it to test many different climate scenarios and the implications that climate change may hold for policy making in the region. One can use the climate modeling method constructed and tested herein to test many different climate scenarios and the implications that climate change may hold for policy making in the region, as well as applying the technique to other semiarid regions. In future research, alternative future scenarios can be defined and used

TABLE 4: Salton Sea (SS) climate sensitivity analysis: one-way ANOVA descriptives.

(I) trial	N	Mean	Std. deviation	Std. error	95% Confidence interval for mean		Minimum	Maximum
					Lower bound	Upper bound		
SS elevation ^a								
1	100	-235.38	0.00	0.00	-235.38	-235.38	-235.39	-235.37
2	100	-233.38	0.01	0.00	-233.38	-233.37	-233.38	-233.37
3	100	-237.09	0.01	0.00	-237.09	-237.08	-237.09	-237.08
Total	300	-235.28	1.52	0.09	-235.45	-235.11	-237.09	-233.37
SS salinity ^a								
1	100	59,292	5	1	59,291	59,293	59,277	59,306
2	100	56,533	5	1	56,532	56,534	56,521	56,546
3	100	61,903	6	1	61,902	61,905	61,891	61,916
Total	300	59,243	2,196	127	58,993	59,492	56,521	61,916
SS elevation ^b								
1	100	-235.36	1.00	0.10	-235.55	-235.16	-238.18	-233.23
2	100	-233.40	1.77	0.18	-233.75	-233.05	-236.52	-227.72
3	100	-237.06	0.90	0.09	-237.24	-236.88	-238.98	-234.35
Total	300	-235.27	1.97	0.11	-235.49	-235.05	-238.98	-227.72
SS salinity ^b								
1	100	59,025	1,450	145	58,737	59,312	56,073	63,380
2	100	56,335	2,245	225	55,890	56,781	49,703	60,731
3	100	61,598	1,415	141	61,317	61,879	57,634	64,712
Total	300	58,986	2,768	160	58,671	59,300	49,703	64,712

Climate sensitivity analysis: ^adeterministic model results; ^bstochastic model results.

(I) trial: 1 = baseline, 2 = +10%, 3 = -10%.

Elevation units = feet above sea level.

Salinity = mg/L.

TABLE 5: Salton Sea (SS) climate sensitivity analysis: one-way ANOVA results.

	Sum of squares	df	Mean square	F	Sig.
SS elevation ^a					
Between groups	689.7	2	344.9	15200536.0	0.000
Within groups	0.0	297	0.0		
Total	689.7	299			
SS salinity ^a					
Between groups	1442505659.6	2	721252829.8	24552559.5	0.000
Within groups	8724.6	297	29.4		
Total	1442514384.2	299			
SS elevation ^b					
Between groups	670.9	2	335.4	203.6	0.000
Within groups	489.2	297	1.6		
Total	1160.1	299			
SS salinity ^b					
Between groups	1385130746.6	2	692565373.3	227.2	0.000
Within groups	905456580.5	297	3048675.4		
Total	2290587327.1	299			

Climate sensitivity analysis: ^adeterministic model results; ^bstochastic model results.

to explore the hydrologic and environmental implications of variations in, among other things, climate change and water-related policy decisions.

Conflict of Interests

The authors declare that there is not a conflict of interests regarding the present research.

Acknowledgments

The authors would like to thank Craig Forster, Edith González Afanador, and Ann L. Kenimer for their assistance. T. W. Clumpkin provided a thorough review. Financial support for this study was provided by the Southwest Consortium for Environmental Research and Policy (SCERP) through a cooperative agreement with the US Environmental Protection Agency.

References

- [1] G. M. MacDonald, "Water, climate change, and sustainability in the Southwest," *Proceedings of the National Academy of Sciences of the United States of America*, vol. 107, no. 50, pp. 21256–21262, 2010.
- [2] J. A. Vano, T. Das, and D. P. Lettenmaier, "Hydrologic sensitivities of Colorado River runoff to changes in precipitation and temperature," *Journal of Hydrometeorology*, vol. 13, pp. 932–949, 2012.
- [3] D. R. Cayan, T. Das, D. W. Pierce, T. P. Barnett, M. Tyree, and A. Gershunova, "Future dryness in the Southwest US and the hydrology of the early 21st century drought," *Proceedings of the National Academy of Sciences of the United States of America*, vol. 107, no. 50, pp. 21271–21276, 2010.
- [4] D. S. Wilks, "Multisite generalization of a daily stochastic precipitation generation model," *Journal of Hydrology*, vol. 210, no. 1–4, pp. 178–191, 1998.
- [5] S. Fatichi, V. Y. Ivanov, and E. Caporali, "Simulation of future climate scenarios with a weather generator," *Advances in Water Resources*, vol. 34, no. 4, pp. 448–467, 2011.
- [6] C. W. Richardson and D. A. Wright, "WGEN: a model for generating daily weather variables," USDA Agricultural Research Service ARS-8, 1984.
- [7] G. A. Baigorria and J. W. Jones, "GiST: a stochastic model for generating spatially and temporally correlated daily rainfall data," *Journal of Climate*, vol. 23, no. 22, pp. 5990–6008, 2010.
- [8] R. Leander and T. A. Buishand, "A daily weather generator based on a two-stage resampling algorithm," *Journal of Hydrology*, vol. 374, no. 3–4, pp. 185–195, 2009.
- [9] A. Mezghani and B. Hingray, "A combined downscaling-disaggregation weather generator for stochastic generation of multisite hourly weather variables over complex terrain: development and multi-scale validation for the Upper Rhone River basin," *Journal of Hydrology*, vol. 377, no. 3–4, pp. 245–260, 2009.
- [10] B. Rajagopalan, U. Lall, D. G. Tarboton, and D. S. Bowles, "Multivariate non-parametric resampling scheme for generation of daily weather variables," *Stochastic Hydrology and Hydraulics*, vol. 11, pp. 65–93, 1997.
- [11] D. S. Wilks, "Simultaneous stochastic simulation of daily precipitation, temperature and solar radiation at multiple sites in complex terrain," *Agricultural and Forest Meteorology*, vol. 96, no. 1–3, pp. 85–101, 1999.
- [12] E. H. Chin, "Modeling daily precipitation occurrence process with Markov Chain," *Water Resources Research*, vol. 13, no. 6, pp. 949–956, 1977.
- [13] T. Chapman, "Stochastic modelling of daily rainfall: the impact of adjoining wet days on the distribution of rainfall amounts," *Environmental Modelling and Software*, vol. 13, no. 3–4, pp. 317–324, 1998.
- [14] R. Srikanthan and T. A. McMahon, "Stochastic generation of annual, monthly and daily climate data: a review," *Hydrology and Earth System Sciences*, vol. 5, no. 4, pp. 653–670, 2001.
- [15] T. I. Harrold, A. Sharma, and S. J. Sheather, "A nonparametric model for stochastic generation of daily rainfall amounts," *Water Resources Research*, vol. 39, no. 12, 2003.
- [16] D. S. Wilks and R. L. Wilby, "The weather generation game: a review of stochastic weather models," *Progress in Physical Geography*, vol. 23, no. 3, pp. 329–357, 1999.
- [17] T. A. Buishand, "Some remarks on the use of daily rainfall models," *Journal of Hydrology*, vol. 36, no. 3–4, pp. 295–308, 1978.
- [18] R. Srikanthan and G. G. S. Pegram, "A nested multisite daily rainfall stochastic generation model," *Journal of Hydrology*, vol. 371, no. 1–4, pp. 142–153, 2009.
- [19] W. P. Miller, T. C. Piechota, S. Gangopadhyay, and T. Pruitt, "Development of streamflow projections under changing climate conditions over Colorado River basin headwaters," *Hydrology and Earth System Sciences*, vol. 15, no. 7, pp. 2145–2164, 2011.
- [20] T. A. McMahon, M. C. Peel, L. Lowe, R. Srikanthan, and T. R. McVicar, "Estimating actual, potential, reference crop and pan evaporation using standard meteorological data: a pragmatic synthesis," *Hydrology and Earth System Sciences*, vol. 17, pp. 1331–1363, 2013.
- [21] J. J. Beersma and T. A. Buishand, "Multi-site simulation of daily precipitation and temperature conditional on the atmospheric circulation," *Climate Research*, vol. 25, no. 2, pp. 121–133, 2003.
- [22] R. L. Snyder, S. Geng, M. Orang, and S. Sarreshteh, "Calculation and simulation of evapotranspiration of applied water," *Journal of Integrative Agriculture*, vol. 11, no. 3, pp. 489–501, 2012.
- [23] N. S. Christensen and D. P. Lettenmaier, "A multimodel ensemble approach to assessment of climate change impacts on the hydrology and water resources of the Colorado River Basin," *Hydrology and Earth System Sciences*, vol. 11, no. 4, pp. 1417–1434, 2007.
- [24] G. A. Baigorria, "Stochastic models to generate geospatial-, temporal-, and cross-correlated daily maximum and minimum temperatures," *Advances in Meteorology*, vol. 2014, Article ID 365362, 14 pages, 2014.
- [25] R. G. Allen, I. A. Walter, R. L. Elliott et al., *The ASCE Standardized Reference Evapotranspiration Equation*, American Society of Civil Engineers, Reston, Va, USA, 2005.
- [26] M. J. Cohen, E. P. Glenn, and J. I. Morrison, "Haven or hazard: the ecology and future of the Salton Sea," A Report of the Pacific Institute, Executive Overview, 1999, <http://www.sci.sdsu.edu/salton/EcoSaltonSeaPacInstExeSum.html>.
- [27] M. J. Cohen and K. H. Hyun, *HAZARD—The Future of the Salton Sea With No Restoration Project*, Pacific Institute for Studies in Development, Environment, and Security, Oakland, Calif, USA, 2006.
- [28] M. E. Kjelland, *The future of the salton sea under proposed lower colorado river basin water management scenarios [Ph.D. dissertation]*, Department of Wildlife & Fisheries Sciences, Texas A&M University, 2008.
- [29] Isee Sytems, "STELLA 8.0 software," Lebanon, New Hampshire, USA, 2006.
- [30] S. Naoum and I. K. Tsanis, "Hydroinformatics in evapotranspiration estimation," *Environmental Modelling and Software*, vol. 18, no. 3, pp. 261–271, 2003.
- [31] L. Castañeda and P. Rao, "Comparison of methods for estimating reference evapotranspiration in Southern California," *Journal of Environmental Hydrology*, vol. 13, no. 14, pp. 1–10, 2005.
- [32] V. P. Singh, *Hydrologic System—Rainfall-Runoff Modeling*, Prentice-Hall, Englewood Cliffs, NJ, USA, 1988.
- [33] R. G. Allen, L. S. Pereira, D. Raes, and M. Smith, "Crop evapotranspiration—guidelines for computing crop water requirements," FAO Irrigation and Drainage No. 56, Food and Agriculture Organization of the United Nations, Rome, Italy, 1998.

- [34] A. Munévar, *Hydrology Development and Future Hydrologic Scenarios for the Salton Sea Ecosystem Restoration Program PEIR: Inflows/Modeling Working Group Preliminary Draft*, 2006.
- [35] R. Scott, D. Entekhabi, R. Koster, and M. Suarez, “Timescales of land surface evapotranspiration response,” *Journal of Climate*, vol. 10, no. 4, pp. 559–566, 1997.
- [36] C. B. Cook, G. T. Orlob, and D. W. Huston, “Simulation of wind-driven circulation in the Salton Sea: implications for indigenous ecosystems,” *Hydrobiologia*, vol. 473, pp. 59–75, 2002.
- [37] W. W. Walker, “Simplified procedures for eutrophication assessment and prediction: user manual,” Instruction Report W-96-2, U.S. Army Corps of Engineers, Water Operations Technical Support Program, U.S. Army Engineer Waterways Experiment Station, Vicksburg, Miss, USA, 1996.
- [38] M. Anderson, “Appendix I—predicted water quality in the southern impoundments,” in *Evaluation of a Proposal for Conversion of the Salton Sea Ecosystem*, U.S.D.I. Salton Sea Science Office, Ed., pp. 1–38, The Pacific Institute for Studies in Development, Environment and Security, Oakland, Calif, USA, 2002.
- [39] Tetra Tech, *Salton Sea Restoration Project Environmental Impact Statement/Environmental Impact Report (Draft)*, Prepared for the Salton Sea Authority and U.S. Department of Interior Bureau of Reclamation, Boulder City, Nev, USA, 2000.
- [40] E. G. Chung, S. G. Schladow, J. Perez-Losada, and D. M. Robertson, “A linked hydrodynamic and water quality model for the Salton Sea,” *Hydrobiologia*, vol. 604, no. 1, pp. 57–75, 2008.
- [41] California Irrigation Management Information System (CIMIS), *Spatial CIMIS*, Department of Water Resources, Office of Water Use Efficiency, Sacramento, California, USA, 2013, <http://www.cimis.water.ca.gov/cimis/cimiSatStationLocation.jsp>.
- [42] National Climatic Data Center (NCDC), *Climate Data Online: Text & Map Search*, National Oceanic and Atmospheric Administration (NOAA), Asheville, NC, USA, 2013, <http://www.ncdc.noaa.gov/cdo-web/#t=firstTabLink>.
- [43] A. A. Voinov, H. C. Fitz, and R. Costanza, “Surface water flow in landscape models: 1. Everglades case study,” *Ecological Modelling*, vol. 108, no. 1–3, pp. 131–144, 1998.
- [44] S. J. Bhuyan, K. R. Mankin, and J. K. Koelliker, “Watershed—scale AMC selection for hydrologic modeling,” *Transactions of the American Society of Agricultural Engineers*, vol. 46, no. 2, pp. 303–310, 2003.
- [45] Salton Sea Ecosystem Restoration Program, *Hydrology Development and Future Hydrologic Scenarios for the Salton Sea Ecosystem Restoration Program PEIR, Inflows/Modeling Working Group Preliminary Draft*, Department of Water Resources, Colorado River and Salton Sea Office, Sacramento, Calif, USA, 2006.
- [46] “MathWave Technologies (EasyFit Version 1.3),” Topol-3, 30/2/27, Dnepropetrovsk, Ukraine, 2006, <http://www.math-wave.com/>.
- [47] A. Agresti, *An Introduction to Categorical Data Analysis*, John Wiley & Sons, New York, NY, USA, 2nd edition, 1996.
- [48] D. W. Hosmer and S. Lemeshow, *Applied Logistic Regression*, John Wiley & Sons, New York, NY, USA, 2nd edition, 2000.
- [49] StataCorp, “Stata Statistical Software: Release 9.0,” College Station, Tex, USA, 2005.
- [50] Environmental Systems Research Institute (ESRI), *ArcGIS Desktop: Release 9 [Software]*, Environmental Systems Research Institute, Redlands, Calif, USA, 2004.
- [51] *Salton Sea Digital Atlas*, Redlands Institute, University of Redlands, Redlands, Calif, USA, 2004, <http://www.spatial.redlands.edu/salton/>.
- [52] S. T. Y. Tong and W. Chen, “Modeling the relationship between land use and surface water quality,” *Journal of Environmental Management*, vol. 66, no. 4, pp. 377–393, 2002.
- [53] SPSS, *SPSS Base 12.0.1 for Windows User’s Guide*, SPSS, Chicago, Ill, USA, 2003.
- [54] Imperial Irrigation District Water Department (IIDWD) and CH2MHill, *Imperial Irrigation Decision Support System Summary Report (Draft)*, Redding, Calif, USA, 2001.
- [55] Department of Water Resources, Colorado River and Salton Sea Office, *Hydrology Development and Future Hydrologic Scenarios for the Salton Sea Ecosystem Restoration Program PEIR, Inflows/Modeling Working Group Preliminary Draft*, Salton Sea Ecosystem Restoration Program, Sacramento, Calif, USA, 2006.
- [56] Colorado River Board of California, *Report to the California Legislature on the Current Condition of the Salton Sea and the Potential Impacts of Water Transfers*, 1992, <http://www.sci.sdsu.edu/salton/PotentialImpactsSaltonSea.html>.
- [57] M. J. Cohen, “Water brief 2—past and future of the Salton Sea,” in *The World’s Water 2008-2009: The Biennial Report on Freshwater Resources*, P. H. Gleick, H. Cooley, and M. Morikawa, Eds., vol. 6 of *World’s Water*, pp. 127–138, Island Press, 2009.
- [58] U.S. Army Corps of Engineers (USACE) and California Natural Resources Agency (CNRA), “Salton sea species conservation habitat project,” Draft Environmental Impact Statement/Environmental Impact Report No. SPL-2010-00142-LLC, State Clearinghouse No. 2010061062, Prepared for the California Natural Resources Agency by the Department of Water Resources and Department of Fish and Game. U.S. Army Corps of Engineers Application, 2011.
- [59] R. Seager, M. Ting, C. Li et al., “Projections of declining surface-water availability for the southwestern United States,” *Nature Climate Change*, vol. 3, pp. 482–486, 2012.

Research Article

Improving Carbon Mitigation Potential through Grassland Ecosystem Restoration under Climatic Change in Northeastern Tibetan Plateau

Lin Huang, Xinliang Xu, Quanqin Shao, and Jiyuan Liu

The Institute of Geographical Sciences and Natural Resources Research, Chinese Academy of Sciences, Beijing 100101, China

Correspondence should be addressed to Xinliang Xu; xuxl@reis.ac.cn

Received 14 February 2014; Accepted 2 April 2014; Published 8 May 2014

Academic Editor: Dong Jiang

Copyright © 2014 Lin Huang et al. This is an open access article distributed under the Creative Commons Attribution License, which permits unrestricted use, distribution, and reproduction in any medium, provided the original work is properly cited.

To protect the water tower's ecosystem environment and conserve biodiversity, China has been implementing a huge payment program for ecosystem services in the three rivers source region. We explored here the dynamics of grassland degradation and restoration from 1990 to 2012 and its relationships with climate mitigation in the TRSR to provide a definite answer as to the forcing and response of grassland degradation and restoration to climate change. Then we estimated its potential of climate mitigation benefits to address the question of whether ecological restoration could be effective in reversing the decline of ecosystem carbon mitigation service. The trend of average annual temperature and precipitation observed by meteorological stations were approximately increased. Compared before and after 2004, the area of grassland degradation was increased slightly. However, nearly one-third of degraded grassland showed improvement, and the grassland vegetation coverage showed significant increase. Comparing current grassland vegetation coverage with healthy vegetation cover with the same grass type, nearly half of the area still needs to further restore vegetation cover. The grassland degradation resulted in significant carbon emissions, but the restoration to its healthy status has been estimated to be technical mitigation potential.

1. Introduction

Ecosystem degradation is causing decline in ecosystem condition and widespread biodiversity loss, leading to reduced provision of ecosystem services [1–3], and may cause the irrevocable loss of ecosystem functions such as soil and soil moisture retention, regulation of water flows, and regulation of carbon and nitrogen cycles [4, 5]. Ecological restoration is regarded as a major strategy for reestablishing and increasing the provision of ecosystem services as well as reversing biodiversity losses [3, 6], but conflicts can arise, especially if single services are targeted in isolation, and the recovery can be slow and incomplete [3]. In addition, a lack of scientific understanding of the factors influencing provision of ecosystem services and of their economic benefits limits their incorporation into land-use planning and decision making [7, 8].

The many ecosystem services from grasslands will be valued variously by different stakeholders, in which local

stakeholders may tend to value productive services and specific ecosystem services such as hydrological services, while international valuations may apply to niche products or for biodiversity conservation services [5]. However, there are usually trade-offs between the different ecosystem services targeted [9]. Restoration of converted grasslands may improve ecosystem services functioning [10, 11], in some cases to levels comparable with nondegraded grasslands, but may not be able to fully restore ecosystem service provision to that of natural grassland [10, 12].

Change in vegetation cover at landscape scale has potential to influence regional climate [13], which may be larger than the effects of global climate change [5]. Various methods of improved grassland management can sequester carbon in soils [14] and in below- and aboveground biomass [15]. Compared to other mitigation options, grassland mitigation is cost-competitive [16, 17]. Climate change mitigation services in grasslands may provide an entry point to the valuation of grasslands for their conservation and restoration.

Globally, grazing land management has been estimated to have a technical mitigation potential of 1.5 Gt CO₂ eq p.a. to 2030 [5]. Degraded grasslands may have significant potential for carbon sequestration [18], through protection and restoration of grasslands. Unfortunately, data on the restoration potential of degraded grassland is not available. Systematic documentation and analysis of costs of protecting and restoring grasslands are still limited [5].

More analysis and evidences are crucially required to provide a definite answer as to the forcing and response of grassland degradation and restoration to climate change and its potential of climate mitigation benefits. Here, we explored in detail the dynamics of grassland degradation and restoration and its relationships with climate mitigation in the TRSR. Specifically, we ask the following questions: (1) how to analyze the dynamics of grassland degradation and restoration under the climate change? (2) Whether ecological restoration could be effective in reversing the decline of ecosystem carbon mitigation service? (3) Will a focus on the ecosystem service enable providing a mechanism for their potential climate benefit?

2. Methods

2.1. Study Area. The TRSR (Figure 1), covering 0.36 million km², is located in the northeast of the Tibetan Plateau. It is the source region of the Yangtze River, the Yellow River, and the Mekong River and also one of the most important biodiversity hotspots in China. Glaciers, permafrost, and snows are widespread here owing to its average altitude of above 4,000 meters and annual temperature of $-5.6\sim -3.8^{\circ}\text{C}$. It is also regarded as a gene bank of 2,238 rare species of vascular plateau plants and suitable habitat for more than 400 endangered animal species. Nearly 600 million people who live downstream depend on the proper functioning of the rivers in this region for their livelihood. About 0.6 million people live in the region, in which 68.15% are herders. The Sanjiangyuan National Nature Reserve (SNNR) located in TRSR is the highest and most extensive wetland protected area in the world and has an area of 0.15 million km², which could be divided to 6 subareas and consists of 18 conservation areas. Since 2005, \$7.5 billion yuan (US \$924.79 million) was provided by Chinese government to conserve and restore the ecological environment in SNNR, with a focus on alpine swamp meadow and natural habitat of the unique wildlife.

2.2. Grassland Vegetation Coverage. Vegetation coverage is one of the most important indicators to measure the status of land surface vegetation, and its changes reflected the growing conditions of the vegetation. In this paper, the semi-monthly 1 km NOAA-AVHRR (1990–2000) and 1 km SPOT-VGT (1998–2012 years) were collected as the data source. We produced the annual maximum NDVI values through maximum value composite (MVC). The linear regression analysis and correlation analysis were processed in overlap years (1998–2000) of AVHRR and VGT by pixel average, and linear regression relationships between AVHRR and VGT data for the three years were established. The AVHRR data were corrected grid by grid applying these relationships.

And then we applied 1 km NDVI data products to calculate and analyze annual average maximum vegetation coverage in the periods before (1990–2004) and after (2004–2012) the implementation of ecological conservation program in TRSR, to show the vegetation growing recovery and/or deterioration.

To illustrate the potential of vegetation growing in this area, we have produced the vegetation coverage distribution map of healthy grass ecosystem, which was extracted from average coverage of typical grass lawn in same zonal groups according to the type of “Qinghai Grassland Survey.” We considered that the healthy vegetation coverage with the same grassland type is future recovery goals that we could achieve.

2.3. Grassland Degradation and Restoration. The remote sensing classification system of grassland degradation in TRSR, according to the principles and characteristics of remote sensing image interpretation, and based on a Chinese national standard “the grading index of natural grassland degradation, desertification, salt marshes (GB19377-20031),” was applied to interpret the trends of grassland degradation by remote sensing. The main data sources were MSS in the 1970s, TM in 1990, and TM/ETM in 2004. Images were acquired concentrating on July and August. And false color composition, geometric correction, images mosaic, and segmentation were processed. The outline of grassland degradation type was delimited by comparison of images in different time periods, with the references from the former. By visual interpretation, we produced the grassland degradation conditions and trends in the periods of 1970s–1990 and 1990–2004 in TRSR.

In order to reflect the changing trend of grassland ecosystems more accurately, especially improved and restored grassland, we developed the change trend classification system of degraded grassland, based on the status of grassland degradation. Based on the remote sensing interpretation map of grassland degradation in the periods of 1990–2004, we produced change situation map of degraded grassland ecosystem from 2004 to 2012, by comparing TM or ETM remote sensing images in 2004 and 2012, which consists of new occurring degradation, intensified degradation, non-change, slight restoration, and substantial slight restoration. According to the change information of degraded grassland, we determined the growth variation of grassland vegetation.

2.4. Climate Change Factors Analysis. The TRSR has few national and local stations with weather records spanning 1960s to present. For the long-term meteorological station, we obtained daily data sets of thirteen national stations, including daily maximum and minimum air temperature, air pressure, daily total water equivalent precipitation, relative humidity, snow depth, and evaporation from China Meteorological Bureau. The temperature and rainfall data sets of well-distributed sites were interpolated by the software ANUSPLIN, which considered the impacts of terrain factors and was suitable for long-term observed data.

The moisture index equals the ratio of annual precipitation and annual potential evapotranspiration (PET).

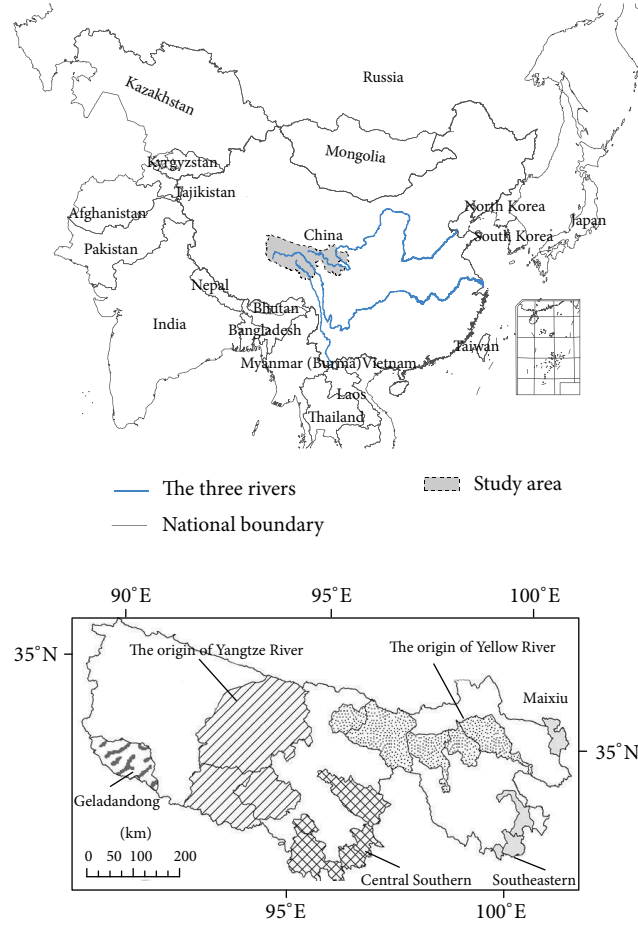


FIGURE 1: Distribution map showing the location of the TRSR.

For each meteorological station, we estimated annual potential evapotranspiration and moisture index using ground meteorological measurement and DEM as input data, applying improved Penman-Monteith and Thornthwaite moisture index to fusion processes and then to estimated water balance of this region for each year. The improved Penman-Monteith recommended by FAO in 1998 presented the PET and Thornthwaite moisture index as follows:

$$I_m = 100 \left(\frac{P}{ET_0} - 1 \right),$$

$$ET_0 = \frac{0.408\Delta (R_n - G) + \gamma (900 / (T + 273)) U_2 (e_s - e_a)}{\Delta + \gamma (1 + 0.34U_2)}. \quad (1)$$

In (1), ET_0 is the potential evapotranspiration (mm day^{-1}), R_n is canopy net radiation ($\text{MJ m}^{-2} \text{day}^{-1}$), G is soil heat fluxes ($\text{MJ m}^{-2} \text{day}^{-1}$), T is the air temperature at 2 m height ($^{\circ}\text{C}$), U_2 is the wind velocity at 2 m height (m s^{-1}), e_s and e_a are saturation vapor pressure and actual water vapor pressure, respectively (kPa), Δ is curve slope of saturation vapor pressure ($\text{kPa } ^{\circ}\text{C}^{-1}$), and γ is constant of psychrometer ($\text{kPa } ^{\circ}\text{C}^{-1}$).

2.5. Carbon Density Change. The conversion of grassland to arable land causes significant emissions of carbon to the atmosphere. For restoration and improved management of grasslands, Table 1 gives some local estimates of mitigation potential per unit area, which was meta-analyzed from other published references [19–25].

3. Results

3.1. Climate Change in Three River's Source Region during 1990–2012. In the periods of 1975–2012, the average annual temperature of meteorological stations in the TRSR was -0.34°C ; the average annual temperature change rate was approximately $0.48^{\circ}\text{C}/10\text{a}$ (Figure 2). During 1990–2004, the average annual temperature was -0.14°C , with the change rate of about $1.38^{\circ}\text{C}/10\text{a}$. During 2004–2012, the annual average temperature was 0.48°C , with the change rate of about $0.19^{\circ}\text{C}/10\text{a}$. Comparing it before and after 2004, the average temperature increased by 0.62°C , but the warming rate is significantly reduced. In the source region of the Yangtze River, the average annual temperature of six meteorological stations from 1975 to 2012 was -1.37°C , and it increased by 0.72°C comparing the period of 2004–2012 with 1990–2004. In the source region of the Yellow River, the average

TABLE I: Carbon density change summarized by restored or degraded grasslands.

Types	Carbon density ($\text{gC}/\text{m}^2/\text{year}$)		
	AGB	BGB	SOC in 0~40 cm
Typical grassland	159.219	990.108	20035.5
Slight grassland degradation	84.533	836.748	16760.0
Middle grassland degradation	79.398	730.600	16145.0
Obvious grassland degradation	36.302	201.672	14360.0
Severe grassland degradation	25.916	50.056	12946.0

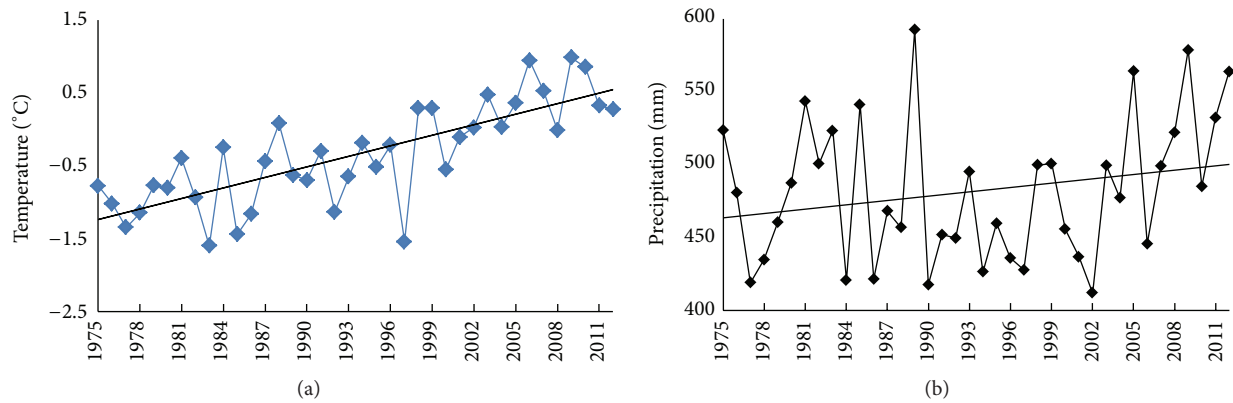


FIGURE 2: The trends of annual average temperature and annual precipitation in 1975–2012.

annual temperature of four meteorological stations from 1975 to 2012 was -0.34°C , and it increased by 0.41°C comparing the period of 2004–2012 with 1990–2004. In the source region of the Lancang River, the average annual temperature of two meteorological stations from 1975 to 2012 was 2.73°C , and it increased by 0.72°C comparing the period of 2004–2012 with 1990–2004. Before 2004 (Figure 3), the temperature change rates in central and southwestern of TRSR were higher than other regions, and they decreased gradually from south to north. The average altitude of average annual temperature greater than 0°C was 3646 m. After 2004, the temperature change in central TRSR was more significant, and the trend was slightly lower in the Northern region. The average altitude of average annual temperature greater than 0°C was 3968 m, reflecting the warming process resulting from the rises of altitude line of average annual temperature greater than 0°C .

During 1975–2012, the average annual precipitation of meteorological stations in the TRSR was 481.83 mm, and variation trend was 9.9 mm/10a (Figure 2). During 1990–2004, the average annual precipitation was 463.56 mm, with trend of about 7.02 mm/10a. During 2004–2012, the average annual precipitation was 518.66 mm, with the trend of about 68.44 mm/10a. Comparing it before and after 2004, annual precipitation increased by 55.10 mm, and increasing trend is more pronounced. In the source region of the Yangtze River, the average annual precipitation of six meteorological stations from 1975 to 2012 was 461.66 mm, and it increased by 64.17 mm comparing the period of 2004–2012 with 1990–2004. In the source region of the Yellow River, the average annual precipitation of four meteorological stations from

1975 to 2012 was 481.78 mm, and it increased by 57.63 mm comparing the period of 2004–2012 with 1990–2004. In the source region of the Lancang River, the average annual precipitation of two meteorological stations from 1975 to 2012 was 542.48 mm, and it increased by 22.84 mm comparing the period of 2004–2012 with 1990–2004. The western and southwestern region of TRSR showed larger increased precipitation; however, the change rate of annual precipitation was increased less in eastern and gradually in central TRSR (Figure 3).

During 1975–2012, the average annual humidity index in TRSR was -57 , with ranges between -86 and -12 (Figure 3). Comparing it during 1990–2004 with 2004–2012, average annual humidity index was increased by about 3.75, from -57 to -53 . Before 2004, humidity index presented a weak decreasing trend, especially in southeastern part. Since 2004, it began an upward trend especially in central regions, but with more significant downward trend in the southern. In the periods of 1975–2012, the average annual humidity index decreased from the southeast to the northwest region. High values of humidity index were mainly distributed in area with relatively lower temperature and potential evapotranspiration and higher rainfall, such as higher mountains in the southeastern and southern part. Low values were mainly distributed in the area of lower temperature, potential evapotranspiration, and annual precipitation, such as alpine steppe and desert areas in northwestern part.

3.2. Grassland Degradation and Restoration over the Past 40 Years. The spatial distribution pattern of degraded grassland in three rivers source region has been basically formed

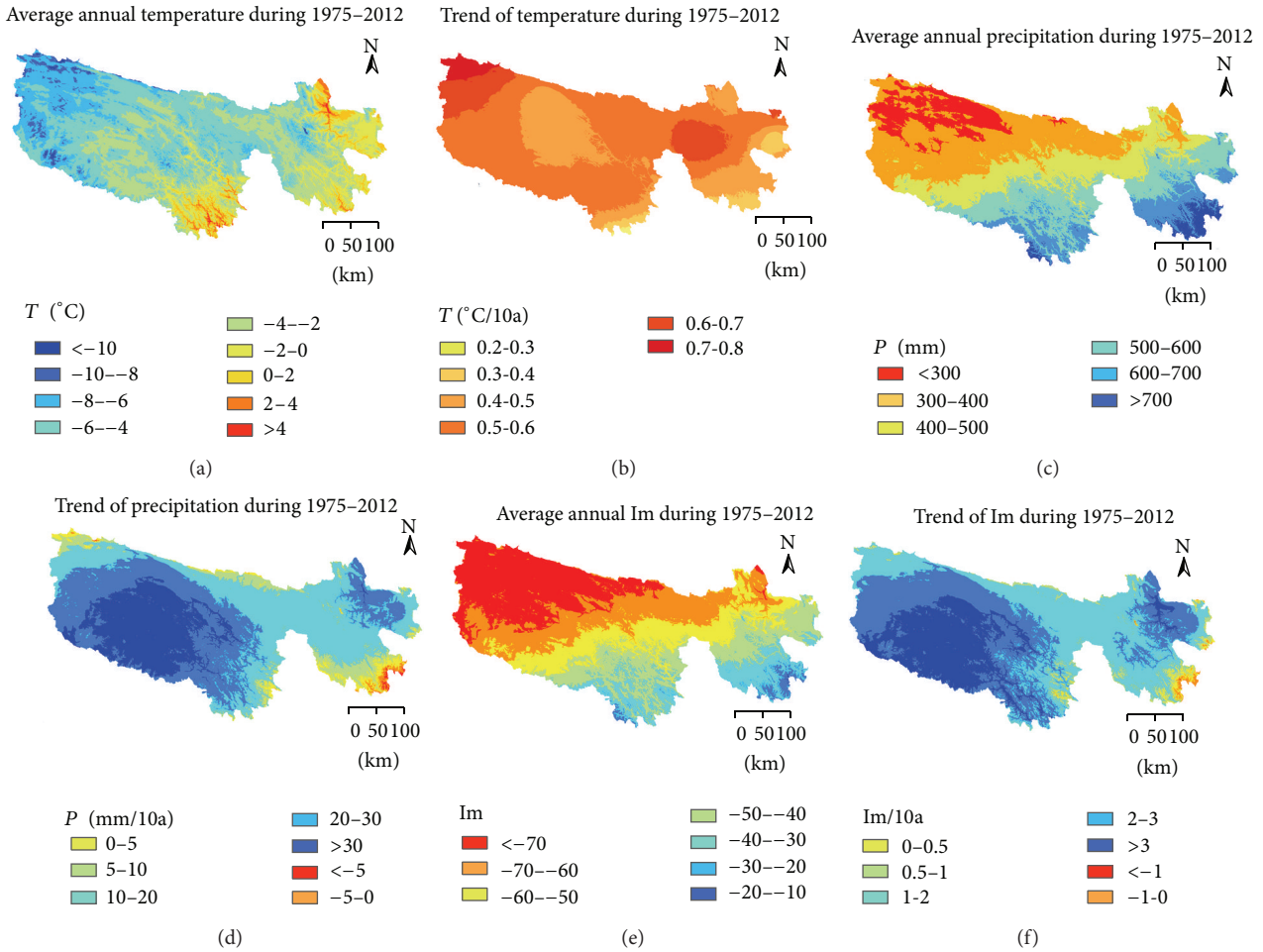


FIGURE 3: The map of temperature, precipitation, and humidity index during 1975-2012.

in 1970s, and the grassland degradation processes continued to occur from the late 1970s to 2004 (Figure 4). During 1970s~1990, area of grassland degradation was 76444.9 km², accounting for 32.83% of the region's grassland area. From 1990 to 2004, area of grassland degradation was 84102.66 km², accounting for 36.12% of the region's grasslands. Comparing the area of grassland degradation before and after 2004, it was increased by 3.87%. From the degree of degradation (Table 2), the grassland degradation in TRSR showed mainly the light and moderate degradation, with severe degradation occurring only in local area. The slightly degraded grassland accounts for 22.88% of the region's total grassland area in 1970s~1990, and it rose to 23.93% from 1990 to 2004, an increase of 1.05%. In the late 1970s to 1990, the moderately degraded grassland accounted for 9.5% of the total grassland, while it rose to 11.74% from 1990 to 2004, an increase of 2.24%.

From 2004 to 2012, the original patches of grassland degradation in the TRSR showed varying degrees of restoration, and the grass situation even improved in some areas. The area of nonchange degradation was 60213.5 km², accounting for 68.52% of the total degraded grassland. Improved grassland was 22927.5 km², accounting for 31.02% of the total

degraded grassland. Among the improved grassland, light improvement of degraded grassland accounted for 24.85% of the total degraded grassland, and obvious improvement accounted for 6.17%. The area of intensified degraded grassland was 297.5 km², accounting for 0.34% of the total degraded grassland. The new occurrence of degraded grassland was 105.9 km². Compared with the early 1990s to 2004, the light, moderate, and severe degraded grassland areas were significantly reduced, especially the moderately degraded grassland which decreased by 5.35%, while the light and severe grassland declined by only 0.33% and 0.09%.

The area of improved grassland in the source region of Yellow River, Yangtze River, and Lancang River were 9145.91 km², 10750.49 km², and 1409.68 km², accounting for 42.93%, 50.46%, and 6.62% of the total improved grassland in TRSR, respectively (Table 3). The grassland degradation in the source region of Yangtze River was more obvious than the Yellow River and the Lancang River, in which intensified grassland degradation was 206.75 km², accounting for 69.85% of intensified degradation in TRSR. And the new occurring degradation in the Yangtze River was 86.34 km², accounting for 86.28% of the total new occurring in TRSR.

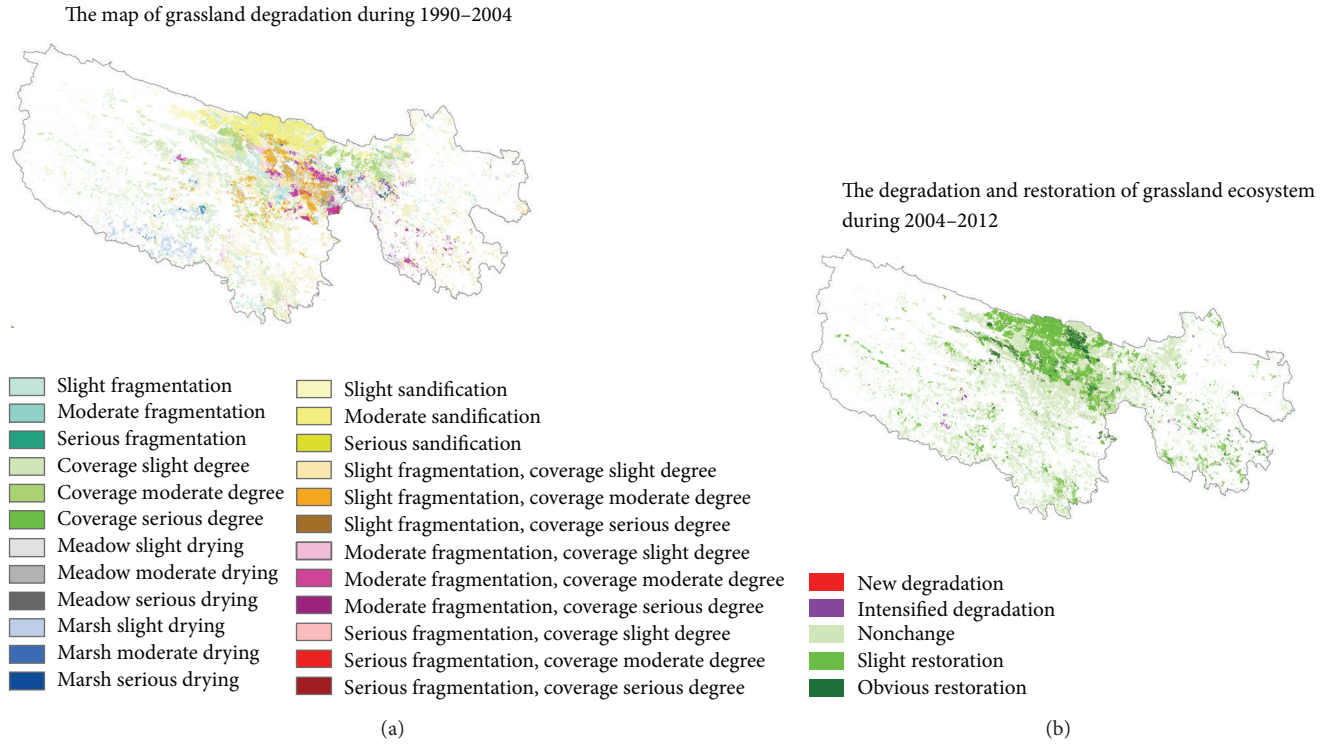


FIGURE 4: The map of grassland degradation during 1990–2004 and 2004–2012 in TRSR.

TABLE 2: The area of grassland degradation and its proportion accounted in total grassland in TRSR.

Type	1970s~1990		1990~2004		2004~2012	
	Area (km ²)	Proportion (%)	Area (km ²)	Proportion (%)	Area (km ²)	Proportion (%)
Light degradation	53283.17	22.88	55724.05	23.93	54948.62	23.60
Moderate degradation	22122.16	9.50	27347.79	11.74	14874.46	6.39
Severe degradation	1039.57	0.45	1030.82	0.44	809.95	0.35
Restoration	674.65	0.29	61.59	0.03	273.49	

TABLE 3: The statistics of grassland degradation/restoration for TRSR (unit: km²).

Type	The source region of			Total
	Yellow River	Yangtze River	Lancang River	
New occurring degradation	19.56	86.34	0	105.9
Intensified degradation	79.16	206.75	11.59	297.5
Non-change	20469.42	30760.46	8983.62	60213.5
Slight restoration	6610.18	8763.27	1304.94	16678.39
Substantial restoration	2535.73	1987.22	104.74	4627.69
Marsh restoration	728.13	819.33	73.91	1621.37

3.3. Grassland Vegetation Coverage Change over the Past 40 Years. Comparing it before and after 2004, the grassland vegetation coverage showed significant increase in TRSR. The area of slightly improved vegetation coverage accounted for 67.62% of total grassland (Table 4) and obvious improvement accounted for 4.58%, while the decreased vegetation coverage only accounted for 3.84%. From the spatial distribution after 2004, obvious improved grassland vegetation coverage was

mainly concentrated in the North Xinghai County and Madoi County (Figure 5), which showed increasing rate of more than 10% in vegetation coverage and could be contributed to ecological protection and construction projects since 2005.

Although the vegetation coverage of TRSR has improved significantly, but comparing it with healthy grassland vegetation coverage, the gap is large (Figure 2, Table 5). Comparing current grassland vegetation coverage with healthy vegetation

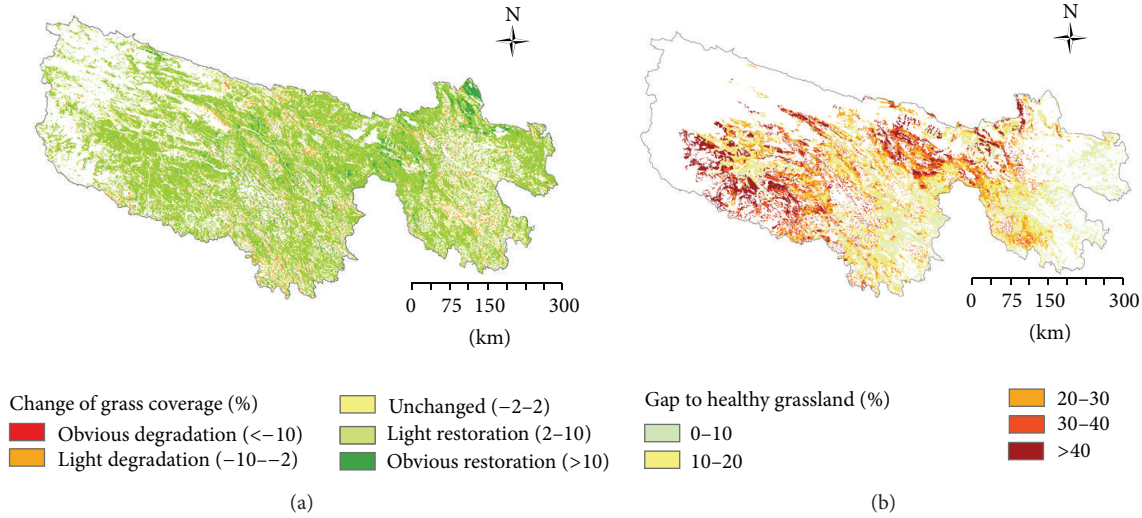


FIGURE 5: The change of vegetation coverage before and after 2004 (a) and the gap between current vegetation coverage and healthy grassland (b).

TABLE 4: The change of vegetation coverage before and after 2004.

Classification of vegetation coverage	The change of vegetation coverage before and after 2004	
	Area (km ²)	Proportion (%)
Obvious degradation (<-10%)	338	0.12
Slight degradation (-10--2%)	10468	3.72
Nonchange (-2%-2%)	67355	23.96
Slight restoration (2%-10%)	190061	67.62
Substantial restoration (>10%)	12868	4.58

cover with the same grass type, 46.11% of the area still needs to further restore vegetation cover, mainly distributed in the source region of the Yellow River and the Yangtze River.

3.4. Climate Change Mitigation Potential of Grassland Restoration. From 1990 to 2004, the grassland degradation caused significant emissions of carbon to the atmosphere, which is estimated to cause an average loss of 6.466 MtC, 16.423 MtC, and 294.464 MtC from above- and belowground biomass and soil carbon pools, the main carbon pool in grassland ecosystem in TRSR (Table 6), in which slight degradation results in large portion of carbon losses and accounts for 64.37%, 52.04%, and 61.99% of the total loss from above- and belowground biomass and soil carbon pools, respectively. However, grassland restoration in the periods only sequestered 0.346 MtC.

From 2004 to 2012, the grassland degradation caused relatively lower emissions of carbon to the atmosphere compared to that before 2004, which is estimated to cause losses of 5.363 MtC, 12.78 MtC, and 241.087 MtC from above-

TABLE 5: The gap between current vegetation coverage and healthy grassland.

Classification of the gap	Area (km ²)	Proportion account in total grassland of TRSR (%)
0~10%	31595	11.24
10~20%	37805	13.45
20~30%	25914	9.22
30~40%	16904	6.01
>40%	17355	6.17
Total	129573	46.11

and belowground biomass and soil carbon pools in TRSR (Table 6), in which slight degradation results in carbon losses accounting for 76.52%, 65.94%, and 74.66% of the total loss from above- and belowground biomass and soil carbon pools, respectively. In addition, grassland restoration in the periods sequestered 1.537 MtC, 4.4 times more than that before 2004.

Various methods of grassland restoration and/or improved management can sequester carbon in soils and in below- and aboveground biomass. For restored and improved grasslands, we give some estimates of mitigation potential per unit area under the scenario of grassland restoring to healthy status. The estimates presented are subject to a range of assumptions and uncertainties. The restoration of degraded grasslands to their healthy status has been estimated to be a technical mitigation potential of 515.074 MtC (167.53 gC/m²/year), 44.568 MtC (344.01 gC/m²/year), and 21.705 MtC (3975.65 gC/m²/year) in soils, and in below- and aboveground biomass.

Figure 6 shows the overlay of grasslands with areas in which there estimated to be a gap between current carbon stocks and their biophysical potential. It is an indicator of potential to sequester additional carbon. The map indicates, for example, areas in the source region of Yellow River and

TABLE 6: Carbon sequestration summarized by types of restored or degraded grasslands.

Types	1990–2004 (MtC)			2004–2012 (MtC)		
	AGB	BGB	SOC in 0~40 cm	AGB	BGB	SOC in 0~40 cm
Slight degradation	-4.162	-8.546	-182.524	-4.104	-8.427	-179.984
Middle degradation	-2.183	-7.097	-106.397	-1.187	-3.860	-57.869
Substantial degradation	-0.127	-0.813	-5.850	-0.100	-0.639	-4.597
Restoration	0.006	0.033	0.307	0.028	0.146	1.363
Total	-6.466	-16.423	-294.464	-5.363	-12.78	-241.087

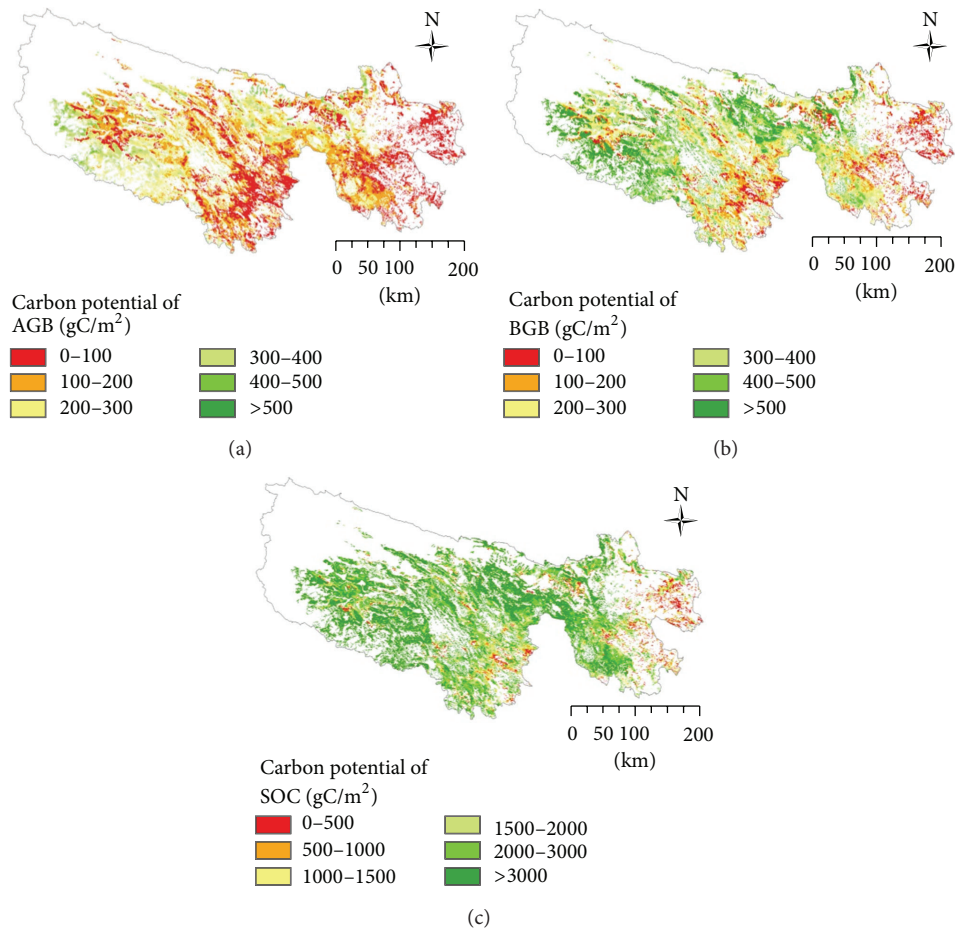


FIGURE 6: The carbon potential of AGB, BGB, and SOC in depth of 40 cm by grassland restoration to healthy status.

Yangtze River with relatively high carbon gaps. In particular the source region of Yellow River is a region with a significant carbon sequestration potential. In this area, the government is already supporting policies such as restoring grassland from grazing, area enclosure programmes, and intensive feed production systems to reduce degradation pressure which restore carbon and close the carbon gap.

4. Discussion and Conclusions

Climate change could impact ecosystems positively in wetter regions and negatively in drier ones. Annual average temperature in TRSR during 2004–2012 increased by 1.29°C

compared with that in 1975–2004. The increasing rate of annual temperature in TRSR was 0.49°C 10 yr⁻¹ and 0.58°C 10 yr⁻¹ during 1975–2004 and 1975–2012, respectively, which illustrates rapid warming over recent years. Warm and wet climatic conditions promote vegetation growth and increase forage yield in TRSR. Average annual precipitation in 2005–2012 increased by 61 mm compared with that during 1975–2004. The change rate of annual precipitation was -4.6 mm 10 yr⁻¹ and 10.2 mm 10 yr⁻¹ during 1975–2004 and 1975–2012, respectively, which shows a clear rise in recent years.

Global environmental change, including climate change, spread of invasive species, and increased pollution, could strongly affect the ability to restore ecosystems. One response

would be to determine how restoration might be used to increase resilience of biodiversity and ecosystem services to global change [26]. Recent progress in understanding the resilience of coupled social-ecological systems [27] provides a basis for understanding how this might be achieved in practice. Further research should identify thresholds beyond which ecological recovery might be slow or impossible and should suggest how changes in human behavior can be achieved to address the causes of ecological degradation [3].

The impacts of climate changes on biological systems are manifested as shifts in phenology and physiology, the composition of and interactions within communities, the range and distribution of species, morphology, net primary productivity, and the structure and dynamics of ecosystems [28]. Ecological responses to recent climate change are already clearly visible by altering their phenology and geographical distributions [29] and changes even greater for the 21st century [30]. Climate change also poses a grave threat to biodiversity by exacerbating existing threats from land-use change, fragmentation, and environmental degradation [31]. Assessments of climate change impacts on biodiversity have often used bioclimatic envelope models [32], to forecast continental-wide impacts of climate change on large numbers of species [33]. However, the complexity of ecological interactions renders it difficult to extrapolate from studies of individuals and populations to the community or ecosystem level. As a result of the widespread loss and fragmentation of habitats, many areas may become climatically unsuitable for many species [28]. It has been brought into a sharper focus by the increasing threats to protected areas through climate change and debate about whether protected areas remain relevant in periods of rapid biophysical and social change [34].

Studies have occasionally examined impacts of climate change on conservation areas. Ecosystem projected to be primarily affected by climate change may require adapted measures, compared to that negatively affected by land-use change that could persist through protection of their remaining natural habitat [34]. The characteristics of protected areas, where planning has to be done decades in advance [35], need to be reviewed under climate change to minimize the effects of climate change as well as for climate refuges of biodiversity [36]. Enhanced conservation efforts will play a critical role in efforts to reduce the impacts of climate change on biodiversity and ecosystem services [37]. It is becoming evident that in addition to providing sustainable management of habitats and ecosystems, effective conservation strategies need to mitigate impacts of climate change [32].

Although the use of ecosystem service markets to support restoration has been questioned in terms of the ability of restoration to deliver specified services [38], it is also appropriate to ask whether payment for ecosystem services (PES) can help achieve restoration goals, such as the convention on biological diversity (CBD) targets. PES might focus restoration activities on a limited set of services, such as carbon sequestration [39], whereas other services or biodiversity is neglected. This could be a particular problem when international markets are brought into play, which might override local concerns. The desired link between

reversing environmental degradation and alleviating poverty might also be undermined by an excessive reliance on market forces, as poor people do not always benefit from PES [10]. For restoration to contribute both to sustainable development and the alleviation of poverty, it is essential that such financial flows compensate landholders adequately for any costs of restoration and provide an effective incentive to initiate restoration actions. Identifying how this might be achieved, based on understanding of the potential distribution of benefits among different stakeholders and the conflicts that could arise, represents a major challenge to future restoration research and practice [3].

Various methods of improved grassland management can sequester carbon [14, 15]. However, the global analysis in particular for some regions has a high level of uncertainty. Primary among these uncertainties are the costs at which carbon sequestration is economically viable. Several studies suggest that compared to other mitigation options, grassland mitigation is cost-competitive [16, 17], but further work is needed to validate this. There are several types of cost to consider regarding any change in management practice, including initial investment costs, annual operating costs, and opportunity costs of income foregone by undertaking the activities needed for avoiding conversion of or improving management of grasslands [40]. While degraded grasslands may have significant potential for carbon sequestration, initial costs of restoration and the delayed return before grasslands recover their productivity imply that costs will not in all cases be low [18].

Conflict of Interests

The authors declare that there is no conflict of interests regarding the publication of this paper.

Acknowledgments

This work was financially supported by the CDM Program (1214115). The authors thank anonymous reviewers for their helpful comments on this paper.

References

- [1] K. M. Havstad, D. P. C. Peters, R. Skaggs et al., "Ecological services to and from rangelands of the United States," *Ecological Economics*, vol. 64, no. 2, pp. 261–268, 2007.
- [2] S. H. M. Butchart, M. Walpole, B. Collen et al., "Global biodiversity: indicators of recent declines," *Science*, vol. 328, no. 5982, pp. 1164–1168, 2010.
- [3] J. M. Bullock, J. Aronson, A. C. Newton, R. F. Pywell, and J. M. Rey-Benayas, "Restoration of ecosystem services and biodiversity: conflicts and opportunities," *Trends in Ecology and Evolution*, vol. 26, no. 10, pp. 541–549, 2011.
- [4] W. H. Schlesinger, J. F. Reynolds, G. L. Cunningham et al., "Biological feedbacks in global desertification," *Science*, vol. 247, no. 4946, pp. 1043–1048, 1990.

- [5] A. Wilkes, K. Solymosi, and T. Tennigkeit, "Options for support to grassland restoration in the context of climate change mitigation," Tech. Rep., UNIQUE Forestry and Land Use, Freiburg, Germany, 2012.
- [6] W. Jordan, M. Gilpin, and J. Aber, Eds., *Restoration Ecology: A Synthetic Approach to Ecological Research*, Cambridge University Press, Cambridge, UK, 1987.
- [7] G. C. Daily and P. A. Matson, "Ecosystem services: from theory to implementation," *Proceedings of the National Academy of Sciences of the United States of America*, vol. 105, no. 28, pp. 9455–9456, 2008.
- [8] J. M. Rey-Benayas, A. C. Newton, A. Diaz, and J. M. Bullock, "Enhancement of biodiversity and ecosystem services by ecological restoration: a meta-analysis," *Science*, vol. 325, no. 5944, pp. 1121–1124, 2009.
- [9] R. Naidoo, A. Balmford, R. Costanza et al., "Global mapping of ecosystem services and conservation priorities," *Proceedings of the National Academy of Sciences of the United States of America*, vol. 105, no. 28, pp. 9495–9500, 2008.
- [10] L. M. Martin, K. A. Moloney, and B. J. Wilsey, "An assessment of grassland restoration success using species diversity components," *Journal of Applied Ecology*, vol. 42, no. 2, pp. 327–336, 2005.
- [11] R. F. Pywell, J. M. Bullock, A. Hopkins et al., "Restoration of species-rich grassland on arable land: assessing the limiting processes using a multi-site experiment," *Journal of Applied Ecology*, vol. 39, no. 2, pp. 294–309, 2002.
- [12] G. Cao and R. Long, "The Bottleneck and its resolutions to the natural recovery of black soil type degraded grassland in the three river Source Region," *Acta Agrestia Sinica*, vol. 17, no. 1, pp. 4–9, 2009.
- [13] T. J. Stohlgren, T. N. Chase, R. A. Pielke Sr., T. G. F. Kittel, and J. S. Baron, "Evidence that local land use practices influence regional climate, vegetation, and stream flow patterns in adjacent natural areas," *Global Change Biology*, vol. 4, no. 5, pp. 495–504, 1998.
- [14] R. T. Conant, K. Paustian, and E. T. Elliott, "Grassland management and conversion into grassland: effects on soil carbon," *Ecological Applications*, vol. 11, no. 2, pp. 343–355, 2001.
- [15] B. Kumar and P. Nair, *Carbon Sequestration Potential of Agroforestry Systems: Opportunities and Challenges*, Springer, New York, NY, USA, 2011.
- [16] P. Smith, D. Martino, Z. Cai et al., "Greenhouse gas mitigation in agriculture," *Philosophical Transactions of the Royal Society B: Biological Sciences*, vol. 363, no. 1492, pp. 789–813, 2008.
- [17] McKinsey & Co, *China's Green Revolution: Prioritizing technologies to Achieve Energy and Environmental Sustainability*, McKinsey & Co, London, UK, 2009.
- [18] L. Lipper, C. Dutilly-Diane, and N. McCarthy, "Supplying carbon sequestration from West African rangelands: opportunities and barriers," *Rangeland Ecology and Management*, vol. 63, no. 1, pp. 155–166, 2010.
- [19] H. Y. Li, H. C. Peng, and Q. J. Wang, "Study on aboveground biomass of plant communities among the stages of regressive succession in alpine *Kobresia humilis* meadow," *Acta Pratacutural Science*, vol. 13, no. 5, pp. 26–32, 2004.
- [20] H. K. Zhou, X. Q. Zhao, L. Zhou et al., "A study on correlation between vegetation degradation and soil degradation in the alpine meadow of the Qinghai-Tibetan Plateau," *Acta Pratacutural Science*, vol. 14, no. 3, pp. 31–40, 2005.
- [21] W. Y. Wang, Q. J. Wang, G. Wang, and Z. C. Jing, "Effects of land degradation and rehabilitation on vegetation carbon and nitrogen content of alpine meadow in China," *Journal of Plant Ecology*, vol. 31, no. 6, pp. 1073–1078, 2007.
- [22] Y. N. Zeng, Z. L. Ma, and Z. D. Feng, "Potential to sequestering carbon from atmosphere through rehabilitating desert land in the head water of the Yellow River," *Journal of Mountain Science*, vol. 27, no. 6, pp. 671–675, 2009.
- [23] J. L. Yu, H. X. Shi, and C. Y. Zhao, "Preliminary study on range conditions of alpine *Kobresia* meadows under different degradation degrees," *Acta Pratacuturae Sinica*, vol. 27, no. 9, pp. 115–118, 2010.
- [24] D. R. Han, G. M. Cao, X. W. Guo et al., "The potential of carbon sink in alpine meadow ecosystem on the Qinghai-Tibetan Plateau," *Acta Ecologica Sinica*, vol. 31, no. 24, pp. 7408–7417, 2011.
- [25] Y. N. Li, S. X. Xu, L. Zhao, and F. W. Zhang, "Carbon Sequestration potential of vegetation and soil of degenerative alpine meadows in Southern Qinghai Province," *Journal of Glaciology and Geocryology*, vol. 34, no. 5, pp. 1157–1164, 2012.
- [26] J. M. Montoya and D. Raffaelli, "Climate change, biotic interactions and ecosystem services," *Philosophical Transactions of the Royal Society B: Biological Sciences*, vol. 365, no. 1549, pp. 2013–2018, 2010.
- [27] J. G. Liu, T. Dietz, S. R. Carpenter et al., "Complexity of coupled human and natural systems," *Science*, vol. 317, no. 5844, pp. 1513–1516, 2007.
- [28] G. R. Walther, E. Post, P. Convey et al., "Ecological responses to recent climate change," *Nature*, vol. 416, no. 6879, pp. 389–395, 2002.
- [29] J. Lenoir, J. C. Gégout, P. A. Marquet, P. De Ruffray, and H. Brisse, "A significant upward shift in plant species optimum elevation during the 20th century," *Science*, vol. 320, no. 5884, pp. 1768–1771, 2008.
- [30] W. Thuiller, S. Lavergne, C. Roquet, I. Boulangeat, B. Lafourcade, and M. B. Araujo, "Consequences of climate change on the tree of life in Europe," *Nature*, vol. 470, no. 7335, pp. 531–534, 2011.
- [31] D. D. Ackerly, S. R. Loarie, W. K. Cornwell et al., "The geography of climate change: implications for conservation biogeography," *Diversity and Distributions*, vol. 16, no. 3, pp. 476–487, 2010.
- [32] M. B. Araújo, D. Alagador, M. Cabeza, D. Nogués-Bravo, and W. Thuiller, "Climate change threatens European conservation areas," *Ecology Letters*, vol. 14, no. 5, pp. 484–492, 2011.
- [33] S. Z. Dobrowski, J. H. Thorne, J. A. Greenberg et al., "Modeling plant ranges over 75 years of climate change in California, USA: temporal transferability and species traits," *Ecological Monographs*, vol. 81, no. 2, pp. 241–257, 2011.
- [34] L. Hannah, G. Midgley, S. Andelman et al., "Protected area needs in a changing climate," *Frontiers in Ecology and the Environment*, vol. 5, no. 3, pp. 131–138, 2007.
- [35] L. Hansen, J. Hoffman, C. Drews, and E. Mielbrecht, "Designing climate-smart conservation: guidance and case studies: special section," *Conservation Biology*, vol. 24, no. 1, pp. 63–69, 2010.
- [36] C. Bellard, C. Bertelsmeier, P. Leadley, W. Thuiller, and F. Courchamp, "Impacts of climate change on the future of biodiversity," *Ecology Letters*, vol. 15, no. 4, pp. 365–377, 2012.

- [37] J. J. Lawler, T. H. Tear, C. Pyke et al., “Resource management in a changing and uncertain climate,” *Frontiers in Ecology and the Environment*, vol. 8, no. 1, pp. 35–43, 2010.
- [38] M. A. Palmer and S. Filoso, “Restoration of ecosystem services for environmental markets,” *Science*, vol. 325, no. 5940, pp. 575–576, 2009.
- [39] F. E. Putz and K. H. Redford, “Dangers of carbon-based conservation,” *Global Environmental Change*, vol. 19, no. 4, pp. 400–401, 2009.
- [40] L. Lipper, A. Wilkes, and N. McCarthy, “Crediting soil carbon sequestration in smallholder agricultural systems: what fits and what will fly?” in *Monitoring, Reporting and Verification Systems for Carbon in Soils and Vegetation in African, Caribbean and Pacific Countries*, D. de Brogniez, P. Mayaux, and L. Montanarella, Eds., EC JRC Scientific and Technical Reports, EC European Commission Joint Research Centre, Brussels, Belgium, 2011.

Review Article

Modeling and Monitoring Terrestrial Primary Production in a Changing Global Environment: Toward a Multiscale Synthesis of Observation and Simulation

Shufen Pan,^{1,2} Hanqin Tian,² Shree R. S. Dangal,² Zhiyun Ouyang,¹ Bo Tao,² Wei Ren,² Chaoqun Lu,² and Steven Running³

¹ State Key Laboratory of Urban and Regional Ecology, Research Center for Eco-Environmental Sciences, Chinese Academy of Sciences, Beijing 100085, China

² International Center for Climate and Global Change Research, School of Forestry and Wildlife Sciences, Auburn University, 602 Duncan Drive, Auburn, AL 36849, USA

³ Numerical Terradynamic Simulation Group, Department of Ecosystem and Conservation Sciences, University of Montana, Missoula, MT 59812, USA

Correspondence should be addressed to Hanqin Tian; tianhan@auburn.edu

Received 24 January 2014; Accepted 13 March 2014; Published 30 April 2014

Academic Editor: Dong Jiang

Copyright © 2014 Shufen Pan et al. This is an open access article distributed under the Creative Commons Attribution License, which permits unrestricted use, distribution, and reproduction in any medium, provided the original work is properly cited.

There is a critical need to monitor and predict terrestrial primary production, the key indicator of ecosystem functioning, in a changing global environment. Here we provide a brief review of three major approaches to monitoring and predicting terrestrial primary production: (1) ground-based field measurements, (2) satellite-based observations, and (3) process-based ecosystem modelling. Much uncertainty exists in the multi-approach estimations of terrestrial gross primary production (GPP) and net primary production (NPP). To improve the capacity of model simulation and prediction, it is essential to evaluate ecosystem models against ground and satellite-based measurements and observations. As a case, we have shown the performance of the dynamic land ecosystem model (DLEM) at various scales from site to region to global. We also discuss how terrestrial primary production might respond to climate change and increasing atmospheric CO₂ and uncertainties associated with model and data. Further progress in monitoring and predicting terrestrial primary production requires a multiscale synthesis of observations and model simulations. In the Anthropocene era in which human activity has indeed changed the Earth's biosphere, therefore, it is essential to incorporate the socioeconomic component into terrestrial ecosystem models for accurately estimating and predicting terrestrial primary production in a changing global environment.

1. Introduction

Terrestrial net primary production (NPP) refers to the net amount of carbon captured by plants through photosynthesis per unit time over a given period and is a key component of energy and mass transformation in terrestrial ecosystems. NPP represents the net carbon retained by terrestrial ecosystems after assimilation through photosynthesis (gross primary production (GPP)) and losses due to autotrophic respiration [1]. NPP is of fundamental importance to humans because the largest portion of our food supply comes from terrestrial NPP [2]. Additionally, NPP is an important indicator of ecosystem health and services [3–5] and a critical

component of the global carbon cycle [6, 7] that provides linkage between terrestrial biota and the atmosphere [8]. Research into terrestrial GPP and NPP, especially at a regional and global scale, has attracted much attention [3, 4, 9–11]. This is because they measure the transfer of energy to the biosphere and terrestrial CO₂ assimilation and provide a basis for assessing the status of a wide range of ecological processes [12].

NPP is an important ecological variable for evaluating trends in biospheric behavior [13] and investigating the patterns of food, fiber, and wood production [4] across broad temporal and spatial scales. Accurate estimations of global

NPP can improve our understanding of the feedbacks among the atmosphere-vegetation-soil interface in the context of global change [14] and facilitate climate policy decisions. Previous studies based on inventory analysis, empirical and process models, and remote sensing approaches have estimated global NPP in the range of 39.9–80 PgC yr⁻¹ [3, 15–17]. In a recent meta-analysis study, Ito [18] reported a global terrestrial NPP of 56.4 PgC yr⁻¹. However, there is large uncertainty ($\pm 8\text{--}9$ PgC yr⁻¹) in the estimation of global terrestrial NPP in recent years (2000–2010) making it difficult to evaluate the transfer of energy and the status of ecological processes [18]. These uncertainties are associated with sensitivity analysis and bias introduced by gap filling of satellite data. In addition, remote-sensing algorithm does not accurately account for environmental stresses such as rooting depth especially in dry areas where plants use deep roots to access and sustain water availability [19].

At a global scale, multiple environmental factors including climate, topography, soils, plant and microbial characteristics, and anthropogenic and natural disturbances control the timing and magnitude of terrestrial NPP [20]; however, the relative contributions of these environmental factors toward global NPP varies over time and space. Globally, climate change including changes in temperature and precipitation had a relatively small-scale positive impact on NPP during the period 1982–1999 [13]. However, during the last decade (2000–2009), the effect of climate on global NPP has been a subject of debate. Zhao and Running [6] reported that warming-related increases in water stress and autotrophic respiration in the Southern Hemisphere resulted in an overall decline in global NPP, whereas Potter et al. [21] found an increasing trend in global NPP due to rapidly warming temperatures in the Northern Hemisphere during the period 2000–2009. While climatic variables such as solar radiation, temperature, and precipitation have been recognized as a key factor controlling the terrestrial NPP [6, 21], other environmental factors such as elevated CO₂, nitrogen deposition, and ozone exposure are also equally important in controlling the timing and magnitude of terrestrial NPP [22]. Additionally, natural and anthropogenic factors such as hurricanes, fires, logging, land cover and land use change, and insect damage also have a significant effect on terrestrial NPP [23–26]. Accurately quantifying the effect of different environmental drivers including climate on global terrestrial NPP requires an understanding of the controlling physiological and ecological processes that determine the timing and magnitude of terrestrial carbon uptake [27, 28].

Because there is substantial uncertainty in our knowledge of the environmental factors that control the magnitude of terrestrial NPP, continuous monitoring of global terrestrial NPP is critical for evaluating trends in biospheric behavior [13], investigating large-scale patterns in food and fiber production [4], and understanding the potential of terrestrial ecosystems for carbon sequestration from the atmosphere. Terrestrial NPP is identified as a primary monitoring variable by a number of studies [4, 29] and

interested organizations (the Environmental Sustainability Index; <http://www.ciesin.columbia.edu/indicators/ESI/> and the National Research Council Report; <http://www.nap.edu/bookds/0309068452/html/>); however, continuous and consistent measurement of global terrestrial NPP that integrates ecosystem processes across broad temporal and spatial scales [30] has not been possible. Although regular monitoring of global terrestrial NPP has been feasible using imagery and the satellite-borne Moderate Resolution Imaging Spectroradiometer (MODIS) sensor, such approaches are limited by their coarse resolution and difficulty in converging with other high resolution datasets and process-based models [14, 31, 32].

Although several approaches have been used to monitor terrestrial primary production over the past two-decades ranging from site-level observations [33–35] to large-scale remote sensing [6, 13] and process-based modeling [3, 36–38], or a combination of site-level observations, remote sensing techniques, and/or process-based models [8, 9, 39], these approaches are associated with significant uncertainties where inconsistent estimates of terrestrial NPP are observed in response to global change [40–42]. A wide range of uncertainty comes from upscaling site- or stand-level primary production to a regional and global scale [14, 43], structural differences among models that are susceptible to forcing-data and parameter values constrained by observations [44, 45], and limitations in the parameterization of light use efficiency [31] and photosynthetically active radiation [31, 46]. Similarly, terrestrial primary production is not directly estimated from the remote sensing measurements but is modeled as a function of leaf area index and fraction of photosynthetically active radiation (fPAR) or greenness index. These indexes used to estimate terrestrial NPP are contaminated by atmospheric particles that would send misleading signals to satellite sensors [47]. Additionally, process-based models integrate the understanding of ecological and physiological processes obtained from field measurements and are particularly important to characterize the response of terrestrial ecosystems to different environmental stressor [23, 48]. It is, therefore, essential to integrate site-level, remote-sensing, and process-based modeling approach to accurately monitor and predict terrestrial primary production across broad temporal and spatial scales.

A variety of reviews have addressed various aspects of NPP [18, 49, 50]; however, none have comprehensively reviewed the existing approaches and associated uncertainties as well as future needs. Therefore, the purpose of this review is to (1) summarize the general approaches to estimate GPP and NPP at multiple scales; (2) review major environmental factors controlling the magnitude and timing of GPP and NPP; (3) identify uncertainties associated with large-scale GPP and NPP estimations; (4) recognize knowledge gaps with possible future direction under changing environmental conditions. Generally, three approaches have been used to estimate gross and net primary productivity in the terrestrial ecosystems: (1) ground-based monitoring including biomass inventory [35] and eddy covariance measurement [9]; (2) remote sensing-based observation [6]; (3) spatially explicit ecosystem modeling [51]. Here, we provide a brief

review of these approaches with an emphasis on satellite-based observation and terrestrial ecosystem modeling.

2. Ground-Based Monitoring of Terrestrial Primary Production

Ground-based monitoring of terrestrial primary production provides a basis for accurately estimating global NPP because it provides direct measurement of terrestrial primary production for scaling up from site to global level as well as calibrating and validating both satellite- and model-based approaches. Ground-based measurements of terrestrial primary production rely on two approaches: biomass and flux measurements. Since the International Biological Program (IBP, 1965–1974), a number of ecosystem surveys have been carried out to measure terrestrial primary production across the globe. Traditionally, terrestrial primary production estimation, using biomass measurement was carried out through periodic measurements of root, stem, leaf, and fruit growth. Recent technological advances allow for ground-based monitoring of terrestrial NPP using meteorological towers that measures the instantaneous exchange of CO₂ (net ecosystem exchange (NEE)) between the atmosphere and terrestrial ecosystems. Terrestrial NPP is calculated indirectly by adding heterotrophic respiration to NEE. Eddy covariance technique [52] is employed worldwide across different biomes including forest, cropland, grassland, and desert. Below, we provide a brief overview of two most widely used ground-based monitoring of terrestrial primary production: (a) biomass inventory and (b) flux measurements using eddy covariance technique.

2.1. Biomass Inventory. The biomass inventory data provide valuable sources of information for estimation of biomass and NPP in forest, cropland, and grassland at landscape and regional scales [53, 54]. Since the early 1980s, regional or national inventories, with a large number of statistically valid plots, have been widely regarded as a powerful tool for estimating forest and crop biomass at broad scales [55, 56]. Inventory-based method estimates forest biomass using biomass expansion factor (BEF) that converts stem volume to biomass to account for noncommercial components, that is, branches, root, and leaves, and so forth [57–59]; however, other studies have indicated that total stem volume varies with forest age, site class, and stand density [60–63]. An alternative approach to tree biomass estimation includes the allometric equation, which can be converted to CO₂ equivalents by scaling [64]. Estimates of forest biomass based on an allometric equation have been used widely to examine the impacts of forest management [65], land-use change [66], and increase in atmospheric CO₂ [67]. While allometric equations are important for estimating forest biomass and are used widely in growth and yield models (e.g., Forest Vegetation Simulator), they fail in distinguishing and quantifying the relative contribution of land cover and land-use change and several environmental factors including climate, elevated CO₂, and air pollution on carbon uptake. Recently, Houghton [68] has recognized that keeping land

cover and land use change exclusive of the environmental change is critically important because it helps to separate direct anthropogenic effects from indirect or natural effects and lower the uncertainty of the land cover and land-use change flux.

2.2. Flux Measurements Using Eddy Covariance Technique. Eddy covariance technique estimates CO₂ exchange rate between atmosphere and plant canopy by measuring the covariance between fluctuation in vertical wind velocity and CO₂ mixing ratio [69, 70]. Eddy covariance technique made it possible to directly and continuously measure vertical turbulent fluxes within atmospheric boundary layers on short and long time scales (from 30 min to year). At the ecosystem scale, FLUXNET towers measure net ecosystem CO₂ exchange (NEE), which is equal to GPP minus ecosystem respiration [70] (i.e., the quantity of CO₂ respired by both autotrophs (plants) and heterotrophs (primarily microbes)). Since the 19 s, there has been increasing interest in estimating net CO₂ exchange in terrestrial ecosystems based on eddy covariance measurements [71]. The eddy covariance approach is capable of detecting small changes in net CO₂ exchange between terrestrial ecosystems and the atmosphere over various time scales [69]. The international FLUXNET [52] has established a network of FLUXNET towers on six of seven continents, including a number of regional networks of eddy covariance measurements (such as CarboEuropeIP, AmeriFlux, Fluxnet-Canada, LBA, AsiaFlux, ChinaFlux, CarboAfrica, KoFlux, TCOS-Siberia, and Afriflux). The flux data derived from these networks provide unprecedented detailed information to the broad community of scientists who need flux data to test, calibrate, validate, and improve land surface schemes in climate models, dynamic vegetation models, remote sensing algorithms, hydrological models, and process-based ecosystem models. Eddy flux measurement also provides a unique tool for understanding eco-physiological mechanisms and environmental controls of ecosystem carbon processes in the context of global change. However, for the large-scale estimation of terrestrial primary production, current eddy covariance measurement sites are still too few and unevenly distributed. The regional extrapolation of carbon-storage capacity from a single field site to the whole study area/region has been based on an assumption of homogeneity in ecosystem functioning across this region, which brings large uncertainties. For instance, Xiao et al. [9] found that the upscaled eddy covariance terrestrial primary production (GPP) for the conterminous US was 14% higher compared to MODIS. The net carbon exchange between the biosphere and the atmosphere at the regional scale, however, can be very different from the product of a site-specific rate of exchange and the area of the region because terrestrial ecosystems have differential responses due to vegetation type, disturbance history, soil, and climate variables that vary over space and time [72]. In addition to upscaling issues, complex topography and unstable atmospheric condition can substantially alter the carbon fluxes due to nighttime gravitational or drainage flows [73], resulting in differences in carbon fluxes in the range of 80–200% compared to measurements based on inventory approach [74].

3. Satellite-Based Monitoring of Terrestrial Primary Production

Ground-based measurements of terrestrial primary production are usually made at spatial scales in the range of less than one to a few hundred square meters making it difficult to estimate terrestrial primary production at a regional and global scale. Additionally, ground-based measurements of terrestrial NPP are constrained by topographic complexity and other adverse environmental factors. Satellite-based monitoring of terrestrial primary production is particularly important over large areas where ground-based methods (inventory and eddy covariance) are not feasible. Satellite-based estimations provide a repeated, consistent measurement of terrestrial primary production across broad temporal and spatial scales. Below we provide a brief overview of satellite-based monitoring of terrestrial primary production with a focus on NASA's Moderate-Resolution Imaging Spectroradiometer (MODIS).

Remote sensing based estimation of terrestrial primary production has advanced tremendously over the past few decades, and these datasets provide essential information associated with emissions of CO₂ into the atmosphere at regional, continental, and global scales. Because carbon fluxes (GPP and NPP) are difficult to measure over larger areas due to high spatial heterogeneity, satellite observations provide consistent, spatially fine-scale estimates [75] and allow us to monitor ecosystem patterns and activities at larger scales [6]. Since the pioneering work of Tucker et al. [76] on the correlation between remote sensing-derived vegetation index (i.e. the Normalized Difference Vegetation Index (NDVI)) and photosynthetic activity, satellite remote sensing has become a primary source of data on regional ecosystem patterns and terrestrial primary production. Additionally, satellite based observations have been coupled with mathematical models to quantify the carbon fluxes across the globe. For instance, over the last decades, production efficiency models (PEM) have been developed based on available satellite data, to monitor primary production and investigate the carbon cycle at large scales [31, 77]. One of the most promising tools to track changes in the productivity of terrestrial and marine ecosystem is based on GPP/NPP products derived from NASA's Moderate-Resolution Imaging Spectroradiometer (MODIS), a satellite-mounted instrument that collects surface spectral signatures to quantify the changes in terrestrial primary production over large areas. Below, we describe detail algorithms on how MODIS keeps track of changes in primary productivity over time to enhance our understanding on how satellite observations are used to estimate terrestrial productivity.

Detailed information on MOD17 algorithm is available in the MOD17 Algorithm Theoretical Basis Document (ATBD) [78] or MOD17 user's guide. Here we provide a simple overview of MOD17. The MOD17 algorithm can be mainly divided into two steps. First, we calculate daily GPP and MODIS photosynthesis product (PSNnet). The daily GPP is calculated as a function of conversion efficiency, incident short wave radiation, and fraction of photosynthetically

active radiation. PSNnet is obtained after subtracting maintenance respiration from the daily GPP. Second, we calculate annual NPP by summation of all 8-day PSNnet products after subtracting maintenance respiration of live wood and growth respiration of whole plant. Below, we provide a detailed description of the two steps.

The first step is calculation of daily GPP ($\text{gC m}^{-2} \text{d}^{-1}$) and PSNnet ($\text{gC m}^{-2} \text{d}^{-1}$), where PSNnet is equal to GPP minus maintenance respiration (MR) ($\text{gC m}^{-2} \text{d}^{-1}$) of leaves and fine roots, for each 8-day period. The standard global 8-day composite MOD17A2 products are formed by summation of these 8-day daily GPP and PSNnet with the first Julian day of the 8-day period as MOD17A2 time information in 10 degree HDF-EOS file name. Daily GPP is calculated similar to Heinsch et al [79] as follows:

$$\text{GPP} \varepsilon \times (\text{SWrad} \times 0.45) \times \text{fPAR}, \quad (1)$$

where ε is the conversion efficiency (i.e., the amount of carbon a specific biome can produce per unit of energy) and SWrad ($\text{MJ m}^{-2} \text{d}^{-1}$) is the daily sum of incident solar short wave radiation, which is multiplied by 0.45 [80] to estimate fraction of photosynthetically active radiation (fPAR; $\text{MJ m}^{-2} \text{d}^{-1}$). SWrad is from the Data Assimilation Office (DAO) at NASA Goddard Space Flight Center (GSFC) and will be discussed in detail later. fPAR is from MOD15A2, 8-day composite fPAR, and LAI, which is based on the maximum fPAR value.

Daily ε (gC MJ^{-1}) is calculated from maximum ε under optimal conditions [79] when controlled by environmental stresses (lower temperature and drought) and is calculated as follows:

$$\varepsilon = \varepsilon_{\max} \times f(T_{\min}) \times f(\text{VPD}), \quad (2)$$

where ε_{\max} is the maximum biome-specific value under well-watered conditions, T_{\min} is daily minimum temperature ($^{\circ}\text{C}$), and VPD is daytime vapor pressure deficits (Pa). Linear interpolation functions of $f(T_{\min})$ and $f(\text{VPD})$ convert T_{\min} and VPD to scalars ranging from 1 (optimal conditions) to 0 (extremely stressed conditions). Currently, ε_{\max} is constant for a given biome. For different days, T_{\min} , VPD, and SWrad are variable to weather conditions; hence, ε would be strongly related to different weather situations and GPP would change daily. For most ecosystems, the scalar of T_{\min} controls photosynthesis during a relative short period at the beginning and end of the growing season. During most of the growing season, the scalar of T_{\min} would be 1 due to higher T_{\min} and would exert no constraint on assimilation so VPD and SWrad would be the two primary meteorological factors governing daily GPP in the MOD17 algorithm.

Maintenance respiration (MR, $\text{gC m}^{-2} \text{d}^{-1}$) by leaf and root is exponentially related to daily average temperature (T_{avg} , $^{\circ}\text{C}$) as follows:

$$\begin{aligned} \text{MR}_{\text{leaf}} &= \text{Leaf.Mass} \times \text{leaf_mr_base} \times Q_{10}^{[(T_{\text{avg}}-20)/10]} \\ \text{MR}_{\text{root}} &= \text{Fine_Root_Mass} \times \text{froot_mr_base} \times Q_{10}^{[(T_{\text{avg}}-20)/10]}, \end{aligned} \quad (3)$$

where Leaf_Mass is retrieved from MOD15A2 LAI using biome-specific specific leaf area (SLA). Fine_Root_Mass is estimated from biome-specific constant ratios between leaf and fine root. Q_{10} is a respiration quotient and is assigned to be 2.0 across biomes. Leaf_mr_base and froot_mr_base are the maintenance respiration of leaves and fine roots per unit mass at 20°C.

The second step is the calculation of annual NPP ($\text{gC m}^{-2} \text{y}^{-1}$) by summation of all 8-day composite PSNnet and subtraction of MR of living wood and growth respiration (GR, $\text{gC m}^{-2} \text{y}^{-1}$) of whole-plant as follows:

$$\begin{aligned} \text{NPP} = & \sum \text{PSNnet} - \text{Livewood_MR} - \text{Leaf_GR} \\ & - \text{Froot_GR} - \text{Livewood_GR} - \text{Deadwood_GR}, \end{aligned} \quad (4)$$

where Livewood_MR and Livewood_GR are the maintenance respiration and growth respiration of living wood, respectively. Leaf_GR, Froot_GR, and Deadwood_GR are the growth respiration of leaves, fine roots, and dead wood, respectively.

The most significant assumption made in the MOD17 logic is that biome specific physiological parameters do not vary with space or time. These parameters are outlined in the Biome Properties Lookup Table (BPLUT). For each pixel, biome types are translated from MOD12Q1 Land Cover into MOD17 biomes. An initial evaluation of the MODIS 2001 GPP product was made by comparing MODIS GPP estimates with ground-based GPP estimates over 25 km² areas at a northern hardwoods forest site and a boreal forest site.

In addition to estimating NPP and vegetation patterns, remote sensing-based observations provide input data (i.e., land cover maps, leaf area index, fPAR, etc.) to set boundary conditions in the climate models, hydrological models, and process-based ecosystem models [81]. While a remote sensing based approach provides continuous and quantitative observations about ecosystem changes at large scale, they are subjected to large errors, if uncorrected. These errors come from atmospheric contamination of the remote sensing signal that interacts with ozone, water vapor, aerosols, and other atmospheric constituents [82]. Additionally, atmospheric haze and scattering from terrestrial surfaces can severely reduce data consistency [83]. There is a need to validate remote sensing based estimates of global primary production against ground measurements on a landscape and regional scale. On the other hand, remote sensing based estimates of terrestrial NPP do not isolate the relative contribution of different environmental and anthropogenic factors. Therefore, a better understanding of terrestrial primary production requires integrating process-based models with remote sensing approaches and validating the model output with field-based measurements (biomass inventory and eddy covariance measurement).

4. Process-Based Model Simulation and Prediction

Terrestrial ecosystem models provide a powerful tool to integrate our understanding on ecosystem processes and

measurements/observations at multiple scales to investigate net primary production in response to multiple environmental factors in the complicated world [38, 51, 84]. Since the 1990s, there has been a dramatic increase in the use of terrestrial ecosystem models to estimate the NPP of terrestrial ecosystems at various spatial and temporal scales. Ecosystem modeling has evolved from empirical modeling that usually considers empirical correlation between ecosystem variables and climate elements (such as temperature, precipitation, and radiation) to process-based modeling, which is capable of investigating multiple responses of ecosystem processes to both environmental and anthropogenic factors at both regional [51, 84, 85] and global scales [3, 48, 86]. Process-based models play a central role in assessing and predicting the primary productivity and carbon cycle of the terrestrial biosphere in past, present, and future conditions [87]. Melillo et al. [3] provide the first NPP estimation using a process-based model (terrestrial ecosystem model (TEM)) at global scale, with an emphasis on responses of terrestrial NPP to climate and atmospheric CO₂ increase. Since then, an array of ecosystem models have been developed and applied to estimate NPP as influenced by multiple environmental factors, including climate, atmospheric CO₂, nitrogen availability, natural disturbances, air pollution, land use, and land cover change [84, 88, 89].

Modeling representation of photosynthesis and autotrophic respiration varies among terrestrial biosphere models. In process-based ecosystem models, a modified Farquhar model is usually used to simulate gross primary production. We take the dynamic land ecosystem model (DLEM, [51]) as an example to address how GPP and NPP are represented in modeling scheme. In DLEM, the canopy is divided into sunlit and shaded layers. GPP ($\text{gC m}^{-2} \text{day}^{-1}$) is calculated by scaling leaf assimilation rates ($\mu\text{mol CO}_2 \text{m}^{-2} \text{s}^{-1}$) up to the whole canopy:

$$\begin{aligned} \text{GPP}_{\text{sun}} &= 12.01 \times 10^{-6} \times A_{\text{sun}} \times \text{Plai}_{\text{sun}} \times \text{day } 1 \times 3600 \\ \text{GPP}_{\text{shade}} &= 12.01 \times 10^{-6} \times A_{\text{shade}} \times \text{Plai}_{\text{shade}} \times \text{day } 1 \times 3600 \\ \text{GPP} &= \text{GPP}_{\text{sun}} + \text{GPP}_{\text{shade}}, \end{aligned} \quad (5)$$

where GPP_{sun} and $\text{GPP}_{\text{shade}}$ are gross primary productivity of sunlit and shaded canopy, respectively; A_{sun} and A_{shade} are assimilation rates of sunlit and shaded canopy; Plai_{sun} and $\text{Plai}_{\text{shade}}$ are the sunlit and shaded leaf area indices; day 1 is daytime length (second) in a day. 12.01×10^{-6} is a constant to change the unit from $\mu\text{mol CO}_2$ to gram C.

The DLEM determines the C assimilation rate (A) as the minimum of three limiting rates, w_c , w_j , w_e , which are functions that represents the assimilation rates as limited by the efficiency of the photosynthetic enzymes system (Rubisco-limited), the amount of PAR captured by the leaf chlorophyll (light-limited), and the capacity of the leaf to export or utilize the products of photosynthesis (export-limited) for C₃ species, respectively. For C₄ species, w_e refer to the PEP carboxylase limited rate of carboxylation. The

canopy sunlit and shaded carbon assimilation rate can be estimated as

$$\begin{aligned}
 A &= \min(w_c, w_j, w_e) \times \text{Index}_{\text{gs}} \\
 w_c &= \begin{cases} \frac{(c_i - \Gamma_*) V_{\max}}{c_i + K_c (1 + o_i/K_o)} & \text{for } C_3 \text{ plants} \\ V_{\max} & \text{for } C_4 \text{ plants} \end{cases} \\
 w_j &= \begin{cases} \frac{(c_i - \Gamma_*) 4.6\phi\alpha}{c_i + 2\Gamma_*} & \text{for } C_3 \text{ plants} \\ 4.6\phi\alpha & \text{for } C_4 \text{ plants} \end{cases} \quad (6) \\
 w_e &= \begin{cases} 0.5V_{\max} & \text{for } C_3 \text{ plants} \\ 4000V_{\max} \frac{c_i}{P_{\text{atm}}} & \text{for } C_4 \text{ plants,} \end{cases}
 \end{aligned}$$

where c_i is the internal leaf CO_2 concentration (Pa); o_i is the O_2 concentration (Pa); Γ_* is the CO_2 compensation point (Pa); K_c and K_o are the Michaelis-Menten constants for CO_2 and O_2 , respectively; α is the quantum efficiency; ϕ is the absorbed photosynthetically active radiation ($\text{W}\cdot\text{M}^{-2}$); V_{\max} is the maximum rate of carboxylation which varies with temperature, foliage nitrogen concentration, and soil moisture:

$$V_{\max} = V_{\max 25} a_{v \max}^{(T_{\text{day}} - 25)/10} f(N) f(T_{\text{day}}) \beta_t, \quad (7)$$

where $V_{\max 25}$ is the value at 25 and $a_{v \max}$ is a temperature sensitivity parameter; $f(T_{\text{day}})$ is a function of temperature related metabolic processes; $f(N)$ is nitrogen scalar of photosynthesis which is related to foliage nitrogen content. β_t is a function, ranging from one to zero, which represents the soil moisture and lower temperature effects on stomatal resistance and photosynthesis.

The DLEM separates autotrophic respiration into maintenance respiration (Mr, unit: $\text{gC m}^{-2} \text{day}^{-1}$) and growth respiration (Gr, unit: $\text{gC m}^{-2} \text{day}^{-1}$). Gr is calculated by assuming that the fixed part of assimilated C will be used to construct new tissue (for turnover or plant growth). During these processes, 25% of assimilated C is supposed to be used as growth respiration. Maintenance respiration is related to surface temperature and biomass nitrogen content [51]. NPP is thus calculated as

$$\begin{aligned}
 \text{Gr} &= 0.25 \times \text{GPP} \\
 \text{NPP} &= \text{GPP} - \text{Mr} - \text{Gr}. \quad (8)
 \end{aligned}$$

Terrestrial ecosystem models are important tools for synthesizing a huge quantity of data, analyzing and predicting large-scale ecosystem processes, and providing a dynamic constraint on uncertainties in a variety of issues related to complex ecosystem processes, as well as heuristics clue for empirical studies [90–92]. This process-based modelling approach avoids many of the limitations of forest biomass inventories, eddy covariance measurement, and inverse modelling by accounting for ecosystem processes and spatial variations in environmental factors. Theoretically, the use of the spatially explicit ecosystem modelling approach provides

us with the ability to determine the relative roles of climate, CO_2 , land use and land cover change, air pollution, and disturbances to changes in terrestrial primary production and other carbon fluxes. However, this approach also has its own limitations because of the uncertainties associated with estimates of key model parameters as well as an incomplete understanding of ecosystem processes [84, 93]. The accuracy of process-based modeling on estimation of terrestrial primary production depends on comparison of simulated NPP across broad temporal and spatial scales with observations at a stand or landscape level (biomass inventory and eddy covariance techniques) and with satellite based estimates at a regional and global level.

5. Evaluating Process-Based Ecosystem Model against Ground and Satellite Observations

Model validation is essential for establishing the credibility of ecosystem models. Rastetter [92] divided various approaches for validating a biogeochemical model into four categories: (1) tests against short-term data; (2) space-for-time substitutions; (3) reconstruction of the past; (4) comparison with other models. To evaluate the accuracy of simulated terrestrial primary production, modeled GPP or NPP has been validated against experimental and observational data from field measurements and biomass inventory and also evaluated against satellite-based estimates and though model intercomparison. Here we use the DLEM model as a case for demonstrating how we validate and evaluate ecosystem models.

5.1. Evaluating against Flux Measurement Data. The DLEM-simulated GPP was compared with the observational data from the AmeriFlux towers in the Southeastern United States. These sites include Duke Forest Hardwoods, Duke Forest Loblolly Pine, Shidler Tallgrass Prairie site, and ARM-Southern Great Plains (SGP) site. We extracted GPP from our regional simulation ($8 \text{ km} \times 8 \text{ km}$ resolution) for the specific sites and compared that with eddy covariance estimates. Our results show that DLEM-simulated GPP is in a good agreement with eddy covariance based GPP for both forests and grassland sites (Figures 1(a)–1(d)). Generally, the model results fit well with observed GPP at Duke Hardwoods, Duke Loblolly, and Shidler Tallgrass except ARM-Southern Great Plain site. The ARM-Southern Great Plain site is a cropland site where measurements were available for limited time period when the vegetation is not in the most active growth period resulting in poor performance of model prediction.

5.2. Evaluating against Stand and Regional Biomass Inventory Data. The DLEM-simulated NPP was also compared to the site observation data in the Southern United States (SUS). We selected 138 measurements from the multibiome forest NPP dataset published by the Oak Ridge National Laboratory (ORNL) Distributed Active Archive Center. We extracted simulated NPP from our regional simulation outputs ($8 \text{ km} \times 8 \text{ km}$ per pixel) to match the geographic information of these

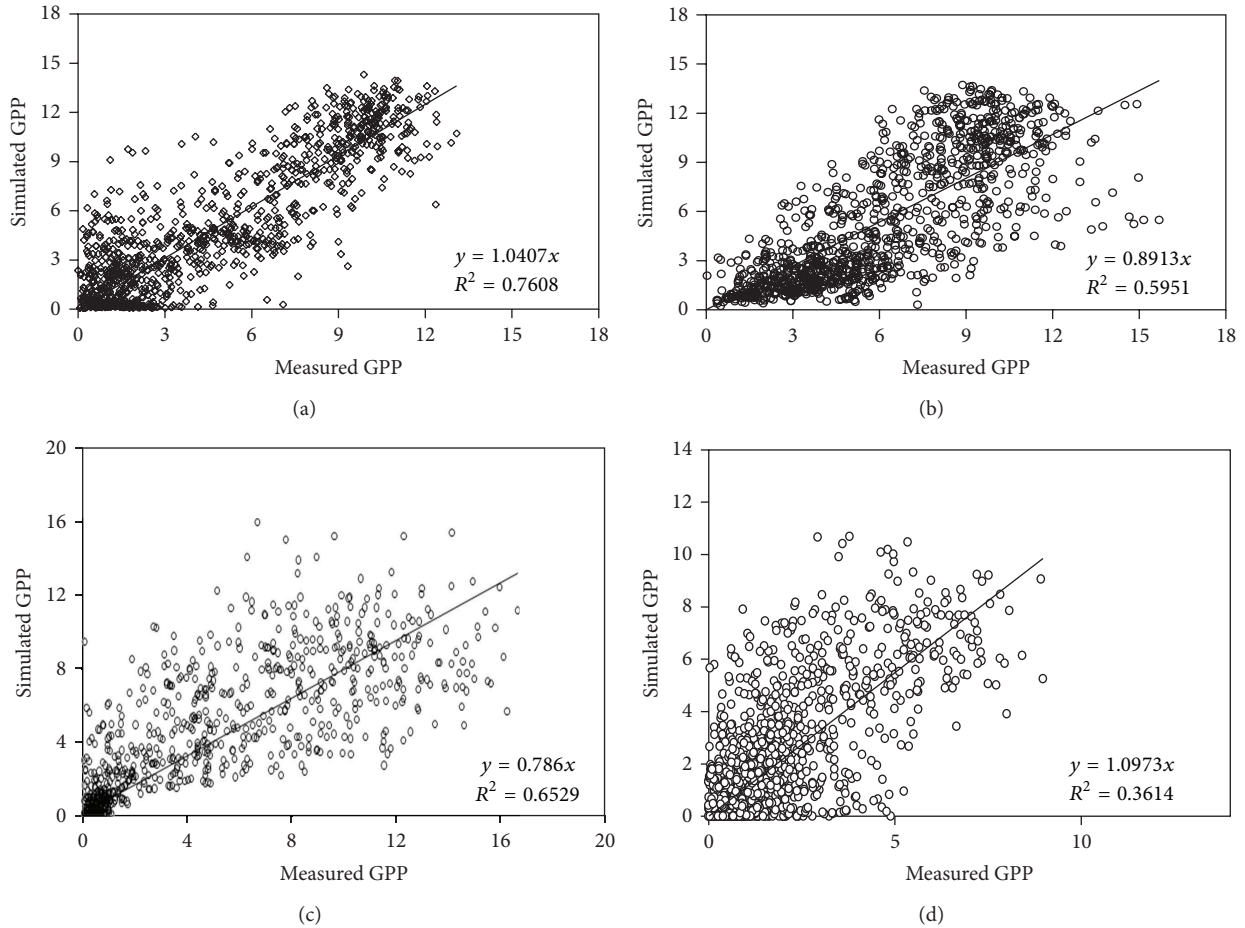


FIGURE 1: Evaluation of DLEM-simulated GPP against eddy covariance measured daily GPP ($\text{gC}/\text{m}^2/\text{day}$) at sites: (a) Duke Forest Hardwoods (US-DK2, NC, USA, deciduous broadleaf forest) from 2003 to 2005; (b) Duke Forest Loblolly Pine (US-DK3, evergreen needleleaf forest) from 2003 to 2005; (c) Shidler Tallgrass Prairie (US-shd, OK, USA, C4 grassland) from 1998 to 1999; (d) ARM SGP Main (US-arm, OK, USA, cropland) from 2003 to 2006.

138 sites. There was a good agreement between the simulated and measured aboveground NPP (Figure 2(a), slope = 1.09, and $R^2 = 0.82$).

For the purpose of regional validation, we compared DLEM simulated crop NPP with survey reports based on Huang et al. [94] at a national level across China. Our DLEM simulated NPP matched well with Huang et al.'s [94] observed NPP collected across 30 provinces in China (Figure 2(b), slope = 0.96, $R^2 = 0.73$). Additionally, we compared the model simulated state-level vegetation carbon of the southern ecosystem against the reported value based on forest inventory dataset (<http://www.fia.fs.fed.us/>). The comparisons (Figure 2(c)) showed that the vegetation carbon simulated by DLEM matched well with the results derived from the forest inventory database for year 1987 and 1997.

5.3. Evaluating against Satellite-Based Estimates. We evaluated the temporal pattern of crop NPP in China during the period 1982–2005 against the remote sensing dataset (Figure 3). We particularly compared our simulated crop

NPP with results from the Global Production Efficiency Model (GLO-PEM), which has a spatial resolution of 8 km and runs at a 10-day time step. GLO-PEM was driven almost entirely by satellite-derived variables, including both the Normalized Difference Vegetation Index (NDVI) and meteorological variables [77, 95]. We overlaid the GLO-PEM NPP images with the yearly cropland distribution data that we had developed and extracted previously. Similarly, we obtained the Moderate Resolution Imaging Spectroradiometer (MODIS) MOD 17 NPP from 2002 to 2005 and the Advanced Very High Resolution Radiometer (AVHRR) NPP from 1981 to 2001 [4]. The results showed that the DLEM-simulated NPP had the same temporal pattern with relatively higher values than those provided by GLO-PEM and by MODIS MOD 17. A possible explanation for the underestimation by GLO-PEM might be due to the fact that nitrogen is not factored into the model. MODIS MOD 17 results might be influenced by the LAI, which tends to be underestimated by MODIS MOD 17 [96]. Similarly, the uncertainties of input data and parameters adopted in DLEM

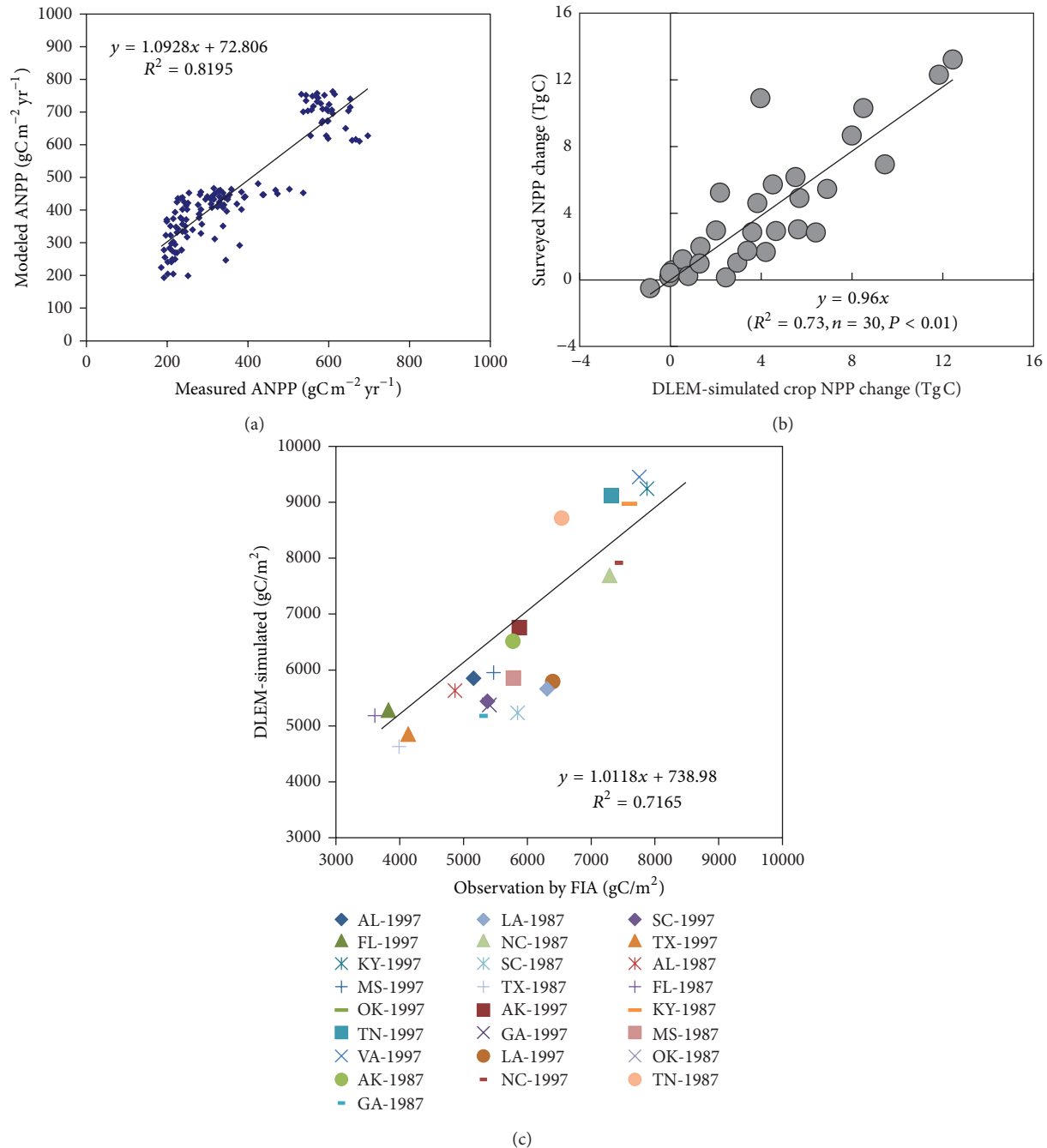


FIGURE 2: Comparisons of (a) modeled annual aboveground NPP against 138 field measurements in the SUS selected from Zheng et al. [120]; (b) modeled annual NPP against survey based crop NPP between 1980's and 1990's from Huang et al. [94]; (c) modeled vegetation carbon against forest inventory outputs in 1987 and 1997 based from Birdsey and Lewis [130].

could lead to higher simulated NPP; for example, we did not include vegetable crop types in this study and assumed that all croplands were dominant by cereal crop types.

We further evaluated DLEM's performance in simulating the spatial pattern of global GPP and NPP across the terrestrial biosphere by comparing it with MODIS product. The spatial pattern of the modeled GPP and NPP is consistent with that of MODIS GPP and NPP (Figure 4). However, the algorithms of MODIS for estimating NPP are not well

calibrated for cropland. A comparison of NPP measured at eddy covariance flux towers in China's cropland with MODIS-estimated NPP [97] indicated that MODIS has significantly underestimated the cropland NPP, which partly explained the higher estimates from the DLEM relative to MODIS products.

Finally, as a surrogate for the direct validation, model intercomparisons can be used to check the applicability of various kinds of ecosystem models [88]. Ecosystem models

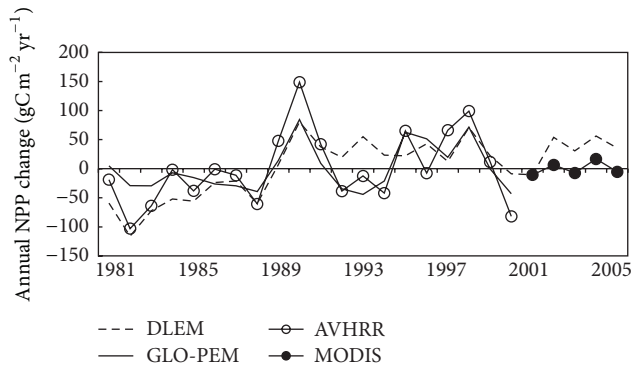


FIGURE 3: Temporal change in annual net primary production (NPP) (relative to the average for 1981–2005) of China's croplands estimated by DLEM-Ag model, GLO-PEM model, AVHRR, and MODIS database during 1981–2005) (modified from Ren et al. [131]).

differ among each other in terms of different model structure, parameters, and the processes that control photosynthetic carbon uptake. The estimates of terrestrial primary production among models, therefore, depend on inherent assumptions and complexity of model structure and formulation. For instance, previous model intercomparison studies [88, 89, 98] report large uncertainty associated with representation of vegetation structure, soil moisture dynamics, and ecosystem response to drought or humidity stress resulting in substantial differences in terrestrial primary production among the models. Although these models differ in assumptions, structure, parameters, and process representation, their intercomparison can highlight model weaknesses, inconsistencies, and uncertainties, which could provide insights for further model improvements. In addition, their intercomparison forces us to examine the interaction among data, model structure, parameter sets, and predictive uncertainty.

6. Assessing Terrestrial Primary Production Response to Climate Change and Increasing Atmospheric CO₂

Previous research has emphasized on how global change factors affect terrestrial primary production across broad temporal and spatial scales. Observational evidence suggest that earth's surface temperature has increased by 0.76°C over the past 150 years and is expected to increase by 1.5–6.4°C by the end of 21st century [99]. Historically, precipitation varied among regions over the period 1900–2005 but is expected to increase by 0.5–1% per decade in the 21st century at a global level [99]. These climate change factors would have a significant effect on ecosystem structure and function resulting in growing season extension [100], carbon loss [101], and changes in water balance [102]. Additionally, studies suggest that elevated CO₂ contributes to an enhancement in terrestrial primary production [67, 103, 104]; however, such enhancement may be counterbalanced by negative effects of ozone [105, 106]. Although tropospheric ozone has been considered as an important environmental factor that

controls terrestrial net primary production, its effect varies depending on regions [105, 106] and therefore could be less important compared to other environmental factors at a global scale. Another factor that might contribute to changes in terrestrial primary production is anthropogenic nitrogen inputs. Nitrogen enrichment has been primarily thought to stimulate terrestrial primary production in the temperate forest [107]; however, excessive nitrogen input likely leads to soil acidification, nutrient cation leaching, thus limiting plant growth [108]. Therefore, in this review, we only considered the effect of climate change and elevated CO₂ because they are the major factors affecting terrestrial primary production at a global scale [6, 13, 21].

6.1. Climate Change Impact on Terrestrial Primary Production.

Climate factors (i.e., temperature, precipitation, and radiation) are key drivers to control changes in terrestrial primary production [38]. Plants assimilate carbon for growth through photosynthesis, which is strongly affected by temperature. Plants also need nutrients from the soil (i.e., nitrogen and phosphorus), and plant responses to climate change can be substantially modified by the nutrient availability. Nutrient availability itself can also be affected by climate factors, especially temperature, because the rate of soil nutrient mineralization strongly depends on temperature. Below the optimum temperature, the activity of photosynthesis increases with increasing temperature in accordance with the Arrhenius relationship [109]. At higher temperature, photosynthesis decreases due to conformational changes in key enzymes. This decrease is reversible at moderately high temperatures but becomes increasingly irreversible with increased duration and intensity of high temperature exposure [110]. Many previous studies suggest that global warming resulted in an increase in NPP [13, 111] during the period 1982–1999, especially in northern high latitude ecosystems. In the low latitude region, changes in long-term NPP patterns were mainly controlled by colimitations of sunlight and precipitation.

The temporal and spatial patterns of precipitation are also critical to terrestrial ecosystem processes [38]. Tao et al. [112] indicate that the precipitation was the key factor determining the spatial distribution and temporal trends of NPP in China during 1981–2000. Zhao and Running [6] suggest a reduction in the global NPP of 0.55 PgC due to large-scale droughts, especially in the Southern Hemisphere, where decreased NPP counteracted the increased NPP over the Northern Hemisphere. However, Potter et al. [21] found an increasing trend in global NPP due to rapid warming trend that alleviated heat limitations in high latitude ecosystems in the Northern Hemisphere during the period 2000–2009. Additionally, comparison of 14 ecosystem models suggested that water availability is the primary limiting factor for NPP in global terrestrial ecosystem models [113].

While Intergovernmental Panel on Climate Change (IPCC, 2007) reported that the earth temperature is projected to increase during the 21st century that could largely alter ecosystem structure and function, it is still unclear how terrestrial primary production would respond to future climate change. Song et al. [114], using a dynamic land

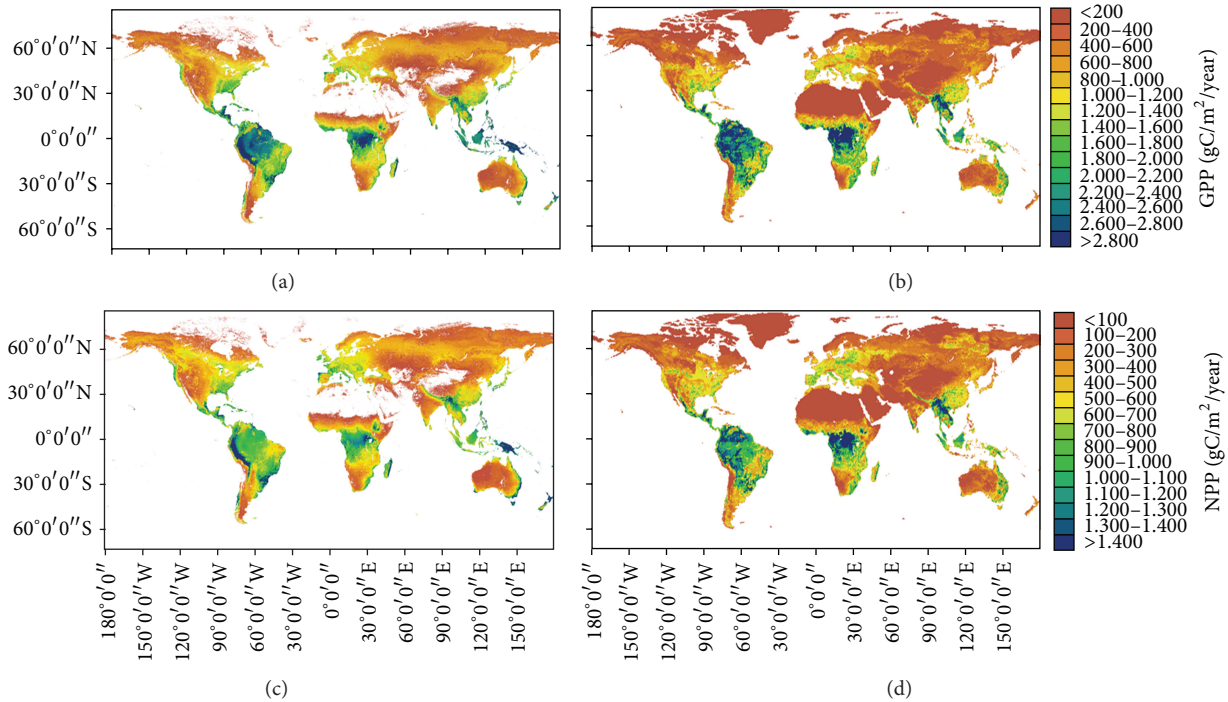


FIGURE 4: Spatial patterns of MODIS-derived and DLEM-simulated GPP and NPP for year 2010. MODIS-derived GPP (a) and NPP (c) and DLEM-simulated GPP (b) and NPP (d).

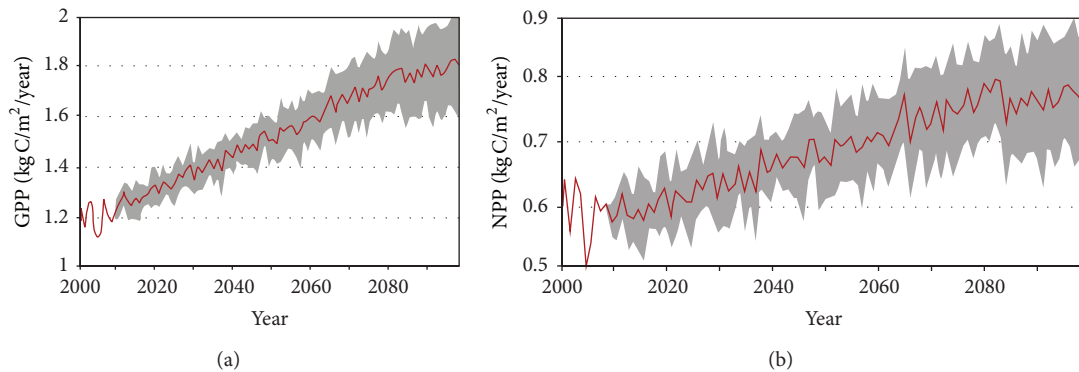


FIGURE 5: Projection of terrestrial primary production in response to climate change and increasing atmospheric CO_2 from 2000 to the 2090 as simulated by DLEM (a) change in gross primary production and (b) change in net primary production (modified from Song et al. [114]).

ecosystem model, projected an increase in GPP and NPP by $0.6 \text{ KgC m}^{-2} \text{ yr}^{-1}$ and $0.2 \text{ KgC m}^{-2} \text{ yr}^{-1}$, respectively, during the period 2000–2099 (Figure 5) across the Southeastern US. Across the globe, Sitch et al. [115] projected global NPP under four SRES scenarios (A1FI, A2, B1, and B2) using five dynamic global vegetation models (DGVMs) and found reduction in terrestrial NPP due to climate. While five models show divergence in their response to climate, all models resulted in decrease in NPP in the tropics and extratropics. These results indicate that the estimated effect of climate on terrestrial NPP varies depending on emission scenarios and model structure and parameters used to simulate plant physiological response to global change.

While inventory and satellite based approaches provide estimates of terrestrial primary production at a global scale, these approaches do not allow us to separate the effects of climate and elevated CO_2 . For instance, Zhao and Running [6] found that extreme events such as drought in the Southern Hemisphere resulted in a decline in terrestrial NPP, while Potter et al. [21] report an increase in NPP during the period 2000–2009. However, these studies do not necessarily specify whether such decline is due to specific climate factors or a combination of climate and elevated CO_2 or other environmental drivers. At a global scale, climate in the absence of elevated CO_2 reduced terrestrial NPP, while doubling CO_2 concentration under changing climatic condition increased global NPP by 25% [37].

TABLE 1: Published values of global terrestrial GPP and NPP based on observations, satellites, and/or process-based model.

Source	Basis	GPP (PgC yr ⁻¹)	NPP (PgC yr ⁻¹)
Melillo et al. [3]	TEM model	NA	53.2
Field et al. [20]	CASA model	NA	48.0
Schlesinger [126]	Review	NA	51.97
Cao and Woodward [37]	CEVSA model	NA	57.0
Ruimy et al. [50]	Model intercomparison	NA	45.5
Cramer et al. [15]	Model intercomparison	113	55.4 (44.4~66.3)
Zhao et al. [127]	MODIS	109.29	56.02
Beer et al. [8]	Diagnostic models	123 ± 8	NA
Yuan et al. [46]	Ameriflux and MODIS	110.5	NA
Ryu et al. [128]	MODIS and process-based model	118 ± 26	NA
Jung et al. [129]	Machine learning approach	119.4 ± 5.9	NA
Ito [18]	Meta-analysis	NA	56.2 ± 14.3
Potter et al. [21]	MODIS and CASA model	NA	50.05
This study	DLEM model	110.4	54.6

6.2. *CO₂ Impact on Terrestrial Primary Production.* The primary responses of plants to elevated atmospheric CO₂ concentration are increased photosynthesis and reduced stomatal conductance [116]. Stomata play an essential role in the regulation of both water losses by transpiration and CO₂ uptake for photosynthesis and plant growth. In order to optimize CO₂ uptake and water losses in rapidly changing environmental conditions, plants have evolved the ability to control stomatal conductance in response to multiple environmental factors such as solar radiation, temperature, VPD, and wind speed. Mechanistic scheme has been developed by Farquhar et al. [109] to describe leaf-level photosynthesis response to CO₂. Ball [117] developed the Ball-Berry empirical model to describe the behavior of stomatal conductance to water vapor as a function of environmental conditions and net photosynthetic rate. These two schemes have been widely used in existing process-based models to describe plant responses to CO₂ increase.

Vegetation/Ecosystem Modeling and Analysis Project (VEMAP) analyzed the responses of NPP to doubled CO₂ from 355 to 710 ppmv among three biogeochemistry models and found that, for the conterminous United States, doubled atmospheric CO₂ causes NPP to increase by 5–11% [10]. King et al. [118] used a georeferenced model of ecosystem dynamics to explore the sensitivity of global carbon storage to changes in atmospheric CO₂ and climate; the results suggest that a doubling of atmospheric CO₂ from 280 ppm to 560 ppm enhances equilibrium global NPP by 16.9%. In a similar model intercomparison study using five dynamic global vegetation models (DGVMs), Sitch et al. [115] found that interaction of climate and atmospheric CO₂ increased terrestrial NPP for four different SRES scenarios over the 21st century.

We also compared DLEM-simulated NPP and GPP with previous studies (Table 1) based on observation, remote sensing, and other process-based models. DLEM simulated a global GPP of 116 PgC yr⁻¹ for year 2010 which is within the range of 109–119 PgC yr⁻¹ based on previous studies. For the same year, DLEM simulated a global NPP of 56.5 PgC yr⁻¹ compared to the range of 44–66 PgC yr⁻¹ estimated by previous studies. While most of the previous studies (Table 1) are based on different approaches, they have their own limitations in terms of field measurements, accuracy associated with satellite estimates, and accuracy of the ecosystem models. For instance, satellite measurements are sensitive to changes in atmospheric chemistry. Similarly, ecosystem models lack structural complexity to capture belowground processes [119]. Therefore, it is necessary to integrate field observations, satellite based approach, and ecosystem models to accurately quantify the terrestrial primary production across broad temporal and spatial scales.

6.3. *Uncertainty in Estimating Terrestrial Primary Production.* Multiple approaches for estimating and predicting terrestrial primary production lead to diversified conclusions (Table 1). Uncertainty in the estimations of terrestrial primary productivity may arise from input datasets (climate, land use, etc.) and inventory datasets (for model calibration and validation) as well as from the model structure itself. The analysis of the seventeen models shows that global NPP ranged from 39.9 to 80.5 PgC [40]. Many factors such as model structure, parameters, input data, and scaling may be responsible for such large uncertainty. One major source of uncertainty is the available inventory NPP datasets for model parameterization, calibration, and validation [120]. The NPP is measured at plot or field scales that may not represent the NPP at the

0.5° by 0.5° grid cell that is commonly used by global scale models. Therefore, direct intercomparison between field data obtained in different studies or comparison of these results with coarse resolution models can be misleading. In a model intercomparison for which all models reported results at 0.5° by 0.5° grid size, there was no suitable and consistent field NPP available since most measurements are conducted in the small areas ranging from <1 to several ha [15]. The second problem with available inventory datasets is the belowground biomass measurement. The belowground biomass is often not measured but is instead estimated using standard formulas. This may provide misleading results. Lauenroth et al. [121] have reported that amount of uncertainty associated with estimates of NPP was significantly influenced by the variability in the input data. For example, due to greater variability in the field measured belowground data than aboveground data, estimates of belowground NPP tended to have more uncertainty than estimates of aboveground NPP. Therefore, lack of available input dataset provides a significant uncertainty in models that estimate NPP at global scale using coarse resolution grid size.

In addition to the inventory NPP datasets for model calibration and validation, the input datasets such as land use and climate are other sources of uncertainty in most of the models. At the global scale, the impacts may be very small for land use as compared to climate or meteorological datasets [122]. Jung et al. [122] estimated GPP using different land cover maps, spatial land cover resolutions, meteorological data sets, and process-based terrestrial ecosystem models. Their results indicate a clear hierarchy of effects: a small effect of using different land cover maps, a somewhat higher but still relatively small effect of the spatial land cover resolution, a substantial effect due to changing the meteorological forcing, and the largest effect caused by using different models. In this way, model structure provides the largest uncertainty in the terrestrial primary productivity.

In the models, uncertainty in the estimation of NPP arises from different representations of ecological processes by different models. Because the components of terrestrial ecosystems and the interactions among them are complicated or not well understood, simplifying assumptions must be made to describe them in numerical models. Different modeling strategies may adopt different simplifying assumptions, leading to different model complexity and behavior. The uncertainties in the models are very large, both in terms of parameter-based and model structure related uncertainty. Models may range from the simple, empirically derived, correlation of net primary productivity with air temperature and precipitation (e.g., [123]) to the detailed models with detailed biochemistry (e.g. DLEM, LPJ, CLM).

Recent studies indicated that major uncertainties in simulating interannual variations of gross carbon uptake are strongly linked to the way of how and if biogeochemical cycles (carbon, water, and nitrogen) interact within the models which controls their sensitivity to meteorological conditions [122]. The observed relationships between forest GPP and mean annual temperature are strongly related to a corresponding gradient of nitrogen availability [124]. Therefore, accurate model representation of interactions among

carbon, nitrogen, and water cycles is the key to reduce uncertainty in simulating terrestrial primary production [51, 125].

7. Toward a Multiscale Synthesis of Observations and Model Simulations

For the NPP estimation at large scales, none of the approaches mentioned above could solely fill in the gap of our understanding. Experiments and observations are always conducted at a specific scale. Multiscale experiments and observations provide data but are not capable of quantifying underlying mechanisms of changes in terrestrial primary production as influenced by multiple environmental factors. At the same time, modeling studies have been developing by integrating better understanding and more representations of biotic and abiotic processes. In order to provide diagnosis, quantification, and attribution of multiscale terrestrial primary production across the globe, it is critically needed to synthesize the various observation data and the modeled output at diverse spatial scales ranging from site to region to globe and temporal steps ranging from day to decade. More specifically, (1) a common driving database needs to be developed to characterize the environmental changes and to drive the model runs. The database includes time series of site-specific and gridded climate, atmospheric composition, land-cover/land-use change, and land management practices and auxiliary dataset on elevation, slope, aspect, vegetation cover types, soil properties, and so on. (2) The magnitude, spatial, and temporal patterns of terrestrial primary production need to be quantified by various approaches and datasets, including site-specific flux measurements, regional inventories, MODIS-derived GPP/NPP, and model simulations in a multimodel fashion. (3) Based on model evaluation and intercomparison, multiple model simulation experiments need to be conducted to distinguish the relative contributions of controlling processes and to identify their changes over space and time. Multiscale synthesis efforts need to provide useful information to reflect the status of terrestrial primary production, which could show further feedback to climate system, as well as to improve our understanding of the mechanisms responsible for terrestrial primary production. (4) Multiple approaches lead to diversified conclusions in terms of quantification and attribution of terrestrial primary production. Therefore, assessments of uncertainty will be an integral part of any synthesis project. In particular, uncertainties associated with each input driving dataset, model structure, parameters, scaling, and measurement need to be addressed. We expect that such a multiscale synthesis will provide a systematic assessment on terrestrial primary production and its driving forces at varied spatial scales.

Moreover, we are living in the new world of the Anthropocene in which human activity has indeed changed the earth's biosphere [132, 133]. Human activity such as land use change has been a primary factor affecting magnitude, spatial, and temporal patterns of terrestrial primary production across the globe. From both scientific and policy perspectives,

therefore, it is essential to incorporate socioeconomic component into terrestrial ecosystem models for better estimating and predicting terrestrial primary production in a changing global environment.

Conflict of Interests

The authors declare that there is no conflict of interests regarding the publication of this paper.

Acknowledgments

This research has been supported by NSF Decadal and Regional Climate Prediction using Earth System Models (AGS-1243220), NSF Dynamics of Coupled Natural and Human Systems (1210360), NSF Computer and Network Systems (CNS-1059376), NASA Land Cover/Land Use Change Program (NNX08AL73G-S01), and NASA Interdisciplinary Science Program (NNX10AU06G, NNX11AD47G).

References

- [1] D. A. Clark, S. Brown, D. W. Kicklighter et al., "Net primary production in tropical forests: an evaluation and synthesis of existing field data," *Ecological Applications*, vol. 11, no. 2, pp. 371–384, 2001.
- [2] F. S. Chapin III, G. M. Woodwell, J. T. Randerson et al., "Reconciling carbon-cycle concepts, terminology, and methods," *Ecosystems*, vol. 9, no. 7, pp. 1041–1050, 2006.
- [3] J. M. Melillo, A. D. McGuire, D. W. Kicklighter, B. Moore III, C. J. Vorosmarty, and A. L. Schloss, "Global climate change and terrestrial net primary production," *Nature*, vol. 363, no. 6426, pp. 234–240, 1993.
- [4] S. W. Running, R. R. Nemani, F. A. Heinsch, M. Zhao, M. Reeves, and H. Hashimoto, "A continuous satellite-derived measure of global terrestrial primary production," *BioScience*, vol. 54, no. 6, pp. 547–560, 2004.
- [5] A. Z. Shvidenko, D. G. Schepashchenko, E. A. Vaganov, and S. Nilsson, "Net primary production of forest ecosystems of Russia: a new estimate," *Doklady Earth Sciences*, vol. 421, no. 2, pp. 1009–1012, 2008.
- [6] M. Zhao and S. W. Running, "Drought-induced reduction in global terrestrial net primary production from 2000 through 2009," *Science*, vol. 329, no. 5994, pp. 940–943, 2010.
- [7] S. Piao, X. Wang, P. Ciais, B. Zhu, T. Wang, and J. Liu, "Changes in satellite-derived vegetation growth trend in temperate and boreal Eurasia from 1982 to 2006," *Global Change Biology*, vol. 17, no. 10, pp. 3228–3239, 2011.
- [8] C. Beer, M. Reichstein, E. Tomelleri et al., "Terrestrial gross carbon dioxide uptake: global distribution and covariation with climate," *Science*, vol. 329, no. 5993, pp. 834–838, 2010.
- [9] J. Xiao, Q. Zhuang, B. E. Law et al., "A continuous measure of gross primary production for the conterminous United States derived from MODIS and AmeriFlux data," *Remote Sensing of Environment*, vol. 114, no. 3, pp. 576–591, 2010.
- [10] Y. Pan, R. Birdsey, J. Hom, K. McCullough, and K. Clark, "Improved estimates of net primary productivity from modis satellite data at regional and local scales," *Ecological Applications*, vol. 16, no. 1, pp. 125–132, 2006.
- [11] W. Ren, H. Tian, B. Tao, Y. Huang, and S. Pan, "China's crop productivity and soil carbon storage as influenced by multifactor global change," *Global Change Biology*, vol. 18, no. 9, pp. 2945–2957, 2012.
- [12] M. Piacentini and K. Rosina, *Measuring the Environmental Performance of Metropolitan Areas with Geographic Information Sources*, OECD Publishing, 2012.
- [13] R. R. Nemani, C. D. Keeling, H. Hashimoto et al., "Climate-driven increases in global terrestrial net primary production from 1982 to 1999," *Science*, vol. 300, no. 5625, pp. 1560–1563, 2003.
- [14] B. E. Law, D. Turner, J. Campbell et al., "Carbon fluxes across regions: observational constraints at multiple scales," in *Scaling and Uncertainty Analysis in Ecology*, pp. 167–190, Springer, New York, NY, USA, 2006.
- [15] W. Cramer, D. W. Kicklighter, A. Bondeau et al., "Comparing global models of terrestrial net primary productivity (NPP): overview and key results," *Global Change Biology*, vol. 5, no. 1, pp. 1–15, 1999.
- [16] N. Gruber, P. Friedlingstein, C. B. Field et al., "The vulnerability of the carbon cycle in the 21st century: an assessment of carbon-climate-human interactions," in *Toward CO₂ Stabilization: Issues, Strategies, and Consequences*, vol. 62, pp. 45–76, Scientific Committee on Problems of the Environment (SCOPE) International Council of Scientific Unions, 2004.
- [17] R. J. Geider, E. H. Delucia, P. G. Falkowski et al., "Primary productivity of planet earth: biological determinants and physical constraints in terrestrial and aquatic habitats," *Global Change Biology*, vol. 7, no. 8, pp. 849–882, 2001.
- [18] A. Ito, "A historical meta-analysis of global terrestrial net primary productivity: are estimates converging?" *Global Change Biology*, vol. 17, no. 10, pp. 3161–3175, 2011.
- [19] D. C. Nepstad, C. R. de Carvalho, E. A. Davidson et al., "The role of deep roots in the hydrological and carbon cycles of Amazonian forests and pastures," *Nature*, vol. 372, no. 6507, pp. 666–669, 1994.
- [20] C. B. Field, J. T. Randerson, and C. M. Malmstrom, "Global net primary production: combining ecology and remote sensing," *Remote Sensing of Environment*, vol. 51, no. 1, pp. 74–88, 1995.
- [21] C. Potter, S. Klooster, and V. Genovesi, "Net primary production of terrestrial ecosystems from 2000 to 2009," *Climatic Change*, vol. 115, no. 2, pp. 365–378, 2012.
- [22] J. Aber, R. P. Neilson, S. McNulty, J. M. Lenihan, D. Bachelet, and R. J. Drake, "Forest processes and global environmental change: predicting the effects of individual and multiple stressors," *BioScience*, vol. 51, no. 9, pp. 735–751, 2001.
- [23] P. E. Thornton, B. E. Law, H. L. Gholz et al., "Modeling and measuring the effects of disturbance history and climate on carbon and water budgets in evergreen needleleaf forests," *Agricultural and Forest Meteorology*, vol. 113, no. 1–4, pp. 185–222, 2002.
- [24] B. D. Amiro, A. G. Barr, J. G. Barr et al., "Ecosystem carbon dioxide fluxes after disturbance in forests of North America," *Journal of Geophysical Research: Biogeosciences (2005–2012)*, vol. 115, no. 4, 2010.
- [25] C. A. Williams, G. J. Collatz, J. Masek, and S. N. Goward, "Carbon consequences of forest disturbance and recovery across the conterminous United States," *Global Biogeochemical Cycles*, vol. 26, no. 1, 2012.
- [26] J. A. Hicke, C. D. Allen, A. R. Desai et al., "Effects of biotic disturbances on forest carbon cycling in the United States and Canada," *Global Change Biology*, vol. 18, no. 1, pp. 7–34, 2012.

- [27] C. M. Gough, C. S. Vogel, K. H. Harrold, K. George, and P. S. Curtis, "The legacy of harvest and fire on ecosystem carbon storage in a North Temperate Forest," *Global Change Biology*, vol. 13, no. 9, pp. 1935–1949, 2007.
- [28] C. M. Gough, C. S. Vogel, H. P. Schmid, and P. S. Curtis, "Controls on annual forest carbon storage: lessons from the past and predictions for the future," *BioScience*, vol. 58, no. 7, pp. 609–622, 2008.
- [29] D. Niemeijer, "Developing indicators for environmental policy: data-driven and theory-driven approaches examined by example," *Environmental Science and Policy*, vol. 5, no. 2, pp. 91–103, 2002.
- [30] D. S. Schimel, "Terrestrial ecosystems and the carbon cycle," *Global Change Biology*, vol. 1, no. 1, pp. 77–91, 1995.
- [31] D. P. Turner, W. D. Ritts, W. B. Cohen et al., "Site-level evaluation of satellite-based global terrestrial gross primary production and net primary production monitoring," *Global Change Biology*, vol. 11, no. 4, pp. 666–684, 2005.
- [32] M. G. Turner, "Landscape ecology: what is the state of the science?" *Annual Review of Ecology, Evolution, and Systematics*, vol. 36, pp. 319–344, 2005.
- [33] E. Falge, D. Baldocchi, J. Tenhunen et al., "Seasonality of ecosystem respiration and gross primary production as derived from FLUXNET measurements," *Agricultural and Forest Meteorology*, vol. 113, no. 1–4, pp. 53–74, 2002.
- [34] B. E. Law, D. Turner, J. Campbell et al., "Disturbance and climate effects on carbon stocks and fluxes across Western Oregon USA," *Global Change Biology*, vol. 10, no. 9, pp. 1429–1444, 2004.
- [35] Y. Pan, R. A. Birdsey, J. Fang et al., "A large and persistent carbon sink in the world's forests," *Science*, vol. 333, no. 6045, pp. 988–993, 2011.
- [36] M. Cao and F. I. Woodward, "Dynamic responses of terrestrial ecosystem carbon cycling to global climate change," *Nature*, vol. 393, no. 6682, pp. 249–252, 1998.
- [37] M. Cao and F. I. Woodward, "Net primary and ecosystem production and carbon stocks of terrestrial ecosystems and their responses to climate change," *Global Change Biology*, vol. 4, no. 2, pp. 185–198, 1998.
- [38] H. Tian, J. M. Melillo, D. W. Kicklighter et al., "Effect of interannual climate variability on carbon storage in Amazonian ecosystems," *Nature*, vol. 396, no. 6712, pp. 664–667, 1998.
- [39] M. Jung, M. Reichstein, H. A. Margolis et al., "Global patterns of land-atmosphere fluxes of carbon dioxide, latent heat, and sensible heat derived from eddy covariance, satellite, and meteorological observations," *Journal of Geophysical Research: Biogeosciences (2005–2012)*, vol. 116, no. 3, 2011.
- [40] W. Cramer, D. W. Kicklighter, A. Bondeau et al., "Comparing global models of terrestrial net primary productivity (NPP): overview and key results," *Global Change Biology*, vol. 5, no. 1, pp. 1–15, 1999.
- [41] P. Friedlingstein, P. Cox, R. Betts et al., "Climate-carbon cycle feedback analysis: results from the C4MIP model intercomparison," *Journal of Climate*, vol. 19, no. 14, pp. 3337–3353, 2006.
- [42] D. Hemming, R. Betts, and M. Collins, "Sensitivity and uncertainty of modelled terrestrial net primary productivity to doubled CO₂ and associated climate change for a relatively large perturbed physics ensemble," *Agricultural and Forest Meteorology*, vol. 170, pp. 79–88, 2013.
- [43] J. Xiao, Q. Zhuang, B. E. Law et al., "Assessing net ecosystem carbon exchange of U.S. terrestrial ecosystems by integrating eddy covariance flux measurements and satellite observations," *Agricultural and Forest Meteorology*, vol. 151, no. 1, pp. 60–69, 2011.
- [44] T. F. Keenan, E. Davidson, A. M. Moffat, W. Munger, and A. D. Richardson, "Using model-data fusion to interpret past trends, and quantify uncertainties in future projections, of terrestrial ecosystem carbon cycling," *Global Change Biology*, vol. 18, no. 8, pp. 2555–2569, 2012.
- [45] W. Wang, J. Dungan, H. Hashimoto et al., "Diagnosing and assessing uncertainties of terrestrial ecosystem models in a multimodel ensemble experiment: 1. Primary production," *Global Change Biology*, vol. 17, no. 3, pp. 1350–1366, 2011.
- [46] W. Yuan, S. Liu, G. Yu et al., "Global estimates of evapotranspiration and gross primary production based on MODIS and global meteorology data," *Remote Sensing of Environment*, vol. 114, no. 7, pp. 1416–1431, 2010.
- [47] A. Huete, K. Didan, T. Miura, E. P. Rodriguez, X. Gao, and L. G. Ferreira, "Overview of the radiometric and biophysical performance of the MODIS vegetation indices," *Remote Sensing of Environment*, vol. 83, no. 1–2, pp. 195–213, 2002.
- [48] A. D. McGuire, S. Sitch, J. S. Clein et al., "Carbon balance of the terrestrial biosphere in the twentieth century: analyses of CO₂, climate and land use effects with four process-based ecosystem models," *Global Biogeochemical Cycles*, vol. 15, no. 1, pp. 183–206, 2001.
- [49] H. Tian, C. A. S. Hall, and Y. Qi, "Modeling primary productivity of the terrestrial biosphere in changing environments: toward a dynamic biosphere model," *Critical Reviews in Plant Sciences*, vol. 17, no. 5, pp. 541–557, 1998.
- [50] A. Ruimy, L. Kergoat, and A. Bondeau, "Comparing global models of terrestrial net primary productivity (NPP): analysis of differences in light absorption and light-use efficiency," *Global Change Biology*, vol. 5, no. 1, pp. 56–64, 1999.
- [51] H. Tian, G. Chen, M. Liu et al., "Model estimates of net primary productivity, evapotranspiration, and water use efficiency in the terrestrial ecosystems of the Southern United States during 1895–2007," *Forest Ecology and Management*, vol. 259, no. 7, pp. 1311–1327, 2010.
- [52] D. Baldocchi, E. Falge, L. Gu et al., "FLUXNET: a new tool to study the temporal and spatial variability of ecosystem-scale carbon dioxide, water vapor, and energy flux densities," *Bulletin of the American Meteorological Society*, vol. 82, no. 11, pp. 2415–2434, 2001.
- [53] M. Zhao and G. Zhou, "Estimation of biomass and net primary productivity of major planted forests in China based on forest inventory data," *Forest Ecology and Management*, vol. 207, no. 3, pp. 295–313, 2005.
- [54] G. Zhou, Y. Wang, Y. Jiang, and Z. Yang, "Estimating biomass and net primary production from forest inventory data: a case study of China's Larix forests," *Forest Ecology and Management*, vol. 169, no. 1–2, pp. 149–157, 2002.
- [55] R. A. Birdsey and L. S. Heath, "Forest inventory data, models, and assumptions for monitoring carbon flux," in *Soil Carbon Sequestration and the Greenhouse Effect*, SSSA Special Publication, pp. 125–135, Soil Science Society of America, Madison, Wis, USA, 2001.
- [56] X. Wang, Z. Feng, and Z. Ouyang, "The impact of human disturbance on vegetative carbon storage in forest ecosystems in China," *Forest Ecology and Management*, vol. 148, no. 1–3, pp. 117–123, 2001.
- [57] S. L. Brown and P. E. Schroeder, "Spatial patterns of above-ground production and mortality of woody biomass for Eastern

- U.S. forests,” *Ecological Applications*, vol. 9, no. 3, pp. 968–980, 1999.
- [58] S. L. Brown, P. Schroeder, and J. S. Kern, “Spatial distribution of biomass in forests of the Eastern USA,” *Forest Ecology and Management*, vol. 123, no. 1, pp. 81–90, 1999.
- [59] J. Y. Fang, T. Oikawa, T. Kato, W. Mo, and Z. Wang, “Biomass carbon accumulation by Japan’s forest from 1947 to 1995,” *Global Biogeochemical Cycles*, vol. 19, no. 2, 2005.
- [60] J. Y. Fang and Z. M. Wang, “Forest biomass estimation at regional and global levels, with special reference to China’s forest biomass,” *Ecological Research*, vol. 16, no. 3, pp. 587–592, 2001.
- [61] Z. Guo, J. Fang, Y. Pan, and R. Birdsey, “Inventory-based estimates of forest biomass carbon stocks in China: a comparison of three methods,” *Forest Ecology and Management*, vol. 259, no. 7, pp. 1225–1231, 2010.
- [62] J. Pajtik, B. Konôpka, and M. Lukac, “Individual biomass factors for beech, oak and pine in Slovakia: a comparative study in young naturally regenerated stands,” *Trees—Structure and Function*, vol. 25, no. 2, pp. 277–288, 2011.
- [63] Y. Luo, X. Wang, X. Zhang, Y. Ren, and H. Poorter, “Variation in biomass expansion factors for China’s forests in relation to forest type, climate, and stand development,” *Annals of Forest Science*, vol. 70, no. 6, pp. 589–599, 2013.
- [64] Z. Somogyi, E. Cienciala, R. Mäkipää, P. Muukkonen, A. Lehtonen, and P. Weiss, “Indirect methods of large-scale forest biomass estimation,” *European Journal of Forest Research*, vol. 126, no. 2, pp. 197–207, 2007.
- [65] W. W. Leighty, S. P. Hamburg, and J. Caouette, “Effects of management on carbon sequestration in forest biomass in Southeast Alaska,” *Ecosystems*, vol. 9, no. 7, pp. 1051–1065, 2006.
- [66] R. Ouimet, S. Tremblay, C. Périé, and G. Prêgent, “Ecosystem carbon accumulation following fallow farmland afforestation with red pine in Southern Quebec,” *Canadian Journal of Forest Research*, vol. 37, no. 6, pp. 1118–1133, 2007.
- [67] R. J. Norby, P. J. Hanson, E. G. O’Neill et al., “Net primary productivity of a CO₂-enriched deciduous forest and the implications for carbon storage,” *Ecological Applications*, vol. 12, no. 5, pp. 1261–1266, 2002.
- [68] R. Houghton, “Keeping management effects separate from environmental effects in terrestrial carbon accounting,” *Global Change Biology*, vol. 19, no. 9, pp. 2609–2612, 2013.
- [69] D. D. Baldocchi, “Assessing the eddy covariance technique for evaluating carbon dioxide exchange rates of ecosystems: past, present and future,” *Global Change Biology*, vol. 9, no. 4, pp. 479–492, 2003.
- [70] S. W. Running, D. D. Baldocchi, D. P. Turner, S. T. Gower, P. S. Bakwin, and K. A. Hibbard, “A global terrestrial monitoring network integrating tower fluxes, flask sampling, ecosystem modeling and EOS satellite data,” *Remote Sensing of Environment*, vol. 70, no. 1, pp. 108–127, 1999.
- [71] B. E. Law, E. Falge, L. Gu et al., “Environmental controls over carbon dioxide and water vapor exchange of terrestrial vegetation,” *Agricultural and Forest Meteorology*, vol. 113, no. 1–4, pp. 97–120, 2002.
- [72] H. Tian, J. M. Melillo, D. W. Kicklighter et al., “Effect of interannual climate variability on carbon storage in Amazonian ecosystems,” *Nature*, vol. 396, no. 6712, pp. 664–667, 1998.
- [73] W. J. Massman and X. Lee, “Eddy covariance flux corrections and uncertainties in long-term studies of carbon and energy exchanges,” *Agricultural and Forest Meteorology*, vol. 113, no. 1–4, pp. 121–144, 2002.
- [74] K. Wilson, A. Goldstein, E. Falge et al., “Energy balance closure at FLUXNET sites,” *Agricultural and Forest Meteorology*, vol. 113, no. 1–4, pp. 223–243, 2002.
- [75] R. DeFries, “Terrestrial vegetation in the coupled human-earth system: contributions of remote sensing,” *Annual Review of Environment and Resources*, vol. 33, pp. 369–390, 2008.
- [76] C. J. Tucker, C. L. Vanpraet, M. J. Sharman, and G. Van Ittersum, “Satellite remote sensing of total herbaceous biomass production in the senegalese sahel: 1980–1984,” *Remote Sensing of Environment*, vol. 17, no. 3, pp. 233–249, 1985.
- [77] S. J. Goetz, S. D. Prince, J. Small, and A. C. R. Gleason, “Inter-annual variability of global terrestrial primary production: results of a model driven with satellite observations,” *Journal of Geophysical Research: Atmospheres (1984–2012)*, vol. 105, no. 15, pp. 20077–20091, 2000.
- [78] S. W. Running, D. D. Baldocchi, D. P. Turner, S. T. Gower, P. S. Bakwin, and K. A. Hibbard, “A global terrestrial monitoring network integrating tower fluxes, flask sampling, ecosystem modeling and EOS satellite data,” *Remote Sensing of Environment*, vol. 70, no. 1, pp. 108–127, 1999.
- [79] F. A. Heinsch, M. Reeves, P. Votava et al., “GPP and NPP, (MOD17A2/A3) products NASA MODIS land algorithm,” in *MOD17 User’s Guide*, pp. 1–57, 2003.
- [80] D. A. Sims, A. F. Rahman, V. D. Cordova et al., “A new model of gross primary productivity for North American ecosystems based solely on the enhanced vegetation index and land surface temperature from MODIS,” *Remote Sensing of Environment*, vol. 112, no. 4, pp. 1633–1646, 2008.
- [81] B. Matsushita and M. Tamura, “Integrating remotely sensed data with an ecosystem model to estimate net primary productivity in East Asia,” *Remote Sensing of Environment*, vol. 81, no. 1, pp. 58–66, 2002.
- [82] J. A. Richards, *Remote Sensing Digital Image Analysis: An Introduction*, Springer, New York, NY, USA, 2013.
- [83] J. M. Chen, G. Pavlic, L. Brown et al., “Derivation and validation of Canada-wide coarse-resolution leaf area index maps using high-resolution satellite imagery and ground measurements,” *Remote Sensing of Environment*, vol. 80, no. 1, pp. 165–184, 2002.
- [84] H. Tian, G. Chen, C. Zhang et al., “Century-scale responses of ecosystem carbon storage and flux to multiple environmental changes in the Southern United States,” *Ecosystems*, vol. 15, no. 4, pp. 674–694, 2012.
- [85] S. R. Dangal, B. S. Felzer, and M. D. Hurteau, “Effects of agriculture and timber harvest on carbon sequestration in the Eastern US forests,” *Journal of Geophysical Research: Biogeosciences*, vol. 119, no. 1, pp. 35–54, 2014.
- [86] C. S. Potter, “Terrestrial ecosystem production: a process model based on global satellite and surface data,” *Global Biogeochemical Cycles*, vol. 7, no. 4, pp. 811–841, 1993.
- [87] IPCC—Intergovernmental Panel on Climate Change, *The Scientific Basis*, Cambridge University Press, New York, NY, USA, 2007.
- [88] D. N. Huntzinger, W. M. Post, Y. Wei et al., “North American carbon program (NACP) regional interim synthesis: terrestrial biospheric model intercomparison,” *Ecological Modelling*, vol. 232, pp. 144–157, 2012.
- [89] K. Schaefer, C. R. Schwalm, C. Williams et al., “A model-data comparison of gross primary productivity: results from the North American carbon program site synthesis,” *Journal of Geophysical Research: Biogeosciences (2005–2012)*, vol. 117, no. 3, 2012.

- [90] H. T. Odum, *Systems Ecology: An Introduction*, John Wiley & Sons, New York, NY, USA, 1983.
- [91] N. Oreskes, K. Shrader-Frechette, and K. Belitz, "Verification, validation, and confirmation of numerical models in the earth sciences," *Science*, vol. 263, no. 5147, pp. 641–646, 1994.
- [92] E. B. Rastetter, "Validating models of ecosystem response to global change," *BioScience*, vol. 46, no. 3, pp. 190–198, 1996.
- [93] S. Piao, S. Sitch, P. Ciais et al., "Evaluation of terrestrial carbon cycle models for their response to climate variability and to CO₂ trends," *Global Change Biology*, vol. 19, no. 7, pp. 2117–2132, 2013.
- [94] Y. Huang, W. Zhang, W. Sun, and X. Zheng, "Net primary production of Chinese croplands from 1950 to 1999," *Ecological Applications*, vol. 17, no. 3, pp. 692–701, 2007.
- [95] S. D. Prince and S. N. Goward, "Global primary production: a remote sensing approach," *Journal of Biogeography*, vol. 22, no. 4–5, pp. 815–835, 1995.
- [96] Y. Q. Zhang, Q. Yu, J. Jiang, and Y. Tang, "Calibration of Terra/MODIS gross primary production over an irrigated cropland on the North China Plain and an alpine meadow on the Tibetan Plateau," *Global Change Biology*, vol. 14, no. 4, pp. 757–767, 2008.
- [97] Y. Q. Zhang, M. Xu, H. Chen, and J. Adams, "Global pattern of NPP to GPP ratio derived from MODIS data: effects of ecosystem type, geographical location and climate," *Global Ecology and Biogeography*, vol. 18, no. 3, pp. 280–290, 2009.
- [98] C. R. Schwalm, C. A. Williams, K. Schaefer et al., "A model–data intercomparison of CO₂ exchange across North America: results from the North American carbon program site synthesis," *Journal of Geophysical Research: Biogeosciences (2005–2012)*, vol. 115, no. 3, 2010.
- [99] S. Susan, "Climate change 2007—the physical science basis," in *Working Group I Contribution to the Fourth Assessment Report of the IPCC*, vol. 4, Cambridge University Press, New York, NY, USA, 2007.
- [100] W. Zhu, H. Tian, X. Xu, Y. Pan, G. Chen, and W. Lin, "Extension of the growing season due to delayed autumn over mid and high latitudes in North America during 1982–2006," *Global Ecology and Biogeography*, vol. 21, no. 2, pp. 260–271, 2012.
- [101] S. Piao, P. Ciais, P. Friedlingstein et al., "Net carbon dioxide losses of northern ecosystems in response to autumn warming," *Nature*, vol. 451, no. 7174, pp. 49–52, 2008.
- [102] M. Jung, M. Reichstein, P. Ciais et al., "Recent decline in the global land evapotranspiration trend due to limited moisture supply," *Nature*, vol. 467, no. 7318, pp. 951–954, 2010.
- [103] D. Schimel, J. Melillo, H. Tian et al., "Contribution of increasing CO₂ and climate to carbon storage by ecosystems in the United States," *Science*, vol. 287, no. 5460, pp. 2004–2006, 2000.
- [104] R. S. Nowak, D. S. Ellsworth, and S. D. Smith, "Functional responses of plants to elevated atmospheric CO₂—do photosynthetic and productivity data from FACE experiments support early predictions?" *New Phytologist*, vol. 162, no. 2, pp. 253–280, 2004.
- [105] B. Felzer, D. Kicklighter, J. Melillo, C. Wang, Q. Zhuang, and R. Prinn, "Effects of ozone on net primary production and carbon sequestration in the conterminous United States using a biogeochemistry model," *Tellus B: Chemical and Physical Meteorology*, vol. 56, no. 3, pp. 230–248, 2004.
- [106] W. Ren, H. Tian, M. Liu et al., "Effects of tropospheric ozone pollution on net primary productivity and carbon storage in terrestrial ecosystems of China," *Journal of Geophysical Research: Atmospheres (1984–2012)*, vol. 112, no. 22, 2007.
- [107] P. M. Vitousek and R. W. Howarth, "Nitrogen limitation on land and in the sea: how can it occur?" *Biogeochemistry*, vol. 13, no. 2, pp. 87–115, 1991.
- [108] J. Aber, W. McDowell, K. Nadelhoffer et al., "Nitrogen saturation in temperate forest ecosystems: hypotheses revisited," *BioScience*, vol. 48, no. 11, pp. 921–934, 1998.
- [109] G. D. Farquhar, S. von Caemmerer, and J. A. Berry, "A biochemical model of photosynthetic CO₂ assimilation in leaves of C₃ species," *Planta*, vol. 149, no. 1, pp. 78–90, 1980.
- [110] J. Berry and O. Bjorkman, "Photosynthetic response and adaptation to temperature in higher-plants," *Annual Review of Plant Physiology*, vol. 31, pp. 491–543, 1980.
- [111] C. S. Potter, S. Klooster, A. Huete et al., "Terrestrial carbon sinks in the Brazilian Amazon and Cerrado region predicted from MODIS satellite data and ecosystem modeling," *Biogeosciences Discussions*, vol. 6, no. 1, pp. 947–969, 2009.
- [112] F. Tao, M. Yokozawa, Y. Hayashi, and E. Lin, "Future climate change, the agricultural water cycle, and agricultural production in China," *Agriculture, Ecosystems and Environment*, vol. 95, no. 1, pp. 203–215, 2003.
- [113] G. Churkina, S. W. Running, and A. L. Schloss, "Comparing global models of terrestrial net primary productivity (NPP): the importance of water availability," *Global Change Biology*, vol. 5, no. 1, pp. 46–55, 1999.
- [114] X. Song, H. Tian, X. Xu et al., "Projecting terrestrial carbon sequestration of the Southeastern United States in the 21st century," *Ecosphere*, vol. 4, no. 7, article 88, 2013.
- [115] S. Sitch, C. Huntingford, N. Gedney et al., "Evaluation of the terrestrial carbon cycle, future plant geography and climate-carbon cycle feedbacks using five dynamic global vegetation models (DGVMs)," *Global Change Biology*, vol. 14, no. 9, pp. 2015–2039, 2008.
- [116] J. S. Amthor and G. W. Koch, "Biota growth factor β : simulation of terrestrial ecosystem net primary production by elevated atmospheric CO₂," in *Carbon Dioxide and Terrestrial Ecosystems*, G. W. Koch and J. Roy, Eds., 1995.
- [117] J. T. Ball, "Calculations related to gas exchange," in *Stomatal Function*, pp. 445–476, 1987.
- [118] A. W. King, W. M. Post, and S. D. Wullschlegel, "The potential response of terrestrial carbon storage to changes in climate and atmospheric CO₂," *Climatic Change*, vol. 35, no. 2, pp. 199–227, 1997.
- [119] N. J. Ostle, P. Smith, R. Fisher et al., "Integrating plant-soil interactions into global carbon cycle models," *Journal of Ecology*, vol. 97, no. 5, pp. 851–863, 2009.
- [120] D. Zheng, S. Prince, and R. Wright, "Terrestrial net primary production estimates for 0.5 grid cells from field observations—a contribution to global biogeochemical modeling," *Global Change Biology*, vol. 9, no. 1, pp. 46–64, 2003.
- [121] W. K. Lauenroth, A. A. Wade, M. A. Williamson, B. E. Ross, S. Kumar, and D. P. Cariveau, "Uncertainty in calculations of net primary production for grasslands," *Ecosystems*, vol. 9, no. 5, pp. 843–851, 2006.
- [122] M. Jung, G. Le Maire, S. Zaehle et al., "Assessing the ability of three land ecosystem models to simulate gross carbon uptake of forests from boreal to Mediterranean climate in Europe," *Biogeosciences*, vol. 4, no. 4, pp. 647–656, 2007.
- [123] C. E. Leith, "Climate response and fluctuation dissipation," *Journal of the Atmospheric Sciences*, vol. 32, no. 10, pp. 2022–2026, 1975.

- [124] F. Magnani, M. Mencuccini, M. Borghetti et al., “The human footprint in the carbon cycle of temperate and boreal forests,” *Nature*, vol. 447, no. 7146, pp. 848–850, 2007.
- [125] C. Lu and H. Tian, “Net greenhouse gas balance in response to nitrogen enrichment: perspectives from a coupled biogeochemical model,” *Global Change Biology*, vol. 19, no. 2, pp. 571–588, 2013.
- [126] W. H. Schlesinger, *Biogeochemistry: An Analysis of Global Change*, Gulf Professional Publishing, San Diego, Calif, USA, 2nd edition, 1997.
- [127] M. Zhao, F. A. Heinsch, R. R. Nemani, and S. W. Running, “Improvements of the MODIS terrestrial gross and net primary production global data set,” *Remote Sensing of the Environment*, vol. 95, no. 2, pp. 164–176, 2005.
- [128] Y. Ryu, D. Baldocchi, H. Kobayashi et al., “Integration of MODIS land and atmosphere products with a coupled-process model to estimate gross primary productivity and evapotranspiration from 1 km to global scales,” *Global Biogeochemical Cycles*, vol. 25, no. 4, p. 24, 2011.
- [129] M. Jung, M. Reischstein, and A. Bondeau, “Towards global empirical upscaling of FLUXNET eddy covariance observations: validation of a model tree ensemble approach using a biosphere model,” *Biogeosciences*, vol. 6, pp. 2001–2013, 2009.
- [130] R. Birdsey and G. Lewis, *Current and Historical Trends in use, Management and Disturbance of U.S. Forest Lands*, CRC Press, New York, NY, USA, 2003.
- [131] W. Ren, H. Tian, X. Xu et al., “Spatial and temporal patterns of CO₂ and CH₄ fluxes in China’s croplands in response to multifactor environmental changes,” *Tellus*, vol. 64, no. 2, pp. 222–240, 2011.
- [132] P. J. Crutzen, “Geology of mankind,” *Nature*, vol. 415, no. 6867, p. 23, 2002.
- [133] J. A. N. Zalasiewicz, M. Williams, W. Steffen, and P. Crutzen, “The new world of the anthropocene,” *Environmental Science and Technology*, vol. 44, no. 7, pp. 2228–2231, 2010.

Research Article

Comparison of Satellite and Ground-Based Phenology in China's Temperate Monsoon Area

Huanjiong Wang,^{1,2} Junhu Dai,¹ and Quansheng Ge¹

¹ Institute of Geographical Sciences and Natural Resources Research, Chinese Academy of Sciences, A 11 Datun Road, Chaoyang District, Beijing 100101, China

² University of Chinese Academy of Sciences, 19A Yuquan Road, Beijing 100049, China

Correspondence should be addressed to Junhu Dai; dajih@igsrr.ac.cn and Quansheng Ge; geqs@igsrr.ac.cn

Received 12 February 2014; Revised 20 March 2014; Accepted 20 March 2014; Published 24 April 2014

Academic Editor: Dong Jiang

Copyright © 2014 Huanjiong Wang et al. This is an open access article distributed under the Creative Commons Attribution License, which permits unrestricted use, distribution, and reproduction in any medium, provided the original work is properly cited.

Continuous satellite datasets are widely used in tracking vegetation responses to climate variability. Start of season (SOS), for example, can be derived using a number of methods from the time series of satellite reflectance data; however, various methods often produce different SOS measures which limit the application of satellite data in phenological studies. Therefore, we employed five methods to estimate SOS from the Advanced Very High Resolution Radiometer (AVHRR)/normalized difference vegetation index (NDVI) dataset. Subsequently, we compared the SOS with the ground-based first leaf date (FLD) of 12 deciduous broadleaved plant species at 12 sites of the Chinese Phenological Observation Network (CPON). The results show that the latitudinal patterns of five satellite-derived SOS measures are similar to each other but different from the pattern of ground phenology. For individual methods, the variability of SOS time series is significantly different from ground phenology except for HANTS, Polyfit, and Midpoint methods. The SOS calculated using the Midpoint method showed significant correlations with ground phenophases most frequently (in 47.1% of cases). Using the SOS derived from the Midpoint method, significantly earlier trends in SOS were detected in 50.7% of the natural vegetation area from 1982 to 2006.

1. Introduction

Phenology, as the study of periodic biological events in the animal and plant world [1], occupies an important position in global change science. Long-term phenological data can provide independent evidence for the effects of environmental change [2, 3]. Impacted by recent climate change [4, 5], trends toward earlier plant phenophases in spring have been observed in many places around the world [6, 7].

Such phenological shifts can influence many properties of terrestrial ecosystems [4, 9]. It is reported that plant phenology is tightly coupled with the seasonal cycles of surface carbon and energy balances in boreal forest ecosystems in western Canada [10]. Modeled spring indices (SI), first bloom date, could serve as proxy for both average spring net ecosystem exchange (NEE) drawdown date and latent-sensible heat crossover date in deciduous forests [11]. Earlier spring onset in combination with delays in the end of the

growing season has also resulted in enhanced vegetation growth in the Northern Hemisphere over the past two decades [12].

Before recent technological advances, the most conventional means to monitor phenological dynamic in plants was through manually recorded human observations at discrete intervals. Recently, researchers began to use eddy covariance towers and satellite sensors to assist in monitoring phenological change on larger spatial scales [4]. Remote sensing phenology or land surface phenology (LSP), defined as the seasonal pattern of variation in vegetated land surfaces observed from remote sensing [13], is the focus of this study. We chose a primary phenological marker—the start of season (SOS)—as the object of this study. The SOS is also called the green-up date, the onset of greenness, or the start of the growing season.

The multiple SOS method can lead to distinct estimates in the same region [14, 15]. For example, based on different

methods, the trends of advance in SOS for China's temperate region ranged from 2.25 days decade⁻¹ [16] to 7.9 days decade⁻¹ [17]. Therefore, the accuracy of SOS methods needs to be carefully evaluated according to ground phenology data. To address this problem, White et al. [18] performed a comprehensive intercomparison of ten SOS methods over broad regions of North America based on ground phenology data and cryospheric/hydrologic seasonality metrics. Schwartz and Hanes [11] further added the latent-sensible heat flux and carbon flux data into the comparison. A comparative study of satellite and ground-based phenology was also made in Switzerland [19]. These studies suggested that not all methods were closely related to ground observations. In temperate China, the accuracy of multiple SOS methods has not been assessed.

As the Institute of Geographical Sciences and Natural Resources Research (IGSNRR) at the Chinese Academy of Sciences has administered the Chinese Phenological Observation Network (CPON) and accumulated a solid database in recent years, we can thoroughly compare Phenological trends derived from remote sensing with those of ground observations and assess the accuracy of different SOS methods. In this study, we employed five methods to estimate SOS for China's temperate monsoon area using a consistently processed satellite dataset. Subsequently, we analyzed the relationships between different SOS measures and ground first leaf dates (FLD) at 12 CPON sites, evaluating which estimation methods for SOS were the best. As a result, we estimated 1982–2006 trends in SOS based on those methods that were most consistent with ground data.

2. Materials and Methods

2.1. Study Area. The temperate monsoon area, located in north and northeast China, was chosen as the study area (Figure 1). Mean annual temperature in this area ranges from -4 to 14°C , while mean annual precipitation decreases from 800 mm in the southeast to 400 mm in the northwest. Affected by the East Asian monsoon, precipitation mainly falls between June and August. The primary natural vegetation in this area, as identified from a digitized 1:1,000,000 vegetation map of China [20], includes needleleaf forests, needleleaf and broadleaf mixed forests, and broadleaf forests.

2.2. Ground and Satellite Dataset. Ground phenological data are derived from CPON, which began its observations in 1963 under the auspices of IGSNRR at the Chinese Academy of Sciences. In this study, data collected from 1982 to 2006 on twelve species of deciduous broadleaved trees and one phase (first leaf date (FLD)) at 12 CPON sites were compared (Figure 1 and Table 1). According to the uniform observation criteria and guidelines of CPON [21], the FLD is defined as the date when a plant forms its first fully unfolded leaf. A total of 85 different cases were therefore available, with one case consisting of a phenological time series at a specific site (Table 1). The FLD time series are not continuous because no observations were carried out in certain periods at each site. Because the missing observation data affects the analysis, the

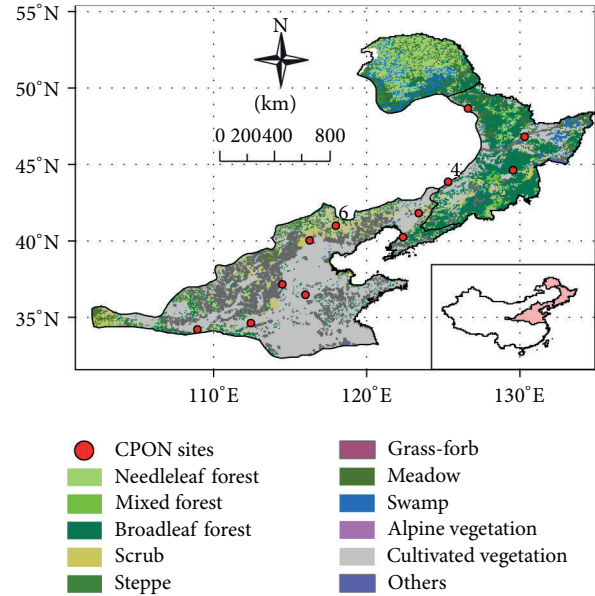


FIGURE 1: Distribution of vegetation types in China's temperate monsoon area and the twelve sites from Chinese Phenological Observation network (CPON) in this study.

missing data are estimated using a phenological model that is driven by temperature data from a nearby weather station. This gap-filling method was described in Ge et al. [8].

With respect to the satellite data, we obtained the data set produced by the Global Inventory Monitoring and Modeling Studies (GIMMS) group of the normalized difference vegetation index (NDVI) for the period 1982 to 2006 at a spatial resolution of 8 km and 15 day intervals. This dataset was observed by Advanced Very High Resolution Radiometer (AVHRR) instruments aboard the NOAA satellite series 7, 9, 11, 14, 16, and 17 and has been corrected for calibration, view geometry, volcanic aerosols, and other effects not related to vegetation change [22]. Sparsely vegetated pixels with annual mean NDVI of less than 0.1 have been excluded to reduce the impact of bare soils [23]. In addition, pixels with cultivated vegetation [20] are excluded because the phenology of cultivated vegetation is strongly impacted by human activity.

2.3. Estimation of SOS. There are several methods to extract SOS from the NDVI dataset. These methods usually consist of two steps [15]. The first step was to reconstruct continuous and daily NDVI series with the noise removed by using curve approaches, such as a polynomial function [17], piecewise logistic functions [24], a Fourier filter [25], spline functions [26, 27], or a Savitzky-Golay filter [28, 29]. In the next step, critical thresholds for SOS were determined from the reconstructed NDVI time series.

Five approaches are commonly used to determine SOS thresholds: (1) thresholds defined by the timing of the greatest relative change in multiyear averaged NDVI series, where

TABLE 1: Study species and their distribution sites with first leaf date (FLD) data. The number of sites for each species is defined in Figure 1.

No.	Species	Phase	Distribution sites	Number of sites
1	<i>Ailanthus altissima</i>	FLD	5, 7, 8, 9, 11, 12	6
2	<i>Salix babylonica</i>	FLD	3, 5, 7, 9, 10, 11, 12	7
3	<i>Robinia pseudoacacia</i>	FLD	5, 6, 7, 8, 9, 10, 11, 12	8
4	<i>Salix matsudana</i>	FLD	1, 3, 5, 7, 8, 9, 10	7
5	<i>Sophora japonica</i>	FLD	6, 9, 10, 11, 12	5
6	<i>Populus × canadensis</i>	FLD	1, 5, 6, 8, 9, 10, 11, 12	8
7	<i>Morus alba</i>	FLD	7, 8, 9, 12	4
8	<i>Amygdalus davidiana</i>	FLD	4, 5, 6, 8, 12	5
9	<i>Armeniaca vulgaris</i>	FLD	2, 3, 7, 8, 9, 10, 12	7
10	<i>Ulmus pumila</i>	FLD	1, 2, 3, 4, 5, 7, 8, 9, 10, 11, 12	11
11	<i>Amygdalus triloba</i>	FLD	1, 2, 4, 7, 8, 9, 12	7
12	<i>Syringa oblata</i>	FLD	1, 2, 4, 5, 6, 7, 8, 9, 11, 12	10

the corresponding NDVI (t) is determined as the NDVI threshold for SOS, where t is the time with the maximum relative NDVI increase [17]; it is worth noting that the SOS threshold is constant for each pixel and does not change with time; (2) maximum relative change, where the SOS is determined as the date with the maximum relative change of NDVI [30]; (3) maximum increase, where the NDVI time series is firstly transformed to its first derivate; in each year, maximum of first derivate marks the SOS [19]; (4) Midpoint, whereby the NDVI time series is first transformed to 0-1 NDVI_{ratio}; Then the SOS is defined as the day of the year when 0.5 NDVI_{ratio} is exceeded [26]; and (5) 20% of NDVI amplitude, where the SOS is defined as the date when the NDVI has increased 20% of the seasonal amplitude from the growing season minimum level [31]. These five methods (Polyfit, Logistic, HANTS, Midpoint, and Timesat) are summarized in Table 2. Specially, in the Logistic method, Zhang et al. [24] recognized that the SOS corresponds to the times at which the rate of change in curvature in the vegetation index data exhibits first local maximums. Other studies have, however, suggested that this metric may be sensitive to early spring understory growth [32], so we utilize the approach of maximum relative change instead (Table 2). All of these five methods were used to estimate SOS for each pixel in the study area over the 1982–2006 period.

2.4. Comparisons and Analyses. We firstly calculated the mean FLD from 1982 to 2006 for each CPON site as well as the mean of satellite-derived SOS measures for each pixel. Then we compared the latitudinal patterns of ground phenophases and five satellite-derived SOS measures. Second, we calculated the coefficient of variation (CV) for ground FLD time series at each site and five satellite-derived SOS measures in pixels with broadleaf forest from 1982 to 2006. Through one-way analysis of variance (ANOVA) and Tukey multiple comparison [34], we assessed the variability of satellite-derived SOS measures. Third, at each site, we calculated Pearson’s correlation coefficients between the FLD time series of each tree species as well as SOS time series averaged from

the closest 49 pixels (excepting cultivated vegetation). Last, we selected the SOS method, the most consistent with the ground phenology, and performed the regression analysis between SOS time series and year for each pixel. The SOS trend is represented by the slope of the regression model.

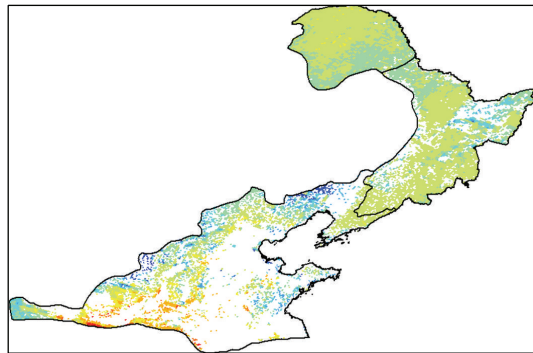
3. Results

3.1. Assessment of Spatial Patterns for Variations of SOS. At first, we studied the spatial pattern of SOS averaged over five SOS measures in the 1982 to 2006 period. The south to north progression of spring phenological events in the study area is shown to be delayed. Mean SOS is delayed from the south to the central study region and then becomes slightly earlier in the northeast region (Figure 2(a)). The SOS in the Changbai Mountains (N38°46′–47°30′, E121°08′–134°) is later than the surrounding area. With regard to the vegetation types, the SOS of the steppe occurs on 16 May, which is the latest. Grass-forb, meadow, swamp, and alpine vegetation have similar SOS patterns ranging from 2 May to 4 May. SOS of needleleaf forest, mixed forest, broadleaf forest, and scrub is the earliest (April 27–30). Individual methods often differ in SOS measures, especially in North China. Across the study area, the maximum differences among the five satellite-derived SOS measures range from 19 to 100 days with a mean of 43 days (Figure 2(b)), suggesting that different SOS methods may detect different portions of the annual vegetation development cycle.

For broadleaf forest, the latitudinal patterns of SOS derived from the five satellite measures are consistent (Figure 3). All five satellite-derived SOS measures along with latitudinal gradients correlated significantly with each other ($P < 0.05$). In general, the ordinal ranking of SOS measures is HANTS > Midpoint > Logistic > Polyfit \approx Timesat. For all of these methods, SOS is stable between 36°N and 50°N and gradually becomes earlier at lower and higher latitudes (Figure 3). This pattern obviously varies with ground phenology. The FLD of woody plants delayed linearly with latitude ($P < 0.05$, Figure 3). Because the entire 8*8 km pixels

TABLE 2: Summary of five methods in estimating SOS from satellite data. The number for each method is defined for the purpose of distinguishing the satellite-derived SOS measures from ground phenophases in Table 1.

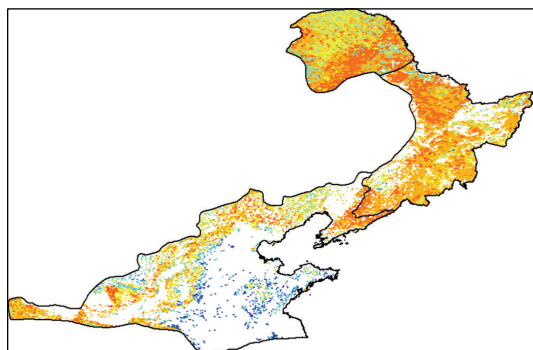
No.	Methods	Curve approaches	SOS determination approaches	Reference
13	Polyfit	Polynomial function	Threshold by the timing of greatest relative change in multi-year averaged series	[17]
14	Logistic	Piecewise logistic functions	Maximum relative change	[24]
15	HANTS	Fourier transformation	Maximum increase	[33]
16	Midpoint	Spline functions	Midpoint	[27]
17	Timesat	Savitzky-Golay filter	20% of NDVI amplitude	[28]



Mean SOS
(DOY)



(a)

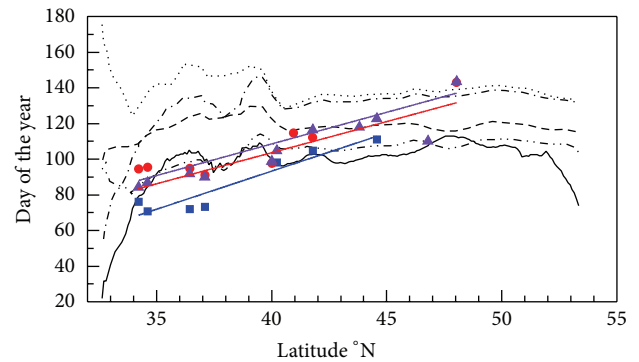


Maximum difference
(days)



(b)

FIGURE 2: (a) The start of season (SOS) averaged from the results of the five methods in the 1982–2006 period and (b) the maximum difference between the five satellite-derived SOS measurements.

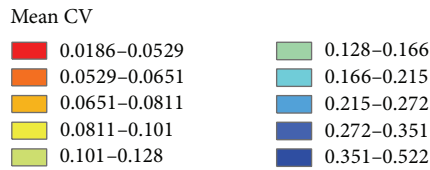
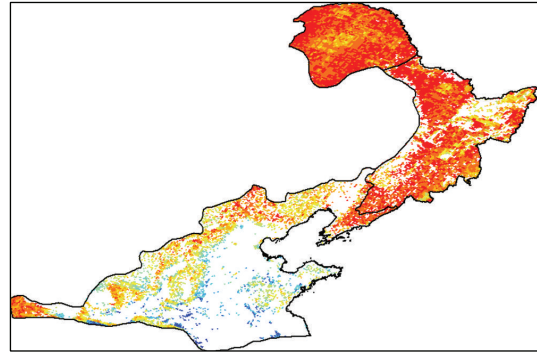


— Polyfit
 --- Logistic
 HANTS
 -.-.- Midpoint
 - - - - Timesat
 ■ *Salix babylonica*
 ● *Populus × canadensis*
 ▲ *Ulmus pumila*

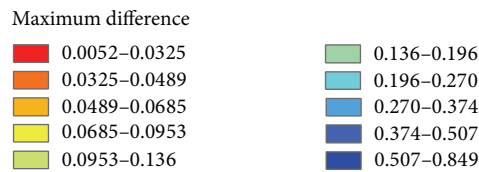
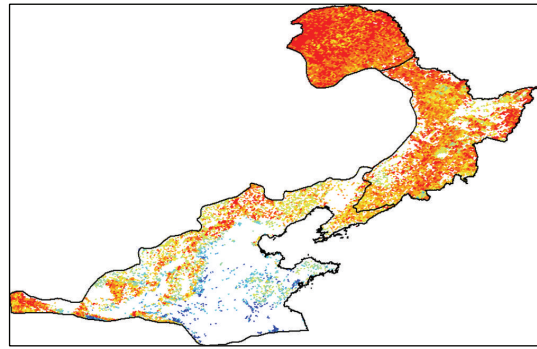
FIGURE 3: The variation of five satellite-derived SOS measures averaged from pixels of broadleaf forest and mean FLD of three broadleaf plants along with latitude. Purple, red, and blue lines are regressions lines for FLD of the three broadleaved plant species, respectively.

along the latitudinal gradient have different plant species compositions, the differences between satellite-derived SOS measures and ground phenology in spatial patterns are expectable.

3.2. Assessment of Temporal Variability of SOS. The variability of SOS obtained through the above five methods is represented by the mean CV of each method. The CV in the northern parts of the study region is relatively smaller, suggesting that the SOS in Northeast China is more stable than that in North China (Figure 4(a)). In regard to vegetation types, the CV of grass-forb reaches up to 0.124, which is the most variable (Table 3). Scrub and steppe both have a CV of 0.088. SOS of the needleleaf forest, mixed forest, broadleaf forest, meadow, swamp, and alpine vegetation is less variable, with their CV ranging from 0.060 to 0.069. Individual SOS methods often differ in CV, especially in North China (Figure 4(b)). Across the study area, the maximum difference between the CV of five satellite-derived SOS measures ranges from 0.019 to 0.523 with a mean of 0.077



(a)



(b)

FIGURE 4: (a) The coefficient of variation (CV) of satellite-derived SOS measures (1982–2006) averaged from the results of the five methods and (b) maximum difference among the CV of five satellite-derived SOS measures.

(Figure 4(b)), suggesting that different SOS methods have different interannual variability.

For the five satellite-derived SOS measures in pixels with broadleaf forest and ground FLD of 12 broadleaf plants, the mean CV (1982–2006) is significantly different (Figure 5, ANOVA, $P < 0.05$). The mean CV of Logistic and Timesat is significantly greater than that of ground phenology (Tukey multiple comparison, $P < 0.05$). The mean CV of HANTS and Polyfit is a little greater than that of ground phenology, but the differences are not statistically significant

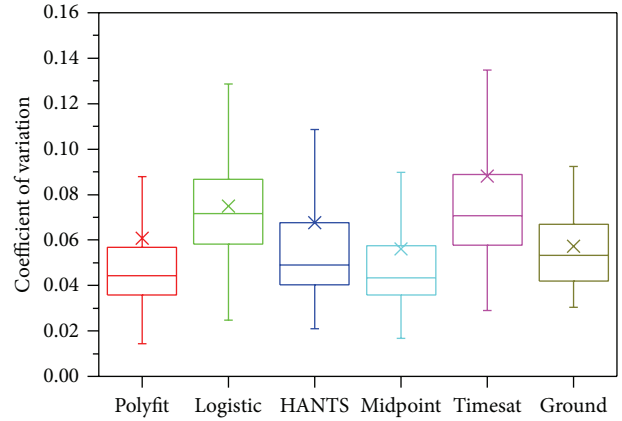


FIGURE 5: Boxplot of the coefficient of variation (CV) for five satellite-derived SOS measures in pixels with broadleaf forest and ground FLD time series at 12 sites. The bottom and top of the box are the 25th and 75th percentile, and the band near the middle of the box is the median. The x designates the mean value.

(see Figure 5). The mean CV of the Midpoint method (0.056) is closest to the CV of ground phenology (0.057).

3.3. Correlation between Satellite and Ground-Based Phenology. The correlation coefficients between time series of five SOS measures and FLD at each CPON site are shown in Figure 6 and summarized in Table 4. The correlations of the five satellite-derived measures are significant in most cases. Especially for the Midpoint method, significant Pearson's correlation coefficients between the Midpoint method and other methods are found at 8 or more sites (Table 4). HANTS method exhibits less consistency with other SOS methods except Midpoint (significant Pearson's correlation coefficients are found at only 1–3 sites).

The time series of plant phenophases observed at the same sites usually correlated significantly with each other (Figure 6). Regarding the relationship between the SOS and ground phenology, at least 14 of 85 cases showed significant correlations (Figure 6, Table 4) and 40 of 85 cases (47.1%) showed significant correlation for the Midpoint method. The numbers of significant correlations for other methods are much less than for the Midpoint method. Only 14, 14, 20, and 23 significant correlations from 85 cases could be detected for Logistic, Timesat, Polyfit, and HANTS methods, respectively. Therefore, SOS measures derived from the Midpoint method show the closest relationship with ground phenology.

In comparison with the 1982–2006 mean dates of ground phenophases, Midpoint, HANTS, Polyfit, and Logistic methods have significant R^2 ($P < 0.05$, Figure 7). Timesat had R^2 close to zero. The SOS measures based on the Midpoint method can explain 45% of interannual variability of ground phenophases at maximum although they are about 20 days later than the ground first leaf date.

3.4. SOS Trends in China's Temperate Monsoon Area. Through the above analysis, the Midpoint method was more

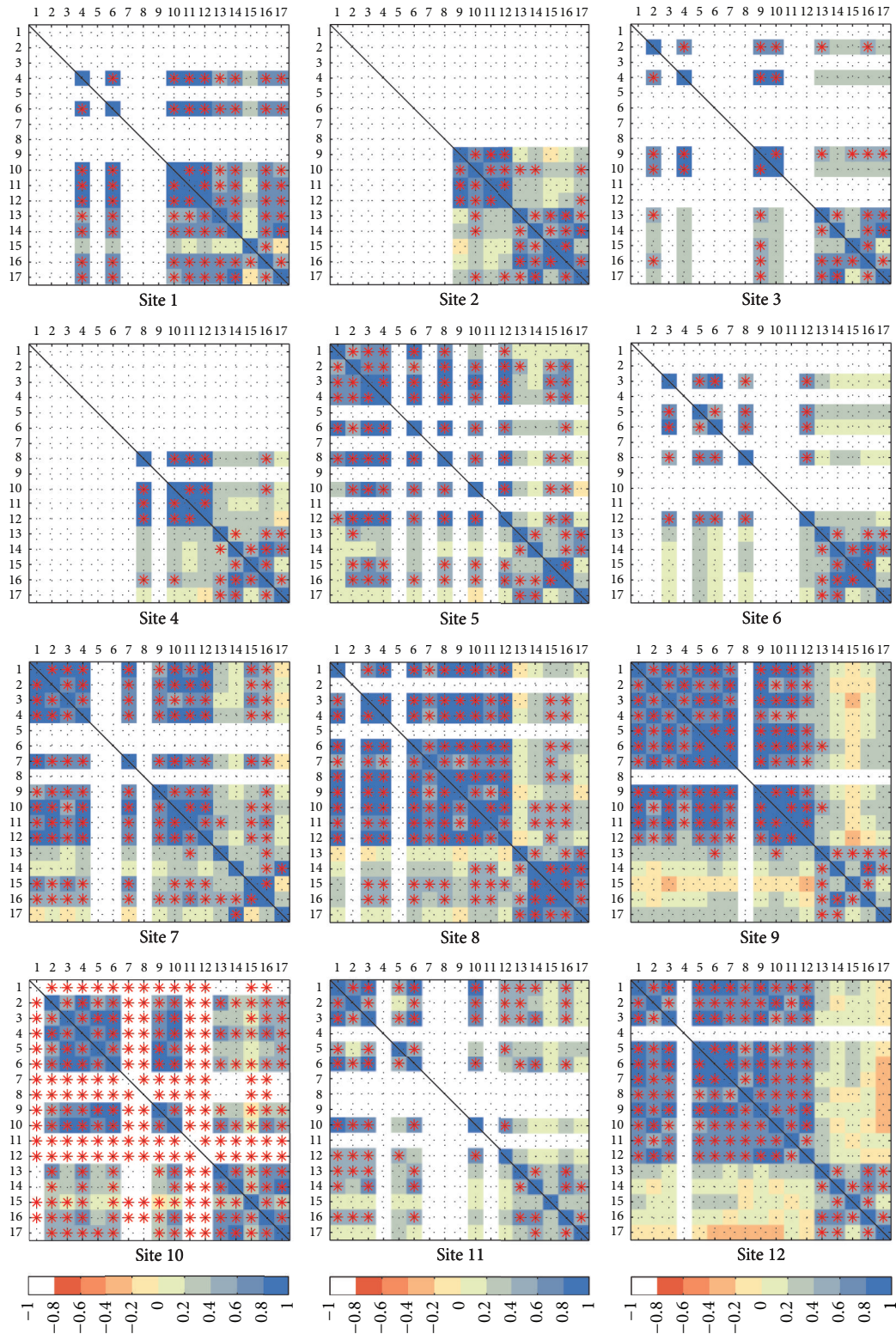


FIGURE 6: Pearson's correlation coefficients between time series of ground phenophases and five satellite-derived SOS measures at each site. The red stars mark the significant correlations ($P < 0.05$). White color indicates no ground observation data. The numbers of ground phenophases (numbers 1–12) correspond to the numbers in Table 1. The numbers of SOS methods (numbers 13–17) correspond to the numbers in Table 2.

TABLE 3: The start of season (SOS) and coefficient of variation (1982–2006) averaged from the results of the five methods for each vegetation type.

Vegetation types	Number of pixels	Mean DOY	Mean SOS	Mean CV
Needleleaf forest	2496	119	4/28	0.069
Mixed forest	263	119	4/27	0.060
Broadleaf forest	4783	119	4/28	0.069
Scrub	1474	121	4/30	0.088
Steppe	401	138	5/16	0.088
Grass-forb	793	123	5/2	0.124
Meadow	1276	125	5/4	0.064
Swamp vegetation	619	124	5/2	0.063
Alpine vegetation	3	125	5/3	0.067

TABLE 4: The proportions of significant Pearson's R ($P < 0.05$) between time series of ground phenophases and five satellite-derived SOS measures.

Methods	Ground	Polyfit	Logistic	Hants	Midpoint	Timesat
Polyfit	20/85	—	11/12	3/12	12/12	9/12
Logistic	14/85	11/12	—	5/12	12/12	12/12
HANTS	23/85	3/12	5/12	—	11/12	1/12
Midpoint	40/85	12/12	12/12	11/12	—	8/12
Timesat	14/85	9/12	12/12	1/12	8/12	—

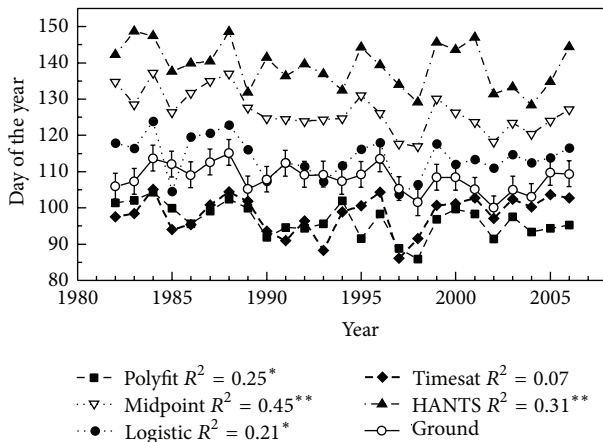


FIGURE 7: Comparison of five satellite-derived SOS measures and ground phenophases averaged over 12 sites from 1982 to 2006. Ground phenophases were first averaged to each site and then for all 12 sites across the region (note that the different sites have different sets of species). The missing ground observation data was interpolated by phenological models described by Ge et al. [8]. The error bar represents the uncertainty due to the interpolated data by models. Variances of ground phenophases explained by each SOS result (R^2) are shown. * $P < 0.05$, ** $P < 0.01$.

closely related to ground observations than other methods, so we investigated the trends of SOS using the Midpoint method. The SOS trends in China's temperate monsoon area from 1982 to 2006 are obvious (Figure 8). For all biomes

(except cultivated vegetation), more than half of the area showed significantly earlier trends ($P < 0.05$). Especially for the needleleaf forest, 57.5% of the distribution area exhibited significantly earlier SOS trends with a mean of -0.22 days year $^{-1}$. The delayed SOS trends ($P < 0.05$) were detected in only 5.3% of the natural vegetation area (Table 5). The swamp had the maximum area proportion of 13.7% towards later SOS, while the needleleaf forest had the minimum area proportion of 1.6% towards later SOS (Table 5). Overall, the linear trends of SOS over the temperate monsoon area of China were -0.13 days year $^{-1}$ ($P = 0.15$, Figure 9). In addition, the year 1998 can be shown to have been a turning point during which the SOS trends changed (Figure 9). The linear trend in SOS before 1998 was -0.39 days year $^{-1}$ ($P = 0.03$), while the SOS showed delaying trends of 0.45 days year $^{-1}$ from 1998 to 2006 ($P = 0.31$).

4. Discussion

Among the satellite-derived SOS measures using the five most common methods, SOS differed in average day of the year by more than 100 days (Figure 2) and in CV by more than 0.8 (Figure 4) in some pixels. These results were in agreement with other studies [11, 18]. The nearly almost consistent latitudinal patterns (Figure 3) and frequent significant correlations among five satellite-derived SOS measures (Figure 6) suggest, however, that the SOS methods may simply detect different portions of the annual vegetation activity [18]. It is worth

TABLE 5: The percentage of pixels with significant earlier or later SOS trends for each vegetation type.

Vegetation Types	Number of pixels	Earlier SOS		Later SOS		No trends
		%	Trends	%	Trends	%
Needleleaf forest	2496	57.5	-0.18	1.6	0.96	40.9
Mixed forest	263	48.7	-0.11	2.7	0.93	48.6
Broadleaf forest	4783	49.1	-0.18	6.1	0.93	44.8
Scrub	1474	49.2	-0.33	2.6	0.96	48.2
Steppe	401	47.1	-0.30	3.7	1.13	49.2
Grass-forb	793	44.5	-0.53	2.3	1.51	53.2
Meadow	1276	49.0	-0.20	11.2	1.04	39.8
Swamp vegetation	619	54.6	-0.15	14.1	1.11	31.3
Alpine vegetation	3	33.3	-0.62	0.0	—	66.7
Total	12108	50.7	-0.22	5.3	1.00	44.0

Unit of trends: days year⁻¹.

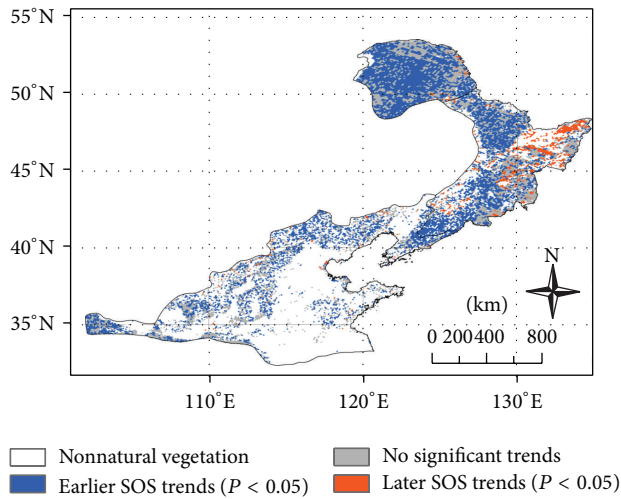


FIGURE 8: Location of trends in SOS (1982–2006) calculated using the Midpoint method. The pixels with earlier SOS trends ($P < 0.05$), no significant trends ($P > 0.05$), and later SOS trends ($P < 0.05$) occupy 50.7%, 44.0%, and 5.3% of the total natural vegetation area, respectively.

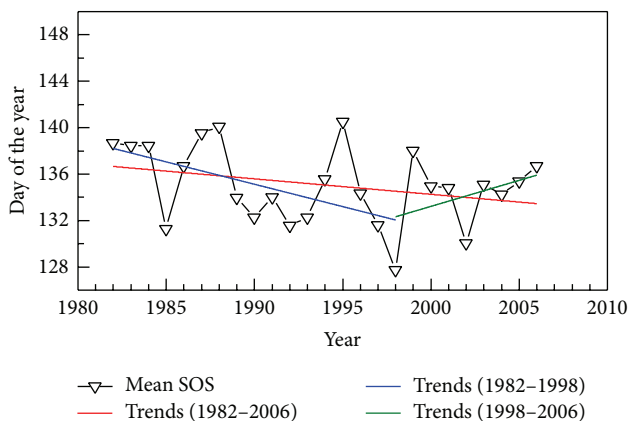


FIGURE 9: The annual SOS in China's temperate monsoon area based on the Midpoint method. Regression for the periods 1982–2006, 1982–1998, and 1998–2006 is shown.

noting that these results were based on a given satellite-based NDVI dataset with identical data sources, durations, compositing schemes, and spatial resolutions. If the data sources were different, the significant correlations between the various satellite-derived SOS measures would be less frequent [11].

Changing temperatures influence the variability of specific plant phenophases observed on the ground as well as spatially integrated SOS as seen from space [35]. Therefore, theoretically, the time series of the ground phenophases and satellite-derived SOS would highly correspond in their inter-annual variability. In this study, however, only 16.5–45.4% of the cases showed significant correlations between time series of FLD and satellite-derived SOS measures. The infrequent correlations can be attributed to the contrasting properties of satellite datasets and ground observation data. Satellite vegetation index datasets typically have coarse temporal resolutions (10–15 days) and spatial resolutions (0.25–8 km), while ground data generally consist of point values. This is the so-called point versus pixel problem [18]. Because the ground data in this study lacked detailed sampling schemes, there is a high probability that the species investigated cannot represent the overall phenological developments in an entire 8 km pixel. In addition, the different sites have different sets of species, which may be a source of variation in the comparison to satellite data. Although these uncertainties exist, the Midpoint method tracked the ground phenophases with high R^2 (45%), suggesting that the interannual variability of satellite-derived SOS measures and spring phenophases of ground observed species is comparable even in a pixel with high land cover heterogeneity.

The time series of mean FLD for the 12 species investigated in this study advanced at a rate of 0.22 days year⁻¹ from 1982 to 2006 ($P < 0.05$, Figure 7). This result agrees with earlier spring phenological trends found in previous studies. For instance, 22 woody plants flowered earlier in eastern China during 1963–2006 period [36]. The modeled first leaf date of *Fraxinus chinensis* advanced at a rate of 0.11 days year⁻¹ from 1952 to 2007 [37]. Compared with ground observations, satellite data can provide comprehensive coverage even though they can only reach back for three decades.

The trends in satellite-derived SOS measures match ground observations. We found a remarkable earlier SOS trend in 50.7% of the natural vegetation area with a mean of 0.22 days year⁻¹ (Figure 8). When the contributions of pixels with insignificant or later trends were considered, the overall trend in SOS across the study area was only 0.13 days year⁻¹ ($P = 0.15$). As indicated by a previous study [38], these changes in SOS are mostly driven by climate change, especially by temperature rise.

Our results highlight that ground observations have a certain linkage with remote sensing data, but approaches using limited numbers of plants face considerable challenges. Integrating and comparing ground phenology and satellite-derived SOS measures need more detailed field observation, such as investigating the land cover of each pixel, the proportions of individual species in a community, and the rate of phenological status (rather than just recording the date of discrete events). For example, Liang et al. [39] employed intensive field observation to address the problem of the significant spatiotemporal scale mismatch between satellite-measured land surface phenology and ground phenology. They found that the MODIS/EVI-derived SOS measure was able to predict landscape phenology of full bud burst date accurately [39]. To make detailed ground-based observations, however, requires much more labor. Recently, “near surface” remote sensing using digital photography has become commonplace [40]. Automated digital cameras, as inexpensive, easy-to-use multispectral sensors, can improve both spatial and temporal resolution with less labor [41]. Therefore, digital repeat photography has great potential for determining the relationships between the various measures of vegetation development in the future.

5. Conclusions

In this study, we assessed five SOS methods based on the ground FLD data of 12 deciduous broadleaf trees at 12 sites of CPON. The satellite-derived SOS measures varied greatly among the five methods. Furthermore, the variability of each of the five satellite-derived SOS measures was significantly different from each other. Through the correlation analysis between time series of five satellite-derived SOS measures and ground phenology, we found that the Midpoint method was most consistent with ground observations. Based on the Midpoint method, therefore, significantly earlier trends in SOS from 1982 to 2006 have been detected in 50.7% of the natural vegetation in the study area.

Conflict of Interests

The authors declare that there is no conflict of interests regarding the publication of this paper.

Acknowledgments

This research was supported by Key Project of National Natural Science Foundation of China (NSFC, no. 41030101), National Basic Research Program of China (2012CB955304),

NSFC project (no. 41171043), and “Strategic Priority Research Program-Climatic Change: Carbon Budget and Relevant Issues” of the Chinese Academy of Sciences (no. XDA05090301).

References

- [1] M. D. Schwartz, *Phenology: An Integrative Environmental Science*, Kluwer Academic Publishers, Dordrecht, The Netherlands, 2003.
- [2] G.-R. Walther, E. Post, P. Convey et al., “Ecological responses to recent climate change,” *Nature*, vol. 416, no. 6879, pp. 389–395, 2002.
- [3] C. Rosenzweig, G. Casassa, D. J. Karoly et al., “Assessment of observed changes and responses in natural and managed systems,” in *Climate Change 2007: Impacts, Adaptation and Vulnerability. Contribution of Working Group II to the Fourth Assessment Report of the Intergovernmental Panel on Climate Change*, M. L. Parry, O. F. Canziani, J. P. Palutikof, P. J. van der Linden, and C. E. Hanson, Eds., pp. 79–131, Cambridge University Press, Cambridge, UK, 2007.
- [4] E. E. Cleland, I. Chuine, A. Menzel, H. A. Mooney, and M. D. Schwartz, “Shifting plant phenology in response to global change,” *Trends in Ecology and Evolution*, vol. 22, no. 7, pp. 357–365, 2007.
- [5] R. Stckli, T. Rutishauser, I. Baker, M. A. Liniger, and A. S. Denning, “A global reanalysis of vegetation phenology,” *Journal of Geophysical Research G: Biogeosciences*, vol. 116, no. 3, 2011.
- [6] F. W. Badeck, A. Bondeau, K. Böttcher et al., “Responses of spring phenology to climate change,” *New Phytologist*, vol. 162, no. 2, pp. 295–309, 2004.
- [7] T. H. Sparks and A. Menzel, “Observed changes in seasons: an overview,” *International Journal of Climatology*, vol. 22, no. 14, pp. 1715–1725, 2002.
- [8] Q. Ge, H. Wang, and J. Dai, “Shifts in spring phenophases, frost events and frost risk for woody plants in temperate China,” *Climate Research*, vol. 57, no. 3, 2013.
- [9] J. T. Morissette, A. D. Richardson, A. K. Knapp et al., “Tracking the rhythm of the seasons in the face of global change: phenological research in the 21st century,” *Frontiers in Ecology and the Environment*, vol. 7, no. 5, pp. 253–260, 2008.
- [10] A. Barr, T. A. Black, and H. McCaughey, “Climatic and phenological controls of the carbon and energy balances of three contrasting boreal forest ecosystems in western Canada,” in *Phenology of Ecosystem Processes*, A. Noormets, Ed., pp. 3–34, Springer, New York, NY, USA, 2009.
- [11] M. D. Schwartz and J. M. Hanes, “Intercomparing multiple measures of the onset of spring in eastern North America,” *International Journal of Climatology*, vol. 30, no. 11, pp. 1614–1626, 2010.
- [12] S. Piao, P. Friedlingstein, P. Ciais, N. Viovy, and J. Demarty, “Growing season extension and its impact on terrestrial carbon cycle in the Northern Hemisphere over the past 2 decades,” *Global Biogeochemical Cycles*, vol. 21, no. 3, p. B3018, 2007.
- [13] M. D. Schwartz and B. C. Reed, “Surface phenology and satellite sensor-derived onset of greenness: an initial comparison,” *International Journal of Remote Sensing*, vol. 20, no. 17, pp. 3451–3457, 1999.
- [14] M. D. Schwartz, B. C. Reed, and M. A. White, “Assessing satellite-derived start-of-season measures in the conterminous USA,” *International Journal of Climatology*, vol. 22, no. 14, pp. 1793–1805, 2002.

- [15] N. Cong, S. Piao, A. Chen et al., "Spring vegetation green-up date in China inferred from SPOT NDVI data: a multiple model analysis," *Agricultural and Forest Meteorology*, vol. 165, pp. 104–113, 2012.
- [16] T. Ma and C. Zhou, "Climate-associated changes in spring plant phenology in China," *International Journal of Biometeorology*, vol. 56, no. 2, pp. 269–275, 2012.
- [17] S. Piao, J. Fang, L. Zhou, P. Ciais, and B. Zhu, "Variations in satellite-derived phenology in China's temperate vegetation," *Global Change Biology*, vol. 12, no. 4, pp. 672–685, 2006.
- [18] M. A. White, K. M. de Beurs, K. Didan et al., "Intercomparison, interpretation, and assessment of spring phenology in North America estimated from remote sensing for 1982–2006," *Global Change Biology*, vol. 15, no. 10, pp. 2335–2359, 2009.
- [19] S. Studer, R. Stöckli, C. Appenzeller, and P. L. Vidale, "A comparative study of satellite and ground-based phenology," *International Journal of Biometeorology*, vol. 51, no. 5, pp. 405–414, 2007.
- [20] Editorial Board of the Vegetation Map of China, *Vegetation Map of the People's Republic of China (1:1000000)*, Geological Publishing House, Beijing, China, 2007.
- [21] M. W. Wan and X. Z. Liu, *China's National Phenological observational Criterion*, Science Press, Beijing, China, 1979.
- [22] C. J. Tucker, J. E. Pinzon, M. E. Brown et al., "An extended AVHRR 8-km NDVI dataset compatible with MODIS and SPOT vegetation NDVI data," *International Journal of Remote Sensing*, vol. 26, no. 20, pp. 4485–4498, 2005.
- [23] L. Zhou, R. K. Kaufmann, Y. Tian, R. B. Myneni, and C. J. Tucker, "Relation between interannual variations in satellite measures of northern forest greenness and climate between 1982 and 1999," *Journal of Geophysical Research D: Atmospheres*, vol. 108, no. 1, p. 4004, 2003.
- [24] X. Zhang, M. A. Friedl, C. B. Schaaf et al., "Monitoring vegetation phenology using MODIS," *Remote Sensing of Environment*, vol. 84, no. 3, pp. 471–475, 2003.
- [25] G. J. Roerink, M. Menenti, and W. Verhoef, "Reconstructing cloudfree NDVI composites using Fourier analysis of time series," *International Journal of Remote Sensing*, vol. 21, no. 9, pp. 1911–1917, 2000.
- [26] M. A. White, P. E. Thornton, and S. W. Running, "A continental phenology model for monitoring vegetation responses to inter-annual climatic variability," *Global Biogeochemical Cycles*, vol. 11, no. 2, pp. 217–234, 1997.
- [27] M. A. White, R. R. Nemani, P. E. Thornton, and S. W. Running, "Satellite evidence of phenological differences between urbanized and rural areas of the eastern United States deciduous broadleaf forest," *Ecosystems*, vol. 5, no. 3, pp. 260–273, 2002.
- [28] P. Jönsson and L. Eklundh, "Seasonality extraction by function fitting to time-series of satellite sensor data," *IEEE Transactions on Geoscience and Remote Sensing*, vol. 40, no. 8, pp. 1824–1832, 2002.
- [29] J. Chen, P. Jönsson, M. Tamura, Z. Gu, B. Matsushita, and L. Eklundh, "A simple method for reconstructing a high-quality NDVI time-series data set based on the Savitzky-Golay filter," *Remote Sensing of Environment*, vol. 91, no. 3–4, pp. 332–344, 2004.
- [30] R. Lee, F. Yu, K. P. Price, J. Ellis, and P. Shi, "Evaluating vegetation phenological patterns in Inner Mongolia using NDVI time-series analysis," *International Journal of Remote Sensing*, vol. 23, no. 12, pp. 2505–2512, 2002.
- [31] W. J. D. van Leeuwen, "Monitoring the effects of forest restoration treatments on post-fire vegetation recovery with MODIS multitemporal data," *Sensors*, vol. 8, no. 3, pp. 2017–2042, 2008.
- [32] J. I. Fisher, J. F. Mustard, and M. A. Vadeboncoeur, "Green leaf phenology at Landsat resolution: scaling from the field to the satellite," *Remote Sensing of Environment*, vol. 100, no. 2, pp. 265–279, 2006.
- [33] G. J. Roerink, M. Menenti, W. Soepboer, and Z. Su, "Assessment of climate impact on vegetation dynamics by using remote sensing," *Physics and Chemistry of the Earth*, vol. 28, no. 1–3, pp. 103–109, 2003.
- [34] The R Core Team, *R: A Language and Environment for Statistical Computing*, R Foundation for Statistical Computing, Vienna, Austria, 2014.
- [35] T. Rutishauser, J. Luterbacher, F. Jeanneret, C. Pfister, and H. Wanner, "A phenology-based reconstruction of interannual changes in past spring seasons," *Journal of Geophysical Research G: Biogeosciences*, vol. 112, no. 4, p. 4016, 2007.
- [36] Q. Ge, J. Dai, J. Zheng et al., "Advances in first bloom dates and increased occurrences of yearly second blooms in eastern China since the 1960s: further phenological evidence of climate warming," *Ecological Research*, vol. 26, no. 4, pp. 713–723, 2011.
- [37] H. Wang, J. Dai, and Q. Ge, "The spatiotemporal characteristics of spring phenophase changes of *Fraxinus chinensis* in China from 1952 to 2007," *Science China Earth Sciences*, vol. 55, no. 6, pp. 991–1000, 2012.
- [38] N. Cong, T. Wang, H. Nan et al., "Changes in satellite-derived spring vegetation green-up date and its linkage to climate in China from 1982 to 2010: a multimethod analysis," *Global Change Biology*, vol. 19, no. 3, pp. 881–891, 2013.
- [39] L. Liang, M. D. Schwartz, and S. Fei, "Validating satellite phenology through intensive ground observation and landscape scaling in a mixed seasonal forest," *Remote Sensing of Environment*, vol. 115, no. 1, pp. 143–157, 2011.
- [40] A. D. Richardson, J. P. Jenkins, B. H. Braswell, D. Y. Hollinger, S. V. Ollinger, and M.-L. Smith, "Use of digital webcam images to track spring green-up in a deciduous broadleaf forest," *Oecologia*, vol. 152, no. 2, pp. 323–334, 2007.
- [41] R. Ide and H. Oguma, "Use of digital cameras for phenological observations," *Ecological Informatics*, vol. 5, no. 5, pp. 339–347, 2010.

Review Article

Integrated Monitoring and Assessment Framework of Regional Ecosystem under the Global Climate Change Background

Qiao Wang, Peng Hou, Feng Zhang, and Changzuo Wang

State Environmental Protection Key Laboratory of Satellite Remote Sensing, Satellite Environment Center, Ministry of Environmental Protection of the People's Republic of China, Beijing 100094, China

Correspondence should be addressed to Peng Hou; houpcy@163.com

Received 12 February 2014; Accepted 17 March 2014; Published 13 April 2014

Academic Editor: Dong Jiang

Copyright © 2014 Qiao Wang et al. This is an open access article distributed under the Creative Commons Attribution License, which permits unrestricted use, distribution, and reproduction in any medium, provided the original work is properly cited.

Global changes are driving ecosystem alterations, and the effects are becoming more and more obvious. Ecosystem management clarifies the fundamental supporting functions of ecosystems for human survival and sustainable development. Integrated ecosystem monitoring and assessment has become a popular topic of ecology study. However, many scientific questions need to be addressed, including what assessment contents and methods are optimal for temporal and spatial measurements. Therefore, the development of a scientific evaluation framework that includes certain core contents and indicators is very important. This paper proposes a regional integrated ecosystem assessment framework involving comprehensive monitoring. Satellite images are the main data source for different ecosystem and ecological parameters, and these need to be supplemented with the help of surveys or field observation data. A healthy ecosystem is the basis of human survival and sustainable development, and ecological service should be taken as the core of integrated ecosystem assessment. This is decided by the spatial distribution, classification, and patterns of regional ecosystems. That is to say, ecological service, together with ecosystems distribution and pattern, ecological problem indicators, and ecological stress, needs to be integrated analyzed and evaluated.

1. Introduction

Global climate change is becoming one of the main driving factors of ecosystem alterations. According to the 2013 Intergovernmental Panel on Climate Change report, the global average temperature exhibits an upward linear trend from 1880 to 2012, with a total increase of 0.85°C. From 2003 to 2012, the annual average temperature has increased by 0.78°C compared to the records from 1850 to 1900. In the past 30 years, the warming magnitude of the surface temperature in every decade is higher than that at any time since 1850 [1]. Because of intense globalization, land resource development has significantly increased in the past 30 years, especially with regard to urban development. The double impact of climate change and human activities is driving obvious ecosystem changes in some regions [2, 3]. For sustainable human development, it is very important to comprehensively measure and assess regional ecosystem statuses over time

to discover the correlation between ecosystem changes and climate and human activity intensities. It is accepted that this is an important area of study in ecology research and ecosystem management.

2. Progress in the Integrated Monitoring and Assessment of Regional Ecosystems

2.1. Ecosystem Management and Ecological Services. Ecosystem issues have increased in numbers and severity in recent decades, such as reductions in ecosystem biodiversity [4]. Scientists and managers have begun to pay more attention to the ecosystem and correlations between its different elements. Such knowledge can provide guidance on how to maintain ecosystem function and support the sustainable development of humankind. This requires the timely assessment and monitoring of ecosystems.

The Research Committee of the Plant and Animal Population of American Ecology Society played an active role in the initial development of ecosystem management. In 1932, the committee considered that American comprehensive nature security system should include natural ecosystem protection [5]. In 1950, the Commission put forward a proposal to perform natural safety investigations [6]. Subsequently, some environment policy researchers had begun to advocate developing public land management policies based on ecosystem management [7]. In the late 1980s, growing numbers of scientists and managers identified and supported the opinion that ecosystem management is an effective measure to protect ecology. The first monograph about ecosystem management appeared in 1988, titled “*Ecosystem Management for Parks and Wilderness*,” and was written by Jim Agee and Darryll Johnson based on the result of a 1987 workshop. In session, a group of managers, scientists, and planners concerned with the future of parks, wilderness areas, and other nature reserves discussed a framework for how to manage these areas most effectively, and the focus was cooperative ecosystem management. This book presented a theoretical framework that included both general goals and processes for achieving these goals [8]. Ecosystem management was summarized by Edward Grumbine in 1994 as ten themes according to papers and books published in that period [9], and ten dominant themes are, respectively, hierarchical context, ecological boundaries, ecological integrity, data collection, monitoring, adaptive management, interagency cooperation, organizational change, humans embedded in nature, and values.

After 2000, the concept of integrated ecosystem management was introduced into the field of ecology research and ecosystem management. In the fifth conference of the “Biodiversity Convention,” ecosystem approach is regarded as a strategy for the integrated management of land, water, and living resources that promotes conservation and sustainable use in an equitable way, and the application of the ecosystem approach will help to reach a balance of the three objectives of the convention: conservation, sustainable use, and the fair and equitable sharing of the benefits arising out of the utilization of genetic resources [10]. Based on this viewpoint, twelve principles of integrated ecosystem management were proposed in detail [10]. The 2010 China International Cooperation Association Annual Meeting selected ecosystem management and green development as the common theme, and the meeting focused on issues related to ecology and economy, environmental protection and green development, and promoting the development of China’s ecosystem management [11]. Some regional ecology management and ecological restoration problems, such as prevention and restoration of land degradation, began to be addressed via integrated ecosystem management [12].

Under ecosystem integrated management, more attention is paid to the ecosystem as a whole rather than dividing the problems and focusing on specific elements. Separate studies of ecosystem elements are helpful for better understanding complex ecosystem relationships and recognizing the factors that affect ecological service [4]. With the development of ecosystem management, knowledge about how ecosystems

support social development has increased, the concept of ecosystem services had been proposed, and it has become a popular topic of ecosystem management research. Ecosystem service refers to a variety of incomes received directly or indirectly from ecosystems by human beings [13]. In 1997, Daily published a groundbreaking book about ecosystem service, which he named as “*natural service*.” In it, he detailed the definition, theory, and other central knowledge about ecosystem services [14]. In the same year, Daily and Costanza’s two important publications on ecosystem service became milestones in the progress of the concept of ecosystem service. Daily outlined the main types of ecosystem services, the major threat factors for maintaining ecosystem services, and discussed how to evaluate these services [13]. Costanza initially estimated the total value of the global ecosystem at about \$30 trillion per year [15]. In 2001, the United Nations launched the Millennium Ecosystem Assessment project, another landmark of ecosystem service, which tremendously promoted the worldwide development of ecosystem service.

2.2. Classical Cases of Integrated Assessment. Lots of classical cases of integrated assessment of ecosystems have been implemented in recent periods, listed in the Table 1. The Millennium Ecosystem Assessment project uses ecosystem service, mainly including supply, regulating, supporting, and cultural services, as the core of the ecological assessment framework. It comprehensively considers the ecosystem on national, regional, and global scales and predicts its possible future statuses in different scenarios. Then, the relationship between ecosystem changes and human wellbeing was analyzed to determine how ecosystem changes were affected by human activities in the past and how the ecosystem will affect the human wellbeing in the future. This project had an important impact on the international community and many governments. The Millennium Ecosystem Assessment project also promoted the development of ecology ecosystem service, confirmed the strong correlation between ecosystems and human wellbeing, and improved the management level of the ecosystem [16–18].

On a national scale, the US has performed two national ecosystem assessments and released the reports in 2002 and 2008. The national assessment divided ecosystems into six types, including farmland, forest, grassland and shrubland, freshwater, urban, and coastal and marine. The assessment framework and core aspects were distribution and pattern, chemical and physical characteristics, biological components, substance supply, and service of ecosystem. Changes and status of national land, water, and biology resources were also analyzed, and a total of 108 key assessment indicators were examined. These reports objectively reflected the real process of ecological change in the national ecosystem [19]. In the UK, the national ecosystem was divided into mountain-moorland-heath, seminatural grasslands, enclosed farmland, forests, open freshwater waters, wetlands-floodplains, urban, coastal, marine, and so on, for a total of 8 first-class and 32 second-class ecosystems. The UK assessment framework and core contents were ecosystem service, material supply, driving force of ecosystem change, and human wellbeing.

TABLE 1: Comparative list of classical cases of integrated assessment.

Case	Scale	Ecosystem type	Framework and content
Millennium ecosystem assessment	Global	Ecosystems were divided into 13 types: Mediterranean forests, woodlands, and scrub; temperate forest steppe and woodland; temperate broadleaf and mixed forests; tropical and subtropical dry broadleaf forests; flooded grasslands and savannas; tropical and subtropical grasslands, savannas, and shrublands; tropical and subtropical coniferous forests; deserts; montane grasslands and shrublands; tropical and subtropical moist broadleaf forests; temperate coniferous forests; boreal forests; tundra.	Assessment focused on the linkages between ecosystems and human well-being and, in particular, on ecosystem services, examined the ecosystem changes affecting human wellbeing, and discovered the critical factors causing ecosystem changes, and put forward the measures managing ecosystems sustainably.
National ecosystem assessment in the US	National	Ecosystems were divided into six types: farmland, forests, grassland and shrublands, freshwater, urban, and coastal and marine.	Assessment focused on the distribution and pattern, chemical and physical characteristics, biological components, substance supply, and ecosystem service.
National ecosystem assessment in the UK	National	Ecosystems were divided into eight types: forests, coastal, marine, mountain-moorland-heath, seminatural grasslands, enclosed farmland, open freshwater waters, urban, and wetlands-floodplains.	Assessment focused on the ecosystem service, material supply, driving force of ecosystem change, and human wellbeing.
National ecosystem assessment in China	National	Ecosystems were divided into eight types: forests, shrublands, wetlands, grassland, farmland, urban, desert, glacier and bare land.	Assessment focused on the ecosystem distribution and pattern, service, quality, problems, driving factors.

Evaluations on the national terrestrial, freshwater, and marine ecological status and its changes on national and regional scales have been performed [20]. In addition, with the implementation of the Millennium Ecosystem Assessment, many European countries also carried out national assessments of the state of ecosystems, including Spain, Portugal, Poland, and other countries [21].

In contrast with the national assessments of ecosystems in developed countries, China first launched a comprehensive assessment of national ecosystems in 2000 and completed the first comprehensive assessment of the ecological status of the whole country. Now the second has been completed, and the assessment report is currently being drafted. This second assessment took full advantage of satellite remote sensing in combination with traditional field survey methods, and the national ecosystem was fully assessed at national, regional, and province scales. The evaluation framework and core content included distribution and pattern, quality, service and function, problems, and ecosystem stress. A lot of key assessment indicators were analyzed, and basic ecosystem information from satellite images has been collected in the past decade. This evaluation revealed the spatial and temporal variation of the ecosystem during this time period, and recognized the effect of protective measures and the influences of social and economic improvement. Because development is moving quickly in China, the relationship between protection and development had received more attention in some regions. Five protected regions and five development regions were selected to better understand this relationship. Compared with the first study, when distribution and ecosystem patterns were the focus, the second study examined ecological service and ecosystem distribution.

3. Key Science Issues Regarding Integrated Monitoring and Regional Ecosystem Assessment

3.1. How to Ascertain the Optimal Assessment Contents and Methods? Ecosystems consist of nonbiological environments, producers, consumers, and decomposers, meaning that they are open, pluralistic, dynamic, hierarchical, self-sustaining, complex systems. Multiple assessments that examine the atmosphere, hydrosphere and biosphere, and lithosphere are necessary to understand such systems. With the improvements of cognizing the relationship between ecosystems and human wellbeing, ecosystem services that support the sustainable development of society have become the core of integrated ecosystem assessments. Ecosystem service is one of the most popular topics of study in ecology and is receiving more attention from governments and organizations. The United Nations Millennium Ecosystem Assessment report found that 15 of 24 global ecosystem services are being degraded, resulting in significant impacts on human wellbeing [16, 17]. Many ecological problems are due to the destruction and degradation of the ecosystem [22]. However, many scientific questions need to be addressed, such as definition, classification, calculation method, and assessment indicators and criteria. However, ensuring that criteria are appropriate is very difficult because factors such as economy levels, society awareness, public diathesis, and consumption habits vary among different regions.

Notwithstanding different definitions of ecosystem service, all of them consider humankind as the beneficial main body. Ecological service classification is difficult because the ambiguities of ecosystem services and benefits result in different classifications of ecological service. Daily generalized

nine types of ecosystem services, including production of ecosystem goods, biodiversity generation and maintenance, climate and life, mitigation of floods and droughts, services supplied by soil, pollination, natural pest control services, seed dispersal, and aesthetic beauty and intellectual and spiritual stimulation [13]. Costanza thought that ecological service included 17 aspects [15]. According to the Millennium Ecosystem Assessment report, ecological services include provisioning, regulating, cultural, and supporting services [16]. Besides these issues, assessment methods lack supporting scientific research and long-term observation data. As such, region assessments often directly apply the evaluation model or model parameters or indicators from other region or research cases, which can lead to inaccurate conclusions. Unique characteristics of the ecosystem must be taken into account to arrive at regional evaluation conclusions. Therefore, it is important to optimize evaluation model parameters and indicators according to the regional nature features and assessment theme.

Due to the complex and interlaced correlations of ecosystems with other nature elements and human activities, it is difficult to quantitatively analyze the driving factors of change. At present, the contribution of different factors is recognized with the help of qualitative methods. The few cases of quantitative analysis that have been published are based on the correlation model, but this model and analysis are lacking in a principle foundation.

3.2. How to Ascertain Optimal Spatial and Temporal Scales?

Ascertaining optimal scales is a foundation of integrated ecological system assessment and directly influences assessment conclusions. It is well known that the ecosystem is an organic whole in a certain spatial area, consisting of organisms and their surroundings, and these components are connected with each other via the exchange of material and energy flow within the system [23]. An ecosystem is a very important level in ecological organization and has comprehensive characteristics of regional, landscape, and population ecology. Ecosystem structure, processes, and function are interacting and interdependent. Structure and process determine ecosystem function; inversely, function influences ecosystem structure and process. Changing scales affect the structure and process of the ecosystem, which affects the methods and conclusions of ecological research and evaluations. That is to say, differences in scale result in different assessment conclusions [24]. For example, the assessment conclusion of the ecosystem service of the Three-River Headwaters region in China was different on the regional and national scales. Because this region is the source of the Yangtze, Yellow, and Lancang Rivers, water conservation and hydrological regulation is the most important ecological service on a national level. However, on the local scale, people are nomadic and there is good pasture; therefore, supplying service is the most important factor.

Ecosystem processes can only be properly understood when the inherent heterogeneity of ecosystems and organisms reacting to this heterogeneity are recognized [25]. The inherent heterogeneity of ecosystems is decided by

the scale. The bigger the scale, the more obvious the inherent heterogeneity. For example, to assess spatial differences of the hydrological regulation abilities of deciduous and coniferous forests on a large scale, it is sufficient to examine vegetation type group differences (e.g., deciduous and coniferous forests). On a moderate scale, there is a need to further distinguish the different hydrological regulation ability resulting from different vegetation types and tree species in the same vegetation type group (e.g., cedar, mason pine). On a small scale, even tree age should be considered. On a temporal scale, heterogeneity is an important characteristic. The wider the time span, the smaller the sampling interval; the more obvious the change trend, the narrower the time span; the smaller the sampling interval, the more unobvious change trend. That is to say, for the same phenomena, it is spatial homogeneity on a large scale and spatial heterogeneity on a small scale.

4. Framework of Comprehensive Ecosystem Monitoring and Assessment

4.1. General Framework and Core Contents. For integrated ecosystem assessment, it is very important to employ a scientific and applicable framework. In general, regional integrated assessment includes comprehensive monitoring and an integrated assessment. Therefore, the general framework of integrated ecosystem monitoring and assessment is shown in Figure 1. This framework pays more attention to the single ecosystem changes and the intertransform of different ecosystems and focuses on the results of these changes, such as change of ecological services, does not take the change of individuals in the ecosystem as the emphasis. It is adaptive to the regional assessments of global, subglobal, continental, national, state or provincial spatial scales or larger drainage area.

Comprehensive monitoring is the fundamental component, and exact model and data precision determine the reliability of the assessment conclusion. Satellite imaging is a powerful tool for monitoring macroecology; it can be used to periodically scan the same regions and synchronize recording information. Thus, it can be used to assess the distributions of different ecosystems and determine the statuses of main ecological parameters, such as vegetation coverage, biomass, and leaf area index of vegetation. Of course, such data must be supplemented by survey or observation data with temporary or permanent field stations. For the sake of ascertaining model parameters, some experiences and parameter data need to be gathered from published books and papers. Because of the inseparable relationship between ecosystems and human beings, data about social, economic, meteorological, hydrological, agricultural, and land and resource exploitation also need to be collected.

Because a healthy ecosystem is the basis of human survival and sustainable development, ecological service must be at the core of integrated ecosystem assessment. Ecological service is decided by the quantity and quality of a regional ecosystem. According to this, regional ecosystem spatial distribution, classification, and pattern need to be analyzed. The same kinds of ecosystems with different spatial patterns result

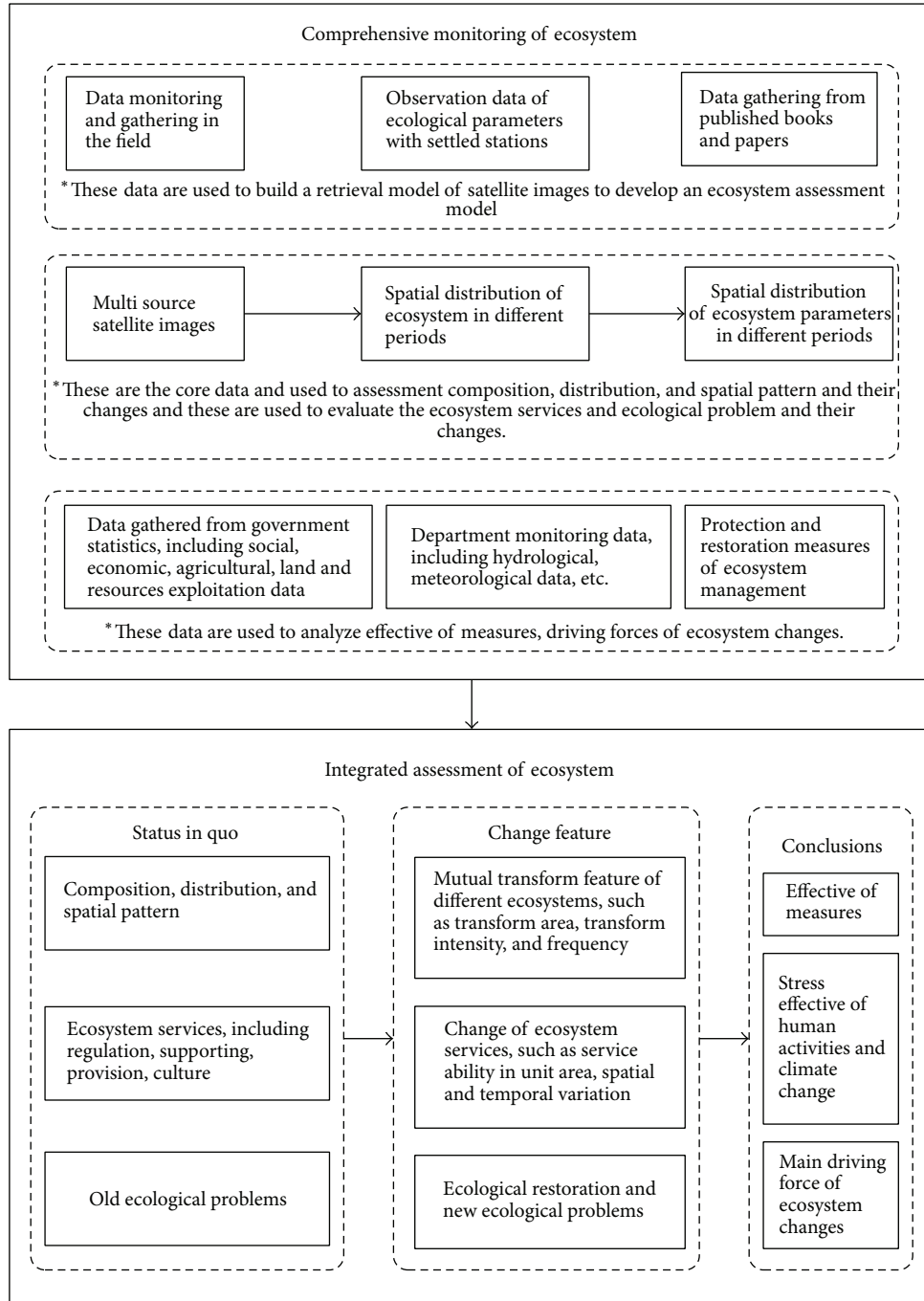


FIGURE 1: General framework of integrated ecosystem monitoring and assessment.

in different ecological processes and functions. Analyzing ecosystem features is important. Firstly, the mutual transform features of different ecosystems are recognized by calculating the transform quantity, intensity, and frequency. The core of ecological change assessment is investigating changes in ecosystem service, including regulation, provision, support, and culture. These assessments can be done with the help of indicators, such as service ability in the unit area and spatial and temporal variations. Notwithstanding, ecosystem change is a basic phenomenon of ecological succession;

the direction of ecosystem change from superior to inferior is not consistent with public requirements and is considered to be indicative of ecological degradation. The ultimate goal of integrated ecosystem assessment is to identify factors driving change, including the positive changes or restoration with the help of management measures, negative change or degradation under the stress of exploitation and construction activities, and the impacts of climate change. The recognition of the driving factors of ecological change is a precondition to design effective measures to protect and utilize nature.

4.2. Indicators of Monitoring and Assessment. According to the core contents of monitoring and assessment, indicators are divided into four groups: distribution and pattern indicators, ecological service indicators, ecological problem indicators, and stress indicators.

Distribution and pattern indicators are used to assess the spatial and temporal distributions and patterns and their changes within regional ecosystems. Ecosystem distribution can be depicted on a spatial distribution by two indicators, namely, area and percentage. (1) Ecosystem patterns can be depicted by landscape pattern indexes, such as number of patches, mean patch area, contagion, Shannon's diversity index, and patch richness. Their ecological meaning and calculation models are detailed and applied in some articles and cases [26–28]. (2) Changes in ecosystem can be shown with two indicators: transform area and percentages between different ecosystems and total transform area and the percentage of all ecosystems. As one of the statistic approaches, transition matrix are usually used, this method can distinctly list the transition area and percentage from one type to another type [28].

Ecological service indicators are mainly used to assess regulation services and their changes. Different services are evaluated by different indicators. (1) Water conservation service is the ability of the ecosystem to conserve water and can be calculated by three indicators: (1) interception ability of rainfall by vegetation canopies and conserving rainfall ability by (2) vegetation litters and (3) topsoil. Interception ability can be obtained by multiplying canopy interception rate and rainfall and forest acreage, as the key parameter, and canopy interception rate of the different forest subplot is observed in the field. Conserving rainfall ability of vegetation litters and topsoil can be estimated with water-holding ability per litter or topsoil and their total volume. This method is carried out in some cases [29]. (2) Soil conservation service is topsoil service, when the surface layer is eroded by water and wind, and it can be calculated by two indicators: the ability of soil and water conservation and the ability of sand fixation. Soil conservation is generally defined as the ability to prevent soil erosion caused by water eroding, widely evaluated with Universal Soil Loss Equation (USLE), and describes soil erosion processes, and is used by United States government agencies to measure water erosion [30–32]. Sand fixation is the ability to prevent soil erosion caused by wind eroding, can be estimated with the Revised Wind Erosion Equation (RWEQ), and has a high accuracy, taking into account the weather, soil, plants, plots, farming and irrigation factor, and so on [33, 34]. (3) Hydrological regulation service is the ability to regulate floodwater and can be calculated by two indicators: the maximum of recharge water by rivers, lakes, and reservoir and decreasing flow speed by the land surface. About hydrological regulation service of the rivers, lakes, and reservoir, maximum of recharge water is estimated by the maximum storage capacity minus the existing water volume. About that of the other ecosystems, hydrological regulation service mainly results from decreasing the flow speed by the land surface, such as grass, forest, and crop; this can be estimated with Soil Conservation Service (SCS) model [35] or Soil and Water Assessment Tool (SWAT)

model [36]. (4) Carbon dioxide gas regulation service is the ability of abstracting, fixating, and releasing carbon, and it can be calculated by quantifying carbon fixation levels. In ecosystem, fixating carbon mainly resulted from three parts: aboveground biomass, belowground biomass, and soil. Carbon fixed by aboveground biomass can be estimated with satellite images [37–39]. According to the aboveground biomass and root-top ratio, belowground biomass and its ability can be calculated. Soil carbon is mainly based on the average soil depth, average bulk density, and average carbon density [40]. In a larger region, soil carbon can estimated from vegetation type, soil type, and other key factors with the help of remote sensing [41].

Ecological problem indicators are mainly used to assess ecosystem degradation intensity and area. (1) Forest degradation can be calculated by three indicators: change of predominant species, change of species construction, and change of biomass. (2) Grass degradation can also be calculated by three indicators: change of predominant species, change of species construction, and change of vegetation coverage. (3) Wetland degradation can be calculated by five indicators: change of indication species, change of species construction, changes in water volume and quality, humidity of the surface layer, and change of area. All these indicators, most of them need to be measured in the field. However, vegetation coverage is usually retrieved from Normal Difference Vegetation Index (NDVI) data, and humidity of the surface layer can be obtained from the radar data scatter features [42].

Stress indicators are mainly used to assess pressure on ecosystems due to natural conditions and human activities, and this information is used to identify reasons underlying ecosystem changes. They can be divided into two groups: nature stress and human activity stress. (1) Nature stress can be analyzed by climate change, and the main indicators are temperature, precipitation, net radiation from the sun, and climate change driving ecosystem change usually analyzed with the statistical correlation and Empirical Orthogonal Functions (EOF) methods [3, 43, 44]. (2) Changes in human activity intensity and distribution. The main indicators of human activity are economic development intensity and impermeable layer expansion. According to the analysis cell, change of centroid location is used to find the relationship between change of economic product population and ecosystem change [45]. Expansion of land exploitation, including impermeable layer expansion and mine resources exploitation, resulting into the change of ecosystem can be analyzed with transition matrix method.

5. Conclusions

Global change, including climate warming and water resource shortages, is driving ecosystem changes, and the effects are becoming more obvious. To better protect and manage ecosystems, the concept of ecosystem management and ecosystem service was proposed to ensure human survival and sustainable development. Integrated ecosystem monitoring and assessment has become a focus of ecology that demands increasing international attention. Many

researchers and governments actively carry out ecosystem assessment cases on different scales. Determining the scientific and rational evaluation framework is the key step, which influences the precision and reliability of conclusions from ecosystem studies. The framework includes assessment scope, contents, indicators, and technical methods.

A regional integrated ecosystem assessment framework is proposed based on the literature and study practices. Regional integrated assessment can be carried out with comprehensive monitoring and integrated assessment. Comprehensive monitoring is fundamental. Satellite images are used as the main data source, and these images are supplemented by surveys or field data from temporary or permanent stations. Other approaches, including collecting statistical data and gathering data from documents, can further supplement satellite imagery and field data. With integrated assessment, ecosystem status, change, and its driving factors are the main contents, and ecological services are at the core. Ecosystem spatial distribution, classification, and their regional patterns need to be analyzed to make informed decisions with regard to ecosystem services. According to the core monitoring and assessment contents, indicators can be divided into four groups: distribution and pattern indicators, ecological service indicators, ecological problem indicators, and stress indicators in turns.

Conflict of Interests

The authors declare that there is no conflict of interests regarding the publication of this paper.

Acknowledgments

This paper benefitted from the assessment framework of the “National ecological survey and assessment of environmental change from 2000 to 2010.” The authors express their heartfelt thanks to the group of scientists, managers, and colleagues involved in the project, especially Zhiyun Ouyang and Hua Zheng, and research team members of Professor Ouyang at the Research Center for Eco-Environmental Sciences, Chinese Academy of Sciences.

References

- [1] Intergovernmental Panel on Climate Change, *Climate Change 2013: The Physical Science Basis*, 2013, <http://www.climate-change2013.org>.
- [2] B. H. Braswell, D. S. Schimel, E. Linder, and B. Moore III, “The response of global terrestrial ecosystems to interannual temperature variability,” *Science*, vol. 278, no. 5339, pp. 870–872, 1997.
- [3] P. Hou, Q. Wang, G. Z. Cao, C. Z. Wang, Z. M. Zhan, and B. F. Yang, “Sensitivity analyses of different vegetations responding to climate change in inland river basin of China,” *Journal of Geographical Sciences*, vol. 22, pp. 387–406, 2012.
- [4] E. Maltby, M. Holdgate, M. Acreman, and A. Weir, *Ecosystem Management: Question for Science and Society*, Royal Holloway Institute for Environmental Research, London, UK, 1999.
- [5] V. E. Shelford, “Ecological society of America: a nature sanctuary plan unanimously adopted by the society, December 28, 1932,” *Ecology*, vol. 14, pp. 240–245, 1933.
- [6] S. C. Kendeigh, H. I. Baldwin, V. H. Calahane et al., “Nature sanctuaries in the United States and Canada: a preliminary inventory,” *The Living Wilderness*, vol. 15, no. 35, pp. 1–45, 1951.
- [7] L. Caldwell, “The ecosystem as a criterion for public land policy,” *Natural Resources Journal*, vol. 10, no. 2, pp. 203–221, 1970.
- [8] J. K. Agee and D. R. Johnson, *Ecosystem Management for Parks and Wilderness*, University of Washington Press, 1988.
- [9] R. E. Grumbine, “What is ecosystem management?” *Conservation Biology*, vol. 8, no. 1, pp. 27–38, 1994.
- [10] The Secretariat of the Convention on Biological Diversity, *Decisions Adopted by the Conference of the Parties to the Convention on Biological Diversity at Its Fifth Meeting: Ecosystem Approach*, 2000.
- [11] China Council for International Cooperation on Environment and Development, “Annual policy report 2010: ecosystem management and green development,” Annual Report, China Environment Science Press, 2011.
- [12] Z. H. Jiang, *Proceedings of the International Workshop: Integrated Ecosystem Management*, China Forestry Publishing House, 2006.
- [13] G. C. Daily, S. Alexander, P. R. Ehrlich et al., “Ecosystem services: benefits supplied to human societies by natural ecosystems,” *Issues in Ecology*, vol. 2, pp. 1–18, 1997.
- [14] G. C. Daily, *Nature's Services: Societal Dependence on Natural ecosystems*, Island Press, 1997.
- [15] R. Costanza, R. D'Arge, R. De Groot et al., “The value of the world's ecosystem services and natural capital,” *Nature*, vol. 387, no. 6630, pp. 253–260, 1997.
- [16] Millennium Ecosystem Assessment, *Ecosystems and Human Well-Being: A Framework for Assessment*, Island Press, 2003.
- [17] Millennium Ecosystem Assessment, *Ecosystems and Human Well-Being: Synthesis*, Island Press, 2005.
- [18] S. D. Zhao and Y. M. Zhang, “Ecosystems and human well-being: the achievements, contributions and prospects of the Millennium Ecosystem Assessment,” *Advances in Earth Science*, vol. 21, no. 9, pp. 896–902, 2006.
- [19] H. The John Heinz III center for science, economics, and the environment, *The State of the National's Ecosystems 2008: measuring the lands, waters and living resources of the United States*, Island Press, 2008.
- [20] U. K. National Ecosystem Assessment, *The UK National Ecosystem Assessment: Synthesis of the Key Findings*, UNEP-WCMC, Cambridge, UK, 2011, <http://uknea.unep-wcmc.org>.
- [21] P. Hou, “Improving the China periodical comprehensive assessment mechanism of ecosystem condition based on Chinese and foreign experience,” *Environment Protect*, vol. 41, no. 23, pp. 71–73, 2013.
- [22] B. J. Fu, G. Y. Zhou, Y. F. Bai et al., “The main terrestrial ecosystem service and ecological security in China,” *Advance in Earth Science*, vol. 24, no. 6, pp. 571–576, 2009.
- [23] G. I. Agren and F. O. Andersson, *Terrestrial Ecosystem Ecology: Principles and Application*, Cambridge University Press, Cambridge, UK, 2012.
- [24] J. A. Wiens, “Spatial scaling in ecology,” *Functional Ecology*, vol. 3, no. 4, pp. 385–397, 1989.
- [25] L. Fahrig, *Theoretical Population Biology: Relative Importance of Spatial and Temporal Scales in a Patchy Environment*, Academic Press, 1992.

- [26] M. G. Turner, R. V. O'Neill, R. H. Gardner, and B. T. Milne, "Effects of changing spatial scale on the analysis of landscape pattern," *Landscape Ecology*, vol. 3, no. 3-4, pp. 153-162, 1989.
- [27] J. Wu, *Landscape Ecology—Pattern, Process, Scale and Hierarchy*, China Higher Education Press, 2nd edition, 2007.
- [28] P. Hou, C. Z. Wang, W. G. Jiang, and Y. W. Zhao, "Ecological effective of land-use and land-cover change in watershed scope," *Geographical Research*, vol. 30, no. 11, pp. 2092-2098, 2011.
- [29] Z. Biao, L. Wenhua, X. Gao, and X. Yu, "Water conservation of forest ecosystem in Beijing and its value," *Ecological Economics*, vol. 69, no. 7, pp. 1416-1426, 2010.
- [30] K. G. Renard, G. R. Foster, G. A. Weesies, D. K. McCool, and D. C. Yoder, "Predicting soil erosion by water: a guide to conservation planning with the revised universal soil loss equation (RUSLE)," in *Agriculture Handbook*, U.S. Department of Agriculture, 1997.
- [31] W. H. Wischmeier and D. D. Smith, "A universal soil-loss equation to guide conservation farm planning," *Transactions of 7th International Congress of Soil Science*, vol. 1, pp. 418-425, 1960.
- [32] N. Hudson, *Field Measurement of Soil Erosion and Runoff*, Food and Agriculture Organization of the United Nations, 1993.
- [33] D. W. Fryrear, A. Saleh, J. D. Bilbro, H. M. Schomberg, J. E. Stout, and T. M. Zobeck, "Revised wind erosion equation (RWEQ)," Technical Bulletin, Wind Erosion and Water Conservation Research University and the USDA-ARS, Southern Plains Area Cropping Systems Research Laboratory, 1998.
- [34] D. W. Fryrear, P. L. Sutherland, G. Davis, G. Hardess, and M. Dollar, "Wind erosion estimates with RWEQ and WEQ," in *Proceedings of the 10th International Soil Conservation Organization*, Sustaining the Global Farm, Purdue University and the USDA-ARS National Soil Erosion Research Laboratory, May 1999.
- [35] P. Hou, W. G. Jiang, Z. L. Chen, and A. M. Luo, "Hydrological recharge effect of precipitation on Dongting Lake Wetland," *Geographical Research*, vol. 28, no. 2, pp. 371-378, 2009.
- [36] Y. Zhang, J. Xia, Q. Shao, and X. Zhai, "Water quantity and quality simulation by improved SWAT in highly regulated Huai River Basin of China," *Stochastic Environmental Research and Risk Assessment*, vol. 27, no. 1, pp. 11-27, 2013.
- [37] J. Estornell, L. A. Ruiz, B. Velázquez-Martí, and A. Fernández-Sarría, "Estimation of shrub biomass by airborne LiDAR data in small forest stands," *Forest Ecology and Management*, vol. 262, no. 9, pp. 1697-1703, 2011.
- [38] R. Nelson, W. Krabill, and J. Tonelli, "Estimating forest biomass and volume using airborne laser data," *Remote Sensing of Environment*, vol. 24, no. 2, pp. 247-267, 1988.
- [39] Y. P. Yang, G. Z. Cao, P. Hou, W. G. Jiang, Y. H. Chen, and J. Li, "Monitoring and evaluation for climate regulation service of urban wetlands with remote sensing," *Geographical Research*, vol. 32, no. 1, pp. 73-80, 2013.
- [40] E. Gorham, "Northern peatlands: role in the carbon cycle and probable responses to climatic warming," *Ecological Applications*, vol. 1, no. 2, pp. 182-195, 1991.
- [41] S. Wang, H. Tian, J. Liu, and S. Pan, "Pattern and change of soil organic carbon storage in China: 1960s-1980s," *Tellus B: Chemical and Physical Meteorology*, vol. 55, no. 2, pp. 416-427, 2003.
- [42] W. X. Liu, X. L. Liu, J. Wang, and W. H. Zeng, "Remote sensing retrieval of soil moisture using ENVISAT-ASAR and MODIS images in vegetated areas of human," *Agricultural Research in the Arid Areas*, vol. 26, no. 3, pp. 39-43, 2008.
- [43] W. Jiang, P. Hou, X. Zhu, G. Cao, X. Liu, and R. Cao, "Analysis of vegetation response to rainfall with satellite images in Dongting Lake," *Journal of Geographical Sciences*, vol. 21, no. 1, pp. 135-149, 2011.
- [44] P. Hou, W. M. Shen, Q. Wang, W. G. Jang, Y. H. Chen, and J. Li, "Quantitative analysis of driving factors for wetland degradation based on hydrology balance," *Acta Ecologica Sinica*, vol. 34, no. 3, pp. 660-666, 2014.
- [45] X. Lei, B. Yang, W. G. Jiang, Y. P. Yang, C. Kuenzer, and Q. Chen, "Vegetation pattern changes and their influencing factors in the East Dongting Lake Wetland," *Geographical Research*, vol. 31, no. 3, pp. 461-470, 2012.

Research Article

Monitoring Grassland Tourist Season of Inner Mongolia, China Using Remote Sensing Data

Quansheng Ge,¹ Xi Yang,² Zhi Qiao,³ Haolong Liu,¹ and Jun Liu^{1,2,4}

¹ Institute of Geographic Sciences and Natural Resources Research, Chinese Academy of Sciences, All Datun Road, Chaoyang District, Beijing 100101, China

² College of Geography and Tourism, Chongqing Normal University, No. 12 Tianchen Road, Shapingba District, Chongqing 400047, China

³ State Key Laboratory of Water Environment Simulation, School of Environment, Beijing Normal University, Xijiekouwai Street, Beijing 100875, China

⁴ Tourism School, Sichuan University, Chengdu 610064, China

Correspondence should be addressed to Jun Liu; liujun_ligsnr@126.com

Received 12 February 2014; Accepted 24 March 2014; Published 10 April 2014

Academic Editor: Dong Jiang

Copyright © 2014 Quansheng Ge et al. This is an open access article distributed under the Creative Commons Attribution License, which permits unrestricted use, distribution, and reproduction in any medium, provided the original work is properly cited.

Phenology-driven events, such as spring wildflower displays or fall tree colour, are generally appreciated by tourists for centuries around the world. Monitoring when tourist seasons occur using satellite data has been an area of growing research interest in recent decades. In this paper, a valid methodology for detecting the grassland tourist season using remote sensing data was presented. On average, the beginning, the best, and the end of grassland tourist season of Inner Mongolia, China, occur in late June (± 30 days), early July (± 30 days), and late July (± 50 days), respectively. In south region, the grassland tourist season appeared relatively late. The length of the grassland tourist season is about 90 days with strong spatial trend. South areas exhibit longer tourist season.

1. Introduction

Phenology-driven events, such as spring wildflower displays or fall tree colour, make some destinations become particularly attractive [1]. During the spring, cherry blossom viewing kicks off the busy tourist season around the world. In Japan, holding flower-viewing parties is a centuries-old practice under blooming cherry trees [2]. The National Cherry Blossom Festival 2013 in Washington DC attracted about 100,000 tourists from around the world. In China, the beautiful and elegant peach blossoms have inspired generations of spectators. In Europe, Netherland's tulips prove huge draw for tourists.

Monitoring the timing of plant life cycle events is an area of science with many practical applications for tourism sector, because the timings determine when tourist season begins and ends. Phenology then can serve as a predictor to inform the public on when certain events take place. Based on phenological information, tourism sector will be better able

to prepare themselves for peak and/or off-season. Tourists would adjust their vacation to nature reserves to the timing of certain life cycle events. As plant phenophases are sensitive to climate change, variations in the timing of vegetation phases are key components to identify and evaluate the effects of climatic change on tourism industry [3].

The timings of plant life cycle events have been detected by ground observations for centuries [4]. However, field phenology observations are difficult to upscale to large spatial scale and labor intensive. Satellite-based measure could provide the potential to extrapolate from species-level observations to regional variations of phenological patterns.

Grasslands play a vital role in tourism sector because grasslands provide recreation and tourism services include horse riding, safari tours, and hunting. At the country level, China takes the third place after Australia and Russia in grassland area. Nearly 42% of China is natural grassland, comprised of a total of 393 million hectares.

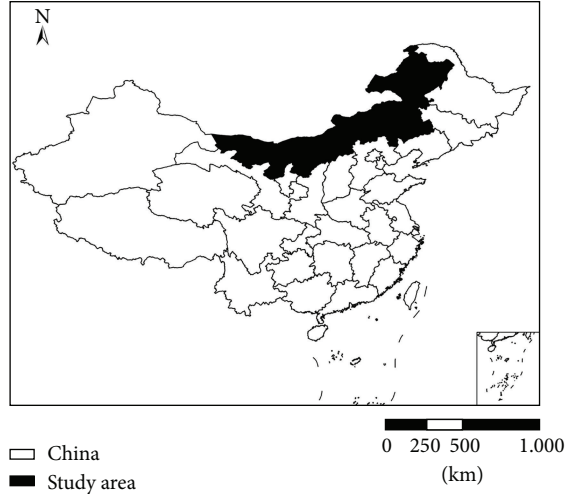


FIGURE 1: The location of study area.

In this paper, we present a satellite-based method to monitor the start and end of the tourist season for grassland in North China. This work can be of crucial importance to better understand how grassland responds to climatic change and, consequently, to design effective adaptation and management policy for tourism sector.

2. Study Area

The Inner Mongolia Autonomous Region is situated between longitude $97^{\circ}12'E-126^{\circ}04'E$ and latitude $37^{\circ}24'N-53^{\circ}23'N$, with an area of 1.183 million km^2 taking up 1/8 of that of China (Figure 1). Situated on the climatic boundary between the humid monsoon region and the inland arid area, Inner Mongolia is a region of extreme contrasts in climate. The annual mean temperature is about $0-3^{\circ}C$. July is on average the warmest month, with an average temperature of $15-25^{\circ}C$. The average sunshine totals throughout the year are more than 2700 hours. Average annual precipitation exhibits a sharp gradient, from 600 mm in the east to <100 mm in the west [5].

Inner Mongolia is one of the most representative grassland regions of China [6]. The area of grassland accounts for 27 percent of the nation's total. With the most representative grassland in China, the region is an appealing destination for grassland tourism in China as well as a sign of ecological tourism. Grassland related tourism has become a vital sector of Inner Mongolia. The number of tourists increased 16.8 percent each year and revenues increased 28.6 percent from 2006 to 2010. By 2015, tourism sector is predicted to generate a direct contribution to GDP of \$25 billion or 8 percent of GDP.

3. Material and Methodology

3.1. Material. MOD13 A2 8-day NDVI and NDVI Quality Assurance products from Terra's Moderate Resolution Imaging Spectroradiometer (MODIS) were obtained from the US

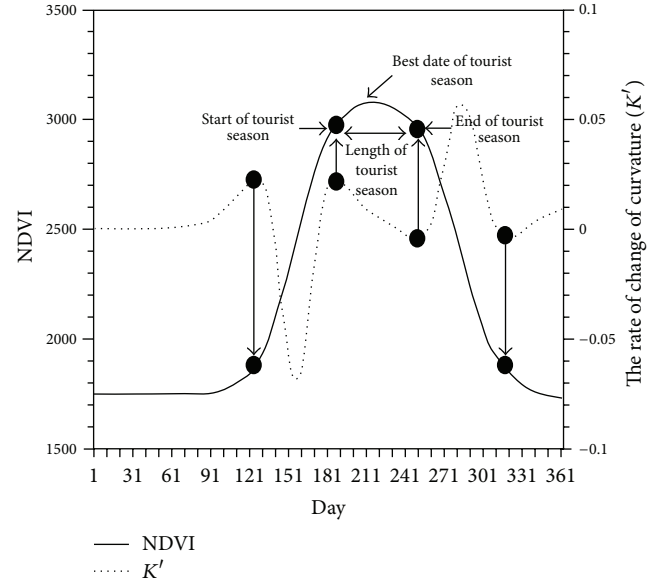


FIGURE 2: The reconstructed NDVI time series and the dates of tourist season.

Geological Survey consisting of a total of 46 images with a spatial resolution of 1 km. The dataset includes 1 year (January 1, 2008, to December 31, 2008), and it is well suited to detect grassland tourist season at the scale of the landscape.

The NDVI is calculated by

$$NDVI = \frac{(NIR - VIS)}{(NIR + VIS)}, \quad (1)$$

where VIS and NIR are the spectral reflectance measurements acquired in the visible (red) and near-infrared regions, respectively.

3.2. Methodology. Grassland tourist seasons define the period of time when grassland conditions are suitable for tourism activities. Zhang et al. [7] defined maturity as the date when vegetation green leaf area reaches a maximum. The senescence is decided to occur when green leaf area begins to rapidly decrease. Figure 2 illustrates how the onset, best date, the end, and thus length of the tourist season are determined based on the satellite derived NDVI. The bottom axis represents time (in days) and the side axis represents reflectance values.

Function (2) is used to model the annual change in satellite derived vegetation index data for a single growth or senescence cycle:

$$y(t) = \frac{c}{1 + e^{a+bt}} + d, \quad (2)$$

where $y(t)$ is the NDVI value at time t , t is time in days, a and b are fitting parameters, d is the initial background NDVI value, and $c + d$ is the maximum NDVI value. Least square fitting was used to determine the fitting parameters a and b .

The onset of transition dates corresponds to the times at which the second derivative gets from positive to negative

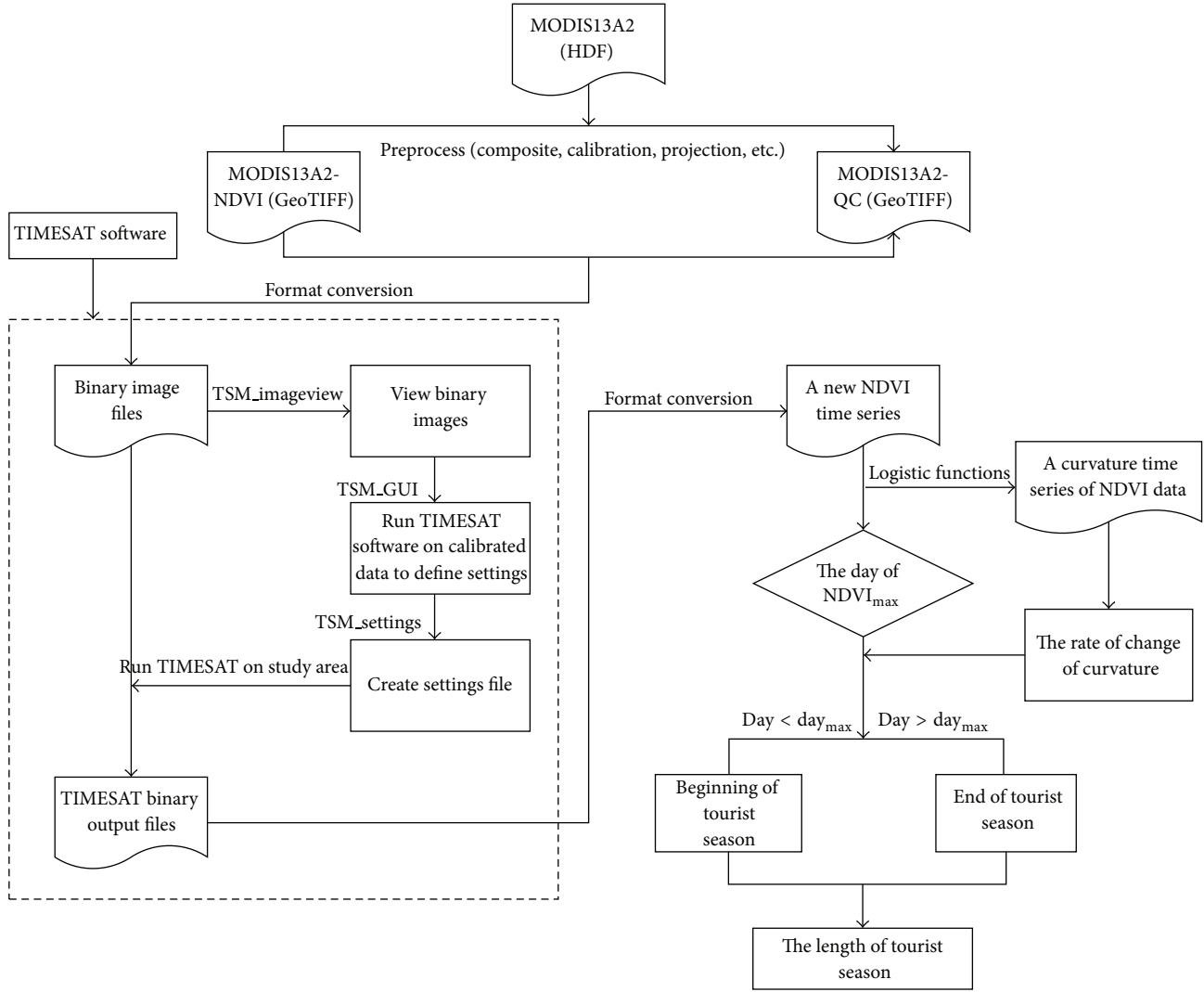


FIGURE 3: Flowchart of grassland tourist season monitoring process.

values. The curvature K for (2) at time t can be calculated by [7]

$$K = \frac{d_a}{d_s} = -\frac{b^2 cz(1-z)(1+z)^3}{[(1+z)^4 + (bcz)^2]^{3/2}}, \quad (3)$$

where $z = e^{a+bt}$, a is the angle of the unit tangent vector at time t along a differentiable curve, and s is the unit length of the curve. The rate of the change in the curvature of the fitted logistic models is used to determine the onset of transition dates (Figure 2). The following is used to compute the rate of change of curvature:

$$K' = b^3 cz \left\{ \frac{3z(1-z)(1+z)^3 [2(1+z)^3 + b^2 c^2 z]}{[(1+z)^4 + (bcz)^2]^{5/2}} - \frac{(1+z)^2(1+2z-5z^2)}{[(1+z)^4 + (bcz)^2]^{3/2}} \right\}. \quad (4)$$

Figure 3 is the detailed flowchart of grassland tourist season monitoring process. To eliminate the abnormal value, that is, cloud and snow, a series of preprocessing steps were performed to smooth satellite data products using TIMESAT software. Then, the VI data could be fit to logistic functions described by (2). For the corrected dataset, we identified the tourist seasons for grassland by Arc Macro Language (AML) programming using the above methods.

4. Results

4.1. The Onset of Grassland Tourist Season. Remote sensing measures of tourist season showed a high degree of spatial variability over the study period. In most regions, grassland tourist season of Inner Mongolia begins in late June (± 30 days). The earliest date was May 30th. The latest date was August Third. Note that north areas exhibit earlier onset of tourist season (Figure 4).

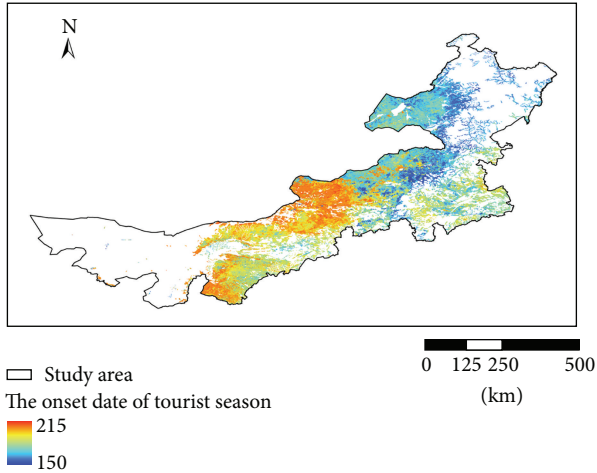


FIGURE 4: The onset of grassland tourist season.

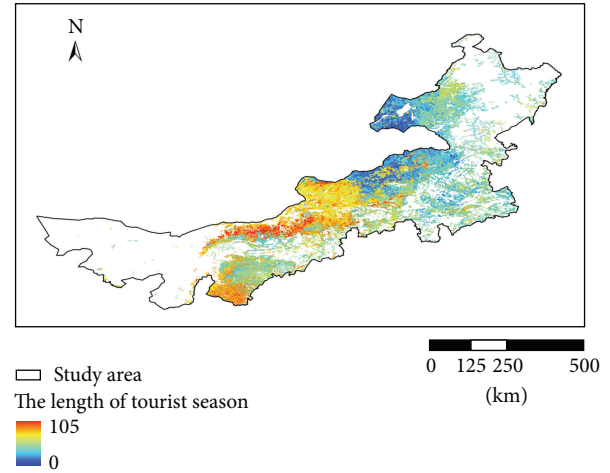


FIGURE 7: The length of grassland tourist season.

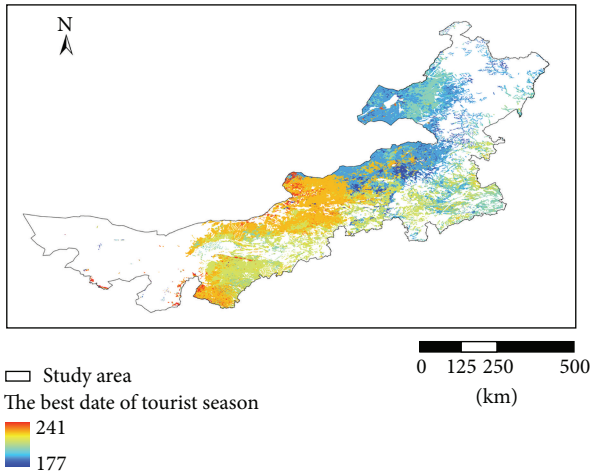


FIGURE 5: The best date of grassland tourist season.

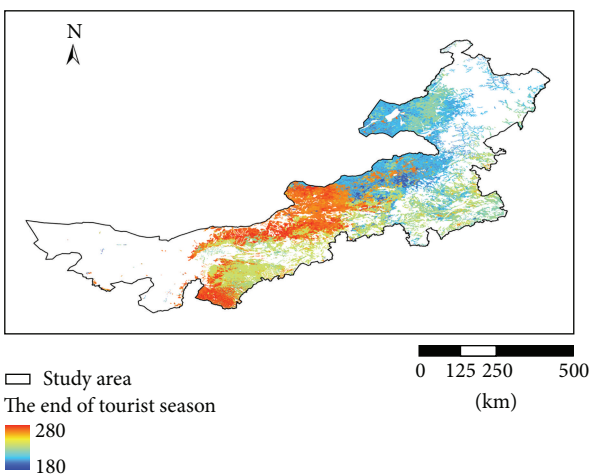


FIGURE 6: The end of grassland tourist season.

4.2. The Best Date of Grassland Tourist Season. The average best date of grassland tourist season in Inner Mongolia started approximately in early July (± 30 days), though the initiation period ranged over more than a 30-day period, beginning in southerly latitudes in late August and advancing northward. The earliest date was June 26th. The latest date was August 29th. Pronounced spatial variability in the timing of best tourist season is particularly evident (Figure 5).

4.3. The End of Grassland Tourist Season. The average end of grassland tourist season started in late July (± 50 days). The earliest date was June 30th. The latest date was October 7th. In south region, the end of grassland tourist season appeared relatively late (Figure 6).

4.4. The Length of Grassland Tourist Season. Satellite-based measurements of the length of grassland tourist season for Inner Mongolia spanned a period of approximately 3 months from late June to late September with strong spatial trend. South areas exhibit longer tourist season (Figure 7).

5. Conclusion and Discussion

A major focus of this research is to present a valid methodology for detecting the grassland tourist season using remote sensing data. On average, the beginning, the best, and the end of grassland tourist season of Inner Mongolia occur in late June, early July, and late July, respectively. The length of the grassland tourist season is about 90 days. The grassland tourist season shows strong spatial variation that might depend on grass species.

Our results indicate that tourist season for grassland can be effectively measured by space-borne radar remote sensing, providing a potentially flexible, repeatable, and realistic way to monitor regional tourist timings. These timings appear to have a major influence on regional patterns of tourist flows. This parameter has implications for tourists and the tourism industry with reference to the timing of trips and their promotion. To improve accuracy, sufficient comparison

between land surface phenology and in situ values is an essential issue.

Conflict of Interests

The authors have declared that no conflict of interests exists.

Acknowledgments

This study was supported by the Key Project of the National Natural Science Foundation of China (NSFC, no. 41030101) and the National Basic Research Program of China (973 Program no. 2010CB950100).

References

- [1] Q. Ge, J. Dai, J. Liu, S. Zhong, and H. Liu, "The effect of climate change on the fall foliage vacation in China," *Tourism Management*, vol. 38, pp. 80–84, 2013.
- [2] Brooklyn Botanic Garden, *Mizue Sawano: The Art of the Cherry Tree*, Brooklyn Botanic Garden, 2006.
- [3] E. Ivits, M. Cherlet, G. Tóth et al., "Combining satellite derived phenology with climate data for climate change impact assessment," *Global and Planetary Change*, vol. 88-89, pp. 85–97, 2012.
- [4] K. Zhu and M. Wan, *Productive Science-Phenology*, Public Science, 1963.
- [5] G. Zhang, Y. Kang, G. Han, and K. Sakurai, "Effect of climate change over the past half century on the distribution, extent and NPP of ecosystems of Inner Mongolia," *Global Change Biology*, vol. 17, no. 1, pp. 377–389, 2011.
- [6] J. Liu, X. Yang, H. Liu, and Z. Qiao, "Algorithms and applications in grass growth monitoring," *Abstract and Applied Analysis*, vol. 2013, Article ID 508315, 7 pages, 2013.
- [7] X. Zhang, M. A. Friedl, C. B. Schaaf et al., "Monitoring vegetation phenology using MODIS," *Remote Sensing of Environment*, vol. 84, no. 3, pp. 471–475, 2003.

Research Article

Characteristics of Spring Phenological Changes in China over the Past 50 Years

Junhu Dai,¹ Huanjiong Wang,^{1,2} and Quansheng Ge¹

¹ Institute of Geographical Sciences and Natural Resources Research, Chinese Academy of Sciences, A 11, Datun Road, Chaoyang District, Beijing 100101, China

² University of Chinese Academy of Sciences, 19A Yuquan Road, Beijing 100049, China

Correspondence should be addressed to Quansheng Ge; geqs@igsnr.ac.cn

Received 13 February 2014; Revised 18 March 2014; Accepted 18 March 2014; Published 7 April 2014

Academic Editor: Dong Jiang

Copyright © 2014 Junhu Dai et al. This is an open access article distributed under the Creative Commons Attribution License, which permits unrestricted use, distribution, and reproduction in any medium, provided the original work is properly cited.

In order to understand past plant phenological responses to climate change in China (1963–2009), we conducted trends analysis of spring phenophases based on observation data at 33 sites from the Chinese Phenological Observation Network (CPON). The phenological data on first leaf date (FLD) and first flowering date (FFD) for five broad-leaved woody plants from 1963 to 2009 were analyzed. Since most phenological time series are discontinuous because of observation interruptions at certain period, we first interpolated phenological time series by using the optimal model between the spring warming (SW) model and the UniChill model to form continuous time series. Subsequently, by using regression analysis, we found that the spring phenophases of woody plants in China advanced at a mean rate of 0.18 days/year over the past 50 years. Changes of spring phenophases exhibited strong regional difference. The linear trends in spring phenophases were -0.18 , -0.28 , -0.21 , -0.04 , and -0.14 days/year for the Northeast China Plain, the North China Plain, the Middle-Lower Yangtze Plain, the Yunnan-Guizhou Plateau, and South China, respectively. The spatial differences in phenological trends can be attributed to regional climate change patterns in China.

1. Introduction

Plant phenology, which is the study of seasonal plant development events and their relationship to environmental factors [1], has attracted much attention in the context of climate change [2, 3]. Plant phenophases can be directly affected by the interannual variations of climate factors, such as temperature, light, and moisture [4]. Also, phenology can in turn affect climate [5, 6]. For example, a longer presence of green cover in large areas should alter physical processes such as albedo, latent and sensible heat, and turbulence [5]. Moreover, a longer growing season can influence ecosystem productivity and vegetation-atmosphere CO₂ exchange [7, 8]. Thus, the study of past phenological changes is beneficial for assessing the impacts of climate change [9].

In recent years, pronounced phenological shifts have been detected on all the continents of the world based on satellite reflectance data [10–12] or ground observation data [13–17]. For example, using the Advanced Very High Resolution Radiometer (AVHRR) Normalized Difference Vegetation

Index (NDVI) dataset, Stöckli and Vidale [10] found a prolonged growing season in Europe over the past two decades. Similar results were also found in North America and China based on the same satellite dataset [11, 12]. Regarding ground-based phenological change, Menzel et al. [14] did a systematic assessment of European phenological responses to climate change and found the spring and summer phenophases such as timing of leaf unfolding and flowering had advanced by a mean trend of 2.5 days/decade from 1971 to 2000. Such earlier spring phenophases in recent decades were also found in North America [18]. In East Asia, several studies showed clear phenological responses to climate change in Japan and South Korea based on ground observations [13, 19, 20]. In China, although some work has been done to assess phenological changes in several locations [16, 21–24], systematic studies of phenological shifts at a national scale over a long time period are still lacking.

In China, phenological observations have been conducted by the Chinese Phenological Observation Network (CPON) in 1963. Since that time, phenophases of typical

TABLE 1: Species selected and corresponding observation sites in the study. Site numbers correspond to site numbers shown in Figure 1.

Species	Numbers of sites	Distribution sites (site number)
<i>Fraxinus chinensis</i>	3	9, 15, 28
<i>Ailanthus altissima</i>	7	8, 9, 12, 14, 15, 17, 21
<i>Melia azedarach</i>	16	14, 15, 17, 18, 23, 24, 24, 25, 26, 29, 30, 31, 33
<i>Paulownia tomentosa</i>	15	9, 10, 13, 15, 18, 19, 20, 21, 24, 25, 26, 28, 29, 30, 32
<i>Ulmus pumila</i>	18	1, 2, 3, 4, 5, 6, 7, 8, 9, 10, 11, 12, 14, 15, 16, 17, 18, 28

plant species at each site of the CPON network were monitored by relevant local organizations, such as botanical gardens, weather stations, research institutions, universities, and middle schools. There was no observation, however, carried out in certain periods. Given that discontinuous time series of phenophases affects the assessment of phenological trends, we firstly interpolated the missing phenological data of five widespread woody plants using phenological models. Subsequently, we systematically studied the characteristics of spatiotemporal changes in spring phenology so as to evaluate the specific impacts of climate change on biological systems.

2. Materials and Methods

2.1. Phenological and Meteorological Data. Phenological data used in this study were derived from CPON. Spring phenophases of five deciduous woody plants, including *Fraxinus chinensis*, *Ailanthus altissima*, *Melia azedarach*, *Paulownia tomentosa*, and *Ulmus pumila*, were investigated. We only used time series with more than 11 years of data from 1963 to 2009. As a result, a total of 33 sites have been included (Figure 1; Table 1). We took first flowering date (FFD) and first leaf date (FLD) as being representative of spring phenophases. According to the uniform observation criteria and guidelines of CPON [25], FFD and FLD are defined as the date when a fixed individual formed its first full flower and first full leaf, respectively. Overall, a total of 118 phenological time series (a phase of a specific species at certain site is considered as one time series) are analyzed (Table 1). As shown in Figure 2, there are a lot of missing data in each year for all phenophases. Especially during the period of 1969–1972, no observation data was made due to the social upheavals of the Cultural Revolution. Similar problems with data collection also existed in the period of 1997–2002 due to funding shortages. The available data (a total of 2316 observations) could only account for 41.8% of the full dataset (118 time series \times 47 years), so these missing data would significantly affect the results of trend estimates. Thus, we interpolated the missing data using phenological models. Although these interpolated phenological data may introduce considerable bias into the results, these uncertainties could be quantified in our analyses (see Section 2.2).

Meteorological data were derived from the Chinese Meteorological Administration (<http://cdc.cma.gov.cn/>) and included daily mean temperatures from 33 meteorological stations (Figure 1). Most of these meteorological stations are relatively close to the corresponding phenological sites

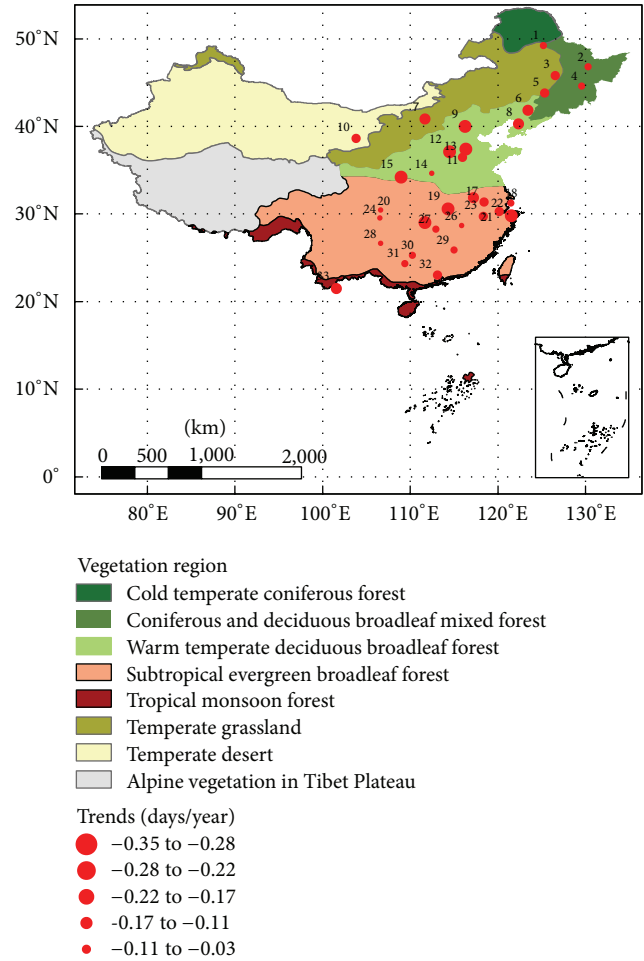


FIGURE 1: Illustration of phenological observation sites and spring phenological trends at each site. Site numbers are shown.

(usually less than 5 km), though for site 8 the corresponding phenological site is about 30 km away.

2.2. Interpolation of Discontinuous Series Using Phenological Models. The spring phenophase of a number of trees has been modeled successfully using accumulated forcing units, which are often calculated by the accumulated degree days above a threshold temperature, regardless of the presence of the additional constraint of a chilling requirement [26]. Since climates over the study area vary in type from site to site, the most applicable models are bound to be different in different places. Thus, we developed two types of models for each

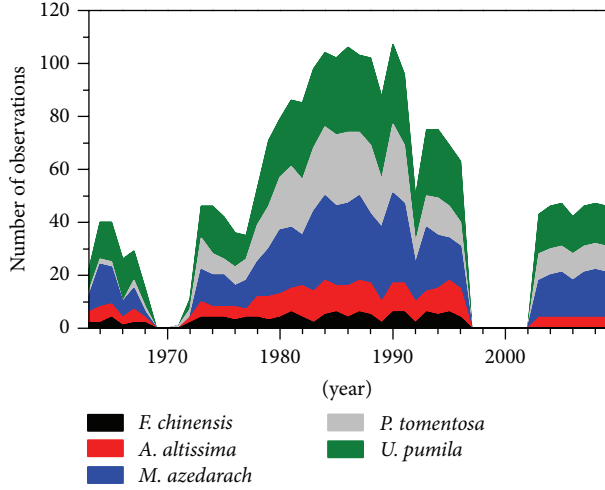


FIGURE 2: Number of phenological observations (including first leaf date and first flowering date) for five plant species from 1963 to 2009.

phenological time series and then chose the most accurate one to interpolate the time series. The first model used is the spring warming (SW) model, which is a model without the constraint of a chilling requirement [27]. Regarding the models with the constraint of a chilling requirement, we chose the UniChill model developed by Chuine [28].

2.2.1. SW Model. In the SW model, plant development occurs in response to aggregated heat sums, or heating degree days (HDD), measured as the sum of $R_f(x_t)$ (daily mean temperature x_t above a base temperature T_b), starting at a day of year t_0 (1). The HDD achieve the critical forcing temperature (F^*) at time t_y , which represent the FFD or FLD that occurred. The equations for SW model are

$$\text{HDD} = \sum_{t_0}^{t_y} R_f(x_t) = F^* \quad (1)$$

$$R_f(x_t) = \begin{cases} 0 & \text{if } x_t \leq T_b \\ x_t - T_b & \text{if } x_t > T_b. \end{cases}$$

2.2.2. UniChill Model. The UniChill model divided the process of bud development into two phases: dormancy and quiescence. Dormancy refers to the physiological state during which development and cell growth are prevented by internal factors despite favorable external conditions [29]. Plants enter the phase of quiescence (during which development and cell growth are triggered by warm temperature) when dormancy is broken. The equations are as follows:

$$S_c = \sum_{t_0}^{t_1} R_c(x_t) = C^* \quad (2)$$

$$S_f = \sum_{t_1}^{t_b} R_f(x_t) = F^* \quad (3)$$

$$R_c(x_t) = \frac{1}{1 + e^{a(x_t - c)^2 + b(x_t - c)}} \quad (4)$$

$$R_f(x_t) = \frac{1}{1 + e^{d(x_t - e)}}, \quad (5)$$

with t_0 set at September 1, and seven species-specific parameters (a, b, c, d, e, C^*, F^*) fitted to phenological observations. Parameters a, b , and c define the response function to temperature $R_c(x_t)$, also called “chilling units”, which models the effect of “cold” temperatures in breaking dormancy (4). The accumulative sum of chilling units is called the state of chilling (S_c). Parameter C^* is the S_c threshold at which bud dormancy is broken (2). Parameters d and e define the response function to temperature ($R_f(x_t)$), also called “forcing units” which conditions the effect of “warm” temperatures during quiescence (5). Forcing units are accumulated as soon as C^* is reached at t_1 . The model predicts that phenophase (T_b) occurs when the state of forcing (S_f) reaches a particular critical value F^* (3).

The above two models were both fitted for respective species at each site using daily mean temperatures and the FLD or FFD time series through the least square method. The function $f(x) = \sum_i [r_i(P)]^2$ is minimized in the parameter space P , where $r_i(P)$ is the residual:

$$r_i(P) = d_i(P) - d_{i\text{obs}} \quad (6)$$

with $d_i(P)$ and $d_{i\text{obs}}$ being the simulated date and the observed date in the year i , respectively. We only used odd years of each time series to fit the parameters. The internal validity of each series was measured by the percentage variance explained by the model (R^2) and the root mean square error (RMSE) between the observed dates and the simulated dates.

The external validity was also measured by the R^2 and RMSE between remaining observed dates in even years and corresponding simulated dates. The external validity measures the goodness of simulation for the years not used to fit the parameters, so the uncertainties of models could be represented by the RMSE of external validity. Between two models we chose the optimal one (with fewest uncertainties) to interpolate the missing data. In addition, in order to minimize the errors, only the time series with associated uncertainties less than seven days (RMSE of external validity < 7) were retained for further analysis.

2.3. Estimation and Comparison of the Phenological Trends. The temporal trends of time series could be calculated as the slope coefficient of a linear regression model with phenophases as the dependent variable and years as the independent variable. Subsequently, we calculated the mean trend of all the phenological time series for each site and investigated the spatial difference of phenological changes in China. Finally, based on the mean phenological series for all five species across the 33 sites, we applied the Mann-Kendall trend test method for detecting monotonic trends in phenological time series [30]. In addition, we used a moving-trend analysis method to investigate the temporal evolution of phenological trends [31], that is, calculating the regression

TABLE 2: Internal and external validity of optimal model for 92 time series of spring phenophases. Each column shows the mean \pm standard deviation.

Species	Phase	N	DOY	Internal validity		External validity	
				R^2	RMSE	R^2	RMSE
<i>Fraxinus chinensis</i>	FFD	2	101.9 \pm 12.2	0.41 \pm 0.18	3.3 \pm 0.3	0.31 \pm 0.18	4.6 \pm 1.6
	FLD	2	100.3 \pm 13.9	0.78 \pm 0.29	2.4 \pm 1.5	0.75 \pm 0.28	3.3 \pm 1.0
<i>Ailanthus altissima</i>	FFD	5	140.1 \pm 9.9	0.69 \pm 0.18	2.4 \pm 1.2	0.42 \pm 0.21	3.6 \pm 0.5
	FLD	7	105.9 \pm 10.0	0.69 \pm 0.15	3.3 \pm 1.0	0.77 \pm 0.12	3.4 \pm 1.5
<i>Melia azedarach</i>	FFD	16	111.2 \pm 19.2	0.67 \pm 0.28	3.6 \pm 1.8	0.66 \pm 0.22	4.1 \pm 1.6
	FLD	9	89.3 \pm 19.7	0.67 \pm 0.28	3.9 \pm 1.4	0.55 \pm 0.28	4.7 \pm 1.4
<i>Paulownia tomentosa</i>	FFD	9	89.3 \pm 16.7	0.85 \pm 0.17	2.3 \pm 0.9	0.69 \pm 0.18	3.4 \pm 1.3
	FLD	12	94.8 \pm 15.2	0.74 \pm 0.17	4.4 \pm 2.3	0.59 \pm 0.21	4.6 \pm 1.1
<i>Ulmus pumila</i>	FFD	13	82.0 \pm 23.8	0.63 \pm 0.34	4.2 \pm 2.1	0.60 \pm 0.17	5.2 \pm 1.4
	FLD	17	103.4 \pm 19.1	0.59 \pm 0.21	4.1 \pm 1.1	0.63 \pm 0.23	4.1 \pm 1.2
Overall		92	N/A	0.67 \pm 0.24	3.7 \pm 1.7	0.62 \pm 0.22	4.2 \pm 1.4

slope for each 31-year period by moving the center year with a step length of one year. For highlighting the decadal variation of spring phenophases, the anomalies (relative to the mean over the 1963–1990 period) of spring phenophases in each decade (1960s, 1970s, 1980s, 1990s, and 2000s) were calculated.

3. Results

3.1. Validity of the Models. The SW model performed better (the RMSE of external validity is less) than the UniChill model in 67 time series, while the UniChill model showed better simulation in the other 51 time series. For each time series of spring phenophases, we used the optimal model to interpolate the missing data. In order to minimize the uncertainty of the interpolation as far as possible, we only retained the time series with models uncertainties less than 7 days. As a result, 92 of 118 time series were chosen for further analysis. The results of model validity for these series are shown in Table 2. The average R^2 of internal validity for each phenophase ranged from 0.41 to 0.85 with an overall mean of 0.67, while the overall mean of R^2 for external validity was 0.62 (0.31–0.77). Accordingly, the overall mean of RMSE for internal validity and external validity was 3.7 days and 4.2 days, respectively. The variances of phenophases (standard deviation) were often more than 3 times stronger than the RMSE (Table 2); therefore, the error introduced by the models was acceptable.

3.2. Spatial Patterns of Spring Phenophases Change. The frequency distribution of the phenological trends is summarized in Figure 3. 88 of 92 spring phenological series showed earlier trends (62 series reached a 0.05 level of significance). Therefore, the earlier trends of spring phenophases from 1963 to 2009 are notable in China. The temporal trends of spring phenophases ranged from -0.35 to -0.03 days/year among different sites (Figure 1). The trends of spring phenophases in the main areas of China are as follows:

- (1) The spring phenophases in the Northeast China Plain, represented by sites 1–6 and 8, showed a strongly earlier trend of 0.18 days/year;
- (2) the spring phenophases in the North China Plain, represented by sites 9 and 11–13, exhibited a very marked trend of -0.28 days/year, which was the strongest change in China;
- (3) the spring phenophases in the Middle-Lower Yangtze Plain, represented by sites 17–19, 21–23, and 26–28, advanced by a mean trend of 0.21 days/year. In the southern part of this area, however, the trends in spring phenophases were relatively weak (e.g., trends at sites 26 and 27 are only -0.07 and -0.14 days/year, resp.);
- (4) mean spring phenophases trend in the area of the Yunnan-Guizhou Plateau (represented by site 28) and the Sichuan Basin (represented by sites 20 and 24) was only -0.04 days/year, which was the weakest change in China;
- (5) the spring phenophases in the South China area (represented by sites 29–32) advanced by 0.14 days/year.

Furthermore, the spring phenophases at other sites also showed consistent shifts (Figure 1). For example, the spring phenophases at site 7 (Hohhot), the only site located in the temperate grassland region, showed a trend of -0.22 days/year, while the spring phenophases at site 10 (Minqin), located in the temperate desert region, showed an advancing trend of 0.18 days/year. The trend at site 14 (Luoyang), located in the Yi-Luo River Basin, demonstrated a very weak trend (-0.07 days/year). The mean trend of -0.28 days/year at site 15 (Xi'an), located in the Weihe River Plain, was comparable with the trend in the North China Plain area. Site 33 (Mengla), the only one located in the tropical monsoon forest area, shows an obvious trend of -0.23 days/year towards earlier spring. Overall, the spring phenophases for most areas over China had advanced very significantly, but the strength of the advance varied among different regions.

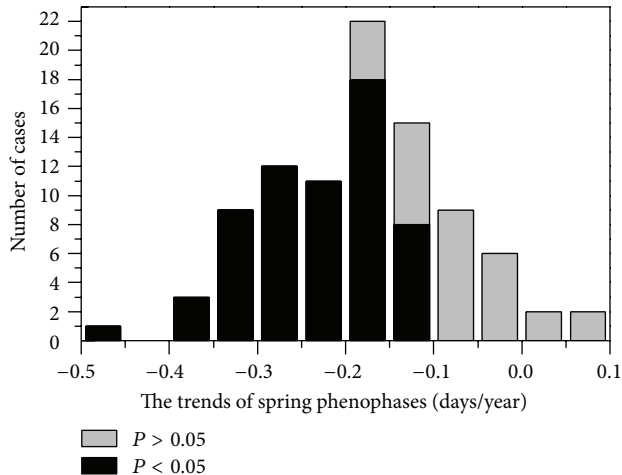


FIGURE 3: Frequency distributions of trends (1963–2009) in spring phenophases. Solid values in columns represent significant trends ($P < 0.05$).

3.3. Temporal Evolutions of Spring Phenophases. The annual changes of mean spring phenophases are shown in Figure 4(a). We found that the spring phenophases have large interannual variation with about 18 days' amplitude. In the context of the last 47 years, 1980 marks the latest spring phenophases and 2002 marks the earliest spring phenophases. The spring phenophase in 1980 was 5.0 days later than the 1963–1990 average, while the spring phenophase in 2002 was 13.2 days earlier than the 1963–1990 average. For the overall period of 1963–2009, the linear trend of spring phenophases was -0.18 days/year ($P < 0.001$), suggesting a significant advance of 8.3 days. The Mann-Kendall trend test also indicates a significantly earlier trend in the mean spring phenophases time series ($Z = -3.72$; $P < 0.001$).

The 31-year moving linear analysis of the spring phenological series indicated that the time periods would affect the estimation of phenological trends (Figure 4(b)). The spring phenophases showed a pronounced advancing trend of 0.30 days/year for the period of 1979–2009. The 31-year periods with the center year from 1989 to 1993 also showed significant advancing trends of around 0.23 days/year, though they were less than the trend over the 1979–2009 period (Figure 4(b)). In the 31-year periods with the center year before 1989, the trends of spring phenophases were insignificant. In general, the trends in the recent 31 years showed an unusual advancing trend that surpasses all previously observed trends in the past 31-year periods before 1979.

Furthermore, in terms of the temporal evolution of spring phenophases, a very apparent decadal change was detected (Figure 5). The spring phenophases in the 1990s and 2000s occurred 2.53 and 6.93 days earlier, respectively, than the 1963–1990 average. However, in the first three decades (1960s–1980s) the spring phenophases were close to the 1963–1990 average. Therefore, the advances in spring phenology can be said to have become evident after the 1980s and then strengthened in the 2000s.

4. Discussion

The significant advance in FFD and FLD of the five tree species observed in this study is consistent with spring phenophase changes in other parts of the world (Table 3). In Europe, an enormous systematic phenological network dataset of more than 100 000 observational series of 542 plants indicates an advance of 0.25 days/year in spring/summer phase for the period of 1971–2000 [14]. In this study, when restricting the time period to 1971–2000, the spring phenophase trend (-0.11 days/decade) is shown to be weaker than that observed in Europe (Table 3). Compared with the Northeastern US, however, the observed trend in the flowering time of lilac from 1965 to 2001 is close to our estimates [32]. This evidence indicates that the onset of spring across the Northern Hemisphere has appeared earlier over the past several decades. In the Southern Hemisphere, Australia has also experienced a warming climate in recent decades, leading to earlier wine grape maturity dates with a trend of -0.8 days/year (1985–2009) [33], which is about two times a stronger advance than indicated by spring phenophases in China (-0.43 days/year).

In addition, another study from China suggested that the spring started 0.41 days earlier per year on average from 1982 to 2006 [34]. The result is stronger than our estimates (-0.33 days/year, Table 3) over the same period. The possible reason is that both the number of plant species and phenological observation sites involved are different from those relied on in this study. In [34], the authors discussed the FLD of 13 plant species at 20 observation sites, while our study consists of FLD and FBD for five plant species at 33 sites. Therefore, differences in species and phases selection, as well as distribution of phenological observation sites, could affect the results of trend estimates.

The advance of spring phenophases in China has obvious regional differences. In general, the trends in northern China are stronger than those in southern China (Figure 1). As a previous study suggested, the trend of annual temperature increase (1961–2000) was about 0.2 – $0.3^\circ\text{C}/\text{decade}$ in northern China and less than $0.1^\circ\text{C}/\text{decade}$ in southern China [35]. Therefore, in China, the phenological response to climate change matches the observed warming pattern. However, the distribution of phenological observation sites involved in this study is uneven, so these sites have limited spatial representativeness. In future, it will be necessary to enlarge CPON and enlist volunteers to help acquire more phenological data, which could minimize the effect of site distribution in estimating phenological change.

Apart from the temperature in spring and the chilling temperature in winter, the photoperiod and evaporative demand also play an important role in regulating the growth and development of plants in temperate regions [36, 37]. Decreasing day lengths are reliable cues of the impending end of the growing season and winter onset for many temperate biomes, while increasing day lengths indicate the arrival of spring [37]. Because photosynthesis and growth are likely to be significantly limited if the vapor pressure deficit (VPD) is at a high value [38], the distribution of vegetation with different phenological patterns is very sensitive to seasonal

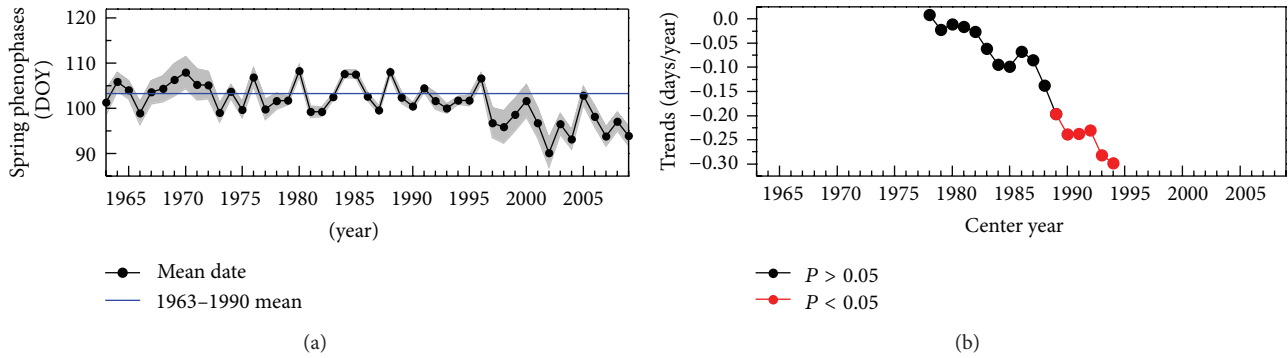


FIGURE 4: The change of spring phenophases from 1963 to 2009 (a) and the 31-year moving trends of the spring phenophases (b) in China. The statistically significant trends ($P < 0.05$) are marked with red circles.

TABLE 3: Comparison of trends in spring phenophases between this study and other studies based on ground phenological observations.

Regions	Objects	Periods	Trends (days/year)	Trends in this study	Source
Europe	Spring/summer events of 542 plant	1971–2000	–0.25	–0.11	[14]
Northeastern USA	The flowering time of lilac	1965–2001	–0.09	–0.12	[32]
Australia	Wine grape maturity date	1985–2009	–0.80	–0.43	[33]
China	The leaf unfolding time of 13 plant species	1982–2006	–0.41	–0.36	[34]

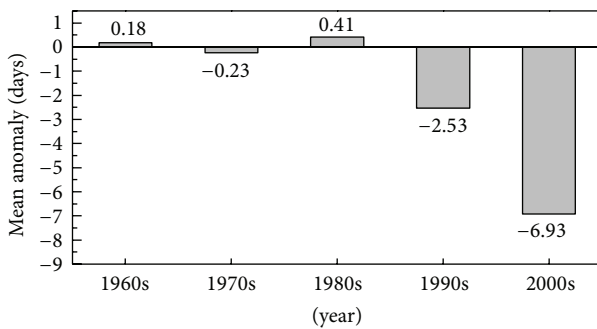


FIGURE 5: The spring phenology anomaly (relative to the 1963–1990 mean) in 1960s (1963–1970), 1970s (1971–1980), 1980s (1981–1990), 1990s (1991–2000), and 2000s (2001–2009).

changes in VPD. Among such influencing factors, the SW model used in this study only considers the effects of spring temperature, but the UniChill model also considers chilling requirements. Thus, the impacts of other potential factors on the model's predictions need to be further studied.

5. Conclusions

Based on observational data from CPON, this study investigated the changes in FFD and FLD of five woody plants (including *Fraxinus chinensis*, *Ailanthus altissima*, *Melia azedarach*, *Paulownia tomentosa*, and *Ulmus pumila*) in China. The results show that the spring phenophases in China became remarkably earlier at a mean rate of 0.18 days/year over the period from 1963 to 2009. The spring phenophases were stable from the 1960s to the 1980s but advanced by 2.5 days during the 1990s and 6.9 days during the 2000s (compared to the 1963–1990 mean). In addition, the

changes of spring phenophases showed noticeable regional difference. The magnitudes of advance in the North China Plain, the Middle-Lower Yangtze Plain, and the Northeast China Plain are the strongest, while the magnitudes of advances in the Yunnan-Guizhou Plateau, the Sichuan Basin, and South China are weaker. In general, the change of spring phenophases in China matches the warming pattern observed over the past 50 years.

Conflict of Interests

The authors declare that there is no conflict of interests regarding the publication of this paper.

Acknowledgments

This study is supported by Strategic Leader Project in Science and Technology, Chinese Academy of Sciences (XDA05090301), National Natural Science Foundation of China (41030101 and 41171043), and the National Basic Research Program of China (2012CB955304).

References

- [1] M. D. Schwartz, *Phenology: An Integrative Environmental Science*, Kluwer Academic Publishers, Dordrecht, The Netherlands, 2003.
- [2] C. Parmesan and G. Yohe, "A globally coherent fingerprint of climate change impacts across natural systems," *Nature*, vol. 421, no. 6918, pp. 37–42, 2003.
- [3] G.-R. Walther, "Plants in a warmer world," *Perspectives in Plant Ecology, Evolution and Systematics*, vol. 6, no. 3, pp. 169–185, 2004.

- [4] E. E. Cleland, I. Chuine, A. Menzel, H. A. Mooney, and M. D. Schwartz, "Shifting plant phenology in response to global change," *Trends in Ecology and Evolution*, vol. 22, no. 7, pp. 357–365, 2007.
- [5] J. Peñuelas, "Phenology feedbacks on climate change," *Science*, vol. 324, no. 5929, pp. 887–888, 2009.
- [6] J. T. Morisette, A. D. Richardson, A. K. Knapp et al., "Tracking the rhythm of the seasons in the face of global change: phenological research in the 21st century," *Frontiers in Ecology and the Environment*, vol. 7, no. 5, pp. 253–260, 2009.
- [7] S. Piao, P. Friedlingstein, P. Ciais, N. Viovy, and J. Demarty, "Growing season extension and its impact on terrestrial carbon cycle in the Northern Hemisphere over the past 2 decades," *Global Biogeochemical Cycles*, vol. 21, no. 3, Article ID GB3018, 2007.
- [8] A. D. Richardson, T. A. Black, P. Ciais et al., "Influence of spring and autumn phenological transitions on forest ecosystem productivity," *Philosophical Transactions of the Royal Society B: Biological Sciences*, vol. 365, no. 1555, pp. 3227–3246, 2010.
- [9] R. Stöckli, T. Rutishauser, D. Dragoni et al., "Remote sensing data assimilation for a prognostic phenology model," *Journal of Geophysical Research G: Biogeosciences*, vol. 113, no. 4, Article ID G04021, 2008.
- [10] R. Stöckli and P. L. Vidale, "European plant phenology and climate as seen in a 20-year AVHRR land-surface parameter dataset," *International Journal of Remote Sensing*, vol. 25, no. 17, pp. 3303–3330, 2004.
- [11] W. Zhu, H. Tian, X. Xu, Y. Pan, G. Chen, and W. Lin, "Extension of the growing season due to delayed autumn over mid and high latitudes in North America during 1982–2006," *Global Ecology and Biogeography*, vol. 21, no. 2, pp. 260–271, 2012.
- [12] X. Wu and H. Liu, "Consistent shifts in spring vegetation green-up date across temperate biomes in China, 1982–2006," *Global Change Biology*, vol. 19, no. 3, pp. 870–880, 2013.
- [13] C.-H. Ho, E.-J. Lee, I. Lee, and S.-J. Jeong, "Earlier spring in Seoul, Korea," *International Journal of Climatology*, vol. 26, no. 14, pp. 2117–2127, 2006.
- [14] A. Menzel, T. H. Sparks, N. Estrella et al., "European phenological response to climate change matches the warming pattern," *Global Change Biology*, vol. 12, no. 10, pp. 1969–1976, 2006.
- [15] H. Doi and I. Katano, "Phenological timings of leaf budburst with climate change in Japan," *Agricultural and Forest Meteorology*, vol. 148, no. 3, pp. 512–516, 2008.
- [16] J. Dai, H. Wang, and Q. Ge, "Multiple phenological responses to climate change among 42 plant species in Xi'an, China," *International Journal of Biometeorology*, vol. 57, no. 5, pp. 749–758, 2013.
- [17] N. L. Bradley, A. C. Leopold, J. Ross, and W. Huffaker, "Phenological changes reflect climate change in Wisconsin," *Proceedings of the National Academy of Sciences of the United States of America*, vol. 96, no. 17, pp. 9701–9704, 1999.
- [18] M. S. Abu-Asab, P. M. Peterson, S. G. Shetler, and S. S. Orli, "Earlier plant flowering in spring as a response to global warming in the Washington, DC, area," *Biodiversity and Conservation*, vol. 10, no. 4, pp. 597–612, 2001.
- [19] H. Doi and M. Takahashi, "Latitudinal patterns in the phenological responses of leaf colouring and leaf fall to climate change in Japan," *Global Ecology and Biogeography*, vol. 17, no. 4, pp. 556–561, 2008.
- [20] H. Doi, "Response of the *Morus bombycis* growing season to temperature and its latitudinal pattern in Japan," *International Journal of Biometeorology*, vol. 56, no. 5, pp. 895–902, 2012.
- [21] J. Bai, Q. Ge, and J. Dai, "The response of first flowering dates to abrupt climate change in Beijing," *Advances in Atmospheric Sciences*, vol. 28, no. 3, pp. 564–572, 2011.
- [22] Q. Ge, J. Dai, J. Zheng et al., "Advances in first bloom dates and increased occurrences of yearly second blooms in eastern China since the 1960s: further phenological evidence of climate warming," *Ecological Research*, vol. 26, no. 4, pp. 713–723, 2011.
- [23] J. Zheng, Q. Ge, Z. Hao, and W.-C. Wang, "Spring phenophases in recent decades over eastern China and its possible link to climate changes," *Climatic Change*, vol. 77, no. 3–4, pp. 449–462, 2006.
- [24] X. Chen and L. Xu, "Phenological responses of *Ulmus pumila* (Siberian Elm) to climate change in the temperate zone of China," *International Journal of Biometeorology*, vol. 56, no. 4, pp. 695–706, 2012.
- [25] M. W. Wan and X. Z. Liu, *China's National Phenological Observational Criterion*, Science Press, Beijing, China, 1979.
- [26] I. Chuine, P. Cour, and D. D. Rousseau, "Selecting models to predict the timing of flowering of temperate trees: implications for tree phenology modelling," *Plant, Cell and Environment*, vol. 22, no. 1, pp. 1–13, 1999.
- [27] A. F. Hunter and M. J. Lechowicz, "Predicting the timing of budburst in temperate trees," *Journal of Applied Ecology*, vol. 29, no. 3, pp. 597–604, 1992.
- [28] I. Chuine, "A unified model for budburst of trees," *Journal of Theoretical Biology*, vol. 207, no. 3, pp. 337–347, 2000.
- [29] E. E. Cleland, I. Chuine, A. Menzel, H. A. Mooney, and M. D. Schwartz, "Shifting plant phenology in response to global change," *Trends in Ecology and Evolution*, vol. 22, no. 7, pp. 357–365, 2007.
- [30] S. Yue, P. Pilon, and G. Cavadias, "Power of the Mann-Kendall and Spearman's rho tests for detecting monotonic trends in hydrological series," *Journal of Hydrology*, vol. 259, no. 1–4, pp. 254–271, 2002.
- [31] T. Rutishauser, J. Luterbacher, F. Jeanneret, C. Pfister, and H. Wanner, "A phenology-based reconstruction of interannual changes in past spring seasons," *Journal of Geophysical Research G: Biogeosciences*, vol. 112, no. 4, Article ID G04016, 2007.
- [32] D. W. Wolfe, M. D. Schwartz, A. N. Lakso, Y. Otsuki, R. M. Pool, and N. J. Shaulis, "Climate change and shifts in spring phenology of three horticultural woody perennials in north-eastern USA," *International Journal of Biometeorology*, vol. 49, no. 5, pp. 303–309, 2005.
- [33] L. B. Webb, P. H. Whetton, and E. W. R. Barlow, "Observed trends in winegrape maturity in Australia," *Global Change Biology*, vol. 17, no. 8, pp. 2707–2719, 2011.
- [34] T. Ma and C. Zhou, "Climate-associated changes in spring plant phenology in China," *International Journal of Biometeorology*, vol. 56, no. 2, pp. 269–275, 2012.
- [35] W. Qian and A. Qin, "Spatial-temporal characteristics of temperature variation in China," *Meteorology and Atmospheric Physics*, vol. 93, no. 1–2, pp. 1–16, 2006.
- [36] W. M. Jolly, R. Nemani, and S. W. Running, "A generalized, bioclimatic index to predict foliar phenology in response to climate," *Global Change Biology*, vol. 11, no. 4, pp. 619–632, 2005.

- [37] A. M. Wilczek, L. T. Burghardt, A. R. Cobb, M. D. Cooper, S. M. Welch, and J. Schmitt, "Genetic and physiological bases for phenological responses to current and predicted climates," *Philosophical Transactions of the Royal Society B: Biological Sciences*, vol. 365, no. 1555, pp. 3129–3147, 2010.
- [38] W. M. Jolly, R. Nemani, and S. W. Running, "A generalized, bioclimatic index to predict foliar phenology in response to climate," *Global Change Biology*, vol. 11, no. 4, pp. 619–632, 2005.

Research Article

Influences of Urban Expansion on Urban Heat Island in Beijing during 1989–2010

Zhi Qiao,¹ Guangjin Tian,¹ Lixiao Zhang,¹ and Xinliang Xu²

¹ State Key Laboratory of Water Environment Simulation, School of Environment, Beijing Normal University, No. 19 Xijiekouwai Street, Haidian District, Beijing 100875, China

² State Key Laboratory of Resources and Environmental Information Systems, Institute of Geographical Sciences and Natural Resources Research, Chinese Academy of Sciences, No. A11 Datun Road, Chaoyang District, Beijing 100101, China

Correspondence should be addressed to Guangjin Tian; tianguangjin@bnu.edu.cn

Received 15 January 2014; Accepted 7 March 2014; Published 31 March 2014

Academic Editor: Dong Jiang

Copyright © 2014 Zhi Qiao et al. This is an open access article distributed under the Creative Commons Attribution License, which permits unrestricted use, distribution, and reproduction in any medium, provided the original work is properly cited.

Beijing has experienced rapid urbanization and associated urban heat island (UHI) effects. This study aimed at analyzing the impact of urban form on UHI in Beijing using TM/ETM images between 1989 and 2010. Spatial analysis was proposed to explore the relationships between area, compactness ratio, the gravity centers of urban land, and UHI. The UHI in Beijing spatially represented a “NE-SW” spindle. The land surface temperature (LST) was higher in south than in north. Urban Heat Island Ratio Index (URI) was well interrelated with urban land area in different zones. Under the similar urban land area condition, UHI and compactness ratio of urban land were in positive correlation. The moving direction of the UHI gravity center was basically in agreement with urban land sprawl. The encroachment of urban land on suburban land is the leading source of UHI effect. The results suggest that urban design based on urban form would be effective for regulating the thermal environment.

1. Introduction

With the background of rapid urbanization, the population living in urban areas is forecasted to be five billion by 2030 [1]. Numerous modifications of land surface will occur as an accumulating number of people migrate into metropolitan areas [2]. The modification of land surface will result in urban climate change. There is a remarkable phenomenon for urban climates that the temperatures of urban land and their surrounding rural regions are different. The distinct differences in the temperature are referred to as urban heat island (UHI) [3, 4]. The UHI would significantly affect the human living conditions and increase energy consumption and atmospheric pollution [5]. The acceleration of urbanization, such as increased impervious surfaces and population density, would increase the UHI [6].

Numerous studies have focused on the impact of the urban form on urban environment. Urban form, which is a term that broadly refers to the layout and design of a city, affects ecological and environmental quality through the composition and fragmentation of land pattern, the water

and energy consumption, and air movement [7–11]. Oke [12] stated urban size as a main factor in the UHI development. Declines in thermal inertia and the vegetation index because of the encroachment of urban land constrain evaporation consequently reduce the loss of heat by latent heat flux [13]. The reduction of wind speeds [14] and sky-view factors [5, 7], higher anthropogenic heat release [5, 7, 14], increased energy demands, and congestion of transportation networks [11] resulting from urbanization will further aggravate UHI effect. However, urban growth is an inevitable tendency following the people migrating into metropolitan areas. “Good urban form” would mitigate the deterioration of the metropolitan environment [15, 16] as recent discussions of “urban sprawl” in the United States and the “compact city” in Europe [17–19]. The relationships between urban form and transportation energy consumption have been examined to reduce CO₂ emissions [20–22]. Marquez and Smith [23] established a land use - transport - environment model linking urban form to improve air quality. So far, no detailed study has been made on the theoretical achievements and practical applications in the relationship between urban form and urban thermal

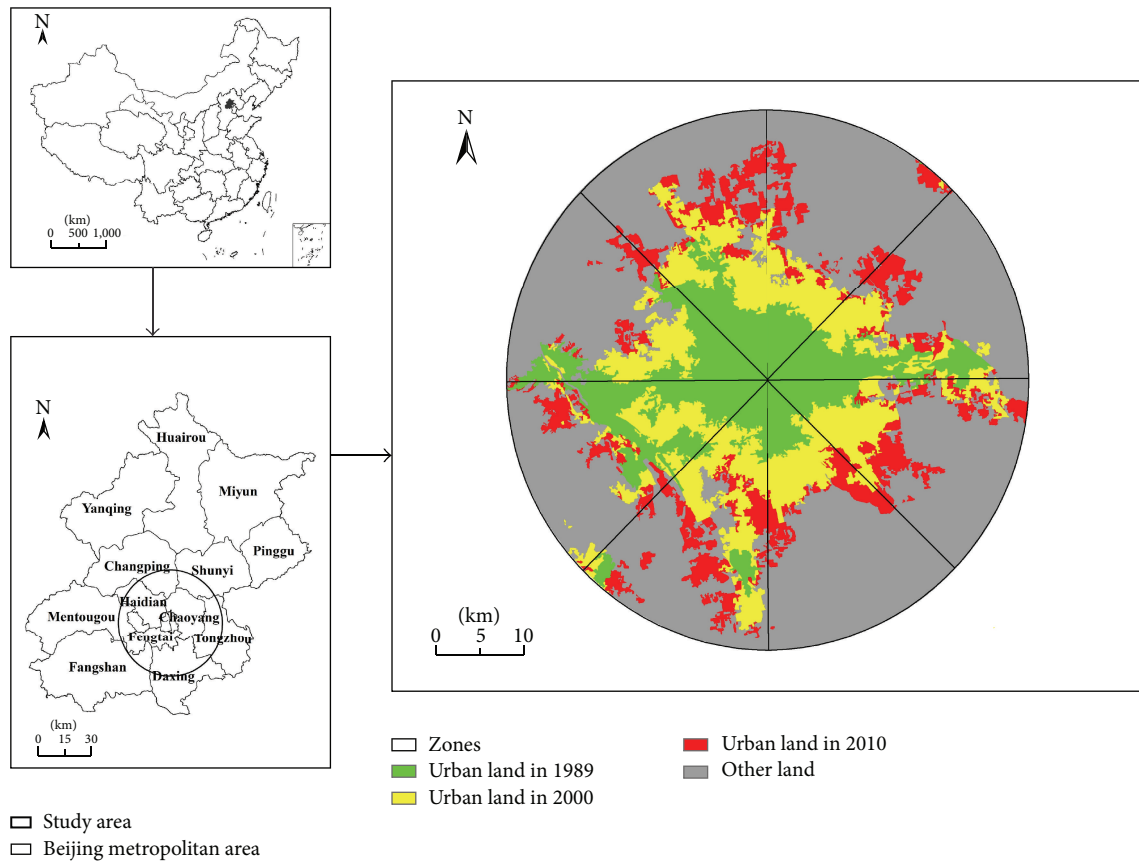


FIGURE 1: The spatial distribution of urban land in Beijing during 1989–2010.

environment in Beijing. The study focused on the following. (1) What were temporal-spatial characteristics of urban form and UHI during the period of 1989–2010? (2) How has urban form impacted UHI effect in Beijing?

To characterize urban growth, form, and spatial structure, various indicators such as density, compactness, complexity, and circularity ratios are used to represent urban characteristics [24]. The zonal strategy also provides us with a scientific method of measuring spatial geographic information for urban agglomeration [25–27]. Similarly to urban form, the measurement of urban heat island also has been the focus of a large number of studies, and for which several indicators have been assigned [9, 28–30]. Satellite observation provides a quantitative measurement of urban sprawl and UHI. Advanced Very High Resolution Radiometer (AVHRR) data from the National Oceanic and Atmospheric Administration (NOAA) [31, 32], Thermal infrared (TIR) data from the Thematic Mapper (TM) and Enhanced Thematic Mapper Plus (ETM) [33, 34], Moderate-Resolution Imaging Spectroradiometer (MODIS) LST products have been successively utilized to study the UHI effect [30]. The present study analyzed LST from TM/ETM collected in 1989, 2000, and 2010, respectively. In addition, Landsat TM images were analyzed to retrieve land use types.

2. Study Area and Data Sources

2.1. Study Area. Beijing, the capital of the People's Republic of China, extends approximately $1^{\circ}37'$ latitudinally

($39^{\circ}26'–41^{\circ}03'N$) and $2^{\circ}05'$ longitudinally ($115^{\circ}25'–117^{\circ}30'E$). It covers fourteen districts and two counties, and the total area is approximately 16410 km^2 [35] (Figure 1). The city has a subhumid warm temperate continental monsoon climate and four distinct seasons, with a cold and windy winter, and a hot and humid summer. Beijing has experienced the rapid urbanization process. The permanent population was 10.75 million in 1989 and reached up to 19.62 million in 2010. In a similar way, Gross Domestic Product (GDP) increased from 45.6 billion to 1411.3 billion with approximate 30 times increase during 1989–2010 [35]. Recently, environmental problems (e.g., UHI, sand and dust storms, and pollution haze) resulting from rapid population and economic growth have negatively affected the quality and comfort of urban living [36].

Environmental problems, especially UHI in Beijing, have drawn international attention. Zhang et al. [37] reported that the average UHI was approximately $4–6^{\circ}C$ when using a suburban area in the northwestern region as the rural baseline and $8–10^{\circ}C$ when using the outer suburban area in the same region. Warmer temperatures even delay the timing of fall foliage vacation [38]. With the diversified and rapid development of the economy and urban society, urban sprawl in Beijing will likely expand and the UHI effect will become more severe [29].

2.2. Data Sources. The land use datasets were provided by the Institute of Geographical Sciences and Natural Resources

Research, Chinese Academy of Sciences. The study collected three periods of land use datasets, that is, 1989, 2000, and 2010. To retrieve the land cover types, Landsat TM images were chosen and radiantly corrected. The visual interpretation was conducted on the false color composites (R/G/B = Band 5/4/3) of TM/ETM+ images. There were six aggregated classes of land use: cropland, forest, grassland, water bodies, built-up land, and bare land. These classes were further divided into 25 land use classes. The built-up land contains urban land, rural residential land, and industrial and mining sites. The average interpretation accuracies were 92.9% for land use and 97.6% for the detection of changes in land cover. For cropland, the accuracy was 94.9%. The built-up area had the highest accuracy of 96.3%. For forest and grassland, the accuracies were 90.1% and 88.1%, respectively [39]. In addition, three high-quality (cloud-free) TM/ETM images on 14 August, 1989, 10 August, 2000, and 8 August, 2010 were applied to retrieve LST, respectively.

3. Methods

3.1. The Measures of Urban Form

3.1.1. *Urban Form Measurement Indices.* The compactness ratio of urban outer contour is an important concept reflecting the urban form [27, 40–42], and it is computed as follows:

$$BCI = 2 \frac{\sqrt{\pi A}}{P}, \quad (1)$$

where BCI is the compactness ratio of urban land, A is the area of urban land, and P is the perimeter of urban contour. BCI ranges from 0 to 1; a higher value indicates a more compacted shape and a value closer to 1 indicates that the shape is closer to a circle, and vice versa. A circle is the most compact shape, and thus the compactness ratio of a long and narrow shape is far smaller than 1.

In general, if urban land expansion changes in the infilling way, the concavity of urban edges will decrease because the urban internal gaps are gradually filled up, and as a result, the urban outer contour form tends to be more compact. If the urban land expansion changes in the edge-expansion way, the urban form tends to be incompact. However, the debate over whether a compact urban form is best for urban thermal environment had lasted for a long history [43, 44]. The heat sources in low-density spreading urban area are relatively dispersed, but the increased fuel consumption by vehicles produces more anthropogenic heat. However, the newly large-area buildings will occupy more green land, increasing the area of impervious surface and enhancing UHI effect.

3.1.2. *Urban Land Expansion Measurement Indices.* The most common method to describe the heterogeneous of urban land expansion is to comparatively analyze the differences of urban expanding speeds at different directions (Figure 1). The method visually and concisely sketches the spatial form of urban expansion and discriminates the spatial heterogeneous in different zones. In this paper, we designed a 30 km buffer

around the city center, which could cover all urban built-up land. We also studied the urban spatial heterogeneous by dividing the buffer zones into eight quadrants.

The speed and intensity of urban land expansion can be used to analyze and describe the land expansion status at all directions in the urban built-up land and to compare the extending intensity, speeds, and trends of urban land in all study areas at different periods [45, 46]. The two indices are expressed as

$$M_{ue} = \frac{\Delta U_{ij}}{\Delta t_j \times ULA_{ij}} \times 100\% \quad (2)$$

$$I_{ue} = \frac{\Delta U_{ij}}{\Delta t_j \times TLA_{ij}} \times 100\%,$$

where M_{ue} is the expanding speed index, I_{ue} is the expanding intensity index, ΔU_{ij} is the expansion area of urban land in study area i (e.g., a zone at certain direction) at period j , Δt_j is the time span, ULA_{ij} is the total area of urban land in study area i at early period j , and TLA_{ij} is the total area of urban land in study area i .

The expanding speed indicates the annual growing rate of urban land at different stages during a whole study period and represents the overall trend of different types of urban land expansion at all stages. The expanding intensity index essentially is used to standardize the annual average expanding speeds of all spatial units, and thus the expanding speeds at different periods can be compared [47].

The centre of gravity is an important indicator describing the spatial distribution transition of a geographic subject [48, 49]. Center of gravity reflects the spatial orientation of a spatial element and the overall heterogeneous and “high-density” parts of a type of land use, and its dynamic transition reflects the overall transfer trajectory of the distribution of spatial elements. The gravity center of urban land is an important spatial index related to urban development and has high applicable value in urban development decision-making.

For multiple geographical objects, the coordinates of gravity center can be computed as follows:

$$X_t = \frac{\sum_{i=1}^n (C_{ti} \times X_i)}{\sum_{i=1}^n C_{ti}} \quad (3)$$

$$Y_t = \frac{\sum_{i=1}^n (C_{ti} \times Y_i)}{\sum_{i=1}^n C_{ti}},$$

where X_t and Y_t are the gravity centers of urban land at time t , X_i and Y_i are the coordinates of geometric center of urban land in block i , and C_{ti} is the area of block i .

We further put forward two variables: gravity center transfer distance (L) and gravity center transfer angle (α). The transfer distance reflects the homogeneous degree of urban land between different periods, and the transfer direction indicates the “high-density” parts of urban land [48, 49]:

$$L_{t+1} = \sqrt{(x_{t+1} - x_t)^2 + (y_{t+1} - y_t)^2}, \quad (4)$$

where L_{t+1} is the gravity center transfer distance of urban land from period t to period $t+1$:

$$\alpha_{t+1} = \begin{cases} \arctan\left(\frac{y_{t+1} - y_t}{x_{t+1} - x_t}\right), & x_{t+1} \geq x_t, y_{t+1} \geq y_t, \\ \pi - \arctan\left(\frac{y_{t+1} - y_t}{x_{t+1} - x_t}\right), & x_{t+1} < x_t, y_{t+1} \geq y_t, \\ \pi + \arctan\left(\frac{y_{t+1} - y_t}{x_{t+1} - x_t}\right), & x_{t+1} < x_t, y_{t+1} < y_t, \\ 2\pi + \arctan\left(\frac{y_{t+1} - y_t}{x_{t+1} - x_t}\right), & x_{t+1} \geq x_t, y_{t+1} < y_t \end{cases} \quad (5)$$

where α_{t+1} is the angle between the transfer direction and the east direction from period t to period $t+1$.

3.2. The Spatiotemporal Pattern of LST

3.2.1. The Retrieval of Brightness Temperature from the Landsat 5 TM Images. Chen et al. [50] proposed a two-step method to derive brightness temperature. First, the digital numbers (DNs) of band 6 are converted to radiation luminance (R_{TM6} , $m \cdot W \cdot cm^{-2} \cdot sr^{-1}$) as follows:

$$R_{TM6} = \frac{V}{255} (R_{max} - R_{min}) + R_{min}, \quad (6)$$

where V is the DN of band 6, and $R_{max} = 1.896 m \cdot W \cdot cm^{-2} \cdot sr^{-1}$, $R_{min} = 0.1534 m \cdot W \cdot cm^{-2} \cdot sr^{-1}$.

Then radiation luminance is converted to at-satellite brightness temperature in Kelvin, $T(K)$, as follows:

$$T = \frac{K1}{\ln(K2/(R_{TM6}/b) + 1)}, \quad (7)$$

where $K1 = 1260.56 K$ and $K2 = 60.766 (m \cdot W \cdot cm^{-2} \cdot sr^{-1})$, which are prelaunch calibration constant, and b is the effective spectral range, when the sensor's response is much more than 50%, $b = 1.239 (\mu m)$.

3.2.2. Retrieval of Brightness Temperature from Landsat 7 ETM+ Images. Landsat 7 ETM products were utilized for retrieving temperature in 2000 according to the User's Handbook. It is also simplified to two steps as follows.

First, the DN of band 6 were converted to radiance as follows:

$$R_{TM6} = \frac{L_{max} - L_{min}}{Q_{cal\ max} - Q_{cal\ min}} \times (Q_{cal} - Q_{cal\ min}) + L_{min}, \quad (8)$$

where the gain and offset can be obtained from the header file, $Q_{cal\ min} = 1$, $Q_{cal\ max} = 255$, $Q_{cal} = DN$, and L_{max} and L_{min} (also given in the header file) are the spectral radiances for band 6 at DN 1 and 255 (i.e., $Q_{cal\ min}$ and $Q_{cal\ max}$), respectively.

Then the effective at-satellite temperature of the viewed Earth-atmosphere system under the assumption of uniform emissivity could be obtained from the above spectral radiance as follows:

$$T = \frac{K2}{\ln(K1/R_{TM6} + 1)}, \quad (9)$$

where T is the effective at-satellite brightness temperature in Kelvin, $K1 = 666.09 (m \cdot W \cdot cm^{-2} \cdot sr^{-1})$ and $K2 = 1282.71 K$ are calibration constants, and R_{TM6} is the spectral radiance in $m \cdot W \cdot cm^{-2} \cdot sr^{-1}$.

3.2.3. Retrieval of LST. The calculated radiant temperatures were corrected for emissivity by using the normalized differential vegetation index (NDVI). The study thresholds the NDVI images into two general vegetation and nonvegetation classes, and assigning emissivity values of 0.95 and 0.92 to them, respectively, produced emissivity images for each data [51]. Then, LST was calculated as below [33, 52–57]:

$$T_s = \frac{T}{1 + (\lambda T / \rho) \ln \varepsilon}, \quad (10)$$

where λ = wavelength of radiance = $11.5 \mu m$, $\rho = hc/\delta = 1.438 \times 10^{-2} mK$ (h = Planck's constant = $6.626 \times 10^{-24} Js$, c = velocity of light = $2.998 \times 10^8 m/s$, and δ = Boltzmann constant = $1.38 \times 10^{-23} J/k$). Because of the importance of vegetation as a temperature controlling factor, the emissivity correction resulted in significant differentiation of classes and increased spatial detail comparable to those of reflective bands. Finally, the images were converted to Celsius.

3.2.4. The Calculation of Urban Heat Island Ratio Index (URI).

In this paper, we aimed to study the spatiotemporal variation of UHI by using LST data inverted from remote sensing (RS) images at different periods. Then based on bright temperature normalization, we introduced URI to quantify UHI [28, 46].

UHI study focuses on the spatial relative intensity of LST. Conditions in surrounding rural areas also affect the magnitude of an UHI [58]. For example, Streutker [32] found that UHI intensity was inversely correlated with rural LST. RS images obtained from different periods only change the values of LST, rather than changing the spatial distribution of LSTs. Therefore, LSTs were normalized to compare the spatial distributions of LSTs at the three periods, and thereby the spatiotemporal pattern variations of UHI in Beijing between 1989 and 2010 were studied.

First, LSTs at different periods were normalized to be between 0 and 1:

$$T_{ni} = \frac{T_{si} - T_{s\ min}}{T_{s\ max} - T_{s\ min}}, \quad (11)$$

where T_{ni} is the normalized value of pixel i ; T_{si} is the LST of pixel i ; $T_{s\ max}$ is the maximum LST in Beijing; and $T_{s\ min}$ is the minimum LST.

Then the normalized LSTs were classified by a density segmentation method into five thermodynamic levels: low, submedium, medium, subhigh, and high. Thereby, the distribution of LST levels in Beijing was characterized, and the area of each level could be calculated according to Table 1.

Finally, URI was introduced to quantify the contribution rate of urban land to UHI [28, 46]:

$$URI = \frac{1}{100m} \sum_{i=1}^n w_i p_i, \quad (12)$$

TABLE 1: The thresholds of different thermodynamic levels (unit: °C).

Level	1989	2000	2010
Low	21–23.46	21–22.33	21–23.82
Submedium	23.46–24.75	22.33–23.35	23.82–25.85
Medium	24.75–25.60	23.35–24.87	25.85–27.10
Subhigh	25.60–26.87	24.87–26.85	27.10–28.91
High	26.87–30	26.85–31	28.91–32

where m is number of normalized temperature levels; i is the level value of temperatures higher than rural areas; n is number of higher temperature levels mainly occurring in urban areas; w denotes weighted value using the value of correspond level i ; and p is the area percentage of level i . Essentially, URI is obtained by computing the ratio of UHI area to urban land with the consideration of weighted values of each temperature level. It reflects the development degree of UHI in built-up land. A larger URI indicates more severe UHI effect.

4. Results

4.1. The Spatiotemporal Pattern of Urban Form. Urban land expansion is a basic characteristic of urban form evolution. The urban land increased by 775.82 km² at a rate of 184.31% between 1989 and 2010 (Table 2). Specifically, the urban land increased by 469.32 km² during 1989–2000 and by 306.50 km² during 2000–2010, respectively. The expanding intensity of urban land (I_{ue}) decreased from 1.51 during 1989–2000 to 1.08 during 2000–2010, indicating the slow-down of expanding speed. Regarding urban form, the urban land was distributed like an “E-W” axis in 1989. The urban land in north of the axis was highly compacted, indicating high clustering degree; the urban land in south of the axis was less compacted, indicating scattered distribution. From 1989 to 2010, the newly urban land sprawled north- and southwards along the axis, and thus the compactness ratio of urban land slightly decreased, showing an overall edge-expansion mode (Figures 2 and 3).

In 1989, the urban lands were concentrated in southwest and west, for example, Xicheng, Fengtai, and Shijingshan Districts, accounting for 41.38% of total built-up land in the study area. The area of urban land in northeast zone was 70.17 km². The urban land in the three zones expanded in an infilling way, and compactness index (BCIs) all increased during 1989–2000. Especially, BCI increased from 0.17 to 0.25 in the southwest zone, which was attributed to the large area of newly urban land in Fengtai District and the continuous infilling expansion of urban land in Xicheng, Haidian, and Shijingshan districts. BCIs in other zones slightly decreased during the same period. These results indicated that the newly urban land were spreading outward, and especially in the south and northwest zones, the expanding intensity (I_{ue}) reached 2.17 and 1.84, respectively. However the BCIs did not change obviously. Urban land in southeast zone also expanded apparently, and the expanding intensity reached 1.63, but BCI dropped in the same zone. The expanding

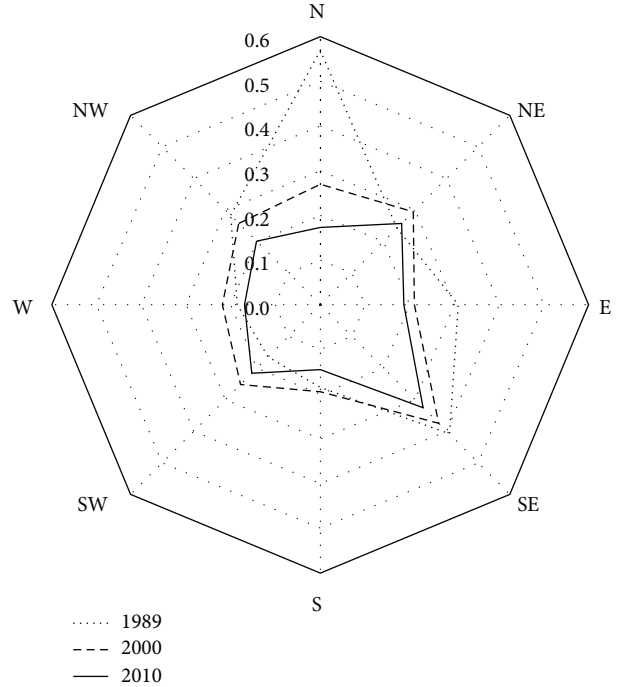


FIGURE 2: Compactness ratio index.

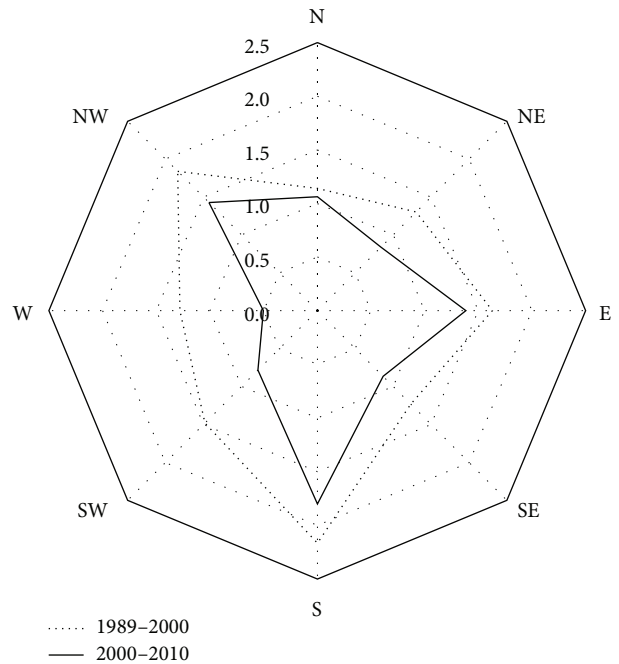


FIGURE 3: Urban land expanding intensity.

speed and the compactness ratio of urban land slightly decreased during 2000–2010, and the urban land was more decentralized. The urban expansion still was apparent in the south, northwest, and southeast zones. Especially, the area of urban land was 185.48 km², a 4-fold increase more than 1989 in Fengtai and Daxing Districts.

TABLE 2: The characteristics of urban land expansion in Beijing during 1989–2010 (unit: area-km²).

Zone	1989		2000		2010		1989–2000		2000–2010	
	Area	BCI	Area	BCI	Area	BCI	M_{ue}	I_{ue}	M_{ue}	I_{ue}
N	27.25	0.57	71.98	0.27	109.93	0.17	14.92	1.14	5.27	1.06
NE	70.17	0.24	120.25	0.29	149.50	0.26	6.49	1.30	2.43	0.84
E	30.82	0.31	93.53	0.21	141.87	0.19	18.50	1.63	5.17	1.38
SE	23.84	0.41	72.19	0.37	103.09	0.33	18.44	1.23	4.28	0.87
S	36.07	0.19	121.20	0.19	185.48	0.14	21.45	2.17	5.30	1.80
SW	102.03	0.17	159.00	0.25	186.34	0.22	5.08	1.48	1.72	0.78
W	72.13	0.19	121.35	0.22	138.86	0.17	6.20	1.28	1.44	0.50
NW	58.60	0.28	130.75	0.26	181.67	0.20	11.19	1.84	3.89	1.43
Built up area	420.93	0.11	890.25	0.11	1196.75	0.09	10.14	1.51	3.44	1.08

TABLE 3: The LST and URI of urban land in Beijing between 1989 and 2010.

Zone	1989		2000		2010	
	LST (°C)	URI	LST (°C)	URI	LST (°C)	URI
N	26.73	0.06	27.47	0.18	27.83	0.23
NE	26.45	0.16	27.22	0.30	27.83	0.32
E	27.32	0.08	27.37	0.23	28.46	0.31
SE	27.57	0.06	27.71	0.18	28.43	0.23
S	27.56	0.09	27.41	0.30	28.35	0.41
SW	26.85	0.25	27.70	0.41	28.54	0.44
W	26.12	0.15	27.44	0.31	27.99	0.31
NW	26.85	0.14	27.10	0.31	27.87	0.38
Beijing	26.78	0.12	27.39	0.27	28.26	0.30

4.2. *The Spatiotemporal Pattern of LST.* The LSTs in Beijing between 1989 and 2010 were quantitatively retrieved from TM/ETM data, and their spatiotemporal patterns were further analyzed (Figure 4). In general, the LSTs and URIs of urban land increased from 1989 to 2010, heat island areas expanded, and the UHI intensity resulting from urban expansion obviously increased (Table 3). LSTs in urban land were higher in south than in north in 1989, mainly because there were more industrial lands in the south of Beijing. However, the spatial distribution became less obvious along with urban expansion during 1989–2000, because some large-scale energy-intensive factories were completely moved out and the released industrial heat sources were reduced.

UHIs in 1989 distributed like an “NE-SW” spindle, as URI in the southwest zone where URI reached up to 0.25 was obviously higher than in other zones (Figure 5), because large-scale energy-intensive enterprises including Shoudu Iron and Steel Company and some thermal power plants were located in Shijingshan district. They discharged abundant heat to cause elevated temperature in atmosphere and land surface. URI was also high in the northeast zone (URI = 0.16) and UHI effect was more severe than the adjacent zones, which mainly were associated with the Beijing Capital International Airport in Shunyi district. URIs increased largely and heat island area expanded obviously between 1989 and 2000. However UHIs were still distributed like an “NE-SW” spindle in the southwest and northeast zones. URIs increased significantly and raised above 0.3 in the west, south, and northwest zones.

Especially the increase of URI was most obvious in the south zone, which was associated with the highest urban expanding intensity. The urban-rural transition belt of the main urban area to Tongzhou/Fangshan districts has clearly manifested UHI characteristics.

URIs in all zones further increased and UHI was more severe in Beijing between 2000 and 2010. URI was still highest in the southwest zone (URI = 0.44), followed by the south zone (URI = 0.41). Noticeably, URI in the northwest zone increased rapidly to 0.38, because of the tremendous expansion of urban land. A mountain of high-tech industry areas and large-scale residential areas emerged and gradually became new heat island centers, such as Zhongguancun, Shangdi, and Sijiqing residential areas. These high-density buildings and dense population were the main reasons of high LSTs. In addition, the east zone gradually connected and jointly developed with the residential areas in Yanjiao of Hebei province, and the population boom, traffic land extension, and increased vehicle flow together resulted in constantly increasing URI.

4.3. *The Impact of the Urban Form on Urban Heat Island.*

In this study, we compared urban land and URIs in the eight zones at three periods. The results showed that the two indices were in high correlation ($R^2 = 0.971$), indicating that the occurrence of UHI effect was likely attributed to the rapid transition from suburban land to urban land (Figure 6). Large-area buildings encroached on more green land, as the

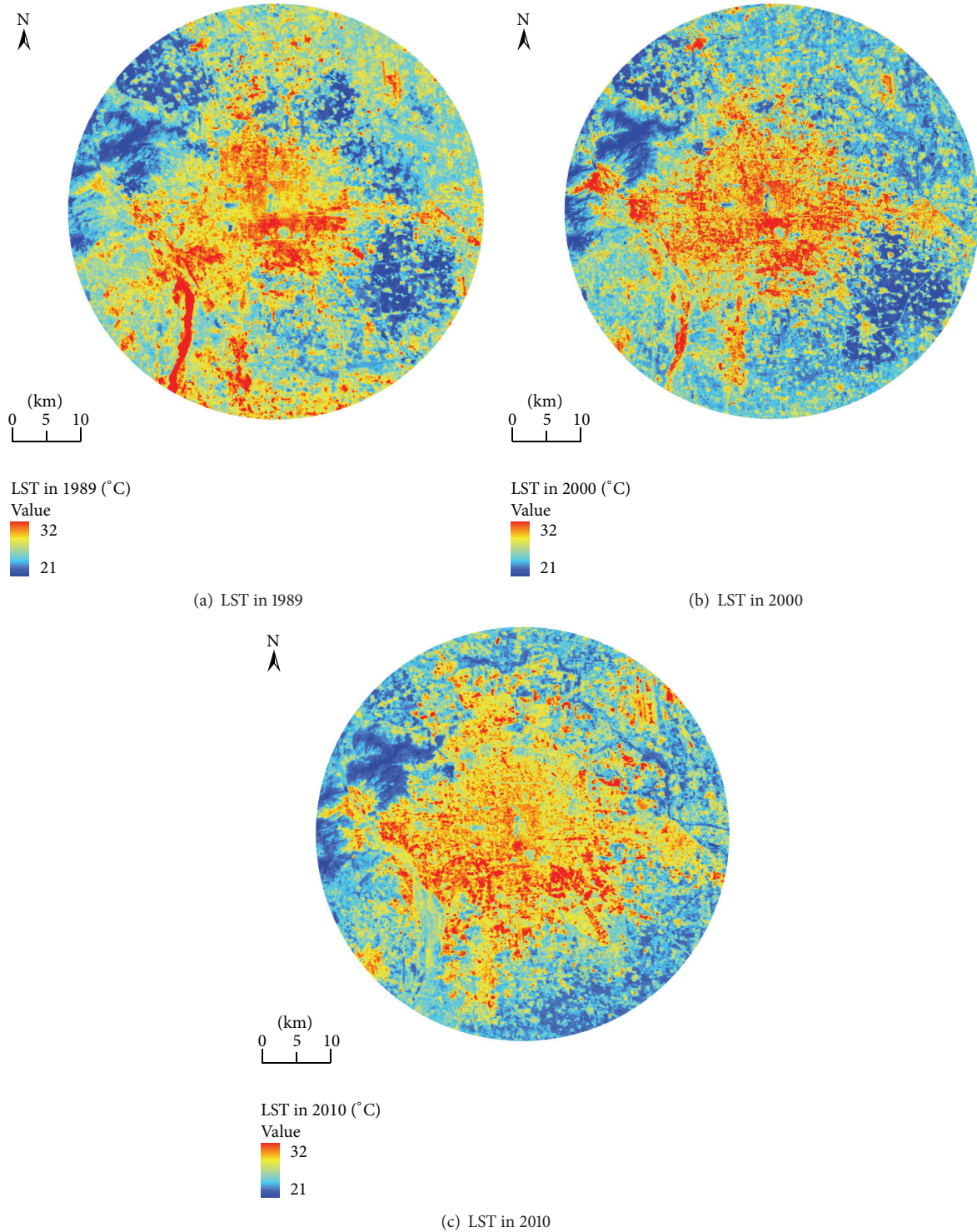


FIGURE 4: Spatiotemporal distributions of LST in Beijing.

increase of impervious surface, declines in thermal inertia, and the vegetation index constrain evaporation, consequently reducing the loss of heat by latent heat flux and enhancing UHI effect.

In addition, at the same urban scale, a more compacted urban form indicated more severe UHI. In 1989, the urban

lands were nearly identical size (70.17 versus 72.13 km²) in the northeast and west zones of Beijing. However, the BCI was obviously higher in the northeast zone, therefore there was a higher URI, indicating stronger UHI effect in the northeast zone than in the west zone of Beijing. Similarly, the southeast and north zones were equally large (103.09 versus 109.93 km²)

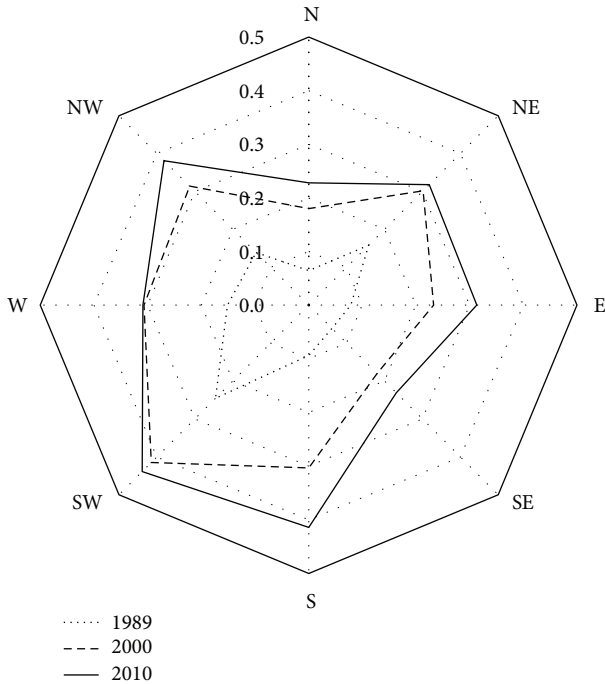


FIGURE 5: Urban Heat Island Ratio Index.

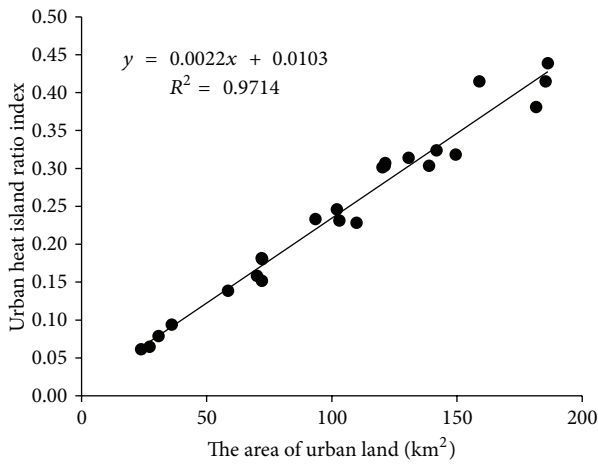


FIGURE 6: The relationship between urban land area and URI.

in 2010; however the urban form was more compacted in the southeast zone, the BCI (0.33 versus 0.17) and thus URI was higher, indicating stronger UHI effect in the southeast zone than in the north zone. Obviously, higher urban density and surface roughness would weaken the urban-rural air ventilation, blocking the urban internal heat diffusion and increasing the temperature differences between urban area and rural area.

Then the effects of urban land on UHI effect were further analyzed from the aspect of spatial distribution (Figure 7). The gravity centers of urban land generally shifted nearly the edges in all zones between 1989 and 2000, and the gravity center transfer distance was longer during 1989–2000 than during 2000–2010 (Table 4). Gravity center transfer

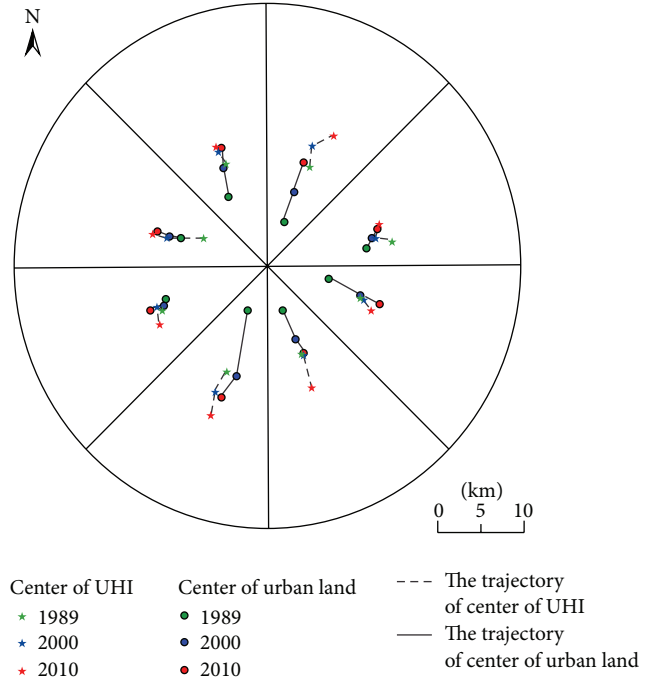


FIGURE 7: Gravity center transfer orbits of urban land and UHI.

in the south zone was more obvious, followed by the east zone, because Fengtai and Daxing Districts in the south zone and Chaoyang District in the east zone experienced the most intense urban land expansion. In the northeast, southwest, and west zones, however, the center transfer distances were shorter between 1989 and 2000 compared with other zones, mainly because the newly urban land in the three zones expanded in an infilling way and thus compactness ratio increased. These results indicated that the expanding intensity and pattern of urban land would largely affect the urban gravity center transfer.

The LSTs in urban land were mainly divided into high and subhigh thermodynamic levels; therefore the two levels were considered as UHI in this paper. The spatial distributions of UHI gravity centers showed that the UHI gravity center was farther away from the city center compared with the gravity center of urban land in the same zone (Figure 7), indicating that the affected area of UHI was greater than urban land. From the aspect of spatial transfer, the gravity centers of UHI and urban land transferred basically in a consistent way and indicated high correlation. Especially in the south zone where urban edge-expansion was more obvious, the gravity centers of UHI and urban land transferred more similarly. However, in the southwest and northeast zones where newly urban land expanded in an infilling way, the gravity center of UHI also transferred irregularly. The encroachment of urban land on the suburb land and a sequence of human activities (e.g., population concentration, increased travel frequency and prolonged trips distance, and industrial restructuring) then resulted in fundamental changes of thermal radiation, heat storage, and heat transfer modes. Therefore, urbanization

TABLE 4: Gravity center transfer distances and angles of urban land and UHI in 1989–2010 in Beijing.

Zones	1989–2000				2000–2010			
	Urban land		UHI		Urban land		UHI	
	Distance	Angle	Distance	Angle	Distance	Angle	Distance	Angle
N	3712.84	72.25	2398.79	74.45	3589.19	71.21	2750.61	18.07
NE	1365.69	61.48	1998.14	163.51	1194.50	61.22	1719.09	67.13
E	4276.40	331.52	480.08	337.33	2361.49	336.04	1483.85	296.58
SE	3731.79	294.68	309.74	328.47	1839.50	300.80	3887.52	276.94
S	7791.64	259.82	2753.14	252.52	2998.27	234.34	2661.15	234.30
SW	773.61	254.10	660.58	331.22	1699.14	198.00	1974.41	271.16
W	1368.30	169.64	4358.77	172.06	1499.32	159.14	1679.55	159.58
NW	3425.77	100.07	1589.25	114.34	2329.85	95.27	693.19	108.85

was the most direct and fundamental driving force of the extension of UHI area.

5. Conclusion

This study explored the relationship between urban form and UHI through GIS spatial analysis. With the superior spatial resolution of the long time sequenced TM/ETM images, the mechanisms involved in generating UHI resulting from urban form could be recognized.

The urban land increased by 775.82 km² at a rate of 184.31% in Beijing during 1989–2010. The urban land distributed like an “E-W” axis in 1989. Urban sprawled in a north-south ward direction in an edge-expansion way in the following two decades, reducing the compactness ratio of urban land. Specifically, the expanding speed index and the expanding intensity slowed down in 2000–2010 than in 1989–2000. The UHIs distributed like an “NE-SW” spindle in Beijing, and the LSTs were obviously higher in the south zone than in the north zone. The LSTs and URIs of urban land in Beijing increased between 1989 and 2010, heat island areas expanded, and the UHI resulting from urban expansion increased obviously.

URI was in high correlation with the urban land area. But at certain urban scale, a more compacted urban form indicated more distinct UHI effect. The gravity centers of UHI and urban land transferred in a basically consistent way. The UHI effect was attributed to the rapid transition from suburban land to urban land. Expansion of urban land also generated larger UHI area than urban area.

The above discoveries about urban form could be very helpful to alleviate urban thermal environment. Urban planning aims at steering land use changes in urban region by assigning new areas for commercial development and residential land and recovering vegetation. The land use changes will inevitably reshape urban form, which in turn alter urban thermal environment. Therefore, an assessment of urban planning policies with regard to effects on urban climate regulation is useful to further integrate them into spatial planning.

Although the paper explored the impact of urban form on UHI, several topics require further investigations. First, the contributions of water bodies and green land inside

the city to the regional LST were not apparent. Increasing greening measures may mitigate UHI effect under the same urban form. Second, the effects of human activities on the urban thermal environment should be investigated to further understand the contributions of urban form to the urban thermal environment.

Conflict of Interests

The authors declare that there is no conflict of interests regarding the publication of this paper.

Acknowledgments

This study was supported by National Key Technology R&D Program of China during the Twelfth Five-Year Plan Period (2012BAC13B01) and the project of National Natural Science Foundation of China under Grant 41071357.

References

- [1] C. Ash, B. R. Jasny, L. Roberts, R. Stone, and A. M. Sugden, “Reimagining cities,” *Science*, vol. 319, no. 5864, p. 739, 2008.
- [2] K. Wang, J. Wang, P. Wang, M. Sparrow, J. Yang, and H. Chen, “Influences of urbanization on surface characteristics as derived from the Moderate-Resolution Imaging Spectroradiometer: a case study for the Beijing metropolitan area,” *Journal of Geophysical Research D: Atmospheres*, vol. 112, no. 22, Article ID D22S06, pp. 1–12, 2007.
- [3] T. R. Oke, “The energetic basis of the urban heat island,” *Quarterly Journal of the Royal Meteorological Society*, vol. 108, no. 455, pp. 1–24, 1982.
- [4] K. P. Gallo, A. L. McNab, T. R. Karl, J. F. Brown, J. J. Hood, and J. D. Tarpley, “The use of a vegetation index for assessment of the urban heat island effect,” *International Journal of Remote Sensing*, vol. 14, no. 11, pp. 2223–2230, 1993.
- [5] A. M. Rizwan, L. Y. C. Dennis, and C. Liu, “A review on the generation, determination and mitigation of Urban Heat Island,” *Journal of Environmental Sciences*, vol. 20, no. 1, pp. 120–128, 2008.
- [6] F. Yuan and M. E. Bauer, “Comparison of impervious surface area and normalized difference vegetation index as indicators of surface urban heat island effects in Landsat imagery,” *Remote Sensing of Environment*, vol. 106, no. 3, pp. 375–386, 2007.

- [7] T. R. Oke, "The urban energy balance," *Progress in Physical Geography*, vol. 12, no. 4, pp. 471–508, 1988.
- [8] J. A. Voogt and T. R. Oke, "Thermal remote sensing of urban climates," *Remote Sensing of Environment*, vol. 86, no. 3, pp. 370–384, 2003.
- [9] X.-L. Chen, H.-M. Zhao, P.-X. Li, and Z.-Y. Yin, "Remote sensing image-based analysis of the relationship between urban heat island and land use/cover changes," *Remote Sensing of Environment*, vol. 104, no. 2, pp. 133–146, 2006.
- [10] U. W. Tang and Z. S. Wang, "Influences of urban forms on traffic-induced noise and air pollution: results from a modelling system," *Environmental Modelling and Software*, vol. 22, no. 12, pp. 1750–1764, 2007.
- [11] Y. Liu, Y. Song, and H. P. Arp, "Examination of the relationship between urban form and urban eco-efficiency in China," *Habitat International*, vol. 36, no. 1, pp. 171–177, 2012.
- [12] T. R. Oke, "City size and the urban heat island," *Atmospheric Environment*, vol. 7, no. 8, pp. 769–779, 1973.
- [13] A. Kondoh and J. Nishiyama, "Changes in hydrological cycle due to urbanization in the suburb of Tokyo Metropolitan area, Japan," *Advances in Space Research*, vol. 26, no. 7, pp. 1173–1176, 2000.
- [14] A. Christen and R. Vogt, "Energy and radiation balance of a central European City," *International Journal of Climatology*, vol. 24, no. 11, pp. 1395–1421, 2004.
- [15] M. Breheny, *Sustainable Development and Urban Form*, Pion Limited, London, UK, 1992.
- [16] G. de Roo and D. Miller, *Compact Cities and Sustainable Urban Development: A Critical Assessment of Policies and Plans from an International Perspective*, Ashgate, Aldershot, UK, 2000.
- [17] R. Ewing, "Is Los Angeles-style sprawl desirable?" *Journal of the American Planning Association*, vol. 63, no. 1, pp. 107–126, 1997.
- [18] J. K. Brueckner, "Urban sprawl: diagnosis and remedies," *International Regional Science Review*, vol. 23, no. 2, pp. 160–171, 2000.
- [19] M. P. Johnson, "Environmental impacts of urban sprawl: a survey of the literature and proposed research agenda," *Environment and Planning A*, vol. 33, no. 4, pp. 717–735, 2001.
- [20] M. Breheny, "The compact city and transport energy consumption," *Transactions of the Institute of British Geographers*, vol. 20, no. 1, pp. 81–101, 1995.
- [21] O. Mindali, A. Raveh, and I. Salomon, "Urban density and energy consumption: a new look at old statistics," *Transportation Research A*, vol. 38, no. 2, pp. 143–162, 2004.
- [22] P. Rickwood, G. Glazebrook, and G. Searle, "Urban structure and energy—a review," *Urban Policy and Research*, vol. 26, no. 1, pp. 57–81, 2008.
- [23] L. O. Marquez and N. C. Smith, "A framework for linking urban form and air quality," *Environmental Modelling and Software*, vol. 14, no. 6, pp. 541–548, 1999.
- [24] J. Huang, X. X. Lu, and J. M. Sellers, "A global comparative analysis of urban form: applying spatial metrics and remote sensing," *Landscape and Urban Planning*, vol. 82, no. 4, pp. 184–197, 2007.
- [25] M. Batty, "New ways of looking at cities," *Nature*, vol. 377, no. 6550, p. 574, 1995.
- [26] P. Frankhauser, "The fractal approach. A new tool for the spatial analysis of urban agglomerations," *Population*, vol. 52, no. 4, pp. 1005–1040, 1997.
- [27] Y. Chen, "Derivation of the functional relations between fractal dimension of and shape indices of urban form," *Computers, Environment and Urban Systems*, vol. 35, no. 6, pp. 442–451, 2011.
- [28] H. Q. Xu and B. Q. Chen, "An image processing technique for the study of urban heat island changes using different seasonal remote sensing data," *Remote Sensing Technology and Application*, vol. 18, no. 3, pp. 129–133, 2003 (Chinese).
- [29] S. Xu, "An approach to analyzing the intensity of the daytime surface urban heat island effect at a local scale," *Environmental Monitoring and Assessment*, vol. 151, no. 1–4, pp. 289–300, 2009.
- [30] Z. Qiao, G. J. Tian, and L. Xiao, "Diurnal and seasonal impacts of urbanization on the urban thermal environment: a case study of Beijing using MODIS data," *Journal of Photogrammetry and Remote Sensing*, vol. 85, pp. 93–101, 2013.
- [31] K. P. Gallo and T. W. Owen, "Assessment of urban heat islands: a multi-sensor perspective for the Dallas-Ft. Worth, USA region," *Geocarto International*, vol. 13, no. 4, pp. 35–41, 1998.
- [32] D. R. Streutker, "A remote sensing study of the urban heat island of Houston, Texas," *International Journal of Remote Sensing*, vol. 23, no. 13, pp. 2595–2608, 2002.
- [33] Q. Weng, "A remote sensing-GIS evaluation of urban expansion and its impact on surface temperature in the Zhujiang Delta, China," *International Journal of Remote Sensing*, vol. 22, no. 10, pp. 1999–2014, 2001.
- [34] J. Nichol and M. S. Wong, "Modeling urban environmental quality in a tropical city," *Landscape and Urban Planning*, vol. 73, no. 1, pp. 49–58, 2005.
- [35] Beijing Statistics Bureau, *Beijing Statistical Yearbook 2010*, China Statistics Press, Beijing, China, 2010.
- [36] X. A. Xia, H. B. Chen, P. C. Wang et al., "Variation of column-integrated aerosol properties in a Chinese urban region," *Journal of Geophysical Research D: Atmospheres*, vol. 111, no. 5, Article ID D05204, 2006.
- [37] J. Zhang, Y. Hou, G. Li, H. Yan, L. Yang, and F. Yao, "The diurnal and seasonal characteristics of urban heat island variation in Beijing city and surrounding areas and impact factors based on remote sensing satellite data," *Science in China D: Earth Sciences*, vol. 48, no. 2, pp. 220–229, 2005 (Chinese).
- [38] Q. S. Ge, J. H. Dai, J. Liu, S. Y. Zhong, and H. T. Liu, "The effect of climate change on the fall foliage vacation in China," *Tourism Management*, vol. 38, pp. 80–84, 2013.
- [39] J. Liu, M. Liu, H. Tian et al., "Spatial and temporal patterns of China's cropland during 1990–2000: an analysis based on Landsat TM data," *Remote Sensing of Environment*, vol. 98, no. 4, pp. 442–456, 2005.
- [40] P. Haggett, A. D. Cliff, and A. Frey, *Locational Analysis in Human Geography*, Edward Arnold, London, UK, 2nd edition, 1977.
- [41] B. Y. Lin, "The calculation method of urban spatial form and its evaluation," *Urban Planning Forum*, vol. 21, no. 3, pp. 42–45, 1998 (Chinese).
- [42] X. Wang, J. Liu, D. Zhuang, and L. Wang, "Spatial-temporal changes of urban spatial morphology in China," *Acta Geographica Sinica*, vol. 60, no. 3, pp. 392–400, 2005 (Chinese).
- [43] P. S. Nivola, *Laws of the Landscape: How Policies Shape Cities in Europe and America*, Brookings Institution Press, Washington, DC, USA, 1999.
- [44] F. Dieleman and M. Wegener, "Compact city and urban sprawl," *Built Environment*, vol. 30, no. 4, pp. 308–323, 2004.

- [45] J. Y. Liu and H. Bu, "Study on spatial-temporal feature of modern land-use change in China: using remote sensing techniques," *Quaternary Sciences*, vol. 20, no. 3, pp. 229–239, 2000 (Chinese).
- [46] H.-Q. Xu and B.-Q. Chen, "Remote sensing of the urban heat island and its changes in Xiamen City of SE China," *Journal of Environmental Sciences*, vol. 16, no. 2, pp. 276–281, 2004.
- [47] J. H. Xu, C. L. Fang, and W. Z. Yue, "An analysis of the mosaic structure of regional landscape using GIS and remote sensing," *Acta Ecologica Sinica*, vol. 23, no. 2, pp. 365–375, 2003 (Chinese).
- [48] S. Q. Zhang, J. Y. Zhang, and F. Li, "Vector analysis theory on landscape pattern in Sanjiang plain marsh, China," *Wetland Science*, vol. 9, no. 3, pp. 161–170, 2004.
- [49] W. Kuang, S. Zhang, Y. Zhang, and Y. Sheng, "Analysis of urban land utilization spatial expansion mechanism in Changchun city since 1900," *Acta Geographica Sinica*, vol. 60, no. 5, pp. 841–850, 2005 (Chinese).
- [50] Y. H. Chen, J. Wang, and X. B. Li, "A study on urban thermal field in summer based on satellite remote sensing," *Remote Sensing for Land and Resources*, vol. 14, no. 4, pp. 55–59, 2002.
- [51] J. E. Nichol, "A GIS-based approach to microclimate monitoring in Singapore's high-rise housing estates," *Photogrammetric Engineering & Remote Sensing*, vol. 60, no. 10, pp. 1225–1232, 1994.
- [52] D. A. Artis and W. H. Carnahan, "Survey of emissivity variability in thermography of urban areas," *Remote Sensing of Environment*, vol. 12, no. 4, pp. 313–329, 1982.
- [53] Q. Weng, "Fractal analysis of satellite-detected urban heat island effect," *Photogrammetric Engineering & Remote Sensing*, vol. 69, no. 5, pp. 555–566, 2003.
- [54] Q. Weng, D. Lu, and J. Schubring, "Estimation of land surface temperature-vegetation abundance relationship for urban heat island studies," *Remote Sensing of Environment*, vol. 89, no. 4, pp. 467–483, 2004.
- [55] Q. Weng and S. Yang, "Managing the adverse thermal effects of urban development in a densely populated Chinese city," *Journal of Environmental Management*, vol. 70, no. 2, pp. 145–156, 2004.
- [56] Q. Weng and S. Yang, "Urban air pollution patterns, land use, and thermal landscape: an examination of the linkage using GIS," *Environmental Monitoring and Assessment*, vol. 117, no. 1–3, pp. 463–489, 2006.
- [57] Q. Weng, "Thermal infrared remote sensing for urban climate and environmental studies: methods, applications, and trends," *ISPRS Journal of Photogrammetry and Remote Sensing*, vol. 64, no. 4, pp. 335–344, 2009.
- [58] T. W. Hawkins, A. J. Brazel, W. L. Stefanov, W. Bigler, and E. M. Saffell, "The role of rural variability in urban heat island determination for Phoenix, Arizona," *Journal of Applied Meteorology*, vol. 43, no. 3, pp. 476–486, 2004.

Research Article

Trends in Moisture Index, Farmland Area, and Their Combined Effects on Grain Production in Northern China

Qingshui Lu,¹ Zhiqiang Gao,¹ Xinliang Xu,² Jicai Ning,¹ and Xiaoli Bi¹

¹ Yantai Institute of Coastal Zone Research, CAS, Yantai, Shandong 264003, China

² State Key Laboratory of Resources and Environmental Information System, Institute of Geographic Sciences and Natural Resources Research, CAS, Beijing 100101, China

Correspondence should be addressed to Xinliang Xu; xuxl@reis.ac.cn

Received 29 November 2013; Revised 17 January 2014; Accepted 16 February 2014; Published 20 March 2014

Academic Editor: Dawei Han

Copyright © 2014 Qingshui Lu et al. This is an open access article distributed under the Creative Commons Attribution License, which permits unrestricted use, distribution, and reproduction in any medium, provided the original work is properly cited.

China policies and Grain-for-Green Project have led to changes in farmland area and grain production. Climate change was also occurring during this period. To analyze the effects of land use and climate change on grain production, the area of farmland in northern China during 1988–2008 was determined from remote sensing images, a moisture index (MI) was calculated from daily meteorological data obtained from weather stations, and unit grain production was obtained from statistical yearbooks. Using statistical and spatial analyses, we determined that MI decreased across most of the study area during this period. This decrease in humidity caused humid zones to decrease and semiarid areas to increase. Combined effects of decreased humid area and conversion of farmland resulted in a decrease in agricultural land in humid areas and an increase in semiarid and arid areas. Increases in unit grain production, machine power, and irrigated farmland area led grain production to increase from 122,799,081 to 188,532,597 ton in humid areas, from 28,875,900 to 115,976,814 in semiarid areas, and from 7,622,100 to 15,490,026 in arid areas, respectively. Increased unit grain production and farmland resulted in increased importance of semiarid areas for grain production.

1. Introduction

Grain production is one of the top priorities for the Chinese government, who has issued a number of policies aimed at maintaining and improving grain production, including “Ten Policies to Further Promote Agricultural Economic Development” in 1985 and “Guidelines to Strengthen Works in Rural Areas” in 1986. These policies encouraged farmers to expand farmland by considering unused land areas. In 1999, the government stopped collecting tax from agricultural products and began to provide subsidies to farmers who planted grains.

In general, those policies caused grain production to increase continuously in China from 1978 to 2000 [1]. However, rapid urbanization caused a significant decline in farmland area. About 17750 km² farmlands were converted to urban use from 1990 to 2010 [2]. The central government launched the Grain-for-Green project in 1999, resulting in

conversion of eroded farmland on slopes to forest or grassland [3–5]. The Ministry of Land Resources has also taken various measures (e.g., farmland replenishing programs) to compensate for loss of farmland by land reclamation [6].

Climate change has also affected agricultural areas in recent decades. The average global surface temperature has increased over the past century by 0.6°C, and precipitation has increased in some regions and decreased in others in the Northern Hemisphere [7]. In China, precipitation increased by 2% from 1950 to 2000 in the south and decreased by 4–11% in the north, while temperature decreased by 1.2°C in the south and increased by 2.5°C in the north [8–10].

Climate zones in northern China are primarily humid, semiarid, and arid. The dynamic spatial patterns of the humidity index in northern China and of farmland characteristics in various moisture zones have not been fully clarified. Grain production is affected by many factors, including climate, chemical fertilizer application, irrigation, cropping

index, and farmland area [11–14]. The combined effects of these factors on the dynamics of grain production remain to be elucidated in northern China. The purpose of this study was to analyze the spatial patterns of the humidity index, changes in farmland area, and their possible effects on grain production.

2. Study Area

Northern China, with ten provinces, three autonomous regions, and two major cities, comprises $5.6 \times 10^6 \text{ km}^2$ and was populated by 0.55 billion inhabitants in 2008 (Figure 1). The average annual temperature varies from -5.5 to 15.3°C , and average annual rainfall is between 5 and 1400 mm. The largest desert (Taklimakan Desert) is located primarily in Xinjiang Autonomous Region. Cropping systems consist mainly of single and double cropping. Single-cropping systems are primarily distributed in the northern part, and double-cropping systems are found in the southern part of this area. The major crops in northern China include rice, corn, wheat, and millet.

3. Data and Methodology

3.1. Data Sources. Three main datasets were used to analyze the effects of humidity and farmland area on grain production. The humidity index was calculated using the Penman-Monteith equation and the Thornthwaite moisture index. The input data were daily maximum and minimum temperatures, daily precipitation, wind velocity, and actual water vapor pressure from 1988 to 2009. Those data were obtained from the 174 weather observation stations in northern China and recorded by the State Meteorological Bureau. The second dataset, comprising farmland cover data in the late 1980s and 2008, was interpreted from Thematic Mapper/Enhanced Thematic Mapper (TM/ETM) images acquired from the United States Geological Survey (USGS) (<http://www.usgs.gov/>). The third dataset, unit grain production, and grain planting area at the district level in 1989 and 2008 were collected from local and state Statistical Bureau yearbooks [15–18]. No grain-production data were available for Inner Mongolia Autonomous Region in 1989, so 1988 data were used.

3.2. Methodology. The moisture index (MI) at each station for each year was calculated by combining the improved Penman-Monteith equation and the Thornthwaite Moisture Index (1) as follows:

$$\text{PET} = \frac{0.408\Delta(R_n - G) + r(900/(T + 273))U_2(e_s - e_a)}{\Delta + r(1 + 0.34U_2)},$$

$$\text{MI} = 100 \times \left(\frac{\text{Precipitation}}{\text{PET}} - 1 \right), \quad (1)$$

where PET is potential evapotranspiration (mm d^{-1}), R_n is net canopy radiation ($\text{MJ m}^{-2} \text{d}^{-1}$), G is soil heat flux ($\text{MJ m}^{-2} \text{d}^{-1}$), T is air temperature at 2 m height ($^\circ\text{C}$), U_2 is wind velocity at 2 m height (m s^{-1}), e_a are actual vapor

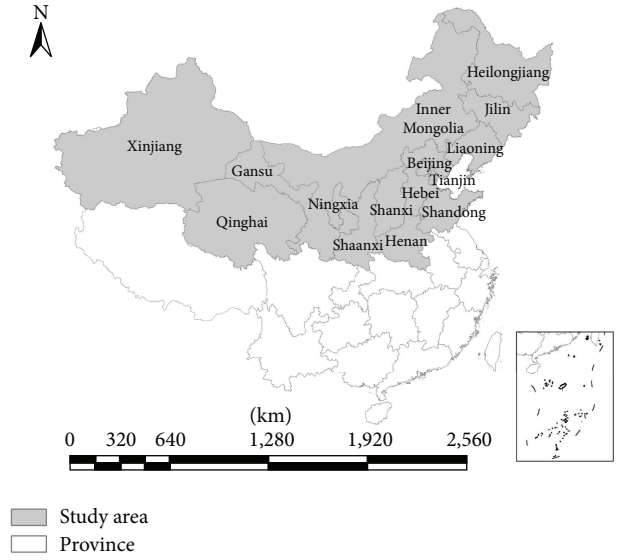


FIGURE 1: Location of study area.

pressure (kPa), Δ is the slope of the saturation vapor pressure curve ($\text{kPa } ^\circ\text{C}^{-1}$), r is the psychrometer constant ($\text{kPa } ^\circ\text{C}^{-1}$), and MI represents the moisture index. The values of T , U_2 , and e_a were obtained from daily weather station data. Recommended FAO values for G , Δ , r , and R_n were used. These values have been widely used for calculating PET.

The MI for all meteorological data in each year was interpolated with ANUSPLINE software to a raster resolution of 100 m. The linear slope of MI in northern China from 1989 to 2008 was calculated using the least-squares method for each pixel in the Economic and Social Research Institute's (ESRI) ArcGIS and was used as the indicator of an average year-to-year trend for each pixel. Positive and negative slopes indicate an overall increase and decrease, respectively, as calculated using

$$S = \frac{n \sum_{i=1}^n m_i x_i - \sum_{i=1}^n m_i \sum_{i=1}^n x_i}{n \sum_{i=1}^n m_i^2 - (\sum_{i=1}^n m_i)^2}, \quad (2)$$

where S is the slope, X_i is the value of precipitation for year i ($i = 1, 2, 3, \dots, n$), and m_i is the sequence number of the year ($m_1 = 1, m_2 = 2, m_3 = 3, \dots$, and $m_n = n$). Positive and negative values indicate increasing and decreasing trends, respectively.

Landsat images covering northern China were preprocessed by correcting for geometric and radiometric distortion. In our previous study, we collected and applied geometric correction to multispectral scanner (MSS) data from the 1980s; these MSS data were used for geometric correction of the Landsat data (late 1980s and 2008). Human-machine interaction interpretation was performed on remote sensing images using ESRI's ArcGIS 9.3 platform. Land cover was classified into six categories: farmlands (cultivated for crops), woodlands (covered with trees including arbors, shrubs, and forestry plantations), grasslands (covered by herbaceous plants), water bodies (natural or facilities for irrigation and water containment), unused lands (areas not

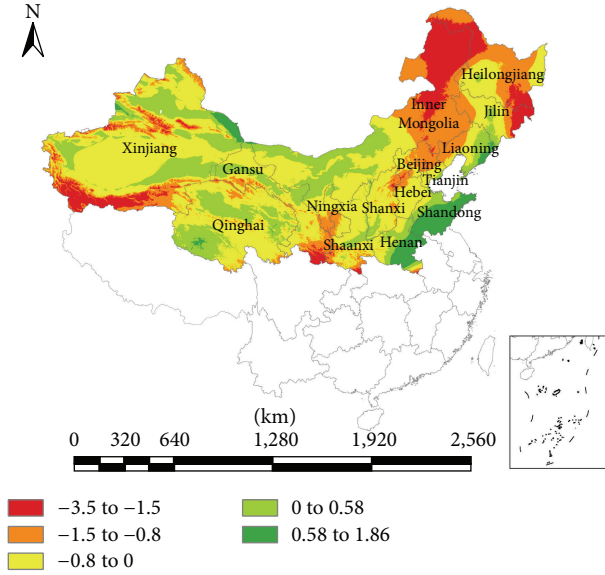


FIGURE 2: Slope of moisture index in northern China from 1989 to 2008.

put into practical use or that are difficult to use), and built environment areas (urban and rural settlements, factories, and transportation facilities). Farmland area in the late 1980s and 2008 was extracted from these combined data.

Total grain production is affected by unit grain production and planting area. Farmland area and grain cropping index are the main factors that determine grain planting area. The grain cropping index was calculated using

$$PI = \frac{A_g}{A_f}, \quad (3)$$

where PI is the cropping index, A_g is the grain planting area (ha), and A_f is the area of farmland in a certain area (ha).

Northern China was classified into three moisture regions according to Feddema [19] and Grundstein [20]. Regions with MI less than -66 were classified as arid, those with MI between -66 and -33 were classified as semiarid, and those with MI greater than -33 were classified as humid. The spatial analysis function of ESRI's ArcGIS was used to analyze the individual and combined effects of moisture index, farmland area, unit grain production, and planting index on grain production.

4. Results and Analysis

4.1. Moisture Index. Daily weather observation data were input into (1) to obtain MI data for 1988–2009 for northern China, and the linear slope of MI from 1989 to 2008 was calculated. MI tended to decrease in most areas (Figure 2), with the most rapid decrease mainly occurring in northeastern areas. Increases in MI occurred in the southeast, north, and some middle areas of northern China.

Annual MI values in northern China for 1988–1990 were considered as the 1989 MI value, and MI values for 2007–2009 were considered as the 2008 value. The mean 1989

TABLE 1: Area of humid, semiarid, and arid zones in northern China.

Humidity region	1989 (ha)	2008 (ha)	Percent change
Humid areas	283,915,219	219,482,992	-22.7
Semiarid areas	105,227,195	153,469,562	45.8
Arid areas	173,833,567	190,023,428	9.3

Note: minus means decrease.

TABLE 2: Area of farmland in humid, semiarid, and arid zones in northern China.

Humidity region	The late 1980s		2008	
	Area (ha)	Percent (%)	Area (ha)	Percent (%)
Humid	70,778,220	72.0	52,196,864	51.0
Semiarid	20,403,300	20.8	40,440,571	39.5
Arid	7,088,430	7.2	9,663,439	9.4
Total	98,269,950	100	102,300,874	100

and 2008 MI values were used to classify areas into humid, semiarid, and arid zones (Figure 3). Humid zones were mainly concentrated in the southern and eastern parts of the study area, with only a small portion in the far northwestern part.

Trends in MI during the study period revealed that humid zones decreased and semiarid and arid zones increased (Table 1 and Figure 3). Humid areas decreased from 283,915,219 ha in 1989 to 219,482,992 ha in 2008, with a decrease of 22.7%. The decrease in humid areas occurred mainly in the middle and northeastern parts of northern China. The area of semiarid zones in 1989 was 105,227,195 ha and increased to 153,469,562 ha, with an increase of 45.8%. The increased semiarid areas mainly occurred in the middle and northeastern parts of northern China. The area of arid zones in 1989 was 173,833,567 ha and increased to 190,023,428 ha in 2008, with an increase of 9.3%. The increase in arid areas occurred mainly in the western part of northern China.

4.2. Farmland Changes. The results of visual interpretation of remote sensing images are presented in Figure 4 and Tables 2 and 3. Farmland is distributed primarily in the eastern and southern parts of northern China. The area of farmlands in the late 1980s was 98,269,950 ha (Table 2), with 70,778,220, 20,403,300, and 7,088,430 ha in humid, semiarid, and arid areas, respectively (Table 2). The net effect of the expansion of farmland and loss of farmed area to urbanization was an increase in agricultural area to 102,300,874 ha in 2008. This net increase suggests that the area of farmland expansion was greater than that of farmland loss.

The rapid expansion of urban areas occurred mostly in eastern China (Figure 5(a)). Approximately 3,808,569 ha of farmland were converted to urban area from the late 1980s to 2008 (Table 3). Most conversion of farmland to urban areas occurred in humid areas because these areas have a greater proportion of the population and a stronger economy.

The area of other land-use categories converted to farmland from the late 1980s to 2008 was 19,078,701 ha (Table 3). In the 1980s, urbanization and industrialization in China were

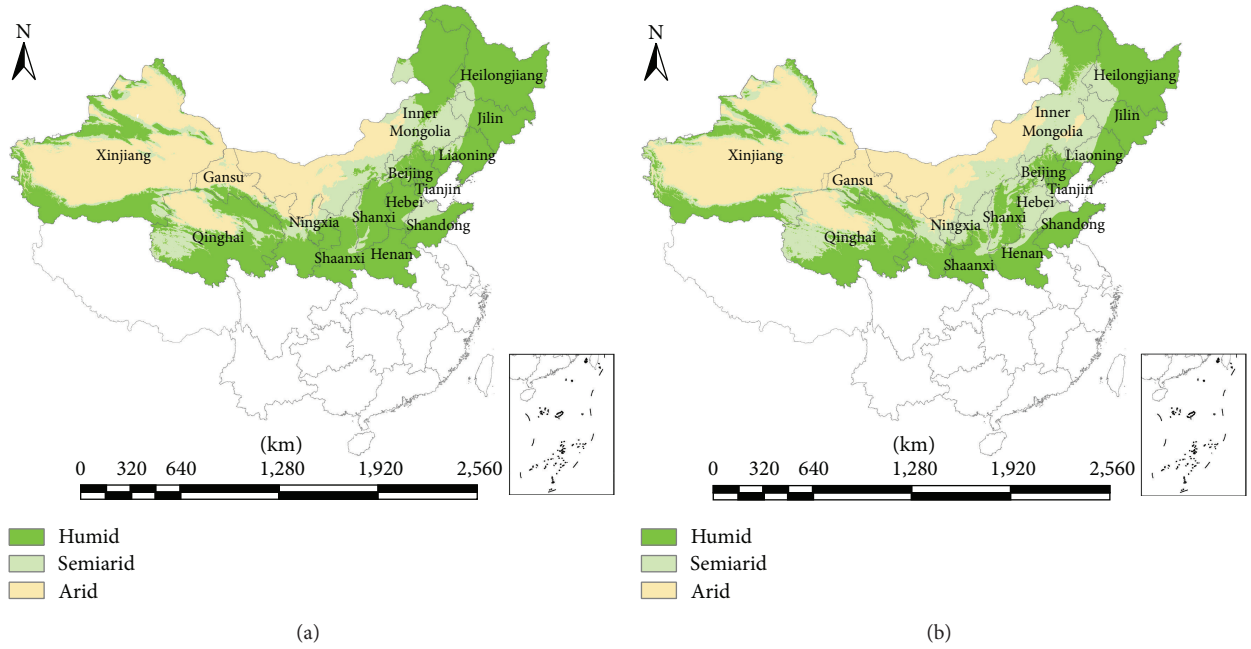


FIGURE 3: Humid, semiarid, and arid zones in northern China: (a) 1989 and (b) 2008.

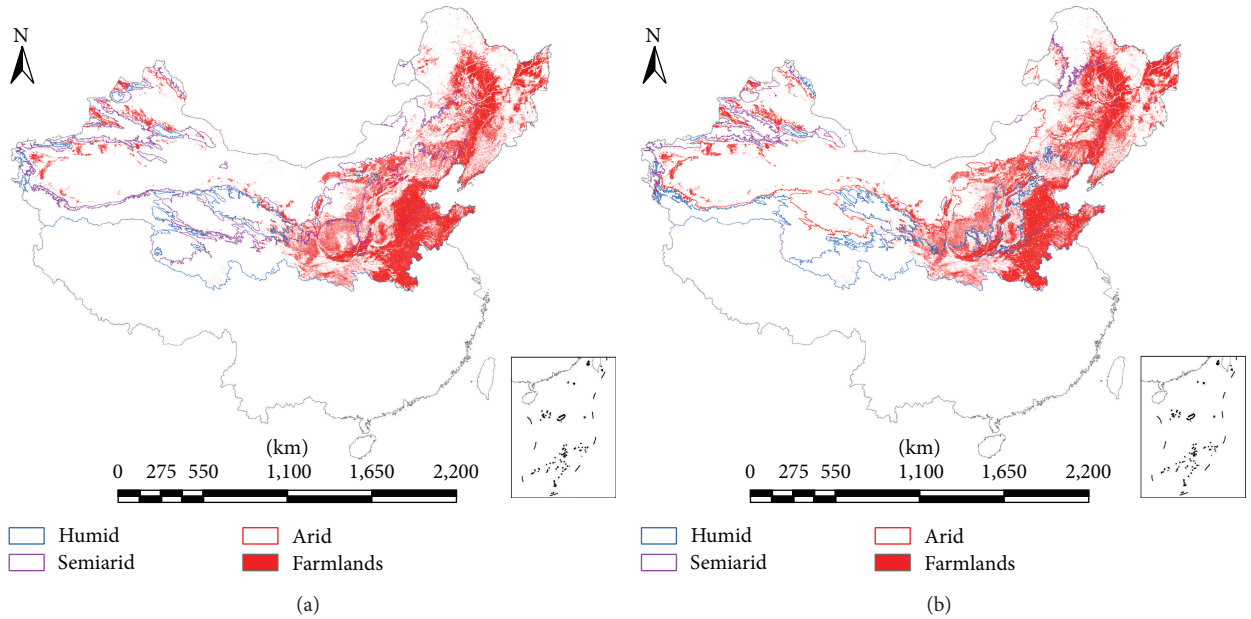


FIGURE 4: Farmland in northern China: (a) the late 1980s and (b) 2008.

TABLE 3: Conversion between farmland and other land-use categories from the late 1980s to 2008.

Humid region	Conversion from farmland to urban area		Conversion from farmland to other land		Conversion from other land uses to farmland	
	Area (ha)	Percent (%)	Area (ha)	Percent (%)	Area (ha)	Percent (%)
Humid	2,832,457	74.4	10,179,839	67.5	11,843,001	62.1
Semi-arid	726,516	19.1	3,668,100	24.3	4,542,250	23.8
Arid	249,596	6.6	1,232,730	8.2	2,693,450	14.1
Total	3,808,569	100	15,080,669	100.0	19,078,701	100.0

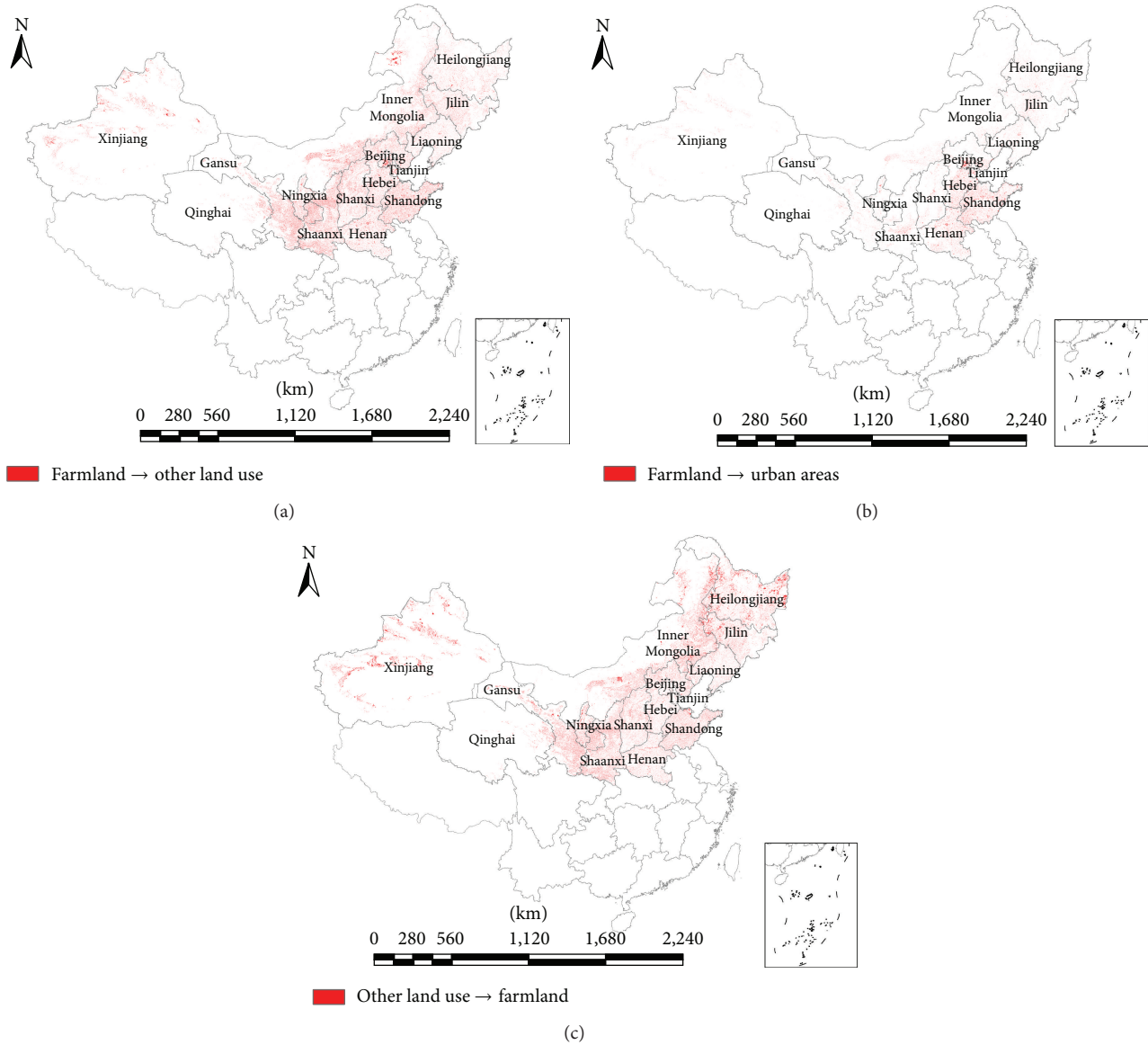


FIGURE 5: Farmland dynamics from the late 1980s to 2008: (a) conversion from farmland to urban areas, (b) conversion from farmland to other land-use types, and (c) conversion from other land-use types to farmland.

still occurring at relatively low rates, and the government's priority was to maintain and improve grain production. The Chinese central government issued policies to ensure sufficient grain production to meet the increasing demand, causing farmland area to increase.

In contrast, the area of farmland that was converted to other land uses during this period was 15,080,669 ha, and most of this conversion took place from 1999 to 2008. The expansion of farmland before 1999 resulted in severe soil erosion, and the government launched the Grain-for-Green project in 1999 to promote conversion of eroded farmland to other land-use categories, such as forest or grassland.

Farmland area tended to increase from the late 1980s to 2008. The decreased humidity index indicated that semiarid and arid areas expanded in the middle and western parts of

northern China. The combined effects of decreased MI and changes in farmland area resulted in a lower percentage of cropland in humid areas and a higher percentage in semiarid and arid areas by 2008.

4.3. Grain Production. Grain production at the district level in the late 1980s and 2008 was calculated and analyzed with MI in ArcGIS (Table 4). Northern China produced 159,297,081 t in the late 1980s, and the percentage of grain production produced in humid areas was higher than that produced in semiarid and arid areas (Table 4).

Conversion of farmland to other land-use categories led to a loss in grain yield, which was estimated by average yield in 2008 at the district level (Table 5). Conversion of

TABLE 4: Grain production in the late 1980s and 2008.

Grain production	The late 1980s		2008		Percent increase (%) (late 1980s–2008)
	Tons	Percent (%)	Tons	Percent (%)	
Humid zone	122,799,081	77.1	188,532,597	58.9	53.5
Semiarid zone	28,875,900	18.1	115,976,814	36.2	301.6
Arid zone	7,622,100	2.4	15,490,026	4.8	103.2
Total	159,297,081	100	319,999,437	100	100.9

TABLE 5: Grain production changes from farmland conversion from the late 1980s to 2008.

Humid zone	Grain production change					
	Conversion of farmland to urban areas		Conversion of farmland to other land		Conversion of other land uses to farmland	
	Tons	Percent (%)	Tons	Percent (%)	Tons	Percent (%)
Humid	-14,593,629	-76.4	-38,795,588	-67.2	46,928,732	58.9
Semiarid	-3,305,860	-17.3	-12,558,400	-21.7	17,639,600	22.1
Arid	-1,205,870	-6.3	-6,411,010	-11.1	15,108,800	19.0
Total	-19,105,359	100	-57,764,998	100	79,677,132	100

farmland to urban areas caused grain production to decrease by 19,105,359 t, and conversion to other land-use categories caused grain production to decrease by 57,764,998 t (Table 5 and Figure 6). Urbanization corresponding to a 0.04% loss of farmland resulted in a 0.06% decrease in grain production across northern China (Figure 6), indicating higher unit grain production in agricultural areas. Conversion of other land-use categories to farmland led to increased grain production, by 79,677,132 t from 1989 to 2008. The net effect of these changes in land use was a slight increase in grain production in northern China.

Grain production in northern China increased from the late 1980s to 2008 (Table 4). Expanded farmland and improved management were the main factors causing the rapid increase in grain production in semiarid areas.

5. Discussion

5.1. Factors That Caused MI Changes. The moisture index tended to decrease in most of the study area and to increase in the southeastern and some western and middle parts of northern China from 1989 to 2008. Temperature and precipitation were the main factors causing these changes. The Juxian, Yuxian, and Kuerle weather observation stations were selected for analysis of the causes of increased MI in humid areas and of decreased MI in semiarid and arid areas (Figures 7–9).

Annual precipitation increased at Juxian station during the study period and decreased at the other stations. The slope of annual precipitation at Juxian station from 1989 to 2008 was 6.6696; annual precipitation in 1989 was 504 mm, increasing to 765.8 mm in 1999 and 841.5 mm in 2008. The slope of annual precipitation at Yuxian station was -3.026. Its annual precipitation was 382 mm in 1989, decreasing to 270.8 mm in 1999 and 289.5 mm in 2006. The slope of

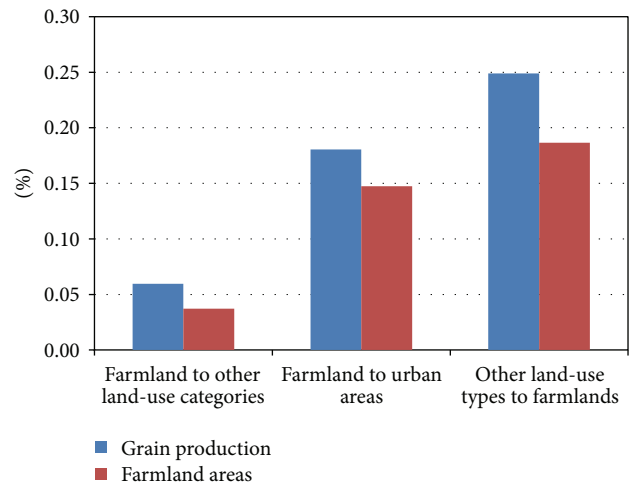


FIGURE 6: Relationship between percentage of farmland area and grain yield.

annual precipitation at Kuerle station was -0.877. Its annual precipitation was 84.4 mm in 1989, decreasing to 78.3 mm in 1996 and 69.5 mm in 2008.

The mean daily temperature showed an increasing trend at all of the weather stations (Figure 8). At Yuxian station, mean daily temperature was 7.3°C in 1989 and increased to 8.2°C in 2000 and 9.1°C in 2007. The mean daily temperature at Kuerle station in 1989, 1998, and 2008 was 12.0, 12.1, and 12.4°C, respectively, and the corresponding values at Juxian station were 12.3, 12.4, and 12.9°C.

The annual PET showed an increasing trend at all of the weather stations (Figure 10). At Yuxian station, annual PET was 630 mm in 1989 and increased to 679 mm in 1999 and 764 mm in 2007. The annual PET at Kuerle station in 1989,

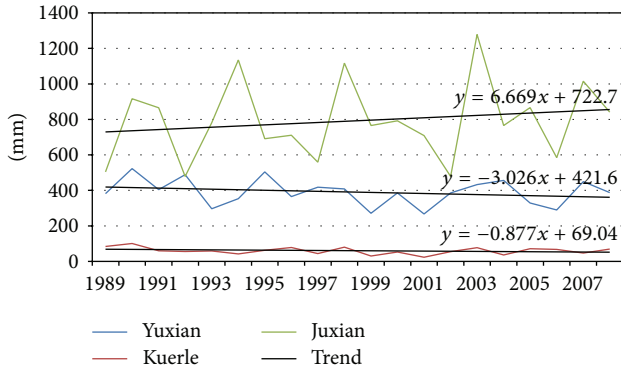


FIGURE 7: Precipitation recorded at the selected weather stations from 1989 to 2008.

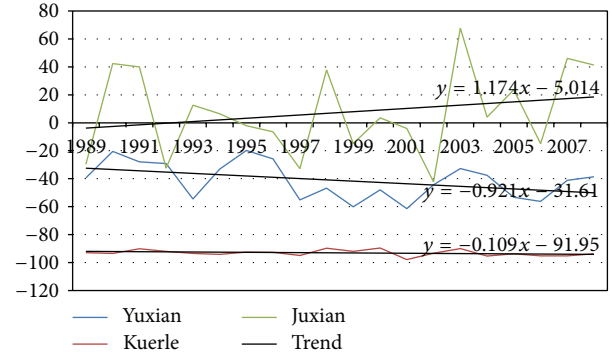


FIGURE 9: Moisture index at the selected weather stations from 1989 to 2008.

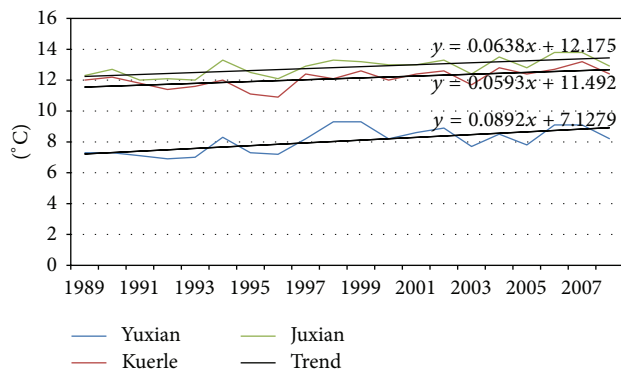


FIGURE 8: Temperature recorded at the selected weather stations from 1989 to 2008.

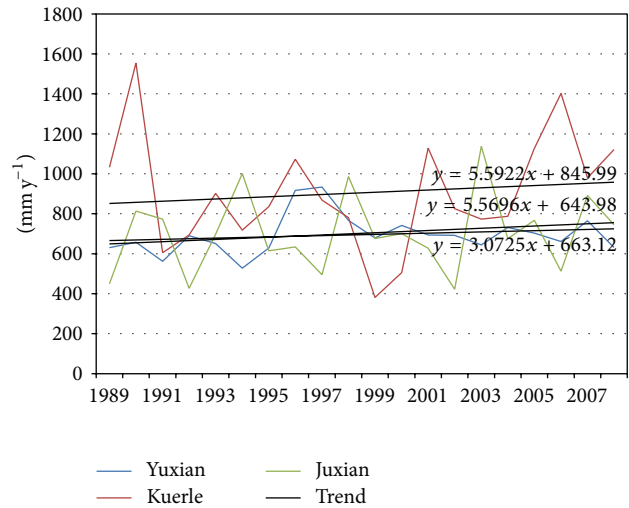


FIGURE 10: PET at the selected weather stations from 1989 to 2008.

1996, and 2008 was 1033, 1072, and 1120 mm, respectively. The annual PET at Juxian station in 1989, 1999, and 2008 was 449, 676, and 745 mm, respectively.

The overall effect of the increased temperature, PET, and precipitation observed at Juxian weather station was an increase in the humidity index such that the annual MI was -29.7 in 1989 and increased to -14.9 in 1999 and 41.3 in 2008. These values indicate that increased annual precipitation was the main factor in the increased MI in the eastern and southern parts of northern China. However, the combined results of increased temperature, PET, and decreased precipitation caused a decrease in MI at the other two stations. At Yuxian, the annual MI was -39.4 in 1989 and decreased to -55.2 in 1997 and -56.2 in 2006; the annual MI at Kuerle was -92.9 in 1989, -94.9 in 1997, and -95.2 in 2007. In combination, the decreased annual precipitation and increased temperature led to decreased MI across most of northern China (Figure 9).

5.2. Grain Production Dynamics and Its Driving Forces. Grain production increased in all areas of northern China from 1989 to 2008. The reasons for this trend included increased farmland area (Table 2) and increased unit grain yield (Table 6). Unit grain yield is affected by many factors, including temperature, precipitation, chemical fertilizer, unit grain yield,

and grain planting area [21–24]. We further analyzed the main factors causing changes in unit grain yield in Yuxian and Juxian counties and determined that the cropping index and irrigated areas decreased in Juxian, indicating that the increased unit grain yield was mainly caused by chemical fertilizer application and increased machine power. In Yuxian County, the cropping index decreased, whereas unit grain yield and other factors increased. Thus, it can be concluded that the increased unit grain yield in semiarid areas was mainly caused by increased chemical fertilizer application, machine power, and percentage of irrigated farmland area.

6. Conclusions

The moisture index in northern China was calculated from daily weather observations at meteorological stations from 1988 to 2008. Farmland area during this time period was determined by visual interpretation of remote sensing images, and grain production at the district level was obtained from statistical data. Using spatial and statistical analyses, we determined that MI decreased across most of northern China and increased only in southeastern areas and some

TABLE 6: Factors that affect grain yield.

County	Year	Unit grain yield (kg/ha)	Cropping index	Chemical fertilizer applied (kg/ha)	Total power of agricultural machinery (W/ha)	Percentage of irrigated area (%)
Juxian	1989	4,635	1.22	304.3	2,648.2	53.9
	2008	6,382.6	0.78	1455.5	10,166.2	50.0
Yuxian	1989	809.8	0.75	65.1	688.3	25.4
	2008	911.0	0.73	106.9	3,453.0	35.0

parts of the middle of northern China during the study period. Decreased MI caused humid zones to decrease and semiarid and arid zones to increase. Loss of farmland due to urbanization mainly occurred in humid areas of eastern China. The combined effects of decreased MI and land-use changes led to a lower percentage of cropland in humid areas and a higher percentage of cropland in semiarid and arid areas by 2008. Unit grain yield increased in northern China. Increased unit grain yield in humid and semiarid areas was mainly caused by chemical fertilizer application and increased machine power; in semiarid areas, increased irrigation also contributed to the increase in unit grain yield. Expanded farmland and increased unit grain yield caused grain production to increase continuously and resulted in increased importance of grain production in semiarid areas.

Conflict of Interests

The authors declare that there is no conflict of interests in this paper.

Acknowledgments

This work is supported by Key Research Program of the Chinese Academy of Sciences (KZZD-EW-14), National Natural Science Foundation of China (41171334 and 41301596), Talent Fund of Yantai Institute of Coastal Zone Research, Ecological Innovation and Breeding Project (Y254021031, Y355031061), and the Science and Technology Project of Yantai (2012132).

References

- [1] State Statistic Bureau, *Statistic Yearbook*, China Statistic Press, Beijing, China, 2010.
- [2] L. Wang, C. C. Li, X. Cheng et al., "China's urban expansion from 1990 to 2010 determined with satellite remote sensing," *Chinese Science Bulletin*, vol. 57, no. 22, pp. 2802–2812, 2012.
- [3] Z. Feng, Y. Yang, Y. Zhang, P. Zhang, and Y. Li, "Grain-for-green policy and its impacts on grain supply in West China," *Land Use Policy*, vol. 22, no. 4, pp. 301–312, 2005.
- [4] X. Wang, C. Lu, J. Fang, and Y. Shen, "Implications for development of grain-for-green policy based on cropland suitability evaluation in desertification-affected north China," *Land Use Policy*, vol. 24, no. 2, pp. 417–424, 2007.
- [5] L. Qingshui, F. Y. Liang, Z. Q. Gao, and J. C. Ning, "Influences of the Grain-for-Green project on grain security in southern China," *Ecological Indicators*, vol. 34, pp. 616–622, 2013.
- [6] C. Ding, "Land policy reform in China: assessment and prospects," *Land Use Policy*, vol. 20, no. 2, pp. 109–120, 2003.
- [7] C. K. Folland, T. R. Karl, J. R. Christy et al., "Observed climate variability and change," in *Climate Change*, The Scientific Basis, Cambridge University Press, Cambridge, UK, 2001, Contribution of Working Group I to the Third Assessment Report of the Intergovernmental Panel on Climate Change.
- [8] B. Liu, M. Xu, M. Henderson, and Y. Qi, "Observed trends of precipitation amount, frequency, and intensity in China, 1960–2000," *Journal of Geophysical Research D: Atmospheres*, vol. 110, no. 8, pp. 1–10, 2005.
- [9] W. Qian and A. Qin, "Precipitation division and climate shift in China from 1960 to 2000," *Theoretical and Applied Climatology*, vol. 93, no. 1-2, pp. 1–17, 2008.
- [10] K. Xu, J. D. Milliman, and H. Xu, "Temporal trend of precipitation and runoff in major Chinese Rivers since 1951," *Global and Planetary Change*, vol. 73, no. 3-4, pp. 219–232, 2010.
- [11] E. Kunzová and M. Hejcman, "Yield development of winter wheat over 50 years of FYM, N, P and K fertilizer application on black earth soil in the Czech Republic," *Field Crops Research*, vol. 111, no. 3, pp. 226–234, 2009.
- [12] M. Miransari and A. F. Mackenzie, "Wheat grain nitrogen uptake, as affected by soil total and mineral nitrogen, for the determination of optimum nitrogen fertilizer rates for wheat production," *Communications in Soil Science and Plant Analysis*, vol. 41, no. 13, pp. 1644–1653, 2010.
- [13] X. Wei, C. Declan, L. Erda et al., "Future cereal production in China: the interaction of climate change, water availability and socio-economic scenarios," *Global Environmental Change*, vol. 19, no. 1, pp. 34–44, 2009.
- [14] L. You, M. W. Rosegrant, S. Wood, and D. Sun, "Impact of growing season temperature on wheat productivity in China," *Agricultural and Forest Meteorology*, vol. 149, no. 6-7, pp. 1009–1014, 2009.
- [15] State Statistic Bureau, *Statistic Yearbook*, China Statistic Press, Beijing, China, 1990.
- [16] State Statistic Bureau, *Statistic Yearbook*, China Statistic Press, Beijing, China, 2009.
- [17] Local Statistic Bureau, *Statistic Yearbook*, China Statistic Press, Beijing, China, 1989-1990.
- [18] Local Statistic Bureau, *Statistic Yearbook*, China Statistic Press, Beijing, China, 2009.
- [19] J. J. Feddema, *Evaluation of Terrestrial Climate Variability Using A Moisture Index*, vol. 47 of *Publications in Climatology*, 1994.
- [20] A. Grundstein, "Evaluation of climate change over the continental United States using a moisture index," *Climatic Change*, vol. 93, no. 1-2, pp. 103–115, 2009.
- [21] K. Neumann, P. H. Verburg, E. Stehfest, and C. Müller, "The yield gap of global grain production: a spatial analysis," *Agricultural Systems*, vol. 103, no. 5, pp. 316–326, 2010.
- [22] X. Zhang, S. Chen, H. Sun, D. Pei, and Y. Wang, "Dry matter, harvest index, grain yield and water use efficiency as affected by

water supply in winter wheat," *Irrigation Science*, vol. 27, no. 1, pp. 1–10, 2008.

- [23] Y. Chen, X. Li, and J. Wang, "Changes and effecting factors of grain production in China," *Chinese Geographical Science*, vol. 21, no. 6, pp. 676–684, 2011.
- [24] G. Pan, P. Zhou, Z. Li et al., "Combined inorganic/organic fertilization enhances N efficiency and increases rice productivity through organic carbon accumulation in a rice paddy from the Tai Lake region, China," *Agriculture, Ecosystems and Environment*, vol. 131, no. 3-4, pp. 274–280, 2009.

Research Article

Evaluating the Marginal Land Resources Suitable for Developing Bioenergy in Asia

Jingying Fu,^{1,2} Dong Jiang,¹ Yaohuan Huang,¹ Dafang Zhuang,¹ and Wei Ji^{1,2}

¹ State Key Laboratory of Resources and Environmental Information Systems,
Institute of Geographical Sciences and Natural Resources Research, Chinese Academy of Sciences, Beijing 100101, China

² University of Chinese Academy of Sciences, Beijing 100049, China

Correspondence should be addressed to Dong Jiang; jiangd@igsrr.ac.cn

Received 23 October 2013; Revised 11 December 2013; Accepted 10 January 2014; Published 13 March 2014

Academic Editor: Shengli Huang

Copyright © 2014 Jingying Fu et al. This is an open access article distributed under the Creative Commons Attribution License, which permits unrestricted use, distribution, and reproduction in any medium, provided the original work is properly cited.

Bioenergy from energy plants is an alternative fuel that is expected to play an increasing role in fulfilling future world energy demands. Because cultivated land resources are fairly limited, bioenergy development may rely on the exploitation of marginal land. This study focused on the assessment of marginal land resources and biofuel potential in Asia. A multiple factor analysis method was used to identify marginal land for bioenergy development in Asia using multiple datasets including remote sensing-derived land cover, meteorological data, soil data, and characteristics of energy plants and Geographic Information System (GIS) techniques. A combined planting zonation strategy was proposed, which targeted three species of energy plants, including *Pistacia chinensis* (*P. chinensis*), *Jatropha curcas* L. (*JCL*), and *Cassava*. The marginal land with potential for planting these types of energy plants was identified for each 1 km² pixel across Asia. The results indicated that the areas with marginal land suitable for *Cassava*, *P. chinensis*, and *JCL* were established to be 1.12 million, 2.41 million, and 0.237 million km², respectively. Shrub land, sparse forest, and grassland are the major classifications of exploitable land. The spatial distribution of the analysis and suggestions for regional planning of bioenergy are also discussed.

1. Introduction

The world is facing problems related to finite availability of fossil fuels, the high price of petroleum, and the environmental impacts caused by the use of traditional fuels. The energy consumption of the world increased from 77,245 thousand barrels per day in 2001 to 88,034 thousand barrels per day in 2011. Asia Pacific accounted for 32% of the total world energy consumption [1]. This increase in energy demand is depleting fossil energy reserves at a high rate. In addition, the use of fossil fuels has caused many environmental problems, such as greenhouse gas (GHG) emissions. Therefore, energy security and climate change mitigation are two main drivers that have pushed renewable energy production to the top of the global agenda [2].

Bioenergy, the most abundant and versatile type of renewable energy, has recently attracted worldwide attention [3]. Biofuels are environmentally friendly and carbon neutral and can play a prominent role in the energy portfolio [4].

The production of liquid biofuels can reduce GHG emissions by 12%–115% compared to traditional fossil fuels. GHG emissions are reduced 12% by the production and combustion of ethanol and 41% by biodiesel according to Hill et al. [5]. Adler et al. found that ethanol and biodiesel reduced GHG emissions by approximately 40% when derived from corn, by approximately 85% when from reed canary grass, and by approximately 115% when from hybrid switch grass and poplar [6]. The global warming potential (GWP, in kg CO₂-equivalent) of the production of biodiesel in the UK was calculated Stephenson et al. The results showed that large-scale production of biodiesel saved 26% of the GWP and small-scale production saved 32% of the GWP when compared to ultralow sulphur diesel [7].

The present global biomass demand for energy purposes is estimated to be 53 Quintillion joules [8]. Overall, global energy demand will grow 35%, even with significant efficiency gains. Energy demand in developing nations will rise 65 percent by 2040 (compared to 2010) as a result of

expanding economies and growing populations. According to the new public energy outlook, 75 percent of the world's population will reside in Asia Pacific and Africa by 2040. India will have the largest population after 2030 [9]. A wide range of indicators suggest that dramatic developments are taking place in Asian energy markets [10], and large-scale bioenergy development is extremely urgent.

Recently, a number of studies have assessed the potential of biofuel. Kumar et al. assessed ethanol and biodiesel development in Thailand in terms of feedstock, production, planned targets, policies, and sustainability (environmental, socioeconomic, and food security aspects) [11]. An assessment of bioenergy potential was also carried out in England, the Midwest United States, China, and other countries [12–15]. The environmental life cycle assessment of lignocellulosic conversion to ethanol was reviewed by Borrion et al. Numerous studies of lignocellulosic ethanol fuel generated significantly different results due to differences in data, methodologies, and local geographic conditions [16]. In addition to feedstock, energy benefits, and GHG reductions, issues related to land resources and food security are an important consideration for Asia-scaled applications.

Schröder et al. considered bioenergy development as an effective way to save the world from an energy crisis. They illustrated the ability to produce novel energy plants for growth on abandoned land [17]. Liu et al. analyzed the bioenergy production potential on marginal land in Canada. The results showed that approximately 9.48 million hectares could be identified as available marginal land in Canada. If this land was fully utilized for growing energy crops, the production of biofuel would be 33 million tons (using switch grass) or 380 million tons (using hybrid poplar). Batidzirai et al. reviewed the current, state-of-the-art approaches and methodologies used in bioenergy assessments and identified key elements that are critical determinants of bioenergy potentials. Bioenergy potential assessments in the US, China, India, Indonesia, and Mozambique were also presented in the paper [18]. Hattori and Morita [19] studied which energy crops can be used for sustainable bioethanol production and where they can be grown. They found that, in Japan and other Asian countries, rice can be grown as an energy crop in unused low-land paddy fields. Bioenergy development in China has also been studied, especially the potential energy production on marginal land in the context of food security [3, 20–22]. The biomass plant *Jatropha curcas L.* (*JCL*) was shown to be a better economic, environmental, and land preservation alternative to corn or millet planted in the poor, gravel soil, and drought land in Taitung, Taiwan [23].

However, the bioenergy development in the above-mentioned studies and most other current research is studied on a regional scale. A potential bioenergy view of the entirety of Asia is not available. The main objective of this study is to present a comprehensive assessment on the marginal land resources which are suitable for developing bioenergy in Asia, without affecting food and environmental security. Asia is the world's largest and most populous continent. It is facing significant pressure for food production. To avoid using the limited amount of arable land, adaptable energy plants that can be grown on marginal land and at scale must

be used. *Cassava*, *P. chinensis*, and *JCL* have been widely proven in existing literature and are further studied in this paper [14, 24–34]. *P. chinensis* and *JCL* are nonfood plants. *Cassava* is used as a food plant in some places. However, we only analyzed its development potential in uncultivated areas (marginal land).

Cassava and *JCL* are classified as second-generation biofuel feedstock, which are derived from crop residues, energy plants, and construction waste [35]. They can reduce GHG emissions and energy dependency during the life cycle when compared to the fossil fuel. The most important advantage of second-generation biofuels is that they will ensure the security of food supply compared with first-generation biofuels which are produced from food-based crops. They are sustainable and environmentally friendly [36]. Bioethanol is produced by hydrolysis and fermentation of carbohydrate feedstock. This type of energy plant usually has high saccharide, starch, and fiber content. *Cassava* which has been widely studied is this kind of plant. Biodiesel is produced from oil plants such as *JCL*. The oil extracted is blended with diesel to produce fuel [34, 37–47].

To achieve our goal, we used Geographic Information System (GIS) technology to identify the spatial distribution of marginal lands which are suitable for bioenergy development. The datasets of growth habits of energy plants, remote sensing-derived land cover, terrain, meteorological data, and soil data were processed to 1 km² grid across Asia.

2. Methodology

Four steps were implemented for this study. First, we identified the marginal land resources suitable for developing bioenergy in Asia. Second, we chose the three aforementioned energy plants that have been proven as biofuels. Third, we reviewed the environmental requirements of each energy plant including preferred meteorological conditions, soil, and terrain. Finally, a multiple factor analysis method was used to evaluate the bioenergy development potential based on the availability of marginal land resources and the growing conditions of the energy plants within the data grid. This analysis was performed using ArcMap software. The specific procedures are presented in Figure 1.

2.1. Data Acquisition. In this study, the land cover, terrain (including elevation and slope), meteorological conditions (including precipitation and temperature), and soil data (including soil organic matter content, soil depth, and soil texture) were used. The data sources and spatial resolutions are listed in Table 1. All the data in this study was resampled to cover the entirety of Asia at a 1 km² resolution.

2.1.1. Land Cover. Land resources defined as marginal must also include land that is considered economically marginal. Therefore, we spatially define marginal land resources based on the land cover classification of unused land. The land cover dataset can be obtained from the GlobCover project. There are 23 land cover types in the dataset. This is the fundamental

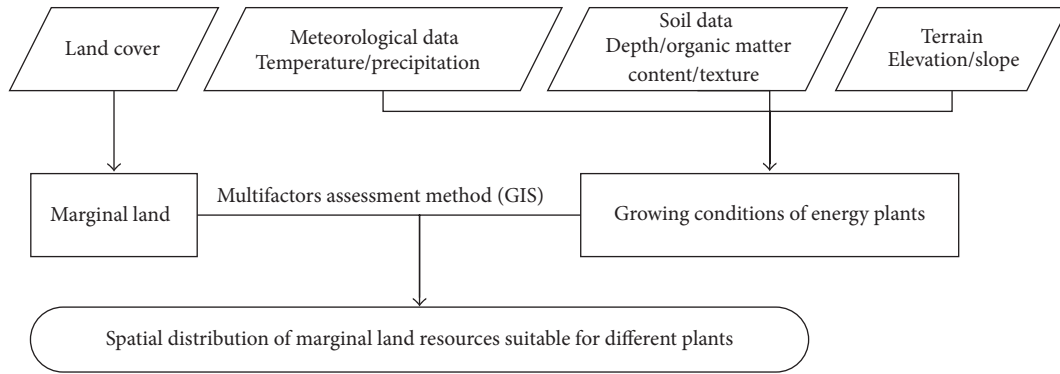


FIGURE 1: Evaluation of spatial distribution and suitability of marginal land resources for energy plants.

TABLE 1: Input data for identification of marginal land resources.

Input data	Data sources	Original spatial resolution
Land cover	ESA 2010 and UCLouvain [48]	1 km
Terrain		
Elevation		90 m
Slope	SRTM [49]	90 m
Meteorological data		
Precipitation		30 arc-seconds (~1 km)
Temperature	WorldClim [50]	30 arc-seconds (~1 km)
Soil data		
Organic matter content		30 arc-seconds (~1 km)
Soil depth	FAO/IIASA/ISRIC/ISS-CAS/JRC [51]	30 arc-seconds (~1 km)
Soil texture		30 arc-seconds (~1 km)

dataset for identification of marginal land that is suitable for bioenergy development.

2.1.2. Terrain. The CGIAR-CSI GeoPortal provides SRTM 90 m digital elevation data for the entire world [49]. The digital elevation models (DEMs) of Asia were extracted from the dataset above, and the slope was calculated using the spatial analysis tool in ArcMap. Thresholds for DEMs and slope, based on the growth habits of each energy plant, were determined (see Section 2.2).

2.1.3. Meteorological Data. WorldClim is a set of global climate layers (climate grids) with a spatial resolution of 30 arc-seconds (often referred to as 1 km resolution). The precipitation and temperature data used in this study were interpolated from observed data from 1950 to 2000 [50]. These two elements are very important for identifying suitable land. The requirement of each energy plant was identified (see Section 2.3).

2.1.4. Soil Data. The Harmonized World Soil Database (HWSD) contributes sound scientific knowledge for planning sustainable expansion of agricultural production and for guiding policies to address emerging land competition issues concerning food production, bioenergy demand, and threats to biodiversity. A resolution of approximately 1 km

was selected to analyze agroecological zoning, food security, and climate change impacts. Soil attribute data were linked with GIS so that specific parameters could be displayed, characterized, and analyzed. These parameters include soil units, organic carbon, pH, water storage capacity, soil depth, cation exchange, clay fraction, total exchangeable nutrients, lime and gypsum contents, sodium exchange percentage, salinity, textural class, and granulometry [51]. Soil texture, organic carbon content, and depth are key factors for growing energy plants.

2.2. Identification of Marginal Land. Marginal land has various meanings in different disciplines and, therefore, the spatial coverage of marginal land differs. Generally, marginal land is evaluated in terms of a cost-benefit analysis and is determined to be economically marginal [3]. Zhuang et al. established a marginal land evaluation system based on the definition of the Ministry of Agriculture (MoA) of China, a qualitative analysis of energy plants in different parts of China, expert suggestions on local planting of energy plants, land resources, and ecology, and other factors [22]. According to the definition of marginal land by MoA of China, marginal land is winter-fallowed paddy land and wasteland that may be used to cultivate energy crops. We only considered the wasteland in this study. Wasteland includes natural grassland, sparse forestland, scrubland, and

TABLE 2: Growing conditions of energy plants.

Growing conditions	<i>Cassava</i> [24]		<i>P. chinensis</i> [52, 53]		<i>JCL</i> [54–56]	
	Suitable	Moderately suitable	Suitable	Moderately suitable	Suitable	Moderately suitable
Meteorological data						
Annual average temperature/ $^{\circ}\text{C}$	21~29	18~21	10~15.3	5.8~10 or 15.3~28.4	20~25	17~20
Average annual extreme lowest temperature/ $^{\circ}\text{C}$	—	—	≥ -15	-26.5~ -15	≥ 2	0~2
Accumulated temperature of $10^{\circ}\text{C}\cdot\text{d}$	—	—	≥ 3800	1180~3800	—	—
Precipitation/mm	1000~2000	600~1000 or 2000~6000	400~1300	1300~1900	600~1000	300~600 or 1000~1300
Soil data [51]						
Soil depth/cm	≥ 75	30~75	≥ 60	30~60	≥ 75	30~75
Soil organic matter content/%	≥ 3.5	1.5~3.5	—	—	≥ 3.5	1.5~3.5
Soil texture/classes	1	2	—	—	1	2
Terrain						
Elevation/m	≤ 1500	1500~2000	—	—	≤ 500	500~1600
Slope/ $^{\circ}$	≤ 15	15~25	≤ 15	15~25	≤ 15	15~25

unused land that may be used to grow energy crops [3]. We selected six land cover types as the available marginal land for growing the energy plants in compliance with the principle that bioenergy development should not compete with cropland and ecologically protected land. These six types were “mosaic vegetation (grassland/shrub land/forest) (50–70%)/cropland (20–50%),” “sparse (<15%) vegetation,” “mosaic grassland (50–70%)/forest or shrub land (20–50%),” “closed to open (>15%) (broad-leaved or needle-leaved and evergreen or deciduous) shrub land (<5 m),” “closed to open (>15%) grassland or woody vegetation on regularly flooded or waterlogged soil,” and “bare areas.” The selection of land cover types for each country can be flexible based on the law, policy, environmental conditions, and special regulations. For example, nature reserves should be excluded in further studies.

2.3. Characteristics of Selected Energy Plants. *Cassava*, as feedstock for fuel ethanol, has three advantages over others. First, *Cassava* is a shrubby tropical plant, widely grown for its large, tuberous, starchy roots, especially on marginal land. Second, *Cassava* is not a staple food for most people in Asia. Third, it is easy to comminute, has short cooking times, and has a low gelatinization temperature. Therefore, *Cassava* is a suitable feedstock for fuel ethanol [33, 57].

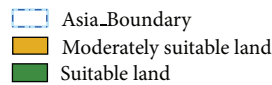
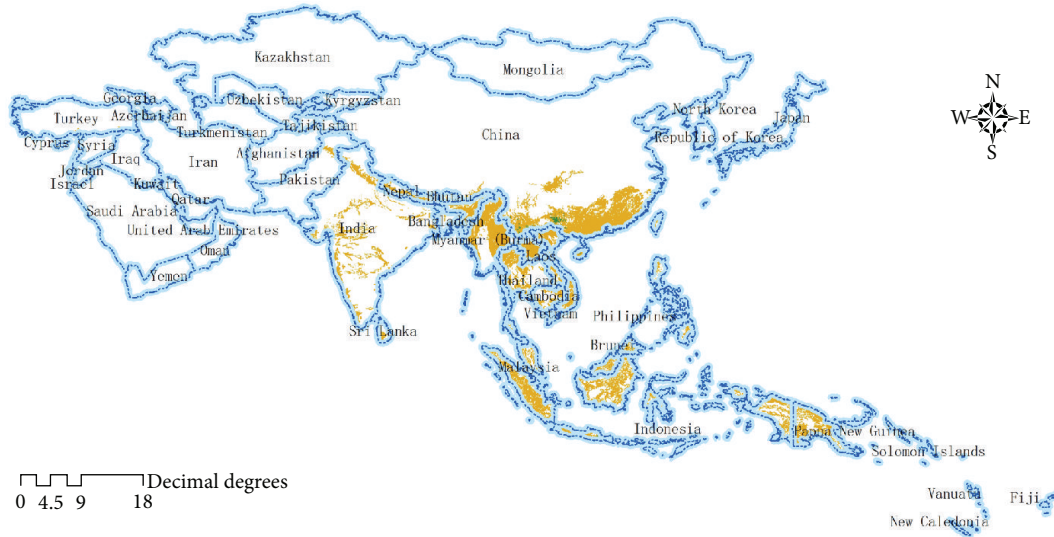
P. chinensis is an ideal species for producing biodiesel. The tree has several outstanding characteristics: drought resistance, tolerance to cold climate, and tolerance to poor, acid, or alkaline soils. It also has some advantages that cannot be replaced by other trees, such as oil yield and its conversion rate, biodiesel quality, geographical distribution, adaptability, and economic benefits cycle. Therefore, *P. chinensis* is considered an important source of biodiesel [34, 47, 52].

JCL is a famous biofuel plant and has been studied globally [31, 58]. It is a tropical species, native to Mexico and Central America, but is widely distributed in wild or semicultivated stands in Latin America, Africa, India, and South-East Asia [59]. The *Jatropha curcas* plant is a nonedible, drought-resistant, perennial plant that has the capability to grow on marginal lands because it requires very few nutrients to survive [34, 44]. *Jatropha* has several other advantages, such as a short gestation period, resistance to common pests, lack of consumption by cattle, and production of biofertilizer and glycerine as useful by-products of biodiesel. In addition, the seed collection period of *Jatropha* does not coincide with the rainy season in June and July, which is when most agricultural activities take place. This makes it possible for people to generate additional income during the slack agricultural season [60, 61].

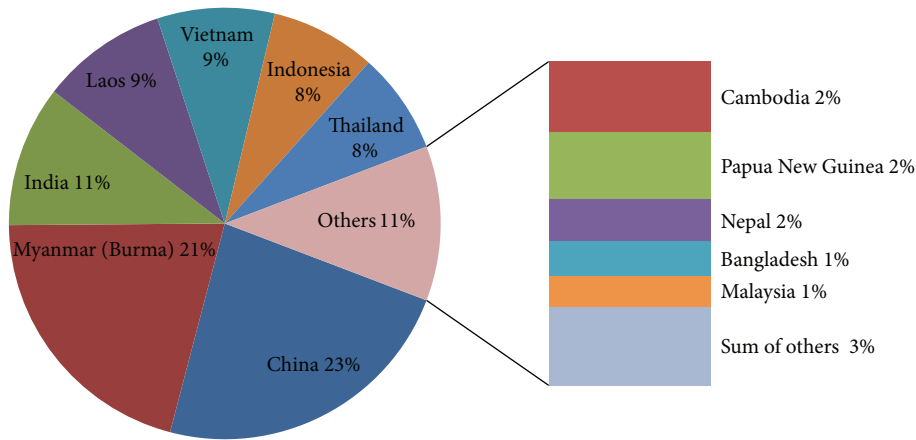
All the specific requirements of the energy plants were chosen according to the literature and advice from experts. The growing conditions of the energy plants are listed in Table 2. The marginal land presented in the previous section was used as the basic condition in the multiple factor analysis.

We used strict criteria during the identification of suitable and moderately suitable areas for energy plants. Marginal land resource areas were only characterized as suitable if all of the suitable conditions were met. If one of the growing conditions was moderately suitable, the land resources were identified as moderately suitable.

The soil texture data used in this paper was classified into two classes. Class 1 was defined as fine textured with more than 35% clay. Class 2 was defined as medium textured with a clay percentage between 18% and 35%. The soil texture requirement of energy plants is that the volumetric ratio of clay should be more than 30% for suitable land and 18%~35% for moderately suitable land. Therefore, there may be more



(a) Spatial distribution



(b) Distribution in different countries

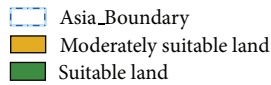
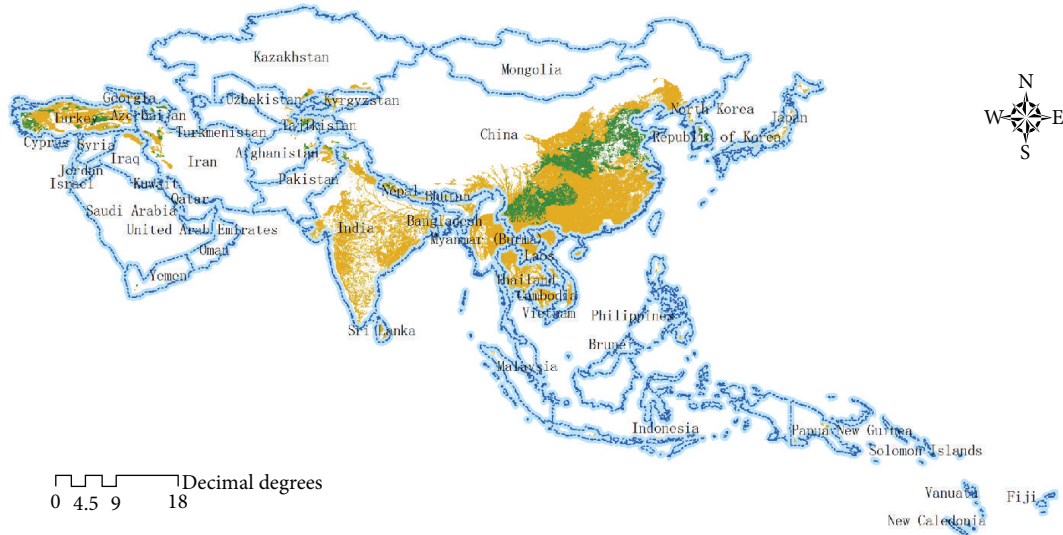
FIGURE 2: Distribution of marginal land resources for *Cassava*.

potential land resource areas available for growing energy plants if more accurate soil data can be obtained.

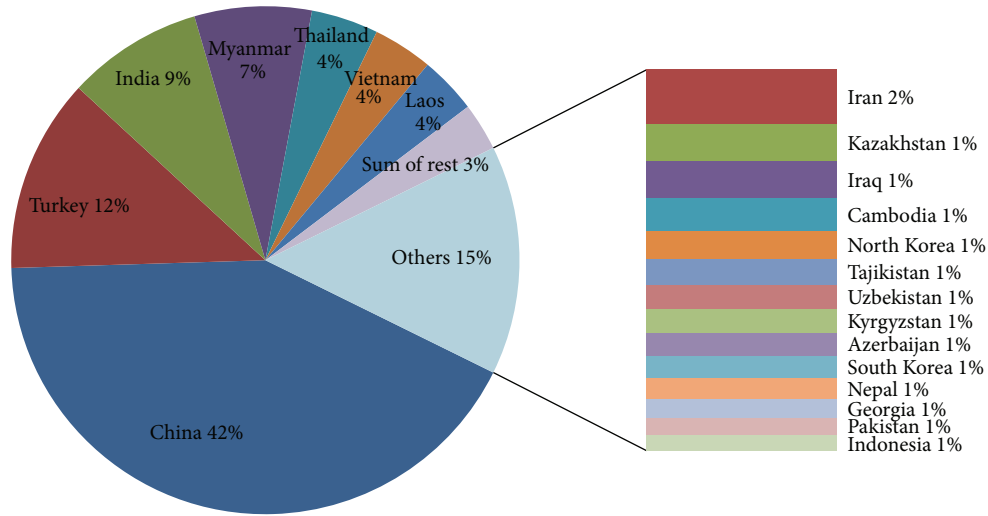
3. Results and Discussion

The planting zones of each energy plant were identified based on marginal land areas and the plant's growth habits. The multiple factor analysis method was adopted to evaluate the suitable marginal land resources based on the evaluation criteria for suitable and moderately suitable growing conditions of each single factor and the type of available land cover. The distributions of marginal land resources suitable for the three energy plants are presented in Figures 2, 3, and 4.

From the figures above, we can see that the area suitable for the growth of *P. chinensis* is much larger than those for the other two plants. Approximately 70% of Asian countries have more than one thousand square kilometers of marginal land resources suitable for *P. chinensis*. *Cassava* and *JCL* resources are limited because they require warmer temperatures than *P. chinensis*, and *Cassava* has a higher precipitation requirement. The results in Table 3 show that the areas of marginal land resources of *Cassava*, *P. chinensis*, and *JCL* are nearly 1.12 million, 2.41 million, and 237 thousand square kilometers, respectively. China has the most marginal land area available for all of the energy plants. Myanmar possesses 21% of the land resources suitable for *Cassava*. Turkey and Thailand have the second largest marginal land resources suitable for *P.*



(a) Spatial distribution



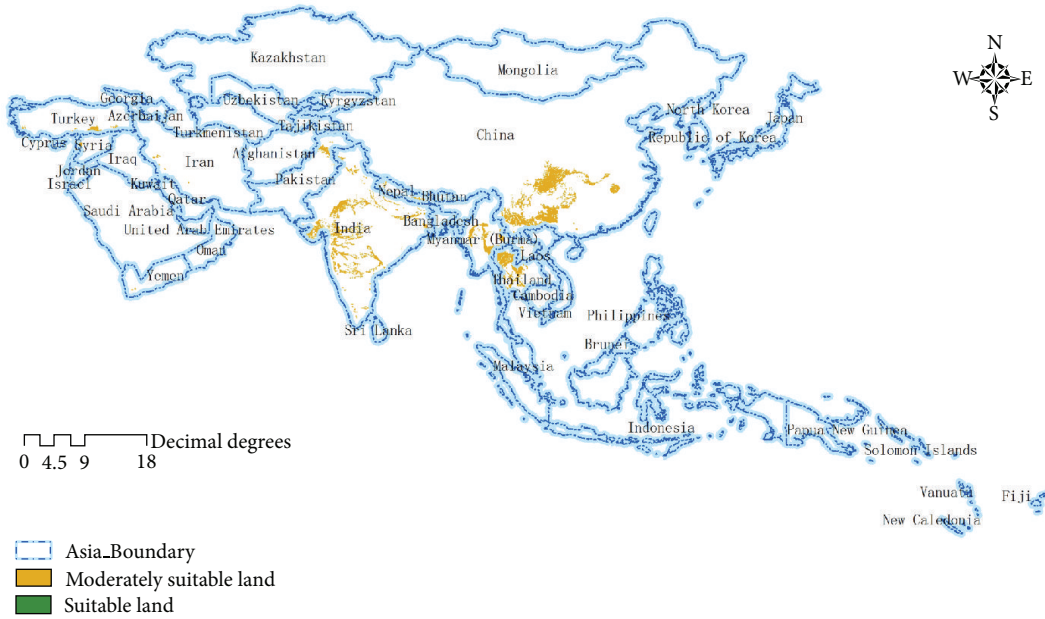
(b) Distribution in different countries

FIGURE 3: Distribution of marginal land resources for *P. chinensis*.

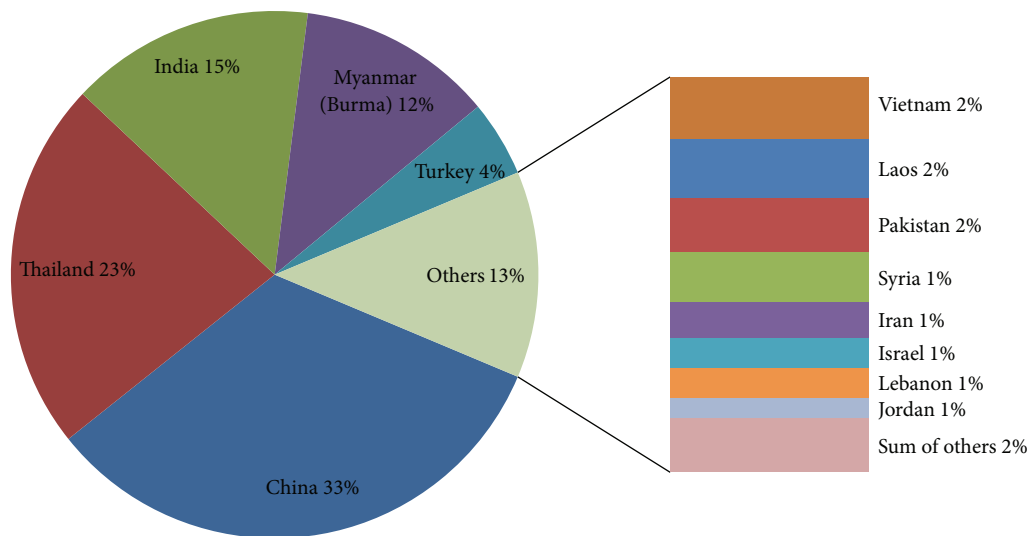
TABLE 3: Marginal land resources suitable and moderately suitable for *Cassava*, *P. chinensis*, and *JCL* planting based on multiple factor analysis in Asia (km²).

Land cover	<i>Cassava</i>		<i>P. chinensis</i>		<i>JCL</i>		Total	
	S	M	S	M	S	M	S	M
Mosaic vegetation	1422	307537	130443	769321	1	92458	131866	1169316
Mosaic grassland	4	3697	17223	73886	0	2461	17227	80044
Shrub land	2089	788006	73008	942428	2	123672	75099	1854106
Herbaceous vegetation	6	16928	9221	89459	0	8794	9227	115181
Sparse vegetation	0	684	28002	180892	0	5732	28002	187308
Bare areas	0	3572	7529	88703	0	4530	7529	96805
Total	3521	1120424	265426	2144689	3	237647	268950	3502760

S: suitable land; M: moderately suitable land.



(a) Spatial distribution



(b) Distribution in different countries

FIGURE 4: Distribution of marginal land resources for JCL.

chinensis and JCL. Shrub land is the dominant land cover type for growing energy plants, which accounts for 51.14% of the total suitable area. Mosaic vegetation is next, accounting for 34.49%.

4. Conclusion

In this paper, a multiple factor analysis method was adopted to identify marginal land resources for three types of energy plants (*Cassava*, *P. chinensis*, and JCL) in Asia based on land cover, meteorological data, soil characteristics, terrain data, and the growth habits of energy plants. GIS was used to

identify potential land resource areas at the resolution of 1 square kilometer. The conclusions of this study are as follows.

- (1) The areas of marginal land suitable for *Cassava*, *P. chinensis*, and JCL were established to be 1.12 million, 2.41 million, and 0.237 million km², respectively. The policy and environmental constraints of each specific county were not considered in this study.
- (2) China has great prospects for bioenergy development. It has the most marginal land resources available for all three energy plants. Myanmar, Turkey, and Thailand have the second largest areas of marginal

land resources available for *Cassava*, *P. chinensis*, and *JCL*, respectively.

- (3) With regard to land cover, shrub land is the dominant land cover type for growing energy plants, accounting for 51.14% of the total suitable area. Mosaic vegetation is second, accounting for 34.49%.

Bioenergy development is important and full of challenges. Further research needs to be performed to choose the best feedstock, improve marginal land resource calculations using more accurate input data, estimate the energy production potential, and analyze the environmental effects coupled with social and economic benefits.

Conflict of Interests

The authors declare that there is no conflict of interests regarding the publication of this paper.

Acknowledgments

Two anonymous referees and the editor of this paper are thanked for their suggestions for the improvement of the paper. The study was supported by the Chinese Academy of Sciences (Grant no. KZZD-EW-08) and the High Resolution Earth Observation Systems of National Science and Technology Major Projects (05-Y30B02-9001-13/15-10).

References

- [1] *BP Statistical Review of World Energy*, 2012.
- [2] A. Karp and I. Shield, "Bioenergy from plants and the sustainable yield challenge," *New Phytologist*, vol. 179, no. 1, pp. 15–32, 2008.
- [3] Y. Tang, J.-S. Xie, and S. Geng, "Marginal land-based biomass energy production in China," *Journal of Integrative Plant Biology*, vol. 52, no. 1, pp. 112–121, 2010.
- [4] J. Zhuang, R. W. Gentry, G.-R. Yu, G. S. Sayler, and J. W. Bickham, "Bioenergy sustainability in China: potential and impacts," *Environmental management*, vol. 46, no. 4, pp. 525–530, 2010.
- [5] J. Hill, E. Nelson, D. Tilman, S. Polasky, and D. Tiffany, "Environmental, economic, and energetic costs and benefits of biodiesel and ethanol biofuels," *Proceedings of the National Academy of Sciences of the United States of America*, vol. 103, no. 30, pp. 11206–11210, 2006.
- [6] P. R. Adler, S. J. del Grosso, and W. J. Parton, "Life-cycle assessment of net greenhouse-gas flux for bioenergy cropping systems," *Ecological Applications*, vol. 17, no. 3, pp. 675–691, 2007.
- [7] A. L. Stephenson, J. S. Dennis, and S. A. Scott, "Improving the sustainability of the production of biodiesel from oilseed rape in the UK," *Process Safety and Environmental Protection*, vol. 86, no. 6, pp. 427–440, 2008.
- [8] *REN21 Renewables 2012 Global Status Report. Renewable Energy Policy Network for the 21st Century*, 2012.
- [9] ExxonMobil, *The Outlook for Energy: A View to 2040*, 2013.
- [10] M. M. Mochizuki, A. Tellis, and M. Wills, *Confronting Terrorism in the Pursuit of Power: Strategic Asia, 2004-2005*, 2004.
- [11] S. Kumar, P. Abdul Salam, P. Shrestha, and E. K. Ackom, "An assessment of Thailand's biofuel development," *Sustainability*, vol. 5, no. 4, pp. 1577–1597, 2013.
- [12] A. Thomas, A. Bond, and K. Hiscock, "A GIS based assessment of bioenergy potential in England within existing energy systems," *Biomass & Bioenergy*, vol. 55, pp. 107–121, 2013.
- [13] I. Gelfand, R. Sahajpal, X. Zhang, R. C. Izaurrealde, K. L. Gross, and G. P. Robertson, "Sustainable bioenergy production from marginal lands in the US Midwest," *Nature*, vol. 493, no. 7433, pp. 514–517, 2013.
- [14] S. Liang, M. Xu, and T. Z. Zhang, "Life cycle assessment of biodiesel production in China," *Bioresource Technology*, vol. 129, pp. 72–77, 2013.
- [15] Y. P. Wu, S. G. Liu, and Z. P. Li, "Identifying potential areas for biofuel production and evaluating the environmental effects: a case study of the James River Basin in the Midwestern United States," *Global Change Biology Bioenergy*, vol. 4, no. 6, pp. 875–888, 2012.
- [16] A. L. Borrión, M. C. McManus, and G. P. Hammond, "Environmental life cycle assessment of lignocellulosic conversion to ethanol: a review," *Renewable & Sustainable Energy Reviews*, vol. 16, no. 7, pp. 4638–4650, 2012.
- [17] P. Schröder, R. Herzig, B. Bojinov et al., "Bioenergy to save the world: producing novel energy plants for growth on abandoned land," *Environmental Science and Pollution Research*, vol. 15, no. 3, pp. 196–204, 2008.
- [18] B. Batidzirai, E. M. W. Smeets, and A. P. C. Faaij, "Harmonising bioenergy resource potentials-methodological lessons from review of state of the art bioenergy potential assessments," *Renewable & Sustainable Energy Reviews*, vol. 16, no. 9, pp. 6598–6630, 2012.
- [19] T. Hattori and S. Morita, "Energy crops for sustainable bioethanol production; which, where and how?" *Plant Production Science*, vol. 13, no. 3, pp. 221–234, 2010.
- [20] Q. Zhang, J. Ma, G. Qiu et al., "Potential energy production from algae on marginal land in China," *Bioresource Technology*, vol. 109, pp. 252–260, 2012.
- [21] H. Qiu, J. Huang, M. Keyzer et al., "Biofuel development, food security and the use of marginal land in china," *Journal of Environmental Quality*, vol. 40, no. 4, pp. 1058–1067, 2011.
- [22] D. Zhuang, D. Jiang, L. Liu, and Y. Huang, "Assessment of bioenergy potential on marginal land in China," *Renewable & Sustainable Energy Reviews*, vol. 15, no. 2, pp. 1050–1056, 2011.
- [23] Y.-K. Tseng, "The economical and environmental advantages of growing *Jatropha curcas* on marginal land," *Advanced Materials Research*, vol. 361–363, pp. 1495–1498, 2012.
- [24] Z.-C. Li and X.-M. Liang, "Analysis of the potential of cassava used as raw materials for fuel alcohol production in China," *Liquor-Making Science & Technology*, vol. 4, pp. 31–33, 2010.
- [25] C. Jansson, A. Westerbergh, J. Zhang, X. Hu, and C. Sun, "Cassava, a potential biofuel crop in China," *Applied Energy*, vol. 86, no. 1, pp. S95–S99, 2009.
- [26] C. Sorapipatana and S. Yoosin, "Life cycle cost of ethanol production from cassava in Thailand," *Renewable & Sustainable Energy Reviews*, vol. 15, no. 2, pp. 1343–1349, 2011.
- [27] K. Sriroth, K. Piyachomkwan, S. Wanlapatit, and S. Nivitchanyong, "The promise of a technology revolution in cassava bioethanol: from Thai practice to the world practice," *Fuel*, vol. 89, no. 7, pp. 1333–1338, 2010.
- [28] S. Kumar, J. Singh, S. M. Nanoti, and M. O. Garg, "A comprehensive Life Cycle Assessment (LCA) of *Jatropha* biodiesel

- production in India,” *Bioresource Technology*, vol. 110, pp. 723–729, 2012.
- [29] Y.-K. Tseng, “The economical and environmental advantages of growing *Jatropha curcas* on marginal land,” *Advanced Materials Research*, vol. 361-363, pp. 1495–1498, 2012.
- [30] H. C. Ong, T. M. I. Mahlia, H. H. Masjuki, and R. S. Norhasyima, “Comparison of palm oil, *Jatropha curcas* and *Calophyllum inophyllum* for biodiesel: a review,” *Renewable & Sustainable Energy Reviews*, vol. 15, no. 8, pp. 3501–3515, 2011.
- [31] K. Openshaw, “A review of *Jatropha curcas*: an oil plant of unfulfilled promise,” *Biomass and Bioenergy*, vol. 19, no. 1, pp. 1–15, 2000.
- [32] L. Axelsson, M. Franzén, M. Ostwald, G. Berndes, G. Lakshmi, and N. H. Ravindranath, “*Jatropha* cultivation in southern India: assessing farmers’ experiences,” *Biofuels, Bioproducts and Biorefining*, vol. 6, no. 3, pp. 246–256, 2012.
- [33] D. Zhuang, D. Jiang, L. Liu, and Y. Huang, “Assessment of bioenergy potential on marginal land in China,” *Renewable & Sustainable Energy Reviews*, vol. 15, no. 2, pp. 1050–1056, 2011.
- [34] M. Tang, P. Zhang, L. Zhang, M. Li, and L. Wu, “A potential bioenergy tree: *Pistacia chinensis* Bunge,” in *Proceedings of the International Conference on Future Energy, Environment, and Materials B*, G. Yang, Ed., pp. 737–746, 2012.
- [35] B. Antizar-Ladislao and J. L. Turrion-Gomez, “Second-generation biofuels and local bioenergy systems,” *Biofuels, Bioproducts and Biorefining*, vol. 2, no. 5, pp. 455–469, 2008.
- [36] A. K. Chandel, E. C. Chan, R. Rudravaram, M. L. Narasu, L. V. Rao, and P. Ravinda, “Economics and environmental impact of bioethanol production technologies: an appraisal,” *Biotechnology and Molecular Biology Review*, vol. 2, no. 1, pp. 14–32, 2007.
- [37] H. Shao and L. Chu, “Resource evaluation of typical energy plants and possible functional zone planning in China,” *Biomass and Bioenergy*, vol. 32, no. 4, pp. 283–288, 2008.
- [38] C. Zhang, W. Han, X. Jing, G. Pu, and C. Wang, “Life cycle economic analysis of fuel ethanol derived from cassava in southwest China,” *Renewable & Sustainable Energy Reviews*, vol. 7, no. 4, pp. 353–366, 2003.
- [39] E. Nuwamanya, L. Chiwona-Karlton, R. S. Kawuki, and Y. Baguma, “Bio-ethanol production from non-food parts of cassava (*Manihot esculenta* Crantz),” *Ambio*, vol. 41, no. 3, pp. 262–270, 2012.
- [40] T. Silalertruksa and S. H. Gheewala, “Security of feedstocks supply for future bio-ethanol production in Thailand,” *Energy Policy*, vol. 38, no. 11, pp. 7476–7486, 2010.
- [41] R. Sarin, M. Sharma, S. Sinharay, and R. K. Malhotra, “*Jatropha*-palm biodiesel blends: an optimum mix for Asia,” *Fuel*, vol. 86, no. 10-11, pp. 1365–1371, 2007.
- [42] S. Jain and M. P. Sharma, “Prospects of biodiesel from *Jatropha* in India: a review,” *Renewable & Sustainable Energy Reviews*, vol. 14, no. 2, pp. 763–771, 2010.
- [43] R. Abdulla, E. S. Chan, and P. Ravindra, “Biodiesel production from *Jatropha curcas*: a critical review,” *Critical Reviews in Biotechnology*, vol. 31, no. 1, pp. 53–64, 2011.
- [44] C.-Y. Yang, Z. Fang, B. Li, and Y.-F. Long, “Review and prospects of *Jatropha* biodiesel industry in China,” *Renewable & Sustainable Energy Reviews*, vol. 16, no. 4, pp. 2178–2190, 2012.
- [45] M. A. Kalam, J. U. Ahamed, and H. H. Masjuki, “Land availability of *Jatropha* production in Malaysia,” *Renewable & Sustainable Energy Reviews*, vol. 16, no. 6, pp. 3999–4007, 2012.
- [46] M. H. Chakrabarti, M. Ali, J. N. Usmani et al., “Status of biodiesel research and development in Pakistan,” *Renewable & Sustainable Energy Reviews*, vol. 16, no. 7, pp. 4396–4405, 2012.
- [47] L. Lu, D. Jiang, D. Zhuang, and Y. Huang, “Evaluating the marginal land resources suitable for developing *pistacia chinensis*-based biodiesel in China,” *Energies*, vol. 5, no. 7, pp. 2165–2177, 2012.
- [48] S. Bontemps, P. Defourny, E. van Bogaert et al., *GlobCover 2009*, vol. 53, European Spatial Agency-Université Catholique de Louvain, 2011.
- [49] A. Jarvis, H. I. Reuter, A. Nelson, and E. Guevara, “Hole-filled SRTM for the globe version 4,” The CGIAR-CSI SRTM 90m Database, 2008, <http://www.cgiar-csi.org>.
- [50] R. J. Hijmans, S. E. Cameron, J. L. Parra, P. G. Jones, and A. Jarvis, “Very high resolution interpolated climate surfaces for global land areas,” *International Journal of Climatology*, vol. 25, no. 15, pp. 1965–1978, 2005.
- [51] *FAO/IIASA/ISRIC/ISS-CAS/JRC Harmonized World Soil Database (Version 1.1)*, 2009.
- [52] X. Hou, H. Zuo, and H. Mou, “Geographical distribution of energy plant *Pistacia chinensis* Bunge in China,” *Ecology and Environmental Sciences*, vol. 19, pp. 1160–1164, 2010.
- [53] Y. Fu, X. Pan, and H. Gao, “Geographical distribution and climate characteristics of habitat of *Pistacia chinensis* Bunge in China,” *Chinese Journal of Agrometeorology*, vol. 30, no. 3, pp. 318–322, 2009.
- [54] J. Heller, *Physic Nut, Jatropha curcas L.*, vol. 1, Bioversity International, 1996.
- [55] R. K. Henning, “*Jatropha curcas* L,” *Plant Resources of the Tropical Africa*, vol. 14, pp. 116–122, 2004.
- [56] K. Eckart and P. Henshaw, “*Jatropha curcas* L. and multifunctional platforms for the development of rural sub-Saharan Africa,” *Energy for Sustainable Development*, vol. 16, no. 3, pp. 303–311, 2012.
- [57] H. Yang, L. Chen, Z. Yan, and H. Wang, “Emergy analysis of cassava-based fuel ethanol in China,” *Biomass and Bioenergy*, vol. 35, no. 1, pp. 581–589, 2011.
- [58] N. Foidl, G. Foidl, M. Sanchez, M. Mittelbach, and S. Hackel, “*Jatropha curcas* L. as a source for the production of biofuel in Nicaragua,” *Bioresource Technology*, vol. 58, no. 1, pp. 77–82, 1996.
- [59] V. C. Pandey, K. Singh, J. S. Singh, A. Kumar, B. Singh, and R. P. Singh, “*Jatropha curcas*: a potential biofuel plant for sustainable environmental development,” *Renewable & Sustainable Energy Reviews*, vol. 16, no. 5, pp. 2870–2883, 2012.
- [60] S. Kumar, A. Chaube, and S. K. Jain, “Sustainability issues for promotion of *Jatropha* biodiesel in Indian scenario: a review,” *Renewable & Sustainable Energy Reviews*, vol. 16, no. 2, pp. 1089–1098, 2012.
- [61] P. Kumar Biswas, S. Pohit, and R. Kumar, “Biodiesel from *jatropha*: can India meet the 20% blending target?” *Energy Policy*, vol. 38, no. 3, pp. 1477–1484, 2010.

Research Article

Changes in Production Potential in China in Response to Climate Change from 1960 to 2010

Luo Liu,^{1,2,3} Xi Chen,² Xinliang Xu,¹ Yong Wang,¹ Shuang Li,^{1,3} and Ying Fu^{1,3}

¹ State Key Laboratory of Resources and Environmental Information System, Institute of Geographic Sciences and Natural Resources Research, Chinese Academy of Sciences, Beijing 100101, China

² State Key Laboratory of Desert and Oasis Ecology, Xinjiang Institute of Ecology and Geography, Chinese Academy of Sciences, Urumqi 830011, China

³ University of Chinese Academy of Sciences, Beijing 100049, China

Correspondence should be addressed to Xinliang Xu; xuxl@reis.ac.cn

Received 9 December 2013; Accepted 27 January 2014; Published 5 March 2014

Academic Editor: Dong Jiang

Copyright © 2014 Luo Liu et al. This is an open access article distributed under the Creative Commons Attribution License, which permits unrestricted use, distribution, and reproduction in any medium, provided the original work is properly cited.

From the Global Agro-Ecological Zone (GAEZ) model, changes in the three climate factors (temperature, precipitation, and solar radiation) over the past five decades showed different trends and that production potential was impacted significantly by the geographic heterogeneity of climate change. An increase of approximately 1.58 million tons/decade in production potential correlated with climate change. Regions with increased production potential were located mainly in the Northeast China Plain, the northern arid and semiarid region, and the Huang-Huai-Hai Plain. Regions with decreased production potential were located mainly in the Middle-lower Yangtze Plain and southern China. The climate factors that impacted production potential varied by region. In the Northeast China Plain, increased temperature was the major cause of the increased production potential. In the northern arid and semiarid region, temperature and precipitation were the major factors affecting production potential, but their effects were in opposition to each other. In southern China, increased temperature and decreased solar radiation caused a decreased production potential. In the Middle-lower Yangtze Plain, a decrease in solar radiation was the major factor resulting in decreased production potential. In the Huang-Huai-Hai Plain, changes in temperature and solar radiation had large but opposite effects on production potential.

1. Introduction

Annual anomalies in global land-surface air temperatures indicate a warming trend of 0.27°C per decade since 1979, with the greatest warming occurring during the winter and spring in the Northern Hemisphere [1]. The effects of this change in temperature on crop growth and production are uncertain.

China has a population of approximately 1.3 billion people, which is expected to increase and then stabilize at approximately 1.5 billion people in the year 2030 [2]. However, the land area suited for agriculture in China is relatively small. Per capita cultivated land is only 0.12 ha, less than half of the world average [3]. The need to provide food for the large population in China has attracted significant attention [4, 5]. Moreover, the rapidly increasing demand for food

and energy has put heavy pressure on natural resources and caused unprecedented environmental degradation. Government policy has long focused on securing a high level of national self-sufficiency especially in grain food production. Attention to the effects of climate change on agricultural production potential over the past few decades throughout China is needed so that sensible agricultural policies can be formulated for the future [6].

The effects of climate change trends on climate-crop relationships and the yields of major crops across China have been investigated over the past few decades [7–9]. In other studies, the Global Agro-Ecological Zone (GAEZ) model was used to assess the impact of climate change on agricultural land productivity [10, 11]. However, these studies addressed only the yields of single crops, such as rice, wheat, or maize, and ignored the multiple cropping systems that are used

on nearly half of the cultivated land in China. A study of the impact of climate change on the overall agricultural production in China at the national and regional levels is yet to be performed.

In this study, meteorological data from 1960 to 2010, including terrain elevation, soil, and farmland distribution data in 2010, were used to calculate the agricultural production potentials in various regions of China based on the GAEZ model, which takes multiple factors into consideration, including light, temperature, moisture, CO₂ fertilization, pests, diseases, soil, and topography. Subsequently, the calculated production potentials were verified using official data on actual productivity. Finally, we analyzed the spatial-temporal changes in the production potential in response to climate change during the past five decades. Our results reveal the impact of climate change on agricultural production and the relationship between climate change and wheat yields. This information will not only help to optimize agricultural practices but also allow adaptation to climate change and the development of national food security policies in China.

2. Materials and Methods

2.1. Data Sources. The input data for this study included terrain elevation, soil, land-use, and meteorological data. The meteorological data included the monthly maximum air temperature, minimum air temperature, precipitation, relative humidity, wind speed, and hours of sunshine.

A 2010 land-use database, with a mapping scale of 1:1,000,000, was developed by the Chinese Academy of Sciences (CAS). The primary data source for the land-use database was Landsat MSS/TM/ETM CCD digital images. Images from the China-Brazil Earth Resources Satellite (CBERS) and Small Satellite Constellation for Environment and Disaster Monitoring and Forecasting (SSCEDMF) HJ-1 satellite were also used as a supplement for the land areas not covered by the Landsat images. The land-use data were classified into 25 categories that were subsequently grouped into six classes: cropland, woodland, grassland, water body, built-up area, and unused land. Detailed information about this land-use database can be found in previous reports [3, 12–15]. Farmland data were extracted from the land-use data for this study.

Meteorological data for the period from 1960 to 2010, including the monthly maximum air temperature, minimum air temperature, precipitation, relative humidity, wind speed at 10 m height, and hours of sunshine, were obtained from national agrometeorological stations maintained by the Chinese Meteorological Administration (CMA) (<http://cdc.cma.gov.cn/>). Because of the diverse terrain across China, the impact of topography on the interpolation of the meteorological data was also considered. The ANUSPLIN software [16, 17], which was designed for spatial interpolation of climate data, was used in this study to interpolate the meteorological data based on the terrain elevation dataset. The monthly data for the above six key plant growth factors were interpolated to 10 km resolution using the ANUSPLIN software based on the digital terrain model of China.

The terrain elevation dataset derived from the Shuttle Radar Topography Mission (SRTM) C-band data was the first publicly available near-global, high resolution raster Digital Elevation Model (DEM) [18]. The SRTM data were publicly distributed with a 90 m spatial resolution around the Earth, reduced from the original 30 m resolution via averaging and subsampling. SRTM data were used for environmental analyses in numerous previous studies.

Soil data were used to calculate the soil-water balance, which was used to determine the potential and actual evapotranspiration for a reference crop and the duration of its growing period. Soil quality was determined based on several parameters, including soil type, effective depth, and water-holding capacity. A nationwide soil dataset, at a scale of 1:1,000,000, was provided by the Data Center for Resources and Environmental Sciences (RESDC) at the Chinese Academy of Sciences.

2.2. Methodology. Simulation of the potential productivity of wheat, maize, rice, sweet potato, and soybean was performed at a spatial resolution of 1 km using the Global Agro-Ecological Zones (GAEZ) model which was developed in the 1970s and updated in 2010 by the Food and Agriculture Organization (FAO) and the International Institute for Applied Systems Analysis (IIASA) [19–22]. These five crops are major crops in China, providing 97.7% of the total grain output of China. The GAEZ model is based on principles of land evaluation. It utilizes meteorological, terrain elevation, soil, and farmland distribution data to calculate the potential productivity, which is dependent upon the supply of water, energy, nutrients, and physical support to plants.

In the GAEZ model, agroclimatic potential yields are determined using mainly the seasonal temperature and the availability of solar radiation, while additional limitations imposed by water availability, soil characteristics, and terrain slopes determine the actual yields that are obtained under rain-fed conditions. To ensure that only areas suitable for agriculture were assessed for heat stress, only cells with actual yields greater than 20% of the potential yields and in which at least 5% of the cell area was cultivated were considered. The optimal crop species were determined by simulating yields for all possible combinations and then selecting the highest yield in each grid cell based on the climate data from 1960 to 2010. We considered irrigated conditions to be appropriate for rice because most rice crops are cultivated under irrigation. For other crops, we considered both irrigated and rain-fed conditions. For crops grown under rain-fed conditions, the date of crop sowing is highly dependent on the presence of sufficient soil moisture for seed germination and seedling establishment. Winter and spring wheat, maize, and maize varieties with an affinity for heat were tested in each grid cell and the crop with the highest productivity was selected. Production potentials of the various crops were calculated using different methods. To calculate the production potential of each crop, growth parameters were adopted based on the growth habits of each crop, including growing period, leaf area index, and harvest index.

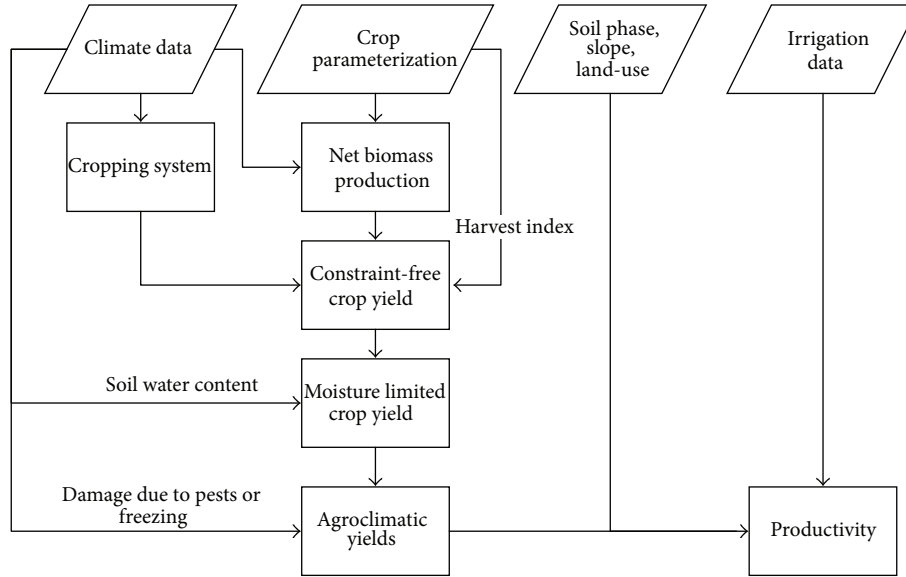


FIGURE 1: Flowchart for calculating potential productivity using the GAEZ model.

China is one of the largest countries and has the highest multiple cropping index [23]. The use of multiple cropping systems in China was considered in the calculation of the potential productivity.

To reveal the impact of water conditions on the production potential, irrigated and rain-fed scenarios were considered. Calculations of production potential for the rain-fed scenarios [24] were based on light, temperature, and water conditions, while the calculations for the irrigated scenarios [25] used only the light and temperature conditions assuming sufficient water for crop growth and no water stress. The two scenarios were consistent with existing agricultural management methods used in China for naturally rain-fed farmland and irrigated farmland. The equation used to calculate crop yields within each grid cell under rain-fed and irrigated scenarios was

$$\text{yield}_{\text{total}} = \text{yield}_{\text{rain-fed}} (1 - i) + \text{yield}_{\text{irrigated}} \times i, \quad (1)$$

where $\text{yield}_{\text{total}}$ is the production potential within each grid cell (kg/ha), $\text{yield}_{\text{rain-fed}}$ is yields under rain-fed scenarios within each grid cell (kg/ha), $\text{yield}_{\text{irrigated}}$ is yields under irrigated scenarios within each grid cell (kg/ha), and i (%) is the ratio of irrigation-cultivated area to total cultivated area based on official statistics of the Chinese Agriculture Ministry (Figure 1).

3. Results

3.1. Verification. To verify the accuracy of our calculated results, the calculated production potential in 2010 was compared with the actual production as reported in official statistics for 2010. The average potential production per hectare in 2010 was 8,316 kg/ha, which was nearly 1.55-fold higher than the actual production. The correlation between the calculated production potential and the actual production

is shown in Figure 2. The cross-correlation coefficient was 0.82 and the standard deviation was 74,000 tons, indicating a good correlation. Consequently, the trend of the calculated production potential reflected, to a great extent, the trend of the actual production.

3.2. Spatial Patterns of Production Potential in China. Based on the GAEZ model, production potential values were calculated for each year based on the climatic conditions from 1961 to 2000. A map of the geographic distribution of production potential in 2010 is shown in Figure 3. In 2010, the total production potential in China was 1.17 billion tons and per hectare production potential was 7,889 kg/ha. The spatial pattern of the production potential was complex, with increasing production potential from north to south and from west to east. The production potential in the southeastern areas was high due to relatively high temperatures and abundant rainfall. The production potential declined with increasing distance from the coast line. In the northwestern part of the country, the production potential was constrained by low temperatures and rainfall. The Middle-lower Yangtze Plain had the greatest total production potential, 0.30 billion tons. In contrast, the area with the least total production potential was the Qinghai-Tibet Plateau, at 4.23 million tons. The area with the greatest per hectare production potential was the Middle-lower Yangtze Plain, at 10,789 kg/ha. In contrast, the area with the least per hectare production potential was the Qinghai-Tibet Plateau, at 3,674 kg/ha (Figure 4).

3.3. Climate Change in China Since 1960. In this study, changes in annual temperature, precipitation, and solar radiation in the major cultivation areas over the past five decades were analyzed statistically. The trends for changes in the climate parameters over the period are shown in Figure 5. Overall, temperature showed an obvious increasing trend

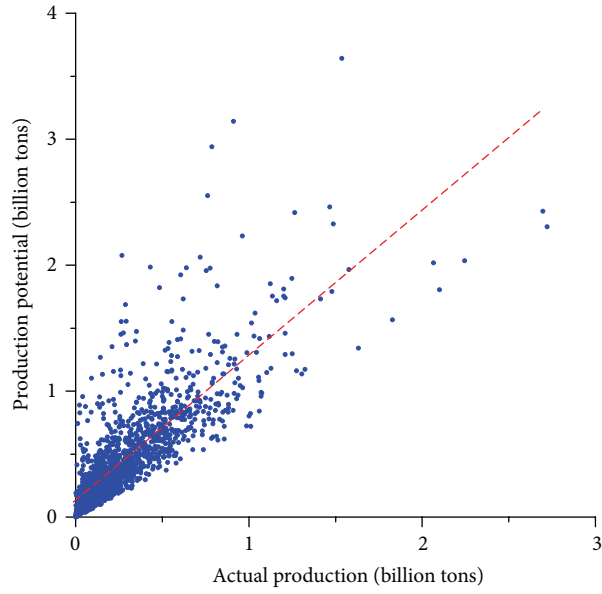


FIGURE 2: Correlation between production potential and actual production.

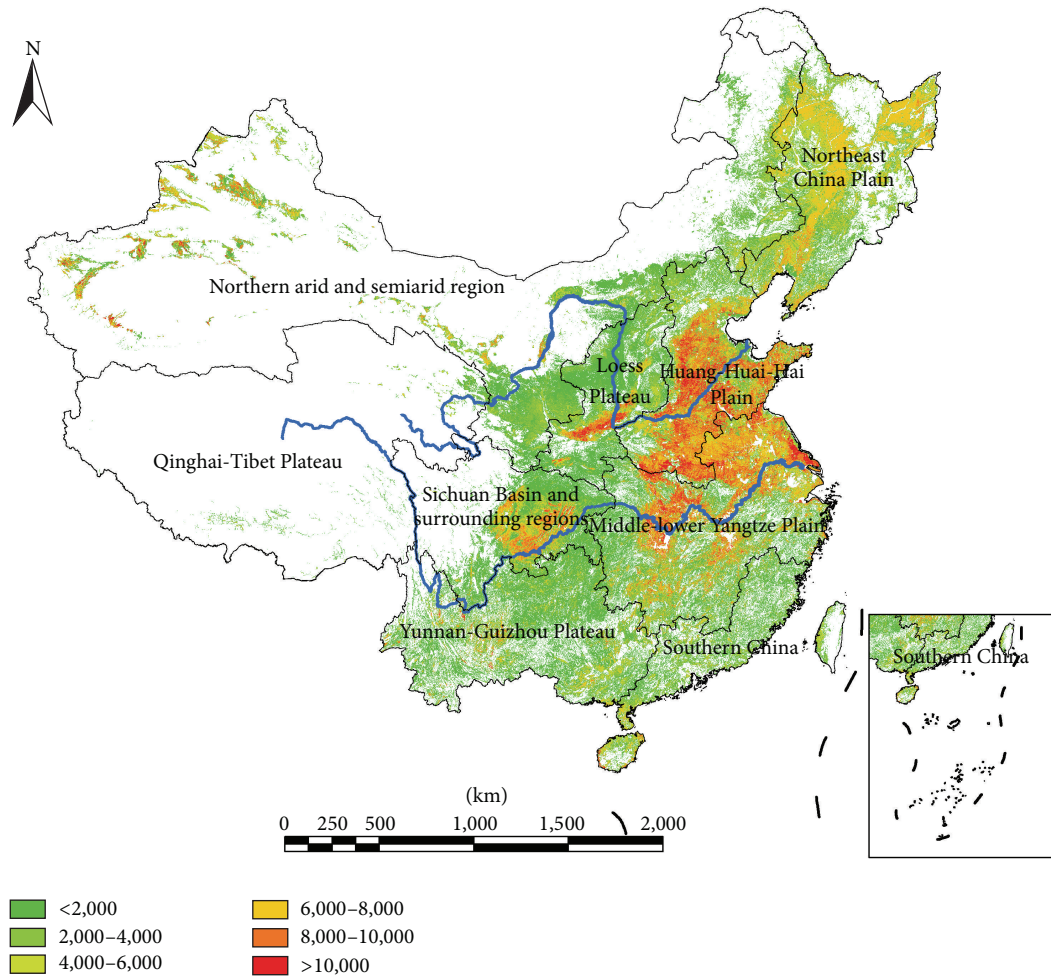


FIGURE 3: Distribution of production potential in China in 2010 (kg/ha).

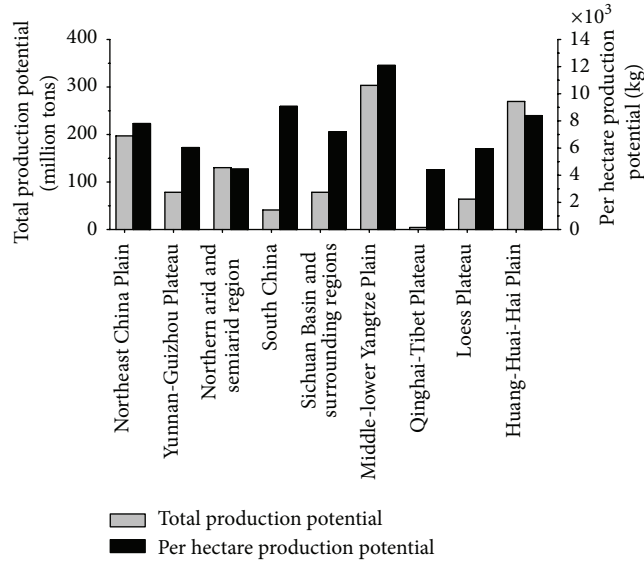


FIGURE 4: Production potential of various regions in 2010.

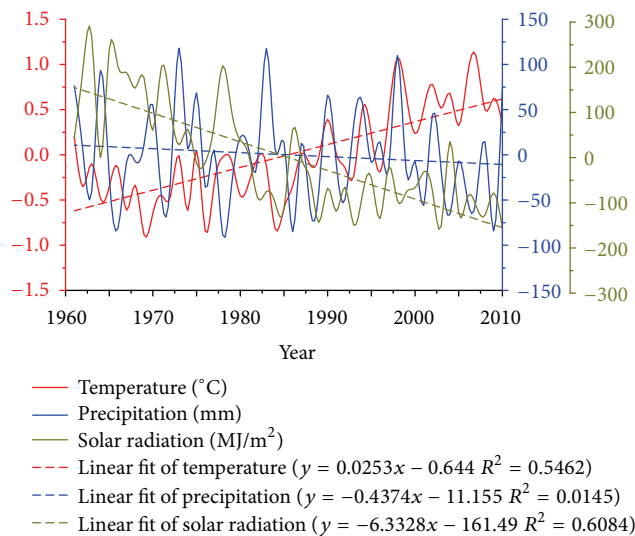


FIGURE 5: Annual anomaly maps of each climatic factor during the past five decades.

since the late 1960s, and the rate of temperature change increased dramatically after the late 1980s relative to the prior years. Mean temperature increased by 0.25°C/decade in the major cultivation areas during the past five decades. Precipitation showed little change, but exhibited clear fluctuations. Since 2000, the annual precipitation each year was less than in the previous years. Total solar radiation showed a decreasing trend (−63.3 MJ/m²·a) during the entire period and, since the 1980s, the annual solar radiation was less than the mean solar radiation for the entire period.

Maps of climate change trends show the spatial distribution of climate change from 1961 to 2010 (Figure 6). Mean temperature generally increased across the major cultivation areas. In particular, it increased by an average rate of more than 0.3°C/decade in the northern arid and semiarid

region, the Northeast China Plain, the Qinghai-Tibet Plateau, and the Loess Plateau. In contrast, the Sichuan Basin and the surrounding regions had the lowest mean temperature increase, 0.1°C/decade. Precipitation increased primarily in southern China and the Middle-lower Yangtze Plain by 21.7 and 9.7 mm/decade, respectively. In northwestern China, the precipitation declined in some locations. In contrast, precipitation generally decreased in the other major farmland areas. In particular, the Loess Plateau showed the largest decrease, of 20.5 mm/decade. Solar radiation decreased in large areas across the major farmland regions. The Huang-Huai-Hai Plain had the largest decrease, 111.5 MJ/m²·decade. Solar radiation decreased in the Middle-lower Yangtze Plain, southern China, and the Sichuan Basin. In contrast, solar radiation showed an increasing trend in a small section of

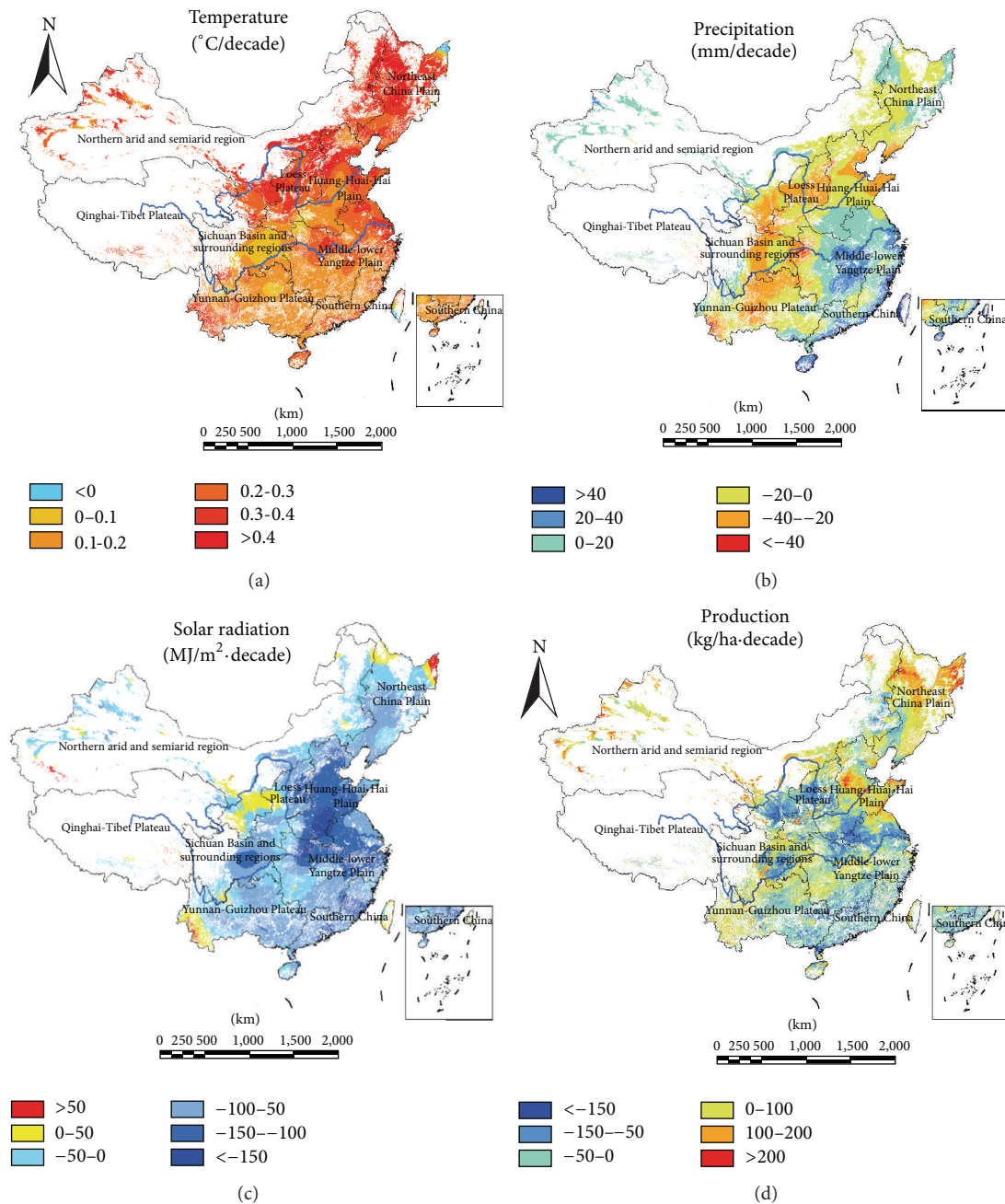


FIGURE 6: Changes in climatic factors and production potential during the past five decades.

northern Heilongjiang Province and in southwestern Yunnan Province.

3.4. Impact of Climate Change on Production Potential. The spatial heterogeneity of climate change during the past five decades had a significant impact on production potential in China (Figure 6). For the entirety of China, the production potential increased by ~ 1.58 million tons/decade as a result of climate change. The geographic distribution of production potential changed over the past five decades, with increases in the north and decreases in the south. The areas with increased production potential were located mainly in the Northeast China Plain, the northern arid and semiarid region,

and the Huang-Huai-Hai Plain, where production potential increased by 3.15, 0.92, and 0.79 million tons/decade, respectively. In contrast, the areas with decreased production potential were located mainly in the Middle-lower Yangtze Plain and southern China, where production potential decreased by 1.53 and 0.83 million tons/decade, respectively.

To analyze the relationship between the changes in production potential and the changes in each climate factor in different regions, correlation coefficients between the production potential and each climatic factor were calculated for each grid.

The change in temperature had a large impact on production potentials, but with different effects in different areas. In

the Northeast China Plain and the Huang-Huai-Hai Plain, the warming trend had a positive effect on the production potential due to increased plant biomass production over the course of the growing season. In the Huang-Huai-Hai Plain, the production potential was increased further by changes in multiple cropping systems made in response to the temperature increase. In contrast, the correlation coefficient between the temperature and the production potential was negative in the Loess Plateau, southern China, and the Yunnan-Guizhou Plateau. Because heat was already sufficient in southern China and the Yunnan-Guizhou plateau, crops did not respond to the increase in temperature with additional growth. The increase in temperature also accelerated crop growth and reduced the required length of the growing season, resulting in a decrease in the production potential. Given the inadequate moisture levels in the Loess Plateau due to low irrigation rates and precipitation, the increase in temperature caused higher evapotranspiration rates, leading to reduced production potential. In contrast, the increase in the temperature had little impact on the production potential in the Middle-lower Yangtze Plain. In summary, the trend for increasing temperature over the past five decades had a positive impact on the production potential in the higher latitudes but had a negative impact on that at the lower latitudes.

The correlation coefficients between precipitation and the production potential were different in the southern and northern regions of China (Figure 7). In northern China, the production potential showed a positive correlation with precipitation, particularly for the rain-fed cropland. However, the limited supply of water in the arid climate of northern China resulted in a decrease in the production potential associated with the trend for decreasing precipitation. In southern China, precipitation and production potential were negatively correlated. An associated effect of excessive rainfall was a decline in solar radiation, which was a significant factor in the decrease in production potential. During the past five decades, the trend in precipitation across China as a whole showed little change but displayed clear geographic differences. Precipitation decreased in northern China and increased in southern China, resulting in a net decrease in the national total production potential.

In southern China and the coastal area of North China, the production potential showed a positive correlation with solar radiation because the abundant water supply supported high rates of photosynthesis, leading to increasing plant biomass with increasing solar radiation. In contrast, solar radiation and production potential were correlated negatively in northern China. The increase in solar radiation may have accelerated the rate of evaporation leading to water deficit in crops. Although northeastern China is an arid region, most of the agricultural production is irrigated so the increase in solar radiation had less impact on the water requirements of the crops. Therefore, the solar radiation and the production potential were positively correlated.

We established a linear regression model using the climatic factors as independent variables and the production potential as a dependent variable to identify the primary factors that impact the production potential. The increase

in temperature had a large and positive influence on the production potential. The contribution rate of temperature to the production potential reached 2137.00% among three factors, while the decreases in precipitation and solar radiation had negative impacts on the production potential, and their contribution rates were -388.06% and -1648.94% , respectively. The increase in temperature was the major contributing factor to the increase in production potential when considering China as a whole, but temperature, precipitation, and solar radiation had varying effects on the production potential in specific regions. In the Northeast China Plain, the increase in temperature was the major factor in the increased production potential, and the contribution rate of temperature to the production potential reached 104.38%. In the northern arid and semiarid region, temperature and precipitation were the major factors in the changes in production potential, but their effects were antagonistic. The increase in temperature had a positive impact on the production potential, with a contribution rate of 431.15%, while the decrease in the temperature had a negative influence on the production potential, and its contribution rate was 290.18%. In southern China, the increased temperature and decreased solar radiation caused a decrease in the production potential, with contribution rates of 53.12% and 48.62%, respectively. In the Middle-lower Yangtze Plain, the decrease in solar radiation was the major factor causing the decrease in the production potential, with a contribution rate of 186.99%. In the Huang-Huai-Hai Plain, the changes in temperature and solar radiation had large and opposing effects on the production potential. The increase in temperature resulted in an increase in production potential, with a contribution rate of 271.38%, but the decrease in solar radiation had a negative impact on the production potential, with a contribution rate of -118.98% (Table 1).

4. Conclusion and Discussion

China faces challenges to its efforts to ensure grain security resulting from an increasing population and the decreasing availability of land for agriculture. One important factor that puts grain security at risk is the high level of climatic variability. Temperature, precipitation, and solar radiation are key climate variables that determine the amount of plant biomass production. In this study, we analyzed the impacts of temperature, precipitation, and solar radiation variability on the agricultural production potential of five major crops in China based on the GAEZ model using meteorological data, including terrain elevation and soil data, collected over the past five decades. Conclusions from this study are as follows.

(1) In 2010, the total production potential was 1.17 billion tons in China, and the per hectare production potential was 7,889 kg/ha. The production potential increased from north to south and from west to east. The region with the highest total and per hectare production potential was the Middle-lower Yangtze Plain, with 0.30 billion tons and 10,789 kg/ha, respectively.

(2) Changes in annual temperature, precipitation, and solar radiation showed different trends over the past five

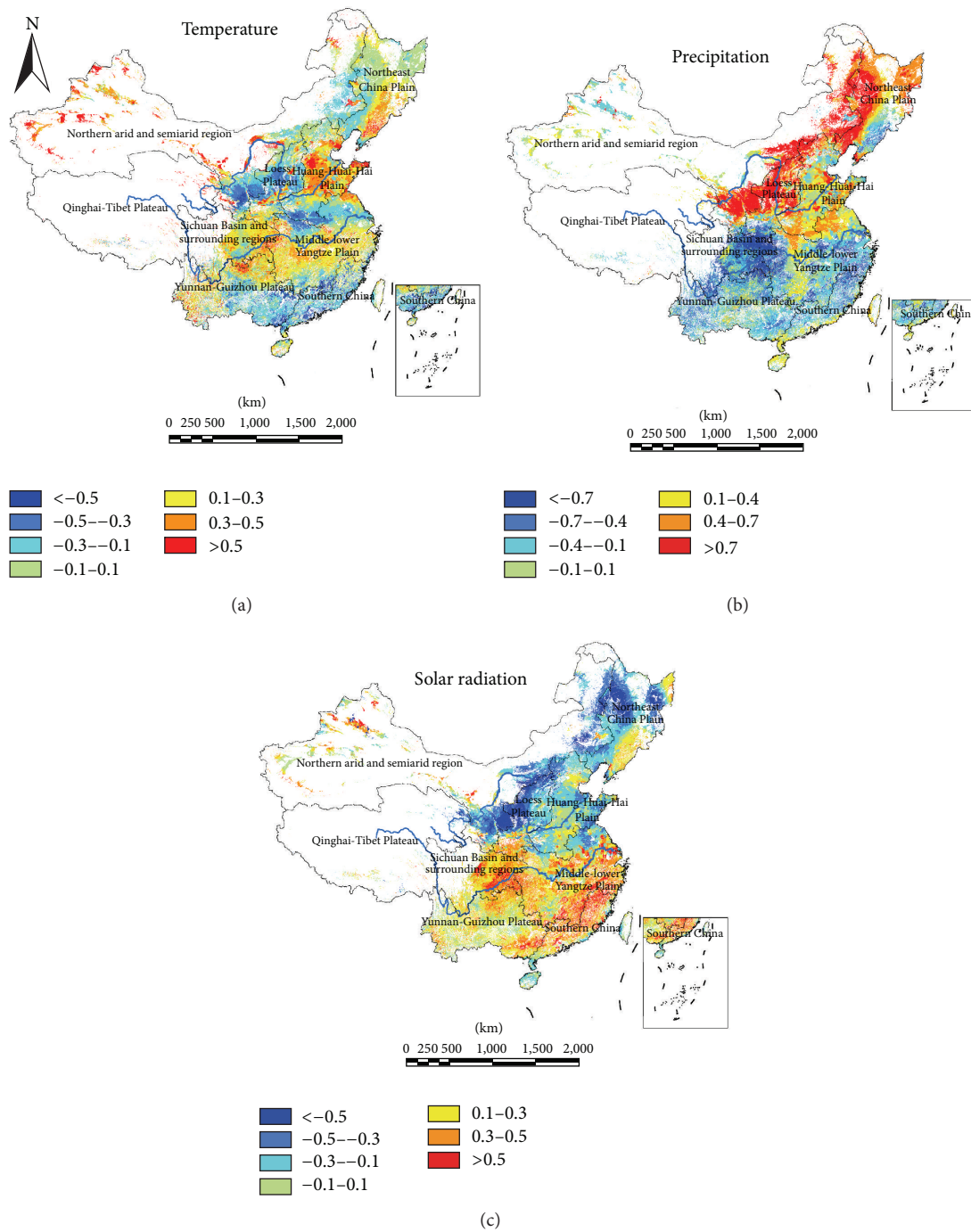


FIGURE 7: Correlation coefficients between production potential and climatic factors.

decades. Temperature showed a clear increasing trend with a dramatically increased rate of temperature change after the late 1980s. Precipitation showed minor change overall but exhibited substantial fluctuation. After 2000, the annual precipitation was consistently less than that in the previous years. Solar radiation showed an obvious decreasing trend during the entire period and the annual solar radiation since

the 1980s was consistently less than the mean solar radiation over the past five decades.

(3) The geographic heterogeneity of climate change had a significant impact on the production potential in China. The overall production potential increased by approximately 1.58 million tons/decade in response to climate change. The areas with increased production potential were located

TABLE 1: Contributions of climatic factors to the production potential in various regions of China (%).

Agriculture zone	Temperature	Precipitation	Radiation
Northeast China Plain	104.38	-24.64	20.26
Yunnan-Guizhou Plateau	102.07	-122.52	120.45
Northern arid and semiarid region	431.15	-290.18	-40.97
Southern China	53.12	-1.74	48.62
Sichuan Basin and surrounding regions	23.12	-381.43	458.31
Middle-lower Yangtze Plain	-58.04	-28.95	186.99
Qinghai-Tibet Plateau	78.86	12.68	8.47
Loess Plateau	-60.65	161.33	-0.67
Huang-Huai-Hai Plain	271.38	-52.40	-118.98
Total	2137.00	-388.06	-1648.94

mainly in the Northeast China Plain, the northern arid and semiarid region, and the Huang-Huai-Hai Plain. In contrast, the areas with decreased production potential were located mainly in the Middle-lower Yangtze Plain and southern China.

(4) The effects of the climate factors that impact production potential in China varied greatly. In the Northeast China Plain, the increase in temperature was the major factor in the increased production potential. In the northern arid and semiarid region, temperature and precipitation were the major factors that led to changes in production potential, but their effects were in opposition to each other. In southern China, the increase in temperature and the decrease in solar radiation led to decreased production potential. In the Middle-lower Yangtze Plain, the major factor causing decreased production potential was the decrease in solar radiation. In the Huang-Huai-Hai Plain, the changes in temperature and solar radiation had large and opposite effects on the production potential.

Finally, we note the limitations of this study. Extreme weather conditions (i.e., freezing or high temperatures, rainstorms, or heavy snow) may have an extreme effect on the production potential, but these factors were not taken into consideration in our study. The irrigated scenarios in this study assumed a sufficient supply of water for crop growth, but the actual availability of water provided by irrigation still poses limitations to crop growth in practice. Crop species selection is determined, in large part, based on farmers' financial interests and not necessarily on which crop is the most suitable.

Conflict of Interests

The authors declare that they have no conflict of interests.

Acknowledgments

This research was supported and funded by the National Key Project of Scientific and Technical Supporting Programs (no. 2013BAC03B01), the project of CAS action-plan for West Development (no. KZCX2-XB3-08-01), and the National Program on Key Basic Research Project (973 Program) (no. 2010CB950901). The authors are particularly indebted

to Günther Fisher from IIASA for his GAEZ model. He made substantial contribution to the production potential estimation of China.

References

- [1] S. Susun, "Climate change 2007-the physical science basis: working group I contribution to the fourth assessment report of the IPCC," Tech. Rep., Cambridge University Press, 2007.
- [2] H. C. J. Godfray, J. R. Beddington, I. R. Crute et al., "Food security: the challenge of feeding 9 billion people," *Science*, vol. 327, no. 5967, pp. 812–818, 2010.
- [3] J. Liu, Z. Zhang, X. Xu et al., "Spatial patterns and driving forces of land use change in China during the early 21st century," *Journal of Geographical Sciences*, vol. 20, no. 4, pp. 483–494, 2010.
- [4] L. R. Brown, *Who Will Feed China?: Wake-Up Call for a Small Planet*, WW Norton & Company, 1995.
- [5] M. E. Brown and C. C. Funk, "Climate: food security under climate change," *Science*, vol. 319, no. 5863, pp. 580–581, 2008.
- [6] H. F. Gale Jr., *China's Food and Agriculture: Issues for the 21st Century*, 2012.
- [7] A. J. Challinor, E. S. Simelton, E. D. Fraser, D. Hemming, and M. Collins, "Increased crop failure due to climate change: assessing adaptation options using models and socio-economic data for wheat in China," *Environmental Research Letters*, vol. 5, no. 3, Article ID 034012, 2010.
- [8] S. Barry and Y. Cai, "Climate change and agriculture in China," *Global Environmental Change*, vol. 6, no. 3, pp. 205–214, 1996.
- [9] F. Tao, Z. Zhang, S. Zhang, Z. Zhu, and W. Shi, "Response of crop yields to climate trends since 1980 in China," *Climate Research*, vol. 54, pp. 233–247, 2012.
- [10] J. Alcamo, N. Dronin, M. Endejan, G. Golubev, and A. Kirilenko, "A new assessment of climate change impacts on food production shortfalls and water availability in Russia," *Global Environmental Change*, vol. 17, no. 3-4, pp. 429–444, 2007.
- [11] E. I. Teixeira, G. Fischer, H. van Velthuizen, C. Walter, and F. Ewert, "Global hot-spots of heat stress on agricultural crops due to climate change," *Agricultural and Forest Meteorology*, vol. 170, pp. 206–215, 2011.
- [12] J. Liu, M. Liu, H. Tian et al., "Spatial and temporal patterns of China's cropland during 1990–2000: an analysis based on Landsat TM data," *Remote Sensing of Environment*, vol. 98, no. 4, pp. 442–456, 2005.

- [13] J. Liu, M. Liu, D. Zhuang, Z. Zhang, and X. Deng, "Study on spatial pattern of land-use change in China during 1995–2000," *Science in China Series D*, vol. 46, no. 4, pp. 373–384, 2003.
- [14] J. Liu, H. Tian, M. Liu, D. Zhuang, J. M. Melillo, and Z. Zhang, "China's changing landscape during the 1990s: large-scale land transformations estimated with satellite data," *Geophysical Research Letters*, vol. 32, no. 2, 2005.
- [15] J. Liu, Q. Zhang, and Y. Hu, "Regional differences of China's urban expansion from late 20th to early 21st century based on remote sensing information," *Chinese Geographical Science*, vol. 22, pp. 1–14, 2012.
- [16] M. F. Hutchinson, "Interpolation of rainfall data with thin plate smoothing splines—part I: two dimensional smoothing of data with short range correlation," *Journal of Geographic Information and Decision Analysis*, vol. 2, pp. 139–151, 1998.
- [17] M. F. Hutchinson, "Interpolation of rainfall data with thin plate smoothing splines—part II: analysis of topographic dependence," *Journal of Geographic Information and Decision Analysis*, vol. 2, pp. 152–167, 1998.
- [18] A. Shortridge and J. Messina, "Spatial structure and landscape associations of SRTM error," *Remote Sensing of Environment*, vol. 115, no. 6, pp. 1576–1587, 2011.
- [19] G. Fischer, M. Shah, F. N. Tubiello, and H. van Velhuizen, "Socio-economic and climate change impacts on agriculture: an integrated assessment, 1990–2080," *Philosophical Transactions of the Royal Society B*, vol. 360, no. 1463, pp. 2067–2083, 2005.
- [20] G. Fischer, M. Shah, H. Velthuisen, and F. Nachtergaele, "Agro-ecological zones assessments. Land use and land cover," in *Encyclopedia of Life Support Systems (EOLSS), Developed Under the Auspices of the UNESCO*, Eolss, Oxford, UK, 2006.
- [21] G. Fischer and L. X. Sun, "Model based analysis of future land-use development in China," *Agriculture, Ecosystems & Environment*, vol. 85, no. 1-3, pp. 163–176, 2001.
- [22] G. Fischer, H. Van Velthuisen, M. Shah, and F. Nachtergaele, *Global Agro-Ecological Assessment for Agriculture in the 21st Century: Methodology and Results*, International Institute for Applied Systems Analysis, 2002.
- [23] H. Yan, J. Liu, and M. Cao, "Remotely sensed multiple cropping index variations in China during 1981–2000," *Acta Geographica Sinica*, vol. 60, no. 4, pp. 559–566, 2005.
- [24] FAO, "Guidelines: land evaluation for rain-fed agriculture," FAO Soils Bulletin 52, 1984.
- [25] FAO, "Guidelines: land evaluation for irrigated agriculture," FAO Soils Bulletin 55, 1985.

Research Article

NDVI-Based Vegetation Change in Inner Mongolia from 1982 to 2006 and Its Relationship to Climate at the Biome Scale

Linghui Guo,^{1,2} Shaohong Wu,¹ Dongsheng Zhao,¹ Yunhe Yin,¹
Guoyong Leng,^{1,2} and Qingyu Zhang^{1,2}

¹ Institute of Geographic Sciences and Natural Resources Research, Chinese Academy of Sciences, Beijing 100101, China

² University of Chinese Academy of Sciences, Beijing 100049, China

Correspondence should be addressed to Dongsheng Zhao; zhaods@igsnr.ac.cn

Received 19 November 2013; Revised 25 January 2014; Accepted 27 January 2014; Published 3 March 2014

Academic Editor: Dong Jiang

Copyright © 2014 Linghui Guo et al. This is an open access article distributed under the Creative Commons Attribution License, which permits unrestricted use, distribution, and reproduction in any medium, provided the original work is properly cited.

Based on the normalized difference vegetation index (NDVI), we analyzed vegetation change of the six major biomes across Inner Mongolia at the growing season and the monthly timescales and estimated their responses to climate change between 1982 and 2006. To reduce disturbance associated with land use change, those pixels affected by land use change from the 1980s to 2000s were excluded. At the growing season scale, the NDVI increased weakly in the natural ecosystems, but strongly in cropland. Interannual variations in the growing season NDVI for forest was positively linked with potential evapotranspiration and temperature, but negatively correlated with precipitation. In contrast, it was positively correlated with precipitation, but negatively related to potential evapotranspiration for other natural biomes, particularly for desert steppe. Although monthly NDVI trends were characterized as heterogeneous, corresponding to monthly variations in climate change among biome types, warming-related NDVI at the beginning of the growing season was the main contributor to the NDVI increase during the growing season for forest, meadow steppe, and typical steppe, but it constrained the NDVI increase for desert steppe, desert, and crop. Significant one-month lagged correlations between monthly NDVI and climate variables were found, but the correlation characteristics varied greatly depending on vegetation type.

1. Introduction

Climate change has resulted in a significant effect on vegetation dynamics during the past decades [1–4] due to the associated alterations to biogeochemical processes, such as plant photosynthesis, respiration, and mineralization of soil organic matter [5–7], and these changes are projected to be enhanced in the future years [8–12].

A number of previous studies have investigated annual variations in vegetation and their responses to climate changes using the normalized difference vegetation index (NDVI), a reliable indicator of vegetation change, at both regional and global scales [13–21]. However, less attention has been paid to vegetation change (NDVI) and its relationships with climatic factors over shorter timescales [22, 23]. For many ecological and agricultural issues, finer temporal resolution is more relevant [23]. Besides, the magnitude of the monthly NDVI and its change over time are vital indicators of

the contribution of vegetation change in different months to annual plant growth [16]. Furthermore, many recent studies have focused mainly on the influence of precipitation and mean temperature on vegetation change, and the important role of other factors has been neglected, such as maximum and minimum temperature and potential evapotranspiration, which also exert considerable influence on patterns of vegetation growth [24–27]. In addition, increasing numbers of studies have confirmed the effect of interannual climate variability on vegetation change, which varies considerably depending on the ecogeographical region and vegetation types [16, 28–30]. Therefore, developing a better understanding of the effect of climate on vegetation growth at the biome scale is of some significance.

The Inner Mongolia Autonomous Region consists of vast forests and the largest grazing area in China and is considered to be an important timber and livestock region in China [31]. As an ecotransition zone, it has a sharp rainfall-temperature

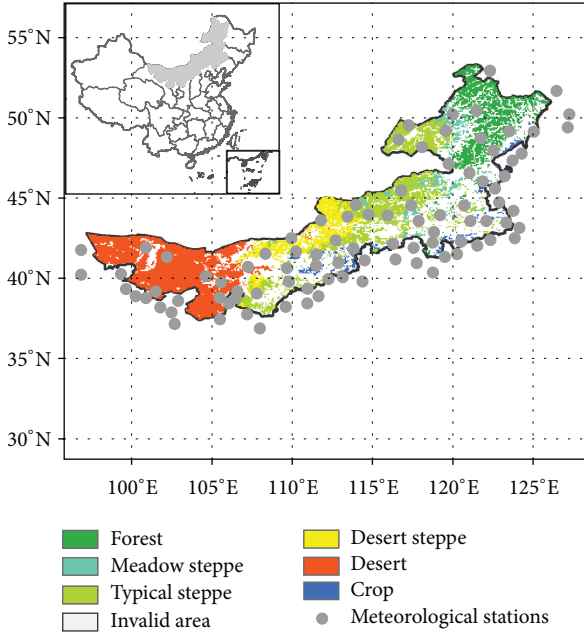


FIGURE 1: The spatial distribution of vegetation types and the 92 meteorological stations used in this study. The inset map indicates the location of the study area in China.

gradient from the southwest to northeast, where vegetation growth is likely to be highly sensitive to climate change [32]. Over recent decades, it has experienced dramatic climate change, which has been more pronounced than most other areas in China [33–36]. The study of climate-related vegetation dynamics here is of fundamental importance to improve our understanding of the mechanisms in the relationship between climate change and vegetation change, and also critical to policy-making for regional adaptation plans. The objective of the present study is to investigate how and why vegetation change has occurred in Inner Mongolia over the past 25 years. Firstly, we examined changes in the growing season NDVI, and variations in NDVI for each month during the growing season to gain further insights into its contribution to the changes in growing season NDVI during the period of 1982–2006, and we further investigated the relationships between climatic factors and NDVI at the growing season and monthly scales, based on vegetation types.

2. Data and Methods

2.1. Study Area. Inner Mongolia is situated in the northern part of China and stretches from approximately 37°N to 53°N and 97°E to 126°E, a total area of nearly 1.2 million km² (Figure 1). The region is dominated by monsoon climate pattern that are controlled by continental Eurasian high and low pressure cells. During the summer, warm and humid air from the Pacific contributes to high temperatures and variable rainfall. In the winter, the region is affected by strong, dry, and cold northwesterly winds regulated by the Siberian-Mongolian atmospheric high pressure cell [31, 37]. The climate is characterized by an increase in precipitation

and a decrease in temperature from southwest to northeast [38]. From southwest to northeast, it can be divided into four major zones [39]. The medium temperate arid region in the southwest is dominated by the desert biome. The medium temperate semiarid region occupying most of the central area (approximately 40°N to 50°N latitude and 110°E to 120°E longitude) is dominated by steppe and fragmented areas of cropland. Finally, the cold temperate humid and medium temperate subhumid regions, occurring mainly in the northeast, are dominated by the forest biome. In this study, we focused on the cultivated and five of the major natural vegetation types of Inner Mongolia: cropland, forest, meadow steppe, typical steppe, desert steppe, and desert. We selected these biomes because they are the dominant vegetation types and follow the rainfall-temperature gradient from the southwest to the northeast.

2.2. Dataset. Vegetation change was identified using NDVI data developed by the global inventory monitoring and modeling studies (GIMMS) group and derived from the NOAA/AVHRR land dataset for the period 1982–2006 (available at <ftp://ftp.glcfc.umd.edu/glcfc/GIMMS/>), which has a resolution of 8 km and an interval of 15 days. The data calibrated to eliminate noise from solar angle and sensor errors has been widely used in analyzing the long-term trends in vegetation cover and activity in China [16, 31, 40]. To further decrease the effects of atmospheric and aerosol scattering, we developed a monthly NDVI data using maximum value composite (MVC) method for each month, as previous study [41]. The growing season was defined as April to October [42–44], and the growing season NDVI data were obtained by averaging these monthly NDVI data during the period of April–October for each year.

The climate variables used were the monthly precipitation amount (P), mean temperature (T_{mean}), maximum temperature (T_{max}), minimum temperature (T_{min}), and potential evapotranspiration (PET). These data were interpolated using ANUSPLIN 4.3 software (<http://fennergchool.anu.edu.au/research/products>) at a resolution of 8 km, based on 92 climatic stations of the China Meteorological Administration in or around Inner Mongolia (Figure 1). To check the performance of the ANUSPLIN 4.3 interpolation for Inner Mongolia, the monthly data in the year of 2000 were interpolated by using ANUSPLIN 4.3, based on observational data from 82 of the 92 climate stations. Then, observational monthly data from the remaining 10 climate stations were compared with corresponding pixel values obtained from the interpolation data in 2000. The coefficients of determination (R^2) between the interpolations and observations indicated that the simulated monthly T_{mean} , T_{max} , T_{min} , PET, and P fitted the observed values reasonably with average R^2 of 0.99, 0.98, 0.98, 0.81, and 0.79, respectively. PET (mm day⁻¹) was calculated using an improved United Nations Food and Agriculture Organization (FAO) Penman-Monteith method [45]:

$$\text{PET} = \frac{0.408\delta(R_n - G) + \gamma(900/(T + 273))U_2(e_s - e_a)}{\delta + \gamma(1 + 0.34U_2)}, \quad (1)$$

where δ is the slope of the saturation vapor pressure versus air temperature curve ($\text{kPa}^\circ\text{C}^{-1}$), R_n is net solar radiation at the plant surface ($\text{MJ m}^{-2} \text{day}^{-1}$), G is soil heat flux density ($\text{MJ m}^{-2} \text{day}^{-1}$), γ is the psychrometric constant ($\text{kPa}^\circ\text{C}^{-1}$), T is mean air temperature at a height of 2 m ($^\circ\text{C}$), U_2 is mean wind speed at a height of 2 m (m s^{-1}), e_s is saturation vapor pressure (kPa), and e_a is actual vapor pressure (kPa).

The information on distribution of vegetation types was obtained from vegetation map of China with a scale of 1:1000000 [46]. Based on this map and the criteria of Editorial Board of Rangeland Resources of China, 1996 [47], vegetation types in Inner Mongolia were further grouped into cropland, forest, meadow steppe, typical steppe, desert steppe, and desert. Then, they were converted to grid maps with a resolution of 8 km, which corresponds to that of the NDVI data.

Digital land-use maps of the scale 1:100000 in 1980s and 2000, provided by the Data Center for Resources and Environmental Sciences of the Chinese Academy of Sciences (<http://www.resdc.cn/>), were used to identify land-use change in 1980s to 2000s. These data based on the Landsat Thematic Mapper (TM)/Enhanced Thematic Mapper (ETM)/Multispectral Scanner System (MSS) images/land-use survey have been proved to be of high accuracy and could better meet the needs of studies on land-use change at regional or national scales [48, 49].

2.3. Method. To remove biases related to the effects of land-use change on NDVI values, pixels affected by land-use change during the study period were excluded. Specifically, we extracted each land-use type for the two periods and converted them to a grid format with a resolution of 8 km, respectively, and then masked them to identify those pixels with no land-use change during the 1980s and 2000s. These pixels were then selected to mask the vegetation types. Results of the vegetation survey are presented in Figure 1.

Linear time trends were evaluated using the ordinary least squares method for the NDVI and climate variables over the growing season and monthly timescales for each vegetation type, and the Pearson correlation coefficients between the NDVI and climatic variables were also calculated to determine the extent of the relationship between them.

3. Results and Discussion

3.1. Changes in Growing Season and Monthly NDVI. From 1982 to 2006, the climate records showed warming and drying trends across the forest, meadow steppe, typical steppes, and crop regions, while they showed wetting and warming in the desert steppes and desert areas (Figure 2). The growing season NDVI for all biomes increased over the past 25 years, with the magnitudes differing greatly by vegetation type (Figure 2). The cultivated ecosystem showed a significant increasing trend, with an average increment of 0.0016 yr^{-1} ($P < 0.01$). In comparison, the natural ecosystems increased only slightly and weakly, with the largest increase (0.0005 yr^{-1} ; $P = 0.50$) occurring in the forest region and

the lowest (0.00001 yr^{-1} ; $P = 0.90$) in the desert. Such an increase in the NDVI indicates that vegetation activity in Inner Mongolia is strengthening during the study period, to some extent. This is generally consistent with previous studies, which demonstrated that the overall state of Inner Mongolia's vegetation developed favorably in the past years [40, 43, 50, 51].

In order to more clearly examine the contribution of each month to the growing season NDVI trend, Figure 3 shows the changes in the trend of monthly NDVI over the period of 1982–2006. For the forest, the monthly NDVI trend at the beginning and end of the growing season (i.e., May and September) increased much larger than that in other months, with an increase of 0.0028 yr^{-1} ($R^2 = 0.05$, $P = 0.26$) and 0.0038 yr^{-1} ($R^2 = 0.18$, $P < 0.05$), respectively. In contrast, there was a marked decrease from June to August, with a minimum rate of -0.002 yr^{-1} ($R^2 = 0.14$, $P < 0.1$) in July (Figure 3(a)-N). This is in agreement with the result from Mao et al. [52], who found that the larger NDVI increase was in May and September in northeast China, at the similar latitude as this region [52]. By comparison, NDVI values for most growing season months tended to increase for the steppes. The largest trends occurred in April and August, with annual rates of 0.0010 yr^{-1} ($R^2 = 0.23$, $P < 0.05$) and 0.0013 yr^{-1} ($R^2 = 0.08$, $P = 0.15$), respectively, for the meadow steppe (Figure 3(b)-N), 0.0009 yr^{-1} ($R^2 = 0.36$, $P < 0.01$) and 0.0017 yr^{-1} ($R^2 = 0.08$, $P = 0.17$), respectively, for the typical steppe (Figure 3(c)-N), and 0.0002 yr^{-1} ($R^2 = 0.02$, $P = 0.56$) and 0.001 yr^{-1} ($R^2 = 0.03$, $P = 0.39$), respectively, for the desert steppe (Figure 3(d)-N). However, the monthly NDVI for the desert exhibited a noticeably different pattern from the other biomes, with the larger increases of 0.0002 yr^{-1} ($R^2 = 0.03$, $P = 0.41$) and 0.0001 yr^{-1} ($R^2 = 0.03$, $P = 0.43$) in September and October, respectively, while that in July decreased significantly by -0.0003 yr^{-1} ($R^2 = 0.10$, $P = 0.12$) (Figure 3(e)-N). For the cropland, monthly NDVI rose significantly in July, August, and September, which played an important role in the growing season NDVI trend. In contrast, monthly NDVI decreased strongly from April to June (Figure 3(f)-N). This could partly be due to the fact that the dominant crop type have been changed from spring wheat to maize [53]. Specifically, the area of spring wheat declined from about 1.1 million hectares in 1990 to 0.4 million hectares in 2006, while that of maize increased greatly from 0.8 million hectares to about 2 million hectares [53, 54].

3.2. The Response of Growing Season NDVI to Climate Change.

Table 1 illustrates the correlations between climatic variables and NDVI for the different vegetation types at the growing season scale. For the forest, the growing season NDVI positively correlated with the corresponding PET ($R = 0.53$, $P < 0.01$) and temperature, especially T_{max} ($R = 0.39$, $P < 0.1$), but related only weakly and negatively to P ($R = -0.30$, $P = 0.16$). Nevertheless, lower growing season NDVI values in 1984, 1993, 1998, and 2003 corresponded well with higher P values (Figure 1(a)). To further analyze the relationship between growing season NDVI and peak precipitation, we

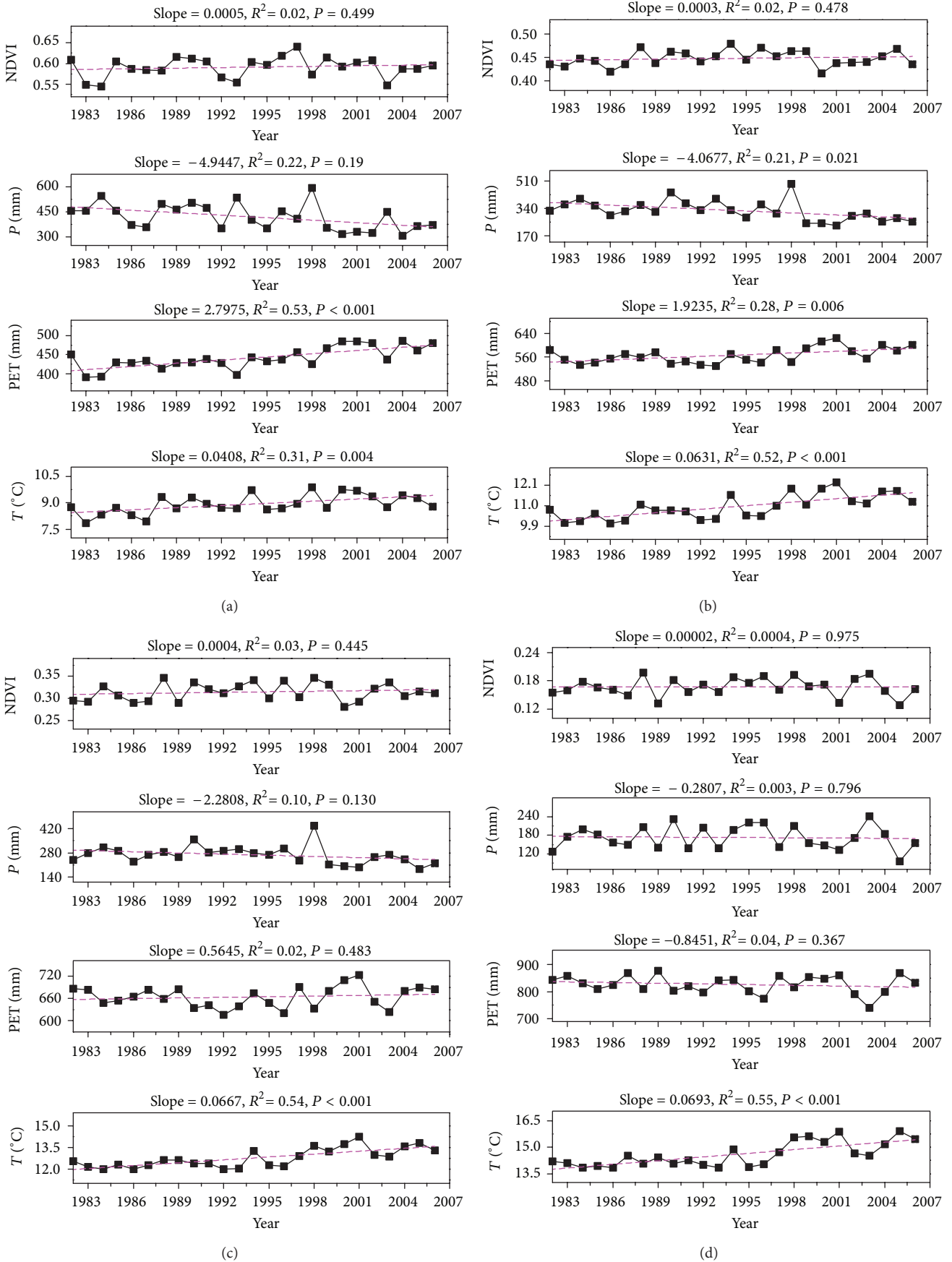


FIGURE 2: Continued.

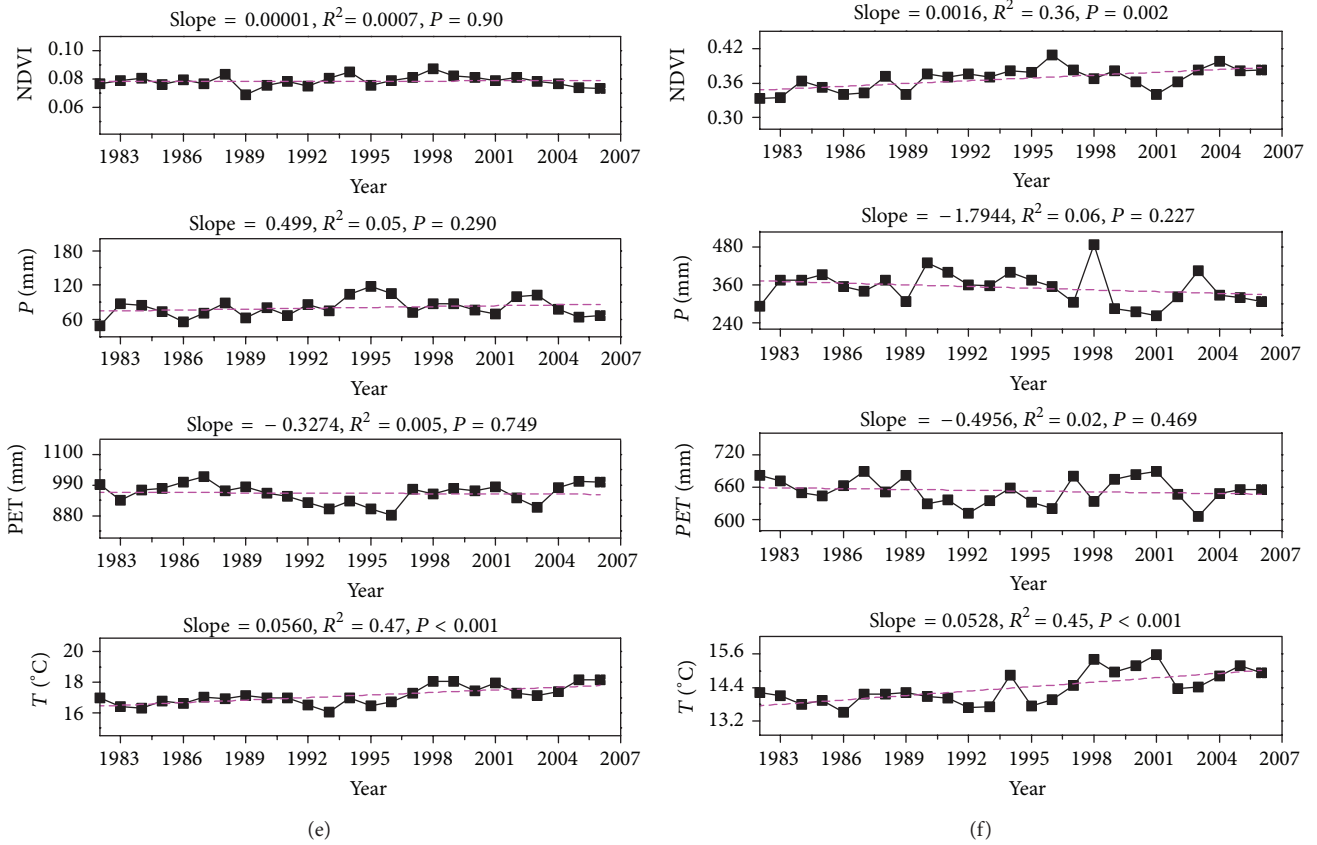


FIGURE 2: Interannual variations of growing season mean NDVI, growing season P , growing season PET, and growing season T_{mean} for (a) forest, (b) meadow steppe, (c) typical steppe, (d) desert steppe, (e) desert, and (f) cropland during the period 1982–2006.

TABLE 1: Correlation between growing season NDVI and corresponding climate variables for different biomes: growing season P , growing season PET, and growing season T_{mean} , T_{max} , and T_{min} .

Climate variables	Correlation coefficient					
	Forest	Meadow steppe	Typical steppe	Desert steppe	Desert	Crop
P	-0.30	0.38*	0.58***	0.84***	0.35*	0.18
PET	0.53***	-0.27	-0.63***	-0.71***	-0.22	-0.58***
T_{mean}	0.29	0.20	-0.04	-0.29	0.02	0.12
T_{max}	0.39*	0.073	-0.13	-0.33	0.09	0.03
T_{min}	0.01	0.36*	0.16	-0.10	-0.02	0.26

***, **, and * indicate $P < 0.01$, $P < 0.05$, and $P < 0.1$, respectively.

calculated the correlation coefficients between precipitation amounts more than 455 mm (a little above the mean) during the growing season and corresponding NDVI value, and a significant negative correlation was observed ($R = -0.55$, $P < 0.1$). These findings suggest that increases in either temperature or potential evapotranspiration boost forest growth, whereas too much precipitation depresses it. In forest dominated areas (cold temperate humid and medium temperate subhumid regions), a negative correlation between the growing season NDVI and precipitation, especially in wetter years, can be attributed to increased cloud cover and the consequent decrease in solar radiation and temperature [52]. In contrast, a positive relationship was observed between the

growing season NDVI and temperature, which is broadly consistent with the results of previous studies performed in northern middle-high latitudes [19, 40, 55]. This may be a consequence of increased temperatures lengthening the growing period and enhancing photosynthesis, while also reducing the negative effect derived from excessive precipitation in summer [56–58].

In contrast, there was a significant positive correlation between growing season NDVI and P for meadow steppes, typical steppes, desert steppes, and desert ($R = 0.38$, $P < 0.1$; $R = 0.58$, $P < 0.01$; $R = 0.84$, $P < 0.01$; and $R = 0.35$, $P < 0.1$, resp.), but a negative correlation between growing season NDVI and PET, especially for the typical

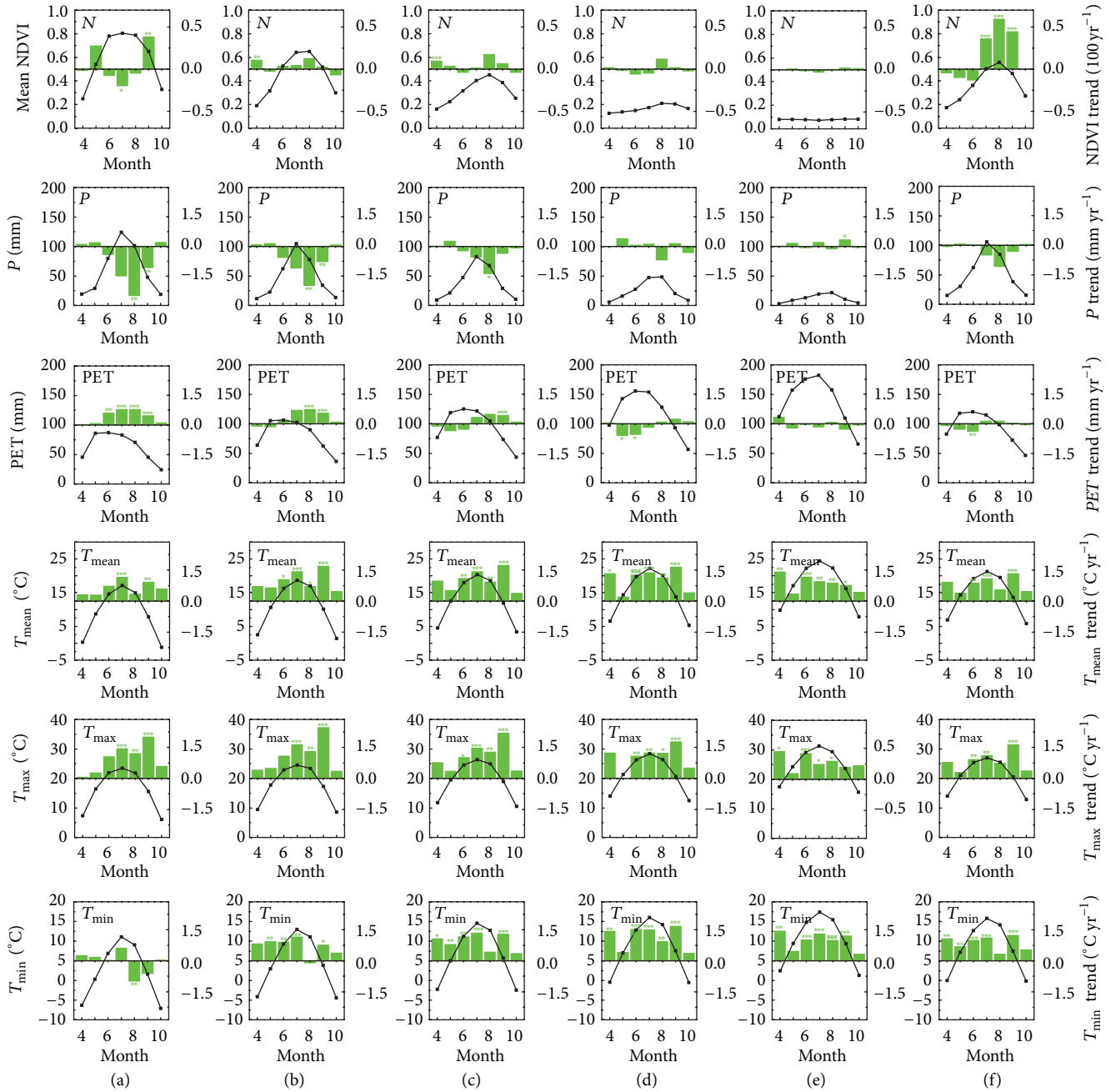


FIGURE 3: Variation in monthly NDVI and climatic variables during growing season over the 25 years for the six vegetation types: (a) forest, (b) meadow steppe, (c) typical steppe, (d) desert steppe, (e) desert, and (f) cropland. Monthly P , monthly PET, and monthly T_{mean} , T_{max} , and T_{min} . The green bars denote the trends, and black lines represent the mean values. * * *, **, and * indicate $P < 0.01$, $P < 0.05$, and $P < 0.1$, respectively.

and desert steppes ($R = -0.63$, $P < 0.01$; and $R = -0.71$, $P < 0.01$, resp.), implying that water may be the key factor controlling grass growth. In addition, growing season NDVI was also positively related to temperature for the meadow steppe, especially to T_{min} ($R = 0.36$, $P < 0.1$), indicating that an increase in temperature can also enhance meadow steppe growth. The steppes and desert biomes are dominated by a medium temperate semiarid and arid climate, and the growing season NDVI rose as

precipitation increased, which agrees with previous findings [28, 44, 59]. These relationships strengthened from meadow steppe to typical steppe and desert steppe, but then weakened to desert, which tends to confirm the general viewpoint that a threshold exists around which vegetation growth is most sensitive to water supply, and below or above which the relationship weakens [29, 60]. Grass in subarid and arid regions is predominantly influenced by precipitation: the more precipitation, the more vegetation growth. However,

TABLE 2: Correlation coefficients between monthly mean NDVI and P , PET, T_{mean} , T_{max} , and T_{min} in the same month for different vegetation types.

Vegetation types	Climate variables	Correlation coefficient						
		4	5	6	7	8	9	10
Forest	P	-0.22	-0.25	0.08	-0.38*	-0.44**	-0.31	0.06
	PET	0.74***	0.43**	0.13	0.35*	0.55***	0.60***	-0.05
	T_{mean}	0.48**	0.74***	0.23	-0.21	0.32	-0.02	0.27
	T_{max}	0.55***	0.69***	0.22	0.06	0.52***	0.24	0.33
	T_{min}	0.28	0.48**	0.25	-0.54***	-0.23	-0.46**	0.20
Meadow steppe	P	0.26	0.30	0.31	-0.14	-0.44**	-0.03	0.32
	PET	0.12	0.02	-0.25	0.07	0.49**	-0.05	0.08
	T_{mean}	0.38*	0.49**	-0.12	0.03	0.13	0.07	0.33
	T_{max}	0.30	0.38*	-0.16	0.07	0.33	-0.03	0.30
	T_{min}	0.50**	0.53***	0.03	0.01	-0.38*	0.12	0.38*
Typical steppe	P	0.30	0.63***	0.54***	0.19	0.10	-0.16	0.23
	PET	-0.11	-0.38*	-0.47**	-0.31	-0.29	0.01	0.05
	T_{mean}	0.21	0.29	-0.37*	-0.15	-0.21	0.23	0.25
	T_{max}	0.10	0.11	-0.41**	-0.19	-0.19	0.22	0.22
	T_{min}	0.34	0.45**	-0.27	0.02	-0.17	0.22	0.30
Desert steppe	P	0.22	0.72***	0.55***	0.60***	0.56***	0.02	0.20
	PET	-0.30	-0.58***	-0.39*	-0.47**	-0.55***	-0.25	-0.30
	T_{mean}	-0.30	-0.20	-0.50**	-0.33	-0.30	-0.00	-0.15
	T_{max}	-0.34*	-0.30	-0.49**	-0.32	-0.32	0.01	-0.14
	T_{min}	-0.21	0.19	-0.37*	-0.160	-0.13	0.00	-0.14
Desert	P	-0.21	0.01	0.09	-0.36*	-0.04	-0.09	-0.05
	PET	0.10	0.08	0.01	0.24	0.07	-0.16	-0.29
	T_{mean}	-0.19	-0.04	0.20	0.11	0.11	-0.17	-0.45**
	T_{max}	-0.10	0.11	0.27	0.20	0.18	-0.09	-0.33
	T_{min}	-0.24	-0.22	0.11	-0.12	-0.02	-0.24	-0.56***
Crop	P	0.21	0.36*	0.37*	0.00	-0.21	-0.22	0.17
	PET	-0.00	-0.21	0.07	-0.12	0.04	0.08	0.06
	T_{mean}	-0.07	-0.10	-0.43**	0.17	0.20	0.40**	0.16
	T_{max}	-0.05	-0.17	-0.45**	0.12	0.21	0.46**	0.12
	T_{min}	-0.02	-0.01	-0.43**	0.28	0.12	0.36*	0.15

***, **, and * indicate $P < 0.01$, $P < 0.05$ and $P < 0.1$, respectively; Bolded numbers denote larger correlation coefficients between the monthly mean NDVI and the corresponding climate variables in the same month, compared with those for climate variables in the preceding month.

in extremely arid conditions, temperature-associated drought generally reduces water availability for vegetation growth, which offsets slight changes in precipitation, leading to a limited effect on vegetation growth [22, 59].

For cropland, growing season NDVI only showed a significant relationship with PET ($R = -0.58$, $P < 0.01$). Nevertheless, considering the different crop growth periods, we calculated the correlation coefficients between NDVI and corresponding climate variables during April to June and July to September, respectively, and nonsignificant correlation was observed. This can be evidenced by ground-based observations. Several studies have revealed that grain yield in this region is probably because of intensive human management, such as fertilization and changing crop type [54, 61, 62].

3.3. The Responses of Monthly NDVI to Climate Changes

3.3.1. The Responses of Monthly NDVI to Climate Changes in the Same Time.

The relationship of the monthly NDVI

to climate variables was complicated and varied temporally among the biomes (Table 2). The forest NDVI was significantly and positively related to T_{mean} , T_{max} , and T_{min} in April and May, but negatively to T_{min} in July, August, and September ($R = -0.54$, $P < 0.01$; $R = -0.23$, $P = 0.26$; and $R = -0.46$, $P < 0.05$, resp.). These findings suggest that an increase in temperature may increase forest growth at the beginning of the growing period, but the minimum temperature increase may depress forest growth in the middle of the growing period. In agreement with previous studies, the large increase in NDVI occurred in the early growing season due to a large temperature rise and advanced growing season [63]. The forest NDVI correlated significantly and negatively with P in July ($R = -0.38$, $P < 0.1$) and August ($R = -0.44$, $P < 0.05$), whereas it significantly and positively related to PET, except in June ($R = 0.13$, $P = 0.54$) and October ($R = -0.05$, $P = 0.82$), indicating that excess rainfall in summer can be an

important limiting factor for forest growth. This is consistent with the results of Fang et al., who reported that forest growth tended to decrease with an increase of precipitation in a relatively cold condition [64]. NDVI for meadow steppe was positively correlated with temperature over almost all of the growing season months, and significantly in April and May. However, NDVI showed a positive correlation with P in April, May, June, and October, but only a significant negative correlation in August ($R = -0.44$, $P < 0.05$). In comparison, although NDVI was positively correlated with P , and negatively related to PET during most growing months for both typical and desert steppe, there was an opposite trend in correlations between NDVI and temperature in April, May, and October. This difference response of steppes to monthly climate change may also be highly correlated with the east-to-west water-temperature gradient. From east to west (i.e., from meadow steppe, typical steppe to desert steppe), the correlation between monthly NDVI and precipitation was strengthened as aridity increased, whereas monthly NDVI was more weakly related to temperature with temperature rising [22].

The NDVI of the temperate desert did not correlate well with climate variables for any month, but most of the correlations between NDVI and T_{mean} , T_{max} , and T_{min} were negative in April, May, September, and October, and especially in October. For cropland, the monthly NDVI was positively related to P , but negatively to T_{mean} , T_{max} , and T_{min} in April, May, and June, and most significantly in June ($R = 0.37$, $P < 0.1$; $R = -0.43$, $P < 0.05$; $R = -0.45$, $P < 0.05$; and $R = -0.43$, $P < 0.05$, resp.), whereas the opposite relationships occurred in July, August, September, and October, but particularly in September ($R = -0.22$, $P = 0.29$; $R = 0.40$, $P < 0.05$; $R = -0.46$, $P < 0.05$; and $R = -0.36$, $P < 0.05$, resp.).

3.3.2. The Response of Monthly NDVI to Climate Change in the Previous Month. Although the monthly NDVI had a similar pattern to that of the climate variables, the monthly peak NDVI was not always coupled with those climatic factors (Figure 2). This discrepancy may suggest a lagged response of NDVI to change in climate [16]. To illustrate and analyze this lagged response of vegetation growth, we also calculated correlation coefficients between monthly NDVI and climatic variables from the preceding month (Table 3). The strength of the relationship varied, however, depending on the biomes and climate variables. For forest, significantly positive correlations were found between the NDVI value in April, May, and September, and PET, T_{mean} , T_{max} , and T_{min} from the preceding month, whereas the NDVI value in April was negatively related to antecedent P ($R = -0.51$, $P < 0.01$). This implies that temperature and potential evapotranspiration in the preceding month are beneficial to forest growth at the beginning and end of the growing season, whereas precipitation during the previous month can depress growth in early spring. The weakly response of forest to preceding P can result from the deeper-rooted system that can maintain amount of moisture during dry periods by absorbing water from the deeper soil and adequate precipitation [52].

Similarly, for the three steppe types, most NDVI values in April and May were positively correlated with T_{mean} , T_{max} , and T_{min} in the previous month, implying that higher temperatures in the preceding month could stimulate grass growth at the beginning of the growing season. In comparison, there were positive correlations between P from the preceding month and monthly NDVI values during the whole growing season (except April for meadow steppe), whereas an almost opposite relationship between NDVI values and corresponding PET appeared at the same time. In addition, during the latter period of the growing season, correlations between the monthly NDVI and climate variables in the previous month were always stronger than the correlations with no time lag, suggesting that the antecedent climate conditions may be critical to grass growth in the latter part of the growing season (Tables 2 and 3). For the cropland, the lagged response of monthly NDVI to changes in climate was not well observed as for the other vegetation types, which is inconsistent with those who concluded that crop seemed to respond more quickly to precipitation than grasslands due to more shallow-rooted system [65]. The difference may be ascribed to different time scale. In this study, we just focused on one month lag effect and could not to detect lag times less than 30 days.

Monthly NDVI increases at the beginning of the growing season (in May for forest, and in April for steppes) were greatly responsible for the growing season NDVI changes, which were almost all strongly and positively related to the current and preceding month's T_{mean} , T_{max} , and T_{min} (Tables 2 and 3). It is possible that, in relatively high latitude regions (forest, as well as meadow and typical steppe areas) where the temperature is relatively low (Figure 2), vegetation growth is highly sensitive to temperature change at the beginning of the growing season [43, 66]. Spring warming can lower levels of frost damage, thaw out the frozen soil, advance the beginning of the growing season, promote plant photosynthesis, and thereby boost vegetation growth [67, 68]. This is partly confirmed by the negative correlation between corresponding precipitation and NDVI in relatively colder regions (Table 2), because spring rainfall can lower temperatures. The disparity between the larger increase at the beginning of the growing season in May for forest, and not in April as for the steppes, can be attributed to the later arrival of spring. Previous studies suggest that the period with daily mean temperatures consistently above 5°C is generally regarded as the growing season for trees [33], with temperatures above 0°C necessary for grass growth [69]. Consequently, the start of the growing season in the steppe regions may be one month ahead of that in the forested areas (on Julian days 79 and 111, resp.).

NDVI variability in spring (April and May) was positively related to T_{mean} , T_{max} , and T_{min} from the preceding month, but almost always negatively related to the temperature range in the current month for desert steppe and desert. The pattern of these relationships may result mainly from differences in regional climate conditions. In the desert steppe and desert regions, where water resources are seriously limited (the ratio of monthly PET to P in April and May is 48.43 and 16.65, resp., for desert steppe, and 93.11 and 34.03, resp., for desert; Figure 2), the heat or water stress induced by climate

TABLE 3: Correlation coefficients between monthly mean NDVI and P , PET, T_{mean} , T_{max} , and T_{min} in the preceding month for different vegetation types.

Vegetation types	Climate variables	Correlation coefficient						
		4	5	6	7	8	9	10
Forest	P	-0.51***	0.11	0.25	-0.05	-0.21	-0.19	0.14
	PET	0.63***	0.32	-0.24	-0.10	0.32	0.49**	0.01
	T_{mean}	0.40*	0.48**	-0.20	0.01	-0.07	0.35*	-0.06
	T_{max}	0.45**	0.36*	-0.32	-0.03	0.09	0.45**	-0.09
	T_{min}	0.37*	0.49**	0.07	0.14	-0.28	-0.09	0.03
Meadow steppe	P	-0.05	0.25	0.50**	0.03	0.01	0.57***	0.48**
	PET	0.51**	0.16	-0.19	-0.27	-0.01	-0.48**	-0.36*
	T_{mean}	0.29	0.33	-0.03	0.06	0.15	-0.30	0.07
	T_{max}	0.30	0.33	-0.16	0.02	0.08	-0.40**	-0.14
	T_{min}	0.28	0.35*	0.14	0.15	0.25	0.11	0.37*
Typical steppe	P	0.04	0.50**	0.39*	0.20	0.53***	0.66***	0.22
	PET	0.37*	-0.14	-0.41**	-0.45**	-0.48**	-0.74***	-0.17
	T_{mean}	0.33	0.41**	0.15	-0.20	0.00	-0.51**	0.19
	T_{max}	0.36*	0.37*	0.01	-0.22	-0.15	-0.59***	0.09
	T_{min}	0.33	0.48**	0.29	-0.14	0.32	-0.15	0.30
Desert steppe	P	0.22	0.71***	0.64***	0.51***	0.71***	0.74***	0.04
	PET	0.16	-0.34*	-0.71***	-0.33	-0.40**	-0.67***	-0.23
	T_{mean}	0.30	0.21	-0.05	-0.41**	0.02	-0.44**	0.01
	T_{max}	0.29	0.14	-0.24	-0.42**	-0.07	-0.47**	0.04
	T_{min}	0.30	0.35*	0.27	-0.27	0.29	-0.21	0.03
Desert	P	0.13	-0.04	0.68***	0.12	0.14	0.40**	-0.18
	PET	0.01	-0.11	-0.44**	-0.02	0.15	-0.27	-0.12
	T_{mean}	0.13	0.18	-0.09	-0.08	0.26	0.02	0.04
	T_{max}	0.17	0.17	-0.16	-0.05	0.25	-0.01	0.09
	T_{min}	0.10	0.18	0.13	-0.06	0.27	0.05	-0.08
Crop	P	0.27	0.08	0.09	0.02	0.11	0.13	0.21
	PET	-0.19	0.04	-0.43**	-0.31	-0.24	-0.32	-0.15
	T_{mean}	0.10	0.23	-0.23	0.23	0.32	-0.02	-0.03
	T_{max}	0.10	0.26	-0.29	0.20	0.20	-0.09	-0.09
	T_{min}	0.11	0.20	-0.14	0.28	0.52***	0.15	0.04

***, **, and * indicate $P < 0.01$, $P < 0.05$, and $P < 0.1$, respectively; Bolded numbers denote larger correlation coefficients between the monthly mean NDVI and the corresponding climate variables in the preceding month, compared with those for climate variables in the same month.

change can adversely affect grass germination and initial growth [27, 70], despite the fact that previous warming can promote germination. These also support the other findings, which report that onset dates of green-up are delayed by the warming trend in the desert steppe [71].

4. Conclusion

Based on the normalized difference vegetation index (NDVI), we have investigated the growing season and monthly NDVI trends and their relationships with climate variables for six biomes in Inner Mongolia over the period 1982–2006. Our results indicated that the growing season NDVI generally increased over the past 25 years for all biomes. The pronounced increase was found in cropland, which almost certainly stemmed from the primary crop type change and the advance of agricultural management. Changes in climate likely functioned as the important controller for

interannual variations in natural vegetation activity. The growing season NDVI was positively related to potential evapotranspiration and temperature, but negatively correlated with higher precipitation for the forest. In contrast, a positive (negative) correlation between NDVI and precipitation (potential evapotranspiration) existed in the steppes and desert. Additionally, monthly changes in climate seemed to influence plant growth in nonlinear fashions at the biome level, depending on times, climate variables, and biome types. Warming-related NDVI at the beginning of the growing season largely contributed to the NDVI increase during the growing season for forest, meadow steppe, and typical steppe but constrained the NDVI increase for desert steppe, desert, and crop. Moreover, our results also suggested that there were complicated one-month lags in vegetation responses to climate changes. However, although this study would greatly improve understanding of the complicated responses of vegetation to climate changes in Inner Mongolia, we could

not determine the relative contribution of these factors. How to separate the contributions from different driving forces remains a big challenge for further studies.

Conflict of Interests

The authors declare that there is no conflict of interests regarding the publication of this paper.

Acknowledgment

This study was supported by the National Scientific Technical Supporting Programs during the 12th Five-year Plan of China (2012BAC19B04) and National Basic Research Program of China (2011CB403206).

References

- [1] T. G. Huntington, "Climate change, growing season length, and transpiration: plant response could alter hydrologic regime," *Plant Biology*, vol. 6, no. 6, pp. 651–653, 2004.
- [2] E. Post, M. C. Forchhammer, M. S. Bret-Harte et al., "Ecological dynamics across the arctic associated with recent climate change," *Science*, vol. 325, no. 5946, pp. 1355–1358, 2009.
- [3] F. Tao, S. Zhang, and Z. Zhang, "Changes in rice disasters across China in recent decades and the meteorological and agronomic causes," *Regional Environmental Change*, vol. 13, no. 4, pp. 743–759, 2013.
- [4] C. J. Tucker, D. A. Slayback, J. E. Pinzon, S. O. Los, R. B. Myneni, and M. G. Taylor, "Higher northern latitude normalized difference vegetation index and growing season trends from 1982 to 1999," *International Journal of Biometeorology*, vol. 45, no. 4, pp. 184–190, 2001.
- [5] S. Wan, D. Hui, L. Wallace, and Y. Luo, "Direct and indirect effects of experimental warming on ecosystem carbon processes in a tallgrass prairie," *Global Biogeochemical Cycles*, vol. 19, no. 2, Article ID GB2014, pp. 1–13, 2005.
- [6] S. Chen, G. Lin, J. Huang, and G. D. Jenerette, "Dependence of carbon sequestration on the differential responses of ecosystem photosynthesis and respiration to rain pulses in a semiarid steppe," *Global Change Biology*, vol. 15, no. 10, pp. 2450–2461, 2009.
- [7] M. U. F. Kirschbaum, "The temperature dependence of soil organic matter decomposition, and the effect of global warming on soil organic C storage," *Soil Biology and Biochemistry*, vol. 27, no. 6, pp. 753–760, 1995.
- [8] D. S. Ojima, W. J. Parton, D. S. Schimel, J. M. O. Scurlock, and T. G. F. Kittel, "Modeling the effects of climatic and CO₂ changes on grassland storage of soil C," *Water, Air, and Soil Pollution*, vol. 70, no. 1–4, pp. 643–657, 1993.
- [9] I. M. D. Maclean and R. J. Wilson, "Recent ecological responses to climate change support predictions of high extinction risk," *Proceedings of the National Academy of Sciences of the United States of America*, vol. 108, no. 30, pp. 12337–12342, 2011.
- [10] R. Warren, J. Price, A. Fischlin, S. de la Nava Santos, and G. Midgley, "Increasing impacts of climate change upon ecosystems with increasing global mean temperature rise," *Climatic Change*, vol. 106, no. 2, pp. 141–177, 2011.
- [11] E. Lugato and A. Berti, "Potential carbon sequestration in a cultivated soil under different climate change scenarios: a modelling approach for evaluating promising management practices in north-east Italy," *Agriculture, Ecosystems and Environment*, vol. 128, no. 1–2, pp. 97–103, 2008.
- [12] D. Zhao, S. Wu, and Y. Yin, "Responses of terrestrial ecosystems' net primary productivity to future regional climate change in China," *PloS ONE*, vol. 8, no. 4, Article ID e60849, 2013.
- [13] X. Wang, S. Piao, P. Ciais et al., "Spring temperature change and its implication in the change of vegetation growth in North America from 1982 to 2006," *Proceedings of the National Academy of Sciences of the United States of America*, vol. 108, no. 4, pp. 1240–1245, 2011.
- [14] J. Harte and R. Shaw, "Shifting dominance within a montane vegetation community: results of a climate-warming experiment," *Science*, vol. 267, no. 5199, pp. 876–880, 1995.
- [15] H. A. Barbosa, A. R. Huete, and W. E. Baethgen, "A 20-year study of NDVI variability over the Northeast Region of Brazil," *Journal of Arid Environments*, vol. 67, no. 2, pp. 288–307, 2006.
- [16] S. Piao, J. Fang, L. Zhou et al., "Interannual variations of monthly and seasonal normalized difference vegetation index (NDVI) in China from 1982 to 1999," *Journal of Geophysical Research D*, vol. 108, no. 14, pp. 1–13, 2003.
- [17] A. K. Knapp and M. D. Smith, "Variation among biomes in temporal dynamics of aboveground primary production," *Science*, vol. 291, no. 5503, pp. 481–484, 2001.
- [18] S. Sarkar and M. Kafatos, "Interannual variability of vegetation over the Indian sub-continent and its relation to the different meteorological parameters," *Remote Sensing of Environment*, vol. 90, no. 2, pp. 268–280, 2004.
- [19] A. Kawabata, K. Ichii, and Y. Yamaguchi, "Global monitoring of interannual changes in vegetation activities using NDVI and its relationships to temperature and precipitation," *International Journal of Remote Sensing*, vol. 22, no. 7, pp. 1377–1382, 2001.
- [20] X. Zeng, P. Rao, R. S. DeFries, and M. C. Hansen, "Interannual variability and decadal trend of global fractional vegetation cover from 1982 to 2000," *Journal of Applied Meteorology*, vol. 42, no. 10, pp. 1525–1530, 2003.
- [21] C. S. Potter, S. Klooster, and V. Brooks, "Interannual variability in terrestrial net primary production: exploration of trends and controls on regional to global scales," *Ecosystems*, vol. 2, no. 1, pp. 36–48, 1999.
- [22] S. Piao, A. Mohammat, J. Fang, Q. Cai, and J. Feng, "NDVI-based increase in growth of temperate grasslands and its responses to climate changes in China," *Global Environmental Change*, vol. 16, no. 4, pp. 340–348, 2006.
- [23] I. Fabricante, M. Oesterheld, and J. M. Paruelo, "Annual and seasonal variation of NDVI explained by current and previous precipitation across Northern Patagonia," *Journal of Arid Environments*, vol. 73, no. 8, pp. 745–753, 2009.
- [24] R. D. Alward, J. K. Detling, and D. G. Milchunas, "Grassland vegetation changes and nocturnal global warming," *Science*, vol. 283, no. 5399, pp. 229–231, 1999.
- [25] J. Szilagyi, D. C. Rundquist, D. C. Gosselin, and M. B. Parlange, "NDVI relationship to monthly evaporation," *Geophysical Research Letters*, vol. 25, no. 10, pp. 1753–1756, 1998.
- [26] W. Yang, L. Yang, and J. W. Merchant, "An assessment of AVHRR/NDVI-ecoclimatological relations in Nebraska, U.S.A.," *International Journal of Remote Sensing*, vol. 18, no. 10, pp. 2161–2180, 1997.
- [27] L. Yang, B. K. Wylie, L. L. Tieszen, and B. C. Reed, "An analysis of relationships among climate forcing and time-integrated NDVI of grasslands over the U.S. northern and central Great Plains," *Remote Sensing of Environment*, vol. 65, no. 1, pp. 25–37, 1998.

- [28] X. Zhao, K. Tan, S. Zhao, and J. Fang, "Changing climate affects vegetation growth in the arid region of the northwestern China," *Journal of Arid Environments*, vol. 75, no. 10, pp. 946–952, 2011.
- [29] B. Li, S. Tao, and R. W. Dawson, "Relations between AVHRR NDVI and ecoclimatic parameters in China," *International Journal of Remote Sensing*, vol. 23, no. 5, pp. 989–999, 2002.
- [30] B. H. Braswell, D. S. Schimel, E. Linder, and B. Moore III, "The response of global terrestrial ecosystems to interannual temperature variability," *Science*, vol. 278, no. 5339, pp. 870–872, 1997.
- [31] Y. Yang, J. Xu, Y. Hong, and G. Lv, "The dynamic of vegetation coverage and its response to climate factors in Inner Mongolia, China," *Stochastic Environmental Research and Risk Assessment*, vol. 26, no. 3, pp. 357–373, 2012.
- [32] G. Zhang, Y. Kang, G. Han, and K. Sakurai, "Effect of climate change over the past half century on the distribution, extent and NPP of ecosystems of Inner Mongolia," *Global Change Biology*, vol. 17, no. 1, pp. 377–389, 2011.
- [33] B. Liu, M. Henderson, Y. Zhang, and M. Xu, "Spatiotemporal change in China's climatic growing season: 1955–2000," *Climatic Change*, vol. 99, no. 1–2, pp. 93–118, 2010.
- [34] W. Qian and X. Lin, "Regional trends in recent temperature indices in China," *Climate Research*, vol. 27, no. 2, pp. 119–134, 2004.
- [35] B. Liu, M. Xu, M. Henderson, Y. Qi, and Y. Li, "Taking China's temperature: daily range, warming trends, and regional variations, 1955–2000," *Journal of Climate*, vol. 17, no. 22, pp. 4453–4462, 2004.
- [36] N. Lu, B. Wilske, J. Ni, R. John, and J. Chen, "Climate change in Inner Mongolia from 1955 to 2005—trends at regional, biome and local scales," *Environmental Research Letters*, vol. 4, no. 4, Article ID 045006, 2009.
- [37] S. Brogaard, M. Runnström, and J. W. Seaquist, "Primary production of Inner Mongolia, China, between 1982 and 1999 estimated by a satellite data-driven light use efficiency model," *Global and Planetary Change*, vol. 45, no. 4, pp. 313–332, 2005.
- [38] L. Zhang, Z. Yang, and G. Chen, "Emergy analysis of cropping-grazing system in Inner Mongolia Autonomous Region, China," *Energy Policy*, vol. 35, no. 7, pp. 3843–3855, 2007.
- [39] S. Wu, Q. Yang, and D. Zheng, "Delineation of eco-geographic regional system of China," *Journal of Geographical Sciences*, vol. 13, no. 3, pp. 309–315, 2003.
- [40] J. Fang, S. Piao, J. He, and W. Ma, "Increasing terrestrial vegetation activity in China, 1982–1999," *Science in China C*, vol. 47, no. 3, pp. 229–240, 2004.
- [41] B. N. Holben, "Characteristics of maximum-value composite images from temporal AVHRR data," *International Journal of Remote Sensing*, vol. 7, no. 11, pp. 1417–1434, 1986.
- [42] Z. P. Wang, X. G. Han, G. G. Wang, Y. Song, and J. Gullledge, "Aerobic methane emission from plants in the Inner Mongolia steppe," *Environmental Science and Technology*, vol. 42, no. 1, pp. 62–68, 2008.
- [43] S. Piao, X. Wang, P. Ciais, B. Zhu, T. Wang, and J. Liu, "Changes in satellite-derived vegetation growth trend in temperate and boreal Eurasia from 1982 to 2006," *Global Change Biology*, vol. 17, no. 10, pp. 3228–3239, 2011.
- [44] S. Peng, A. Chen, L. Xu et al., "Recent change of vegetation growth trend in China," *Environmental Research Letters*, vol. 6, no. 4, Article ID 044027, 2011.
- [45] Y. Yin, S. Wu, and E. Dai, "Determining factors in potential evapotranspiration changes over China in the period 1971–2008," *Chinese Science Bulletin*, vol. 55, no. 29, pp. 3329–3337, 2010.
- [46] Editorial Board of Vegetation Map of China, *Vegetation Atlas of China*, Science Press, Beijing, China, 2001.
- [47] Editorial Board of Rangeland Resources of China, *Rangeland Resources of China*, Science Press, Beijing, China, 1996.
- [48] J. Liu, M. Liu, D. Zhuang, Z. Zhang, and X. Deng, "Study on spatial pattern of land-use change in China during 1995–2000," *Science in China, Series D*, vol. 46, no. 4, pp. 373–384, 2003.
- [49] B. Liu, Y. Huang, J. Fu, and D. Jiang, "Analysis on Spatio-temporal change and driving forces of land use in Tianjin Harbor," *Journal of Geo-Information Science*, vol. 14, no. 2, pp. 270–278, 2012.
- [50] X. Zhang and J. Zhu, "Variations in fractional vegetation coverage over Eastern China during 1982–2006," *Climatic and Environmental Research*, no. 3, pp. 365–374, 2013.
- [51] G. Bao, Z. Qin, Y. Bao, and Y. Zhou, "Spatial-temporal change of vegetation cover in Mongolian Plateau during 1982–2006," *Journal of Desert Research*, vol. 33, no. 3, pp. 918–927, 2013.
- [52] D. Mao, Z. Wang, L. Luo, and C. Ren, "Integrating AVHRR and MODIS data to monitor NDVI changes and their relationships with climatic parameters in Northeast China," *International Journal of Applied Earth Observation and Geoinformation*, vol. 18, pp. 528–536, 2012.
- [53] X. Wang, Y. Li, G. Cui, X. Wu, M. Yu, and W. Ma, "Review of wheat production in inner Mongolia and its actuality analysis," *Inner Mongolia Agriculture Science and Technology*, no. 6, pp. 5–6, 2010.
- [54] R. Luo, B. Zhang, J. Gao, Z. Wang, J. Sun, and X. Yu, "Climate change impacts on corn production as evidenced by a model and historical yields in Inner Mongolia, China," *Journal of Food, Agriculture & Environment*, vol. 10, no. 2, pp. 976–983, 2012.
- [55] K. Ichii, A. Kawabata, and Y. Yamaguchi, "Global correlation analysis for NDVI and climatic variables and NDVI trends: 1982–1990," *International Journal of Remote Sensing*, vol. 23, no. 18, pp. 3873–3878, 2002.
- [56] E. S. Euskirchen, A. D. McGuire, D. W. Kicklighter et al., "Importance of recent shifts in soil thermal dynamics on growing season length, productivity, and carbon sequestration in terrestrial high-latitude ecosystems," *Global Change Biology*, vol. 12, no. 4, pp. 731–750, 2006.
- [57] T. A. Black, W. J. Chen, A. G. Barr et al., "Increased carbon sequestration by a Boreal deciduous forest in years with a warm spring," *Geophysical Research Letters*, vol. 27, no. 9, pp. 1271–1274, 2000.
- [58] R. R. Nemani, C. D. Keeling, H. Hashimoto et al., "Climate-driven increases in global terrestrial net primary production from 1982 to 1999," *Science*, vol. 300, no. 5625, pp. 1560–1563, 2003.
- [59] M. Zhao and S. W. Running, "Drought-induced reduction in global terrestrial net primary production from 2000 through 2009," *Science*, vol. 329, no. 5994, pp. 940–943, 2010.
- [60] C. J. Tucker, H. E. Dregne, and W. W. Newcomb, "Expansion and contraction of the Sahara desert from 1980 to 1990," *Science*, vol. 253, no. 5017, pp. 299–301, 1991.
- [61] L. Zhao and L. Duan, "The analysis of main factors affecting grain yield in Inner Mongolia Autonomous Region," *Journal of Northwest Sci-Tec University of Agriculture and Forest*, vol. 29, no. 4, pp. 77–80, 2001.

- [62] L. Zhang, X. Zhao, D. Zhao, F. Yang, and L. Zhang, "Dynamic analysis of grain production and evaluation of food security of Inner Mongolia," *Agricultural Research in the Arid Areas*, vol. 28, no. 5, pp. 190–195, 2010.
- [63] L. Zhou, C. J. Tucker, R. K. Kaufmann, D. Slayback, N. V. Shabanov, and R. B. Myneni, "Variations in northern vegetation activity inferred from satellite data of vegetation index during 1981 to 1999," *Journal of Geophysical Research D*, vol. 106, no. 17, pp. 20069–20083, 2001.
- [64] J. Fang, S. Piao, L. Zhou et al., "Precipitation patterns alter growth of temperate vegetation," *Geophysical Research Letters*, vol. 32, no. 21, Article ID L21411, pp. 1–5, 2005.
- [65] J. Wang, P. M. Rich, and K. P. Price, "Temporal responses of NDVI to precipitation and temperature in the central Great Plains, USA," *International Journal of Remote Sensing*, vol. 24, no. 11, pp. 2345–2364, 2003.
- [66] S. Tanja, F. Berninger, T. Vesala et al., "Air temperature triggers the recovery of evergreen boreal forest photosynthesis in spring," *Global Change Biology*, vol. 9, no. 10, pp. 1410–1426, 2003.
- [67] A. D. Richardson, T. A. Black, P. Ciais et al., "Influence of spring and autumn phenological transitions on forest ecosystem productivity," *Philosophical Transactions of the Royal Society B*, vol. 365, no. 1555, pp. 3227–3246, 2010.
- [68] L. R. Welp, J. T. Randerson, and H. P. Liu, "The sensitivity of carbon fluxes to spring warming and summer drought depends on plant functional type in boreal forest ecosystems," *Agricultural and Forest Meteorology*, vol. 147, no. 3–4, pp. 172–185, 2007.
- [69] D. J. Moot, W. R. Scott, A. M. Roy, and A. C. Nicholls, "Base temperature and thermal time requirements for germination and emergence of temperate pasture species," *New Zealand Journal of Agricultural Research*, vol. 43, no. 1, pp. 15–25, 2000.
- [70] S. Wan, J. Xia, W. Liu, and S. Niu, "Photosynthetic overcompensation under nocturnal warming enhances grassland carbon sequestration," *Ecology*, vol. 90, no. 10, pp. 2700–2710, 2009.
- [71] F. Yu, K. P. Price, J. Ellis, and P. Shi, "Response of seasonal vegetation development to climatic variations in eastern central Asia," *Remote Sensing of Environment*, vol. 87, no. 1, pp. 42–54, 2003.

Research Article

Spatially Explicit Assessment of Ecosystem Resilience: An Approach to Adapt to Climate Changes

Haiming Yan,¹ Jinyan Zhan,¹ Bing Liu,² Wei Huang,³ and Zhihui Li^{4,5,6}

¹ State Key Laboratory of Water Environment Simulation, School of Environment, Beijing Normal University, Beijing 100875, China

² College of Geomatics, Shandong University of Science and Technology, No. 579 Qianwangang Road, Economic & Technical Development Zone, Qingdao, Shandong 266590, China

³ Department of Agricultural Economics and Rural Development, Georg-August-Universität Göttingen, Raum MZG 2016, Platz der Göttinger Sieben 5, 37073 Göttingen, Germany

⁴ Institute of Geographic and Natural Resources Research, Chinese Academy of Sciences, Beijing 100101, China

⁵ University of Chinese Academy of Sciences, Beijing 100049, China

⁶ Center for Chinese Agricultural Policy, Chinese Academy of Sciences, Beijing 100101, China

Correspondence should be addressed to Jinyan Zhan; zhanjy@bnu.edu.cn

Received 2 November 2013; Revised 4 January 2014; Accepted 11 January 2014; Published 19 February 2014

Academic Editor: Dong Jiang

Copyright © 2014 Haiming Yan et al. This is an open access article distributed under the Creative Commons Attribution License, which permits unrestricted use, distribution, and reproduction in any medium, provided the original work is properly cited.

The ecosystem resilience plays a key role in maintaining a steady flow of ecosystem services and enables quick and flexible responses to climate changes, and maintaining or restoring the ecosystem resilience of forests is a necessary societal adaptation to climate change; however, there is a great lack of spatially explicit ecosystem resilience assessments. Drawing on principles of the ecosystem resilience highlighted in the literature, we built on the theory of dissipative structures to develop a conceptual model of the ecosystem resilience of forests. A hierarchical indicator system was designed with the influencing factors of the forest ecosystem resilience, including the stand conditions and the ecological memory, which were further disaggregated into specific indicators. Furthermore, indicator weights were determined with the analytic hierarchy process (AHP) and the coefficient of variation method. Based on the remote sensing data and forest inventory data and so forth, the resilience index of forests was calculated. The result suggests that there is significant spatial heterogeneity of the ecosystem resilience of forests, indicating it is feasible to generate large-scale ecosystem resilience maps with this assessment model, and the results can provide a scientific basis for the conservation of forests, which is of great significance to the climate change mitigation.

1. Introduction

There is ample evidence of the ecological impacts of climate change, which may pose considerable challenges to the terrestrial ecosystems and change the provided ecosystem services in the future [1, 2], and the forest ecosystem resilience plays an important role in maintaining the desirable ecosystem states that allow these ecosystem services to be delivered, and enables quick and flexible responses to climate changes [3]. For example, forests are major reservoirs of terrestrial biodiversity and contain about 50% of the global terrestrial biomass carbon stocks, emissions from deforestation and degradation remain a significant source of annual greenhouse gas emissions into the atmosphere, and therefore the

conservation, appropriate management, and restoration of forests will make a significant contribution to climate change mitigation [4]. Resilience is the capacity of an ecosystem to withstand external pressures and return to its predisturbance state over time, the loss of ecosystem resilience indicates that ecosystems are prone to the shifts to undesirable states in which the ecosystem services needed by humans can no longer be delivered, and maintaining or restoring the forest ecosystem resilience is often cited as a necessary societal adaptation to climate change [5, 6]. However, forest ecosystem resilience has continually declined at the regional scale and even global scale due to the climate change and human disturbance [7]. The quantitative assessment of ecosystem resilience can provide a scientific basis for the forest resource

management and conservation and therefore is of great significance to the maintenance of critical ecosystem services [8].

The concept of resilience has been widely used, and there have been some ecological theories that attempt to explain the mechanism of resilience through a variety of models [9, 10], for example, “species richness-diversity” [11], “functional redundancy” [12], “keystone species hypothesis” [13], “resilience-productivity hypothesis” [14]. However, these theories are generally based on the concept of species populations as the basic functional unit and therefore fail to capture the importance of the interactions amongst individual organisms in the ecosystem [10]. Among the current theories, the theory of dissipative structures seems particularly suitable for investigating the dynamics of structural change and resilience of ecosystems [15, 16]. It shows that the open and self-organizing systems maintain their structural order by keeping their internal state far from thermodynamic equilibrium through active exchanges with their environment [16]. Those dissipative structures are in principle stable as long as the exchanges with the environment are maintained and the continuous perturbations are absorbed within the framework of the given dynamic regime [15, 16]. The theory of dissipative structures provides a scientific theoretical framework for explaining the mechanism of the ecosystem resilience; however, there have been very few researches on the quantitative measurement of ecosystem resilience on the basis of this theory; more in-depth research should be carried out on how to more scientifically and accurately assess the ecosystem resilience with reasonable indicators of the ecosystem resilience.

Resilience can be measured in terms of change in a system level property and function following perturbation, and the perturbation can be simulated [10]. In previous research, the ecosystem resilience was generally measured by the rate of return of the ecosystem state after disturbance or the maximum disturbance that the ecosystem can absorb before shifting to another state [17]. Currently, researchers generally select one key indicator associated with the ecosystem, for example, the key species and vigor of the ecosystem, and they then simulate the time for the key indicator to return from the stressed state to the normal state (Tr) and the maximum stress that the ecosystem can withstand (MS) with models such as the CENTRURY model and the GAP model [18]. Ecosystem resilience can be represented by the values of MS , $1/Tr$, or MS/Tr [19]. This approach assumes that the dynamics of the ecosystem can be understood by analyzing a few key variables, which is termed the “rule of hand” [5]. However, the concept of “rule of hand” is limited and relatively unrepresentative because it is impossible to represent the complete recovery of ecosystem function by the recovery of only a few key variables [20]. In addition, although it is in principle possible to measure ecosystem resilience by fitting a dynamic model to time series, this approach imposes extraordinary data requirements. It is usually difficult to obtain the data that can meet such requirements in practice [17].

It is more plausible to measure resilience in terms of the factors influencing resilience. The literature reported a number of factors that influence the ecosystem resilience,

for example, the diversity within functional groups and variability of habitats [21]. However, these factors have not previously been considered comprehensively by researchers. The operational indicators of resilience have received little attention in the literature, and there is no consensus-based view of how to measure resilience or even of the exact nature of resilience [22]. Rosset and Oertli assessed the resilience of species to warming with five ecological and biogeographical metrics and explained their theoretical basis [23]; however, this approach may be relatively biased since these researchers simply used equal weights for each metric.

This study aims to develop a conceptual framework for the spatially explicit assessment of the forest ecosystem resilience based on the theory of dissipative structures, and the rest of this paper is organized as follows. The second part presents a brief overview of the study area and explains how the indicator system was constructed, how the indicator weights were determined, and how the resilience index was calculated. Besides, this part also shows the data used in this study and how they were processed. The third part presents the results and discusses the underlying reasons for the spatial heterogeneity of the forest ecosystem resilience, and the final part concludes.

2. Data and Methodology

2.1. Study Area. Yongxin County is representative of the subtropical mixed conifer and broadleaved forest area in the Poyang Lake watershed, with a forest area of 143,980 ha and a forest coverage rate of 65.6%. It is located between $26^{\circ}47' - 27^{\circ}14'N$ and $113^{\circ}50' - 114^{\circ}29'E$, in the upper and middle reaches of the Heshui River which is the largest secondary tributary of Poyang Lake (Figure 1). The northern and southern parts of Yongxin County primarily include mountains and hills, where there are a lot of forests, whereas the central part of the county includes hills and plains, most of which are covered by cultivated land. It is the subtropical monsoon climate in this region, with an annual average temperature of $18.2^{\circ}C$ and an annual average precipitation of 1,530.7 mm, and the zonal vegetation is the evergreen broadleaved forest, but the existing forests primarily consist of *Pinus massoniana* and *Cunninghamia lanceolata* (*C. lanceolata*), and the current state of the forests is the result of both the long-term human disturbance and restoration and the natural recovery under the influence of the regional natural background [24].

2.2. Data and Processing. The data used primarily include the forest inventory data, remotely sensed data, and statistical data. The forest inventory data in 2009 were obtained from the Yongxin Forestry Bureau, including the forest resource distribution map, data for 707 sample plots, and data for 41603 sample trees. We obtained the forest distribution map by integrating the forest form map with the Landsat Thematic (TM) image covering the study area. Besides, we interpolated the sample plot data and sample tree data into $30\text{ m} \times 30\text{ m}$ grid data with the Kriging method to obtain the data of specific indicators of the internal memory, such as the average stand age, average DBH growth rate, and mature

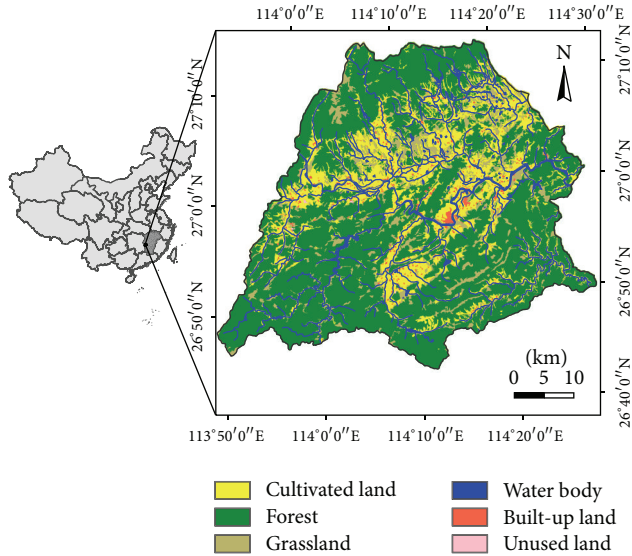


FIGURE 1: Location of Yongxin County and the distribution map of forests.

dominant tree density [25]. The external memory was then calculated on the basis of the internal memory. Besides, the factor influencing the availability of the external memory was indicated with the proximity index, which was calculated on the basis of the forest distribution map. In addition, the data of indicators of the stand conditions were prepared with the remote sensing data, observation data, and statistical data. For example, the climatic data were from the observation stations in Jiangxi Province and Hunan Province maintained, and the original data were interpolated into $30\text{ m} \times 30\text{ m}$ grid data using the gradient plus inverse distance squares method and then extracted the part of Yongxin County. The soil data were extracted from the forest inventory data of the second nationwide general soil survey and were interpolated into $30\text{ m} \times 30\text{ m}$ grid data with the Kriging method [26]. The terrain data were obtained with the $30\text{ m} \times 30\text{ m}$ digital elevation model (DEM) data. The distance to the nearest river was obtained from the 1:250,000 topographic maps of Jiangxi Province. The population data were obtained from China Population Statistics Yearbook 2010 and were spatially disaggregated into $30\text{ m} \times 30\text{ m}$ grid data with the spatial disaggregating method [27].

2.3. Model Development. The forest ecosystem resilience is quantitatively measured with its influencing factors on the basis of the theory of dissipative structures in this study. First, some definitions related to the ecosystem resilience were clarified, which lay the foundation for the ecosystem resilience assessment. Then based on the theory of dissipative structures, a hierarchical indicator system was constructed according to the factors influencing the forest ecosystem resilience, most of which have some impacts on the energy and material flows between the forest ecosystem and the environment. Thereafter, the indicator weights were determined with the combined weighting method, including the

analytic hierarchy process (AHP) and coefficient of variance (CV) method [28]. Finally, the resilience index of forests was calculated as the weighted sum of these indicators at the grid scale.

2.3.1. Definition of Ecosystem Resilience, State, and Scale. It is necessary to make some definitions related to the ecosystem resilience so as to make the results comparable. First and foremost, it is necessary to clarify the definition of ecosystem resilience since the literature offers various definitions of ecosystem resilience and includes a controversy about the existence of different ecosystem states [16]. The current viewpoints can be summarized into ecological resilience and engineering resilience, and forests are engineering resilient in the sense that they may in time return to their predisturbance state and maintain approximately the original species composition [3]. Therefore the definition of the engineering resilience has been adopted in this study, referring to the capacity of an ecosystem to absorb disturbance and return to its predisturbance state following a perturbation [29].

Secondly, it is crucial to specify the ecosystem state of interest since the forest ecosystems have multiple states under which different ecosystem services may be delivered [17]. This study has only focused on the resilience under the current state, which is defined with the dominant tree species [3], and it is assumed that there will be no state transformation during the study period. In addition, it is necessary to specify the scale in the resilience assessment since the different scales may lead to different assessment results [30, 31], and when viewed over an appropriate time span, a resilient forest ecosystem is able to maintain its “identity” in terms of taxonomic composition, structure, ecological functions and process rates [3]. As for the spatial scale, this study proposes to measure the absolute and relative conditions (e.g., space, environmental characteristics, and resource availability) at the patch scale and to analyze questions of resilience at the multipatch scale [31], and the 30 m resolution patch has been used to analyze the resilience in this study. As for the time scale, the forest ecosystem resilience is analyzed at the annual scale, and it is assumed that no ecosystem state transformations would occur during the study period since the ecosystem generally fluctuates near equilibrium and remains essentially stable during a given period.

2.3.2. Indicator System. A hierarchical model was developed with factors influencing the forest ecosystem resilience according to the theory of dissipative structures. The theory of dissipative structures shows that the forest ecosystem as a system of dissipative structures will soon collapse on condition that there is no input of energy and material [15], and the ecosystem resilience depends on both the favorable stand conditions and the biological and ecological resources in the ecosystem, all of which influence the input of energy and material into the forest ecosystem. Therefore the resilience index that evaluates the forest ecosystem resilience was disaggregated into the stand conditions and the ecological memory, which were finally disaggregated into simple indices that are measurable and can be observed in the field.

The indicators of the stand conditions include the terrain, soil, climate, water conditions, and human disturbance, which interact with each other and jointly affect the resilience of the forest ecosystem [32]. The terrain has obvious impacts on the factors required for plant growth, for example, the water and soil nutrients. For example, there is richer soil fertility and seed bank in the lower slope position than the middle and upper slope positions, and the seed germination rate at the lower slope position is higher [33], and the terrain indicators in this study include the aspect, slope, and slope position. Besides, the resilience at the local level depends on the ability of the landscape to maintain infiltration, water storage capacity and nutrient cycles, all of which are threatened by soil loss and structural change [34]. In this study, we selected the soil depth, humus horizon depth, and loam quantity for use as soil structure indices and used the humus quantity, soil nitrogen (N) quantity, soil phosphorus (P) quantity, and soil potassium (K) quantity as indices of soil fertility. In addition, the climate primarily influences photosynthesis, respiration, and other ecosystem processes through medium-term and long-term temperature, radiation and wetness and consequently exerts great impacts on the plant growth [4], and water conditions also have significant influence on plant growth through influencing the availability of water [35]. The climate indices used in this study included the annual accumulated temperature above 10°C, the annual precipitation, and the annual hours of sunshine, and the distance to the nearest river was used as the indicator of the water conditions. What is more, there is still controversy over the identification of humans as a component of natural ecosystems, but human beings have altered the resilience of ecosystems [36]; therefore the population density that is closely related with human activities has been used as the indicator of human disturbance in this study.

The ecological memory include the internal memory within the foci forest patch and external memory in the neighbor patches of the foci forest patch [37, 38], which were further represented with more specific indicators. The internal memory includes the species that survive within the disturbed area (i.e., the biological legacies) and the remaining dead organic structures that serve as foci for regeneration and allow species to colonize (i.e., the structural legacies) [38]. The biological legacies include the seed, vegetation materials, and animal communities, while the structural legacies provide critical protective cover, habitat, and food and nutrient sources for a variety of organisms and influence geomorphic processes such as erosion and the deposition of sediments [38]. First, the seed bank is the material basis for the natural regeneration of forests [37]. Since it is difficult to measure the soil seed bank in a large area, we used the factors influencing the soil seed bank as the specific indicators, including the density of the mature dominant trees and the stand canopy [39]. Besides, the ecosystem resilience resides in both the diversity of the drivers and the number of passengers who are potential drivers, which are of different significance to the ecosystem [40], and the selected indicators of the diversity of the drivers include the species number of the dominant trees and the subdominant trees and the grass and shrub canopy. In addition, ecophysiological characteristics

of the vegetation also contribute to ecosystem resilience [3], the indicators of which include the average stand age and the average growth rate of the diameter at breast height (DBH) in this study. What is more, structural legacies provide critical protective cover that allows species to colonize [21], and the litter depth was used as the indicator of structural legacies in this study. More importantly, the recovery of an ecosystem from disturbance requires an area that is sufficiently large and abundant internal memory to guarantee a rapid reorganization, and a larger and less fragmented forest ecosystem is more resilient [3]. In this study, the patch area and perimeter-to-area ratio were used to represent the patch size and patch shape, respectively.

Ecosystem reorganization requires both the internal memory within the disturbed patch and the external memory within neighboring patches, which provides seed flows among forest patches and influence the species composition and facilitate the resilience of disturbed patches [28]. Since it is difficult to measure long-distance seed dispersal, we measured the external memory by the density of mature dominant trees within neighboring patches of corresponding patch types whose edges are within a specified distance of the focal patch (1000 m in this study). In addition, many plant species are dispersal limited and are influenced by various factors such as the distance to the seed sources and the availability of dispersal agents [41], and therefore we have used a proximity index that combines the area of the neighboring patch and the distance to the focal patch as the indicator of the factors that influence the availability of external memory (Table 1).

2.3.3. Calculation of the Resilience Index. There are many methods to synthesize the basic indicators into one index, such as the fuzzy comprehensive evaluation method, Delphi method, and comprehensive index method [42]. This study used the classic comprehensive index method to calculate the resilience index of the forest ecosystem. First, the assessment indicators of the forest ecosystem resilience were assigned with different weights; then the weighted sum of the assessment indices was calculated with a spatial overlay of these indices. The resilience of the forest ecosystem is calculated with the following formula:

$$\text{resilience}_j = \sum_{i=1}^n w_i x_i, \quad (i = 1, 2, 3, \dots, n), \quad (1)$$

where resilience_j is the resilience index of the j th assessment unit, w_i is the weight of the i th assessment index, x_i is the value of the i th assessment index, which is normalized with the extreme value method, and n is the number of the assessment indices.

Besides, there are many methods to determine the index weights, which can be generally classified into the subjective weighing method and objective weighing method, both of which have some disadvantages [43, 44]. The combinatorial weighing method was used to determine the indicator weights to reduce the possible errors in this study. The indicator weights were first determined with AHP and the coefficient of variation method and then combined as follows

TABLE 1: The assessment system and weights of specific indicators. W_{AHP} and W_{CV} refer to the weights determined with the analytic hierarchy process (AHP) and coefficient of variation method (CV), respectively. The weights were calculated as the average of W_{AHP} and W_{CV} .

Medium-level indicators	Bottom indicators	W_{AHP}	W_{CV}	Weights
<i>Stand conditions</i>				
Terrain	Slope position	0.0123	0.0386	0.0254
	Slope	0.0088	0.0209	0.0148
	Aspect	0.0257	0.0417	0.0337
Climate				
Temperature	Annual average temperature	0.0138	0.0503	0.0320
	Cumulative temperature above 10°C	0.0292	0.0543	0.0417
Precipitation	Annual precipitation	0.0356	0.0289	0.0322
Solar radiation	Annual sunshine hour	0.0102	0.0467	0.0284
Water condition	Distance to the nearest river	0.0194	0.0075	0.0134
Soil				
Soil structure	Soil depth	0.0063	0.0177	0.0120
	Humus depth	0.024	0.0168	0.0204
	Loam quantity	0.0035	0.00001	0.0017
Soil fertility	Soil organic quantity	0.0045	0.0073	0.00591
	Soil nitrogen quantity	0.0065	0.0016	0.00406
	Soil phosphorus quantity	0.0036	0.00001	0.0018
	Soil kalium quantity	0.0044	0.0016	0.00301
Human disturbance	Population density	0.0237	0.0273	0.0255
<i>Ecological Memory</i>				
Internal memory				
Biological legacies	Species number of dominant and subdominant trees	0.0459	0.0824	0.0641
	Grass-shrub canopy	0.0145	0.0308	0.0226
	Average stand age	0.0293	0.0106	0.0199
	Average DBH growth rate	0.0206	0.0342	0.0274
	Mature dominant tree density	0.0568	0.0487	0.0527
	Vegetation canopy	0.0171	0.0257	0.0214
Structural legacies	Litter depth	0.0828	0.0384	0.0606
Patch area and shape	Patch area	0.2487	0.1001	0.1744
	Perimeter area ratio	0.0749	0.0058	0.0403
External memory and factors influencing its availability	Density of mature dominant tree within neighbor patches of corresponding types	0.0552	0.0665	0.0608
	Proximity index	0.1227	0.1949	0.1588

(see (2)) in order to take full advantage of expert knowledge and give full consideration to specific conditions of the study area:

$$w_i = \frac{w_j^{(1)} \times w_j^{(2)}}{\sum_{j=1}^m [w_j^{(1)} \times w_j^{(2)}]}, \quad (2)$$

where $w_j^{(1)}$ is the weight vector obtained with the coefficient of variation method, $w_j^{(2)}$ is the weight vector obtained with AHP, and j is the number of assessment indices. The final index weights are listed in Table 1.

3. Results and Discussion

3.1. Result of the Assessment of Resilience. The indicator system was finally established and indicator weights were determined (Table 1), with which the forest ecosystem resilience in the study area was calculated and was further divided into five levels (Figure 2), with the thresholds of the resilience index determined with the natural breaks method (Table 2).

The forests with the highest resilience were mainly located in the middle of the southwestern mountain area. The result indicated that the forest ecosystem resilience in Yongxin County ranged from 0.1803 to 0.6919, with an average value of 0.3821. Only 40.4% of the forests were above the average resilience level, and the forest ecosystem resilience in the

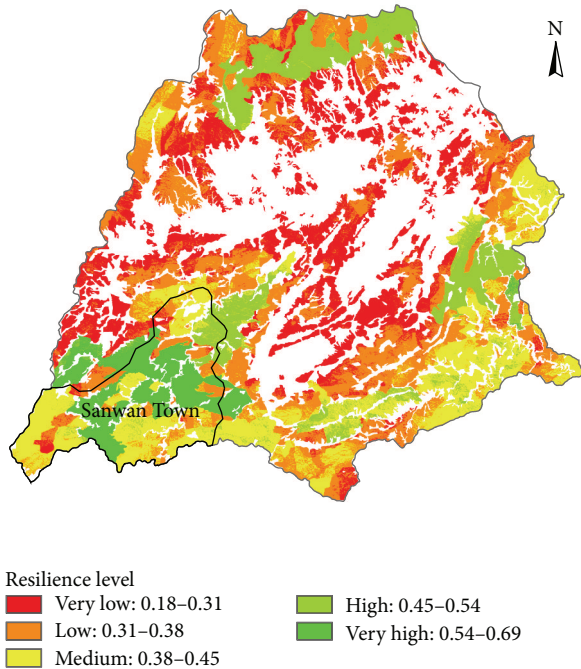


FIGURE 2: Spatial pattern of the forest ecosystem resilience level in Yongxin County and the location of Sanwan Town where Sanwan National Forest Park is located.

study area was not very high on the whole. Besides, the forest ecosystem resilience is generally above the average level occurred in the southwestern mountain area, the southeastern mountain area, and the northern mountain area, while the resilience was generally below the average level in the middle plain and hill area. The map of the forest ecosystem resilience level clearly showed the spatial heterogeneity of the pattern of resilience (Figure 2). The forests reaching a high or very high resilience level generally occurred around the center of the southwestern mountain area and the eastern part of the southeastern mountain area, and they extended from east to west in the northern mountain area. The forests with a medium level of resilience generally occurred in the area of the southern boundary, whereas the forests with a low or very low level of resilience were generally located in the central plain and hill area. The forests in the southwestern mountain area generally reached or exceeded a medium level of resilience, with a large area reaching the very high resilience level. The forests only reached a medium or low level of resilience in the southeastern mountain area except in the eastern part and the area near the administrative boundary, where the forests reached a high level of resilience. In the northern mountain area, only the forests extending from east to west, whose type species was *C. lanceolata*, reached a medium or high level of resilience. The remainder of the forests in the northern mountain area only reached a low or very low level of resilience. In contrast, the forests in the central area were almost entirely at a low or very low level of resilience.

The total forest area at each resilience level was further summarized (Table 2). In total, 57.5% of the forests

TABLE 2: Threshold of forest resilience level and total area at each resilience level.

Resilience level	Threshold of resilience levels	Total area (ha)	Area percent (%)
Very low	0.18–0.31	35835.93	25.60
Low	0.31–0.38	44688.15	31.90
Medium	0.38–0.45	30632.22	21.90
High	0.45–0.54	18448.29	13.20
Very high	0.54–0.69	10386.63	7.40

were at a low or very low level of resilience; 21.9% reached a medium level of resilience. Only 20.6% reached or exceeded a high level of resilience, indicating the resilience of the forest was not good. Besides, only five forest types reached the very high resilience level, among which the *C. lanceolata* forest accounted for the largest area proportion of forests with very high resilience, with the total area of 10381.2 ha reaching the very high resilience level. In addition, many forest types reached the high resilience level, but only the area of *C. lanceolata*, other sclerophyllous forest, and Theaceae was relatively large, reaching 16,457.6 ha, 1,951.02 ha, and 12.42 ha, respectively. In summary, most forest types only reached a medium level of resilience, only the forest types with a large total area, such as *C. lanceolata*, tended to have large areas exceeding the medium resilience level.

The key factors influencing the resilience of the forest ecosystem varied among different areas, these spatial patterns of which may provide significant information for formulating appropriate forest resource management measures. For example, in the southwestern mountain area, the stand condition was not favorable due primarily to the terrain, which makes this area susceptible to soil erosion. However, the rich ecological memory found in this area substantially offsets this disadvantage. The patch area, with a weight of 0.1744, is one of the most important indicators at the bottom level, and the patch area of most forest types was generally very large and the fragmentation was not serious in this area. By comparison, the stand condition is very favorable in the southeastern mountain area, with higher temperature and more precipitation that had favorable effects on the forests. However, the internal memory in this area only reached the medium level; only very few parts were rich in external memory. In the northern mountain area, especially in its western portion, the stand condition is not very good, and the ecological memory was only rich in a *C. lanceolata* forest extending from east to west due primarily to the abundant internal memory. However, the ecological memory of other forest types was very poor in this area, primarily due to the serious fragmentation. In the central plain and hill area, where there are primarily plain and low hills, the stand condition is very favorable for humans as well as forests. But this area has a long history of human disturbance, and the forests were seriously fragmented, leading to the very poor ecological memory.

The current spatial heterogeneity of the forest ecosystem resilience is the result of the cumulative effects of long-term

human intervention and the influence of natural conditions [45]. The human disturbance plays a subordinate role in influencing the forest ecosystem resilience on the whole; however, it still may be the dominant influencing factor at the local scale. For example, there is still very serious human disturbance in the plain area, and the human activities still play a dominant role in influencing the forest ecosystem resilience, especially in the plain area in the middle part of the study area, where there is a high population density and a lot of forests have been reclaimed for cropland. In fact, the accumulative effects of historical human activities make great contribution to the current spatial pattern of the species composition of the forests. For example, the zonal vegetation is the evergreen broad-leaf forest, which has been seriously damaged during the historical period, and the gradual recovery of the local forests is due primarily to the reconstruction and conservation since the 1980s. As a result, *C. lanceolata*, which has been widely used in the afforestation projects, has accounted for the largest proportion of the forests at present. Overall, the result objectively reflects the spatial pattern of the forest ecosystem resilience in the study area, indicating that it is a practical approach to spatially measure the ecosystem resilience with its influencing factors.

3.2. Discussion. This study indicates that the ecosystem resilience can be quantitatively measured with its influencing factors; however, more efforts should be made to further explore how to more scientifically and accurately measure the ecosystem resilience since there are various challenges in both the spatially explicit assessment of the ecosystem resilience and its application. First and foremost, more efforts should be made to explore the theory and assessment of the ecosystem resilience. Although previous researches have provided some methods to measure the ecosystem resilience, there remains an urgent need for an operational tool for assessing and mapping the ecosystem resilience [46], and it is necessary to make more efforts to select and integrate the resilience indicators according to the research object and data availability based on firm theoretical foundations. Besides, methods for spatially assessing many resilience factors have not yet been developed, and the comparative study is crucial since the ecosystem resilience cannot always be directly observed [46]. In addition, since there may be multiple indicators to measure the ecosystem resilience, it is of great importance to explore how to integrate these indicators. The resilience was represented with weighted sum of indices of its influencing factors in this study; the result may be not very accurate since there may be some nonlinear relationship between the ecosystem resilience and its influencing factors, but it still provides a useful method to the spatially explicitly assess the ecosystem resilience.

There is also a great challenge to operationalize the resilience concept for ecosystem management in a dynamic world; one of the major challenges for progressing resilience-based management lies in successful application. In fact, the general resilience principles have been influencing the way of the ecosystem management and conservation and have been consciously or unconsciously applied in the ecosystem

management. For example, the biosphere reserves have been generally demarcated into core area(s), buffer area(s), and transition area(s) according to guidelines of the United Nations Educational, Scientific and Cultural Organization [47]. The demarcation of the biosphere reserves into three areas can promote the ecosystem resilience, although the ecosystem managers may have been not aware of that. For example, in fact there is a forest park in Sanwan Town where the forest ecosystem resilience is the highest, that is, Sanwan National Forest Park, which has a forest coverage rate of 90.5% (Figure 2). This forest park was initially established in order to promote the development of the local tourism and pursue more economic benefit rather than improve the ecosystem resilience; however, it has unexpectedly increased the resilience of local forests. Therefore, establishing forest parks may be an effective way to conserve ecosystems and maintain the desirable ecosystem state.

4. Conclusions

Drawing on principles of the ecosystem resilience highlighted in the literature this study selected the indicators that capture the influencing factors of the ecosystem resilience and quantitatively assessed the forest ecosystem resilience in Yongxin County. The result indicates that it is feasible to generate large-scale ecosystem resilience maps with this assessment model and spatially explicitly identify the areas essential to the ecosystem conservation. Besides, the result show that there is significant spatial heterogeneity of the forest ecosystem resilience in the study area, which can provide a scientific basis for the local forest resource management and conservation to maintain critical ecosystem services and adapt to the climate change. But it is still necessary to make further improvement in the future research since there are still some controversies on the selection and integration of the specific indicators of ecosystem resilience, and it is possible to more accurately measure the ecosystem resilience if high resolution data in a large area are available. Although there are still some uncertainties, the results still can provide a scientific basis for the conservation of the forests, which is of great significance to the climate change mitigation.

Conflict of Interests

The authors declare that there is no conflict of interests regarding the publication of this paper.

Acknowledgments

This research was supported by the Project of the National Natural Science Foundation of China (Grant no. 41071343), the National Basic Research Program of China (973 Program) (Grant no. 2010CB950900), and the Key Project in the National Science & Technology Pillar Program of China (no. 2013BAC03B00). Data support from the projects funded by the National Natural Science Foundation of China (Grant no. 71225005, and Grant no. 40801231) is also greatly appreciated.

References

- [1] T. Prato, "Increasing resilience of natural protected areas to future climate change: a fuzzy adaptive management approach," *Ecological Modelling*, vol. 242, no. 1, pp. 46–53, 2012.
- [2] E. J. Ma, A. P. Liu, X. Li, F. Wu, and J. Y. Zhan, "Impacts of vegetation change on the regional surface climate: a scenario-based analysis of afforestation in Jiangxi province, China," *Advances in Meteorology*, vol. 2013, Article ID 796163, 8 pages, 2013.
- [3] I. Thompson, B. Mackey, S. McNulty, and A. Mosseler, *Forest Resilience, Biodiversity, and Climate Change. A Synthesis of the Biodiversity/Resilience/Stability Relationship in Forest Ecosystems*, Secretariat of the Convention on Biological Diversity, Montreal, Canada, 2009.
- [4] Intergovernmental Panel on Climate Change (IPCC), *Climate Change 2007: The Physical Science Basis*, Cambridge University Press, Cambridge, UK, 2007.
- [5] F. Brand, "Critical natural capital revisited: ecological resilience and sustainable development," *Ecological Economics*, vol. 68, no. 3, pp. 605–612, 2009.
- [6] F. S. Chapin III, K. Danell, T. Elmqvist, C. Folke, and N. Fresco, "Managing climate change impacts to enhance the resilience and sustainability of Fennoscandian forests," *AMBIO*, vol. 36, no. 7, pp. 528–533, 2007.
- [7] C. Folke, S. Carpenter, T. Elmqvist, L. Gunderson, C. S. Holling, and B. Walker, "Resilience and sustainable development: building adaptive capacity in a world of transformations," *AMBIO*, vol. 31, no. 5, pp. 437–440, 2002.
- [8] J. K. Strickland-Munro, H. E. Allison, and S. A. Moore, "Using resilience concepts to investigate the impacts of protected area tourism on communities," *Annals of Tourism Research*, vol. 37, no. 2, pp. 499–519, 2010.
- [9] G. C. Gallopín, "Linkages between vulnerability, resilience, and adaptive capacity," *Global Environmental Change*, vol. 16, no. 3, pp. 293–303, 2006.
- [10] C. Hawes and C. Reed, "Theoretical steps towards modelling resilience in complex systems," in *Computational Science and Its Applications—ICCSA 2006*, Lecture Notes in Computer Science, pp. 644–653, Springer, Berlin, Germany, 2006.
- [11] R. MacArthur, "Fluctuations of animal populations and a measure of community stability," *Ecology*, vol. 36, no. 3, pp. 533–536, 1955.
- [12] D. R. Bellwood, A. S. Hoey, and J. H. Choat, "Limited functional redundancy in high diversity systems: resilience and ecosystem function on coral reefs," *Ecology Letters*, vol. 6, no. 4, pp. 281–285, 2003.
- [13] B. H. Walker, "Biodiversity and ecological redundancy," *Conservation Biology*, vol. 6, no. 1, pp. 18–23, 1992.
- [14] J. C. Moore, P. C. de Ruiter, and H. W. Hunt, "Influence of productivity on the stability of real and model ecosystems," *Science*, vol. 261, no. 5123, pp. 906–908, 1993.
- [15] V. L. Scarborough and W. R. Burnside, "Complexity and sustainability: perspectives from the ancient Maya and the modern Balinese," *American Antiquity*, vol. 75, no. 2, pp. 327–363, 2010.
- [16] G. Nicolis, I. Prigogine, and P. Carruthers, *Exploring Complexity: An Introduction*, W. H. Freeman, New York, NY, USA, 1989.
- [17] S. Carpenter, *Alternate States of Ecosystems: Evidence and Some Implications*, Cambridge University Press, New York, NY, USA, 2001.
- [18] R. Costanza, "Ecosystem health and ecological engineering," *Ecological Engineering*, vol. 45, pp. 24–29, 2012.
- [19] E. M. Bennett, G. S. Cumming, and G. D. Peterson, "A systems model approach to determining resilience surrogates for case studies," *Ecosystems*, vol. 8, no. 8, pp. 945–957, 2005.
- [20] O. J. Schmitz, "Combining field experiments and individual-based modeling to identify the dynamically relevant organizational scale in a field system," *Oikos*, vol. 89, no. 3, pp. 471–484, 2000.
- [21] J. F. Franklin and J. A. MacMahon, "Message from a mountain," *Science*, vol. 288, no. 5469, pp. 1183–1185, 2000.
- [22] M. T. Gibbs, "Resilience: what is it and what does it mean for marine policymakers?" *Marine Policy*, vol. 33, no. 2, pp. 322–331, 2009.
- [23] V. Rosset and B. Oertli, "Freshwater biodiversity under climate warming pressure: identifying the winners and losers in temperate standing waterbodies," *Biological Conservation*, vol. 144, no. 9, pp. 2311–2319, 2011.
- [24] X. Z. Deng, J. K. Huang, E. Uchida, S. Rozelle, and J. Gibson, "Pressure cookers or pressure valves: do roads lead to deforestation in China?" *Journal of Environmental Economics and Management*, vol. 61, no. 1, pp. 79–94, 2011.
- [25] X. Z. Deng, F. Yin, E. Uchida, and S. Rozelle, "A complementary measurement of changes in China's forestry area using remote sensing data," *Journal of Food, Agriculture & Environment*, vol. 10, no. 3–4, pp. 1355–1358, 2012.
- [26] F. Wu, J. Y. Zhan, H. M. Yan, C. C. Shi, and J. Huang, "Land cover mapping based on multisource spatial data mining approach for climate simulation: a case study in the farming-pastoral ecotone of North China," *Advances in Meteorology*, vol. 2013, Article ID 520803, 12 pages, 2013.
- [27] Y. Jing, X. H. Yang, and D. Jiang, "The grid scale effect analysis on town leveled population statistical data spatialization," *Journal of Geo-Information Science*, vol. 12, no. 1, pp. 40–47, 2010.
- [28] B. Wolfslehner, H. Vacik, and M. J. Lexer, "Application of the analytic network process in multi-criteria analysis of sustainable forest management," *Forest Ecology and Management*, vol. 207, no. 1–2, pp. 157–170, 2005.
- [29] C. Folke, "Resilience: the emergence of a perspective for social-ecological systems analyses," *Global Environmental Change*, vol. 16, no. 3, pp. 253–267, 2006.
- [30] B. Walker, C. S. Holling, S. R. Carpenter, and A. Kinzig, "Resilience, adaptability and transformability in social-ecological systems," *Ecology and Society*, vol. 9, no. 2, article 5, 2004.
- [31] A. Jentsch, C. Beierkuhnlein, and P. S. White, "Scale, the dynamic stability of forest ecosystems, and the persistence of biodiversity," *Silva Fennica*, vol. 36, no. 1, pp. 393–400, 2002.
- [32] D. Zirlewagen, G. Raben, and M. Weise, "Zoning of forest health conditions based on a set of soil, topographic and vegetation parameters," *Forest Ecology and Management*, vol. 248, no. 1–2, pp. 43–55, 2007.
- [33] T. J. Martin and J. Ogden, "The seed ecology of *Ascarina lucida*: a rare New Zealand tree adapted to disturbance," *New Zealand Journal of Botany*, vol. 40, no. 3, pp. 397–404, 2002.
- [34] S. Carpenter, B. Walker, J. M. Anderies, and N. Abel, "From metaphor to measurement: resilience of what to what?" *Ecosystems*, vol. 4, no. 8, pp. 765–781, 2001.
- [35] Q. L. Shi, J. Y. Zhan, F. Wu, X. Z. Deng, and L. R. Xu, "Simulation on water flow and water quality in Wuliangshai lake using a 2-D hydrodynamic model," *Journal of Food, Agriculture & Environment*, vol. 10, no. 2, pp. 973–975, 2012.

- [36] H. T. Dublin, A. R. E. Sinclair, and J. McGlade, "Elephants and fire as causes of multiple stable states in the Serengeti-Mara woodlands," *Journal of Animal Ecology*, vol. 59, no. 3, pp. 1147–1164, 1990.
- [37] J. Bengtsson, P. Angelstam, T. Elmqvist et al., "Reserves, resilience and dynamic landscapes," *AMBIO*, vol. 32, no. 6, pp. 389–396, 2003.
- [38] M. Nyström and C. Folke, "Spatial resilience of coral reefs," *Ecosystems*, vol. 4, no. 5, pp. 406–417, 2001.
- [39] A. B. Khattak, A. Zeb, and N. Bibi, "Impact of germination time and type of illumination on carotenoid content, protein solubility and in vitro protein digestibility of chickpea (*Cicer arietinum* L.) sprouts," *Food Chemistry*, vol. 109, no. 4, pp. 797–801, 2008.
- [40] F. Berkes and D. Jolly, "Adapting to climate change: social-ecological resilience in a Canadian western Arctic community," *Conservation Ecology*, vol. 5, no. 2, 2002.
- [41] J. Ehrlén and O. Eriksson, "Dispersal limitation and patch occupancy in forest herbs," *Ecology*, vol. 81, no. 6, pp. 1667–1674, 2000.
- [42] A. Borja, S. B. Bricker, D. M. Dauer et al., "Overview of integrative tools and methods in assessing ecological integrity in estuarine and coastal systems worldwide," *Marine Pollution Bulletin*, vol. 56, no. 9, pp. 1519–1537, 2008.
- [43] N. Mantua, "Methods for detecting regime shifts in large marine ecosystems: a review with approaches applied to North Pacific data," *Progress in Oceanography*, vol. 60, no. 2–4, pp. 165–182, 2004.
- [44] R. C. Rooney and S. E. Bayley, "Quantifying a stress gradient: an objective approach to variable selection, standardization and weighting in ecosystem assessment," *Ecological Indicators*, vol. 10, no. 6, pp. 1174–1183, 2010.
- [45] J. Y. Zhan, N. N. Shi, S. J. He, and Y. Z. Lin, "Factors and mechanism driving the land-use conversion in Jiangxi province," *Journal of Geographical Sciences*, vol. 20, no. 4, pp. 525–539, 2010.
- [46] G. Rowlands, S. Purkis, B. Riegl, L. Metsamaa, A. Bruckner, and P. Renaud, "Satellite imaging coral reef resilience at regional scale. A case-study from Saudi Arabia," *Marine Pollution Bulletin*, vol. 64, no. 6, pp. 1222–1237, 2012.
- [47] UNESCO, "Action plan for biosphere reserves," *Nature and Resources*, vol. 12, no. 1, pp. 1–12, 1984.